Synthesis and characterization of Schiff bases and their diverse applications

THESIS SUBMITTED FOR THE DEGREE OF

DOCTOR OF PHILOSOPHY (SCIENCE)

JADAVPUR UNIVERSITY

KOLKATA – 700032,

WEST BENGAL, INDIA

September, 2022

BY

SUKANYA PAUL, M. Sc.

DEPARTMENT OF CHEMISTRY

JADAVPUR UNIVERSITY

KOLKATA – 700 032

WEST BENGAL, INDIA

Registration No. SCHEM1100419

Index No. 4/19/Chem./26

Prof. (Dr.) C. Sinha, Ph. D.
Professor & Former Head
Department of Chemistry

JADAVPUR UNIVERSITY KOLKATA - 7 0 0 0 3 2, I N D I A Telephone: 91+033+ 2414-6666. Ext. 2453 (O), Mobile: +91-9433621872/ 7044231277
e-mail: crsjuchem@gmail.com

To Whom It May Concern

This is to certify that the thesis entitled **"Synthesis and characterization of Schiff bases and their diverse applications."** submitted by Smt. Sukanya Paul, M.Sc., who got her name registered on 05.08.2019 (Registration No.- SCHEM1100419) For the award of Ph.D. (Science) degree of Jadavpur University, is absolutely based upon her own work under the supervision of Dr. Chittaranjan Sinha, Professor, Department of Chemistry, Jadavpur University, Kolkata-700 032 and that neither this thesis nor any part of it has been submitted for either any degree / diploma or any other academic award anywhere before.

It is also certified that she has fulfilled all the requirements of the regulations relating to the nature, period and ethical guideline of research.

C. Sinha 27/09/2022

(Signature of the Supervisor, date with official Seal)

(C. SINHA)
Professor of Chemistry
Department of Chemistry
Jadavpur University
Kolkata-700 032

Declaration of the Scholar

I declare that this written submission suggests my creative approaches in my own words and where other's ideas have been included. I have properly cited with suitable reference from the authentic sources. I also declare that I have adhered to all origins of academic principle and honesty and have not misled or fabricated or falsified any approach/ data/ origin in my submission. I understand such violation of the above will cause for disciplinary action by University and can evoke penal action from the sources which have thus not been properly cited or from whom proper permission has not been taken when needed.

Sukanya Paul 27.09.22

Sukanya Paul

Department of Chemistry

Jadavpur University

Dedicated to Maa and Baba…

Acknowledgement

It is one of the finest moments in my academic life when I get the opportunity to express my indebtedness to all of my near and dear ones and to all who have been attached to my academic career.

First and foremost, I sincerely convey my deepest gratitude to my Supervisor Prof. Chittaranjan Sinha, Professor, Department of Chemistry, Jadavpur University, Kolkata - 700 032, who allowed me to be one of the Research Scholars under his supervision. It's been a privileged and integral part of my academic phase to be under his constant guidance, support and tutelage during the course of my Ph.D. degree. His meticulous attention to the work and incisive decision has guided me to accomplish my research project successfully. Thank you so much Sir for letting me that opportunity, believing in me and most importantly for being such a wonderful guide at every stage of my Ph.D. career.

I record my sincere thanks to Prof. Swapan K Bhattacharya, Head, Department of Chemistry; Prof. Saurabh Das, Section-in-Charge, Inorganic Chemistry Section and Prof. Ambikesh Mahapatra, Prof. Sujoy Baitalik, Prof. Jnan Prakas Naskar, Prof. Partha Roy, Prof. Samaresh Bhattacharya, Prof. Subrata Mukhopadhyay, Dr. Partha Mahata, Prof. Mahammad Ali, Prof. K. K. Rajak, Prof. K. S. Pramanik, Prof. Subratanath Koner, Dr. Bibhuti Bhushan Show, Prof. Tapan Kumar Mondal, Prof. Amrita Saha, Prof. Shouvik Chattopadhyay and other faculty members of the Department of Chemistry, Jadavpur University; I remember my indebtedness to all the staff members of this department for their help in various respects.

I am also extremely thankful to my Research Advisory Committee (RAC) members, Prof. Nikhil Guchhait (CU, Kolkata), Prof. Chittaranjan Sinha (JU, Dept. of Chemistry, Kolkata) and Prof. Swapan Kumar Bhattacharya (JU, HOD, Dept. of Chemistry, Kolkata) for their valuable suggestions, advices and support during the RAC meetings.

It has been a great pleasure for me to be a part of the Research group of Prof. Sinha. I fail to utter my heartfelt thanks with appropriate words to seniors Dr. Basudeb Dutta, Dr. Suvendu Maity and Dr. Sunanda Dey for their constant co-operation, encouragement and kind support at every stage of my research tenure. I

express my gratitude towards Dr. Rakesh Purkait and Dr. Angeera Chandra for their generous support and contribution throughout my research career.

I am also thankful to all the past and present members of this research group *viz.*, Dr. Kaushik Naskar, Mr. Srikanta Jana, Mr. Suprava Bhunia, Mr. Manik Shit, Dr. Arup Kumar Adak, Dr. Chiranjit Patra, Ms. Ananya Dasmahapatra, Ms. Sangita Ghosh, Mr. Mukul Bikash Maity, Mr. Samrat Dev, Mr. Himadri Shekhar Chatterjee, Mr. Soumya Jyoti Ghosh, Mr. Sambhunath Bera, Mr. Abhishek Karmakar, Mr. Arka Patra, Mr. Koushik Saha, Dr. Debasis Mallick, Dr. Souvik Panday, Dr. Abhijit Das, Mr. Sabir Ahmed, Mrs. Nivedita Roy, Mr. Gurupada Bairy, Mr. Kumarjit Chowdhury.

I am extremely thankful to Mr. Satyajit Halder, Mr. Kingshuk Debsharma, Ms. Pubali Das, Ms. Taposi Chatterjee, Mr. Kunal Pal for their contribution in my research. I sincerely thanks to all my collaborators- Prof. Partha Pratim Ray (Department of Physics, Jadavpur University, Kolkata- 700032) and Prof. Kuladip Jana (Division of Molecular Medicine, Bose Institute, Kolkata-, India) for their kind cooperation in research works.

I would like to acknowledge Council of Scientific and Industrial Research (CSIR), New Delhi for the Financial Assistance. I would also like to thank Wiley, Royal Society of Chemistry (RSC) for the research articles that I managed to publish during the tenure of my Ph.D. career.

I am also thankful to my friends Pritam, Saswati Di, Suman, Biplab, Sabuj Da, Souvik, Bishu, Deep Da, Lipi, Abani Da, Ipsita, Suvendu for their pleasant association, which directly or indirectly helped me in both academic and non-academic affairs.

Whatever I am and whatever I intend to be in future are because of the goodwill and unstinted encouragements that I have received from my parents, Mrs. Kabita Paul and Mr. Radha Nath Paul for their selfless sacrifices, relentless motivation and emotional support which help me a lot throughout the whole academic career and in pursuing the Ph.D. study and no words are enough to acknowledge them. I also pay my deepest thanks to Dr. Totan Ghosh and Mr. Jayanta Dutta for their constant encouragement. Last but not the least, my sincere acknowledgement to Jadavpur University Administration for providing academic, financial and administrative support for this research.

Sukanya Paul
27.09.22
(Sukanya Paul)

Preface

The present dissertation entitled "**Synthesis and characterization of Schiff bases and their diverse applications.**" is submitted to fulfil the requirements for the Degree of Doctor of Philosophy (Science) of Jadavpur University. The study concerns the synthesis and structural characterization of different Schiff bases and their evolution in the sensing of bio-relevant analytes such as Cu^{2+}, Zn^{2+}, CN^-, $H_2PO_4^-$, Cysteine and TFA acid vapour through fluorometric or colorimetric techniques at a trace level concentration followed by intracellular imaging applications. The Schiff base ligand has been also employed in the synthesis of Zn(II) Coordination Polymer that functions as Schottky diode device and exhibits anti-carcinogenic property. In this work, five Schiff bases framed on triphenylamine, coumarin, pyrazole, benzimidazole, naphthyl moieties are accomplished through extensive characterization techniques along with X-ray crystallographic measurement. Some selected ligand has been utilized for the fabrication of Zn(II) coordination complex and polymer. Theoretical calculations have been done to compare with experimental findings.

The thesis contains six chapters. **Chapter I** contain a concise description on the benefit and toxicity associated with cations, anions, Cysteine and TFA acid vapour, different fluorescent mechanism, Schottky device parameters and a brief review on some selected Schiff probes for detections of analytes in relevance to the present work. It also covers a summarized discussion on synthetic outline of different molecular probes used in present research work. **Chapter II** includes triphenylamine based Schiff base as a reversible fluorescence sensor to Cu^{2+} and Cysteine along with live cell imaging and logic gate construction. **Chapter III** contains a reversible benzimidazole derivative chemosensor for Zn^{2+} and $H_2PO_4^-$ through fluorescent techniques and theoretical calculations. **Chapter IV** covers on pyrazole appended probe which enables simultaneous fluorescence detections of Zn^{2+} and CN^- at distinctive regions followed by intracellular imaging of the respective analytes. **Chapter V** is focused on AIEE active naphthyl derivative which exhibits solid-phase acidochromism and a promising CN^- sensor in solution medium. **Chapter VI** is depicted on two dimensional

coumarin based Zn(II) Coordination Polymer which functions as Schottky diode device and explored as an effective anti-carcinogenic agent.

From my research work, I have published some of the above works in high impact SCI journals and more results will be published shortly.

Sukanya Paul 27.09.22

Sukanya Paul

Index No. 4/19/Chem./26

Registration No. SCHEM1100419

Department of Chemistry

Jadavpur University

Abstract

Index No. 4/19/Chem./26

Title of Thesis: Synthesis and characterization of Schiff bases and their diverse applications.

The structures of Schiff bases consist of exocyclic imine/azomethine (C=N) functional unit who is considered as a versatile component for various applications. The imine unit can serve as coordinating group or chelating site in the coordination chemistry. Some of the properly functionalised Schiff bases have been used as a functional material for recognition of bio-relevant ions/molecules at a very low concentration (μM to nM) level. Cations, Anions and certain molecules regulate concentration dependent bioactivity in human body and can be beneficial or toxic than the requisite amount to trigger health issues. Therefore, for normal functioning of the living system, the determination of concentration of these active species must be monitored carefully. Considerable efforts have been invested for the development of efficient chemosensor based on imine framework (CH=N) for sensitive detection of analytes. In addition, the coordinating environment of such molecule with metal centre can form discrete complex and coordination polymers (CPs) which is considered as the natural extension of coordination compounds towards polymerization. In my research work, five Schiff bases bearing different fluorogenic entities such as triphenylamine, benzimidazolyl, pyrazolyl, coumarinyl, naphthyl have been formulated. The probes are synthesized by Schiff's condensation reaction followed by extensive characterization through different spectroscopic techniques (IR, Mass, NMR, elemental analysis) and structural confirmation of some of the molecules by Single Crystal X-Ray Diffraction measurements, **Chapter II:** Triphenylamine-naphthyl appended Schiff base, an emissive probe, (λ_{em}, 550 nm) selectively senses Cu^{2+} through fluorescence quenching (CHEQ) with a LOD value of 7.3 nM in 7:3 (v/v) CH_3CN/H_2O medium (HEPES buffer, pH 7.2) which exhibits reversibility in presence of Cysteine and restores the emission of the probe due to strong binding of Cysteine to Cu^{2+} and the LOD of sensing is 36 nM. The probe has been used in cytotoxicity analysis in normal WI-38 Cell line and intracellular imaging was performed with HepG2 Cell line. **Chapter III:** Benzimidazolyl-ethoxysalicyldehyde derivative recognizes Zn^{2+} in 9:1 (v/v) $DMSO/H_2O$ (HEPES Buffer, pH=7.4) medium through chelation and fluorescence intensity (λ_{em}, 461 nm) is

enhanced and the LOD is 3.2 nM. The emissive [Zn(L^1)OAc] complex is further capable of disclosing a selective fluorescence 'turn-off' detection towards $H_2PO_4^-$ (LOD: 0.238 μM) accomplishing the reversibility of Chemosensor. **Chapter IV:** Coumarin-Pyrazolyl appended probe detects Zn^{2+} (λ_{em}, 497 nm) and CN^- (λ_{em}, 447 nm) with two distinctive emissive responses in CH_3CN/H_2O (99:1, v/v) (HEPES Buffer, pH 7.5) medium and the LOD values are 34.76 nM (Zn^{2+}) and 19.91 nM (CN^-). On interaction of the probe with Zn^{2+} a hexanuclear metallocryptand [Zn_6L_6] is structurally verified by Single Crystal X-Ray Diffraction data. The probe is successfully applied for biological applications such as MTT Assay, cellular imaging and FACS in MD-MBA cells. **Chapter V:** Naphthyl-dimethoxy scaffold is AIE active probe and a strong solid-state emitter which enables a reversible acidochromic behaviour in presence of HTFA/TEA vapour. The LOD estimated for HTFA vapour is found to be 1.41 ppm. The probe further detects a chromogenic and fluorogenic receptor selectively towards CN^- (λ_{em}, 565 nm) in CH_3CN/H_2O (99:1, v/v) (HEPES Buffer, pH 7.3) and the LOD is 45.42 nM. MTT analysis and AIE phenomena along with CN^- detection of the probe is clearly depicted from the intracellular imaging. **Chapter VI:** Coumarinyl-pyridine molecule has been utilized for the fabrication of Zn(II) 2D coordination polymer (Zn(II)-CP) which has been explored as a semiconducting Schottky diode device and possess effective anticancer efficacy against HeLa cell line.

From my research work, I have published a total of six original research articles and more results will be published shortly.

Contents

Chapter II: A Fluorogenic Triphenyl-Amine-Naphthyl-Hydrazide Probe Selective for Cu^{2+} and Cysteine Detection via an ON-OFF-ON Logic path with Real Applications.

Chapter III: A Highly Emissive Zn(II)-pyridyl-benzimidazolyl-phenolato based Chemosensor : Detection of $H_2PO_4^-$ via "Use" and "Throw" Device Fabrication.

Chapter IV: Idiosyncratic recognition of Zn^{2+} and CN^- using Pyrazolyl-Hydroxy-Coumarin scaffold and live cell imaging: Depiction of Luminescent Zn(II)-Metallocryptand.

Chapter VI: Tangible Coumarinyl-Pyridyl Schiff base Appended Carboxylato Bridging Zinc(II) 2D Coordination Polymer : Electrical Property and Anti-carcinogenic Application.

Chapter I

Introduction

CHAPTER I

Abstract

Partial Review on Design and Use of Schiff bases in the Fluorescence Sensing of Ions and Molecules.

A molecule consisting of exocyclic imine/azomethine (C=N) function belongs to a class of Schiff base. Ease to synthesis, moderate stability in biological pH (7.0-7.5) and conventional characterization procedure makes their utility in versatile fields- chemistry to biological applications as well as industrial purpose. Appending a fluorogenic or choromphoric unit to a Schiff Base makes a fluorescent active molecule. Additional functional groups in a suitable position may design a chelating ligand that may coordinate to metal ions and thus the metal complexes may be used for different applications. Similarly, a metal centres can form a synthon for a coordination polymer or metal-organic framework who have multifacetated applications. The research in this thesis is focused to fluorogenic responsive trace quantity detection of toxic ions and molecules with orientation to this direction an entitled partial review is reported in this chapter.

I.1. Introduction

The Schiff base, reported first by Hugo Schiff in 1864 and synthesized from the reaction of $–NH_2$ (an amino) and carbonyl compound (aldehyde or ketone), has active imine or azomethine (C=N) group. Although the C=N is a stable double bond but susceptible to hydrolysis and even catalysed by Lewis Acid, like metal ions. Aromatic frame of Schiff base is appropriately functionalised so that it may serve as multidentate chelating ligand and can form coordination complexes with transition and post-transition metal ions of innumerable stereochemistry.[1,2] The Schiff bases show highly challenging medicinal applications in the field of pharmacology, biology and chemistry.[3-5] The Schiff bases (**Scheme I**) show different biological activity like analgesic,[6] anti-inflammatory,[7,8] antifungal,[9,10] antibacterial,[11,12] anticonvulsant,[13,14] antioxidant[15,16] and anticancer activity.[17-19] Variation of both aldehyde/ketone and amine part can develop multidentate and structurally flexible Schiff bases those play important role in diverse areas such as sensing, coordination polymer, biological activity and other fields.

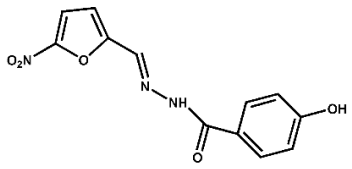

Dantrolene (Muscle relaxant)

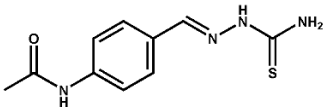

Thiacetazone (Anti-tuberculosis)

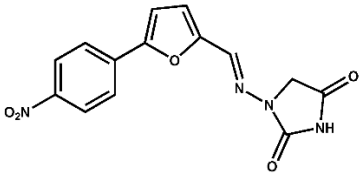

Nifuroxazide (Antibiotic)

Scheme I Drugs bearing C=N group

A number of Schiff base ligands have been designed, synthesized and well-characterized via different analytical techniques and used for the synthesis of coordination complex and coordination polymers. Towards design of fluorogenic Schiff base a planned strategy has to be outlined either using photosensitive amine/aldehyde or both. Ions and molecules play a significant role in biology and environment which are closely associated with health issues of living being. Cation, anions and some selective molecules are both

present as beneficial as well as non-essential toxic elements. Depending on concentration they can be crucial for survivability of the cells if its presence is either surplus or deficient than the requisite amount for proper functioning of cells. Therefore, an optimum concentration of ions and molecules must be maintained for normal functioning and thus its measurement must be monitored carefully. Therefore, efforts are being devoted towards the advancement of efficient detection and quantitative estimation of ions and molecules. The probe follows plausible conventional signalling mechanism such as Photoinduced Electron Transfer (PET), Excited State Intramolecular Proton Transfer (ESIPT), Foster Resonance Energy Transfer (FRET), Charge Transfer (CT) and excimer/exciplex formation, Aggregation Induced Emission (AIE) etc., has been used for the optical recognition of various analyte based on the primary photophysical properties of fluorescent chemosensors.[20]

The Coordination polymers (CPs) can be considered as the natural extension of coordination compounds towards polymerization. These are popularly named as crystalline inorganic organic hybrid material where metal entities act as nodes and are coordinated to organic or anionic linkers through covalent or other weak chemical bonds and extends into structural framework forming highly ordered crystalline structures with remarkable chemical and thermal stability. The architectures and dimensionalities of the coordination polymer are defined by its capabilities of the building blocks to extend substantially into one, two or three dimensions (1D, 2D or 3D respectively) through repeating coordination units.[21-23] Many unusual properties are discovered within CPs and have been applied in sensing of ions/molecules, gas sensing and separation, drug delivery and diseases diagnosis, fabrication of energy saving materials etc. Incorporation of metal ions in the organic polymer backbone makes electronically conductive coordination polymers (CPs), are considered as a separate class conductive solid materials which have emerged as of great scientific interest in the recent years.[24-26]

I.2. Cations, Anions and Molecules in Human Health

I.2.1. Cations

Alkali and Alkaline earth metals such as Sodium (Na), Potassium (K), Magnesium (Mg), Calcium (Ca) and some selective transition metals such as Iron (Fe), Copper (Cu), Zinc (Zn), Vanadium (V), Chromium (Cr), Manganese (Mn), Cobalt (Co), Nickel (Ni), Molybdenum (Mo) are classified for the essential metal ions.

These cations contributes a major role in biological process, Sodium (Na^+) occupies the sixth most abundant elements in Earth's Crust constitute about 2.83% and are located in extracellular part of animal cells regulates osmotic equilibrium, blood pressure, pH as well as it maintains the electrostatic charge transportation and helps in neurotransmission.[27,28] Low sodium concentration induces an electrolytic disorder while an excess has an adverse effect on Kidney and increases blood pressure.[29] Potassium (K^+) constituting 0.4% of mass of the body depending on its concentration inside the cells or in the extracellular fluid plays diverse roles in the intracellular part and is associated with the maintenance of electrolytic balance with the Na^+ and involved in modulating biochemical signal transduction throughout the nervous system.[30,31] Potassium uptake is required for plants and animal for normal functioning of the system. However, imbalances in potassium level are associated with health problems. High concentration leads to severe cardiac disorder while its deficiency causes nausea, muscle weakness and fatigue.[32] Magnesium (Mg^{2+}), a member of the alkaline earth series, is the fourth abundant metals in human body, a key component of chlorophyll and executes the photosynthetic process in plants and a vital cofactor on cell proliferation, numerous enzymatic catalysis like phosphorylation of proteins, DNA Synthesis.[33-35] Different distribution of Mg^{2+} in sub-cellular compartment accomplish its varying biological function. Abnormal concentrations of Mg^{2+} are in close association with diseases like Alzheimer, Epilepsy, diabetes and hypertension.[36-38] Calcium (Ca^{2+}), the largest intracellular concentration of the alkaline earth series with around 100 nM in its free form in living system, is the primary constituent of bones and teeth as well as monitors cellular process like hormonal secretion, muscle contraction, fertilization, gene transcription and signal transduction. Notably, imbalances in intracellular Ca^{2+} concentration are responsible for physiological disorder such as obesity and Alzheimer's disease.[39,40]

Of the heavy metal transition series, Vanadium ranks the second most abundant ubiquitous metal which exists exclusively in the form of ion-pair as Na^+ $H_2VO_4^-$ in sea water with concentration limits to 35 nM.[41,42] Vanadium, an essential trace element, plays a favourable role in the prevention of heart-disease. Apart from the oxides, other salts of vanadium exhibit moderate toxicity.[43] Chromium commonly shows +3 oxidation state and is less harmful while those are at higher states (+4 and+6) are potentially toxic.[44] Chromium (Cr^{3+}) is considered as the essential trace element in nutritional diet for human and had significant influences on the

metabolism of carbohydrates, proteins fats and nucleic acids, and also it helps to activate insulin to reduce blood sugar.[45,46] US Environmental Protection Agency (USEPA) has classified chromium species as a mutagenic and carcinogenic agent.[47,48] Below the adequate level of Cr^{3+} in living system triggers diabetes and cardiovascular diseases. While excessive concentration of Cr^{3+} binds with DNA through guanine N7 and phosphate backbone; thus, affect and damage the cellular components.[49,50] Manganese (Mn) is important trace nutrient with diverse biological roles, participates as structural component in varied enzymes that is activating metabolic process and in photosynthetic oxygen evolution. Elevated level of Mn damages Central Nervous System resulting called Mn-induced Parkinsonism.[51-53] Manganese exhibits a variable oxidation state ranging from +2 to +7. Mn^{2+}, (d^5), excellent magnetic resonance imaging (MRI) relaxation agent used as a tool in neurobiological research. Mn^{3+} is comparatively more cytotoxic than Mn^{2+}.[54,55] Iron occupies as the most abundant and significant transition trace element in living body and exists in both form Fe^{2+} and Fe^{2+} which plays vital biological function. In living systems Fe^{2+} serves as oxygen carrier in the tissues and Fe^{3+} helps transportation of electrons. Iron deficiency causes anaemia, which can be harmful or even fatal.[56,57] However excessive accumulation leads to dysfunction of organs as well. In addition, presence of Iron has severe impacts on the quality of crops and water bodies through industrial and agricultural activities.[58] Cobalt abundance in both forms Co^{2+} and Co^{3+} found in rock, minerals, soils and seawater in trace level and is beneficial to organism as primary constituent of Cobalamin, known as vitamin B_{12} that plays essential role in the metabolism of iron and the synthesis of haemoglobin.[59,60] Deficiency causes haematological and neurological disorders while excessive intake causes toxicological effects including asthma, vasodilation, dermatitis and cardiomyopathy in human and animals.[61,62] Nickel (Ni^{2+}), another divalent essential trace nutrient related to the metabolism, biosynthesis and respiration of organism.[63] Metalloenzyme, Urease contains nickel ion at its active site and plays an effective role for domestic animals and plants. Overdose of Ni^{2+} consumption responsible for various pathological effects such as dermatitis, pneumonitis, disorders of CNS. International Agency for Research on Cancer (IARC, 1990) classified Ni(II)-compounds as group 1 carcinogenic substances.[64,65] Copper (Cu^{2+}), available in two oxidation states (Cu^{+} and Cu^{2+}), is the third most available essential nutrient in human body. Cu^{+} is predominantly found in anaerobic environments which is readily oxidized to Cu^{2+} accounting for its

divalent existence, Cu^{2+} plays diverse significant roles as an active centres and catalytic co-factors for metalloenzymes likes superoxide dismutase, cytochrome oxidase and tyrosinase for several biochemical and energy transport processes. Insufficiency of copper in the system can cause bone, arterial, and anaemia abnormalities while surplus amounts induce toxicity due to initiation of uncontrollable Reactive Oxygen Species (ROS) which give rise to neurodegenerative disease like Wilson's Alzheimer's and Parkinson's disease, Meknes syndrome and adversely affects lungs and Kidney. In addition, Copper is also an essential micronutrient for plants cellular process which on excessive causes chlorosis.[66-72] Zinc (Zn^{2+}) found in its divalent form ranks as the second most essential micronutrient in biological system. Zn^{2+}, mother of metalloenzyme, constitutes more than 300 proteins and are present at the active site of enzymes like carbonic anhydrase and carboxypeptidase and proteins acts as a structural and catalytic co-factor for vital process like regulation of enzymes, gene expression, cellular metabolism, apoptosis, neural signal transmission, DNA binding. Lack of Zinc contributes to metabolic disorder such as retarded and impaired growth, gastrointestinal, weaker immune response, diarrhoea, dermatitis, hypotension, and hypothermia while the overload of Zinc in body is detrimental to vital organs and are responsible for Parkinson's and Alzheimer's disease.[73-76] Molybdenum can exist in five oxidation states (II–VI) and actively participates and regulates the enzymatic redox reactions and protein synthesis in living organisms. Excess accumulation of Mo from industrial activities results in contaminations which has detrimental influences on the environment.[77,78]

I.2.2 Anions

Anions are biologically relevant for its versatile role in cellular process such as to balance pressure, energy transport and act as template for capturing cations. Anions listed are essential CO_3^{2-}, NO_3^-, NO_2^-, Phosphates (PO_4^{3-}, HPO_4^{2-} , $H_2PO_4^-$, $P_2O_7^{4-}$), Cl^-, Br^-, I^-, CN^-, SCN^-, OCl^-, SO_3^{2-}, SO_4^{2-}, $S_2O_3^{2-}$ appear and functions accordingly in different stages of metabolic process.

Cyanide (CN^-) till date has been recognized by WHO and Environmental Protection Agency (EPA) as the potent toxic anion for all form of life depending on its exposure, absorption and distributions. Cyanide can bind with Fe of Cytochrome C-oxidase which may interferes with the cellular respiration which can cause

hypoxia. Presence of CN^- in living system inhibits normal function of lungs and brain which can turned out to be fatal. Despite its toxicity, the scaled-up utilization of CN^- in gold mining, synthetic and plastics manufacturing resulting in increased exposure to the environment.[79-83] Sulfide (S^{2-}) generated as a by-product of drug synthesis and industrial production are potentially threat to the environment and human health when present in excess and can cause diseases like diabetes, high blood pressure, liver cirrhosis.[84-86] Thiocyanate (SCN^-), widely used in electroplating, pesticide manufacturing printing and textile dyeing . On irradiation or chlorination SCN^- can gets chemically converted to CN^- and CNCl which are classified as toxic agents. Surplus concentration of SCN^- in the body than the permitted level affects the protein dialysis and resulting in coma.[87,88] Sulfite (SO_3^{2-}) commonly used as preservatives for food storage known for its antimicrobial and antioxidizing agent property. On excess accumulation of diet enriched with sulfiting agent has considerable side effects and leads to respiratory related allergy, reduction in thiamine in stomach.[89-92] Sulfate and Bisulfate (SO_4^{2-}/HSO_4^-) are essential macronutrient participates in series of cellular process including detoxification and biosynthesis through sulfation of compound required for the development of cell organism. However at higher pH it exhibits toxicity with symptoms like eye and skin irritation, respiratory paralysis etc.[93-95] Thiosulfate ($S_2O_3^{2-}$) exceptionally hazardous dispersed in the blood and urine are used as a reliable parameter for detection of sulfur poisoning.[96-98] Phospate (PO_4^{3-}, $H_2PO_4^-$, HPO_4^{2-}, $P_2O_7^{2-}$) anions are of biological importance owing to essential functions in energy transduction, gene regulation, muscle contraction, signal processing and information storage, They are well-known ground and surface water contaminants and excess discharge in the water generates algal blooming and eutrophication responsible for depletion of dissolved oxygen in water.[99-105] Chloride (Cl^-) is ubiquitous class of halides with extensive utilization in fertilizers and food additives; it assists the tracing of pollutant movements within a natural water body, monitoring of landfills for leaks and detection of salt water interruption into drinkable ground or surface waters.[106,107] Hypochlorite (OCl^-) anion is a well-known bleaching material/disinfectant generates reactive oxygen species (ROS) in cells and possesses exceptional antibacterial properties. But, OCl^- at higher concentration results in oxidative stress which leads to neuron degeneracy, atherosclerosis, arthritis, and cancers.[108-112] Fluoride ions are biologically relevant for their role in dental care and the treatment of osteoporosis, Overload of fluoride deposition in the

human body results in Fluorapatite in the bones and teeth which causes dental fluorosis, osteoporosis and skeletal fluorosis.[113,114] Bromide ions are commonly available in aquatic environment and biological fluids. On increased exposure, it has serious side effects on health problems including skin and tissue damage, respiratory dysfunction, and cancer induction.[115] Iodine is an essential micronutrient predominantly exist in the bioavailable form as iodide in body regulates vital biological processes like growth hormone, thyroid functioning and neurological activity. Iodine is widely utilized in diverse fields like manufacturing of dyes, synthesis of chemicals, medicine, bio-labelling and foods. However, excessive utilization results in environmental pollution and physiological problems.[116-118] Nitrite ion is a well-known preservative in meat and fish products and involved in nitrogen fixation, denitrification which influences the quality of natural and underground water. However, controlled monitoring of nitrite level is relevant as it undergoes chain reactions generating carcinogenic nitrosamines.[119-120] Nitrate used in fertilizer gets accumulated in water surface causes eutrophication disrupts the aquatic stable ecosystem. Increased nitrate level generates carcinogenic nitrosamines and can cause methemoglobinemia (blue-baby syndrome) in infants.[121-123] Carbonate are extensively used as an additive electrolyte in Li-ion batteries for hybrid electric vehicle. Further, carbonate has vital application in agricultural planting, hydrology, geology and fire retardant. In large doses, carbonate ion turn out to be toxic to human health which leaves a strong caustic effect gastro-intestinal tract causes severe abdominal pain, vomiting, and even fatal sometimes.[124-126] For the healthy living, different internationally accreditation organizations like World Health Organization (WHO), United States Environmental Protection Agency (USEPA), Central Pollution Control Board (CPCB) in India, Indian Council of Medical Research (ICMR) and Indian Standard Institution (ISI) defined the safe limits or maximum contaminant levels of ions in drinking water (**Table I.1)**[127]

Table I.1: Acceptable limits in drinking water (in the unit of mg/liter)

Parameters	WHO	ICMR	ISI	USEPA	CPCB
Iron	0.1	1.0	0.3	-	1.0
Copper	1.0	1.5	0.05	1.3	1.5

Magnesium	50	-	30	-	100
Sodium	200	1100-3300 mg/day	-	20	-
potassium	-	1100-3750 mg/day	-	-	-
Calcium	75	200	75	-	200
Cadmium	0.005	0.01	0.01	0.005	No relaxation
Lead	0.05	0.05	0.10	-	No relaxation
Mercury	0.001	0.001	0.001	0.002	No relaxation
Arsenic	0.01	0.01	0.01	0.01	No relaxation
Zinc	5.0	0.10	5.0	-	15.0
Chromium	-	-	0.05	0.1	No relaxation
Selenium	0.01	-	-	0.05	No relaxation
Nitrate	-	100	45	-	100
Sulfate	-	400	150	-	400
Fluoride	1.5	1.5	0.6-1.2	4.0	1.5

I.2.3. Amino Acids: Cysteine

Cysteine, the thiol containing amino acids amongst all biothiols (Cysteine, Homocysteine, Glutathione) having molecular formula HOOC-CH(NH_2)-CH_2-SH exists as zwitterion, are chemically labile and has physiological and biological importance. The structure of Cysteine exhibits L chirality and plays pivotal role in cellular functions. The thiol group of the Cysteine (30–200 μM) provides as sulphide source for proteins synthesis and maintaining its highly ordered structure, detoxification and metabolism.[128-131] Cysteine itself a strong antioxidant has the potential to trap ROS. Cysteine accelerates the mechanism for the pheomelanin production and simultaneously inhibits eumelanin formation that produces dark colours thereby functions as a skin-

whitening agent.[132] Unbalanced Concentrations of intracellular cysteine are often responsible for physiological problems like retarded growth, haematopoiesis decrease, hair depigmentation, liver damage, skin lesions and weakness.[133-135]

I.2.4. TFA Acid Vapour

The intracellular and extracellular pH of a system is regulated through different physiological processes. Inflammation and tumour growth are often associated with low or acidic pH. Therefore, use of pH sensor at intricate level is applicable in early diagnosis or treatment.[136-138] Trifluoroacetic acid (TFA) is synthetically produced from the resulting hydrochlorofluorocarbons (HCFC) used as refrigerants and as breakdown by-products from the chemicals used for pharmaceuticals, pesticides, and polymers. TFA generated on degradation of HCFC may have long-term impact environmental health which can be a potentially threat to range of organisms.[139-141]

I.3 Preference towards Optical Sensing over other analytical techniques

Common Technique such as Gravimetry, Electrochemical and Spectrophotometric method are generally used for quantitative detection of analytes at ultra-trace concentration. Classical Techniques involving inductively coupled plasma-atomic emission spectrometry (ICP-AES),[142,143] voltammetry,[144] atomic absorption spectroscopy (AAS),[145] inductively coupled plasma mass spectrometry (ICPMS),[146] flame atomic absorption spectroscopy (FAAS),[147] thin chitosan films[148,149] and functionalized metal nanoparticles[150,151] involves an expensive, labour-intensive and complex technique for estimation. On the other hand, Spectrophotometric approach based on optical chemosensor involving UV-Visible and Fluorescence technique have emerged as the most convenient method for recognition and determination of physiologically and environmentally important analyte respectively for low detection limit and intracellular imaging of analyte for biological applications. Addressing the potential hurdles in other techniques, Fluorescence and Absorption Methods of the optical sensing strategy are gaining importance due to cost-effectiveness, feasible synthetic route, operational simplicity, rapid responsive, substantial selectivity and sensitivity, appreciable detection limit and easy analysis.

I.3.1 Chemosensor

A sensor is a device which measures a physical quantity and converts it into a useful detectable form as "signal" that can be read by an observer or by an analytical instrument. By Cambridge Definition Chemical sensor is elucidated "*a portable miniaturized analytical device, which can deliver real-time and on-line information in presence of specific compounds or ions in complex samples*".[152] For fabrication of chemosensor, it must compromise three units : (a) a receptor consisting of two subunits attached by spacer and the ensemble known as the binding unit for recognition and interactions with the specific analyte prior to its selectivity and sensitivity, (b) signalling unit represents the measurable physical signal which arise when receptor recognize the analyte and (c) instruments and techniques to determine this useful signal and converting it into valued information. (**Fig.I.1**) The change in the absorbance or fluorescence behaviour dictates its nature of response towards analytes. Chromogenic receptor responses through colorimetric change in presence of analyte that can be detected by UV-Visible absorption method whereas fluorogenic receptor responds through a modification in the fluorescence property of the molecule on interaction with the analyte that can be recognized through Fluorometric spectrophotometer.

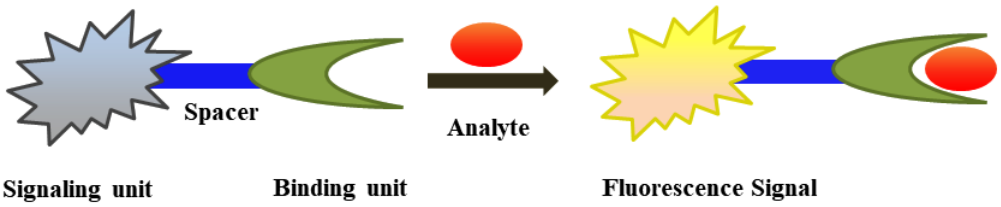

Fig. I.1 Schematic representation of Chemosensor demonstrating binding of an analyte (guest) through host-guest interaction.

I.3.2. Different Fluorescence Sensing Mechanism

In a fluorescent molecule, the absorption of light at a given wavelength effects the radiative emission from excited state. For Fluorescent sensor, two types of signalling corresponding to "Turn On" and "Turn Off" response are observed. For "Turn On" sensing, fluorescence enhancement, ratiometric enhancement and wavelength shift are the phenomena commonly associated while for the "Turn Off" sensing decrement in the emission intensity or quenching only takes place which may sometimes associate with wavelength shift.

I.3.2.1 Photoinduced Electron Transfer (PET)

Structural aspects of PET active probe consist of fluorophore-spacer-receptor unit. PET exhibits charge transfer from lone pair of electrons resides in HOMO of N, O, S and P donor centers to the LUMO of acceptor. In free or unbound state of the probe, an intramolecular electronic excitation occurs from HOMO of the free receptor to LUMO of the fluorophore, that causes a non-radiative transition and no fluorescence is observed. However, in the bounded state of the receptor electron pair interacts with analyte, which reasons lowering of energy of the HOMO corresponds to the receptor than that from the fluorophore inhibiting the PET process and causing a "Turn On" fluorescence enhancement phenomena (**Fig.I.2**). Solvent polarity largely influences PET process as with increased solvent polarity facilities favorable electron transfer.[153]

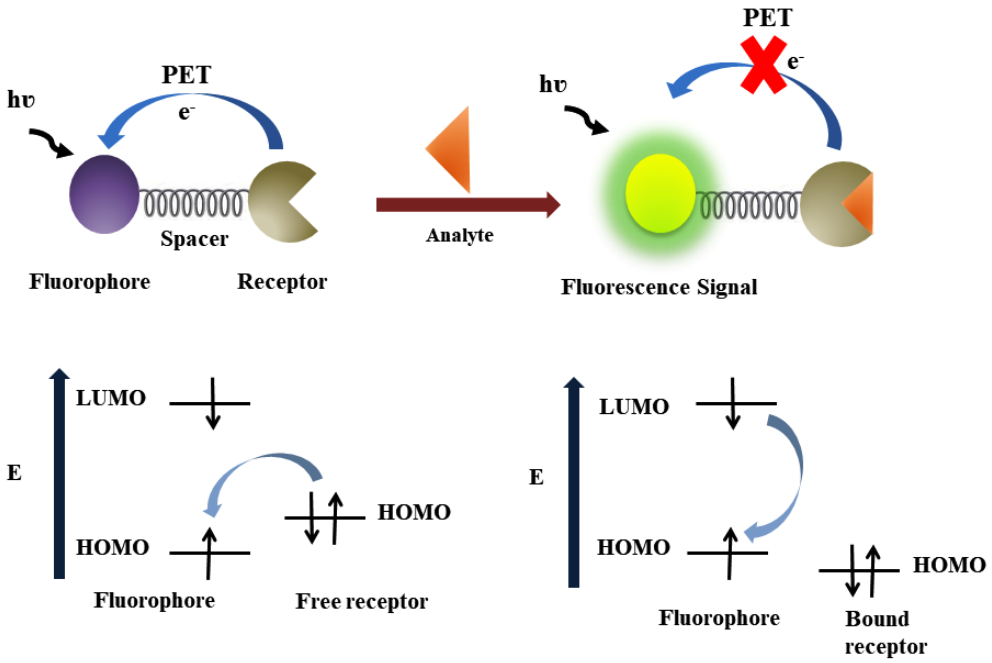

Fig. I.2. Schematic representation of PET mechansim.

I.3.2.2 Excited-State Intramolecular Proton Transfer (ESIPT):

Fundamental concept of ESIPT was first introduced by Weller in 1950. The mechanism is based on the relaxation of photoexcited molecules through tautomerization by transfer of protons. ESIPT occurs in the molecules capable of forming a five/six membered ring transition state during tautomerization and is based on the large Stokes' shift (**Fig.I.3**). This represents an exclusive four-state photochemical process where the ground state represents typically the enol (E) form which on photo excitation undergoes tautomerization to

keto ($^1E^* \rightarrow {}^1K^*$) form *via* intramolecular hydrogen-bonding through five/six membered cyclic transition state. Then, it reverts into its ground state where the reverse protons transfer (RPT) occurs to generate the initial enol form. Such process occurs at ultrafast rate usually in the femtosecond to picosecond time scale (10^{-15}–10^{-12} s). Both the radiative decay and the non-radiative ESIPT follows similar path from excited keto (K*) form into the ground state keto (K) form. However, ESIPT is comparatively faster than that of the radiative decay. ESIPT chromophores mainly show fluorescence due to the keto tautomer (K) with a few exceptions and are substantially sensitive to its surroundings. Presence of polar and hydrogen-bonding donating solvents induces an inhibition of the ESIPT mechanism.[154]

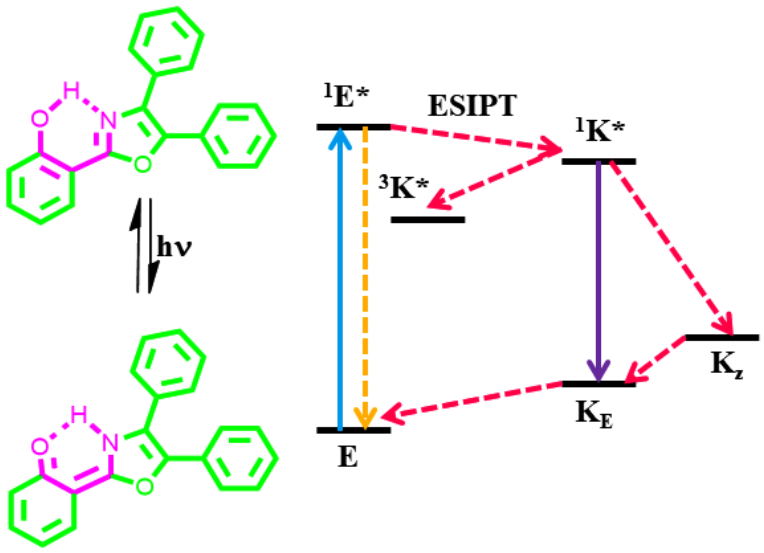

Fig. I.3. Schematic Representation of ESIPT pathway.

I.3.2.3 Intra and Intermolecular Charge Transfer (ICT)

A mechanism by which molecules in excited state undergoes energy relaxation through charge transfer process which may be intermolecular or intramolecular Intermolecular occurs when an excited molecule and a neighbouring molecule, serves as an acceptor and donor while intramolecular forms when the charge redistribution takes place in the excited state within the same molecule having both donor acceptor component producing a large dipole moment. In an ICT system, a fluorophore is in direct interaction with a receptor; compromises of electron rich and electron deficient units resembling a 'push–pull' mechanism. (**Fig.I.4**). The fluorescence output during the recognition processes of interaction between the receptor unit and the analyte

dictates the change in electron density in the fluorophore. ICT causes substantial shifts in absorption and fluorescence emission of the probe on analyte binding and may exhibits ratiometric fluorescence shifts.[155]

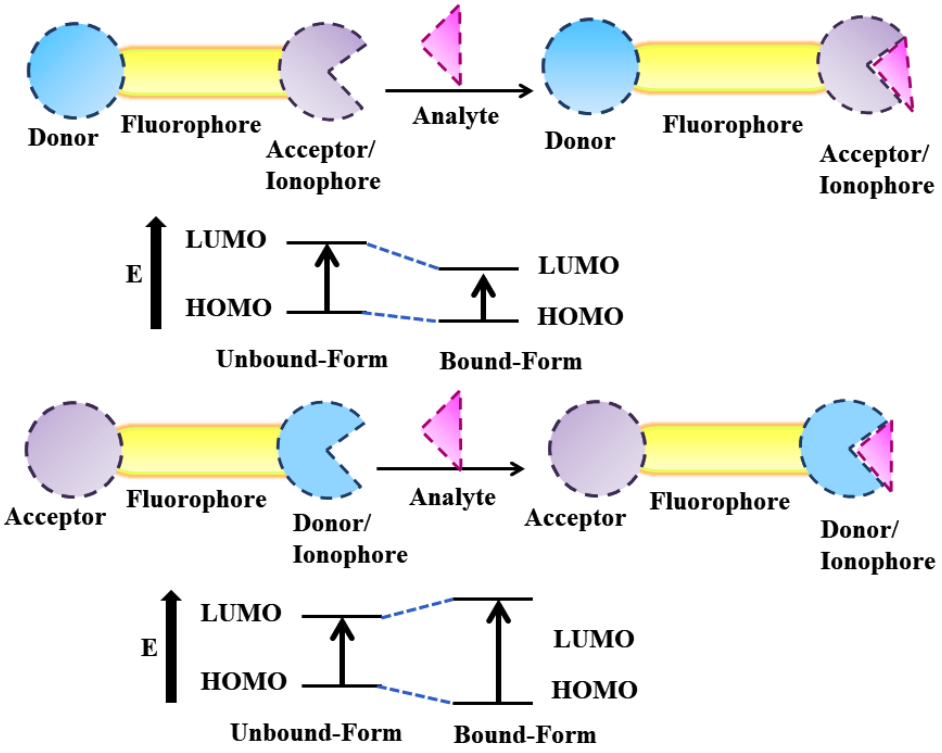

Fig. I.4. Schematic Representation of ICT phenomena.

I.3.2.4. Fluorescence Resonance Energy Transfer (FRET)

FRET is a distance-dependent phenomena where the energy transfer takes place from an excited fluorophore as donor to an acceptor as the other fluorophore through intermolecular long-range dipole–dipole coupling. Degree of FRET proficiency depends on overlapping of emission and absorption spectra of donor and acceptor species; proximity between the two specifically lies within Förster radius (3-6 nm), dipole-dipole interaction. (**Fig. I.5**) In FRET, transfer of energy occurs from the excited donor fluorophore to the acceptor fluorophore having longer-wavelength (D* + A→D + A*), and acceptor emits light with the resulting loss of emission from donor. Efficiency of FRET is guided by the inverse relation with sixth power of intermolecular distance ($E_{FRET} = 1/[1 + (r/R_0)^6]$; R_0 is the Förster radius and it's the distance where E exhibits at its 50% of its maximum intensity.) for analytes that produces changes in molecular proximity with the receptor.[156,157]

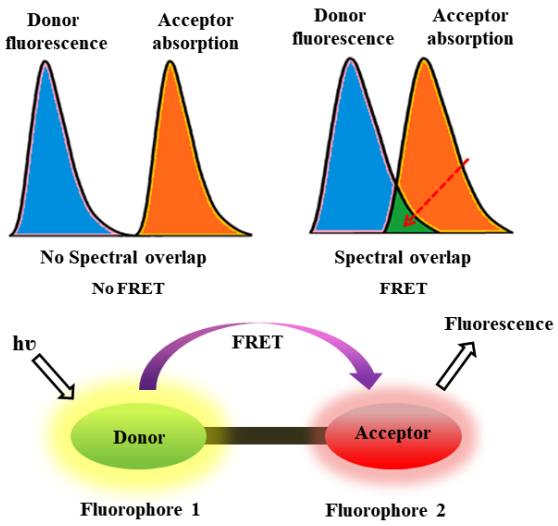

Fig. I.5. Schematic Representation of FRET Mechanism.

I.3.2.5. Chelation Enhanced Fluorescence and Chelation Enhanced Quenching (CHEF & CHEQ):

When a fluorogenic molecule coordinates with metal ion, a change in the fluorescence signal is reflected either to enhance or get quenched. Depending on the fluorescence emission behaviour on binding to the analyte, it's been designated as CHEF for increasing the emission intensity and CHEQ for reducing the emission intensity. (**Fig. I.6**) A red or blue shift in the emission band could be observed due to CHEF and CHEQ. In case of CHEF, on chelation the rigidity of the resulting complexes enhances the radiative process. In CHEQ, the spin-forbidden intersystem crossing (ISC) become faster in presence of paramagnetic centers (radical or transition metal ions) in close proximity to the fluorogenic species. On excitation, it may undergo ISC from S_1 to T_1 state of the fluorophore and subsequently deactivated through the non-radiative pathway.[158]

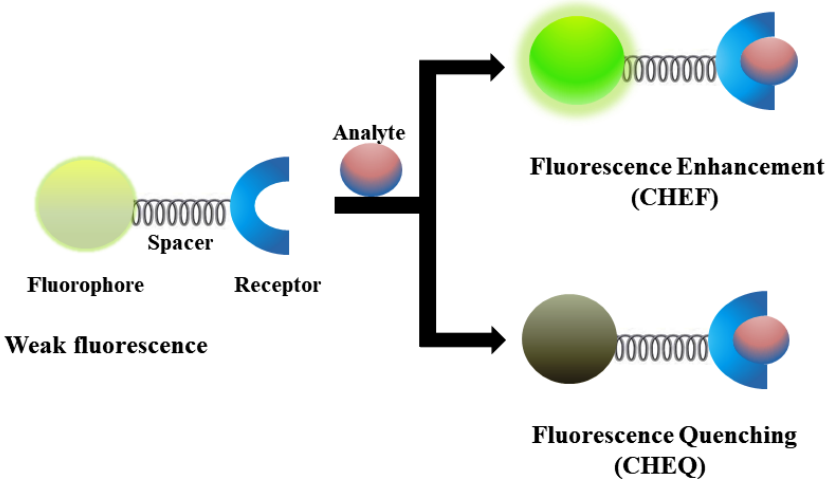

Fig. I.6. Schematic Diagram of CHEF and CHEQ process.

Further quenching process (**Fig. I.7**) invariably governs the lifetime profile of the probe and further classified into two types (i) Static and (ii) Dynamic.

(i) Static Quenching: In presence of large excess (Q>>A) of quencher (Q) a stable ground state complex with the analyte (A) may immediately be formed (A+Q → AQ) and the resulting component may be non-fluorescent then emission is statically quenched. Static quenching will not alter or lessen the lifetime of the sample as tit form the non-fluorescent ground state complex with the quencher. So, they will have normal excited state properties. Since the quencher is basically diminishing the quantity of fluorophores that emits, the emission from the sample is decreased.

(ii) Dynamic Quenching: At Q>A collisional quenching occurs; excited-state of the fluorophore, A*, gets deactivated on contact with Q, [A*Q]. Heavy atoms have large number of L-S coupled states, quenching occurs due to spin-orbit coupling and inter-system crossing to the triplet state. Collisional quenching also diminishes the lifetime of the fluorophore.

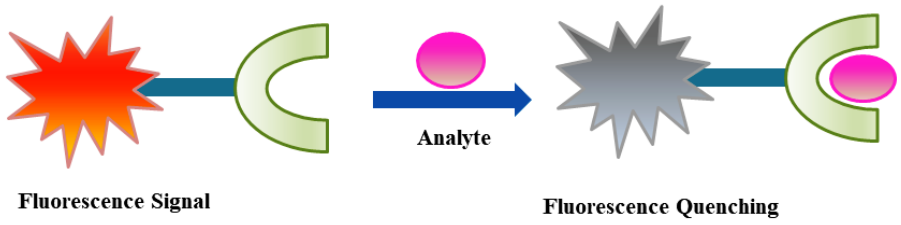

Fig. I.7. Schematic Diagram of Quenching Response.

I.4. Electrical Conductivity

Electrical conductivity is a property of a material to accommodate electrical charge under certain physical conditions like - temperature, pressure, applied current, etc. Ohm's law states that conductivity can quantitively measure the value of resistance by passing the current and measuring the potential value as R = V/I where V is voltage and I is current. Additionally, resistance is dependent on geometrical parameters and the magnitude can be expressed as resistivity $\rho = R \times (A/l)$, [A depicts cross-sectional area of conducting material (A represents product of a and d) and l denotes the distance between points where voltage is applied. However, resistivity is inversely proportional to the conductivity $\sigma = 1/\rho$, where it is estimated in International System unit (SI), $\Omega^{-1}\ m^{-1} = S\ m^{-1}$ (Ω^{-1} = S = Siemens)

I.4.1. Schottky Diode

An electronic device which permits current flow in one direction in a two-terminal system called diode that opposes the current with a high resistance in the reverse direction. A Schottky diode, a semiconductor device, is also recognized as a hot carrier diode. It has a low forward voltage drop which offers improved efficiency and superior switching speed. A semiconductor in contact with a metal has created a Schottky diode which is the Schottky barrier. The n-type semiconductor in Schottky diode acts as the cathode and the metal portion acts as the anode of the diode.

1.4.2. Schottky Barrier

The rectifying property of a MS (metal-semiconductor) contact depends on the presence of an electrostatic barrier between the semiconductor and the metal. This barrier emerges due to the dissimilarity in work functions of the metal and semiconductor. For n type Schottky diodes, work function of the metal (ϕ_m) surpasses work function of the semiconductor (ϕ_s) and electron transfer occurs from semiconductor to metal to maintain equilibrium with Fermi levels and creates a depletion region behind the semiconductor along with the upward bending of the band in the semiconductor. The charge transfer continues till thermal equilibrium is achieved. This is known as a Schottky barrier. We can write the diffusion potential V_{do} as

$$V_{do}=\phi_m-\phi_s \qquad \text{(I. 1)}$$

Upward bending is observed when V_{do} (Eq.I.1) is positive ($\phi_m>\phi_s$), for n-type semiconductor, the electrons must overcome this barrier in order to get transferred from the semiconductor to the metal regions **(Fig. I.8(a))**; this indicates its rectifying properties. In **Fig. 1.8(b)** the bending causes no obstruction to the holes motion for a p-type semiconductor and rectification does not take place by giving an 'ohmic' contact. Downward bending is observed when $\phi m<\phi s$. For n-type semiconductor, an ohmic contact is generated as shown in **Fig. 1.8(c)** whereas for a p-type, a rectifying contact is formed **(Fig. 1.8(d))**.

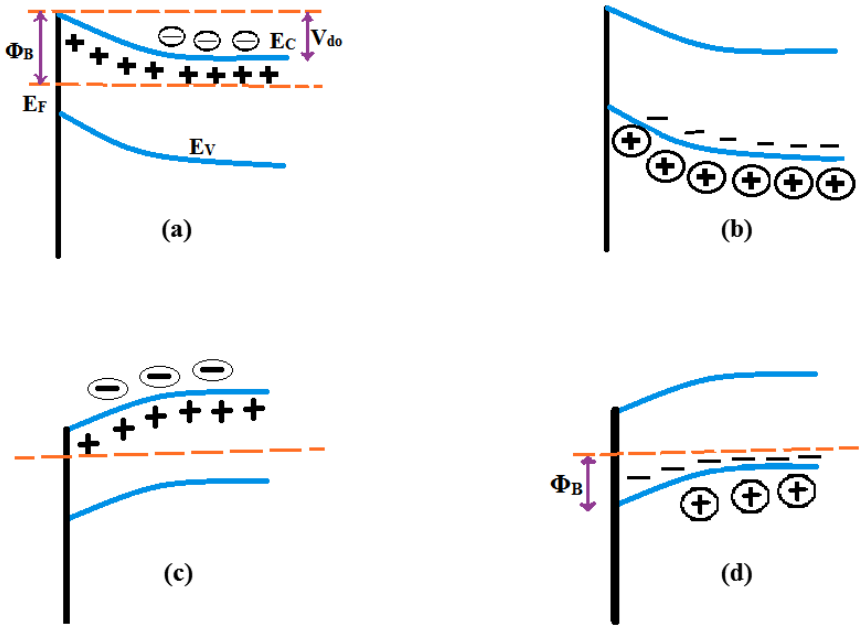

Fig. I.8. Types of Schottky barriers for semiconductors and their work function.

Advantages of Schottky Diode

Advantages of Schottky Diode are (i) Low turn on voltage in between 0.2 and 0.45 volts, (ii) Fast recovery time and (iii) Low junction capacitance.

Applications

A Schottky diode more correctly Schottky barrier diode (SBD)is widely used in different mixer, in radio frequency applications, as a rectifier in power applications, in power OR Circuits. Major field of applications is Solar Cell devices, Clamp diodes etc.

I.4.3. Charge transport parameter

Mobility: The rate of charge carrier transference through a metal or semiconductor is indicated by the carrier mobility. Semiconductor mobility is dependent on factors such as concentration (donor, acceptor, electron, hole, defect concentrations are included), the electric field and temperature.

Carrier Transit time: The time required by a carrier to travel in between cathode and anode. It covers the total time spent as a free carrier and a trapped carrier.

Diffusion Length: Current across a MS junction depends on the carriers. Diffusion of the carriers generating from semiconductor into the metal, is an important mechanism among the existing mechanism.

I.4.4. Diode Parameters

For an efficient SBD the parameters are Ideality Factor (η) obtained from I (current) vs. d*V*/dln*I* plot in low voltage region; Series Resistance (Rs), Schottky barrier height (SBH) (Φ_B) at MS junction of a metal/n-type semiconductor.

I.5. Extension of the scope of the work to Fluorogenic Responsive Schiff bases

Literature review (above discussion) reveals on two aspects of Schiff bases with application in sensing of ions (cations and anions) and small molecules to the use of the materials for sustainable energy conservation policy. Schiff base scaffold with chromophore receptor such as Triphenylamine, Coumarinyl, Naphthyl, Pyrazolyl and benzimidazolyl are specially mentioned to the research reported in this Thesis.

I.5.1. Triphenylamine appended probe

Triphenylamine is one of the most frequently used functional units in opto- and electro-active materials It is recognized as sensitive platform for detection of bio-relevant ions ascribing to their fluorogenic influences on sensing applications (**Table I.2**). In 2013, Malkondu et al. reported Schiff receptor based on triphenylamine–aminophenol conjugate (**T-1**) that displays ratiometric fluorescence changes towards Zn^{2+} and Cd^{2+} giving red and yellow emissions, respectively in CH_3CN medium with detection limit of $(3.43 \pm 0.21) \times 10^{-6}$ M for Cd^{2+} and $(3.16 \pm 0.18) \times 10^{-6}$ M for Zn^{2+}.[159] Qu et. al. in 2017 presented probe as composite of triphenylamine-diaminobutane (**T-2**) which shows reversible acid-base fluorescence behaviour and the highly emissive aqueous solution get selectively quenched in presence of Fe^{3+} and a detection limit to 0.511 μM. Chelation with Fe^{3+} facilates intramolecular charge transfer (ICT) and attributes to quenching.[160] In 2019 Erdimir, reported triphenyamine-rhodamide derivatives (**T-3**) which serves as dual channel sensor via "FRET on" for Hg^{2+} and via "PET-off" Al^{3+} at two different emissive wavelength in $MeCN/H_2O$ (9/1, v/v) medium with a limit of detection 71.8 nM for Al^{3+} and 0.46 μM for Hg^{2+}.[161] Kaya et. al. reported in 2020 another Schiff base

designed on triphenylamine-thiophene entities (**T-4**) for sensitive detection of Cr^{3+} analysed by enhancement of the fluorescence emission through coordination resulting in color change into saxon blue in THF/deionized H_2O (1:1, v/v) and a LOD of 1.5 x 10^{-6} (M) emphasize its sensitivity at micromolar concentration.[162] In 2020 Hung's group synthesized molecule on triphenylamine-salicyldehyde framework (**T-5**) that exhibits Aggregation Induced Emission (AIE) and displays maximum emission at DMF/H_2O (50/50, v/v) and shows specific sensitivity towards hydrazine over other analytes due to blocking of AIE process and chemical transformation from CH=N into $-CH_2$-NH- group after hydrazine addition. The detection yield found to have lower LOD of 55.1 nM.[163] In 2020, Xing and his group reported a triphenylamine-carbazole condensed probe (**T-6**) which shows colorimetric and fluorescence sensor towards Al^{3+} with calculated detection limit of 6.7 × 10^{-7} mol/L in EtOH solvent. Transformation of the light-yellow colour to orange and enhanced emission are due to hydrolysis of the probe in presence of Al^{3+}, along with the formation of new complex with the carbazole amide framework.[164] Wang and his group in 2021 developed a receptor (**T-7**) based on triphenylamine-naphthyl substituent that turn out selective fluorescent sensor in presence of Zn^{2+} in DMF:H_2O solvent with an estimated LOD of 19.34 nM. Chelation Enhanced Fluorescence (CHEF) is the mechanism for its "turn on" response.[165] Xu et.al. in 2021 designed a triphenylamine-benzothiazole fluorophore for efficient sensing of CN^- (**T-8).** The probe undergoes a colorimetric change from red to colourless on addition of CN^- in DMSO-Tri Buffer and exhibits a bright luminescence. The C=N of the indole salt undergoes nucleophilic addition by CN^- which block the ICT effect of the probe and accounts for its enhanced emission. The LOD for CN^- was found 2.62 × 10^{-8} M.[166] Mishra and his group in 2022 synthesized a AIEgenic probe in 90:10 water/DMF mixture (**T-9**) that simultaneously detects Cu^{2+} and Fe^{3+} through quenching response with detection limit of 0.4 and 0.2 ppb for Fe^{3+} and Cu^{2+}.[167] In 2022, Rajesh and Kumar reported another fluorophore on Triphenylamine-sulfonyltoluene framework (**T-10**) which shows selective colorimetric quencher towards Cu^{2+} in CH_3CN:H_2O (7:3, v/v) solvent and LOD value of 1.25 × 10^{-8} M.[168]

Table I.2: Selective Reported Probes on Triethylamine Schiff base Probe:

Probe	**T-1** 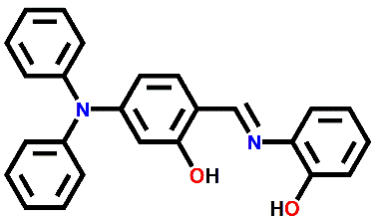	**T-2** 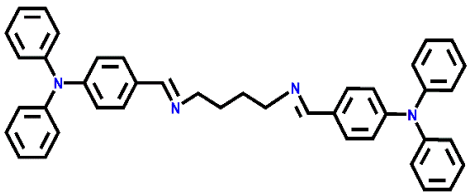
LOD	**3.43 ± 0.21 × 10^{-6} M (Cd^{2+})** **3.16 ± 0.18 × 10^{-6} M (Zn^{2+})**	**0.511 µM (Fe^{3+})**
Solvent	**CH_3CN**	**Aqueous Solution**
Probe	**T-3** 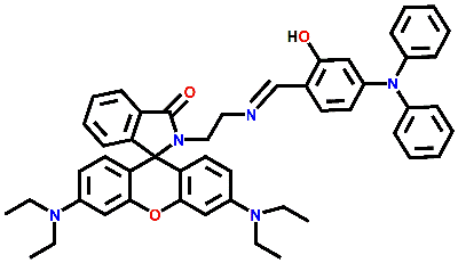	**T-4** 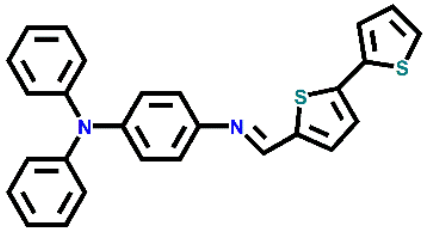
LOD	**71.8 nM (Al^{3+})** **0.46 µM (Hg^{2+})**	**1.5 x 10^{-6} (M) (Cr^{3+})**
Solvent	**CH_3CN /H_2O (9:1, v/v)**	**THF/ H_2O (1/1, v/v)**
Probe	**T-5** 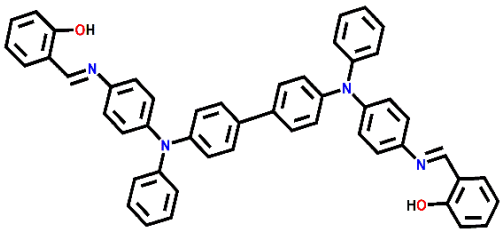	**T-6** 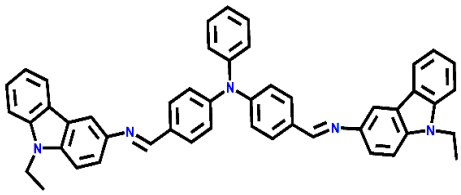
LOD	**55.1 Nm (N_2H_4)**	**6.7 × 10^{-7} mol/L (Al^{3+})**
Solvent	**DMF/H_2O (50/50, v/v)**	**EtOH**

Probe	**T-7** 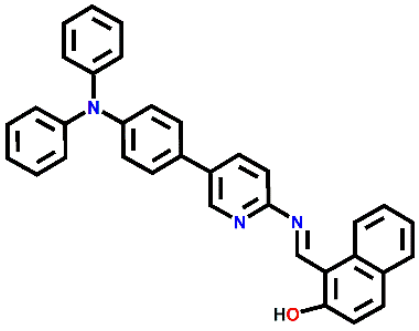	**T-8** 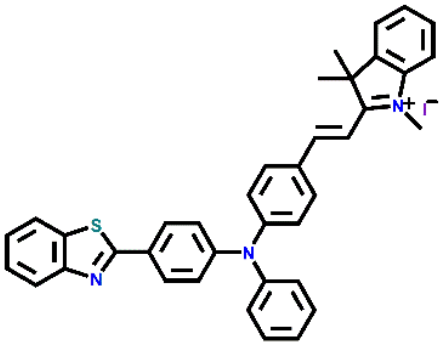
LOD	**19.34 nM (Zn^{2+})**	**2.62×10^{-8} M (CN^-)**
Solvent	**DMF: H_2O**	**DMSO-Tri Buffer**
Probe	**T-9** 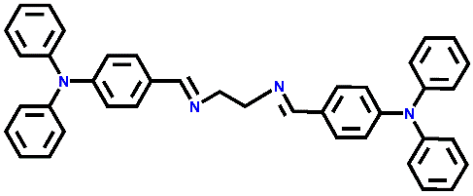	**T-10** 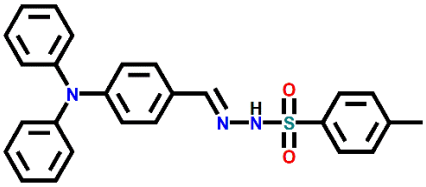
LOD	**0.4 ppb (Fe^{3+})** **0.2 ppb (Cu^{2+})**	**1.25×10^{-8} M (Cu^{2+})**
Solvent	**90:10 water/DMF**	**CH_3CN:H_2O (7:3, v/v)**

I.5.2. Coumarin appended Probe

Coumarin-scaffold is a fluorogenic system to serve as fluorescent chemosensor or chemodosimeter and the substituents influence the emissivity. They participate in the photoinduced electron transfer (PET) process, isomerization etc. and follow non-radiative mechanistic pathway. On interactions with analytes, these quenching effects are inhibited resulting in intense emission. Coumarin, classified as benzopyrone-containing phytochemical, has emerged as an interesting organic fluorophore for detection and estimation of trace levels of environmentally and biologically relevant ions as well as pathological markers **(Table I.3).** Khatua et. al. in 2017 developed a coumarin-salicyldehyde derivative (**C-1**) which shows sensitive sensor towards Al^{3+} through inhibition of C=N isomerization and chelation (CHEF) in a mixed HEPES buffer: methanol (1:9; v/v) phase and detects at a limiting value of 1.34 μM.[169] Kong et. al. in 2017 reported coumarin-naphthol conjugate (**C-2**) in 2017 that severs as fluorescent receptor for Cu^{2+} in HEPES buffer (1% DMSO) media via metal

assisted imine hydrolysis mechanism with a LOD value of 12.7 nM.[170] In 2018, Seferoglu et.al synthesized molecule based on coumarin-thiophene hybrid (**C-3**) which shows remarkable colorimetric and fluorescence recognition for CN- in DMSO/water (6/4, v/v) solvent through deprotonation and ICT mechanism. The detection limit experimentally evaluated to be 1.69 μM.[171] Zhu et.al. synthesizes tripodal molecule on coumarin-triamine scaffold (**C-4**) in 2019 which senses Cd^{2+} specifically with fluorescence enhancement in CH_3CN-HEPES solution (90:10, v/v) with the limit of detection for Cd^{2+} at 1.16×10^{-7} M.[172] Xu et. al. in 2019 reported a reversible probe for Ca^{2+} and F^- (**C-5)** sensor based on coumarin-mandelohydrazide framework. The emission of the probe gets amplified in presence of Ca^{2+} ascribing to the ICT effect in DMF/HEPES buffer (1:1) while the resultant species gets selectively quenched by F^-. The LOD experimentally calculated as 5.81×10^{-7} M for Ca^{2+} and 4.28×10^{-7} M for F^- respectively.[173] Sinha et. al. developed a AIE active coumarin-picolylhydrazide derivative (**C-6**) that detects Al^{3+} with cyan blue emission on account of withdrawal of ESIPT and introduction of CHEF. The emissive Al^{3+} complex goes sequential quenching in presence of nitroexplosives like DNP and TNP in pure water. The corresponding LOD value obtained are 6.99 nM (Al^{3+}), 9.97×10^{-7}(TNP) and 1.67×10^{-6} M (DNP).[174] Zhao et. al. in 2020 group fabricated AIE active coumarin-tetraphenylethene probe that **(C-7)** behaves as Cu^{2+} selective receptor through "turn off" mechanism of the emissive core in THF/H_2O (10:90, v/v) and a limit of detection of 0.36 μM is reported.[175] Zhag's group synthesized a fluorescent coumarin-diethylaminosalicylaldehyde probe in 2021 (**C-8**) offers selective and discriminative emissions of dual recognition of toxic heavy metal ions of Hg^{2+} and Pb^{2+} in aqueous Hepes buffer solution through inhibition of PET and ESIPT pathway and detection limit calculated as 8.3 nM (Hg^{2+}) and 10.5 nM (Pb^{2+}).[176] In 2021, Chaudhury et. al. presented molecule fluorogenic receptor coumarin-dimethyethylene diamine (**C-9**) towards Zn^{2+} through inhibition of PET in ethanol solvent and a LOD value of 0.272 nM.[177] Elmas et. al. reported a coumarin-furan scaffold (**C-10**) that serves a discriminative dual channel emissive sensor of Al^{3+} and ClO^- in different solvents. The probe detects Al^{3+} in ethanolic medium with LOD value of 14.2 nM while for ClO^- the LOD reports to 0.238 μM in DMSO solvent.[178]

Table I.3: Selective Reported Probes on Coumarin Schiff base Probe:

Probe	**C-1** 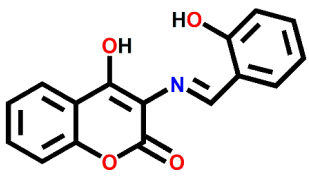	**C-2** 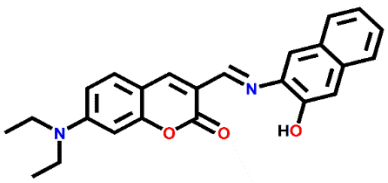
LOD	**1.34 μM (Al^{3+})**	**12.7 nM (Cu^{2+})**
Solvent	**HEPES buffer: methanol (1:9; v/v)**	**HEPES buffer (1% DMSO)**
Probe	**C-3** 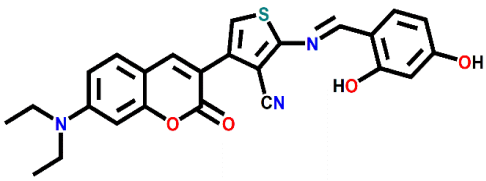	**C-4** 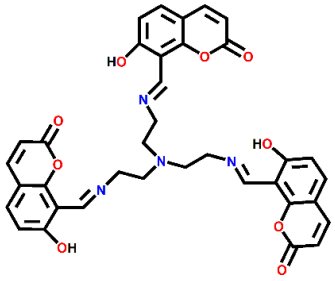
LOD	**1.69 μM (CN^-)**	**1.16 x 10^{-7} (M) (Cd^{2+})**
Solvent	**DMSO/water (6/4, v/v)**	**CH_3CN-HEPES (90:10, v/v)**
Probe	**C-5** 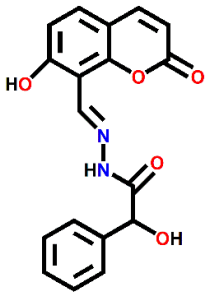	**C-6** 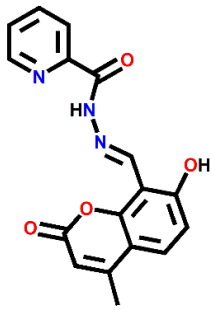
LOD	**5.81 × 10^{-7} M (Ca^{2+})** **4.28 × 10^{-7} M (F^-)**	**6.99 nM (Al^{3+})** **9.97 x 10^{-7} (TNP)** **1.67 × 10^{-6} M (DNP)**
Solvent	**DMF/HEPES buffer (1:1)**	**H_2O**
Probe	**C-7** 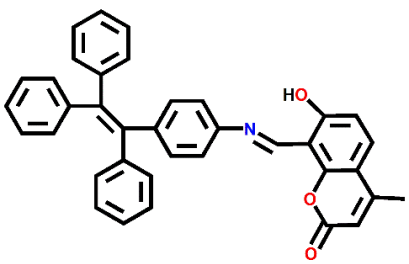	**C-8** 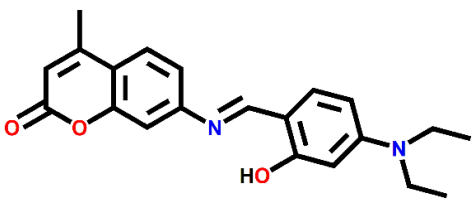

LOD	**0.36 μM (Cu^{2+})**	**8.3 nM (Hg^{2+})** **10.5 nM (Pb^{2+})**
Solvent	**THF/H_2O (10/90, v/v)**	**Aqueous Hepes buffer**
Probe	**C-9** 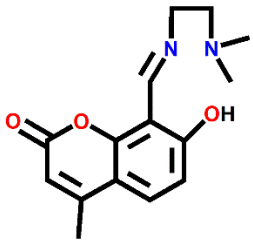	**C-10** 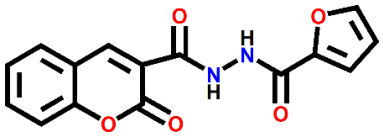
LOD	**0.272 nM (Zn^{2+})**	**14.2 nM (Al^{3+})** **0.238 μM (ClO^-)**
Solvent	**Ethanol**	**DMSO**

I.5.3. Pyrazol appended Probe

Pyrazol Schiff Base probes are known for their interesting photophysical and sensing. Behaviour. A few reports on pyrazol derivatives are discussed here (**Table I.4**). In 2016, Guchhait and Bhattacharya's group synthesized pyrazol-naphthyl hybrid receptor (**P-1**) gives discriminative and selective emission in presence of Mg^{2+} and Zn^{2+} in 7 : 3 (v/v) MeCN–water medium. Enhancement of emission can be attributed to the blocking of PET followed by activation of CHEF. The fabricated probe shows a low sensing limit towards Mg^{2+} (3.9×10^{-7} M) & Zn^{2+} (2.2×10^{-7} M).[179] Yang et. al. in 2017 reveals pyrazol-diamine conjugate (**P-2**) displayed Al^{3+} recognition through CHEF mechanism which imparts rigid stable conformation on coordination with Al^{3+} in DMF solution with a detection limit of up to 1 nM.[180] Prasad's group demonstrated in 2018 pyrazol-anisaldehyde ligand (**P-3**) that presented a colorimetric sensor for Cu^{2+} ion in water/DMSO (9 : 1, v/v) and a detection limit was found to be 1.6 μM.[181] Pu et. al. in 2018 fabricated pyrazol-diarylethene probe (**P-4**) that mediates different absorption and fluorescence behaviours towards Al^{3+} and Zn^{2+} in methanol. The LOD are 2.7×10^{-7} mol L^{-1} (Al^{3+}) and 4.0×10^{-8} mol L^{-1} (Zn^{2+}).[182] In 2019, Xu and his group have developed pyridine substituted pyrazolhydrazide-diethylaminosalicyldehyde probe (**P-5**) which has shown reversible chemosensor towards Al^{3+} and F^- in HEPES buffer. The enhancement in emission resulted on interaction with

Al^{3+} coupled with AIEE effect. Conversely the emission gets quenched in presence of F^- and the LOD calculated for Al^{3+} and F^- are 0.062 μM and 0.326 μM respectively.[183] In 2020, Ayyanar et. al. reported pyrazole-benzimidazole molecule which shows notable ratiometric sensing (**P-6**) for Fe^{3+} and Al^{3+} in CH_3CN-H_2O (7:3, v/v) solution with a LOD value detected is 2.12×10^{-7} M(Al^{3+}) and 5.77×10^{-6} M (Fe^{3+}).[184] Mishra et. al. in 2021 (**P-7**) reported a pyrazole hydrazide-pyridine derivative as Al^{3+} sensor that caused increased emission accompanied by change into greenish color. The combined effect of inhibition of PET, restricted rotation and CHEF are the reason behind high fluorescence response in MeOH–H_2O (9 : 1,v/v). Submicromolar detection level is exhibited by the probe (LOD = 4.78 μM) for Al^{3+}.[185] Mondal et. al. in 2021 synthesized another receptor based on pyrazol-dihydroxysalicyldehyde (**P-8**) scaffold that triggers a turn-on chelation-enhanced Al^{3+}-responsive fluorescence in DMSO–water (1 : 1) solution and calculated detection limit of 0.216 μM.[186] The emissive complex further utilized for picric acid sensing at a LOD value of 1.2257 × 10^{-4} (M). Kumar's group developed a synthesized pyrazol-pyran probe (**P-9**) that serves as a turn-on colorimetric sensor for arginine in DMSO–PBS (8 : 2 v/v) and a LOD value of 1.8 x 10^{-5} M.[187] Ren in 2022 developed a pyrazole-picolyl hydrazide derivative (**P-10**) for significant increase in emission intensity selective to Cu^{2+} ascribing due to the Intramolecular Charge Transfer (ICT) effect in DMF/H_2O (v/v, 1:2) solution The detection limit estimated for the Cu^{2+} detection is 1.6×10^{-8} mol·L^{-1}.[188]

Table I.4: Selective Reported Probes on Pyrazol Schiff Base Probe:

Probe	**P-1**	**P-2**
	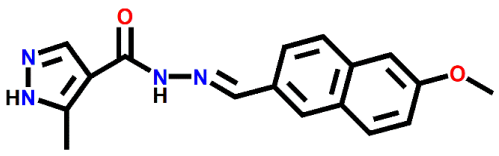	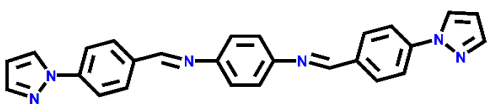
LOD	**2.2×10^{-7} M (Zn^{2+})** **3.9×10^{-7} M (Mg^{2+})**	**1 nM (Al^{3+})**
Solvent	**7 : 3 (v/v) MeCN–water**	**DMF solution**
Probe	**P-3**	**P-4**

	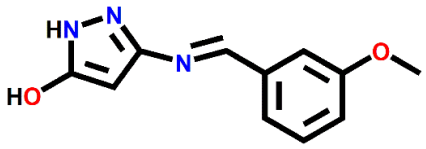	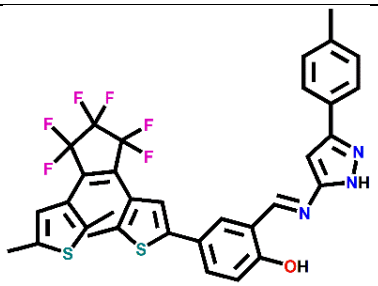
LOD	**1.6 µM (Cu^{2+})**	**2.7×10^{-7} mol L^{-1} (Al^{3+})** **4.0×10^{-8} mol L^{-1} (Zn^{2+})**
Solvent	**water/DMSO (9 : 1, v/v)**	**Methanol**
Probe	**P-5** 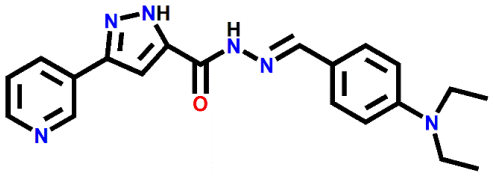	**P-6** 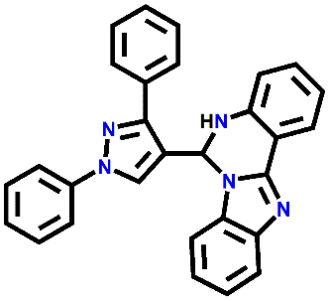
LOD	**0.062 µM (Al^{3+})** **0.326 µM (F^-)**	**2.12×10^{-7} M (Al^{3+})** **5.77×10^{-6} M (Fe^{3+})**
Solvent	**HEPES Buffer**	**ACN-H_2O (7:3, v/v)**
Probe	**P-7** 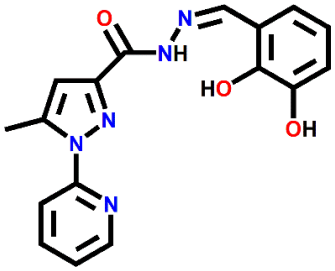	**P-8** 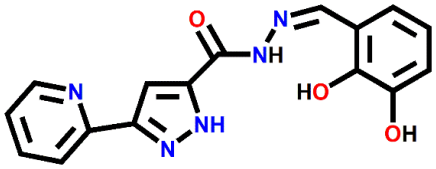
LOD	**4.78 µM (Al^{3+})**	**0.216 µM (Al^{3+})** **1.2257×10^{-4} (M) (TNP)**
Solvent	**MeOH–H_2O (9 : 1 v/v).**	**DMSO–water (1 : 1)**
Probe	**P-9** 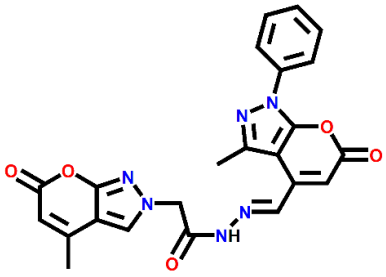	**P-10** 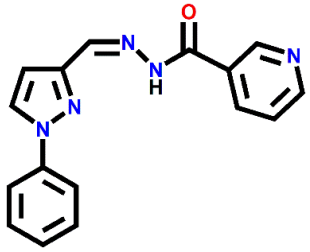

LOD	**1.8 x 10^{-5} M (Argenine)**	**1.6 × 10^{-8} mol L^{-1} (Cu^{2+})**
Solvent	**DMSO–PBS (8 : 2 v/v)**	**DMF/H_2O (V/V = 1:2)**

I.5.4. Benzimidazole appended Probe

Benzimdazole substituted ligand possesses unique fluorescence properties that caters as promising materials for chemosensor. Till date, considerable efforts are devoted to the synthesis of benzimidazole designed probe. (**Table I.5**). Chellappa in 2015 synthesized azobenzimidazole-salicyldehyde system (**B-1**) as bifunctional chromogenic and fluorogenic receptor towards Al^{3+} and F^- in DMSO medium. The probe facilitate receptor–F^- interaction through deprotonation which leads to a degree of increased conjugation causing colorimetric change for Al^{3+} attributed to the ligand to metal charge transfer (LMCT) mechanism resulted for enhanced fluorescence and prominent color transformation and the reported detection limit are 3.41×10^{-7} M (Al^{3+}) and 9.189×10^{-8} M (F^-).[189] In 2016, Tian-Jiang's group developed benzimdazole-salicyldehyde probe that **(B-2)** enables simultaneous reversible recognitions of multifunctional analytes like Al^{3+}, Cu^{2+}, F^- and S^{2-} in CH_3OH-PBS buffer. The distinctive red-shifted emission enhancement caused due to Al^{3+} reverts to its original state on treatment with F^- while that of the quenched state occurs due to Cu^{2+} on account of its paramagnetic induced CHEQ effect which exhibits reversibility in presence of S^{2-}. The estimated detection limit estimated for analytes are and are 0.31 μM (Al^{3+}), 0.54 μM (Cu^{2+}), 3.8 μM (F^-) and 1.4 μM (S^{2-}).[190] Kim et al. in 2016 synthesized a molecular system composed of benzimidazole-diethylaminosalicyldehyde unit that behaves efficient colorimetric receptor towards Fe^{3+}/Fe^{2+} and fluorometric sensor for Zn^{2+} in aqueous solution. **(B-3)** The dark green colorimetric response for Fe^{3+}/Fe^{2+} might be ascribed to a metal-to-ligand charge-transfer (MLCT) while for Zn^{2+} fluorescence enhancement resulted on effective coordination refers to the CHEF effect along with inhibition of ESIPT. The LOD calculated are 1.21 μM (Fe^{3+}), 1.18 μM (Fe^{3+}) and 1.05 μM (Zn^{2+}).[191] In 2017, Gao and Chen et. al. developed fluorescent probe based on benzimidazole-coumarin conjugate that detects Hg^{2+} and Cu^{2+} through different sensing pathway in HEPES buffer/DMSO (v:v = 9:1) medium.**(B-4)** In case of Hg^{2+}, emission enhancement caused from mercury-promoted hydrolysis of probe while for Cu^{2+} colorimetric change can be explained on the basis of chelation and fluorescence quenching because of its

paramagnetic nature. The detection limits are 90 nM for Hg^{2+} and 1.59 μM for Cu^{2+}.[192] Steinberg and his group in 2018 presented another cyano substituted benzimidazole-salicyldehyde hybrid that **(B-5)** serves colorimetric detection of Al^{3+} a colour change from light- to dark-yellow which can be ascribed to deprotonation of the ligand and a selective Cu^{2+} quencher in ethanol with limit of detection determined as 1.3×10^{-7} M and 3.7×10^{-7} M for Cu^{2+} and Al^{3+} respectively.[193] Das et. al. in 2019 reported a Schiff base benzimidazole-naphthyldehyde molecule that **(B-6)** applied for selective sensing of Zn^{2+} via inhibition of internal charge transfer (ICT) followed by activations of CHEF. The probe further detects N_3^- through enhance fluorescence that occurs through formation of supramolecular H-bonded rigid assembly. The sensing process with distinctive emission for the two analytes are carried out in DMSO-H_2O, 1:3, v/v, 0.1 M HEPES buffer medium and the corresponding detection limit for Zn^{2+} and N_3^- are 6.85×10^{-8} M and 1.82×10^{-7} M, respectively.[194] Bubbly's group in 2019 synthesized hydroxobenzimidazole-salicyldehyde composite probe as selective sensor for Zn^{2+} and Al^{3+} in DMF/water (9:1 v/v) solvent **(B-7)** and the detection limit for the receptor was found to 0.21 μM and 0.11 μM for Zn^{2+} and Al^{3+}.[195] Fan and Li's group in 2020 reported fluorophore core based on AIE active benzimidazole-pyrrole derivative and allows for selective sensing of Cu^{2+} through metal induced quenching assembly through complexation. **(B-8)** The restoration of emission is achieved on addition of PPi to Cu^{2+} complex. The detection studies have been performed in H_2O/CH_3CN (99.5%, v/v) with LOD value of 49.6 nM (Cu^{2+}) and 0.55 μM (PPi) respectively.[196] Anbu et. al. reported in 2021, a multi-responsive benzimidazole-diformyl chemosensor which (**B-9**) is moderately emissive and undergoes sequential detections for Cu^{2+}, CN^-, Zn^{2+}, $P_2O_7^{4-}$, DNA in CH_3CN / (50 mM) HEPES buffer medium. The emissive probe exhibits paramagnetic quenching to Cu^{2+} and the complex serves as secondary sensor to CN^- classify as reversible probe. Simultaneously the emission of the probe gets enhanced in presence of Zn^{2+} via inhibition of PET between donor and Zn^{2+}. The emissive Zn^{2+}-complex was further utilized as sensor for PPi and DNA components recognition. The LOD values reported are 24.4 nM (Cu^{2+}), 9.43 nM (CN^-), 2.4 nM (Zn^{2+}), 2.9 nM (PPi) and 5.5×10^{-7}, 4.5×10^{-7} and 5.7×10^{-7} M (XOF, XAPF and CT-DNA).[197] In 2022, Balakrishnan's group developed a chemosensor based on benzimidazole-indole system for detection of analytes Hg^{2+}, F^- and Histidine. The probe response through diminishing of emission for Hg^{II} and histidine while it is ratiometric

towards F^- ions in methanol/aqueous HEPES buffer (1:9 v/v). **(B-10)** Chelation enhanced quenching (CHEQ) mechanism in Hg^{2+} and the participation of imidazole ring in histidine in hydrogen bonding and π-π stacking interactions via., PET may be responsible for quenching process. However, for F^-, the ratiometric sensing attributed to the extent of intramolecular charge transfer (ICT) from the imidazolate anion to other aromatic rings. The detection limit estimated for the probe are 8.24 nM (for Hg^{II}), 7.72 nM (for F^-) and 8.03 nM (for histidine).[198]

Table I.5: Selective Reported Probes on Benzimidazole Schiff base Probe

Probe	**B-1**	**B-2**
	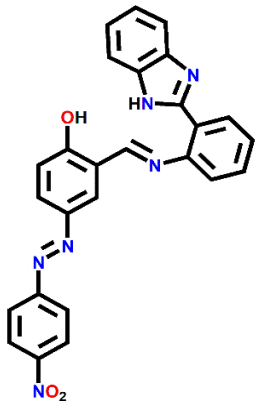	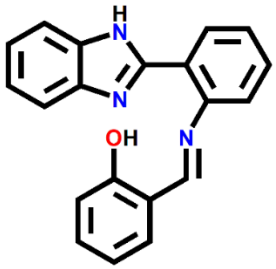
LOD	**3.41×10^{-7} M (Al^{3+})** **9.189×10^{-8} M (F^-)**	**0.31 µM (Al^{3+})** **0.54 µM (Cu^{2+})** **3.8 Mm (F^-)** **1.4 µM (S^{2-})**
Solvent	**DMSO**	**CH_3OH-PBS buffer.**
Probe	**B-3**	**B-4**
	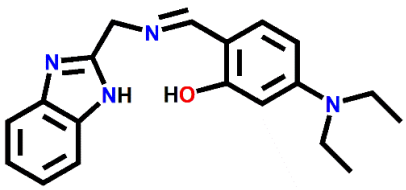	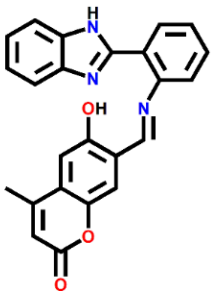
LOD	**1.21 µM (Fe^{3+})** **1.18 µM (Fe^{3+})** **1.05 µM (Zn^{2+})**	**90 nM (Hg^{2+})** **1.59 µM (Cu^{2+})**
Solvent	**Aqueous Solution**	**HEPES buffer/DMSO (v:v = 9:1)**

Probe	**B-5** 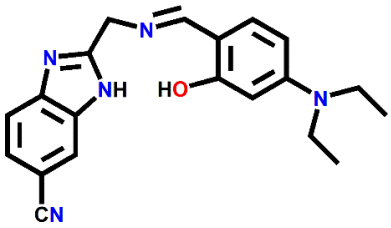	**B-6** 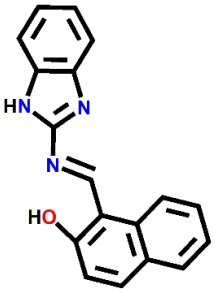
LOD	**1.3×10^{-7} M (Cu^{2+})** **3.7×10^{-7} M (Al^{3+})**	**6.85×10^{-8} M (Zn^{2+})** **1.82×10^{-7} M (N_3^-)**
Solvent	**Ethanol**	**DMSO-H_2O, 1:3, v/v**
Probe	**B-7** 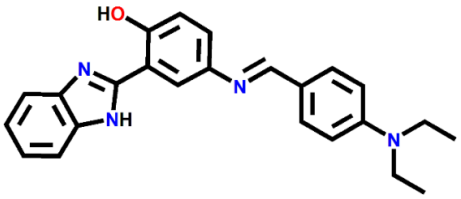	**B-8** 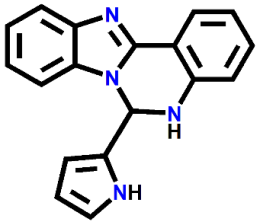
LOD	**0.21 µM (Zn^{2+})** **0.11µM (Al^{3+})**	**49.6 nM (Cu^{2+})** **0.55 µM (PPi)**
Solvent	**DMF/water (9:1 v/v)**	**H_2O/CH_3CN (99.5%, v/v)**
Probe	**B-9** 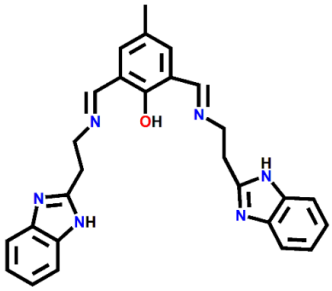	**B-10** 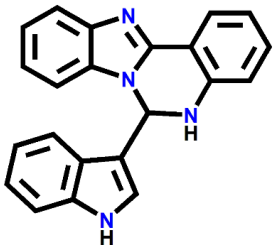
LOD	**24.4 nM (Cu^{2+})** **9.43 nM (CN^-)** **2.4 nM (Zn^{2+})** **2.9 nM (PPi)** **5.5×10^{-7}, 4.5×10^{-7}, 5.7×10^{-7} M (XOF, XAPF, CT-DNA).**	**8.24 nM (for Hg^{II})** **7.72 nM (for F^-)** **8.03 nM (for histidine).**
Solvent	**CH_3CN / HEPES buffer medium**	**Methanol/ HEPES buffer (1:9 v/v).**

I.5.5. Naphthyl Appended Probe

Naphthyl scaffolds emerges as versatile fluorescent unit for advancement of sensors for recognition of important analytes. Different approach of sensing mechanism by naphthalene-based sensors also extends its applications in biological assay (**Table I.6**). In 2017, Roy et. al developed an azine based naphthyl-p-nitrosalicyldehyde **(N-1)** system used for selective recognition for Al^{3+} in water:methanol (1:9, *v/v*) solvent causing an enhanced emission due to the inhibition of PET and a limit of detection of 4.39 μM.[199] Yan and his group in 2018 presented a probe with naphthyl-aminophenol composite as **(N-2)** colorimetric sensor for Fe^{2+} and Fe^{3+} in ethanol-H_2O (v/v = 4:6) medium. The detection limit experimentally evaluated for Fe^{2+} and Fe^{3+} are 4.2 nmol/L and 8.3 nmol/L, respectively.[200] Qi's group in 2019 synthesized the Schiff molecule containing naphthyl-aminosalicylic acid conjugate that **(N-3)** undergoes colorimetric changes with Cr^{3+}, Cu^{2+} and Fe^{3+} as well as for Al^{3+} in DMF/water (1:1) and it displays a blue shifted emission enhancement while in case of Fe^{3+} the existing emission of the probe gets quenched. The limit of detection of the probe for the respective ions are 3.37×10^{-7} M (Cr^{3+}), 4.65×10^{-7} M (Cu^{2+}), 3.58×10^{-7} M (Fe^{3+}) and 4.89×10^{-7} M (Al^{3+}) and are below than the recommended limit.[201] In 2019 Sinha et. al. reported an AIE active naphthyl-picolylhydrazide probe that able to detect Al^{3+} attributing cyan blue emission in pure aqueous medium following the mechanism of inhibition of PET and inclusion of CHEF. **(N-4)** The emissive probe in 95% aqueous medium was further applied as sensory device for nitro explosives like TNP and DNP sensing. The lower value of limit of detection obtained for the probe 2.09 nM (Al^{3+}), 0.779 μM (TNP) and 0.908 μM (DNP) certifies the probe to efficient in sensing applications.[202] Ramu's group in 2020 fabricated a condensed probe with naphthyl-aminothiodiphenyl entities for the **(N-5)** chromogenic and fluorescent recognition of Al^{3+} via CHEF and ICT mechanistic pathway in DMSO medium with a LOD value of 13×10^{-7} M range.[203] Kaur et. al. in 2020 synthesized naphthyl-anthracene Schiff base as **(N-6)** a sensitive probe towards Al^{3+} and F^- with distinguished emissive responses in CH_3CN. Further F-complex has been employed detection of Cu^{2+} through quenching process. The LOD value reported for sensitive detections are 1.48(Al^{3+}), 1.44(F^-) and 2.05 μM (Cu^{2+}).[204] Erdemir' group developed a naphthyl-triazole-anthracene receptor towards **(N-7)** enhanced fluorescence response selective to Al^{3+} in EtOH/H_2O (v/v, 6/4) via imine hydrolysis approach. The limit of detection of the

receptor towards Al^{3+} was calculated as 0.117 μM.[205] Dong et. al. in 2021 designed a flexible naphthyl-salamo derivatives that **(N-8)** itself undergoes deprotonation and stacking interaction for recyclable chemonsensor for CN^- with a LOD of 0.128 μM in in DMSO/H_2O solution.[206] Das et.al. in 2022 defined functionalized naphthyl-ninhydrin as reversible chemosensor for detection of Al^{3+} and F^- and a colorimetric sensor for Cu^{2+} with detection limits amounts to 1.97, 4.0 and 0.34 μM respectively in methanol/aqueous HEPES. **(N-9)** [207] Wang and his group in 2022 reported naphthylhydrazono-thiophene derivative **(N-10)** in 2 vol% DMSO exhibits a emissive probe that gets selectively quenched in presence of Cr^{3+} through CHEQ and limit of detection is 41 nM.[208]

Table I.6: Selective Reported Probes on Naphthyl Schiff base Probe

Probe	**N-1** 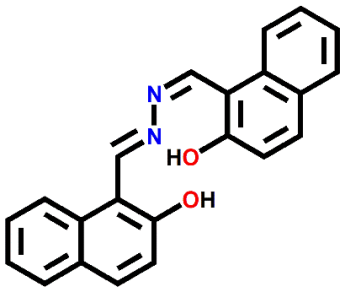	**N-2** 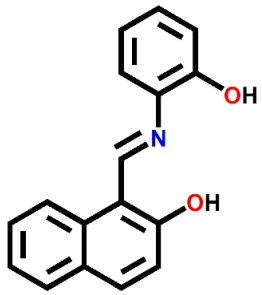
LOD	**4.39 μM (Al^{3+})**	**4.2 nmol/L (Fe^{2+})** **8.3 nmol/L (Fe^{3+})**
Solvent	**water:methanol (1:9, *v/v*)**	**ethanol-H_2O (v/v = 4:6)**
Probe	**N-3** 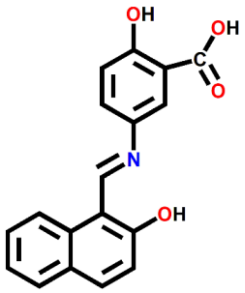	**N-4** 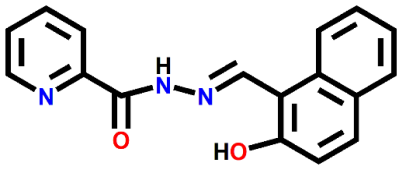
LOD	**3.37×10^{-7} M (Cr^{3+})** **4.65×10^{-7} M (Cu^{2+})** **3.58×10^{-7} M (Fe^{3+})** **4.89×10^{-7} M (Al^{3+})**	**2.09 nM (Al^{3+}),** **0.779 μM (TNP)** **0.908 μM (DNP)**
Solvent	**DMF/H_2O (1:1)**	**Pure aqueous medium**

Probe	**N-5** 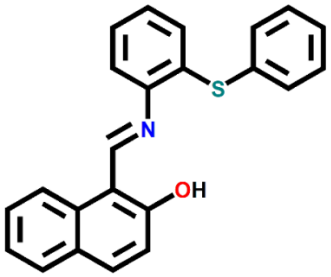	**N-6** 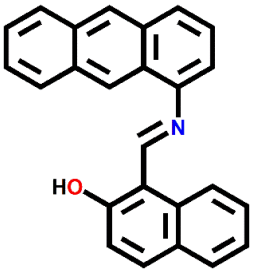
LOD	**13×10^{-7} M (Al^{3+})**	**1.48 μM (Al^{3+})** **1.44 μM (F^{-})** **2.05 μM (Cu^{2+})**
Solvent	**DMSO**	**ACN-H_2O (7:3, v/v)**
Probe	**N-7** 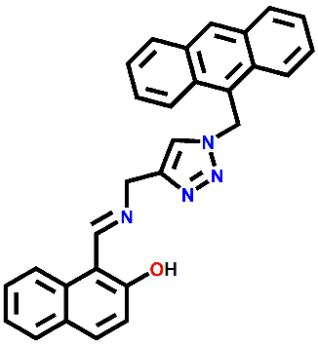	**N-8** 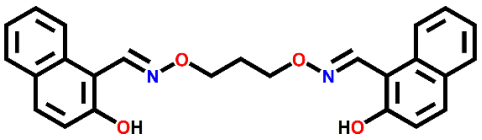
LOD	**0.117 μM (Al^{3+})**	**0.128 μM (CN^{-})**
Solvent	**EtOH/H_2O (v/v, 6/4)**	**DMSO/H_2O**
Probe	**N-9** 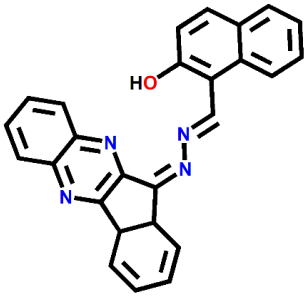	**N-10** 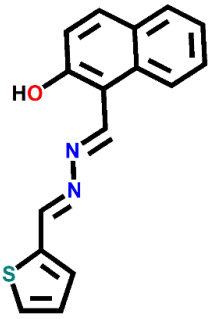
LOD	**1.97μM (Al^{3+})** **4 μM (F^{-})** **0.34 μM (Cu^{2+})**	**41 nM (Cr^{3+})**
Solvent	**methanol/aqueous HEPES Buffer**	**2 % vol DMSO**

I.6. Aims and Dissertation of the scope

The research work presented in this thesis work divulges on the synthesis, characterization and applications of different Schiff bases functionalized with fluorescent chromophores. The dissertation study focuses on (i) Design and synthesis of different Schiff base attributing interesting photophysical properties, (ii) Exploring the role of such molecule in sensing applications of different analytes (ions and molecules) (iii) Utilizing in the fabrication of Zn coordination polymer with its application in electrical conductivity and biological study. Herein, we represent the five synthesized Schiff bases in relevance to my thesis work.

Chapter 2: A symmetrical Schiff Base is reported on 1,1′-((1E,1′E)-((2E,2′E)(((phenylazanediyl)bis(4,1-phenylene))bis-(methanylylidene))bis-(hydrazine-2,1-diylidene))bis(methanylylidene))bis(naphthalen-2-ol) which has been synthesized following the condensation method and well characterized. (**Scheme I.6.a**)

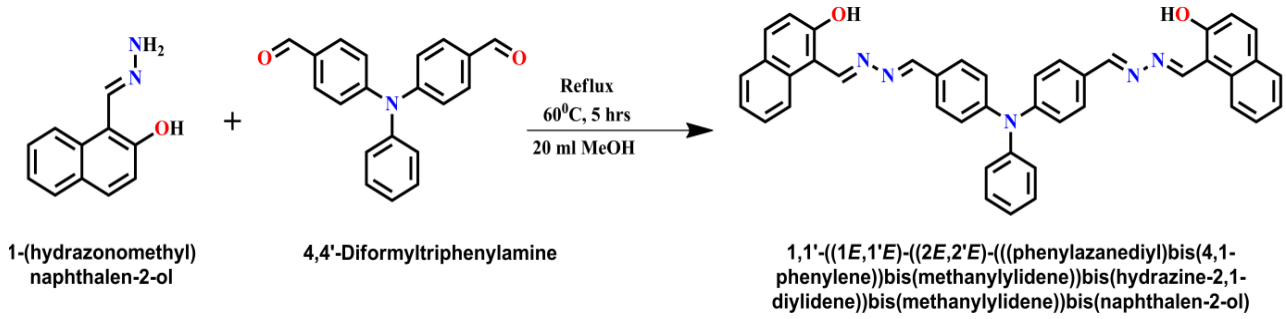

Scheme I.6.a. Synthesis of Ligand

Chapter 3: The work reports on benzimidazole derived Schiff ligand 2-Ethoxy-6-[1-(phenyl-pyridin-2-yl-methyl)-1H-benzimidazol-2-yl]-phenol has been synthesized by Schiff's reaction along with detailed characterization. **(Scheme I.6.b)**

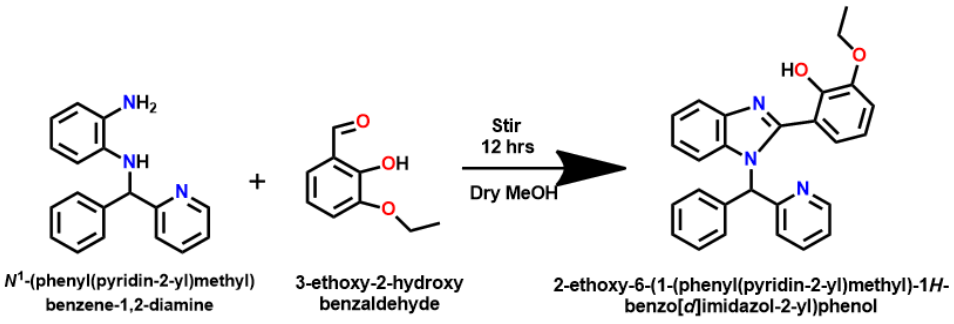

Scheme I.6.b. Synthesis of Ligand

Chapter 4: This chapter reports an interesting coumarinyl-pyrazole scaffold 7-hydroxy-4-methyl-8-(((5-phenyl-1Hpyrazol-3-yl)imino)methyl)-2H-chromen-2-one synthesized by one step Schiff base reactions. Single crystal X-Ray Diffraction confirms its structural framework. **(Scheme I.6.c)**

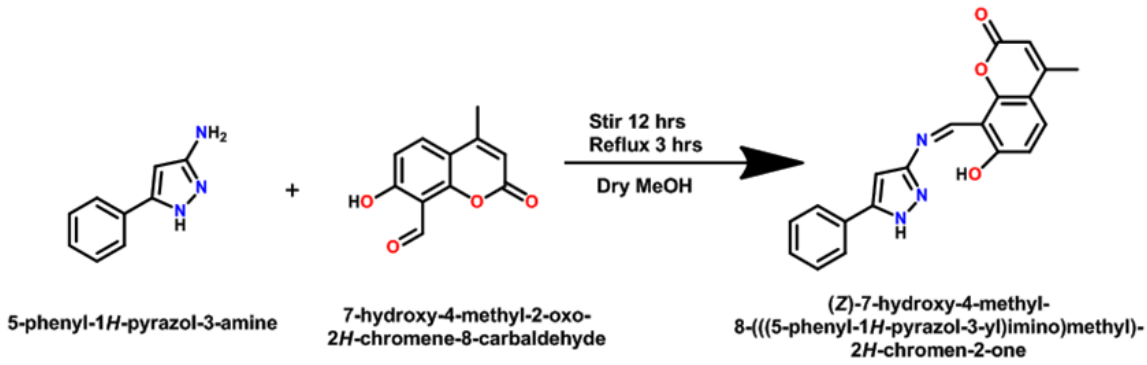

Scheme I.1.6.c. Synthesis of Ligand

Chapter 5: Schiff's Molecule based on napthyl derivative 1-[(2-Hydroxy-4,6-dimethoxy-benzylidene)-hydrazonomethyl]-naphthalen-2-ol has been reported in this work. The probe synthesized by simplest C=N imine condensation approach has been structurally validated through different spectroscopic techniques. **(Scheme I.6.d)**

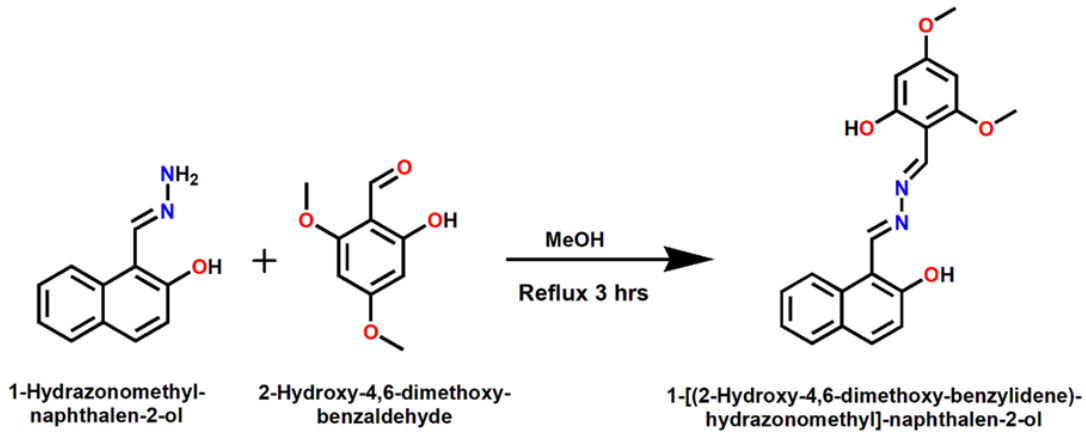

Scheme I.6.d Synthesis of Ligand

Chapter 6: Coumarin-pyridine pendant Schiff base ligand 7-[(Pyridin-4-ylmethylene)-amino]-chromen-2-one synthesized and characterized for the implementation of Zn based coordination polymer. **(Scheme I.6.e)**

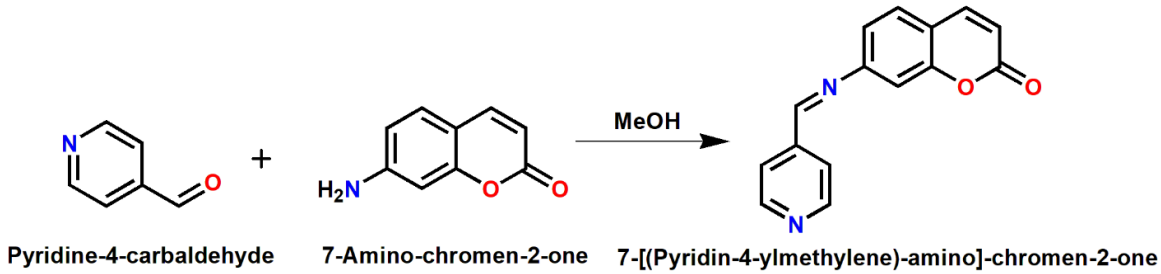

Scheme I.6.e. Synthesis of Ligand

I.7. Physical measurement:

(i) ***Elemental analysis*****:** Microanalytical data (C, H, N) were collected on Perkin Elmer 2400 Series-II CHN analyzer, USA elemental analyzer using the pure solid sample.

(ii) ***FT-IR spectra*****:** FT-IR spectra (4000–400 cm^{-1}) by Perkin Elmer LX-1 FTIR and LITA FT-IR spectrophotometer with samples.

(iii) ***UV-Vis spectra*****:** UV-Vis spectra were recorded by Perkin Elmer UV-Vis spectrophotometer with model Lambda 25 using the solution as required concentration. Solution will be kept in a quartz cell with 1 cm path length and absorption spectra were recorded starting from visible to UV region.

(iv) ***^{1}H NMR spectra*****:** ^{1}H NMR spectra were taken by Bruker (AC) 300, 400, 500 and 600 MHz FTNMR spectrometer with trimethylsilane (TMS) as internal standard.

(v) ***Single crystal X-ray diffraction study*****:** Single crystals of the ligands and their complexes were obtained by slow evaporation of solvent from solution, or from the diffusion of another solvent into the solution. Data collected on a Bruker SMART Apex CCD area detector by graphite monochromated MoKα radiation with wavelength of 0.71073 Å. X-ray data reduction, structure solution and refinement were done by using ORTEP-32,[209] SHELXL-97,[210] and PLATON-99[211] programs. The structures were solved by direct method.

(vi) ***Mass Spectroscopy*****:** A Water HRMS model XEVO-G2QTOF#YCA351 spectrometer has been used to record ESI mass spectra.

(vii) ***Theory and Computational Methods:*** Optimization of ground-state structures and energy calculations for all the fluorescence probe and their complexes were carried out by DFT (density functional theory) method using the Gaussian 09 package**,** where B3LYP was chosen as the basis function.[212,213] For C, H, N, O 6-311G basis set[214-220] were assigned, while for Zn and Cu the LanL2DZ basis set[221] with effective core potential were employed. Vibrational frequency calculations were performed for confirmation the optimized geometries represent the local minima, and these only yielded positive eigenvalues. Time Dependent Density Functional Theory (TD-DFT) was also performed by the use of conductor-like polarizable continuum model (CPCM),[222-224] from this theoretical UV-Vis spectral transitions are observed. The fraction of contributions of various groups in each molecular orbital were calculated by carrying out GAUSSSUM.[225]

(viii) Live cell imaging: Cell images were taken using fluorescence microscope.

I.8. References:

1. A. B. P. Lever, I. M. Walker, P. J. McCarthy, K. B. Mertes, A. Jircitano, R. Sheldon, *Inorg. Chem.* 1983, **22,** 2252−2258

2. L. Fabbrizzi, *J. Org. Chem.* 2020, **85**, 12212–12226.

3. P. G. Cozzi, *Chem. Soc. Rev.* 2004, **33**, 410–421.

4. M. S. Karthikeyan, D. J. Prasad, B. Poojary, K. S. Bhat, B.S. Holla, N.S. Kumari, Bioorganic Med. Chem. 2006, **14**, 7482–7489.

5. K. Singh, A. Prakash, H.K. Rajour, N. Bhojak, D. Adhikari, *Spectrochim. Acta A Mol. Biomol. Spectrosc.* 2010, **76**, 376–383.

6. A. M. Alafeefy, M. A. Bakht, M. A. Ganaie, M. N. Ansarie, N. N. El-Sayed, A. S. Awaad. *Bioorganic Med. Chem. Lett.* 2015, **25**, 179–183.

7. A. A. Bekhit, H.T.Y. Fahmy, S.A.F. Rostom, A.M. Baraka, *Eur. J. Med. Chem.* 2003, **38**, 27–36.

8. B. M. Sahoo, S. C. Dinda, BVV R. Kumar, J.Panada, *Lett. Drug Des. Discov.* 2014, **11**, 82–89.

9. A. Bacchi, M. Carcelli, P. Pelagatti, G. Pelizzi, M. C. Rodriguez-Arguelles, D. Rogolino, C. Solinas, F. Zani, *J. Inorg. Biochem.* 2005, **99**, 397–408.

10. Y. Liu, L. Yang, D. Yin, Y. Dang, L. Yang, Q. Zou, J. Li, J. Sun, *J. Organomet. Chem.* 2019, **899**, 120903.

11. W. H. Mahmoud, R. G. Deghadi, G. G. Mohamed, *Appl. Organomet. Chem.* 2016, **30**, 221– 230.

12. M. Rao, L. Shadap, V. Banothu, *J. Organomet. Chem.* 2020, 915, 121246.

13. S. Smitha, S. N. Pandeya, J. P. Stables, S. Ganapathy, *Sci. Pharm.* 2008, **76**, 621–636.

14. M. Verma, S. N. Pandeya, K. N. Singh, J. P. Stables, *Acta Pharm.* 2004, **54**, 49–56.

15. S. S. Shah, D. Shah, I. Khan, S. Ahmad, U. Ali, A. U. Rahman, *Biointerface Res. Appl. Chem*. 2020, **10**, 6936–6963.

16. S. Saroya, S. Asija, N. Kumar, Y. Deswal, J. devi, *J. Ind. Chem. Soc.*, 2022, **99**, 100379.

17. B. Iftikhar, K. Javed, M.S.U. Khan, Z. Akhter, B. Mirza, V. Mckee, *J. Mol. Struct.* 2018, **1155**, 337–348.

18. R. V Kupwade, V. J. Sawant, J. Chem. Sci. 2020, **132**, 1–12.

19. I. Ali, L.M.A. Mahmood, Y. T. H. Mehdar, H. Y. Aboul-enein, *Inorg. Chem. Commun*. 2020, **118**, 108004.

20. C. I. David, N. Bhuvanesh, H. Jayaraj, A. Thamilselvan, D. P. devi, A. Abiram, J. Prabhu, and R. Nandhakumar, *ACS Omega* 2020, **5**, 3055−3072.

21. D. Wang, K. Chen, M. Wang, Y. You, X. Zhou, *J. Mol. Struc.* 2021, **1239**, 130486.

22. Z. Shi, Z. Pan, L. Qin, J. Zhou, H. Zheng, *Cryst. Growth Des.* 2017, **17,** 2757-2766.

23. F. Kateshali, S. G. Dogaheh, J. Soleimannejad, A. J. Blake, *Coord. Chem. Rev.* 2020, **419**, 213392.

24. F. Ahmed, B. Dutta, M. H. Mir, *Dalton Trans.* 2021**, 50** , 29-38.

25. B. Dutta, K. Pal, K. Jana, C. Sinha, M. H. Mir, *ChemistrySelect* 2019**,** 4, 9947-9951.

26. G. Givaja, P. A.-Ochoa, Carlos J. G.-García and F. Zamora, *Chem. Soc. Rev.*, 2012, **41**, 115-147

27. M. Constantin, I. Alexandru, The role of sodium in the body, Balneo-Research 2011, **2**, 70-74

28. P. Nandhikonda, M. P. Begaye and M. D. Heagy, *Tetrahedron Lett*., 2009, **50**, 2459–2461.

29. T. Clausen, *Physiol. Rev.*, 2003, **83**, 1269–1324.

30. J. M. Burnell, B. H. Scribner, B. T. Uyeno and M. F. Villamil, *J. Clin. Invest.*, 1956, **35**, 935–939.

31. J. M. Berg, J. L. Tymoczko and L. Stryer, Biochemistry, W. H. Freeman, New York, 5th edn, 2002

32. H.-R. Yu, X.-J. Ju, R. Xie, W. Wang, B. Zhang and L.-Y. Chu, *Anal. Chem.*, 2013, **85**, 6477–6484.

33. N. Singh, N. Kaur, R. C. Mulrooney and J. F. Callan, *Tetrahedron Lett.*, 2008, **49**, 6690–6692.

34. F. H. Nielsen and H. C. Lukaski, *Magnesium Res.*, 2006, **19**, 180–189.

35. J. R. Moll, A. Acharya, J. Gal, A. A. Mir and C. Vinson, *Nucleic Acids Res.*, 2002, **30**, 1240–1246.

36. H. Komatsu, N. Iwasawa, D. Citterio, Y. Suzuki, T. Kubota, K. Tokuno, Y. Kitamura, K. Oka and K. Suzuki, *J. Am. Chem. Soc.*, 2004, **126**, 16353–16360.

37. O. B. Stepura and A. I. Martynow, *Int. J. Cardiol.*, 2009, **134**, 145–147

38. T. Shoda, K. Kikuchi, H. Kojima, Y. Urano, H. Komatsu, K. Suzukic and T. Nagano, *Analyst*, 2003, **128**, 719–723.

39. S. Kim, J. Kim, N. H. Lee, H. H. Jang and M. S. Han, *Chem. Commun*., 2011, **47**, 10299–10301.

40. H. M. Kim and B. R. Cho, *Acc. Chem. Res*., 2009, **42**, 863–872.

41. G. Arena, C. Copat, A. Dimartino, A. Grasso, R. Fallico, et al. *J. Water Health* 2015, **13**, 522–530.

42. D. Rehder, *Metallomics*, 2015, **7**, 730–742.

43. M. J. C. Taylor, J. F. V. Staden. *Analyst*, **119**, 1263-1276.

44. D. Bagchi, S. J. Stohs, B. W. Downs, M. Bagchi, H.G. Prcuss. *Toxicology*, 2012, **180**, 5-22

45. A. K. Singh, V. K. Gupta, B. Gupta, *Anal. Chim. Acta*, 2007, **585**, 171-178.

46. J. Mao, L. Wang, W. Dou, X. Tang, Y. Yan, W. Liu. *Org. Lett.*, 2007, **9**, 4567-4570

47. J.B. Vincent. *Nutr. Rev.*, 2000, **58**, 67-72.

48. D. Li, C.-Y. Li, H.-R.Qi, K.-Y. Tan, Y-F. Li, *Sens. Actuators. B* 2016, **223**, 705–712.

49. H. Arakawa, R. Ahmad, M. Naoui, H. Ali and T. Riahi, *J. Biol. Chem.*, 2000, **275**, 10150–10153.

50. X. Hu, X. Zhang, G. He, C. He, C. Duan. Tetrahedron, 2011, **67**, 1091-1095.

51. N. Hayakawa, S. Asayama, Y. Noda, T. Shimizu, H. Kawakami, *Mol. Pharm.* 2012, **9**, 2956–2959.

52. B. Michalke, K. Fernsebner, *J. Trace Elem. Med. Biol.* 2014, **28**, 106–116.

53. V. Raju, R. Selva Kumar, Y. Tharakeswar, S.K. Ashok Kumar. *Inorg. Chim. Acta* 2019, **493**, 49-56.

54. J. H. Lee, A. P. Koretsky, *Curr. Pharm. Biotechnol.* 2004, **5**, 529–537.

55. S. A. Lee, J. J. Lee, G. R. You, Y. W. Choi and C. Kim. *RSC Adv.*, 2015, **5**, 95618-95630

56. A. Luo, H. Wang, Y. Wang, Q. Huang, Q. Zhan. *Spectrochim. Acta A: Mol. and Biomol. Spec.* 2016, **168**, 37-44

57. S. Sen, S. Sarkar, B. Chattopadhyay, A. Moirangthem, A. Basu, K. Dhara and P. Chattopadhyay *Analyst*, 2012, **137**, 3335-3342

58. J. Hofmann, V. Watson, B. Scharaw, *Environ. Earth. Sci* 2014, **73**, 629-648.

59. S. Okamoto, L.D. Eltis, *Metallomics* 2011, **3**, 963–970.

60. B. E. Kim, T. Nevitt, D.J. Thiele, *Nat. Chem. Biol.* 2008, **4**, 176–185.

61. Y. J. Na, Y. W. Choi, G. R. You, C. Kim. *Sens. Actuators B* 2016, **223**, 234–240.

62. W. C. Chan, H. M. Saad, K. S. Sim, V. S. Lee, C. W. Ang, K. Y. Yeong, K. W. Tan. *Spectrochim. Acta A: Mol. and Biomol. Spectrosc.* 2021, **262**, 120099.

63. E. Denkhaus, K. Salnikow, *Crit. Rev. Oncol. Hematol.* 2002, **42**, 35–56.

64. K. Alizadeh, H. Nemati, S. Zohrevand, P. Hashemi, A. Kakanejadifard, M. Shamsipur, M. R. Ganjali and F. Faridbod, *Mater. Sci. Eng. C*, 2013, **33**, 916–922.

65. S. Y. Lee, C. Kim, *Inorg. Chemi. Commun.*, 2017, 77, 6-10.

66. G.-Bi Li, H.-C. Fang, Y.-P. Cai, Z.-Y. Zhou, P. K. Thallapally, and J. Tian *Inorg. Chem.* 2010, **49**, 7241–7243

67. B. Wang, W. Xu, K. Gan, K. Xu, Q. Chen, W. Wei, W. Wu. *Spectrochim. Acta A: Mol. and Biomol. Spectrosc.* 2022, **277**, 121245

68. C. Joel, D. J. Livingston, R. B. Bennie, D. Jeyanthi, R.V. Solomon *J. Photochem. and Photobio A: Chem.* 2022, **423**, 113612

69. P. Srisuwan, A. Sappasombut, W. Thongyod, T. Jantarat,V. Tipmanee, N. Leesakul, D. Sooksawat. *J. Photochem. and Photobio. A: Chem.* 2022, **427**, 113841

70. X. Liu, P. Xu, X. Zhao, J. Ge, C. Huang, W. Zhu, C. Li, L. Du, M. Fang, *Inorg. Chim, Acta* 2019, **495** 118975.

71. H. So, J. B. Chae, C. Kim, *Inorg. Chim, Acta* 492 2019 429 83-90.

72. S. Anbu, A. Paul, K. Surendranath, N. Shaikh, S. Armando J. L.Pombeiro. *Sens. Actuators. B: Chem.* 2021, **337**, 129785.

73. P. Jiang and Z. Guo, *Coord. Chem. Rev.*, 2004, **248**, 205–229.

74. J. M. Berg and Y. Shi, *Science*, 1996, **271**, 1081–1085.

75. C. J. Frederickson, *Int. Rev. Neurobiol.*, 1989, **31**, 145–238.

76. A. Takeda, *BioMetals*, 2001, **14**, 343–351.

77. E. J. Hewitt, *Biol. Rev.*, 1959, **34**, 333–375.

78. E. J. Underwood, Trace Elements in Human and Animal Nutrition, 4th Edn., Academic Press, New York, 1977.

79. M. Sharma, Y. Akhter, S. Chatterjee. *World J Microbiol Biotechnol,* 2019, **35**, 1-14

80. P.G. Rao, B. Saritha, T.S. Rao *J. Photochem. Photobiol.,* A, 2019, **372**, 177-185

81. P.B. Pati. *Sens. Actuators B Chem.,* 2016, **222,** 374-390

82. S. Chakraborty, S. Paul, P. Roy, S. Rayalu. *Inorg. Chem. Commun.,* 2021, **128**, 108562

83. S. Munusamy, S. Swaminathan, D. Jothi, V. P. Muralidharan and S. K. Iyer. *RSC Adv.,* 2021, **11**, 15656-15662.

84. Y. Zhang, Y.Chen, Y. Bai, X. Xue, W. He and Z. Guo. *Analyst,* 2020, **145**, 4233-4238

85. P. Xiao, J. Liu, Z. Wang, F. Tao, L.Yang, G. Yuan, W.Sun and X. Zhang. *Chem. Commun.,* 2021,**57**, 5012-5015.

86. D. A. Jose, R. Sakla, N. Sharma, S. Gadiyaram, R. Kaushik, and A. Ghosh. *ACS Sens.* 2020, **5**, 3365–3391.

87. E. Sundaram, K. L. Servarayan, V. S. Vasantha. *Spectrochimi. Acta A: Mol. and Biomole. Spectrosc.,* 2022, **266**, 120423.

88. S. Wirojsaengthong, D. Aryuwananon, W. Aeungmaitrepiroma, B. Pulpoka, T. Tuntulani. *Talanta.* 2021, **231**, 122371

89. A. Liu, R. Ji, S. Shen, X. Cao and Y. Ge. *New J. Chem.*, 2017, **41**, 10096-10100.

90. G. Xu, H. Wu, X. Liu, R. Feng, Z. Liu. *Dyes and Pigments* 2015, **120**, 322-327.

91. L. Tan, W. Lin, S. Zhu, L. Yuana and K. Zheng. *Org. Biomol. Chem.*, 2014,**12**, 4637-4643.

92. J. Wang, L. Long, X. Xiao. *Luminiscence.,* 2016, **31**, 775-781.

93. R. Sainia and S. Kumar. *RSC Adv.*, 2013, **3**, 21856-21862.

94. Z. Luo, K. Yin, Z. Yu, M. Chen, Y. Li J. Ren. *Spectrochim. Acta A: Mole. and Biomole. Spectrosc*. 2016, **169**, 38-44.

95. B.-Y. Kim, H.-S. Kim, A. Helal. *Sens. Actuators B: Chem*. 2015, **206**, 430-434.

96. M. Torun, A. Bayhan, G. Yenturm. *Clin. Chem.,* 1989, **35**, 1792-1793.

97. C. Dong, Z. Wang, Y. Zhang, X. Ma, M. Z. Iqbal, L. Miao, Z. Zhou, Z. Shen, and A. Wu. *ACS Sens.* 2017, **2**, 1152–1159.

98. Y. Wang, Y. Hu, W. Weng, S. Chang, H. Xu, D. Li, D. Li. *J. Photochem. and Photobio. A: Chem.* 2021, **412**, 113234.

99. L. S. Mittal, P. Sharma, N. Kaur and P. Singh. *Anal. Methods*, 2019, **11**, 5320-5327.

100. W.Du, C. Jia, Y. Zhang, Q. Chen, Y. Wang, Y. Huang and Q. Zhang. *Anal. Methods*, 2018, **10**, 1993-1998.

101. S. K. Asthana, A. Pandey, A. Kumar and K. K. Upadhyay. *New J. Chem.*, 2020, **44**, 2201-2205.

102. C. H. Santos, N. M. Uchiyama, I. A. Bagatin. *Spectrochim. Acta A: Mole. and Biomole. Spectrosco.* 2019, **210**, 355-361.

103. P. Kumar, S. Pachisia and R. Gupta. *Inorg. Chem. Front.*, 2021, **8**, 3587-3607

104. S. Jiang, J. Qiu, S. Chen, H. Guo, F. Yang. *Spectrochim. Acta A: Mole. and Biomole. Spectrosco.* 2020, **227**, 117568

105. D. Bansal and R. Gupta. *Dalton Trans.*, 2019, **48**, 14737-14747.

106. T. J. D. W. Sweeney, G. V. Granade, M. G. Eversmeyer, D. A. Whitney. *J. Plant Nutr.*, 23 2000, 23, 1267-1281.

107. Jentsch, V. Stein, F. Weinreich, A. A. Zdebik. *Physiol Rev.*, 2002, **82**, 503-568.

108. S. I. Reja, V. Bhalla, A. Sharma, G. Kaur and M. Kumar. *Chem. Commun.*, 2014, **50**, 11911-11914.

109. C. Maa, G. Zhong, Y. Zhao, P. Zhang, Y. Fu, B. Shen. *Spectrochim. Acta A: Mole. and Biomole. Spectrosco.* 2020, 240, 118545

110. N. Kwon, Y. Chen, X. Chen, M. H. Kim, J. Yoon. *Dyes and Pigments* 2022, **200**, 110132.

111. P. Chen, Z. Zheng, Y. Zhu, Y. Dong, F. Wang, and G. Liang. *Anal. Chem.* 2017, **89**, 5693–5696.

112. Y. Sun, C. Liu, X. Jiao, Y. Shang, X. Zeng, L. Zhao, J. Zhao. *J. Mole. Struct.* 2021, **1227**, 129523.

113. A. Dhillon, M. Nair and D. Kumar. *Anal. Methods* 2016, **8**, 5338-5352.

114. D. Udhayakumari. *Spectrochim. Acta A: Mole. and Biomole. Spectrosco.* 2020, **228**, 117817

115. Y. G. Ko, Mayank, N. Singh, D. O. Jang. *Tetrahedron Letters*, 2018, **59** , 3839-3844.

116. L.-R Lina, W. Fang,Y. Yub, R.-B. Huang, L.-S. Zheng. *Spectrochim. Acta A Mol. and Biomole. Spectrosco.* 2007, **67**, 1403-1406.

117. X. Wang, C. Zhang, L. Feng, L. Zhang. *Sens. Actuators B: Chem.* 2011, **156**, 463-466.

118. A. Thakur, S. R. Bhatta, B. Mondal, D. Kakash, P. Chawla. *Sens. Actuators B: Chem*. 2018, **267**, 617-626.

119. C.-X. Jiao, C.-G. Niu, S.-Y.Huan, Q. S. Y. Yang, G.-L. Shen, R.-Q. Yu. *Talanta* 2004, **64**, 637-643.

120. K. S. Abou-Melha. *ChemistrySelect*, 2020, **5**, 6216-6223.

121. L. Wang, B. Lia, L. Zhang, L. Zhang, H. Zhao. *Sens. Actuators B: Chem.* 2012, **171-172**, 946-953.

122. L. Yang, F. Wang, J. Zhao, X. Kong, K. Lu, M. Yang, J. Zhang, Z. Sun, J. You. *Talanta* 2021, **221**, 121477.

123. Y. Yang, S. Chen, and X.-L. Ni. *Anal. Chem.* 2015, **87**, 7461–7466

124. H. Tavallali, G. D. Rad, A. Parhami, S. Lohrasbi. *Talanta*, 2016, **149**, 168-177.

125. A. Ghorai, J. Mondal, R. Chandra and G. K. Patra. *RSC Adv.*, 2016, **6**, 72185-72192

126. Ş. N. K. Elmas, F. Ozen, K. Koran, A. O. Gorgulu, G. Sadid, I. Yilmaza, S. Erdemir. *Talanta* 2018, **188**, 614-622

127. M. Kumar and A. Puri. *Indian J. Occup. Environ. Med.*, 2012, **16**, 40–44.

128. S. Das, A. Ghosh, S. Kundu, S. Saha, H.S. Sarkar, P. Sahoo. *Anal. Bioanal. Chem*, 2019, 411, 6203-6212

129. Z. Tang, T. Bai, and P. Zhou. *J. Phys. Chem. A* 2020, **124**, 6920–6927

130. P. Zhang, Y. Xiao, Q. Zhang , Z. Zhang , H. Yu and C. Ding. *New J. Chem.*, 2019, **43**, 7620-7627

131. Y.-F. Li, C.-Y. Li, F. Xu, Y. Zhou, Q.-C. Xiao. *Sens. Actuators B: Chem.* 2011, **155**, 253-257.

132. C. E. Paulsen, K. S. Carroll. *Chem. Rev.*, 2013, **113**, 4633-4679.

133. J. Duperray, R. Sergheraert, K. Chalothorn, P. Tachalerdmanee, F. Perin. *J. Cosmet. Dermatol.* 2022, **21**, 802-813.

134. Y. Yue, F. Huo, P. Ning, Y. Zhang, J. Chao, X. Meng, C. Yin. *JACS*, 2017, **139**, 3181-3185

135. C. Milanese, C. Payán-Gómez, P.G. Mastroberardino. *Curr. Opin. Physiol.*, 2019, **9**, 73-78.

136. S. Lee, S. H. Kim, S. Lee, Y. Lee, Y. S. Lee, K. H. Yang, K.-K.Wang, W.-S. Hana. *Dyes and Pigments* 2021, **194**, 109613.

137. J. V. L. S. Néto, R. I. Teixeir, R. B. da Silva, N. C. de Lucas, S. J. Garden. *Dyes and Pigments* 2021, **193**, 109536

138. X. Niu, H. Zhang, X. Wu, S. Zhu, H. Feng, W. Liu. *J. Mol. Struct.* 2022, **1259**, 132754.

139. Y. Chen, B. Bai, Q. Chai, M. Zhang, J. Wei, H. Wang and M. Li. *Soft Matt*, 2019, **15**, 6690-6695.

140. Y. Zhan, P. Yang, G. Li, Y. Zhang and Y. Bao. *New J. Chem.*, 2017, **41**, 263-270.

141. K. R. Solomon, G. J. M. Velders, S. R. Wilson, S. Madronich, J. Longstreth, J. Aucamp, J. F. Bornman. *J. Toxicol. Environ. Health B Crit. Rev*, 2016, **19**, 289-304.

142. K. Pomazal, C. Prohaska, I. Steffan, G. Reich and J. F. K. Huber, *Analyst*, 1999, **124**, 657–663.

143. P. Vanloot, B. Coulomb, C. Brach-Papa, M. Sergent and J. L. Boudenne, *Chemosphere*, 2007, **69**, 1351–1360.

144. C. M. G. Berg, *Anal. Chem.*, 2006, **78**, 156–163.

145. G. Cerchiaro, T. M. Manieri and F. R. Bertuchi, *Metallomics*, 2013, **5**, 1336–1345.

146. A. A. Ammann, *J. Mass Spectrom.*, 2007, **42**, 419–427.

147. T. Shamspur, I. Sheikhshoaie and M. H. Mashhadizadeh, *J. Anal. At. Spectrom.*, 2005, **20**, 476–478.

148. H. A. McIlwee, C. L. Schauer, V. G. Praig, R. Boukherroub and S. Szunerits, *Analyst*, 2008, **133**, 673–677.

149. T. I. Nasution, I. Nainggolan, D. Dalimunthe, M. Balyan, R. Cuana and S. Khanifah, *IOP Conf. Ser.: Mater. Sci. Eng.*, 2018, **309**, 012080.

150. V. N. Mehta, S. K. Kailasa and H. F. Wu, *New J. Chem.*, 2014, **38**, 1503–1511.

151. Z. Z. Yin, Y. Li, L. P. Jiang, R. K. Rana and J. J. Zhu, *Anal. Chim. Acta*, 2013, **781**, 48-53.

152. Cammann, G. G.; Guilbault, E. A.; Hal, H.; Kellner, R.; Wolfbeis, O. S. The Cambridge Definition of Chemical Sensors, Cambridge Workshop on Chemical Sensors and Biosensors; Cambridge University Press: New York, 1996.

153. R. A. Marcus, *Angew. Chem. Int. Edit.*, 1993, **32**, 1111–1121.

154. T. Iijima, A. Momotake, Y. Shinohara, T. Sato, Y. Nishimura and T. Arai, *J. Phys. Chem. A*, 2010, **114**, 1603–1609

155. Y. Jiao, B. Zhu, J. Chen and X. Duan, *Theranostics*, 2015, **5**, 173–187.

156. M. A. Rizzo, G. H. Springer, B. Granada and D. W. Piston, *Nat. Biotechnol.*, 2004, **22**, 445–449.

157. W. M. Shih, Z. Gryczynski, J. R. Lakowicz and J. A. Spudich, *Cell*, 2000, **102**, 683–694.

158. P. Li, X. Zhou, R. Huang, L. Yang, X. Tang, W. Dou, Q. Zhaoa and W. Liu, *Dalton Trans.*, 2014, **43**, 706–713.

159. S. Erdemir, S. Malkondu. *Sens. Actuators B*, 2013, **188**, 1225– 1229.

160. L. Wang, X.Yang, X. Chen, Y. Zhou, X. Lu, C. Yan, Y. Xu, R. Liu, J. Qu. *Materials Science and Engineering C* 2017, **72**, 551–557.

161. S. Erdemir. *Sens. Actuators: B Chem.*, 2019, **290**, 558–564

162. F. Kolcu, D. Erdener, İ. Kaya. *Inorg. Chim. Acta* 2020, **509**, 119676

163. X. Wang, G. Ding, Y. Duan, Y. Zhu, G. Zhu, M. Wang, X. Lia, Y. Zhang, X. Qin, C.-H. Hung. *Talanta* 2020, **217**, 121029.

164. Y.-l. Mu, C.-j. Zhang, Z.-l. Gao, X. Zhang, Q. Lu, J.-s. Yao, S. Xing. *Synthetic Metals* 2020, **262**, 116334.

165. D. Wang, Q. Yin, M. Zheng, Y. Xie, W. He, Z. Li, S. Hou, H. Wang. *Spectrochim. Acta A* 2021, **251**, 119480.

166. Y. Liu, J. S. Du, S. Qi, L. Zhu, Q. Yang, H. Xu, Y. Li. *Luminescence.* 2020, **36**, 336-344.

167. Y. B. Barot, V. Anand, R. Mishra. *J. Photochem. & Photobio. A: Chem.* 2022, **426** 113785.

168. D. Mohanasundaram, R. Bhaskar, N. Lenin, K. Nehru, G. Rajagopal, G. G. V. Kumar, J. Rajesh. *J. Photochem. & Photobio. A: Chem.* 2022, **427,** 113850.

169. B. Sen, S. K. Sheet, R. Thounaojamb, R. Jamatia, A. K. Pal, K. Aguan, S. Khatua. *Spectrochim. Acta A: Mol. Biomol. Spectrosc.* 2017, **173**, 537–543.

170. S. Wang, Z. Wang, Y. Yin, J. Luo, L. Kong *J. Photochem. Photobio. A: Chem.* 2017, **333**, 213–219.

171. M. Chemchem, I. Yahaya, B. Aydıner, N. Seferoglu, O. Doluca, N. Merabet, Z. Seferoglu. *Tetrahedron* 2018, **74**, 6897-6906.

172. Y. Tang, Y. Huang, Y. Chena, L. Lu, C. Wang, T. Suna, M. Wang, G. Zhu, Y. Yang, L. Zhang, J. Zhu. *Spectrochim. Acta A: Mol. Biomol. Spectrosc* 2019, **218**, 359–365.

173. K. Yao, Y. Chang, B. Li, H. Yang, K. *Spectrochim. Acta A: Mol. Biomol. Spectrosc* Xu. 2019, **216**, 385–394.

174. R. Purkait, A. Dey, S. Dey, P. P. Ray and C. Sinha. *New J. Chem.*, 2019, **43**, 14979.

175. Y. Wang, X. Hao, L. Liang, L. Gao, X. Ren, Y. Wua and H. Zhao. *RSC Adv.*, 2020, **10**, 6109.

176. S. Muthusamy, K. Rajalakshmi, D. Zhu, W. Zhu, S. Wang, K.-B. Lee, H. Xu, L. Zhao. *Sens. Actuators B Chem.* 2021, **346**, 130534.

177. A. K. K. Bhasin, P. Chauhan, S. Chaudhary. *Sens. Actuators B Chem.* 2021, **330**, 129328.

178. S. N. K. Elmas. *Inorg. Chim. Acta.* 2022, **573**, 120953.

179. A. Dhara, N. Guchhait, I. Mukherjee, A. Mukherjee and S. C. Bhattacharya. *RSC Adv.*, 2016, **6**, 105930.

180. F. Wang, H. Duan, D. Xing, G. Yang. J. Fluoresc., 2017, **27**, 1721–1727.

181. N. Nayak, K. S. Prasad, R. R. Pillai, S. Armakovi´c and S. J. Armakovi´c. *RSC Adv.*, 2018, 8, 18023.

182. W. Gao, Y. Zhang, H. Li, S. Pu. *Tetrahedron*, 2018, **74**, 6299-6309.

183. Y. Wang, Y.-F. Song, L. Zhang, G.-G. Daia, R.-F. Kanga, W.-N Wua, Z.-H. Xu, Y.-C. Fan, L.-Y. Bian. *Talanta*, 2019, **203**, 178–185.

184. J. S. Ganesan, M. Sepperumal, B. Ashokkumar, S. Ayyanar. *Spectrochim. Acta A: Mol. Biomol. Spectrosc* 2020, **230**, 117993.

185. B. Das, M.Dolai, A. Ghosh, A. Dhara, A. D. Mahapatra, D. Chattopadhyay, S. Mabhai, A. Jana, S. Dey and A Misra. *Anal.Methods*, 2021, **13,** 4266.

186. Sayan Saha, A. De, A. Ghosh, A. Ghosh, K. Bera, K. S. Das, S. Akhtar, N. C. Maiti, A. K. Das, B. B. Das and R. Mondal. *RSC Adv*., 2021, **11**, 10094.

187. R. Bawa, N. Deswal, S. Negi, M. Dalela, A. Kumar and R. Kumar. *RSC Adv*., 2022, **12**, 11942.

188. Q. Huang, L Zhang, J. Liu, T. Liu, G. Li, W. Wu, T. Ren. *J. Mol. Struct.* 2022, **1263** 133119.

189. M. Iniya, D. Jeyanthi, K. Krishnaveni, D. Chellappa. *J. Lumin*,. 2015, **157**, 383–389.

190. H. Liu, B. Zhang, C. Tan, F. Liu, J. Cao, Y. Tan, Y. Jiang. *Talanta*, 2016, **161**, 309–319.

191. Y. S. Kim, J. J. Lee, S. Y. Lee, T. G. Jo and C. Kim. *RSC Adv.*, 2016, **6**, 61505.

192. Y. Gao, C. Zhang, S. Peng, H. Chen, *Sens. Actuators B Chem.,* 2017, **238**, 455–461.

193. E. Horak, R. Vianello, M. Hranjec and I. M. Steinberg. *Supramol. Chem.*, **30**, 891-900.

194. S. Ta, S. Das, M.Ghosh, M. Banerjee, S. K. Hira, P. P. Manna, D. Das. *Spectrochim. Acta A: Mol. Biomol. Spectrosc* 2019, **209**, 170-185.

195. G. R. Suman, S. G. Bubbly, S. B. Gudennavar, V. Gayathri. *J. Photochem. & Photobio. A: Chem.* 2019, **382**, 111947.

196. W.-W. Wang, Y. Wang, W.-N. Wu, X.-L. Zhao, Z.-Q. Xu, Z.-H. Xu, X.-X. Li, Y.-C. Fan. *Spectrochim. Acta A: Mol. Biomol. Spectrosc*. 2020, 226, 117592.

197. S. Anbu, A. Paul, K. Surendranath, N. S. Solaiman, A. J. L. Pombeiro. *Sens. Actuators B Chem.,* 2021, **337**, 129785.

198. D. Jeyanthi, C. Joel, R. B. Bennie, D. J. Livingston, C. Balakrishnan. *J. Photochem. & Photobio. A: Chem.* 2022, **430**, 113950.

199. A. Roy, S. Dey, S. Halder, P. Roy. *J. Lumin.* 2017, **192**, 504-512.

200. L. Xing, X. Zheng,W. Sun, H. Yuan, L. Hu, Z. Yan. *Spectrochim. Acta A: Mol. Biomol. Spectrosc* 2018, **203**, 455–460

201. M. Zhang, L. Gong, C. Sun, W. Li, Z. Chang, D. Qi. *Spectrochim. Acta A: Mol. Biomol. Spectrosc.,* 2019, **412,** 7-13.

202. S. Dey, R. Purkait, K. Pal, K. Jana, and C. Sinha. *ACS Omega* 2019, **4**, 8451−8464.

203. W. A. Durai, A. Ramu, A. Dhakshinamoorthy. *Inorg. Chem. Commun.* 2020, **121,** 108191.

204. B. Kaur, A. Gupta, N. Kaur. *J. Photochem. & Photobio. A: Chem.* 2020, **389**, 112140.

205. S. Erdemir, S. Malkondu and S. Kararkurt. *Analyst*, 2020,**145**, 3725-3731.

206. G.-H. Liu, Z.-Z. Chen, Y.-H. Deng, W.-K. Dong. *J. Photochem. & Photobio. A: Chem.* 2021, **414**, 113271.

207. A. Das, S. De, G. Das. *J. Photochem. & Photobio. A: Chem.* 2021, **418**, 113442.

208. B. Musikavanhu, Y. Zhang, D. Zhu, Z. Xu, R. Yuan, S. Wang, L. Zhao. *Spectrochim. Acta A: Mol. Biomol. Spectrosc.*, 2022, **281**, 121599.

209. L. J. Farrugia, *J. Appl. Crystallogr.*, 1997, **30**, 565−565.

210. G. M. Sheldrick, *Acta Crystallogr., Sect. A: Found. Crystallogr.*, 2008, **64**, 112−122.

211. A. L. Spek, *J. Appl. Cryst.*, 2003, **36**, 7−13.

212. M. J. Frisch, G. W. Trucks, H. B. Schlegel, P. M. W. Gill, B. G. Johnson, M. A. Robb, J. R. Cheeseman, T. A. Keith, G. A. Petersson, J. A. Montgomery, K. Raghavachari, M. A. Al-Laham, V. G. Zakrzewski, J. V. Ortiz, J. B. Foresman, J. Cioslowski, B. B. Stefanov, A. Nanayakkara, M. Challacombe, C. Y. Peng, P. Y. Ayala, W. Chen, M. W. Wong, J. L. Andres, E. S. Replogle, R. Gomperts, R. L. Martin, D. J. Fox,

J. S. Binkley, D. J. Defrees, J. Baker, J. P. Stewart, M. Head-Gordon, C. Gonzalez, J. A. Pople, Gaussian 98, Gaussian Inc. Pittsburgh, PA, (**1998**).

213. C. Lee, W. Yang and R. G. Parr, *Phys. Rev. B*, 1988, **37**, 785–789.

214. H. G. Korth, M. I. De Heer and P. Mulder, *J. Phys. Chem. A*, 2002, **106**, 8779–8789.

215. B. G. Johnson, P. M. W. Gill and J. A. Pople, *J. Chem. Phys.*, 1993, **98**, 5612–5626.

216. P. K. Chowdhury, *J. Phys. Chem. A*, 2003, **107**, 5692–5696.

217. V. Chis, *Chem. Phys.*, 2004, **300**, 1–11.

218. A. Asensio, N. Kobko and J. J. Dannenberg, *J. Phys. Chem. A*, 2003, **107**, 6441–6443.

219. A. Müller, M. Losada and S. Leutwyler, *J. Phys. Chem. A*, 2004, **108**, 157–165.

220. N. S. Goncalves, R.Cristiano, M. G. Pizzolatti and F.da Silva Miranda, *J. Mol. Struct.*, 2005, **733**, 53–61.

221. P. J. Hay and W. R. Wadt, *J. Chem. Phys.*, 1985, **82**, 270–283.

222. A. D. Becke, *J. Chem. Phys.*, 1993, **98**, 5648–5652.

223. M. Cossi and V. Barone, *J. Chem. Phys.*, 2001, **115**, 4708–4717.

224. M. Cossi, N. Rega, G. Scalmani and V. Barone, *J. Comput. Chem.*, 2003, **24**, 669–681.

225. N. M. O'Boyle, A. L. Tenderholt and K. M. Langner, *J. Comput. Chem.*, 2008, **29**, 839–845.

Chapter II

A Fluorogenic Triphenyl-Amine-Naphthyl-Hydrazide Probe Selective for Cu^{2+} and Cysteine Detection via an ON-OFF-ON Logic path with Real Applications.

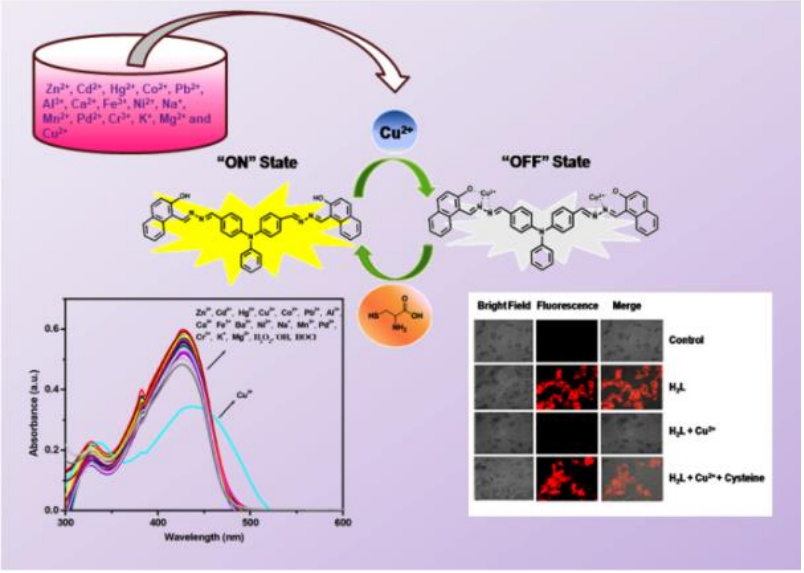

CHAPTER II

Abstract

This Chapter deals with the hydrazide based probe which is 1,1'-((1E,1'E)-((2E,2'E)(((phenylazanediyl)bis(4,1-phenylene))bis-(methanylylidene))bis-(hydrazine-2,1-diylidene))bis(methanylylidene))bis(naphthalen-2-ol), H_2L which shows high fluorescence emission (λ_{em}, 550 nm; λ_{abs}, 420 nm) and gets selectively quenched by Cu^{2+} in presence of many other biologically important ions. The limit of detection (LOD), 7.3 nM is much lower than WHO recommended maximum permissible limit (20 μM) of Cu^{2+}consumption in human body. The binding fashion of the probe to Cu^{2+} ion is 1:2 mole ratios and has been confirmed by Job's plot and ESI-MS spectral data. The binding constant for Cu^{2+} is 4.93 × 10^{-10} M^{-2} which also indicates sufficient stability and 1:2 complexations. On addition of cysteine to L-Cu^{2+}ensemble, the emission intensity (550 nm) enhances which accounts the release of Cu^{2+} from the non-emissive complex and restores the total fluorogenic efficiency of probe, H_2L (LOD (Cysteine), 36 nM). Thus, ON-OFF-ON mechanism of H_2L has been utilized for selective and specific detection of Cu^{2+} and Cysteine over several other amino acids. In addition to this, the probe is treated on WI-38 cell line to check cytotoxicity. This chemosensor, H_2L has been successfully applied to examine intracellular trace quantity of Cu^{2+} and Cysteine concentration in Hep G2 Cell lines.

II.1. Introduction

One-third of naturally abundant elements constitute life in different proportions. Amongst nine 3d transition elements, Copper (II) ion occupies the third most abundant transition metal ions in human bodies and plays vibrant roles in many essential physiological processes in organisms. Many biochemical reactions are directly/indirectly regulated by copper such as oxygen transportation by hemocyanin, electron transport redox enzymes, Blue copper protein, lactase, Cytochrome *c* oxidase, superoxide dismutase, ascorbate oxidase, pigmentation of the skin, repairing of connective tissues, etc.[1,2] However, congestion of copper can cause unadorned neurodegenerative diseases such as Alzheimer's, Parkinson's and prion diseases.[3-5] Biological requirement of copper in the normal human body is 15.7 – 23.6 μM.[6] So, a constant monitoring of Cu^{2+}ion concentration in environment and health is very much important. Under the guideline of US Environmental Protection Agency (EPA) the maximum permissible limit of Cu^{2+} ion concentration in drinking water is 1.3 ppm (20 μM).[7] For these reasons, considerable efforts have been devoted to the development of analytical techniques for the accurate and precise measurements of copper in the consumed items and body organs. Therefore a facile analytical method for specific and sensitive detection for Cu^{2+} must be developed. Spectrofluorometric method is more convenient and approachable for detection of ions and molecules by qualitative and quantitative analysis owing to their interesting features such as easy modification, simplicity, cost effective and time saving over various known techniques such as redox titration, complexometric titrations, atomic absorption spectrometry,[8] inductively coupled plasma mass spectroscopy (ICPMS),[9] inductively coupled plasma–atomic emission spectrometry (ICPAES), and voltammetry which requires a much more costly and sophisticated management.[10,11] Design of chemosensors aimed at detection of ions and molecules are increasingly drawing attention in different fields of science and technology.[12,13] Chemosensors based on Schiff base scaffold with Coumarin,[14-16] Rhodamine B,[17-19] Fluorescein,[20] Pyrrole,[21] derivatives has been used for Cu^{2+} detection.

Biothiols mainly Cysteine (Cys), Homocysteine (Hcy) and Glutathione (GSH) play a prominent role in various cellular processes. Cysteine one of the essential thiol containing amino acids serves as building block of protein

synthesis and helps in detoxification and metabolism of living systems.[22] Free intracellular concentration of cysteine in human body is of the order 20-300 μM.[23] Scarcity in the level of cellular Cys could induce diseases such as retarded growth, fat loss, lethargy, skin lesions and hematopiesis decrease.[24-28] On the other hand an increase in Cys concentration would lead to neurotoxicity.[29,30] A balanced concentration and important role of cysteine in living system leads to monitoring and detection of cysteine essential for human health concern. An effective method for detection and discrimination of Cys amongst various others biothiols and amino acids is quite challenging and much more essential as it would help in better understanding of its role in physiological system and early diagonisis of its related disease.

Recent works focused on designing chemosensors which includes metal complex as well as organic fluorophores for specific detection of Cys where the functional unit of the probes interacts with the thiol group of Cys which enables for selective response towards Cys sensing. Different chemosensors responds towards Cys sensing through different reaction mechanism such as nucleophilic aromatic substitution,[31,32] addition,[33] intramolecular reaarangement,[34,35] and displacement approach.[36] Based on the displacement approach, the probe has been developed for detection of Cys.

In this work, we report a Schiff base probe obtained by linking two units namely 1-(hydrazonomethyl)naphthalene-2-ol and 4,4'-diformyl triphenylamine. Details of probe characterization, spectral studies along with the theoretical computation has been reported in this work. The strong emissive nature of the ligand is distinctive for Cu^{2+} amongst all other competitive cations in the solution phase. The sensing is analyzed through “turn-off” fluorescence of probe on interaction with selectively Cu^{2+} ion in the solution state. The non-fluorescent L-Cu^{2+} in presence of Cysteine leads to decomplexation of Cu^{2+} from H_2L resulting in “turn on” fluorescence approach for detection of Cys as well as in cellular level. A MTT assay for the probe and Cell-imaging were done for the highly fluorescent probe H_2L along with intracellular detection of Cu^{2+} and Cys in HepG2 cell line. Increase or decrease of biologically relevant ion and molecular concentration from a permissible limit in cells is toxic and sometimes fatal. Hence, determination of ion and

molecule concentration in trace level is a challenging task. Herein, we report a system which detects Cu^{2+} and Cysteine (Cys) with a very low detection limit.

II.2. Experimental section

II.2.1 Materials and methods

All the reagents of analytical grade (A.R) were collected from the commercial suppliers and used without further purification. 2-Hydroxy-1-napthaldehyde, 4,4'-Diformyltriphenylamine, Hydrazine Hydrate, inorganic salts ($ZnCl_2$, $CdCl_2$, $HgCl_2$, $CuCl_2.2H_2O$, $CoCl_2.6H_2O$, $PbCl_2$, $AlCl_3$, $CaCl_2.6H_2O$, $FeCl_3.6H_2O$, $BaCl_2.2H_2O$, $NiCl_2.6H_2O$, NaCl,$MnCl_2.4H_2O$, $PdCl_2$, $CrCl_3.6H_2O$, KCl, $MgCl_2$,H_2O_2, ·OH, HOCl, $Na_2S_2O_3.5H_2O$, K_3PO_4, NaCl, NaF, NH_4HF_2, KNO_3, KBr, $NaNO_2$, NaN_3, Na_3AsO_4, CH_3COONa, NaAsO2, KIO_3, $Na_4P_2O_7$, KI, Na_2SO_4, Na_2S, $Na_2S_2O_5$, H_2O_2, HOCl) amino acids (Alanine (Ala), Lysine(Lys), Aspartic Acid (Asp), Glutathione(GSH), Cysteine (Cys), HomoCysteine (Hcy), Glutamic Acid (Glu), Glycine(Gly), Histidine (His), Valine(Val), Leucine (Leu), Serine (Ser), Proline (Pro), Methionine (Met)) and organic chemicals were bought from TCI chemicals and Merck. For spectroscopic measurement solvents with spectroscopic grade were used. The solvents were dried by standard procedure[37] for spectroscopic studies. Milli-Q water (Millipore) has been used for preparation of aqueous solutions of metal salts. Perkin-Elmer (2400 Series-II, Perkin Elmer, USA) CHN analyser has been used for elemental analysis purpose. The spectra were recorded by Lambda 25 spectrophotometer: UV-Vis; LS55: fluorescence and LX-1FTIR spectrophotometer: FT-IR spectra (KBr disk, 4000-400 cm^{-1}) on Perkin Elmer instruments. ^{1}H and ^{13}C NMR spectra were taken by Bruker 300 MHz FT-NMR spectrometer. The chemical shift (δ) of the respective NMR spectra were recorded in parts per million (ppm) with respect to trimethylsilane internal standard. ESI-MS spectra were obtained from HRMS spectrometer (model, XEVO-G2QTOF#YCA351). The HPLC system consisted of a Hewlett-Packard quaternary HPLC model HP 1100 series (Hewlett-Packard, Palo Alto, CA), fitted with a Waters μ-Bondapack (Waters Corp., Milford, MA). C18 column (300 × 4.6 mm i.d.). The injection system (Rheodyne) used was a 20 μL sample loop. An HP 1100 series variable-wavelength detector used at a wavelength of 425

nm was used for detection. A Millipore Swinnextype filter (pore size) 0.45 μm) was obtained from Millipore (Bangalore, India).

II.2.2. Synthesis of 1,1'-((1E,1'E)-((2E,2'E)(((phenylazanediyl)bis(4,1-phenylene))bis-(methanylylidene))bis(hydrazine-2,1-diylidene))bis(methanylylidene))bis(naphthalen-2-ol) (H_2L)

1-(Hydrazonomethyl)naphthalene-2-ol was synthesized following the literature procedure.[38] To solution of 1-(hydrazonomethyl)naphthalene-2-ol (0.373 g, 2 mmol) in 10 ml methanol, 4,4'-Diformyltriphenylamine (0.301g, 1mmol) was added slowly and stirred for overnight and the resulting solution was refluxed for 5 h generating an yellow precipitate. The bright yellow precipitate then filtered, washed with cold methanol for several times and dried under vacuum to obtain 1,1'-((1E,1'E)-((2E,2'E)(((phenylazanediyl)bis(4,1-phenylene))bis-(methanylylidene))bis(hydrazine-2,1-diylidene))bis(methanylylidene))bis(naphthalen-2-ol) **(**H_2L**)** with 79% of yield (0.504 g) (**Scheme II.a**). ^{1}HNMR ($CDCl_3$, 300 MHz) δ(ppm): 13.44 (s, 2H, OH), 9.72 (s, 2H, HC=N), 8.65 (s, 2H, CH=N), 8.21(d, 2H, Ar-H), 7.89-7.78(m, 8H, Ar-H), 7.58(d, H, Ar-2H), 7.43-7.37(m, 4H, Ar-H) and 7.28-7.20 (m, 9H, Ar-H) (**Fig. II.1**); ^{13}CNMR ($CDCl_3$ 300 MHz) δ (ppm): 161.13, 160.91, 160.79, 150.01, 146.28, 134.44, 132.84, 129.98, 129.93, 129.22, 128.24, 128.22, 127.89, 126.44, 125.30, 123.71, 123.41, 120.21, 119.28 and 108.48. (**Fig. II.2**); ESI-MS (m/z): 638.2539 for $[M+H]^+$ (Calculated 638.2556) and 639.2458 for $[M+2H]^+$ (Calculated 639.2634)(**Fig. II.3**).IR: 1624-1590 cm^{-1}(C=N stretching), 1467-1416 cm^{-1}(C=C stretching), 1317 cm^{-1}(O-H bending), 1280cm^{-1}(C-N stretching) and1172 cm^{-1}(C-O stretching) (**Fig. II.4**). The product was dissolved and purified using HPLC chromatography showing an intense signal with a retention time of 7.211 min. (**Fig. II.5**).

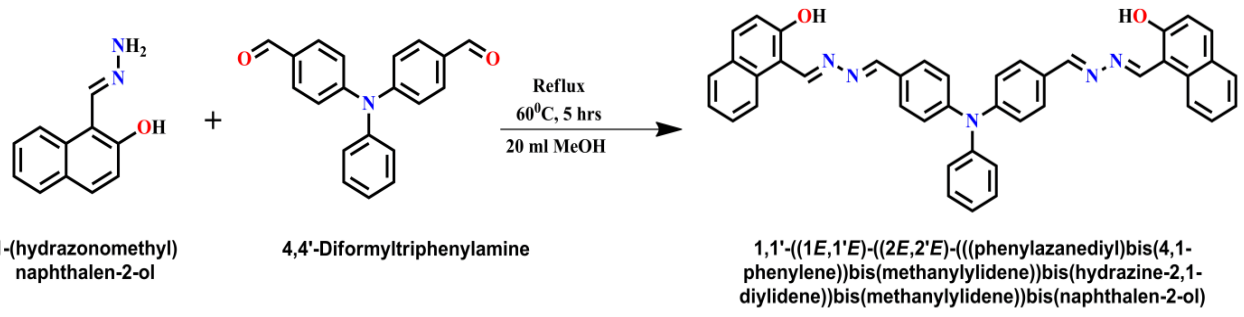

Scheme II.a. Synthesis of Ligand

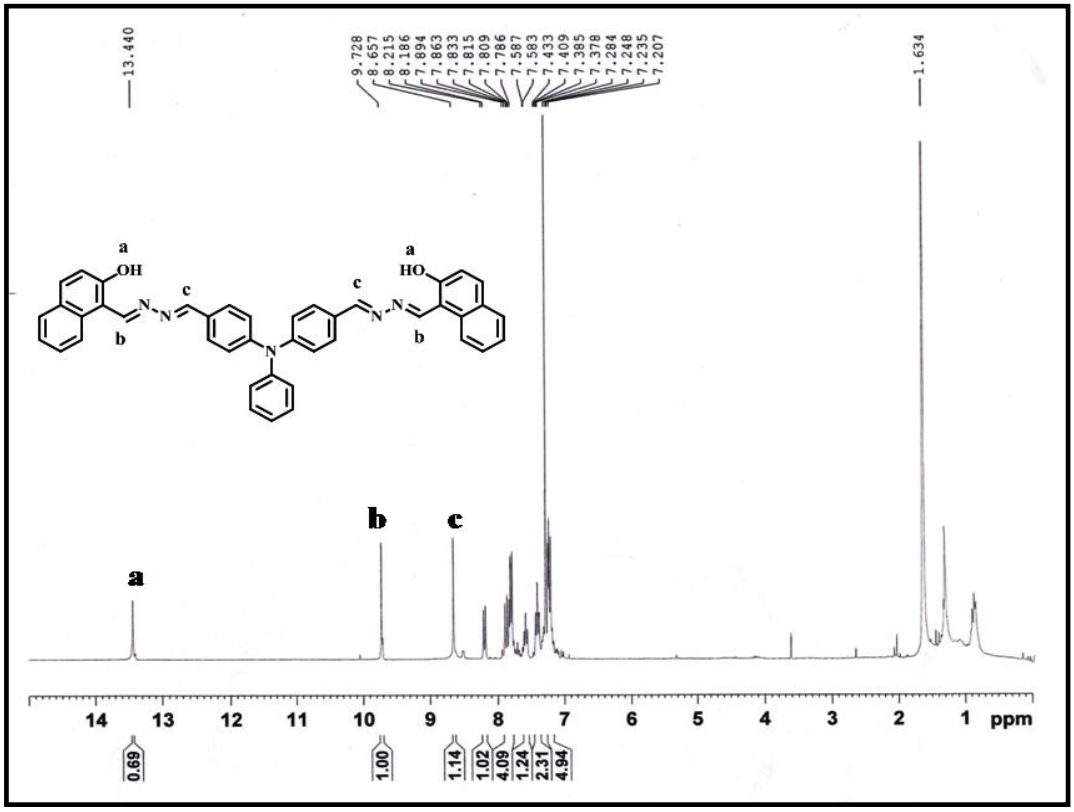

Fig.II.1. ^{1}HNMR Spectrum (300 MHz) of H_2L in $CDCl_3$.

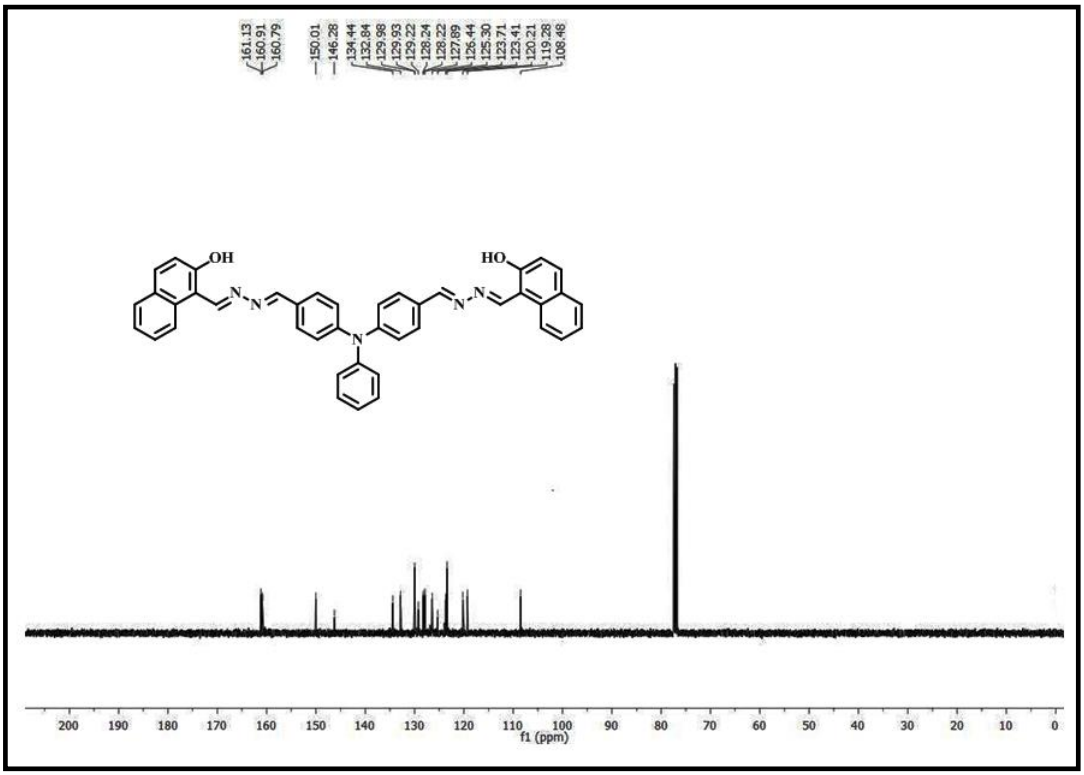

Fig.II.2.^{13}CNMR Spectrum (300 MHz) of H_2L in $CDCl_3$.

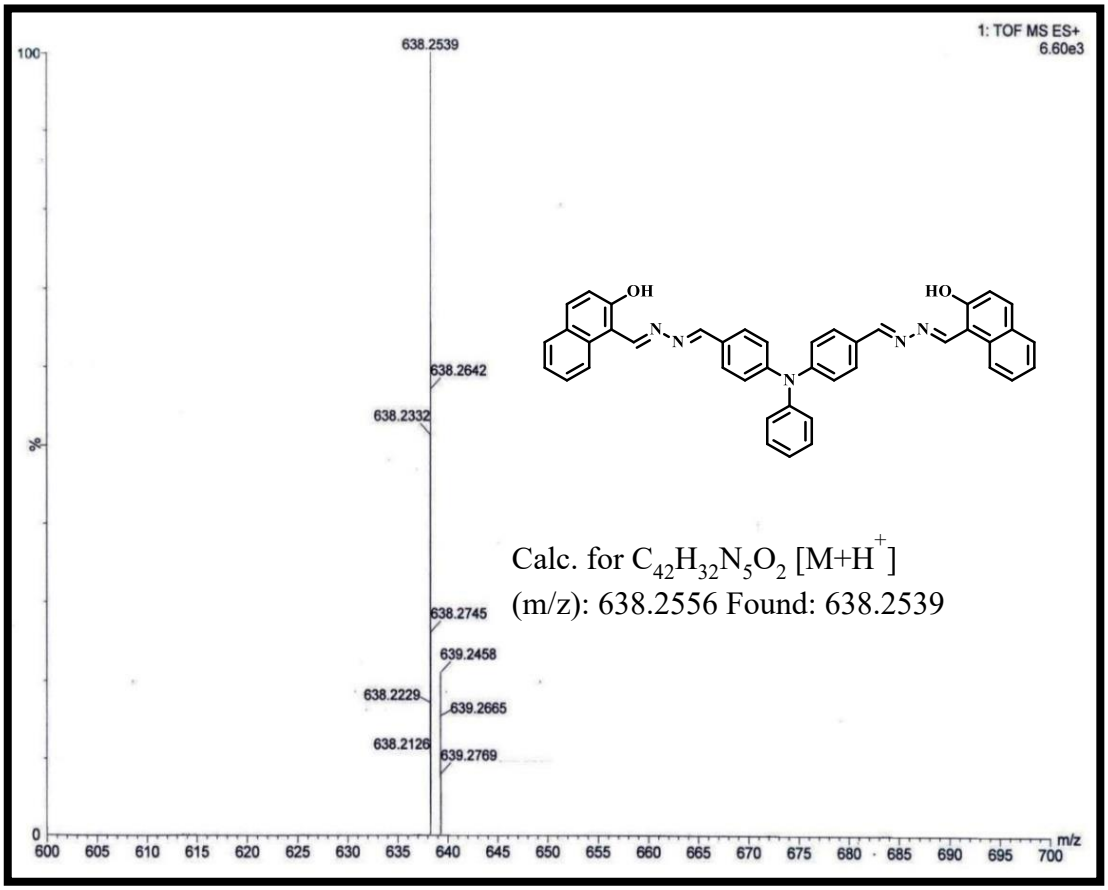

Fig.II.3. ESI-MS spectrum of H_2L.

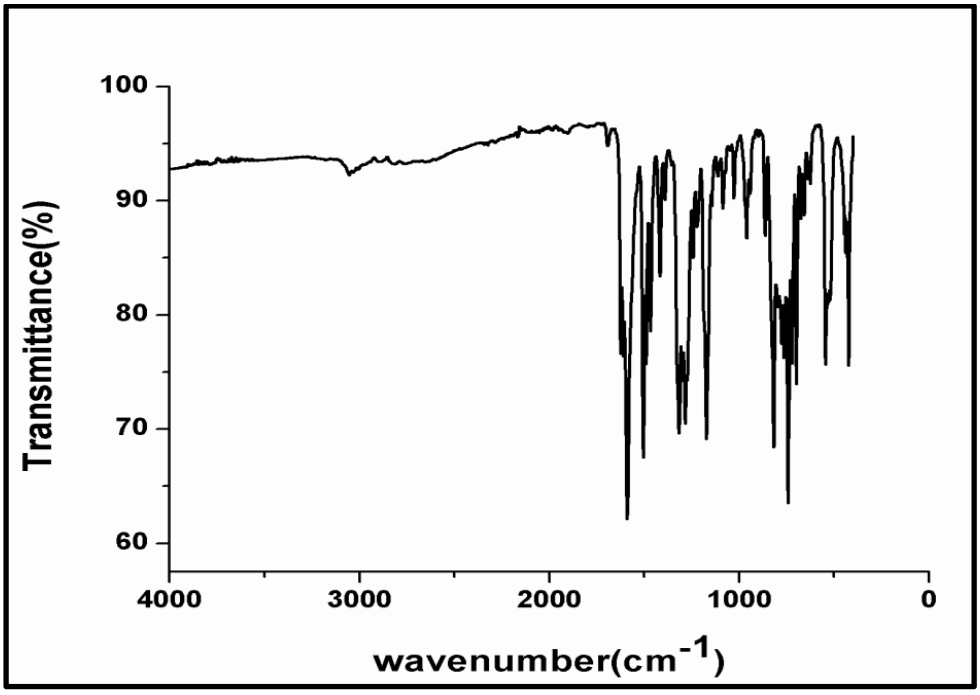

Fig. II.4. IR Spectrum of H_2L.

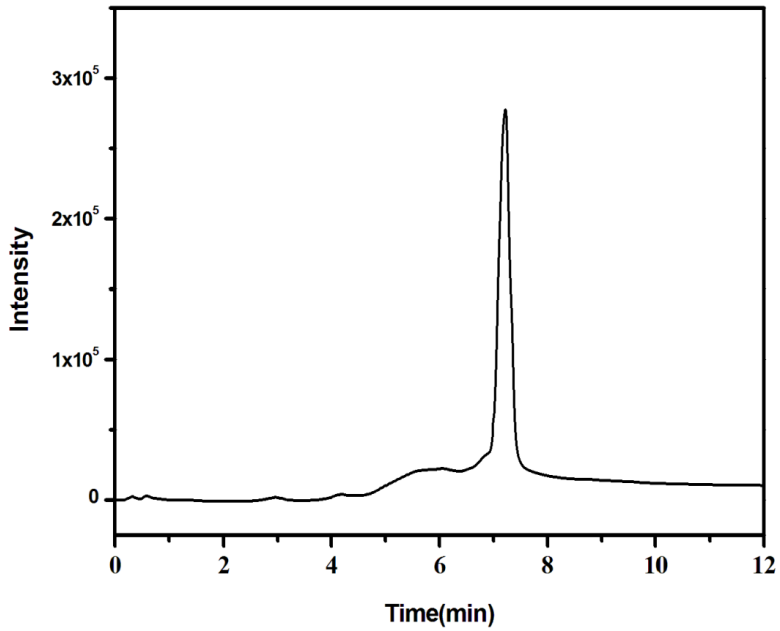

Fig. II.5. HPLC Chromatogram recorded at 254 nm for 2 mL of 10^{-3}(M) solution of H_2L.

II.2.3. Solution Spectral measurements

A stock solution of $H_2L$with concentration 1×10^{-3}M was prepared in DMSO. Stock solutions of all salts and amino acids with 1×10^{-3} M concentration were prepared in deionized water. An aliquot of 20 μL H_2L stock solution was taken in a quarts cuvette and made up to 2mLvolume with 7:3(v/v) CH_3CN:H_2O (HEPES Buffer, pH 7.2) making a concentration of 10μM and with the respective solution the sensitivity and selectivity of the probe was examined. UV-Vis and fluorescence spectral studies of the probe towards metal cation have been conducted with the prepared solution and to the solution a 2.0 equivalent of metal cation was added. Titration of the probe (10μM) was conducted by successive addition of Cu^{2+} ion (0-20μM). Upon addition of Cu^{2+} the solution was well mixed and then the spectra were obtained. The absorption and emission path length of quartz cell used was 1 cm. Fluorescence experiments performed with both the excitation and emission slit of 10 nm. Fluorescence quantum yields (Φ) were obtained by using the equation:

$$\Phi_{sample} = (OD_{std.} \times A_{sample})/(OD_{sample} \times A_{std.}) \times \Phi_{std.}$$

Where, A_{sample} and A_{std} represent the areas under the fluorescence spectral curves for sample and standard respectively. OD_{sample} and OD_{std} represents the optical densities of the sample and standard respectively at the

excitation wavelength.[39] In this work, acidic quinine sulfate (0.1(N) H_2SO_4 solution) was taken as the standard with known quantum yield, $\Phi_{std.}$ = 0.54 for the quantum yield calculation of ligand H_2L.

II.2.4. Biological Studies

II.2.4.1. Cell line culture

Human liver cancer cell line Hep G2 and human lung fibroblast cells, WI-38 were obtained from National Centre for Cell Science (NCCS) Pune, India. The cells were grown in DMEM with 10% FBS (Fetal Bovine Serum), penicillin/streptomycin(100units/ml) at 37ºC and 5%CO_2. All the treatments were conducted at 37ºC[40] and at a cell density allowing exponential growth**.**

II.2.4.2. Cell survivability assay

Cell survivability was estimated for WI-38 following reported procedure.[41] Viability of WI-38 cells was assessed through MTT assay. The cells were seeded in 96-well plates at 1×10^4 cells per well and exposed to H_2L at different concentrations of 0 µM, 20 µM, 40 µM, 60 µM, 80 µM, 100 µM for 24 h. After incubation cells were washed with 1×PBS twice and incubated with MTT solution (450µg/ml) for 3-4h at 37ºC. The resulting formazan crystals were dissolved in an MTT solubilisation buffer and the absorbance measured at 570 nm by using a spectrophotometer (BioTek) and the value has been compared with control cells.

II.2.4.3. Cell Imaging

The Hep G2 cells were grown in coverslips for 24h. Then the cells were treated with 10µM of H_2L**,** 20µM salts $Cu^{2+}$and 40µM Cysteine were incubated for 24h at 37ºC. The cells were washed with 1×PBS. Then they were mounted on a glass slide and observed under fluorescence microscope (Leica).

II.2.5. Computational methods

The optimized structures of the probe H_2L and L-Cu^{2+} were generated by DFT computation of Gaussian 09 (G09) Program Package with B3LYP exchange correlation functional for C, H, N, O and LanL2DZ basis set for Cu.[42-44] The vibrational frequency calculation has been performed with the complexes using B3LYP/6-311G basis sets for C, H, N, O and LaLn2DZ basis set to Cu. The vibrational frequency calculation has been

performed with the complexes to ensure that the optimized geometries represent the local minima and the only positive Eigen values are used. The lowest 25 singlet – singlet transition in acetonitrile using the conductor-like polarizable continuum model (CPCM) and results of the Time Dependent Density Functional Theory (TD-DFT) calculations was qualitatively very similar.[45-47] For calculating the fractional contributions of various groups GaussSum calculations were done.[48]

II.3 Results and Discussion

II.3.1. Characterization of H_2L

The condensation of 4,4-Di formylTriphenylamine and1-(hydrazonomethyl)naphthalene-2-ol in 1:2 molar ratio synthesizes the probe H_2L. (**Scheme II.a**). The probe H_2L shows relatively better solubility in $CDCl_3$, so the probe has been well characterized by ^{1}HNMR and ^{13}CNMR in $CDCl_3$ solvent. ^{1}HNMR($CDCl_3$) of the probe represents a strongly deshielded singlet peak at 13.440 ppm for the phenolic (–OH) proton. Another sharp singlet appears at 9.728 ppm is attributed to imine proton (CH=N) attached to the naphthyl moiety and a peak at 8.657 ppm is assigned for the imine proton (CH=N) bonded to the diformyl unit of triphenyl amine in relatively deshielded zone confirms the formation of Schiff base. A doublet signal at 8.215 ppm corresponds to proton peak situated at para position to the imine group of the naphthyl fragment. The signals from 8.186 to 7.207 ppm represent the protons of aromatic region of the molecule. (**Fig.II.1**) ^{13}CNMR ($CDCl_3$) of the probe H_2L includes a signal at 161.13 to 160.79 ppm which corresponds for two imine carbon (CH=N) and phenolic (C-OH) peaks. The peaks at 150.01 and 146.28 ppm may be due to C-N carbon of triphenyl fragment. The regions from 134.44 to 108.48 ppm may include the rest of the carbon atom and thus confirms the formation of Schiff base (**Fig.II.2)**. ESI-MS analysis shows the spectral peak with m/z at 638.2539 and 639.2458 and supports the desired formulation of the probe. (**Fig. II.3**) In FTIR spectrum of H_2L, the elimination of ν(CHO), 1690 cm^{-1} from 4,4'-diformyltriphenylamine and ν(NH_2) at 3312cm^{-1} of 1-(hydrazonomethyl)naphthalene-2-ol along with appearance of new band at 1605 cm^{-1}which is assigned to ν(C=N) and supports the coupling of –CHO and -NH_2 (**Fig.II.4**). The purity of the ligand H_2L was further analyzed by High-performance Liquid Chromatograhy (HPLC) technique. The probe H_2L was eluted using

0.012% TFA as the aqueous mobile phase and 40% acetonitrile medium as the organic mobile phase having a flow rate of 1 mL/min. The result shows that the signal appeared in chromatogram was observed for 10^{-3}(M) concentration of the probe H_2L with retention time at 7.211 min. (**Fig.II.5**)[49]

II.3.2. Sensing of Cu^{2+}

In UV-Vis spectral studies, H_2L exhibits a high intense absorption band at 428 nm with a shoulder hump at 326 nm in 7:3(v/v) CH_3CN/H_2O medium (HEPES buffer, pH 7.2) which may arise due to π-π* transition. Sensitivity of probe H_2L has been checked in presence of various metal ions (Zn^{2+}, Cd^{2+}, Hg^{2+}, Co^{2+}, Pb^{2+}, Al^{3+}, Ca^{2+}, Fe^{3+}, Ni^{2+}, Na^{+}, Mn^{2+}, Pd^{2+}, Cr^{3+}, K^{+}, $Mg^{2+}$and Cu^{2+}) and selective oxidizing agents (·OH, H_2O_2, HOCl) in 7:3(v/v) CH_3CN/H_2O medium (HEPES buffer, pH 7.2) and it shows appreciably no change in the characteristic absorption band of the ligand while it shows unprecedented effect upon addition of Cu^{2+} ion. The absorption band in UV-Vis spectrum of the corresponding ligand H_2L is red shifted upon addition of 2 equivalent (20 µM) Cu^{2+}ion from 326 to 335 nm and 428 to 439 nm which accounts for its specificity towards Cu^{2+} ion even in presence of other competitive ions and oxidizing agents. (**Fig. II.6**).

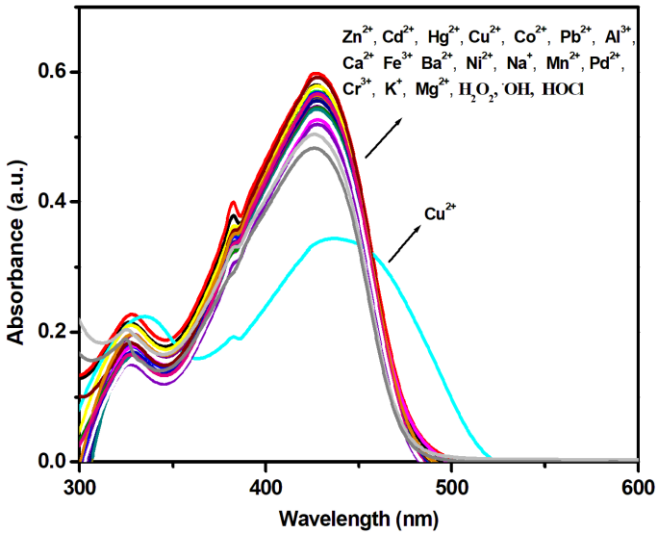

Fig.II.6. UV-Vis spectra of H_2L in presence of various cations and oxidizing agents (H_2L: cations and oxidizing agent; 1:2) in in CH_3CN/H_2O (7:3, v/v) medium HEPES Buffer pH=7.2.

With incremental addition of Cu^{2+} ion (0-20 µM) to the probe solution in 7:3(v/v) CH_3CN/H_2O medium (HEPES buffer, pH 7.2), the absorption intensity at 428 nm gradually decreases while that of the peak at 326 nm shows a slight increase in the absorption intensity with two isosbestic points at 354 nm and 461 nm. On increasing concentration of Cu^{2+} to probe the characteristic band at 428 nm is shifted to 439 nm (**Fig.II.7**).

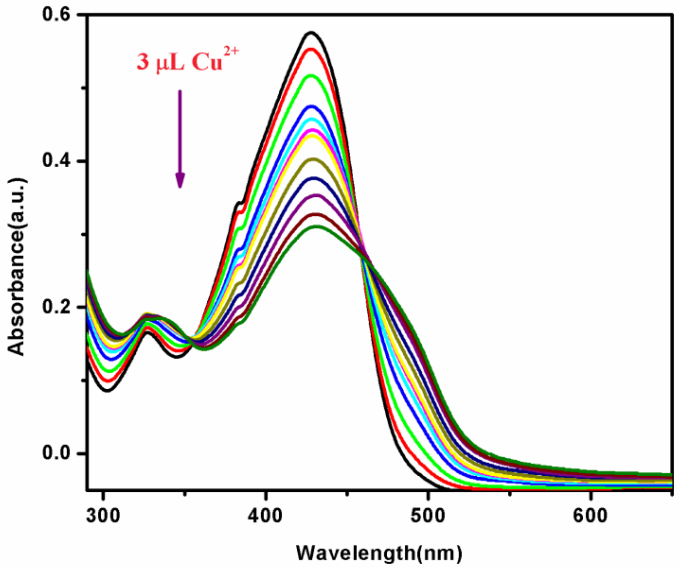

Fig.II.7. Change in absorption spectrum of H_2L (10 µM) upon gradual addition of Cu^{2+} ions (0-20 µM).

Luminophores based on hydrazide Schiff Base shows strong fluorescence in solid state.[50,51] Enhancement of emission intensity in solid state may be attributed to the Restricted Intramolecular Rotation (RIR) inhibiting the non radiative decay through rotation around C=N.[52] The probe, H_2L, in solid state shows strong emission at 540 nm with a shoulder at 570 nm upon excitation on 430 nm (**Fig.II.8**). H_2L may exist in keto and enol form which may exhibit emission at two different wavelengths; 540 and 570 nm respectively. The proton transfer may assist imine-phenol to keto-amine tautomerisation.[53-57] (**Scheme II.b**) The probe H_2L in solution phase exhibits only single band at 550 nm.

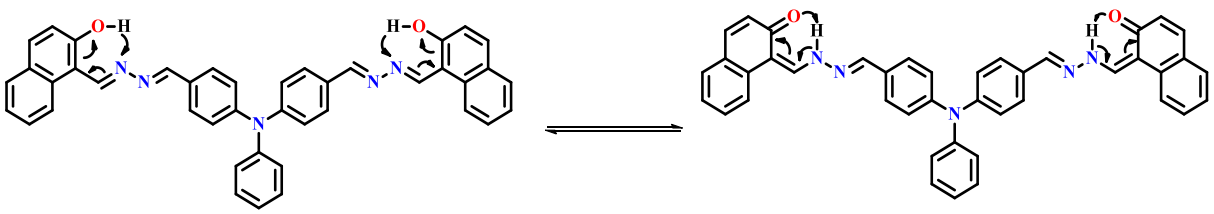

Scheme II.b. Keto-Enol Tautomerism in H_2L.

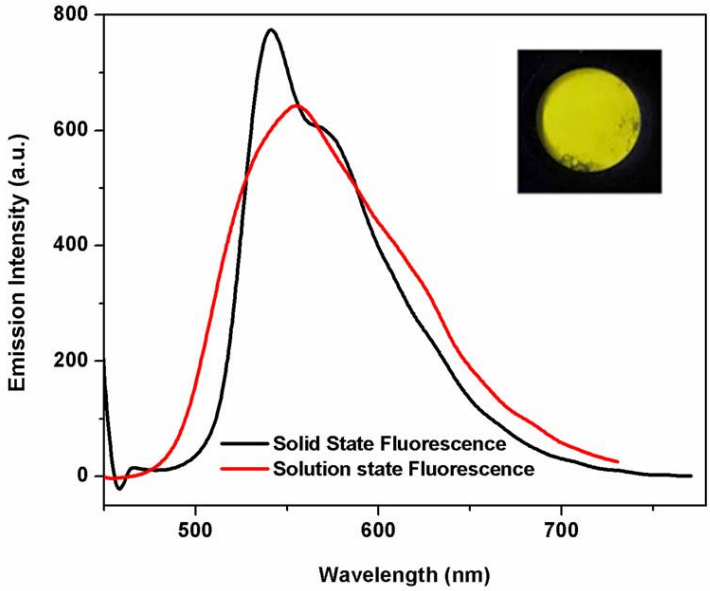

Fig.II.8. Solid and solution state emission spectra of H_2L (λ_{ex} 430 nm); Inset: solid state images under UV Chamber (λ_{ex} 365 nm).

The effect on emissive properties of H_2L in semi-aqueous phase was checked by adding various cations like Zn^{2+}, Cd^{2+}, Hg^{2+}, Co^{2+}, Pb^{2+}, Al^{3+}, Ca^{2+}, Fe^{3+}, Ni^{2+}, Na^{+}, Mn^{2+}, Pd^{2+}, Cr^{3+}, K^{+}, Mg^{2+}, Cu^{2+} and oxidizing agents like H_2O_2, $^{\cdot}OH$, HOCl in which the probe gets selectively quenched only in presence of Cu^{2+} ion (**Fig. II.9.**).

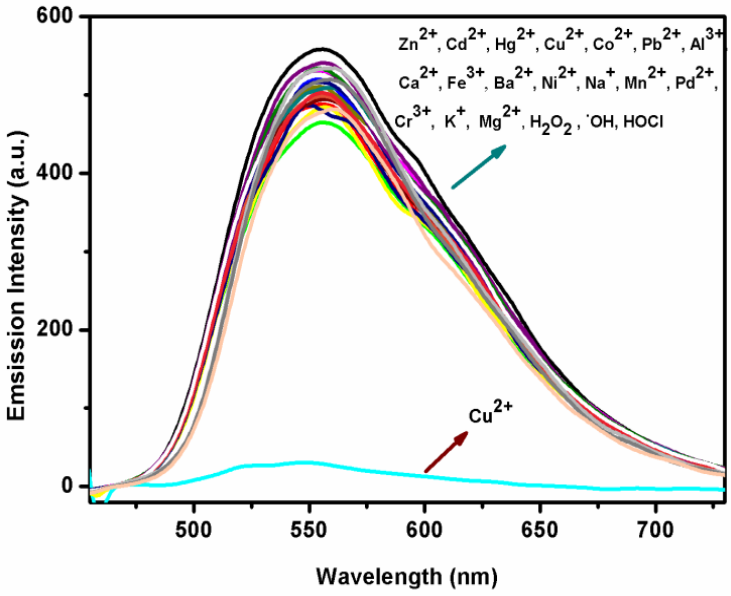

Fig.II.9 Fluorescence spectra of H_2L in presence of different cations and oxidizing agents (2 equivalent).

Vial images were taken in presence of various metal ions in 7:3(v/v) CH_3CN/H_2O medium (HEPES buffer, pH 7.2) at room temperature with ligand to metal in the ratio of 1:2 (**Fig. II.10**) and it shows negligible effect on the emission of the probe except Cu^{2+} ion.

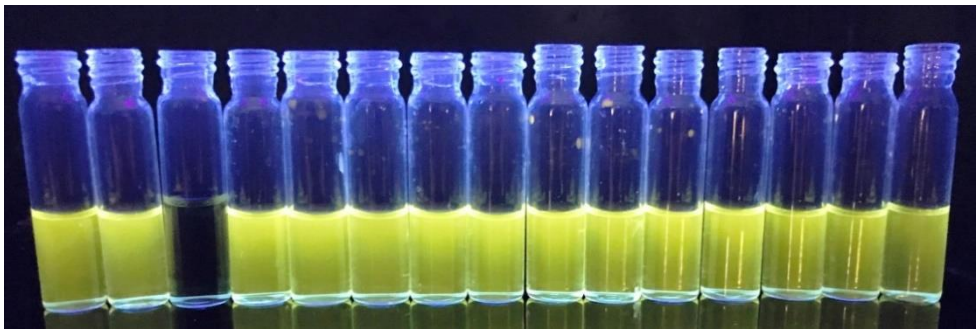

Fig.II.10 Image of the probe with various cations (left to right: H_2L, Zn^{2+}, Cu^{2+},Cd^{2+}, Hg^{2+}, Co^{2+}, Al^{3+}, Ca^{2+}, Fe^{3+}, Ni^{2+}, Na^{+}, Mn^{2+}, Pd^{2+}, $Cr^{3+}$and Mg^{2+}) in 7:3(v/v) CH_3CN/H_2O medium under 365 nm UV light.

The change in the emission spectrum in its fluorometric titration of H_2L upon addition of Cu^{2+} was carried out in 7:3(v/v) CH_3CN/H_2O medium (HEPES buffer, pH 7.2) (**Fig.II.11**). A quantitative analysis was done on quenching the emission of H_2L by successive addition of 2μL of Cu^{2+} (0-20μM) stock solution to 20μL of ligand (10μM) in 7:3(v/v) CH_3CN/H_2O medium (HEPES buffer, pH 7.2). The emission intensity at 550 nm (quantum yield Φ= 0.23) gradually decreases on titration with incremental addition of Cu^{2+} concentration and exhibited a good linearity. The H_2L scaffold has a pair of N, O chelating sites and can chelate to two Cu^{2+} ions. On addition of 2 equivalent of Cu^{2+} the emission intensity is quenched with a stoichiometric preference of the Ligand:Metal in 1:2 mole ratio. The ligand, H_2L chelates Cu^{2+}, the paramagnetic and Chelation Enhanced Quenching (CHEQ) may be the reason to sequester the emission.[58-60] Detection for Cu^{2+} by H_2L using a semi aqueous medium enables the use of green and safe solvent system for sensing studies.

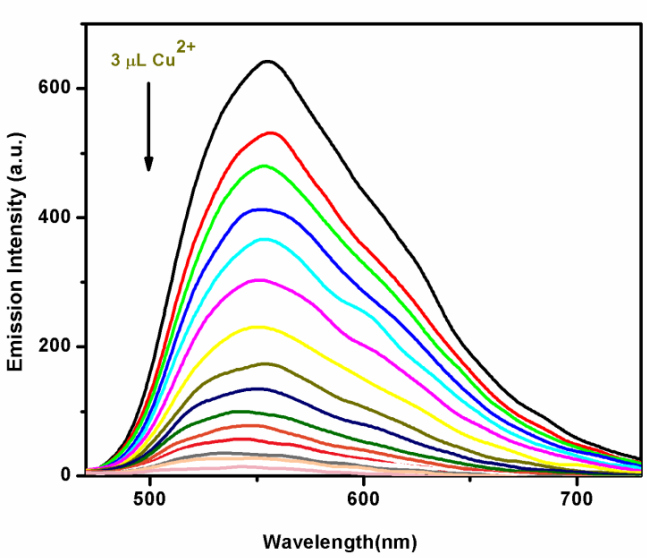

Fig.II.11. Fluorescence titration profile of H_2L on successive addition of Cu^{2+} in CH_3CN/H_2O (7:3,v/v) medium HEPES Buffer pH=7.2 , λ_{ex}, 430 nm.

The competitive study was conducted to check the selectivity of H_2L towards Cu^{2+} ion in presence of other cations such as Zn^{2+}, Cd^{2+}, Hg^{2+}, Co^{2+}, Pb^{2+}, Al^{3+}, Ca^{2+}, Fe^{3+}, Ni^{2+}, Na^{+}, Mn^{2+}, Pd^{2+}, Cr^{3+}, K^{+}, Mg^{2+} and anions (F^{-}, HF_2^{-}, PO_4^{3-}, $H_2PO_4^{-}$, IO_3^{-}, $S_2O_3^{2-}$, $S_2O_5^{-}$, I^{-}, HPO_4^{2-}, $PO_4^{3-}OAc^{-}$,SO_4^{2-},F^{-}, NO_3^{-}, Cl^{-}, Br^{-}, CN^{-}, AsO_2^{-}, S^{2-}, AsO_4^{3-} and $P_2O_7^{4-}$). The experiment was carried out on addition of 2.0 equivalent Cu^{2+} to the solution of 1.0 equivalent H_2L in 7:3 (v/v) CH_3CN/H_2O medium (HEPES buffer, pH 7.2) and to this complex solution, 2.0 equivalent of other cations are added at each time. Results (**Fig.II.12**) shows that there is no such interference in the detection of Cu^{2+} ion in presence of other cations. The "turn-off" response of Cu^{2+} was examined in presence of co-existed ions which could minimally affect its quenching phenomenon.

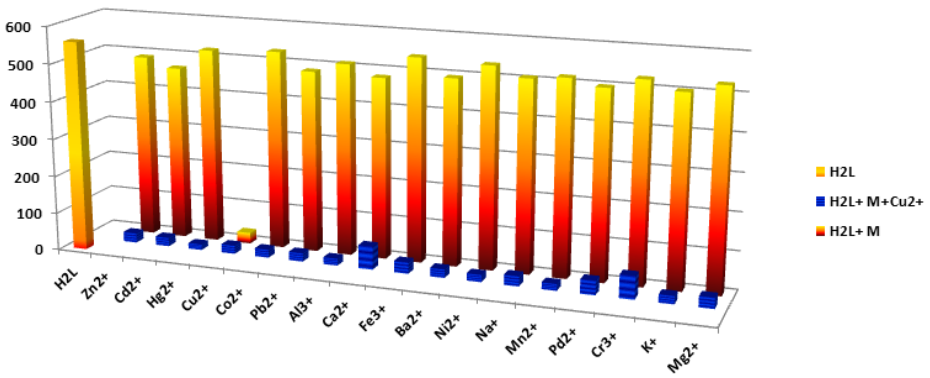

Fig.II.12 Interference study of cations on Cu^{2+} sensing in 7:3(v/v) CH_3CN/H_2O medium.

The effect of anions on the analysis of Cu^{2+} is also checked (**Fig.II.13**) and it is found that no anion (2.0 equivalent Cu^{2+} to the solution of 1.0 equivalent H_2L and 4.0 equivalent of anions) has impact on the determination of it. So, the probe detects efficiently in presence of external ions and can be accredited as highly sensitive probe in detection of Cu^{2+} ions.

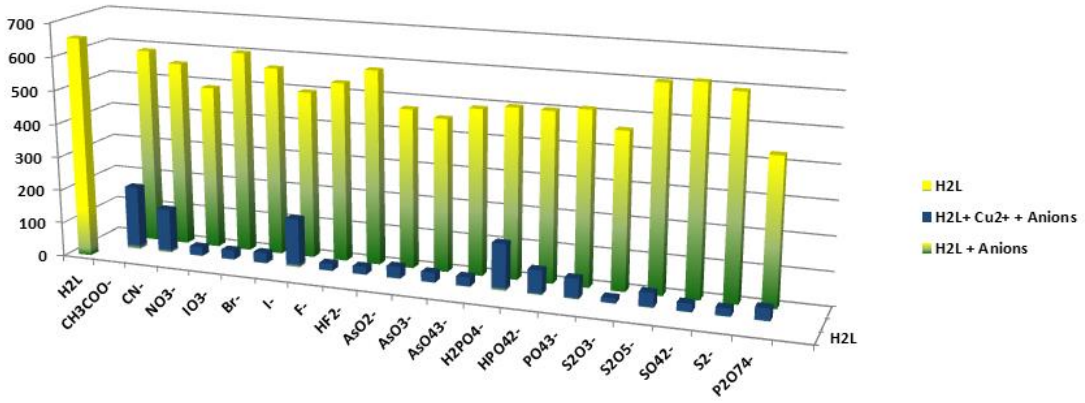

Fig.II.13. Interference study of anions on Cu^{2+} sensing in 7:3(v/v) CH_3CN/H_2O medium.

The fluorescence intensity of H_2L remains unchanged under a series of pH from 2.0 to 8.0. Upon addition of Cu^{2+} to H_2L solution emission is quenched within pH, 6.0 – 8.0 (**Fig.II.14**). Hence the probe can be used for detection of Cu^{2+} under normal physiological pH.

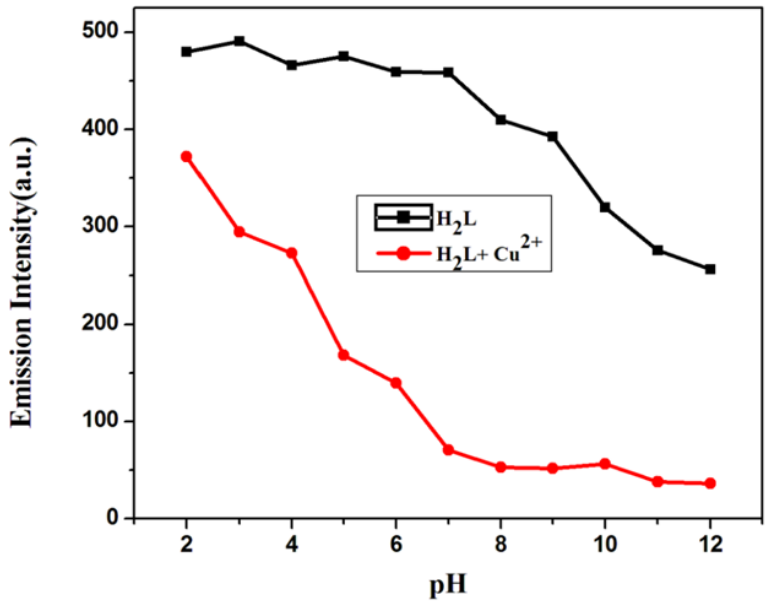

Fig.II.14. pH effect on Cu^{2+} sensing by H_2L.

The limit of detection (LOD) of Cu^{2+} by H_2L was experimentally determined by (3σ/S) method where σ is the standard deviation; S is the slope of the calibrated curve resulted from fluorescence titration profile of H_2L by successive addition of Cu^{2+} ions**.** From the titration, detection limit (LOD) calculated for Cu^{2+} was found to be 7.3 nM (**Fig.II.15**) which is fairly less than the recommended permissible limit for Cu^{2+} (20μM) in drinking water by WHO.[7]

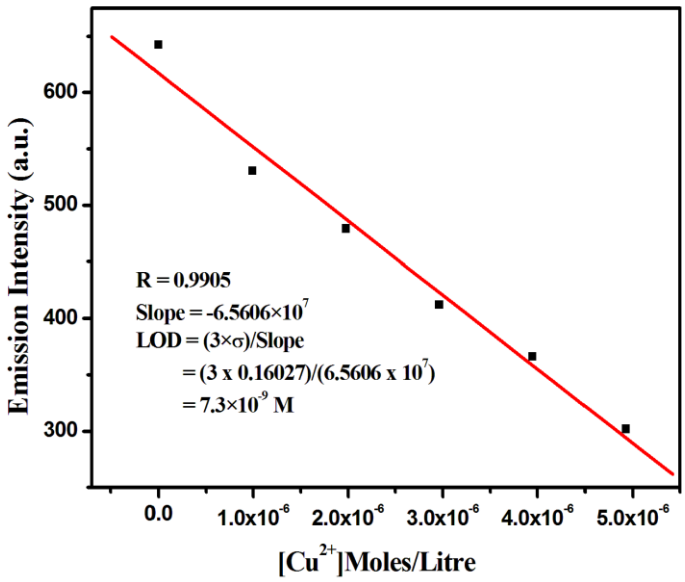

Fig.II.15. Limit of Detection (LOD) for Cu^{2+} sensing by H_2L.

The LOD was experimentally calculated and it is compared with some published data (**Table II.1**). The reports are available for Cu^{2+} sensing using different fluorogenic sensors like pyrene appended imine-phenol (LOD,1.21 μM in CH_3CN/HEPES Buffer),[7] Coumarin-napthol probe (LOD, 12.7 nM in DMSO/HEPES buffer),[14] Rhodamine-benzothiazole (LOD, 6.89 μM in CH_3CN/water)[20], pyrrole appended chromen-ol (LOD, 0.512 μM in DMSO/PBS buffer)[57] ,naptholhydrazide (LOD, 223 nM in PBS buffer)[58] and dicyanomethylene-4H-pyran picolinate derivative (LOD, 23 nM in DMSO/PBS Buffer)[61]; The present probe H_2L shows better efficiency (LOD, 7.3 nM). Hence, the probe is applicable and suitable for detection of Cu^{2+} in trace quantity.

Table II.1. Some reported Cu^{2+} sensor with their LOD value

SL. No.	Ligand	(LOD, Cu^{2+})	Solvent	Ref.
1.	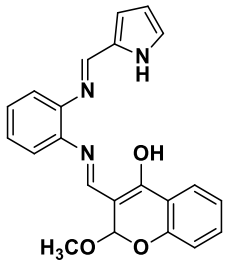	0.512 μM	DMSO/PBS Buffer (1:99)	[62]
2.	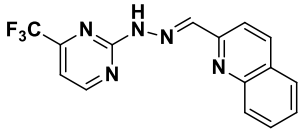	0.02 μM	DMF/bis-Tris Buffer (1:4)	[63]
3.	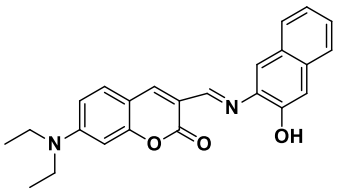	12.7 nM	DMSO/HEPES Buffer (1:99)	[66]
4.	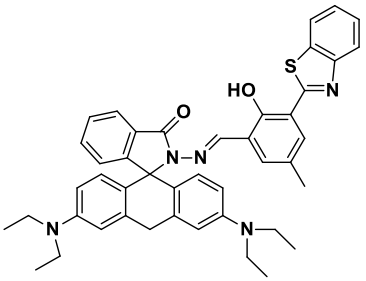	6.89 μM	CH_3CN/HEPES Buffer (1:1)	[65]
5.	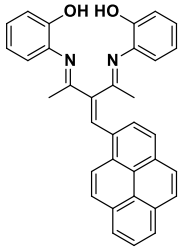	1.21 μM	CH_3CN/HEPES Buffer (7:3)	[64]
6.	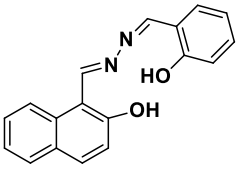	223 nM	PBS Buffer	[67]

7.	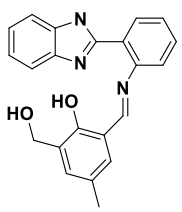	18.2 nM	CH_3OH/H_2O HEPES Buffer (1:1)	[68]
8.	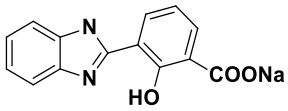	2.77 μM	HEPES Buffer	[69]
9.	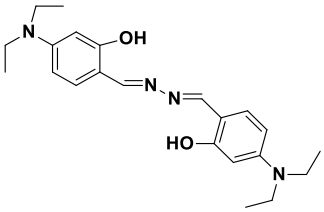	0.98 μM	CH_3CN	[70]
10.	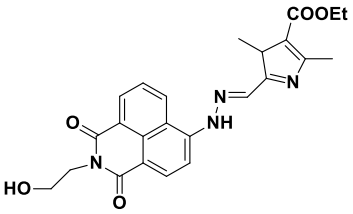	1.5 μM	CH_3CN/H_2O (9:1)	[71]
11.	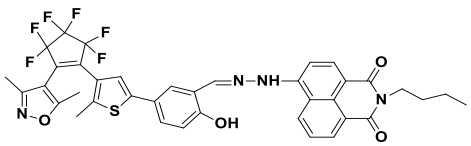	2.4 μM	CH_3CN	[72]
12.	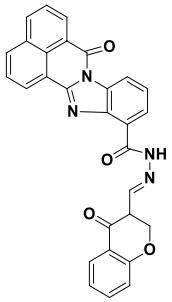	13 nM	CH_3CN/H_2O HEPES Buffer (9:1)	[73]
13.	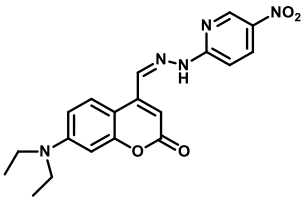	2.1 nM	DMSO/PBS Buffer (1:1)	[74]

14.	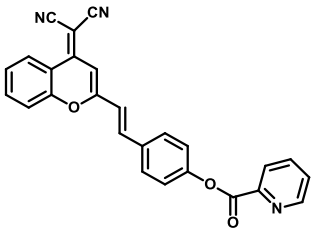	23 nM	DMSO/PBS Buffer (1:1)	[75]

II.3.3. Binding preference and stoichiometric study for Cu^{2+} ion

Analysis of binding of ligand with Cu^{2+} in (7:3(v/v) CH_3CN/H_2O medium (HEPES buffer, pH 7.2)) was evident from Job's Plot which hints the stoichiometric preference of H_2L complexation towards Cu^{2+} (**Fig. II.16**).[76] The maxima in Job's plot correspond to mole fraction of 0.67 which indicates a complex formation of H_2L to Cu^{2+} in 1:2 modes.

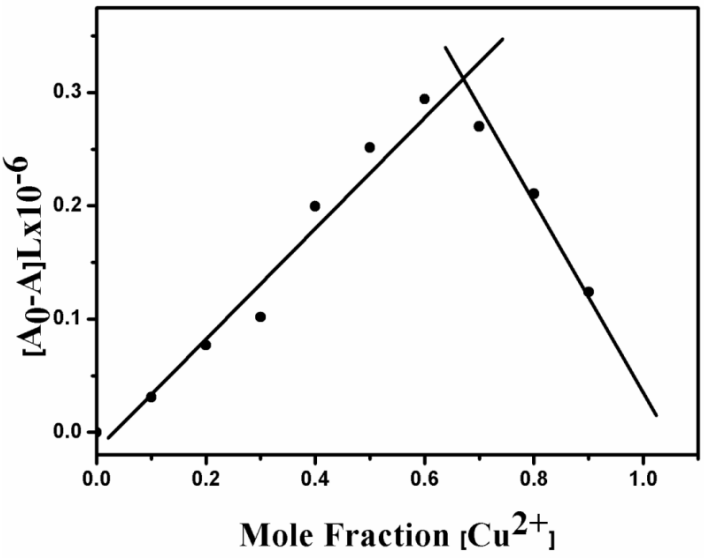

Fig.II.16 Job's Plot for determination of stoichiometric binding preference for Cu^{2+}.

A change in the ^{1}HNMR spectra of H_2L was observed on addition of varying concentration of Cu^{2+} in DMSO-d_6 (**Fig.II.17.**). The ^{1}HNMR spectral difference of H_2L, on addition of Cu^{2+} in varying proportion observes a significant change to peak at 13.2 ppm, phenolic proton attached to the naphthyl moiety. In presence of 1 equivalent of Cu^{2+}, phenolic OH proton peak gets attenuated and on 2.0 equivalents it vanishes completely which is an indication of deprotonation of H_2L and complexation to Cu^{2+} through O donor centres. Due to

gradual addition of Cu^{2+}, the aromatic protons get broadened and a slightly downshifted. The complete disappearance of hydroxyl proton peak of H_2L on 2.0 equivalent additions of Cu^{2+} intimates at preferential complex formation in 1:2 ratios. The reduced peak of imine CH=N peak also indicates its participation in binding.

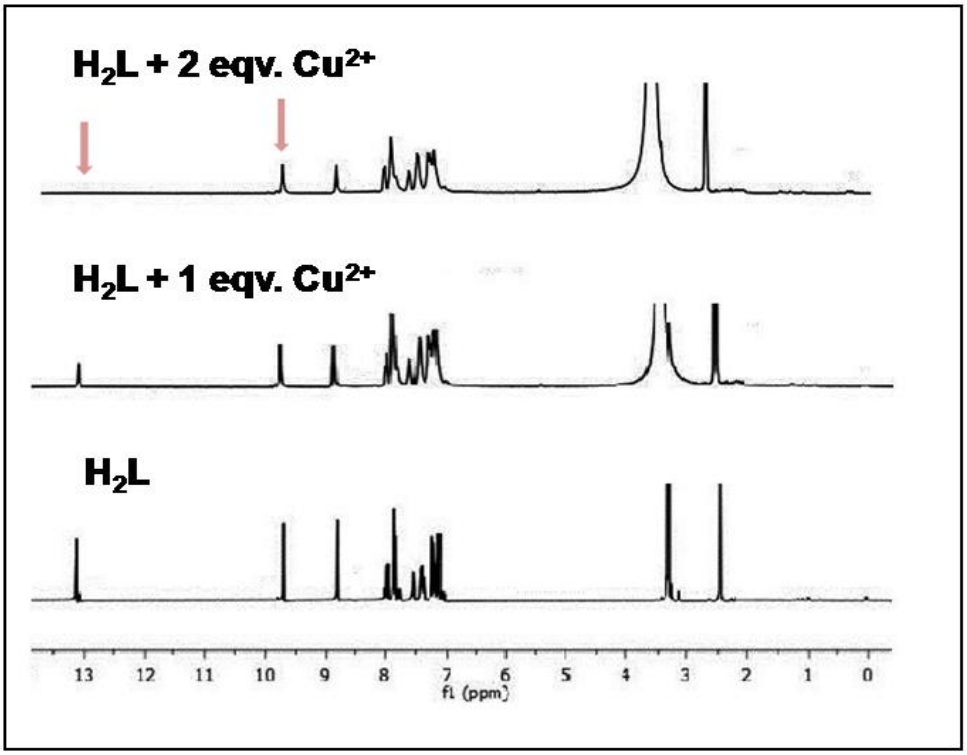

Fig.II.17. ^{1}HNMR titration of **H_2L** on successive addition of Cu^{2+} in DMSO-d_6.

On ESI-MS analysis, a molecular ion peak appears at m/z = 767.0098 corresponds to $[HL+Cu^{2+}+Cl^-+MeOH]$ reveals a 1:1 binding stoichiometry between H_2L and Cu^{2+} and confirms 1:1 complex formation and another peak at 895.9957 corresponds to $[L+2Cu^{2+}+2Cl^-+2MeOH]$ which reveals interaction of H_2L to Cu^{2+} in 1:2 stoichiometry binding mode (**Fig.II.18.**). Infrared spectrum of the complex shows a broad peak at 3370 cm^{-1} which may be due to ν(OH) of coordinated MeOH and a high intense broad peak at 1585 cm^{-1} is assigned to coordinated C=N and in free ligand (H_2L) it appears at 1605 cm^{-1}. The coordination of imine-N to Cu^{2+} is supposed to responsible for elongation of C=N bond length and is shifting to lower energy. A band at 1317 cm^{-1} corresponds to O-H bending; the C-N and C-O stretching appear at 1280 and 1172 cm^{-1}respectively in the complex. (**Fig.II.19**).

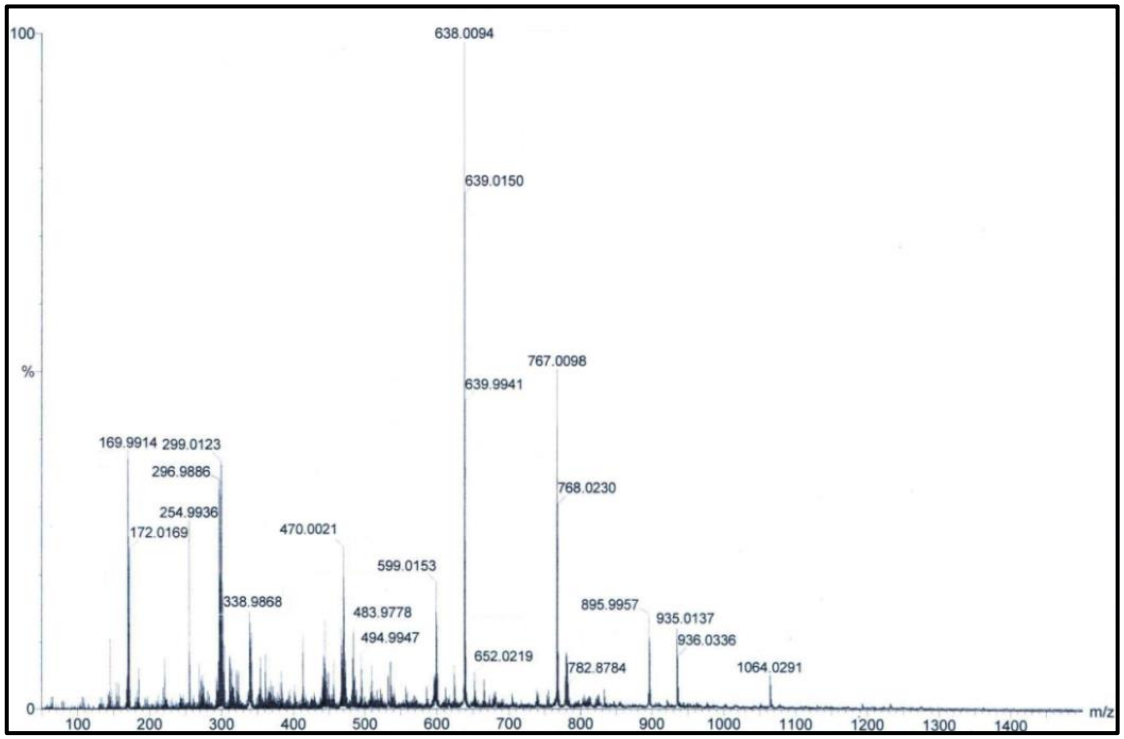

Fig.II.18. ESI-MS Spectrum of L- Cu^{2+}.

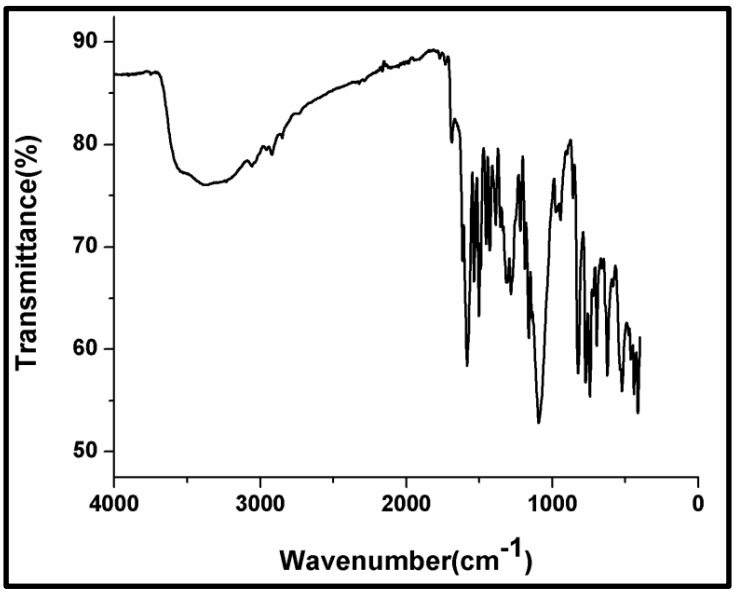

Fig.II.19. IR Spectrum of L -Cu^{2+}.

The binding constantis K_D= 4.93 × 10^{10} M^{-2} (R= 0.99637) as obtained from the plots of ((F_{max}-F_0)/(F-F_0)) vs. 1/[Cu^{2+}]^2 using the linear Benesi-Hildebrand expression (**Fig.II.20.**). This also supports the fact that Cu^{2+} has a strong binding affinity for ligand with N and O chelating centres with results of 1:2 binding mode of H_2L to Cu^{2+} and thus have a sufficient stability.[77]

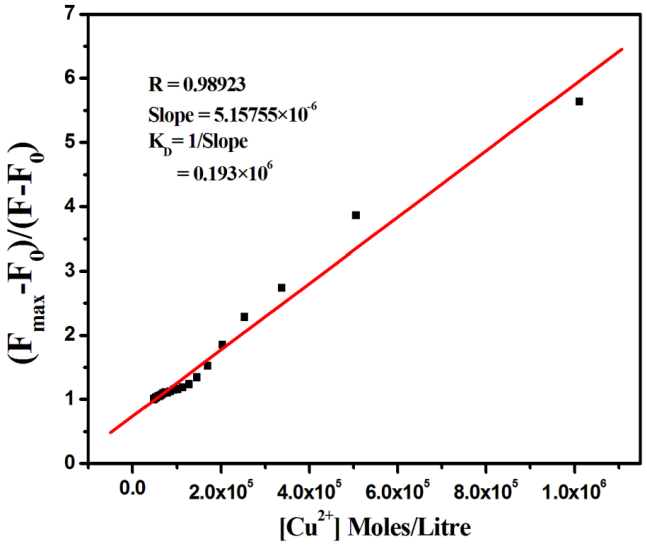

Fig.II.20. B-H Plot for calculating binding constant (K_d) of H_2L with Cu^{2+} ions.

The Stern Volmer (S-V) constant, K_{sv}= 0.217 × 10^6 M^{-1} (R = 0.98719) as calculated using the equation $[I_0/I]$ = 1+K_{sv}[Q] for static quenching (**Fig.II.21 (a)& (b)**). The plot shows linearity up to 20μM and accounts the static quenching and on above 20μM of [Cu^{2+}] it shows an upward bend along with inclusion of dynamic process. The constancy of lifetime of the excited state fluorophore even on addition of Cu^{2+}further confirms the static quenching.[78, 79]

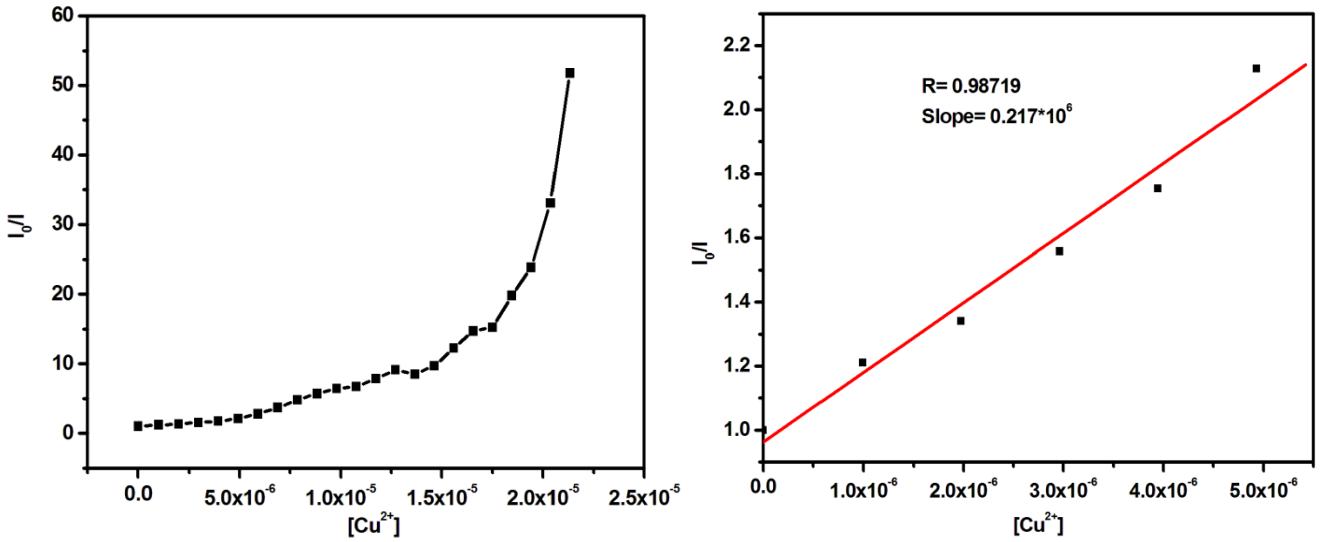

(a) **(b)**

Fig.II.21. (a) Stern-Volmer plot of [Cu^{2+}] against I_0/I. **(b)** Stern-Volmer constant (K_{sv}) obtained from the above given plot.

II.3.4. Time -Correlated Single Photon Counting (TCSPC) (Lifetime Measurement):

The lifetime decay profile of H_2L and L-Cu^{2+} fits well into bi-exponential fashion. The time resolved fluorescence spectroscopic study reveals a lifetime of 0.32688 ns (H_2L) which on addition of Cu^{2+} decreases to 0.298222 ns (**Fig.II.22**). On increasing the concentration of Cu^{2+}, lifetime of the complex remains invariant which signifies a static quenching and the quenching takes place at ground state complex formation.[80]

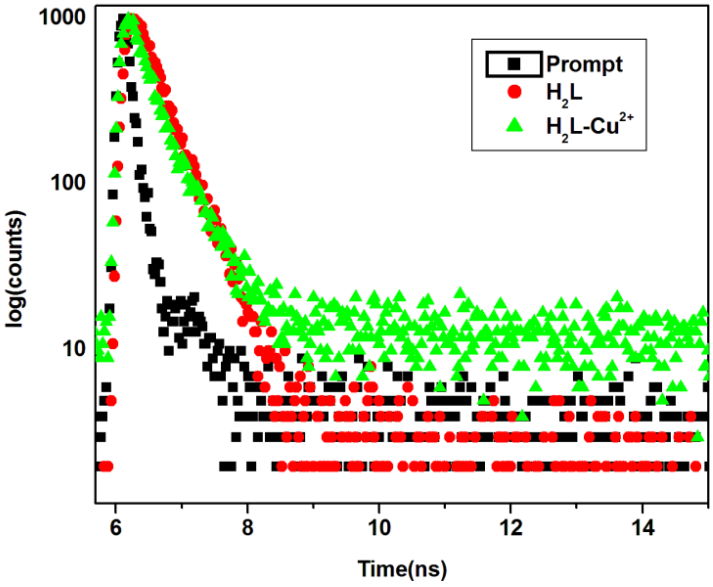

Fig.II.22. Fluorescence lifetime plot of H_2L and on Cu^{2+} addition in CH_3CN/H_2O (7:3, v/v) HEPES Buffer medium pH=7.2.

II.3.5. Recovery Study from Municipal supplied Water Sample

To analyse the reliability of the use of H_2L for the fluorescence detection method of Cu^{2+}, a recovery study was performed utilizing municipal supplied water in Kolkata by Standard addition method. The calibration plot on varying the concentration of Cu^{2+} from 0 to 10 μM and keeping the concentration of ligand 10μM fixed 7:3(v/v) CH_3CN/H_2O medium (HEPES buffer, pH 7.2) (**Fig.II.23**). The drinking water was collected from Jadavpur, Kolkata supplied by Kolkata Municipal Corporation in specific bottle. Unknown concentration of Cu^{2+} is determined from the calibration plot (**Table II.2**). The recovery study of $Cu^{2+}$is satisfactory to >85 %. This experiment exhibited a rapid and inexpensive application for sensing of Cu^{2+} even in municipal supplied water.[81]

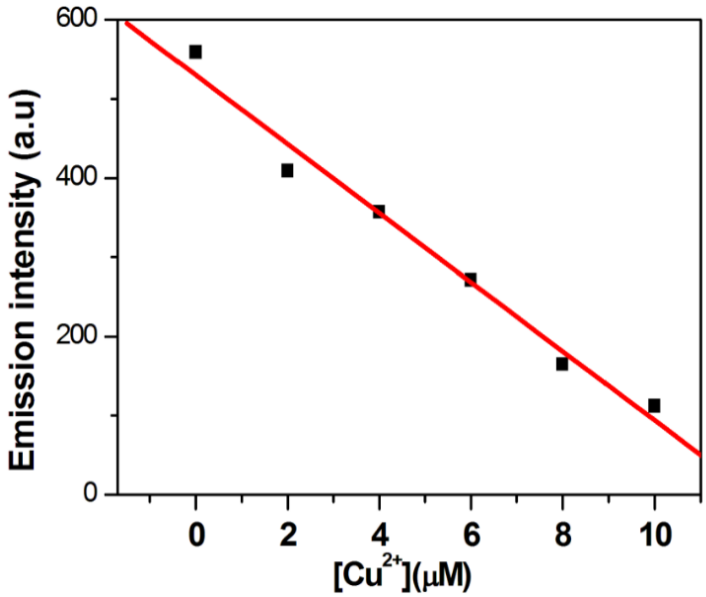

Fig.II.23. Calibration Plot for detection of Cu^{2+} by H_2L.

Table II.2: Recovery of Cu^{2+} from drinking water sample using **H_2L**

Sample	**Added (Cu^{2+}) μL**	**Emission Intensity (a.u.)**	**Experimentally Found (μL)**	**Recovery (%)**
Drinking Water	2	410	1.73	86.5
	4	357	3.52	88
	6	271	5.51	91.18

II.3.6. DFT Computational Study:

The DFT computation technique is used to calculate the molecular energy levels of H_2L and its Cu^{2+}-complex. The HUMO-LUMO energies (**Fig.II.24**) for H_2L are -5.61 eV and -2.24 eV and the energy difference is 3.37eV and after interaction with Cu^{2+} the HOMO LUMO energies are -3.51 eV and -0.52 eV and the energy gap is diminished to 2.99 eV. The UV-Vis absorption spectrum of L-Cu^{2+} (335, 439 nm) is red shifted

compared to H_2L (326, 428 nm) and has been supported by energy calculation. TD-DFT study reveals the theoretical aspects of the observed spectroscopic changes of H_2L towards Cu^{2+}. (**Tables II.3 and II.4**).

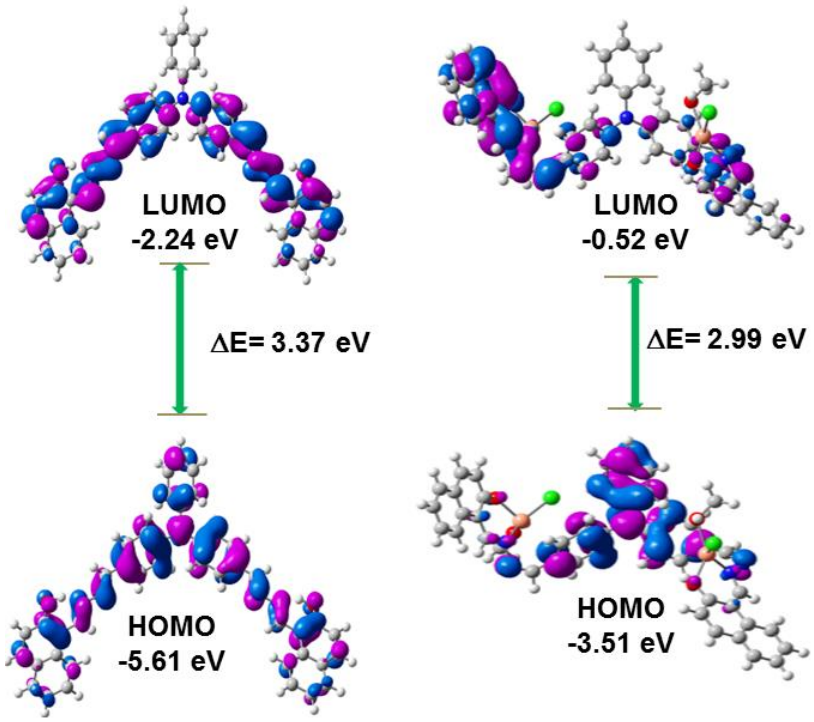

Fig.II.24. HOMO-LUMO gap of **H_2L** and L-Cu^{2+}.

Optimized geometry of H_2L and L-Cu^{2+} along with some selected frontier molecular functions with their energy were listed in the **Fig.II.25, 26** and **27**. Fractional contribution of groups in frontier molecular orbitals for H_2L and its L-Cu^{2+} were calculated by GASSSUM and are listed in **Table II.5 &II.6**

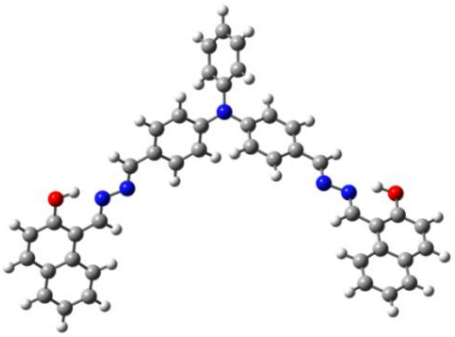	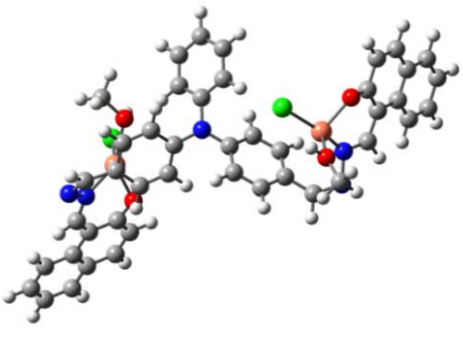
H_2L	**L-Cu^{2+}**

Fig.II.25. Optimized structure of **H_2L** and L-Cu^{2+}.

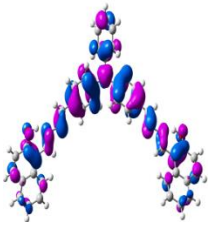	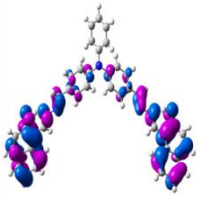	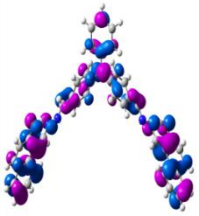	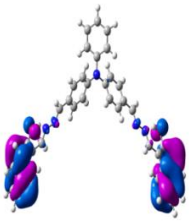	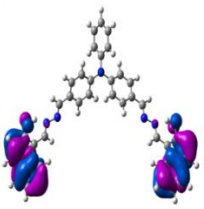
HOMO **-5.61eV**	**HOMO-1** **-5.73 eV**	**HOMO-2** **-5.85eV**	**HOMO-3** **-6.37eV**	**HOMO-4** **-6.39eV**
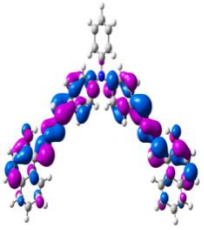	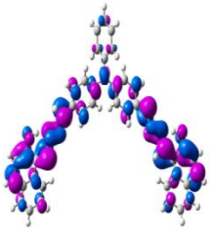	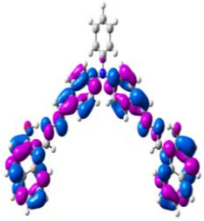	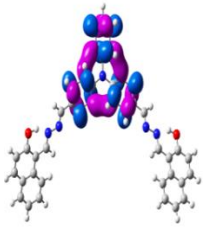	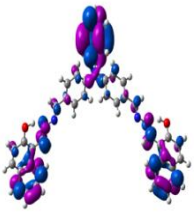
LUMO **-2.24 eV**	**LUMO + 1** **-2.05 eV**	**LUMO + 2** **-1.16 eV**	**LUMO + 3** **-1.02 eV**	**LUMO + 4** **-0.64 eV**

Fig.II.26. Energy of some selected frontier molecular orbital of ligand H_2L.

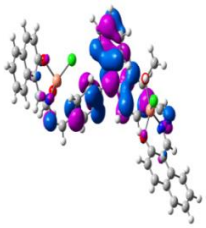	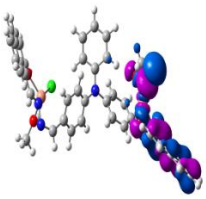	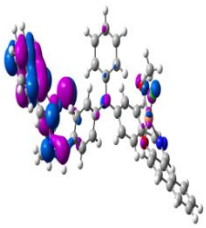	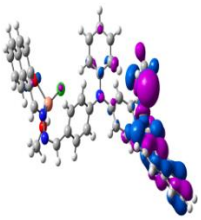	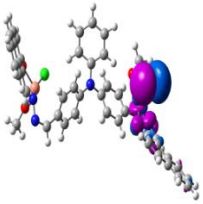
HOMO **-3.51 eV**	**HOMO – 1** **-4.24 eV**	**HOMO - 2** **-4.36 eV**	**HOMO – 3** **-4.47 eV**	**HOMO – 4** **-4.59 eV**
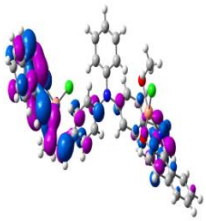	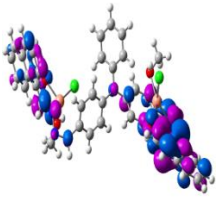	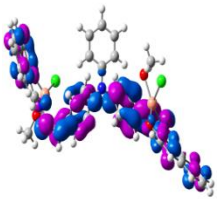	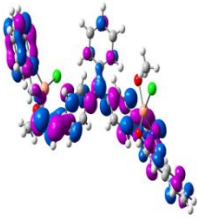	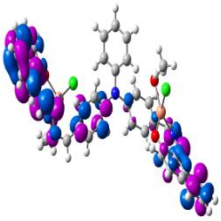
LUMO **-0.52 eV**	**LUMO + 1** **-0.41eV**	**LUMO + 2** **0.35 eV**	**LUMO + 3** **0.63 eV**	**LUMO + 4** **1.25 eV**

Fig.II.27. Energy of some selected frontier molecular orbital of L-Cu^{2+}.

Table II.3: Possible Transition of Ligand H_2L from TD-DFT

Excitation Energy	Exp. Wavelength	Theor. Wavelength	Oscillation Frequency (f)	Key Transition	Nature of Transition
3.0851 eV	429 nm	401.88 nm	0.4135	HOMO-1→ LUMO	ILCT
3.7445 eV	325 nm	331.11 nm	0.0586	HOMO→ LUMO+3	ILCT

Table II.4: Possible Electronic Transition of L-$Cu^{2+}$from TD-DFT

Excitation Energy	Exp. Wavelength	Theor. Wavelength	Oscillation Frequency (f)	Key Transition	Nature of transition
2.7893 eV	439 nm	444.51 nm	0.0448	HOMO→LUMO	ILCT
3.4608 eV	335 nm	358.25 nm	0.0380	HOMO -1→LUMO	ILCT

Table II.5: MOs Contribution for ligand H_2L

MOs	Energy(eV)	Triphenylamine	Imine	Nahpthyl
LUMO+4	-0.64	99	0	0
LUMO+3	-1.02	35	19	45
LUMO+2	-1.16	27	20	52
LUMO+1	-2.05	17	45	38
LUMO	-2.24	25	46	29
HOMO	-5.61	63	16	22
HOMO-1	-5.73	8	20	72
HOMO-2	-5.85	27	11	62
HOMO-3	-6.37	2	2	96
HOMO-4	-6.39	1	1	98

Table II.6: Contribution of MOs for its L-Cu^{2+}

MOs	Energy (eV)	Naphthyl	Cl	imine	Triphenylamine	MeOH	Cu
LUMO+4	1.25	60	0	10	25	0	4
LUMO+3	0.63	20	0	49	29	0	2
LUMO+2	0.35	26	0	38	33	0	3
LUMO+1	-0.41	46	0	47	6	0	0
LUMO	-0.52	44	0	47	8	0	0
HOMO	-3.51	3	0	6	90	0	1
HOMO-1	-4.24	43	25	12	2	8	11
HOMO-2	-4.36	61	9	18	4	2	6
HOMO-3	-4.47	35	23	7	5	20	9
HOMO-4	-4.56	5	79	5	1	0	9

II.3.7. Detection of Cysteine

The strong affinity of Cysteine (Cys) towards Cu^{2+} has shown the use of L-$Cu^{2+}$for the sensing of Cysteine in 7:3(v/v) CH_3CN/H_2O medium (HEPES buffer, pH 7.2). The selectivity of Cys to Cu^{2+} from in situ generated L-Cu^{2+} non emissive complex, results in recovery of emission and turn on response towards Cys detection in semi-aqueous medium. To a solution of L-Cu^{2+} in 7:3(v/v) CH_3CN/H_2O medium (HEPES buffer, pH 7.2) 5 equivalent of amino acids (Alanine (Ala), Leucine (Leu), Methionine (Met), Serine (Ser), Proline (Pro), Glutamic acid (Glu), Aspartic acid (Asp), Glycine (Gly), Histidine (His), Valine (Val), Lysine (Lys), Homocysteine (Hcy)) were added and their fluorescence spectra were measured (**Fig.II.28**). The result shows that the fluorescence of the probe (H_2L) is recovered from the quenched complex, L-Cu^{2+} ensembles only in case of Cys whereas for other amino acids/biothiols remain unaffected. On addition of 40 μM Cys, a 30 fold significant fluorescence enhancement was observed whereas only 5.6 and 9.7 fold enhancement was observed in case of GSH and Hcy.

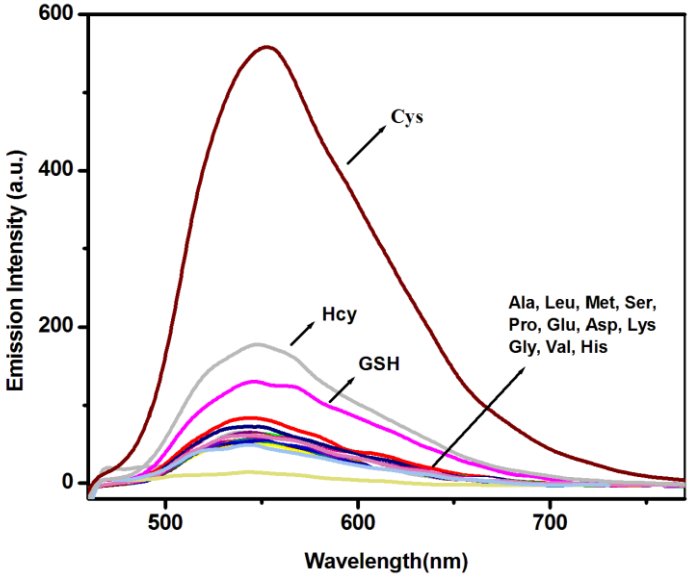

Fig.II.28. Fluorescence spectra of L-Cu^{2+} in presence of different biothiols and amino acids (4 equivalent) in 7:3(v/v) CH_3CN/H_2O medium (HEPES buffer, pH 7.2).

Fluorescence titration was conducted on addition of varying amounts of Cys to the solution of L-Cu^{2+}. On gradual addition of (0-40μM) Cys to a solution of 10 μM L-Cu^{2+} in7:3(v/v) CH_3CN/H_2O medium (HEPES buffer, pH 7.2), the intensity of spectra gradually increases and recovers to that of H_2L (**Fig.II.29**).

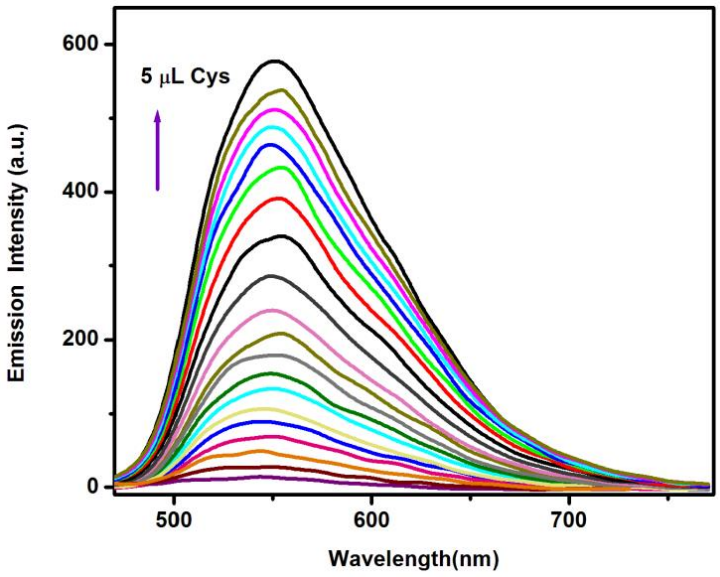

Fig.II.29. Fluorescence Spectra of L-Cu^{2+} on addition of varying amounts of Cys (0-40μM) λ_{ex}= 430 nm.

Scheme II.c represents the reversibility of the emissive probe H_2L which quenches in presence of Cu^{2+} and simultaneously the ensemble L-Cu^{2+} detect Cys by restoring the emission of the probe. The emission intensity

changes at 550 nm when plotted against Cys concentration exhibited a linear correlation. The detection limit (3σ/S method) for Cys is 36 nM (R= 0.99695) which is sufficiently low making it applicable for sensitive detection in living system (**Fig.II.30**).

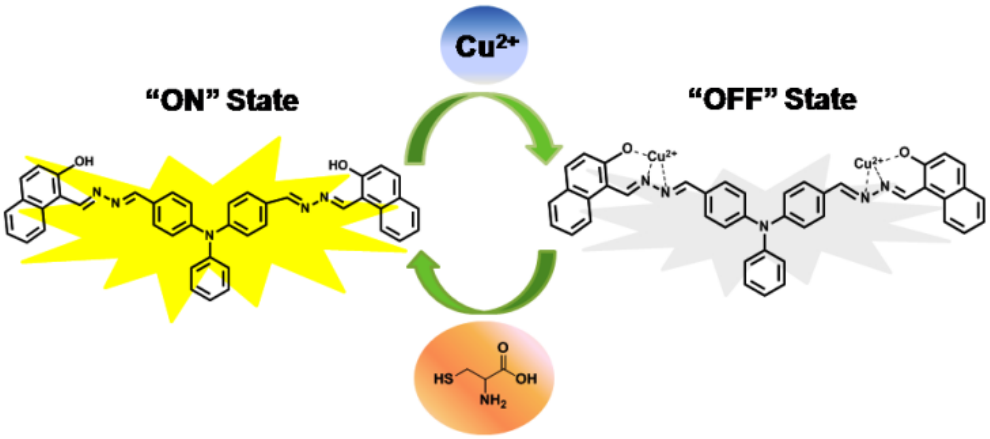

Scheme.II.c. Schematic Representation for Cys sensing by non-fluorescent L-Cu^{2+} ensemble.

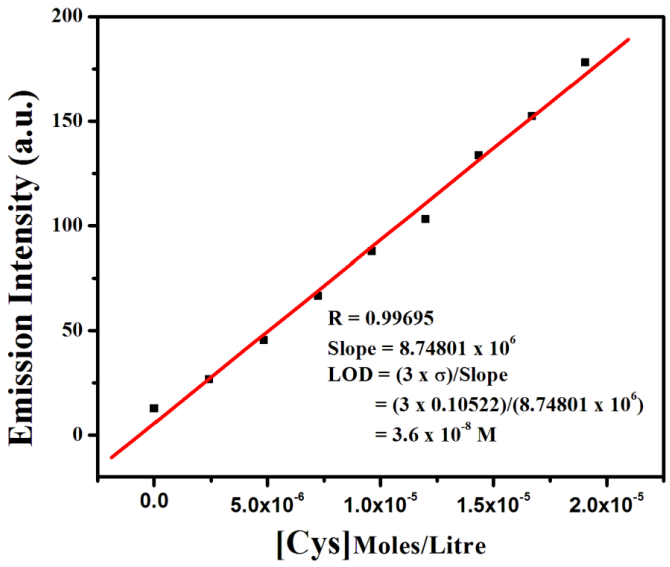

Fig.II.30. Limit of Detection (LOD) for Cys by L-Cu^{2+}.

The LOD value has also been compared with the reported LOD value of Cu^{2+} selective probes for cysteine (Cys) detection which are listed in the **Table II.7**. Most of the Cu^{2+} selective probes available in literature can detect in μM concentration while few reported are shown with LOD in nM range such as Zhang et al reported a Cu^{2+} selective PSMA coated carbon dot chemosensor which detects Cys with LOD value of 78 nM.[82] Wu

reported an aminoantipyrine-napthyl moiety for Cys sensor (LOD 84 nM).[83] Zhang and his co-workers synthesized a coumarin-appended naphthyl Cu^{2+} selective ensemble for cysteine detection (LOD- 15 nM).[84]

Table II.7. Some Reported LOD value for Cu^{2+} Selective Cys Sensor

Sl No.	Probe	Detection Limit Cu	Detection limit Biothiols	Solvent	Ref.
1.	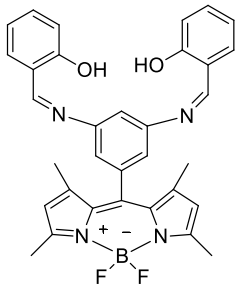	0.1 μM	Cys-0.17 μM Hcy-0.25 μM	CH_3CN/H_2O HEPES Buffer (1:1)	[85]
2.	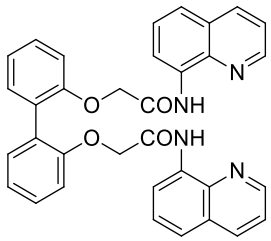		Cys-0.192μM	CH_3CN/H_2O PBS Buffer (1:9)	[86]
3.	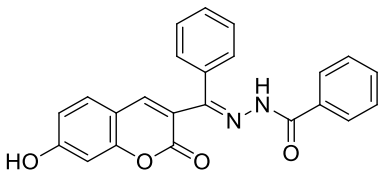	8 μM	Cys-10 μM Hcy-10 μM Glu-16 μM	CH_3CN/H_2O (9:1)	[87]
4.	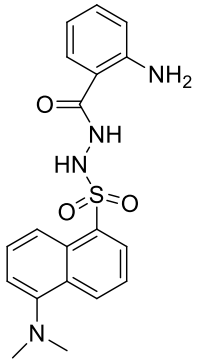	0.97 μM	Cys- 1.76 μM	DMSO/H_2O (1:1)	[88]

5.	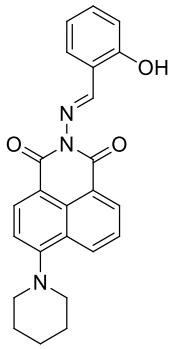		Cys- 0.42 µM Hcy- 0.10µM Glu- 4.24µM	EtOH/HEPES Buffer (9:1)	[89]
6.	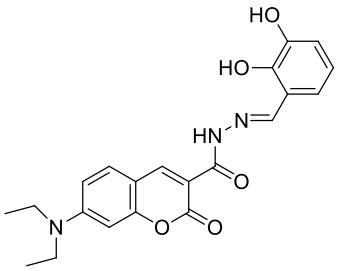	0.25 µM	Cys- 0.72 µM	DMSO/H_2O HEPES Buffer (1:1)	[90]
7.	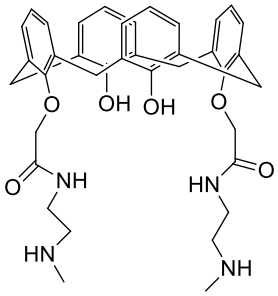	63 µM	Cys-0.5 µM	CH_3CN/H_2O (1:1)	[91]
8.	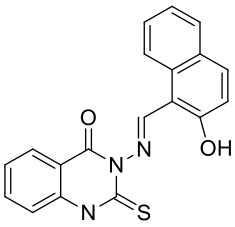	20 nM	Cys- 0.54 µM	DMSO/H_2O HEPES Buffer (1:9)	[92]
9.	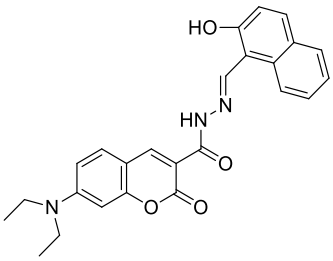		Cys-15 nM	CH_3CN/H_2O HEPES Buffer (7:3)	[93]

10.	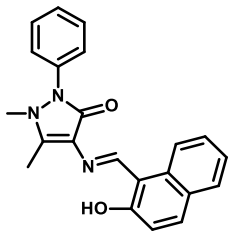		Cys- 84 nM	CH_3CN/PBS Buffer (1:99)	[94]
11.	PSMA coated carbon dot	107 nM	Cys-78 nM	(H_2O)	[95]

The Binding constant from B-H plot is 0.95 × 10^4 M^{-1} which sugggests Cys forms stable association with Cu^{2+} which release the probe and resulted in regeneration of emission (**Fig.II.31**). The overall pattern of the emission spectrum after addition of 40 μM of Cys matches closely with the native fluorescence spectrum of H_2L**.** This clearly supports the fact that on addition of cysteine, it leads to the liberation of H_2L.

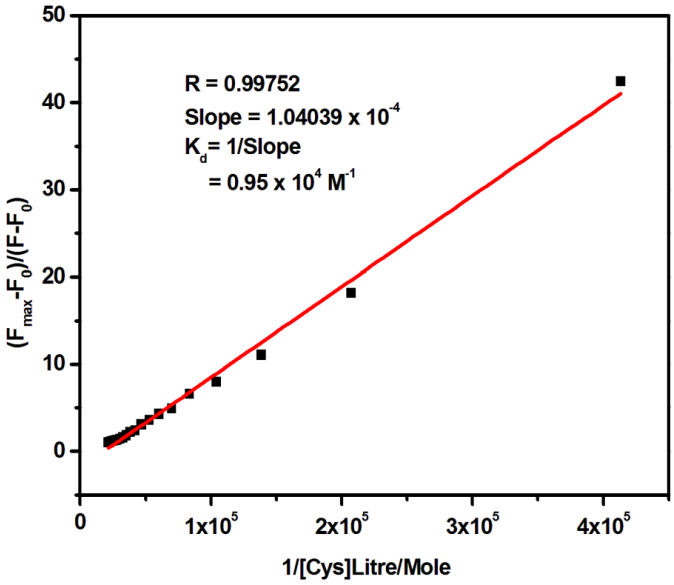

Fig.II.31. Benesi-Hildrebrand Plot for calculating binding constant (K_d) of L-Cu^{2+} with Cys.

The specificity of L-Cu^{2+} towards Cys was further checked in presence of competitive amino acids and the resulting emission intensities illustrates the fact that the response of L-Cu^{2+} to Cys is highly specific without any interference of the added competitive amino acids (**Fig.II.32**). This behavior may reasonably due to high nucleophilicity of thiolate group and steric influence may play a pivotal role in its selectivity to Cys.[96,97]

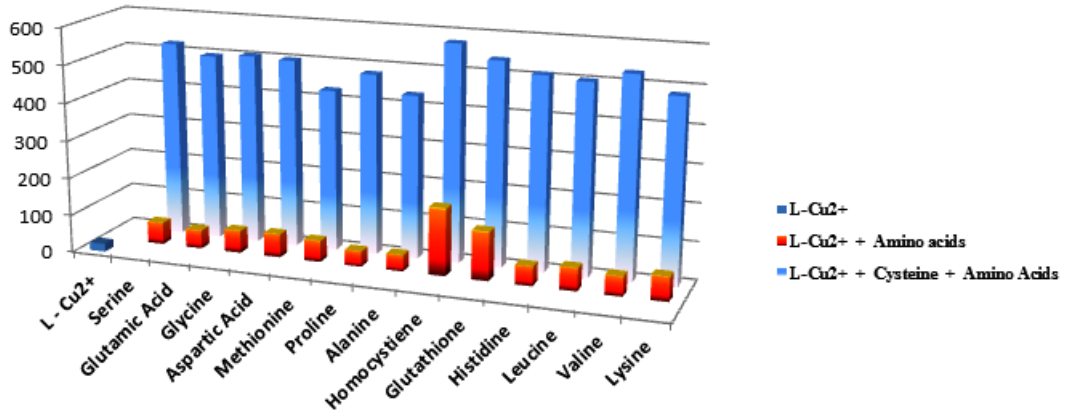

Fig.II.32. Interference study of amino acids on Cys sensing in7:3(v/v) CH_3CN/H_2O medium.

The UV-Vis absorption spectra of L-Cu^{2+} on addition of biothiols and several other amino acids were investigated in 7:3(v/v) CH_3CN/H_2O medium (HEPES buffer, pH 7.2). Noticeably the addition of other amino acids and biothiols induces no such effect on the absorption spectrum of L-Cu^{2+} (**Fig.II.33.(a)**). On addition of increasing concentration of (0-40 μM) Cys the band intensity at 439 nm gradually increases and shifted to the absorption spectrum of the probe H_2L at 430 nm and gets completely recovered on addition of 40 μM of Cys to L-Cu^{2+} (**Fig.II.33.(b)**).

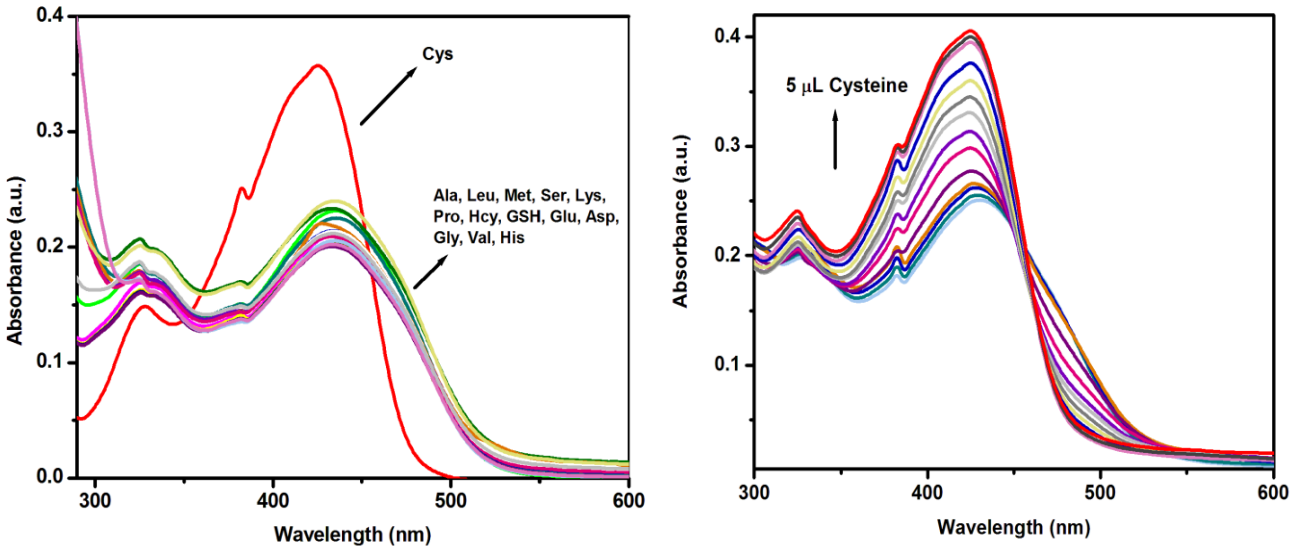

(a) **(b)**

Fig.II.33. (a) Absorption Spectra of L-Cu^{2+} on addition of different Amino Acids (4 equivalent) in 7:3(v/v) CH_3CN/H_2O medium (HEPES buffer, pH 7.2). **(b)** Change in the Absorption Spectra of L-Cu^{2+} on gradual addition of (0-40 μM) Cys.

The formation of Cu-Cys Complex on addition of Cys to L-Cu^{2+} was further confirmed from ESI-MS Spectrum. The peak at m/z = 239 may be due to [Cys+Cu+Cl+H_2O+H^+] and confirms the formation of 1:1 stochiometric complex between Cys and Cu. Another peak appears at m/z = 302 may be assigned to [2Cys + Cu+ H^+] reveals a 1:2 stochiomeric complex along with liberation of H_2L which is clearly confirmed from the peak at m/z =638 (**Fig.II.34**).

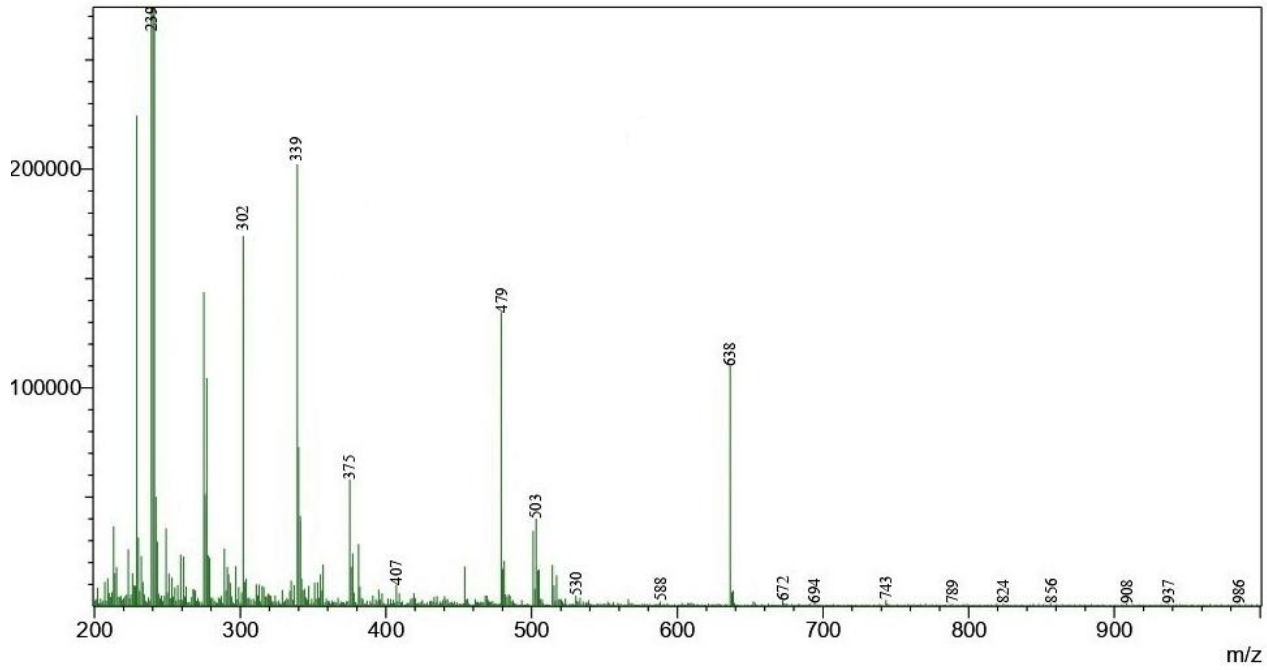

Fig.II.34. ESI-MS of Cu-Cys Complex.

II.3.8. Reversibility

Reversibility is one of the prominent factors for chemosensors for recognition of important analytes. The regeneration of H_2L on addition of Cys to the solution of L-Cu^{2+} results in reversibility of fluorescence response which can be repeated upto 5 times by modulation of Cu^{2+}/Cys addition in 7:3(v/v) CH_3CN/H_2O medium (HEPES buffer, pH 7.2) making the probe H_2L as reversible fluorescence ON-OFF-ON chemosensor for detection of Cu^{2+} and Cys (**Fig .II.35**).

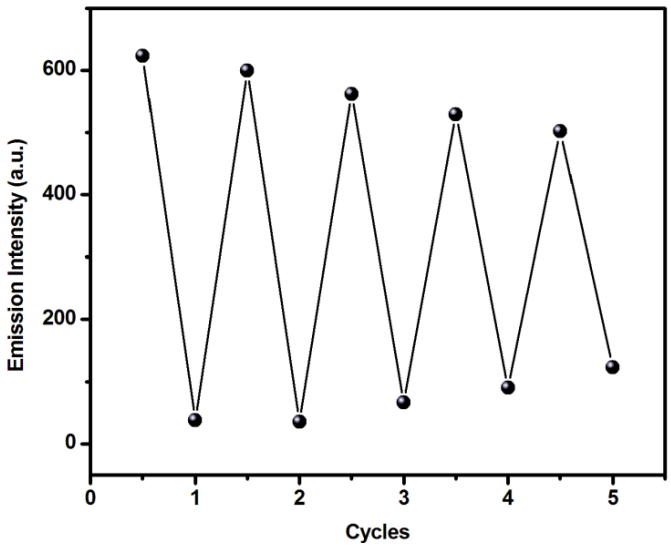

Fig.II.35. Emission Intensity at 550 nm change on alternative addition of Cu^{2+}/Cys with concentration in 7:3(v/v) CH_3CN/H_2O medium (HEPES buffer, pH 7.2).

II.3.9. Logic Behaviour

A molecule with appreciable sensitivity can be beneficial for construction of intregated logic gates.[96] The probe generates a highly emissive band at 550 nm in 7:3(v/v) CH_3CN/H_2O medium (HEPES buffer, pH 7.2) which selectively quenches by Cu^{2+} and this ensemble in presence of Cys results regeneration of emission. Here the probe H_2L operates on two emission states 'ON' and 'OFF' which can be analysed as a molecular logic gate with two chemical inputs. The two input-1(Cu^{2+}) and input-2(Cys) can be considered for the development of IMPLICATION logic gate. Monitoring the fluorescent emission as the output signal, 1 is considered if it is present and 0 if it is absent. The input and output string are connected with combination of H_2L, Cu^{2+} and Cysteine and represented in the truth table (**Fig.II.36**).

INPUT 1 Cu^{2+}	INPUT 2 Cys	OUTPUT λ_{em} = 550 nm
0	0	1
1	0	0
0	1	1
1	1	1

Fig.II.36. Molecular IMPLICATION Logic gate construction for Cu^{2+} and Cys.

II.3.10. Cell Study

In order to check the cellular toxicity of the probe H_2L, an in vitro cytotoxicity study was estimated for assuring its biocompatibility on WI-38 cell line. The cells were treated with five different concentrations (20 µM, 40 µM, 60 µM, 80 µM and 100 µM ml^{-1}) for 24 h and followed by MTT assay. It was evaluated from the experimental observation that the ligand exhibited no significant toxicities even at the highest concentration of 100 µM (**Fig.II.37**). Therefore the results ensure that the biocompatibility of H_2L applicable to living systems.

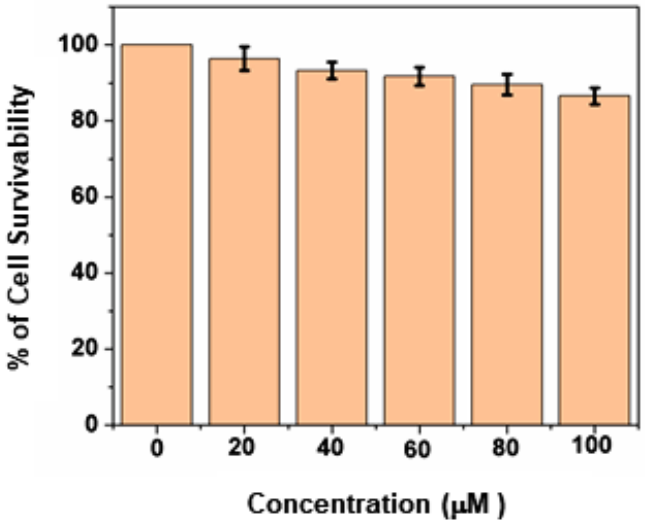

Fig.II.37. Cell survivability of the ligand on WI-38 cell line.

The cellular internalisation study of H_2L was carried out in the hepatocellular carcinoma cells. The cellular uptake of H_2L (10μM), Cu^{2+}salt (20 μM) and cysteine (40μM) by HepG2 cells were examined through the fluorescence microscopy study. A prominent red signal observed for cells treated with the probe. The prominent red fluorescence is observed as the compound penetrates into the cells which in turn results in the red emission. The red signal immediately disappears after addition of 20 μM of Cu^{2+} salt. To perform the fluorescence imaging of Cys in Hep G2 cells, 40μM of Cys added to cells incubated with L-Cu^{2+} which resulted in reappearance of bright red fluorescence.

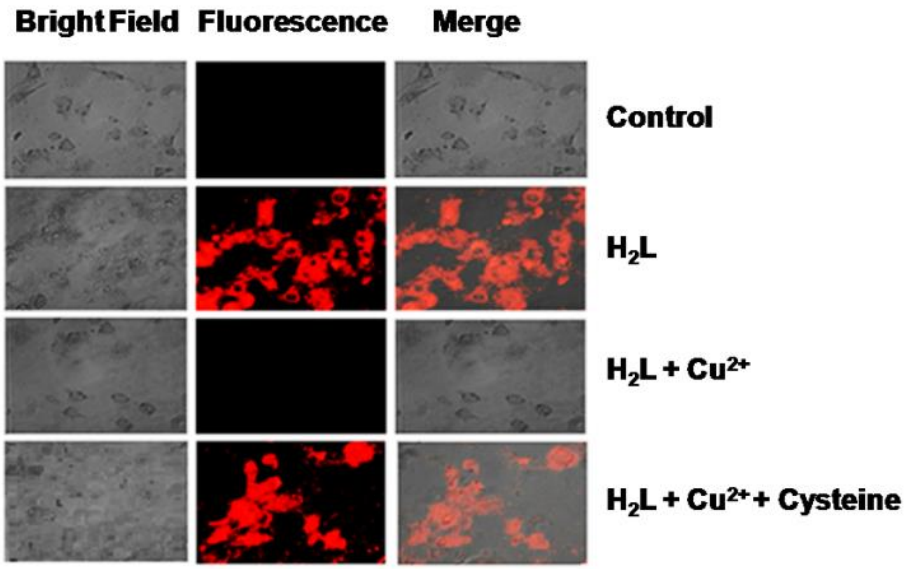

Fig.II.38. Bright field, fluorescence and merged microscopic images of untreated HepG2 (Control), cells treated with H_2L(10 μM), Cu^{2+}(20 μM), Cys(40 μM).

The concentration of free copper ions has been estimated to be of the order of 10^{-18}–10^{-13} M in yeast cells and in human cells. So we can easily comprehend that the quantity within the cellular mileu is too low for our sensor H_2L to detect (Limit of detection 7.3 nM) Therefore the insitu detection of Cu^{2+}/Cys is not possible by employing our sensing probe, H_2L.[97] However, the overall results show that the cells can readily uptake H_2L, Cu^{2+} and Cys with a prominent response at cellular level (**Fig.II.38**).

II.4. Conclusion

A Highly Emissive Difomyl triphenyl-napthyl hydrazide based probe has been Synthesized and well characterized. The strongly emissive probe shows efficient sensitivity and selectivity for Cu^{2+} ion through turn off approach over a series of important cations with a low detection limit of 7.3 nM under physiological condition. The interaction of Cu^{2+} with the probe has been experimentally determined. DFT and TDDFT calculation were in accordance with the experimental results. The L-Cu^{2+} complex is applied for selective detection of Cys amongst other biothiols and amino acids with LOD value of 36 nM for Cys. The strong affinity of Cys towards Cu^{2+} leads to the recovery of emission of H_2L turning it to be a reversible ON-OFF-ON chemosensor and can be beneficial for construction of IMPLICATION logic gate. A MTT studyinWI-38 Cell and fluorescence cell imaging in Hep G2 cells shows biocompatibility of the probe for sensing application at cellular level.

II.5. Reference:

1. P. Kaur, S. Kaur and K. Singh, *Inorg. Chem. Commun.*, 2009, **12**, 978-981.

2. W. Wang, A. Fu, J. You, G. Gao, J. Lan and L. Chen, *Tetrahedron*, 2010, **66**, 3695-3701.

3. K. J. Barnham, C. L. Masters and A. I. Bush, *Nat. Rev. Drug Discov.*, 2004, **3**, 205–214.

4. Y. K. Jang, U. C. Nam, H. L. Kwon, I. H. Hwang and C. Kim, *Dyes Pigment*., 2013, **99**, 6-13.

5. E. Gaggelli, H. Kozlowski, D. Valensin, G. Valensin, *Chemical Reviews* 2006, **106,** 1995-2044.

6. M. Li, H. Ge, R. L. Arrowsmith, V. Mirabello, S. W. Botchway, W. Zhu, S. I. Pascu and T. D. James, *Chem. Commun*., 2014, **50**, 11806-11809.

7. S. Goswami, S. Chakraborty, S. Paul, S.Halder, S.Panja and S. K. Mukhopadhyay, *Org. Biomol. Chem.*, 2014, **12**, 3037–3044.

8. J. S. Becker, A. Matusch, C. Depboylu, J. Dobrowolska and M. V. Zoriy, *Anal. Chem.*, 2007, **79**, 6074–6080.

9. Y. Liu, P. Liang and L. Guo, *Talanta*, 2005, **68**, 25–30.

10. Y. Zheng, Q. Huo, P. Kele, F. M. Andreopoulos, S. M. Pham and R. M. Leblanc, *Org. Lett*. 2001, **3**, 3277–3280.

11. C. Sinha, A. Adak, R. Purkait, S. K. Manna, B. Ghosh and S. Pathak, *New J. Chem.*, 2019, **43,** 3899-3906

12. S. Dey, S. Maity, K. Pal, K. Jana and C. Sinha, *Dalton Trans.*,2019, **48**,17818-17830.

13. B. Dutta, R. Purkait, S. Bhunia, S. Khan, C. Sinha and M. H. Mir., *RSC Adv*., 2019, **9**, 38718-38723.

14.S. Wang, Z. Wang, Y. Yin, J. Luo, L. Kong, *J. Photochem. Photobiol. A: Chem.*, 2017, **333**, 213–219.

15. O. García-Beltrán, N. Mena, L.C. Friedrich, J.C. Netto-Ferreira, V. Vargas, F.H. Quina, M.T. Nú˜nez, B.K. Cassels, *Tetrahedron Lett.*, 2012, **53**, 5280–5283.

16. G. Yin, J. Yao, S. Hong, Y. Zhang, Z. Xiao, T. Yu, H. Li and P. Yin, *Analyst*, 2019, **144**, 6962-6967.

17. V. Dujols, F. Ford, A.W. Czarnik, *J. Am. Chem. Soc.*, 1997, **119**, 7386–7387.

18. L. Tang, X. Dai, X. Wen, D. Wu and Q. Zhang, *Spectrochimica Acta A: Mol. Biomol. Spectrosc.* 2015, **139**, 329-334.

19. Z.-H. Xu, H.-W. Wang, X.-F.Hou, W.-L.Xu, T.-C.Xiang, C.-Z. Wu, *Sens. Actuators B*, 2014, **201** 469–474.

20. B. Muthuraj, R. Deshmukh, V. Trivedi, P.K. Iyer, *ACS Appl. Mater.Interfaces*, 2014, **6**, 6562–6569

21. Y. Wang, H.Wu, W.-N.Wu, S.-J.Li, Z.-H.Xu, Z.-Q.Xu, Y.-C.Fan, X.-L.Zhao, B-Z.Liu, *Sens. Actuators B*, 2018, **260**, 106–115 .

22. T. P. Dalton, H. G. Shertzer and A. Puga, *Pharmacol. Toxicol*., 1999, **39**, 67-101.

23. E. Weerapana, C. Wang, G. Simon, F. Richter, S. Khare, M. Dillon, D. Bachovchin, K. Mowen, D. Baker and B. Cravatt, *Nature*, 2010, **468**, 790–795.

24. J. Shao, H. Guo, S. Ji, J. Zhao, *Biosen.Bioelectron*., 2011, **26**, 3012-3017.

25. H.-Y. Shiu, M.-K. Wong, C.-M.Che, *Chem.Commun.*, 2011, **47**, 4367-4369.

26. Y. Tang, H.-R. Yang, H.-B.Sun, S.-J.Liu, J.-X.Wang, Q. Zhao, X.-M.Liu, W.-J.Xu, S.-B. Li, W.Huang, *Chem. Eur. J.*, 2013, **19**, 1311-1319.

27. F. Wang, Z. Guo, X. Li, X. Li, C. Zhao, *Chem. Eur. J.*, 2014, **20**, 11471-11478.

28. Y. Shi, J. Yao, Y. Duan, Q. Mi, J. Chen, Q. Xu, G. Zhang, Y. Zhou and J. Zhang, *Med. Chem. Lett.*, 2013, **23**, 2538–2542.

29. X. Chen, H. Xu, S. Ma, H. Tong, K, Lou and W. Wang, *RSC Adv.*, **2018**, *8*, 13388–13392.

30. D. Maheshwaran, S. Priyanga and R Mayilmurugan, *Dalton Trans.*, **2017**, *46*, 11408–11417.

31. X. Gao, X. Li, L. Li, J. Zhou and H. Ma, *Chem. Commun.*, **2015**, *51*, 9388-9390.

32. G. Yin, T.Niu, Y. Gan, T. Yu, P. Yin, H. Chen, Y. Zhang, H. Li, and S. Yao, *Angew. Chem. Int. Ed.*, 2018, **57**, 4991-4994.

33. Z. Mao, M. Wang, J.Liu, L.-J.Liu, S. M.-Y. Lee, C.-H. Leung and D.-L. Ma, *Chem. Commun.*, 2016, **52**, 4450-4453.

34. M. Tang, L. Wu, D. Wu, C.Huang, W.Zhu, Y.Xu and X. Qian, *RSC Adv.*, 2016, **6**, 34996-35000

35. R. Xie, Y. Li, Z. Zhou, X. Pang, C. Wu, P. Yin, H. Li, *Anal.Bioanal.Chem.*, 2020, **412**, 5539-5550.

36. Y. W. Choi, J. J.Lee,G. R.Youand C. Kim, *RSC Adv.*, 2015, **5**, 38308-38315.

37. D. D. Perrin, W. L. F. Armarego, D. R. Perrin, Purification of Laboratory Chemicals, Pergamon Press, Oxford, U.K., 1980.

38. S. Samanta, S. Goswami, Md. N. Hoque, A. Ramesh and G. Das, *Chem. Commun.,* 2014, **50,** 11833-11836.

39. D. Maiti, A. S. M. Islam, M. Sasmal, C. Prodhan and M.Ali, *Photochem. Photobiol.Sci.* 2018, **17**,1213-1221.

40. A. Samui, K. Pal, P. Karmakar and S. K. Sahu, *Mater. Sci. Eng. C,* 2019, **98**, 772-781.

41. K. Pal, S. Roy, P. K. Parida, A. Dutta, S. Bardhan, S. Das, K. Jana and P. Karmakar, *Mater. Sci. Eng. C,* 2019, **95,** 204-216.

42. M. J. Frisch, G. W. Trucks, H. B. Schlegel, G. E. Scuseria, M. A. Robb, J. R. Cheeseman, G. Scalmani, V. Barone, B. Mennucci, G. A. Petersson, H. Nakatsuji, M. Caricato, X. Li, H. P. Hratchian, A. F. Izmaylov, J. Bloino, G. Zheng, J. L. Sonnenberg, M. Hada, M. Ehara, K. Toyota, R. Fukuda, J. Hasegawa, M. Ishida, T. Nakajima, Y. Honda, O. Kitao, H. Nakai, T. Vreven, J. A. Montgomery Jr., J. E. Peralta, F. Ogliaro, M. Bearpark, J. J. Heyd, E. Brothers, K. N. Kudin, V. N. Staroverov, R. Kobayashi, J. Normand, K. Raghavachari, A. Rendell, J. C. Burant, S. S. Iyengar, J. Tomasi, M. Cossi, N. Rega, J. M. Millam, M. Klene, J. E. Knox, J. B. Cross, V. Bakken, C. Adamo, J. Jaramillo, R. Gomperts, R. E. Stratmann, O. Yazyev, A. J. Austin, R. Cammi, C. Pomelli, J. W. Ochterski, R. L. Martin, K. Morokuma, V. G. Zakrzewski, G. A. Voth, P. Salvador, J. J. Dannenberg, S. Dapprich, A. D. Daniels, O. Farkas, J. B. Foresman, J. V. Ortiz, J. Cioslowski and D. J. Fox, Gaussian 09, Revision D.01, Gaussian Inc., Wallingford, CT, **2009**.

43. A. D. Becke, *J. Chem. Phys.*,1993, **98**, 5648–5652.

44. W.R. Wadt and P.J. Hay, *J. Chem. Phys*., 1985, **82**, 299-310

45. R. Bauernschmitt and R. Ahlrichs, *Chem. Phys. Lett*., 1996, **256**, 454–464.

46. M. Cossi and V. Barone, *J. Chem. Phys*., 2001, **115**, 4708–4717.

47. M. Cossi, N. Rega, G. Scalmani and V. Barone, *J. Comput. Chem.*, 2003, **24**, 669–681.

48. N. M. O'Boyle, A. L. Tenderholt and K. M. Langner, *J. Comput. Chem*., 2008, **29**, 839–845.

49. D. Śmiłowicz, N. M.-Nolte, *J. Inorg. Bio.,* 2020, **206**, 111410.

50. V.S. Padalkar, S. Seki, *Chem. Soc. Rev*., 2016, **45**, 169–202.

51. R. Hu, S. Li, Y. Zeng, J. Chen, S. Wang, Y. Li, *Phys. Chem. Chem. Phys*., 2011, **13,** 2044–2051.

52. P.P. Soufeena, T.A. Nibila, K.K. Aravindakshan, *Spectrochimica Acta A: Mol.Biomol. Spectrosc.*,2019, **223**, 117201

53. Z. Tu, M. Liu, Y. Qian, G. Yang, M. Cai, L. Wang, W. Huang, *RSC Adv*., 2015, **5**, 7789–7793.

54. Z. Tu, Q. Zhang, M. Liu, Y. Qian, L. Wang, W. Huang, *J. Mater Sci.* 2016, **51**, 2972–2979.

55. G. Yang, K. Zhang, F. Gong, M. Liu, Z. Yang, J. Ma, S. Li, *Sens. Actuators B.*, 2011, **155** 848–853

56. R. Hu, J. Feng, D. Hu, S. Wang, S. Li, Y. Li, G. Yang, *Angew. Chem.* **2010**, *49*, 4915 –4918.

57. S. Bhardwaj, N.Maurya, A. K. Singh, R.Varshney, P.Roy, *RSC Adv.* **2016**, *6,*102096-102101.

58. B. Liu, H. Zhou, B. Yang, X. Hu, *Sens. Actuators B.*, 2017, **246**, 554–562.

59. H. S. Jung, J. H. Han, Z. H. Kim, C. Kang, J. S. Kim, *Org. Lett,* 2011, **13**, 5056-5059.

60. C. Yin, J. Li, F. Huo, *Curr. Med. Chem.*, 2019, **26**, 3958-4002.

61. B. Gu, L. Huang, Z. Xu, Z. Tan, M. Hu, Z. Yang, Y. Chen, C. Peng, W. Xiao, D. Yu, H. Li, *Sens. Actuators B.*, 2018, **273**, 118-125.

62. S. Bhardwaj, N. Maurya, A. K. Singh, R. Varshney, P. Roy, *RSC Adv.* 2016, **6,** 102096-102101.

63. M. S. Kim, S. Y. Lee, J. M. Jung, C. Kim, *Photochem. Photobiol. Sci.*, 2017, **16,** 1677-1689.

64. S. Wang, Z. Wang, Y. Yin, J. Luo, L. Kong, *J. Photochem. Photobiol. A: Chem.*, 2017, **333**, 213–219.

65. L. Tang, X. Dai, X. Wen, D. Wu and Q. Zhang, *Spectrochimica Acta A: Mol. Biomol. Spectrosc.* 2015, **139**, 329-334.

66. S. Goswami, S. Chakraborty, S. Paul, S. Halder, S. Panja and S. K. Mukhopadhyay, *Org. Biomol. Chem.*, 2014, **12,** 3037–3044.

67. B. Liu, H. Zhou, B.Yang, X. Hu, *Sens. Actuators B,* 2017, **246**, 554–562.

68. L. Tang, M. Cai, *Sens. Actuators B,* 2012, **173**, 862– 867.

69. Y. Fu, Q.-C.Feng, X.-J.Jiang, H. Xu, M. Li and S.-Q.Zang, *Dalton Trans.*, 2014, **43**, 5815–5822

70. N. Narayanaswamy, T. Govindaraju, *Sens. Actuators B.*, 2012, **161**, 304– 310

71. Y. Wang, P.-D. Mao, W.-N.Wu, X.-J.Mao, X.-L. Zhao, Z.-Q.Xu, Y.-C.Fan, Z.-H.Xu, *Sens. Actuators B,* 2017, **251,** 813–820.

72. Y. Fu, C. Fan, G. Liu, S. Pu, *Sen. Actuators B,* 2017, **239**, 295–303

73. W. He and Z. Liu, *RSC Adv*. 2016, **6**, 59073-59080.

74. G. Yin, J. Yao, S. Hong, Y. Zhang, Z. Xiao, T. Yu, H. Li and P. Yin, *Analyst*, 2019, **144**, 6962-6967.

75. B. Gu, L. Huang , Z. Xu , Z. Tan, M. Hu, Z. Yang, Y. Chen, C. Peng, W. Xiao, D. Yu, H. Li *Sens. Actuators B,* 2018, **273**, 118-125.

76. P. Singha,, H. Singha , G. Bhargavab and S. Kumara, *J. Mater. Chem. C.*, 2015, **3**,5524-5532

77. D. Zhao, T.M. Swager, *Macromolecules* 2005, **38**, 9377–9384.

78. S. Dey, R. Purkait, K. Pal, K. Jana, and C. Sinha, *ACS Omega*, 2019, **4**, 8451−8464.

79. V. Sharma, D. De, S. Pal, P. Saha, and P. K. Bharadwaj, *Inorg.Chem*. 2017, **56**, 8847−8855.

80. J. Ding, L. Yuan, L. Gao, J. Chen, *J. Lumin* **2012**, **132**, 1987–1993.

81. R. Jiang, N. Liu, F. Li, W. Fu, Y. Zhou and Y. Zhang, *Polymer.*, 2018, *10*,786.

82. H. Fang, N. Wang, L. Xie, P. Huang, K.-Y. Deng, F.-Y. Wu, *Sens. Actuators B*, 2019, **294**, 69-77.

83. Y. Wang, Q. Meng, Q. Han, G. He, Y. Hu, H.Feng, H. Jia, R. Zhang and Z. Zhang, *New J. Chem*., 2018, **42,** 15839-15846.

84. H. Zhao, Y.Luo, H.Wang, T.Guo, H.Zhou, H.Tan, Z.Zhou, Y.Long, Z. Tang, *ChemistrySelect*, 2018, **3**, 1521-1526.

85. Q. Li , Y. Guo, S. Shao, *Sens. and Actuators B*, 2012, **171– 172,** 872– 877.

86. G. Chai, Q. Liu, Q. Fei, J. Zhang, X. Sun, H. Shan, G. Feng, Y. Huan, *Luminiscience*, 2018, **33**, 153-160.

87. H. Li, X. Sun, T. Zheng, Z. Xu, Y. Song, X. Gu., *Sens. Actuators B*, 2019, **279**, 400-409.

88. T.Anand, V. Bhardwajand S. K. Sahoo, *Photochem. Photobiol. Sci***.,** 2019, **18**, 1533-1539.

89. Y. G. Shi, J. H. Yao, Y. L. Duan, Q. L Mi, J. H. Chen, Q. Q. Xu, G. Z. Gou, Y. Zhou, J. F. Zhang, *Bioorg. Med. Lett*. **2013**, *23*, 2538-2542.

90. Q. Meng, H. Jia, P. Succar, L. Zhao, R. Zhang, C. Duan, Z. Zhang *Biosens. And Bioelectron.,* **2015**, *74*, 461-468.

91. M. Bhatt, D. Maity, V. Hingu, E. Suresh, B. Ganguly, and P. Paul., *New J. Chem.* **2017**, *41*, 12541-12553.

92. T. Anand, G. Sivaraman, D. Chellappa, *J. Photochem. Photobio. A: Chem.* **2014**, *281*, 47-52.

93. Y. Wang, Q. Meng, Q. Han, G. He, Y. Hu, H. Feng, H. Jia, R. Zhang and Z. Zhang, *New J. Chem.* **2018**, *42*, 15839-15846.

94. H. Fang, N. Wang, L. Xie, P. Huang, K.-Y. Deng, F.-Y. Wu, *Sens. Actuators B*, 2019, **294**, 69-77.

95. R. Jiang, N. Liu, F. Li, W. Fu, Y. Zhou and Y. Zhang, *Polymer*, 2018, **10**,786.

96. X. Tian, Z.P. Dong, J. R. Hou, R. Wang and J.T. Ma, *J. Lumin*, 2014, **145**, 459-465.

97. H. Tapiero, D.M. Townsend and K.D. Tew, *Biomed Pharmacother.*, 2003, **57**, 386–398.

Chapter III

A Highly Emissive Zn(II)-pyridyl-benzimidazolyl-phenolato based Chemosensor : Detection of $H_2PO_4^-$ via "Use" and "Throw" Device Fabrication.

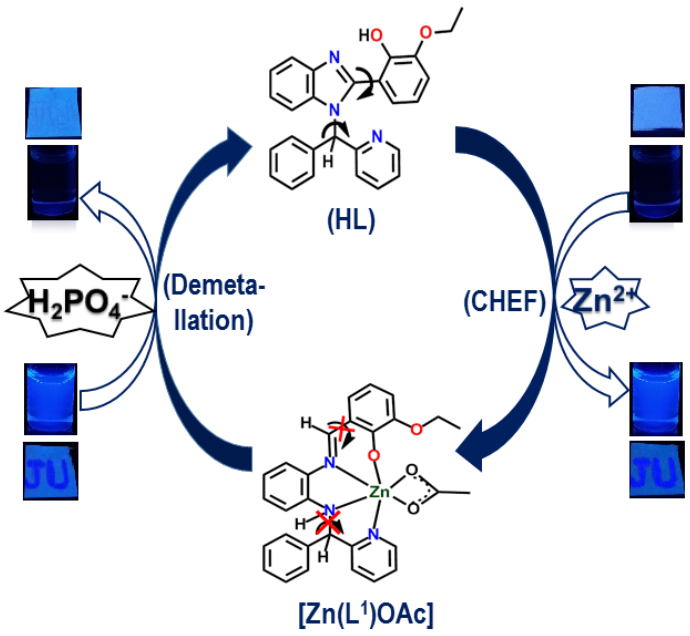

CHAPTER III

Abstract

2-Ethoxy-6-[1-(phenyl-pyridin-2-yl-methyl)-1H-benzoimidazol-2-yl]-phenol (HL) selectively serves as sensitive 'turn on' Zn^{2+} sensor in 9:1 (v/v) DMSO/H_2O (HEPES Buffer, pH=7.4) medium in presence of sixteen other cations at the limit of detection (LOD) 3.2 nM. The stronng blue emission of the complex, {[Zn(L^1)OAc]} (HL^1 = benzimidazolyl ring opening structure of HL) (λ_{em}, 461 nm), is quenched by the $H_2PO_4^-$ in presence of eighteen other anions and the LOD is 0.238 μM. The cause of the emission of the complex, is due to the restricted intramolecular rotation (RIR) followed by the chelation enhanced fluorescence (CHEF). The quenching of the emission of [Zn(L^1)OAc] by $H_2PO_4^-$ (in presence of other P^Vs (inorganic and biological) as well as additional anions) is due to 'turn off' fluorescence via demetalltion and releasing of nonfluorescent ligand, HL and $[Zn(H_2PO_4)]^+$. An INHIBIT logic gate memory circuit of the probe, HL, is devised with Zn^{2+} and $H_2PO_4^-$ as two consecutive inputs. The percentage of $H_2PO_4^-$ recovery is excellent and is obtained from distilled, tap and drinking water sources. The bright blue emission of [Zn(L^1)OAc] further triggers to fabricate ready-made portable thin films of the Zn-complex which executes a cost-effective 'on-site' solid state contact mode detection of $H_2PO_4^-$ at the selectivity of picogram level (10.97 pg/cm^2) by monitoring the intensity of quenched spots under UV light upon varying the analyte concentration from 10^{-8} to 10^{-3} M. Finally, taking the advantage of reversible fluorescence switching, a simple and definite ion responsive security feature is successfully embedded into a "Use" and "Throw" solution coated paper strip of the present Zn(II)-pyridyl-benzimidazolyl-phenolato based chemosensor, which efficiently detects $H_2PO_4^-$ from water by a successive 'ON-OFF' fluorescence switching driven security activity without any exhaustion in emission phenomenon.

III.1. Introduction

Phosphates (P^V, inorganic phosphates (PO_4^{3-}, $H_2PO_4^-$, HPO_4^{2-}, $P_2O_7^{4-}$, $P_3O_{10}^{5-}$, polyphosphates) and biogenic phosphates (AMP^{2-}, ADP^{3-} and ATP^{4-}, nucleic acids, phospholipids) are ubiquitous in ecology and environment, and have attracted considerable attention owing to their inevitable relevance in energy metabolism, signal transduction, regulation of protein and genetic information transfer[1,2] and manufacturing of antiviral as well as chemotherapeutic drugs.[3,4] Khoshiniat *et al*. reviewed and suggested that, the local phosphate concentration in serum acts as a signal regulating agent for some important biological events like bone, teeth and muscles or vascular calcification.[5] Phosphates are useful genetic components for development of essential biopolymers - DNA, RNA and phospholipids along with transcription of energy and signal *via* development of bioproteins like Adenosine triphosphate (ATP).[6,7–9] Essentially, phosphates have extensively been utilized as nutrient and fertilizer for all plants and crops in agricultural processes.[10] However, excessive dispensation together with uncontrolled discharge of such ions/compounds in environment through wind erosion, surface runoff from terrestrial to aquatic ecosystems, triggered by the agriculture, animal husbandry and other anthropogenic activities causes a severe threat for the human health and living organisms. Over-leakage of inorganic phosphates as agricultural wastes eventually results in eutrophication for the aquatic bodies via decomposition and depletion of dissolved oxygen due to excessive algal growth in water.[11] Therefore, the permissible level of phosphate in drinking water has been minimized by WHO to 1 mg/L.[6] Side-by-side, irregular concentration of phosphate in human body leads to the clinical diagnostics of various disorders related to vitamin D deficiency, mineral and bone syndrome,[12] illness of hyperparathyroidism, hypertension,[13] Franconia disorder,[14,15] hyperphosphatemia and cardiovascular complications.[6] On considering their importance in both biology and environment, a great effort has been made for the trace level detection of P^V in analytical biochemistry.

Various techniques based on gravimetry, volumetry, spectrophotometry, electrochemistry, enzymatic coupled reactions have been adopted for quantitative estimation of P^V.[16] In most cases, the methods have been developed with the reference to yellow molybdophosphate. However, these methods are suffering from a

serious drawback of acidic pH condition (conc. HNO_3) and the usage of hazardous chemicals. Out of these methods, fluorescence molecular sensors specific to inorganic phosphate (Pi) is turned out to be highly sensitive, selective, inexpensive and simple. Hydrogen bonding, pi-interaction, self-assembly for Aggregation Induced Emission/Quenching, coordination of oxoanions, chemical reaction, displacement approach etc. are the advanced procedures for ion detection by molecular fluorescence sensing techniques.[17-19] Due to their importance in biology and environment, considerable attention has been made to develop systems capable of selective sensing of phosphates and their related compounds. Several comprehensive reviews describing the recognition of phosphate molecules by artificial receptors have been published.[20–28]

Out of various intrinsic forms of phosphorus, dihydrogen phosphate ($H_2PO_4^-$) has been considered as a predominant component of inorganic phosphate owing to its prevailed equilibrium between other two basic anions HPO_4^{2-} and PO_4^{3-} at physiological pH.[16] Therefore, sensitive and selective detection of $H_2PO_4^-$ as a primary target analyte is a topic of paramount importance. In this aspect, design of fluorogenic metal complex which could selectively interact with $H_2PO_4^-$ through altering its emission by desire physical or chemical methods is of uppermost priority.[1,6]

Sequential “ON-OFF” fluorescence switching formulated on the direct coordination of a metal ion to the organic scaffold followed by its demetallation with the desired anion based on the relay displacement process not only successfully resolves the prolonged dearth of phosphate detection but also enjoys the added benefit of dual sensing (metal ions and anions) with the exchangeable indicator in a single chemosensor framework, where the sensing mechanism remains independent of analyte structure.[29, 30] Amongst different metal ions, second most abundant essential element Zn(II) imparts a sensitive recognition towards $H_2PO_4^-$ and is biologically important.[31–36] The lack of spectroscopic signature of Zn(II) due to its intrinsic ($3d^{10}$) electronic configuration can successfully be resolved by its spontaneous tendency to divulge a feasible complexation with varied organic chemosensors, which ultimately tune the photophysics of luminogenic receptor through the real-time modulation in fluorescence signal upon hampering the metal-induced electronic communication in presence of required anion.[37] Taking the inspiration from the simultaneous detection of multi-analytes, the

present study unearths an easy-made novel benzimidazole appended probe, 2-ethoxy-6-[1-(phenyl-pyridin-2-yl-methyl)-1H-benzoimidazol-2-yl]-phenol (HL) based on a single step Schiff base condensation, where the targeted detection requires merely ambient conditions. Unlike most of the unstable phosphate sensors having poor sensitivity,[38] the present receptor unveils sensitive and selective relay recognition of $H_2PO_4^-$ both in solution and solid state *via* "ON-OFF" fluorescence switching of the sensor, triggered by a ring opening chelation of Zn^{2+} followed by its displacement by $H_2PO_4^-$, with desired accuracy and comparability in each recognition step.

III.2. Experimental section

III.2.1. Materials and methods

2-Benzoylpyridine, o-Phenylenediamine, 3-Ethoxysalicyldehyde were purchased from Sigma-Aldrich. Inorganic salts (Cation sources: $Zn(OAc)_2.2H_2O$, $Cd(OAc)_2$, $Hg(OAc)_2$, $CuCl_2.2H_2O$, $CoCl_2.6H_2O$, $PbCl_2$, $Al(NO_3)_3.9H_2O$, $CaCl_2.6H_2O$, $FeCl_3.6H_2O$, $BaCl_2.2H_2O$, $NiCl_2.6H_2O$, NaCl, $MnCl_2.4H_2O$, $PdCl_2$, $CrCl_3.6H_2O$, KCl, $MgCl_2$; Anion sources: KH_2PO_4, $Na_2S_2O_3.5H_2O$, K_3PO_4, NaCl, NaF, NH_4HF_2, KNO_3, KBr, $NaNO_2$, NaN_3, Na_3AsO_4, CH_3COONa, $NaAsO_2$, KIO_3, $Na_4P_2O_7$, KI, Na_2SO_4, Na_2S, and $Na_2S_2O_5$,) were bought from Merck. For spectroscopic measurement, spectroscopic grade solvents were used from TCI. The solvents were dried by standard procedure for spectroscopic studies.[39] Milli-Q water (Millipore) was used for preparation of aqueous solutions of metal salts. Perkin-Elmer (2400 Series-II, Perkin Elmer, USA) CHN analyzer was utilized for elemental analysis purpose. The spectra were recorded by Lambda 25 spectrophotometer: UV-Vis; LS55: fluorescence and LX-1FTIR spectrophotometer: FT-IR spectra (KBr disk, 4000-400 cm^{-1}) on Perkin Elmer instruments. ^1H and ^{13}C NMR spectra were taken by Bruker 500 MHz FT-NMR spectrometer. The chemical shift (δ) of the respective NMR spectra were recorded in parts per million (ppm) with respect to Trimethylsilane (TMS) as internal standard. ESI-MS spectra were obtained from HRMS spectrometer (model, XEVO-G2QTOF#YCA351).

III.2.2. Synthesis of 2-Ethoxy-6-[1-(phenyl-pyridin-2-yl-methyl)-1H-benzoimidazol-2-yl]-phenol (HL)

N-(Phenyl-pyridin-2-yl-methyl)-benzene-1,2-diamine was synthesized by following literature procedure.[40] To dry methanol solution (10 mL) of N-(Phenyl-pyridin-2-yl-methyl)-benzene-1,2-diamine (0.275 g, 1.0 mmol), 3-Ethoxy-Salicyldehyde (0.166 g, 1.0 mmol in 15 mL methanol) was added gradually and the mixture was stirred for 12 h. Clear solution was allowed to evaporate slowly (**Scheme III.a**) to isolate yellow coloured prismatic crystals (0.305 g, Yield ~72 %) after two weeks, which was characterized by various spectroscopic techniques including single crystal X-ray diffraction measurement.

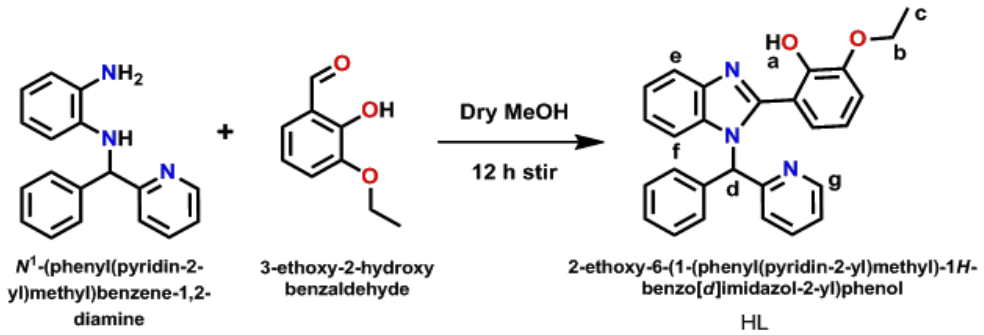

Scheme III.a : Synthesis of the ligand HL.

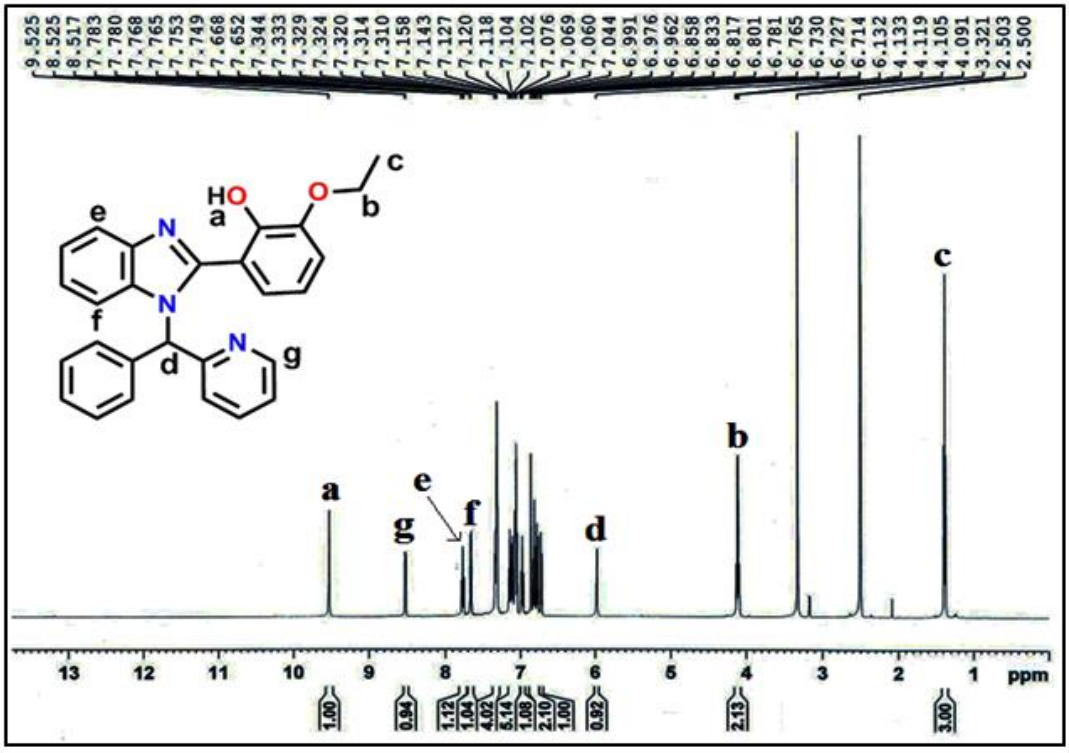

Fig.III.1 ^{1}H NMR spectrum of HL.

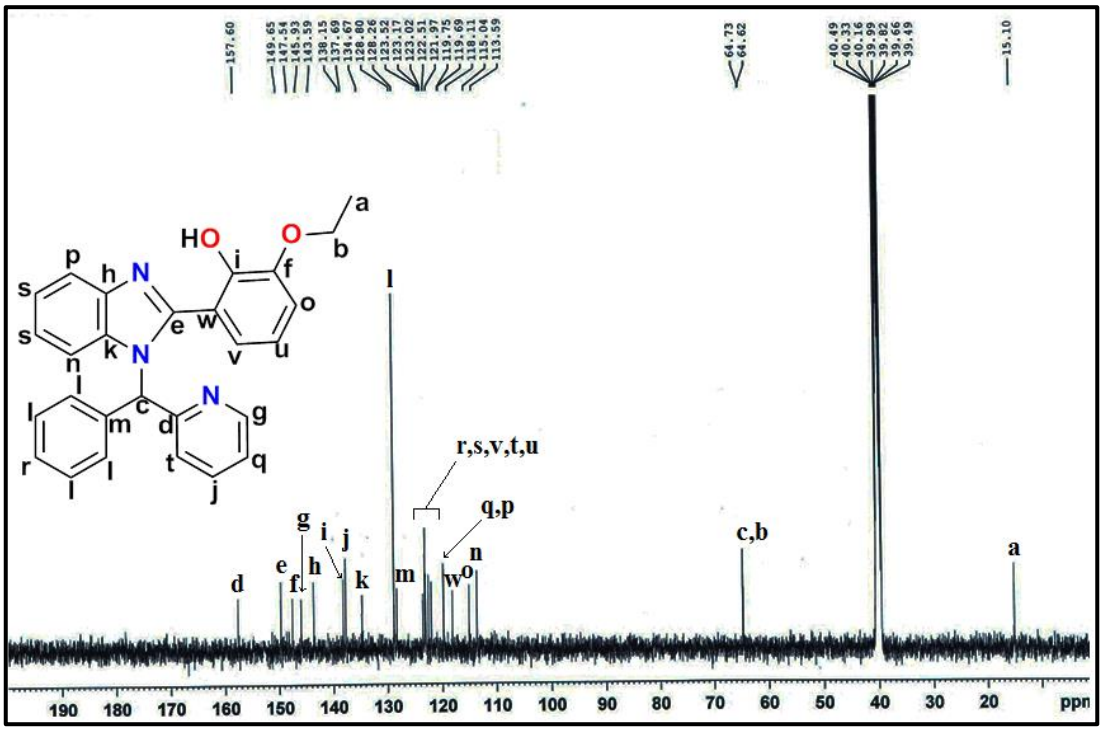

Fig.III.2 ^{13}C NMR spectrum of HL.

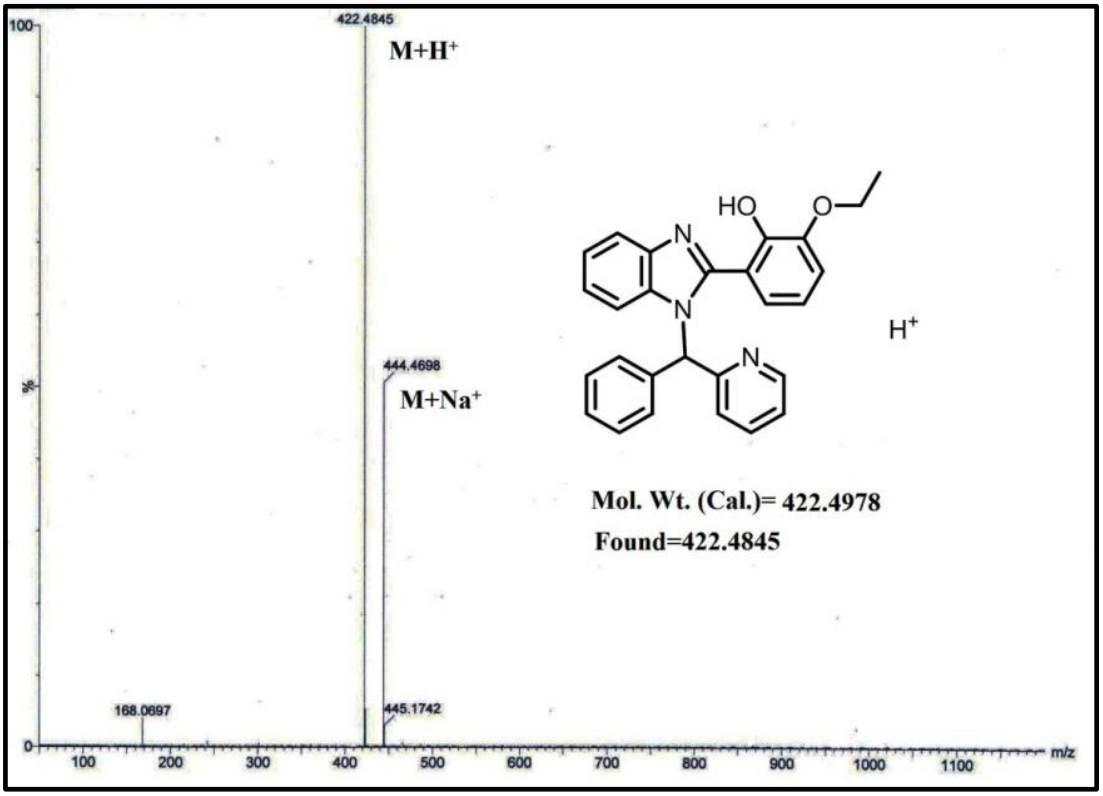

Fig.III.3 ESI-MS spectrum of HL.

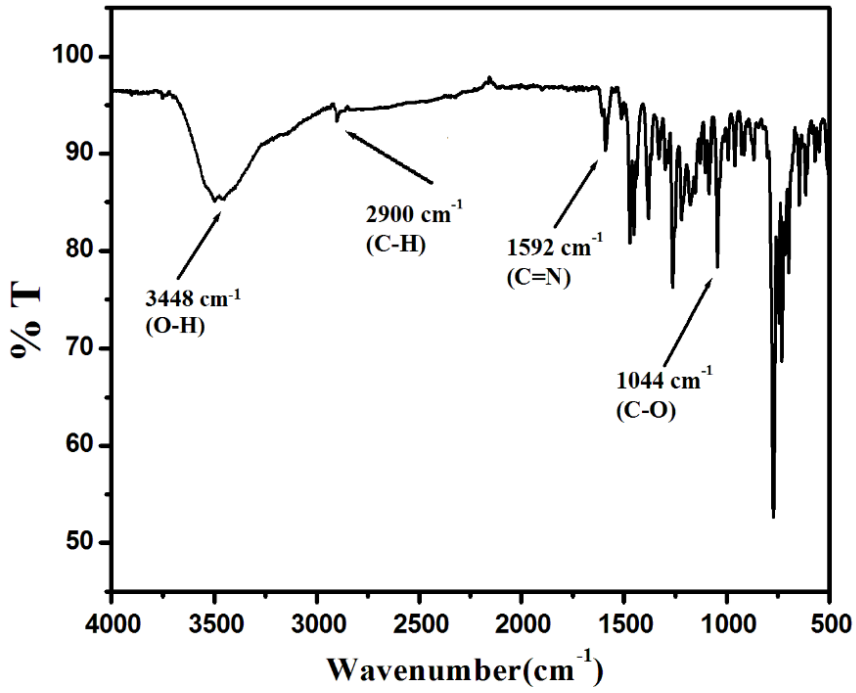

Fig.III.4 IR Spectrum of HL.

III.2.3. Quantum yield and limit of detection calculation

Fluorescence quantum yields (φ) were obtained by using the equation:

$$\varphi_{sample} = (OD_{std.} \times A_{sample})/(OD_{sample} \times A_{std.}) \times \varphi_{std.}$$

where, A_{sample} and A_{std} represent the areas under the fluorescence spectral curves for sample and standard respectively. OD_{sample} and OD_{std} represent the optical densities of the sample and standard respectively at that excitation. wavelength. In this work, acidic quinine sulfate (0.1(N) H_2SO_4 solution) was taken as the standard with known quantum yield of 0.54.[41] LOD was calculated from fluorescence titration experiment on gradual addition of Zn^{2+} into the solution of probe, HL. Standard deviation was measured from emission intensity of probe at varying concentration. Limit of detection was determined from the equation, LOD = 3σ/m, where, σ represents standard deviation and the slope (m) was acquired from the plot of fluorescence titration experiment.

III.2.4. Solution preparation for UV-Vis and fluorescence spectral measurement

The probe (HL, 1×10^{-3} M) was prepared in DMSO (AR) solution. All the salt solutions (1×10^{-3} M) were taken in deionized water. A 50 μM of HL solution was prepared with (9:1, v/v; DMSO/H_2O (HEPES Buffer, pH 7.4)). To this solution, 1.0 equivalent of salt solution was added under room temperature (298 K) with proper correction of dilution factor and the sensitivity and selectivity were checked by spectroscopic measurements. A two and four faced quartz cells of path length equalled to 1 cm were used for absorption and emission measurements respectively. Fluorescence experiments were carried out with 15 and 5 nm excitation and emission slit widths.

III.2.5. X-Ray Crystallography of HL

The yellow prismatic crystals of HL (0.19 × 0.03 × 0.06 mm^3), suitable for diffraction study were obtained upon slow evaporation of ethanolic solution of the probe under room temperature. Single crystal X-Ray data were collected by Bruker Apex II CCD Area Detector at 273(2) K. The crystal data and refine parameters are tabulated in **Table III.1.** Graphite-monochromatized MoKα radiation (λ= 0.71073 Å) was used in fine-focus sealed tube. The *hkl* range for data collection was $-10 \le h \le 10$; $-12 \le k \le 12$; $-27 \le l \le 27$. Diffraction was recorded within the angular range of $2.185 \le \theta \le 24.993^o$. The intensity was corrected for Lorentz and polarization effects with application of rectified empirical absorption data, collected under the condition of $I > 2\sigma(I)$. The structure was solved by direct method followed by successive Fourier and difference Fourier syntheses. All non-hydrogen atoms were refined anisotropically. The hydrogen atoms were geometrically fixed and refined using the riding model. All calculations were carried out using SHELXL-97,[42] ORTEP-32[43] and PLATON-99[44] programs. The crystal data of HL were deposited to Cambridge Crystallographic Data Centre with CCDC 2038659. The copies of this data may be picked up free of cost from the Director, CCDC, 12 Union Road, Cambridge CB2 1EZ, UK (e-mail:deposit@ccdc.cam.ac.uk or www:htpp://www.ccdc.cam.ac.uk).

Table III.1: Crystal data and refine parameters for probe HL.

Empirical formula	$C_{27}H_{23}N_3O_2$
Formula weight	421.48
Temperature (K)	273(2)
System	orthorhombic
Space group	$P2_12_12_1$
a (Å)	9.0805(9)
b (Å)	10.1637(10)
c (Å)	23.374(2)
α=β=γ /°	90
V $(Å)^3$	2157.2 (4)
Z	4
D(cal)/g cm^{-3}	1.298
μ/mm^{-1}	0.083
λ(Å)	0.71073
data[$I > 2\sigma(I)$]/params	3805/279
Final R indices [$I > 2\sigma(I)$][a,b]	R_1= 0.1007 wR_2= 0.1951
GOF[c]	1.118

[a]$R_1 = \Sigma||F_o|-|F_c||/\Sigma|F_o|$; [b]$wR_2 = \{\Sigma[w(F_o^2-F_c^2)^2]/\Sigma[w(F^2_o)^2]\}^{1/2}$; $w = [\sigma^2(F_o)^2 + (0.1003P)^2 + 4.9693P]^{-1}$ $(F_o^2 + 2F_c^2)/3$; [c] Goodness-of-fit

III.2.6. Time-resolved fluorescence decay measurement

A time correlated single photon counting spectrometer (Horiba Jobin Yvon) having a diode laser as an excitation source (λ_{ex} = 390 nm) with the pulse repetition rate equaled to 1 MHz was utilized for fluorescence

decay profiles measurement. The respective emission maxima were taken for the collection of decay curves, which were further analyzed using an IBH DAS6 software with proper fitting according to the following equation:

$$I(t) = \sum_i A_i e^{-\tau/\tau_i}$$

where, τ_i is the luminescence lifetime of i^{th} species and A_i represents the amplitude of the corresponding decay. During fitting, a range of valid $\chi 2$ values were employed accordingly.

For evaluating the characteristic times, a bi-exponential decay model was utilized based on the following equation:

$$\tau_{avg} = \frac{\sum \tau_{i\,B_i}}{\sum_i B_i}$$

where, τ, B represent the lifetime and its respective amplitude.

III.2.7. DFT computations

Density Functional Theory (DFT) and TD-DFT calculations were performed to explicate theoretical correlation with experimental analyses. The gas phase full geometry optimization of HL was carried out using GEN basis set with the B3LYP functional in Gaussian program package Gaussian09.[45] The LanL2DZ basis set was employed for full geometry optimization of the Zn complex. The absence of any imaginary frequencies in the vibrational frequency calculations of probe and its complex ensured that the optimized geometries attained the respective energy minima.[46] Subsequently, the entire vibrational analyses were performed with respect to all geometrical variables, regardless of any geometrical constrains. Electronic transitions were obtained theoretically by Time Dependent-DFT (TD-DFT) calculation in DMSO medium using Conductor like Polarizable Continuum Model (CPCM)[47,48] and the GAUSSSUM[49] was used for calculation of fractional contribution of groups in the molecular orbitals.

III.3 Results and discussion

III.3.1 Characterization of the probe, HL

The ^{1}H NMR spectrum of 2-ethoxy-6-[1-(phenyl-pyridin-2-yl-methyl)-1H-benzoimidazol-2-yl]-phenol (HL) shows a singlet peak at 9.52 ppm which is assigned to the phenolic proton (-OH). Also, a singlet signal at 8.52 ppm is allotted to aromatic-C-H (H_g) adjacent to Pyridyl-N. The remaining aromatic protons appear from 6.71 to 7.78 ppm. The sharp singlet peak due to the tertiary C-H (H_d) appears at 6.13 ppm. The methylene (-CH_2-) proton (H_b) of ethoxy (-O-CH_2-CH_3) group seems to be at 4.09-4.13 ppm and methyl (-CH_3) proton (H_c) observes at 1.32 ppm (**Fig.III.1**). ^{13}C NMR spectrum shows a peak at 157.6 ppm due to the presence of C-N of pyridine ring and other aromatic carbon appears between 113.59-149.65 ppm. The resonance signals for methylene carbon (-CH_2-) of -O-CH_2-CH_3 and primary carbon (-CH_3) appear at 64.73 and 15.10 ppm, respectively (**Fig.III.2**). The ESI-MS analysis shows two molecular ion peaks at m/z, 422.1845 and 444.4698 which could be assigned for [M + H^+] and [M + Na^+] ions peaks respectively and support the structure of HL (**Fig.III.3**). The FT-IR spectrum exhibits stretching frequency at 2900 and 1591 cm^{-1} respectively correspond to the vibrations of tertiary C-H and C=N units in the probe (**Fig.III.4**). Thus, probe carries benzimidazole derivative. This is confirmed from the single crystal structure determination as well. The phenolic –OH stretching is observed at 3448 cm^{-1}. The single crystal X-Ray structure of HL is shown in (**Fig.III.5(a)**), it crystallizes in orthorhombic crystal system with space group of $P2_12_12_1$. The molecular lattice is consisted of one discrete unit and details of the bond parameters like selected bond length and bond angle are listed in **Table III.4 &Table III.5**. The bond lengths of C(007)-N(2) and C(007)-N(1) are 1.307(9) and 1.374(9) Å respectively which confirm the formation of imine and amine linkage in the probe. The HL has three N and one O donor for chelation with metal ions, which behaves as tetra-dentate NNNO type coordination with respect to the proximity of chelating sites. A supramolecular assembly is formed in this crystal unit along 'c-axis' through weak intermolecular interaction (**Fig.III.5(b)**)

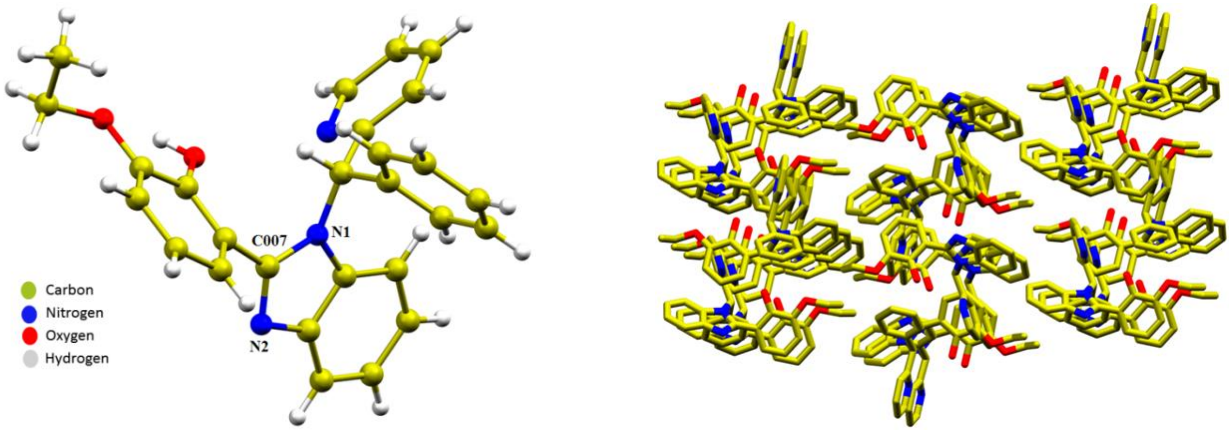

Fig.III.5 (a) Single crystal X-Ray structure of the probe, HL. **(b)** Supramolecular assembly of HL along 'c-axis'.

III.3.2 Spectroscopic behaviour of HL to metal ions and selectivity to Zn^{2+} ion

The UV-Vis absorption spectrum of the probe, HL (9:1 (v/v) DMSO/H_2O; HEPES Buffer, pH=7.4) exhibits absorption bands at 265 and 285 nm and a weak shoulder at 335 nm (**Fig.III.6**).

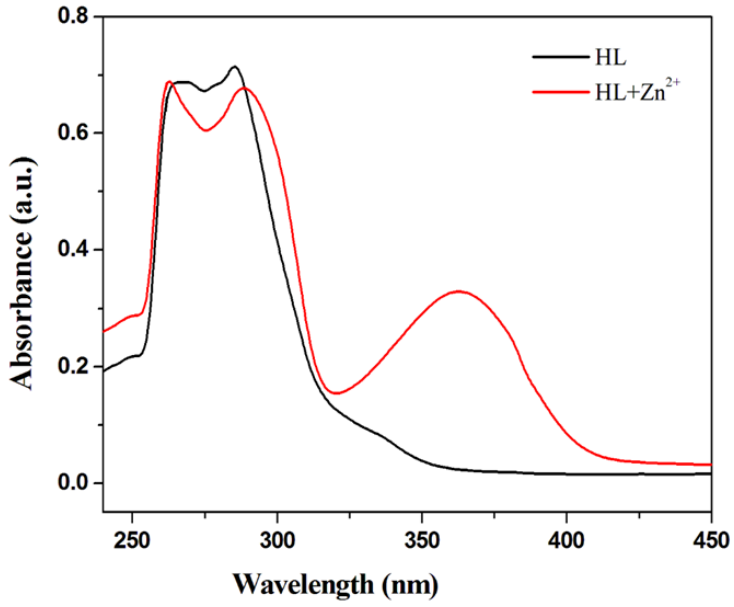

Fig.III.6 Change in absorption spectrum of HL (50 µM) on addition of Zn^{2+} (0-50 µM)

The fluorescence spectrum exhibits very weak emission ($\varphi_{[HL]}$=0.0051) upon excitation at 350 nm in the same medium (9:1 (v/v) DMSO/H_2O (HEPES Buffer, pH=7.4)). The poor luminogenic behavior of the probe in

free-state is ascribed by twisting of structural framework, which enables the unrestricted rotation of tethered 2-ethoxy phenol and phenyl pyridine substituents with respect to the benzimidazole unit (**Fig.III.7).**

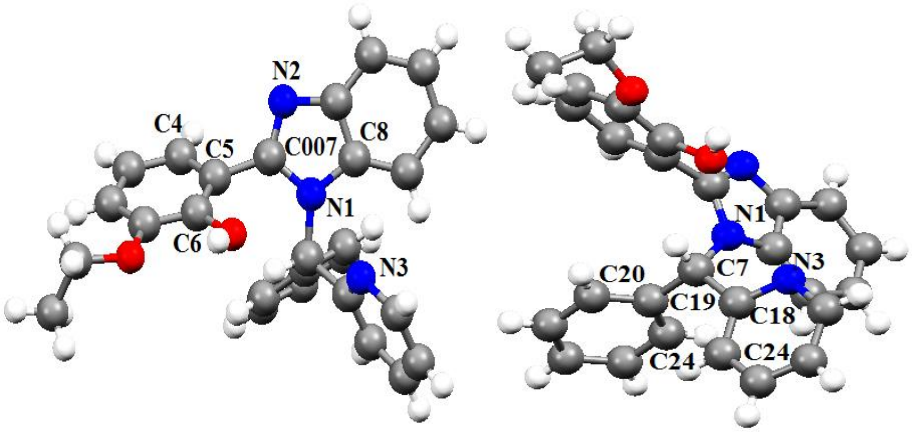

Fig.III.7 X-Ray structure of HL exhibiting twisting framework (two different view)

The torsional angles of the planes C4-C5-C007-N2, C6-C5-C007-N1 and N1-C7-C18-N3 are 58.14°, 64.18° and 38.09°, respectively (**Table III.2**), which ascertains the free rotation of the probe and results weak luminescence at excited state.[50, 51]

Table III.2: Some selective torsional angles present in the free probe HL (obtained from X-Ray structure).

Bonds	**Angle (°)**
C8 N1 C7 C18	47.3(10)
N2 C007 C5 C4	58.1(10)
N1 C7 C19 C24	57.1(7)
N2 C007 C5 C6	-116.5(8)
N1 C7 C18 N3	38.1(9)
N1 C7 C18 C17	-144.1(7)
N1 C7 C19 C20	-121.6(6)
N1 C007 C5 C4	-121.2(8)
C007 N1 C7 C19	86.5(8)
N1 C007 C5 C6	64.2(10)

Sensitivity experiments of the probe was carried out in presence of 1.0 equivalent of different essential cations such as Cu^{2+}, Co^{2+}, Pb^{2+}, Zn^{2+}, Cr^{3+}, Cd^{2+}, Ca^{2+}, Al^{3+}, Fe^{3+}, Hg^{2+}, Ni^{2+}, Mn^{2+}, Ba^{2+}, Na^{+}, K^{+}, Mg^{2+} and Pd^{2+} in 9:1 (v/v) DMSO/H_2O (HEPES Buffer, pH=7.4) and the fluorescence spectra were recorded (**Fig.III.8(a)**). Interestingly, out of all the cations, the probe selectively senses Zn^{2+} ion with enhancement of emission band centered at 461 nm (λ_{ex} = 350 nm). A significant enhancement (~80 fold) of emission has been observed in case of Zn^{2+} ion whereas ~6 folds enhancement was observed for Cd^{2+} ion and rest of the metal ions exert insignificant change in the emission intensity. The probe shows a distinctive blue emission only in presence of Zn^{2+} ion (**Inset of Fig.III.8(b)**) and such high emission may be explained on account of the suppression of existing free rotations in HL accompanied by the introduction of Chelation Enhanced Fluorescence (CHEF) with augmentation of molecular rigidity.[52,53] Inspired from the selective 'turn-on' recognition towards Zn^{2+}, gradual addition of the analyte to 50 µM probe solution (9:1 (v/v) DMSO/H_2O; HEPES Buffer, pH=7.4), the emission intensity at 461 nm significantly increases (**Fig.III.8(b)**) and varies linearly with [Zn^{2+}] until emission reaches the saturation level of 1.0 equivalent of Zn^{2+}. At this stage the probe shows remarkable turn on sensitivity towards Zn^{2+} ion. Eventually, the Limit of detection (LOD) has been determined from fluorescence titration profile by following the 3σ/slope method. The calculated LOD for Zn^{2+} is 3.2 nM (**Fig.III.9**), which is much lower than the WHO recommended permissible level and implies that the probe is highly sensitive towards Zn^{2+} ion with a very efficient LOD than most of the reported probe (**Table III.3**).

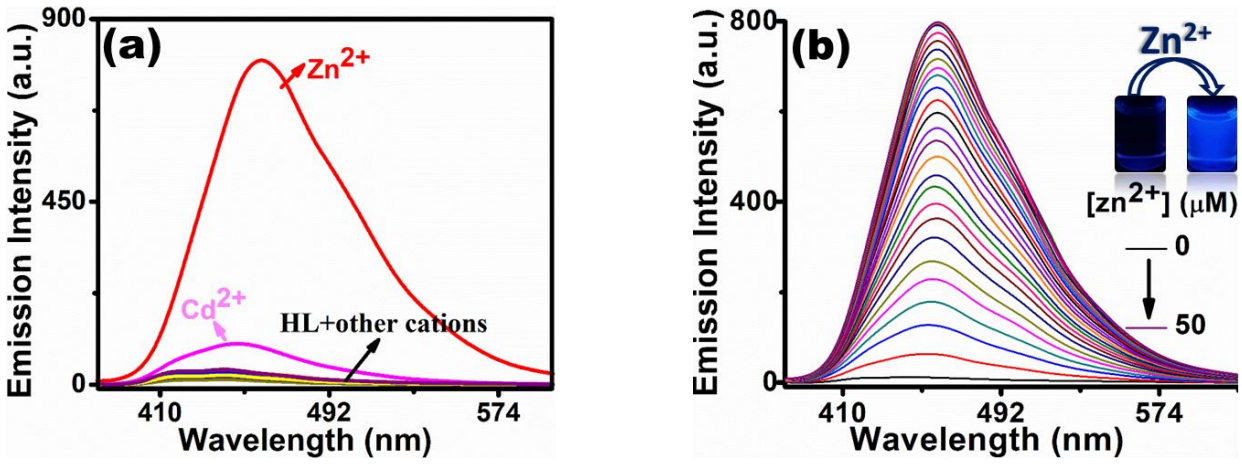

Fig.III.8 (a) Emission spectra of HL (50 µM) in presence of different cations (1.0 equivalent) in 9:1 (v/v) DMSO/H_2O (HEPES Buffer, pH=7.4) (λ_{ex} = 350 nm). **(b)** Change in the fluorescence spectrum of HL (50

μM) on successive addition of Zn^{2+} ion (0-50 μM) in 9:1 (v/v) DMSO/H_2O (HEPES Buffer, pH=7.4) (λ_{ex} = 350 nm). Inset: photographs of HL (50 μM) and its Zn(II)-complex taken under UV lights (λ_{ex} = 365 nm) .

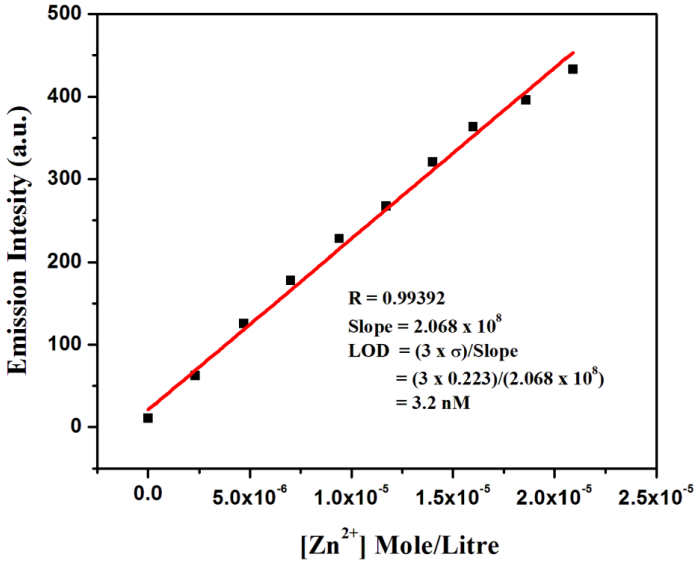

Fig.III.9. Limit of detection (LOD) for Zn^{2+} by the probe, HL.

Table III.3: Some of the reported $Zn^{2+}/H_2PO_4^-$ selective probe along with LOD.

SL No.	Probe	Selectivity (LOD)	Solvent	Ref.
1.	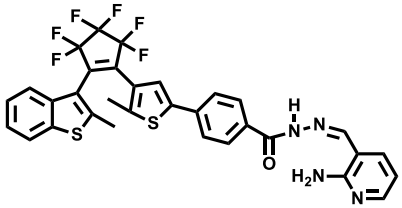	Zn^{2+} (0.562 μM) $H_2PO_4^-$ (0.0314 μM) HSO_4^- (0.0304 μM)	CH_3CN	[54]
2.	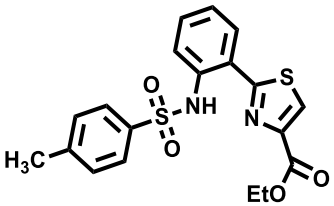	Zn^{2+} (20 μM) $HP_2O_7^{3-}$ (1 μM) $H_2PO_4^-$ (1 μM)	EtOH	[55]
3.	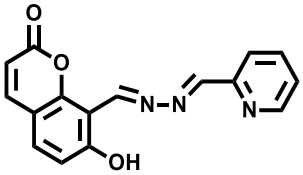	Zn^{2+} (0.103 μM) HPO_4^{2-} (0.207 μM)	DMF/HEPES Buffer (5:1)	[56]

4.	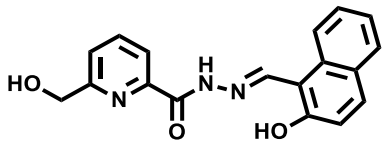	Zn^{2+} (5.7 nM) Cd^{2+} (1.09 µM) Al^{3+} (1.64 µM) F^- (21.1 µM) H_2PO4^- (2.56 µM)	MeOH/HEPES Buffer (7:3)	[57]
5.	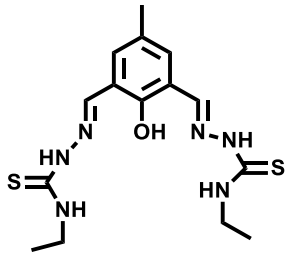	Zn^{2+} (0.59 nM) $H_2PO_4^-$ (26 µM)	MeOH/H_2O (4:1)	[58]
6.	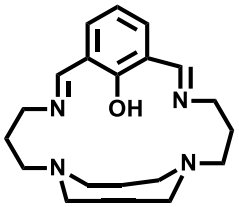	Zn^{2+} (5.4 µM) $H_2PO_4^-$ (-)	CH_3CN/HEPES Buffer (1:1)	[59]
7.	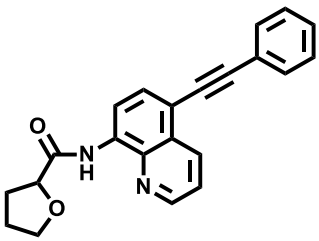	Zn^{2+} (41 nM) $H_2PO_4^-$ (49 nM)	DMSO/H_2O (8:2)	[60]
8.	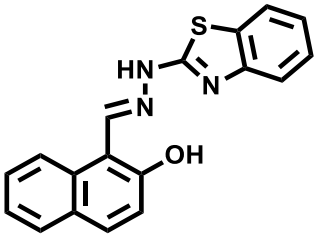	Zn^{2+} (0.65 µM) Cd^{2+} (2.1 µM) $H_2PO_4^-$ (-) HPO_4^{2-} (-)	CH_3OH/H_2O (7:3)	[61]
9.	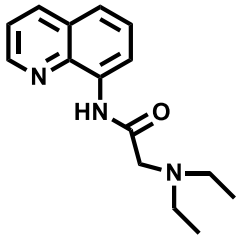	Zn^{2+} (8.8 nM) $H_2PO_4^-$ (0.05 µM)	CH_3CN/H_2O (8:2)	[62]

10.	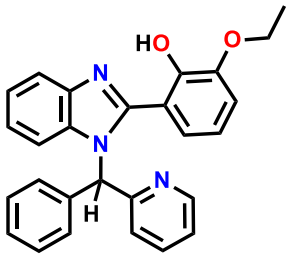	Zn^{2+} (3.2 nM) $H_2PO_4^-$ (0.238 µM)	DMSO/H_2O 9:1 (v/v)	This Work

The sensitivity of the probe has further tested in presence of other co-cations to check the interference in the detection of Zn^{2+}. The competitive study is performed by addition of 2.0 equivalent of other cations into the solution containing HL and Zn^{2+}, *i.e.* in-situ generated [Zn(L^1)OAc] complex. It is found that the interfering effects are negligible in the detection of Zn^{2+} in presence of external cations (**Fig.III.10**)

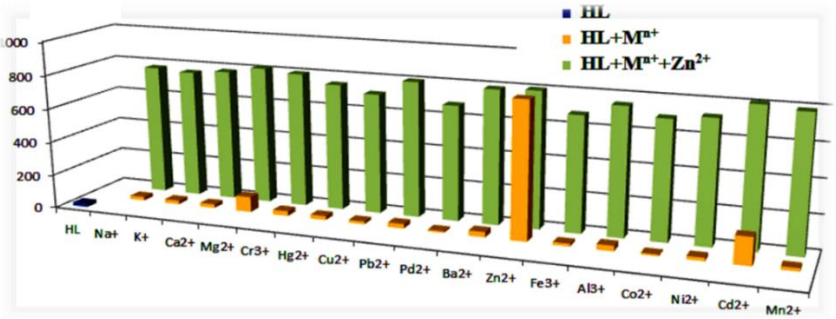

Fig.III.10. Interference study on Zn^{2+} sensing in presence of external cations.

The change in the emission of the probe is insensitive to a wide range of pH (2-12). However, on addition of 1.0 equivalent of Zn^{2+} to the probe solution, the emission intensity increases from pH 5 to 12 and appreciable emission is observed in the basic pH (>7) regime (**Fig.III.11**). The effect of pH values on the luminescence properties of [Zn(L^1)OAc] is examined. The non-luminescence nature of free probe owing to the unrestricted rotation of its twisted counterparts is hardly affected by the variation of pH values, which results more or less unaltered photoluminescence characteristics of HL throughout the entire pH regime (2-12). However, in acidic pH (<5), the N, N, N and O units in HL become inefficient for binding with Zn^{2+} presumably due to the possible protonation of coordinating sites, which eventually leads to poor emission feature. Conversely, with increased pH values, the respective coordinating units become available for efficient chelation with 1 equivalent Zn^{2+} where vigorous restriction of existing free rotation in [Zn(L^1)OAc] complex effectuates

chelation enhanced fluorescence (CHEF) emission from pH 5 to 12 and appreciable emission is observed in the basic pH (>7) regime. Hence, the probe is applicable for recognizing Zn^{2+} at normal physiological pH.

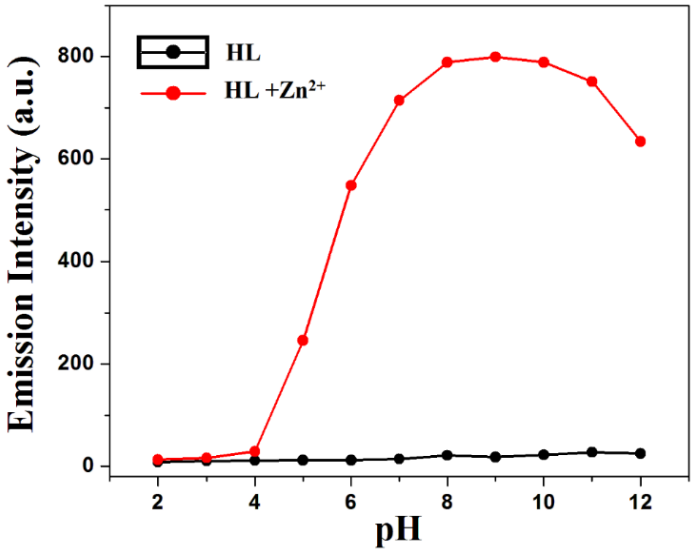

Fig.III.11. pH effect on HL for Zn^{2+} sensing.

Quantum yield calculated for the complex $[Zn(L^1)OAc]$ ($\varphi = 0.391$) is found to be reasonably higher than that of free probe, HL ($\varphi_{[HL]} = 0.0051$). Since the non-emissive probe HL becomes highly luminescent selectively on coordination to Zn^{2+} ($\lambda_{em} = 461$ nm) out of sixteen biologically important metal ions, the specific behavior of Zn^{2+} can presumably be explained on the basis of suitable size of the ion which fits in the NNNO chelate cavity and elevates the CHEF process in a dominating fashion. Furthermore, the Lewis acidity of Zn^{2+} makes it appropriate for robust and selective interactions with hard N and O centers of the probe, which reinforces the emission intensity by resisting the free rotations and also the vibrational relaxation of the pendant substituents in HL. The disfavored size and electronic characteristics of other ions in the present case make them unfit for such emission enhancement. The absorbance change of HL is also recorded by the incremental addition of Zn^{2+} (9:1 (v/v) DMSO/H_2O, HEPES Buffer, pH=7.4), where the absorption intensity at 325 nm increases with a red shifting to 362 nm (**Fig.III.12**). On further addition of Zn^{2+}, the unchanged absorbance spectrum indicates that the saturation is attained with a stoichiometry of 1:1 for complexation and the red shift in absorption spectra also remains unchanged with successive addition of Zn^{2+} when 1:1 complexation is attained.

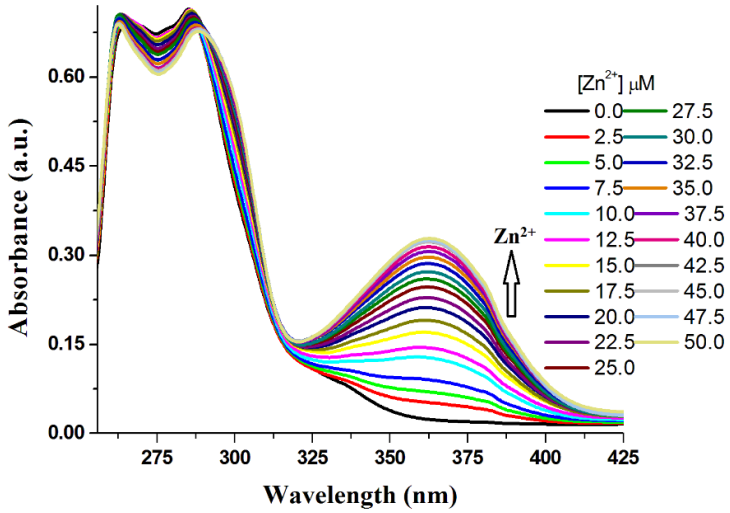

Fig.III.12. Change in the absorption spectrum of HL (50 µM) on gradual addition of Zn^{2+} (0-50 µM).

The binding affinity of HL towards Zn^{2+} has experimentally determined from Benesi-Hildebrand equation ($[(F_{max} - F_0)/(F - F_0)]$ *vs.* $1/[Zn^{2+}]$) and the binding constant, K_d is estimated is 2.93×10^4 M^{-1}, which suggests a strong interaction and association between HL and Zn^{2+} (**Fig.III.13(a)**). The stoichiometry of the complex Zn^{2+}-HL has been examined by the Job's plot which shows an inflexion corresponds to the mole fraction of 0.5 and suggests 1:1 complexation (**Fig.III.13(b)**).

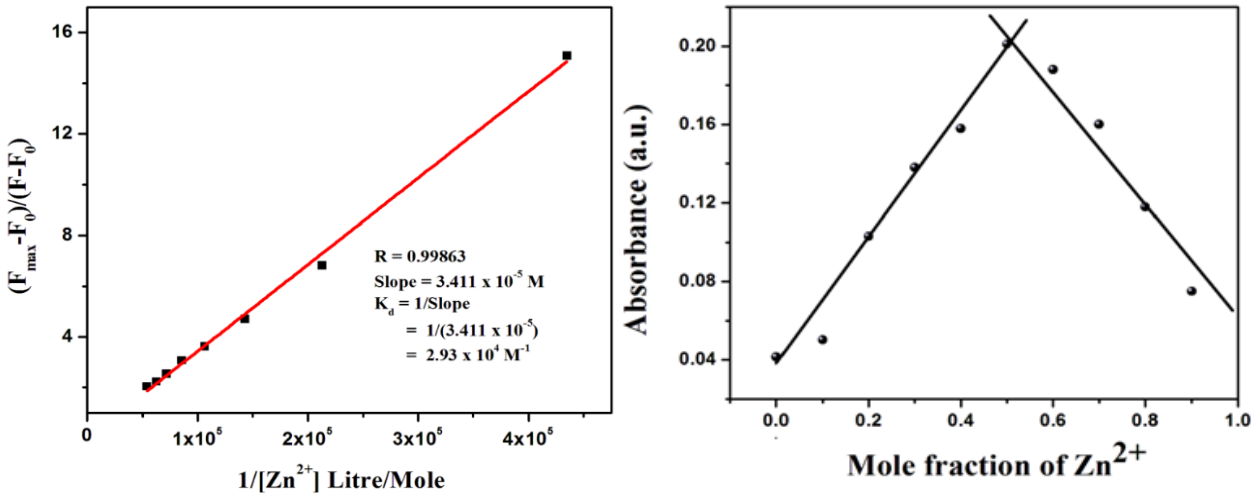

Fig.III.13. (a) Binding constant K_d evaluated from Benesi-Hildebrand plot of probe HL towards Zn^{2+} ion. **(b)** Job's plot between $Zn^{2+}$and HL.

ESI-MS of [HL-Zn^{2+}] complex also supports the 1:1 complex formation. The mass peak at m/z = 486.0937 corresponds to the $[HL–H+Zn]^+$ ion, accounts1:1 binding along with ring opening of the cyclic benzimidazole moiety (**Fig.III.14**).

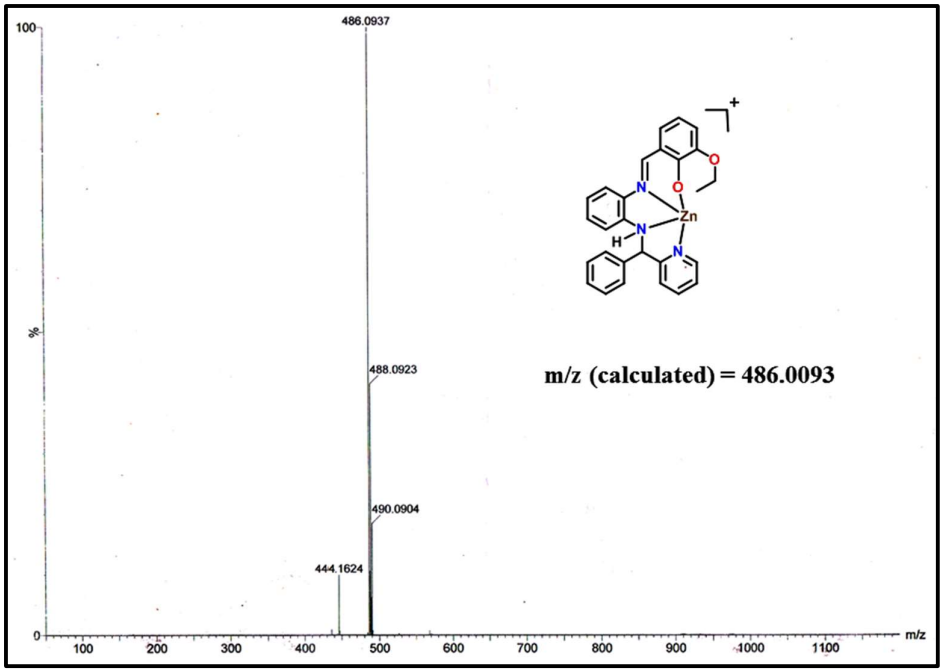

Fig.III.14. ESI-MS spectrum of HL-Zn^{2+} complex.

III.3.3. ^{1}HNMR Titration

To understand the binding approach of HL towards Zn^{2+} and proposed composition of the zinc complex, ^{1}H-NMR titration (500 MHz, DMSO-d_6) of the probe with addition of Zn^{2+} has been examined (**Fig.III.15**). On successive addition of different concentration of $Zn(OAc)_2.2H_2O$ into the probe solution, the phenolic OH peak intensity at 9.52 ppm gradually disappears and gets completely vanished at 1:1 stoichiometric addition. The appearance of two new peaks at 8.90 and 5.02 ppm can be assigned to the imine (CH=N) and NH protons which suggest that chelation prefers the ring opening event in presence of Zn^{2+}. The arrival of a peak at 1.88 ppm indicates the presence of acetate (AcO^-) in the [Zn(L^1)OAc] complex. The broadening of aromatic peak also confirms participation of Zn^{2+} in binding. The results together clearly explain the ring opening phenomena on participation towards Zn^{2+} binding. This is reasonably due to involvement of Zn^{2+} chelation induced five membered ring opening reaction.[63]

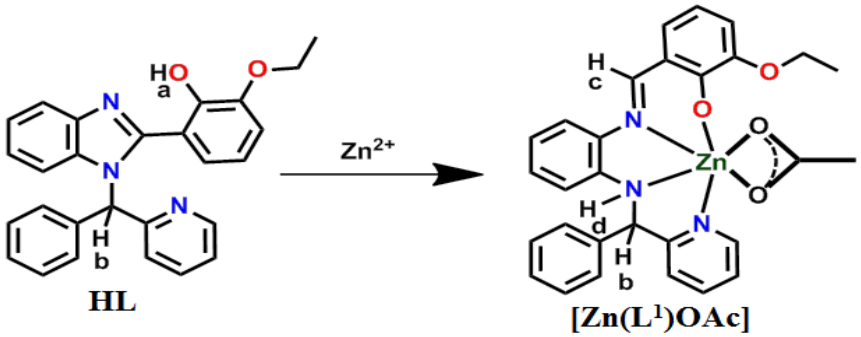

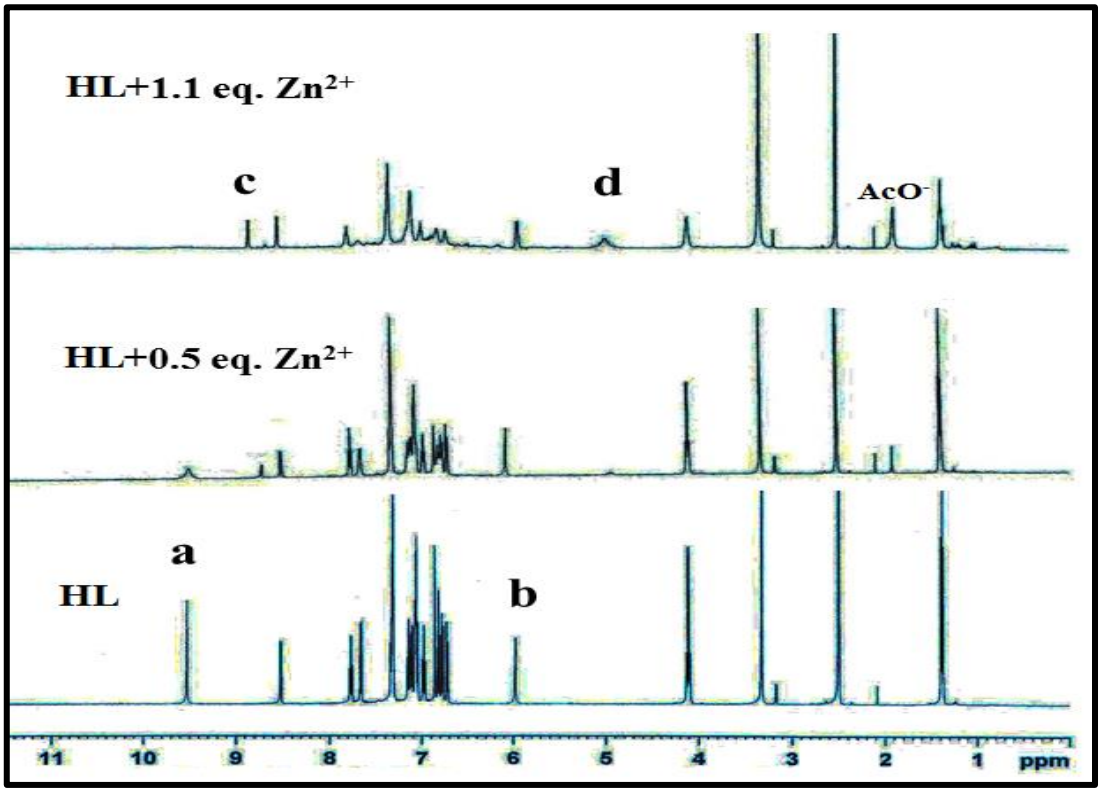

Fig.III.15 ^{1}H-NMR titration of HL on successive addition of Zn^{2+} in DMSO-d_6.

The kinetics of Zn^{2+} sensing via ring opening of the cyclic benzimidazole moiety of HL has been evaluated by fitting the emission intensity into a single exponential equation,[64,65] and the response time has been calculated to be as low as 0.05 s (**Fig.III.16**). The rapid response time ascertains instantaneous reaction of the probe towards Zn^{2+} ion.

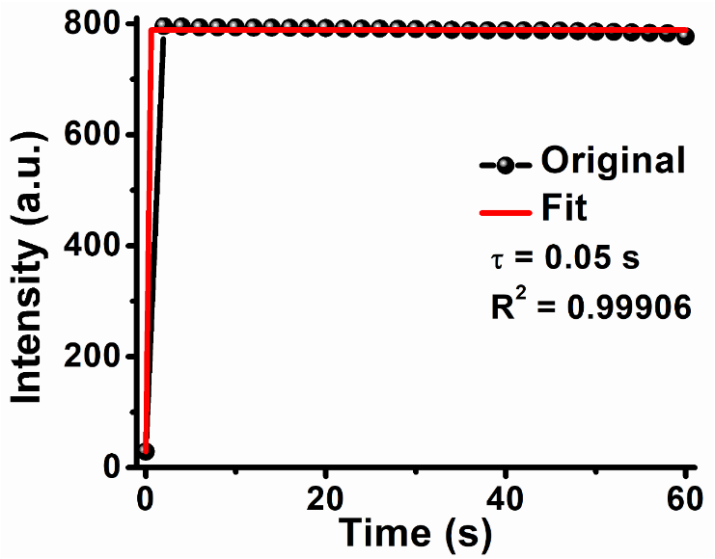

Fig.III.16 Time-course emission intensity of HL upon addition of 1 equivalent Zn^{2+}.

The presence of medium intense broad stretching band at 3343 cm^{-1} indicates υ(N-H) along with the presence of tertiary υ(C-H) at 2975 cm^{-1} (**Fig.III.17(a)&(b)**) which confirms the chelation that proceeds through ring opening reaction. A shift in υ(C=N) from 1592 to 1599 cm^{-1} indicates its participation in chelation process with Zn^{2+}, and the appearance of an intense band at 1614 cm^{-1} presumably ascribes υ(N-H) bending as well. The acetate (–COO) group might associates with metal ions in different modes, which is assigned by the [Zn–(O–C–O)] chelation. For [Zn(L^1)OAc] complex the bands at 1585 and 1393 cm^{-1} plausibly refer to asymmetric and symmetric binding of acetate group. Merged IR spectra of HL and its Zn-complex also included in the **Fig.III.18** for better understanding.

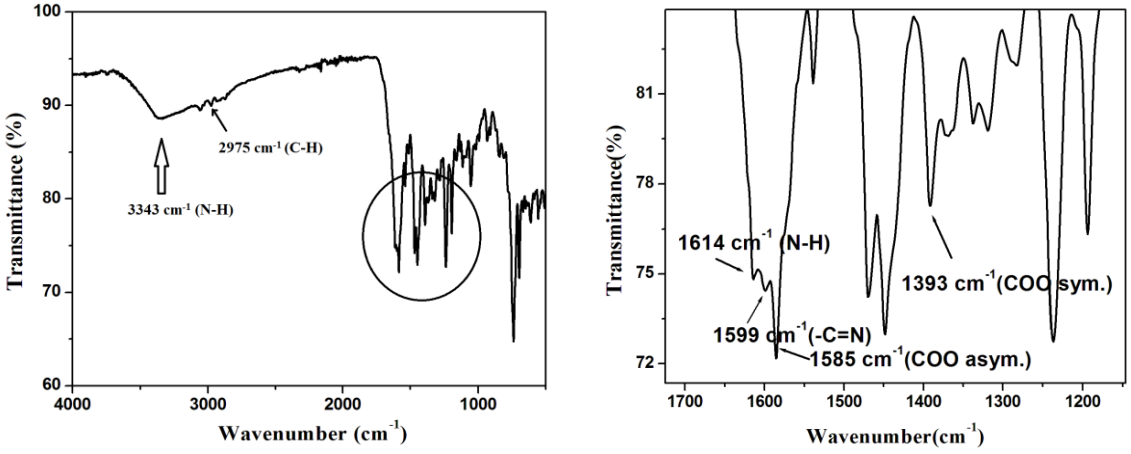

Fig.III.17 (a) IR spectrum of HL-Zn^{2+} complex; **(b)** zoom image in wavenumber around 1200-1700 cm^{-1}.

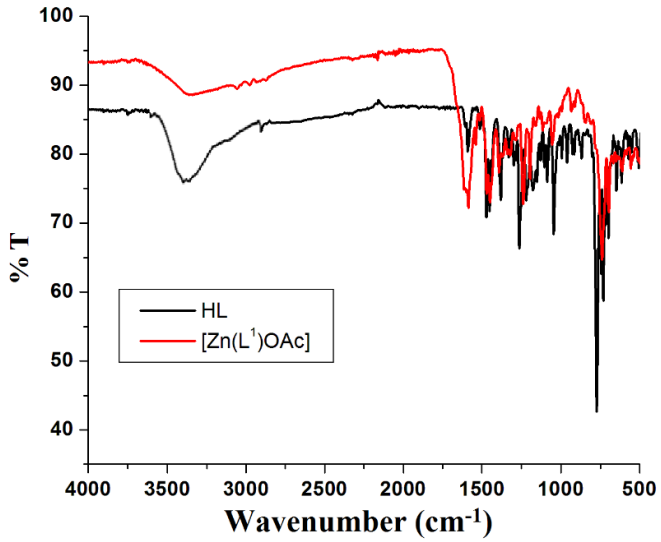

Fig.III.18 Merge IR spectrum of HL and HL-Zn^{2+} complex ([Zn(L^1)OAc]).

III.3.4. DFT Computation:

In order to explain the change in bond parameters on interaction of HL with Zn^{2+}, the optimized structure of HL and [Zn(L^1)OAc] are calculated using DFT/B3LYP computational method (**Fig.III.19**). The Bond lengths and bond angles are calculated from the optimized cyclic structure of HL (**Tables III.4&5**) which eventually are in good correlation with the parameters obtained from X-ray measurements as shown for HL (length; Å) calc. (exp.): C007-N1 1.39 (1.37), N1-C7 1.46 (1.47), C18-N3 1.33 (1.39), C007-N2 1.31 (1.30), O2-H2 0.96 (0.82) and bond angle (°): calc.(exp.) C007-N1-C7 124.89 (124.48), N1-C7-C18 111.70 (112.10), C18-N3-C14 118.48 (118.39), N1-C007-N2 113.01 (112.6), C007-N2-C9 105.60 (105.22), N2-C007-C5 121.69 (123.36), C6-C1-O1 113.28 (114.51), C6-O2-H2 107.78 (110).

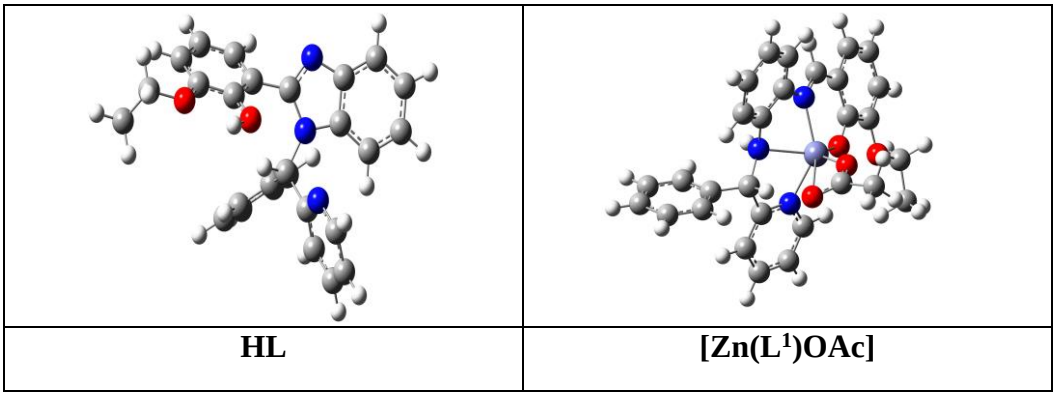

HL	**[Zn(L^1)OAc]**

Fig.III.19. DFT optimized structure of probe HL and its zinc complex using B3LYP method.

Table III.4: Some selected bond length of HL obtained from single crystal and compared with theoretical optimized structure.

Bond-Length	Experimental bond length (Å)	Theoretically bond length (Å)
C007-N1	1.374(9)	1.39
N1-C7	1.475(10)	1.46
C7-C18	1.527(10)	1.53
C18-N3	1.392(12)	1.33
C7-H7	0.98	1.08
C007-N2	1.307(9)	1.31
C007-C5	1.497(10)	1.47
C5-C6	1.390(10)	1.39
C6-O2	1.366(9)	1.36
O2-H2	0.82	0.96
C1-C6	1.392(10)	1.40
C1-O1	1.383(9)	1.37

Table III.5: Selected bond angles of probe HL from crystal unit and its comparison with optimized structure.

Bond Angles	Experimental angle(°)	Theoretically calculated Angle(°)
C007-N1-C7	124.5(5)	124.89
N1-C7-C18	112.1(6)	111.70
C7-C18-N3	118.7(7)	115.06
C18-N3-C14	118.4(8)	118.48
N1-C007-N2	112.6(6)	113.01
C007-N2-C9	105.2(6)	105.60

N2-C007-C5	123.4(6)	121.69
C007-C5-C6	120.9(6)	123.14
C6-C5-O2	118.0(6)	120.16
C6-C1-O1	114.5(7)	113.28
C6-O2-H2	110	107.78

To explain the spectroscopic response of HL towards Zn^{2+}, Time Dependent Density Functional Theory (TD-DFT) has been performed. Using CPCM method in DMSO solvent medium, the ground state electronic spectra for both the probes and its zinc complexes has been determined. The absorption band at 335 nm of HL may be ascribed to HOMO-1→LUMO transition and that for the complex the absorption maximum at 362 nm contributed from HOMO-1→LUMO transition. Some electronic transitions are tabulated (**Table III.6&7**).

Table III.6: Probable electronic transition of HL from TD-DFT calculation.

Excitation Energy (eV)	Wavelength Exp. (nm)	Wavelength Theor. (nm)	Oscillator strength(f)	Key Transition	Nature of Transition
4.2538	335	291.47	0.0589	HOMO-1→ LUMO	ILCT
4.3614	285	284.28	0.0937	HOMO-2→ LUMO	ILCT

Table III.7: Probable electronic transition of [Zn(L^1)OAc] from TD-DFT calculation.

Excitation Energy	Wavelength Exp. (nm)	Wavelength Theor. (nm)	Oscillation Frequency (f)	Key Transition	Nature of Transition
3.6399 eV	362	340.62	0.4568	HOMO-1 →LUMO	ILCT
4.1028 eV	289	302.19	0.1619	HOMO-2→ LUMO	ILCT

The highest occupied molecular orbital (HOMO) and lowest unoccupied molecular orbital (LUMO) of HL and its zinc complex ([Zn(L^1)OAc]) along with some selected frontier molecular orbitals are shown in **Tables III.8 &9.**

Table III.8: Selected frontier molecular orbitals of HL along with their energies.

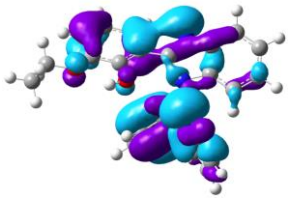	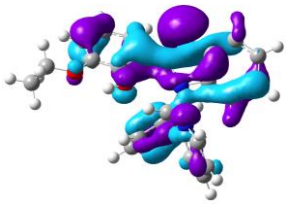	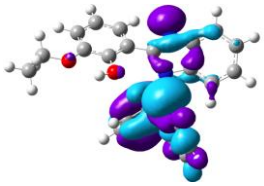	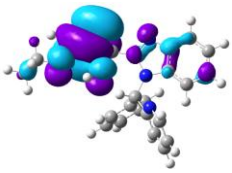
HOMO-5 **-7.150 eV**	**HOMO-4** **-6.957 eV**	**HOMO-3** **-6.888 eV**	**HOMO-2** **-6.047 eV**
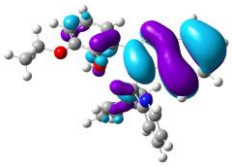	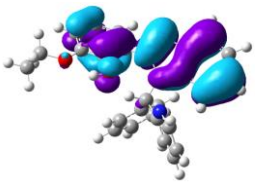	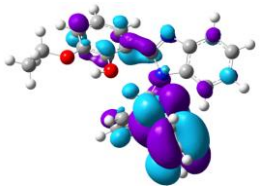	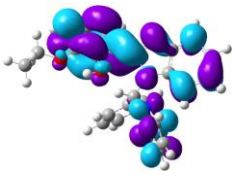
HOMO-1 **-5.980 eV**	**HOMO** **-5.826 eV**	**LUMO** **-1.280 eV**	**LUMO+1** **-0.919 eV**
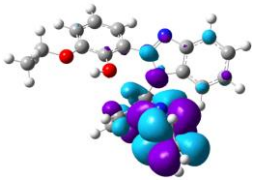	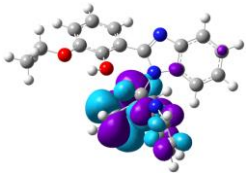		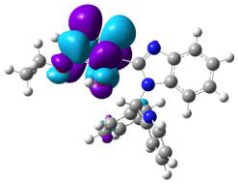
LUMO+2 **-0.821 eV**	**LUMO+3** **-0.630 eV**	**LUMO+4** **0.518 eV**	**LUMO+5** **0.442 eV**

Table III.9: Selected frontier molecular orbitals of [Zn(L^1)OAc] complex along with their energies.

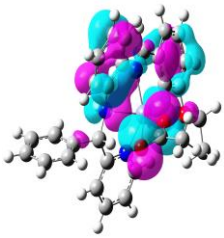	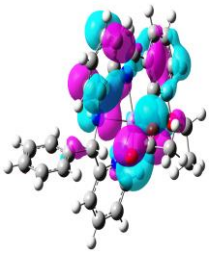	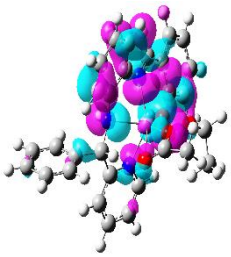	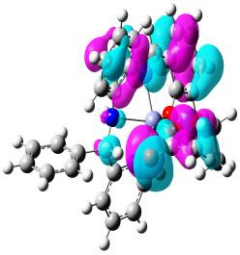
HOMO-5 **--6.62 eV**	**HOMO-4** **-6.52 eV**	**HOMO-3** **-6.42 eV**	**HOMO-2** **-5.94 eV**
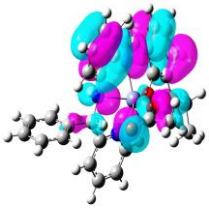	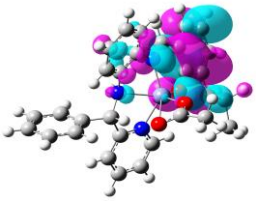	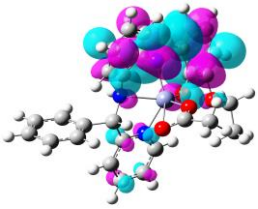	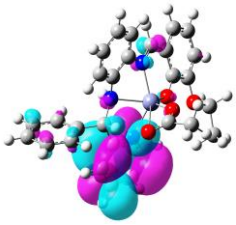
HOMO-1 **-5.87 eV**	**HOMO** **-5.0 eV**	**LUMO** **-1.74 eV**	**LUMO+1** **-1.61 eV**
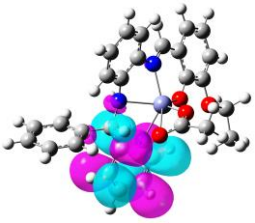	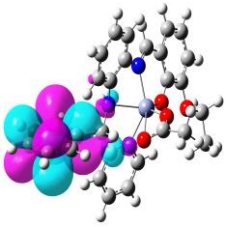	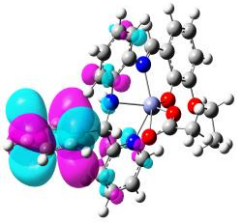	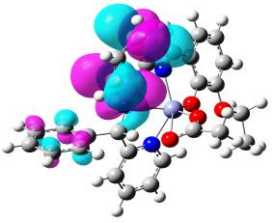
LUMO+2 **-1.03 eV**	**LUMO+3** **-0.69 eV**	**LUMO+4** **-0.58 eV**	**LUMO+5** **-0.3 eV**

Subsequently the band gap of 4.7 eV is calculated for HL, which is further diminished to 4.13 eV for the complex [Zn(L^1)OAc]. This decrement by 0.57 eV clearly explains the red shift behavior in UV-Vis absorption spectra of Zn-complex in respect to HL itself (**Fig.III.20**). The band gap does not support for examination of the compounds for the photo conductivity experiments.

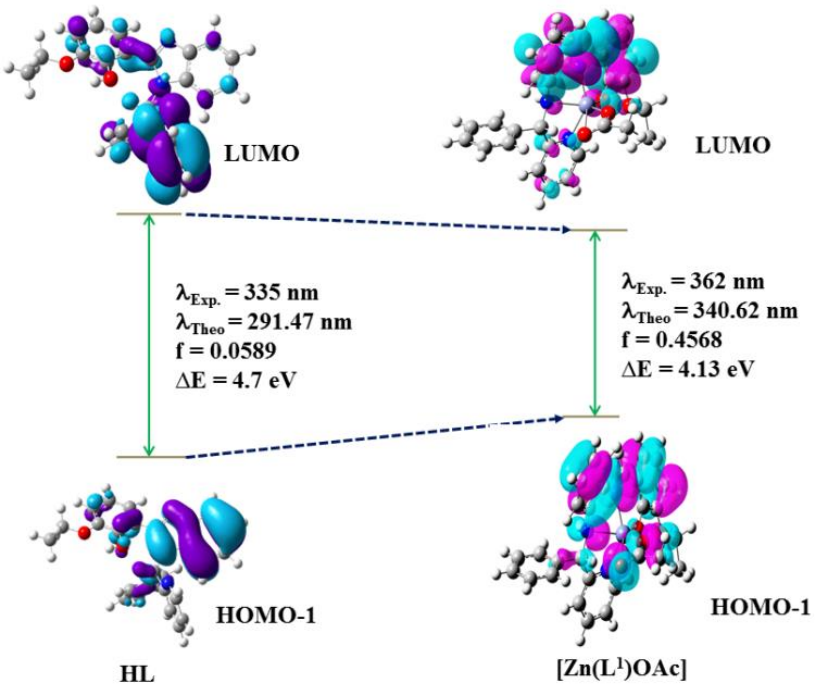

Fig.III.20. Electronic transition for HL and its respective zinc complex.

The coordination of HL with Zn^{2+} opens the ring and makes more planar structure compared to that of the free one. This is quite evident from the energy optimized structure of [Zn(L^1)OAc], where the dihedral angles 162.40° (45–17–47– 3), 170.12° (17–47–3–10) and 149.07° (13–1–47–17) (**Table III.10**) in the energy optimized complex were found to be comparatively lower compared to HL (**Fig.III.21**). Thus, the planar geometry helps better electronic delocalization throughout the structure and has lowered energy gap with respect to that of HL, which possibly explained the red-shifted absorption spectrum of the Zn-complex.[65]

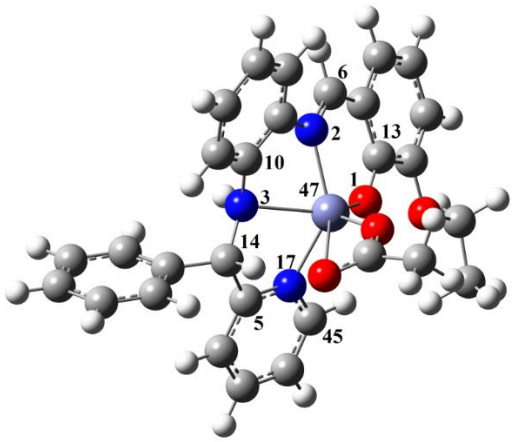

Fig.III.21 DFT optimized structure of Zn-complex exhibiting twisting framework.

Table III.10: Some selective torsional angles present in the Zn-complex (from DFT-optimized structure).

Bonds	Angle (°)
6 – 2 – 47 – 3	-147.25
45 – 17 – 47 – 3	162.40
2 – 47 – 3 – 14	-168.12
17 – 47 – 3 – 10	170.12
13 – 1 – 47 – 17	149.07
1 – 47 – 17 – 5	-158.45

III.3.5. Detection of $H_2PO_4^-$ by emissive [Zn(L^1)OAc]

The complex, [Zn(L^1)OAc] shows strong emission at 461 nm upon excitation at 350 nm (9:1 (v/v) DMSO/H_2O, HEPES Buffer, pH=7.4). Interestingly, the higher emission of [Zn(L^1)OAc] is quenched upon addition of $H_2PO_4^-$ ion, where other P^Vs remain silent. Henceforth, fluorescence quenching of [Zn(L^1)OAc] was monitored through titration experiment with increasingly added $H_2PO_4^-$ (**Fig.III.22**). On gradual addition of $H_2PO_4^-$ (0-50 μM) to the [Zn(L^1)OAc] complex in 9:1 (v/v) DMSO/H_2O (HEPES Buffer, pH=7.4), the emission intensity decreases linearly and completely quenches on addition of 1.0 equivalent of $H_2PO_4^-$.

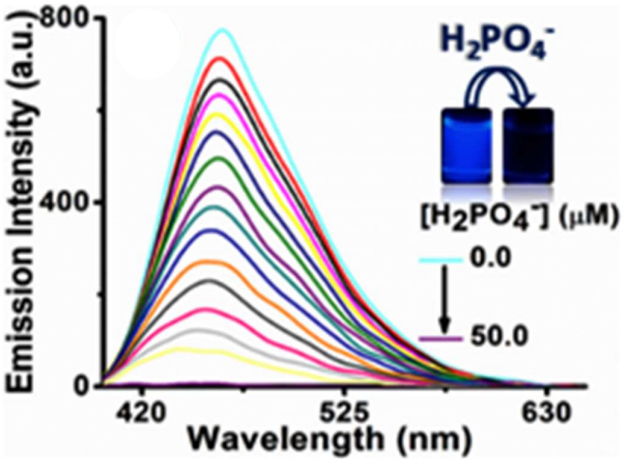

Fig.III.22. Change in emission spectra of [Zn(L^1)OAc] complex upon successive addition of $H_2PO_4^-$ (λ_{ex} = 350 nm). Inset of the figure represents photographs of Zn(II)-complex before and after treatment with $H_2PO_4^-$, taken under UV lights (λ_{ex} = 365 nm).

From the fluorescence titration curve, the detection limit is experimentally determined to be 0.238 μM based on then 3σ/Slope, method (**Fig.III.23(a)**). The binding constant has also been calculated and found to be 3.224 × 10^4 M^{-1} which shows sufficient stability on binding with $H_2PO_4^-$ (**Fig.III.23(b)**).

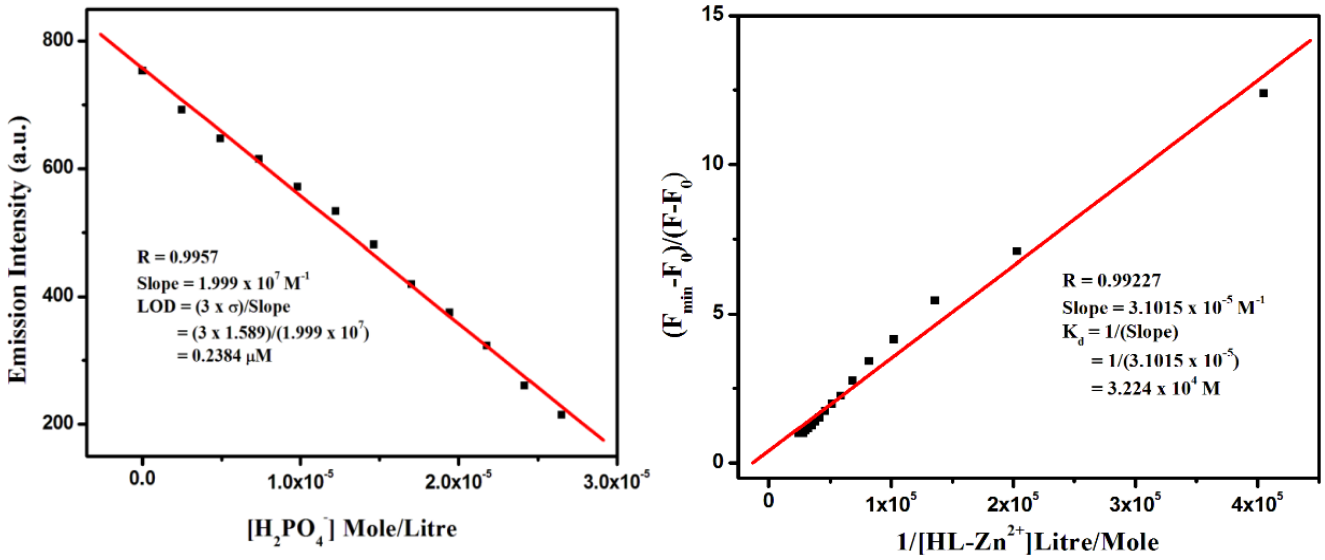

Fig.III.23.(a) Limit of detection (LOD) determination for $H_2PO_4^-$ by [Zn(L^1)OAc] complex. **(b)** Binding constant, K_d for $H_2PO_4^-$.

Moreover, selectivity over additional anions, such as Cl^-, Br^-, I^-, HPO_4^{2-}, CN^-, S^{2-}, PO_4^{3-}, AcO^-, $S_2O_3^{2-}$, IO_3^-, SO_4^{2-}, citrate, F^-, $S_2O_5^{2-}$, AsO_3^{3-}, AsO_2^-, SCN^-, NO_3^-, NO_2^-, HF_2^- towards [Zn(L^1)OAc] emission is also inspected by adding 1.0 equivalent into the complex solution which do not show any significant effect on the emission intensity of the Zn-complex (**Fig.III.24**).

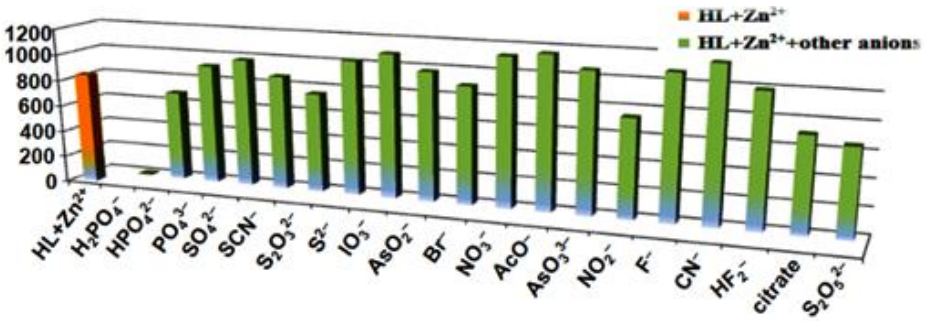

Fig.III.24. Emission intensity of [Zn(L^1)OAc] in presence of 1.0 equivalent various anions in 9:1 (v/v) DMSO/H_2O (HEPES Buffer, pH=7.4) (λ_{ex} = 350 nm).

IV.3.6. Time -Correlated Single Photon Counting (TCSPC) (Lifetime Measurement):

The average fluorescence lifetime decay for the probe fits into bi-exponential decay ((τ_{HL} 1.909 ns) and is lower than that of Zn(II)-complex (τ_{comp}, 2.907 ns) (**Fig.III.25**). Upon addition of $H_2PO_4^-$ the lifetime of the resultant system is further decreased to 1.829 ns. The enhanced lifetime value of the Zn-complex was justified by the decrement of nonradiative relaxation from 521.16×10^6 to 209.5×10^6 s^{-1} of the excited state (**Table III.12**) because of rigidification of overall structural framework on coordination to Zn(II).[66,67] Eventually, the increased radiative dissipation of excited energy from 2.67×10^6 to 134.5×10^6 s^{-1} resulted higher fluorescence quantum yield (0.391 vs. 0.0051 in free HL) and caused ~1.52 times enhancement in fluorescence lifetime of [Zn(L^1)OAc]. On the other hand, the decrement in τ of [Zn(L^1)OAc] on addition of $H_2PO_4^-$ is quite comparable to that of average lifetime of free probe.[68]

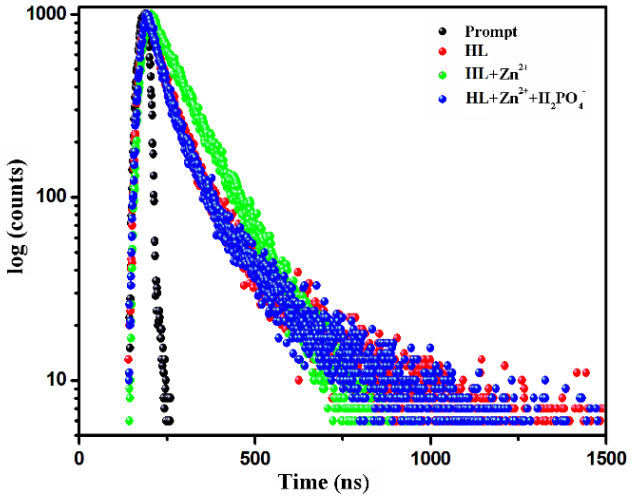

Fig.III.25. Time resolved fluorescence spectroscopy of probe, HL on addition of Zn^{2+} and $H_2PO_4^-$ in 9:1 (v/v) DMSO/H_2O (HEPES Buffer, pH=7.4).

Table III.12. Photophysical parameters of HL, HL+Zn^{2+} and HL+Zn^{2+}+$H_2PO_4^-$

Systems	λ_a (nm)	λ_f (nm)	τ_f (ns)	φ_f	$^ak_r(s^{-1})/10^6$	$^bk_{nr}$ $(s^{-1})/10^6$
Free HL	265, 285, ^{s}335	~460	1.91	0.0051	2.67	521.16
HL+Zn^{2+}	262, 288, 362	461	2.91	0.391	134.50	209.50
HL+Zn^{2+}+$H_2PO_4^-$	264, 288, ^{s}334	~460	1.83	0.0039	2.13	544.62

$^ak_r = \varphi_f/\tau_f$; $^bk_{nr} = (1/\tau_f) - k_r$; ^{s}shoulder band

Concurrently, the quenching can be explained by its favorability towards Zn^{2+} ion which may tend to demetallate [Zn(L^1)OAc] complex. Thus, the probe, HL can be used for simultaneous detection of Zn^{2+} and $H_2PO_4^-$. The UV-Vis absorption spectrum shows decrease in intensity at 362 and 285 nm upon gradual addition of $H_2PO_4^-$ (0-50 µM) (**Fig.III.26**).

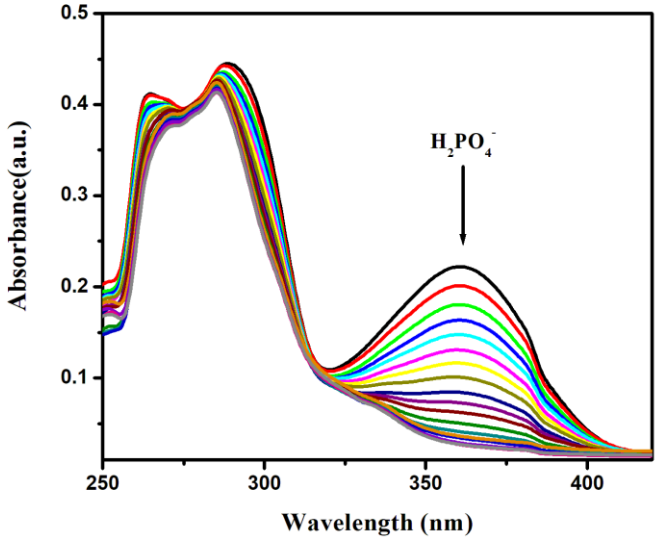

Fig.III.26. Change in UV-Vis absorption spectra of [Zn(L^1)OAc] on gradual addition of $H_2PO_4^-$.

To verify the respective interaction between $H_2PO_4^-$ and [Zn(L^1)OAc], ESI-MS has inspected by adding $H_2PO_4^-$ into the in-situ generated complex in solution phase. The mass spectrum shows a base peak at 422.1367, which ascertains the mass of HL+H^+ and at 162.3632 corresponds to [Zn(H_2PO_4)]$^+$ (**Fig.III.27**).

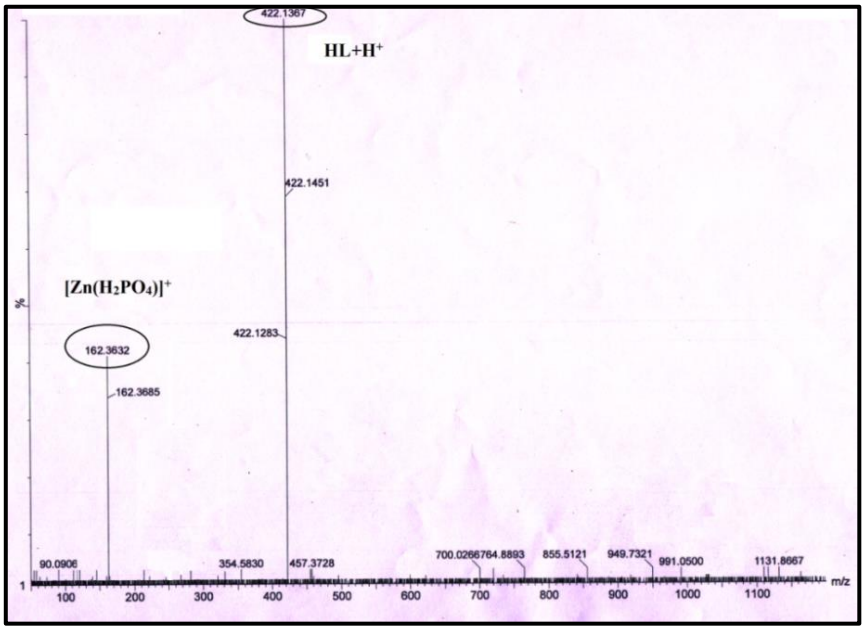

Fig.III.27. ESI-MS spectrum in addition of $H_2PO_4^-$ to in-situ generated HL-Zn^{2+} complex.

In the ^1H NMR measurement, addition of $H_2PO_4^-$ (1.1 eqv.) to the resulting mixture of HL and Zn^{2+} (1.0 eqv.) regenerates the probe HL by removing Zn^{2+} from [Zn(L^1)OAc] complex and is shown in (**Fig.III.28**).

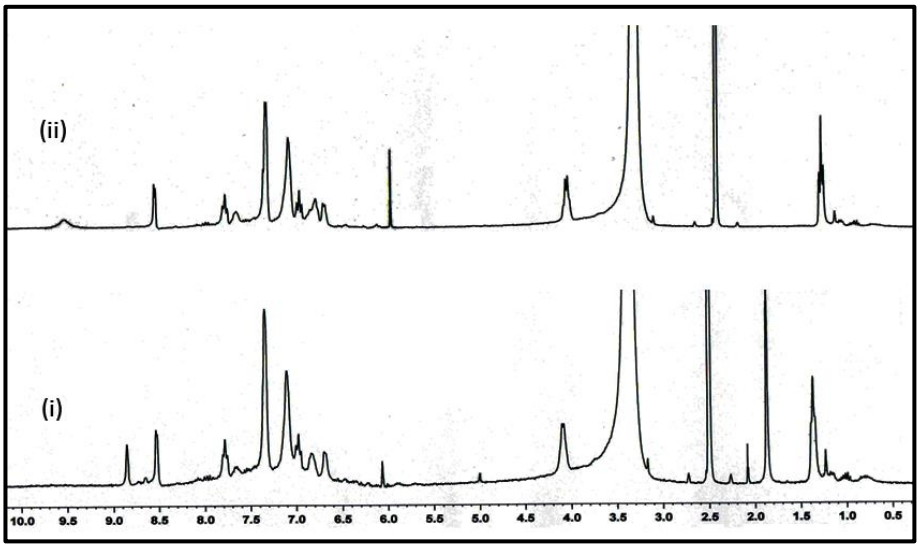

Fig.III.28. ^1H NMR spectra (i) HL+Zn^{2+} (1.0 eqv.) (ii) HL+Zn^{2+}(1.0 eqv.)+$H_2PO_4^-$ (1.0 eqv.)

Evidently, kinetics of the fluorescence quenching of emissive [Zn(L^1)OAc] in presence of $H_2PO_4^-$ has also been monitored by fitting the intensity decay in a single exponential equation and the calculated response time is found to be 0.02 s (**Fig.III.29**)

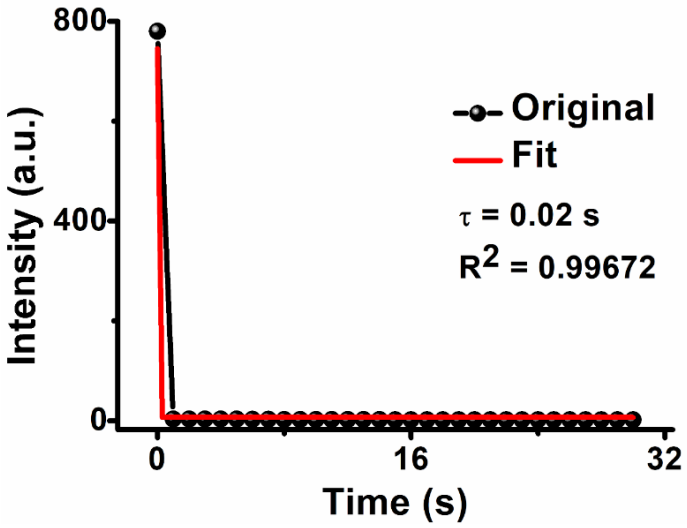

Fig.III.29. Time-course of emission intensity quenching of [Zn(L^1)OAc] upon addition of 1 eqv. $H_2PO_4^-$.

Due to strong affinity towards Zn^{2+}, $H_2PO_4^-$ is used for gravimetric estimation in analytical chemistry and in present case removal of Zn^{2+} from the complex has been assessed as the recovery incident of free probe, HL.

Hence, the proposed mechanism for the sensing of $H_2PO_4^-$ ions by [Zn(L^1)OAc] complex can be represented by **Scheme III.b.**

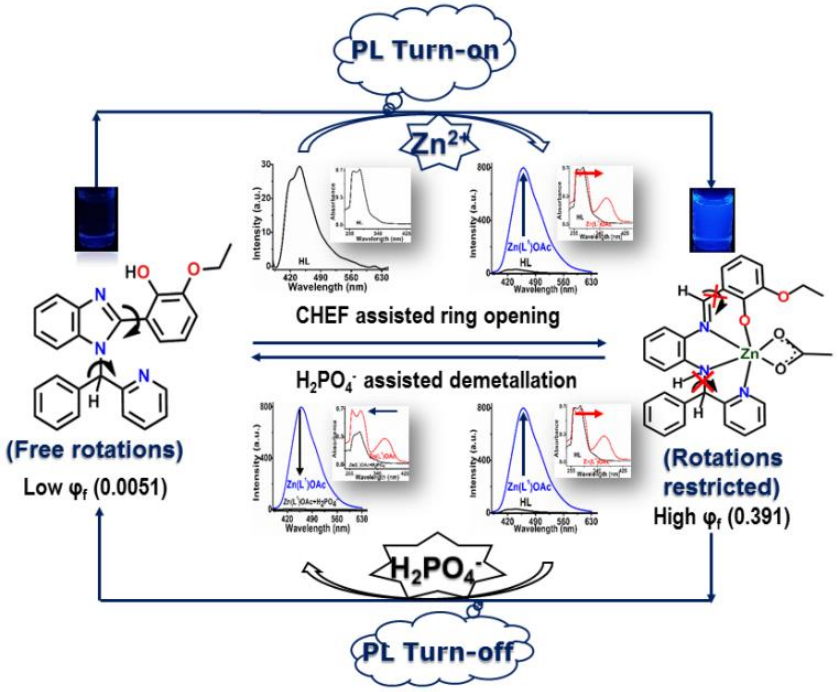

Scheme III.b Proposed mechanism for the sensing of $H_2PO_4^-$ ion by [Zn(L^1)OAc] complex.

Recently, accumulation of phosphate in surface water creates a great concern for water bodies and human health.[6] Henceforth, it is of importance to track and recover phosphates from the real water sources in order to maintain the quality of the potable water. The excellent selectivity of [Zn(L^1)OAc] towards $H_2PO_4^-$ together with reasonable sensitivity inspire us to further explore its practical application as a sensing as well as recovery agent for $H_2PO_4^-$ from the real water samples. In this regard, we have utilized tap water, distilled water and drinking water spiked with trace quantity of the requisite analyte (0.5–2.0 μM) without any further processing. The percentage of $H_2PO_4^-$ recovery by the Zn(II) complex (**Table III.13**) is in the range of 95.8 to 101 with minimal percentage of error (0.5–4.2).

Table III.13: Recovery of $H_2PO_4^-$ by [Zn(L^1)OAc] complex from real water samples.

Sample	**Added $H_2PO_4^-$ (M)**	**Detected $H_2PO_4^-$ (M)**	**Recovery (%)**	**Error (%)**
Tap water	0.5×10^{-6}	0.505×10^{-6}	101	1.0
	1.0×10^{-6}	0.991×10^{-6}	99.1	0.9
	2.0×10^{-6}	1.99×10^{-6}	99.5	0.5
Distilled water	0.5×10^{-6}	0.493×10^{-6}	98.6	1.4
	1.0×10^{-6}	0.992×10^{-6}	99.2	0.8
	2.0×10^{-6}	1.94×10^{-6}	97.0	3.0
Drinking water	0.5×10^{-6}	0.479×10^{-6}	95.8	4.2
	1.0×10^{-6}	0.972×10^{-6}	97.2	2.8
	2.0×10^{-6}	1.934×10^{-6}	96.7	3.3

III.3.7. Reversibility study and logic gate behavior

Reversibility and recyclability are considered the most prominent factors when it comes to the practicability of the chemosensor.[69] The CHEF induced fluorescence of HL on addition of Zn^{2+} and its simultaneous quenching in presence of $H_2PO_4^-$ can be repeated upto 6 cycles upon modulation $Zn^{2+}/H_2PO_4^-$ addition in 9:1 (v/v) DMSO/H_2O (HEPES Buffer, pH=7.4) (**Fig.III.30(a)**). Based on the switchable emissive characteristics of HL towards Zn^{2+} and $H_2PO_4^-$ (**Fig.III.30(b)**), an INHIBIT logic gate can be constructed with input signals Zn^{2+} and $H_2PO_4^-$ as INPUT 1 (In Z) and INPUT 2 (In P) and emission intensity at 461 nm as the output signal. The truth table (**Fig. 30(c**)) and the set-reset memory device (**Fig. 30(d)**) are constructed for the given logical circuit and the output is considered as 1 when it results in enhancement of emission.[70]

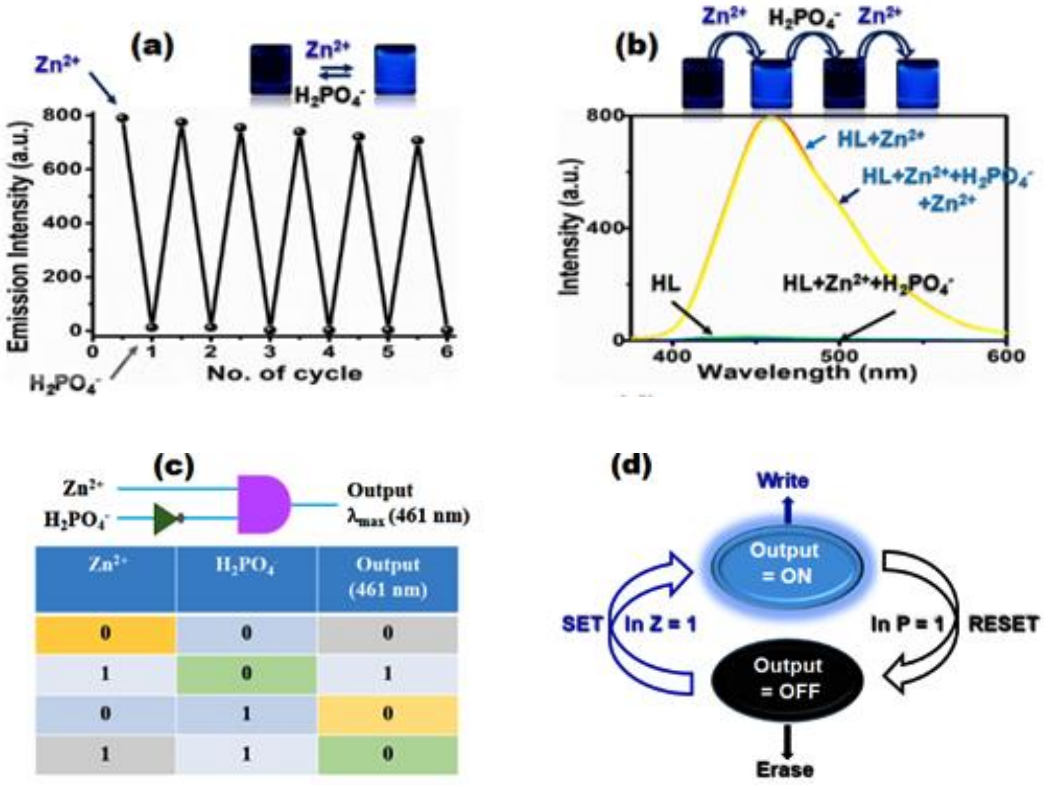

Zn^{2+}	$H_2PO_4^-$	Output (461 nm)
0	0	0
1	0	1
0	1	0
1	1	0

Fig.III.30. (a) Recyclability of HL on addition of Zn^{2+}/$H_2PO_4^-$ up to 6 cycles. (b) Variation in PL characteristics of HL (50 μM; λ_{ex} = 350 nm) upon simultaneous addition of Zn^{2+} and $H_2PO_4^-$ (1 cycle). Insets of figures **(a)** and **(b)** represent chronological changes in emission color of HL upon successive addition of Zn^{2+} and $H_2PO_4^-$, taken under UV light (λ_{ex} = 365 nm). **(c)** INHIBIT logic gate and truth table for two inputs: Zn^{2+} and $H_2PO_4^-$ and single output: λ_f = 461 nm. **(d)** Schematic representations of SET/RESET memorized write/erase logic circuit based on reversible ON/OFF fluorescence switching behavior.

III.3.8. Practical application of [Zn(L^1)OAc] complex for sensing of $H_2PO_4^-$ in solid state with devising a "Use" and "Throw" security marker

Fluorescent chemosensors, capable of exhibiting quantitative detection of bioactive analytes in solid state overrules the traditional sensors owing to their additional advantages in term of cost-effective 'on-site' recognition of particular analyte with better sensitivity and improved LOD without much necessity of sophisticated instruments.[71,72] Considering the importance of phosphates in environment and industry, it is necessary to detect $H_2PO_4^-$ in solid platform which practically offers quick response and easy to handle. In order to achieve selective solid state detection of $H_2PO_4^-$, disposable paper strips of Whatman 41 are soaked

readily with probe solution (HL) and air dried. Then the aqueous solution of Zn^{2+} (10^{-3} M) is sprayed over the strip which in turn reveal blue fluorescence from the treated area while illuminating it under UV light (λ_{ex} = 365 nm) (**Fig.III.31(i)**). Interestingly, the bright blue fluorescence is noticed to be selectively fades away when above strip is allowed to be treated with aqueous solution of $H_2PO_4^-$ (10^{-3} M) (**Fig.III.31(ii)**) out of eighteen other anions. The observation clearly indicates selective detection of $H_2PO_4^-$ by the Zn(II) complex of pyridyl-benzimidazolyl-phenolato in solid state.

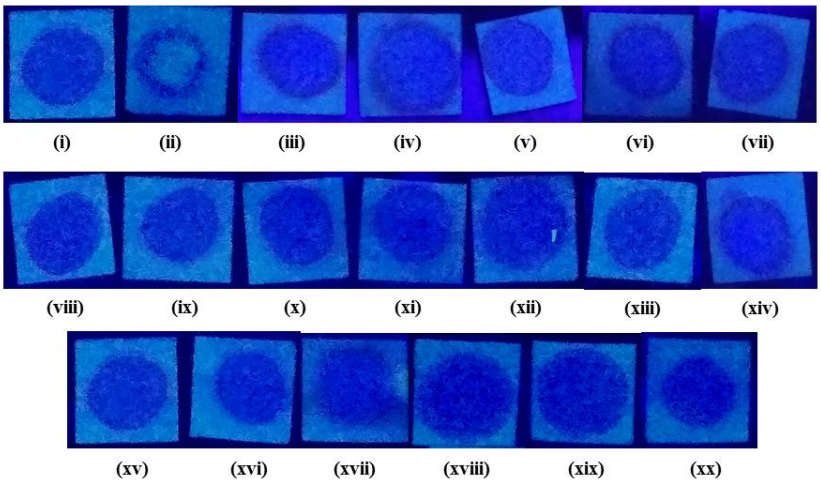

Fig.III.31 Paper kit detection: Zn-complex in presence of different anions; (i) [Zn(L^1)OAc], (ii) $H_2PO_4^-$, (iii) I^-, (iv) Br^-, (v) Cl^-, (vi) $H_2PO_4^-$, (vii) S^{2-}, (viii) PO_4^{3-}, (ix) $S_2O_3^{2-}$, (xx) IO_3^-, (xi) citrate, (xii) AcO^-, (xiii) F^-, (xiv) AsO_2^-, (xv) AsO_3^{3-}, (xvi) CN^-, (xvii) SCN^-, (xviii) SO_4^{2-}, (xix) NO_2^-, (xx) NO_3^-.

Subsequently, to inspect the sensitivity of Zn(II)-coated paper strips, the concentration-dependent fluorescence quenching of the Zn(II) complex is readily monitored by simply varying the aqueous concentration of $H_2PO_4^-$ from 10^{-3} M to 10^{-8} M upon spotting different concentrations on the fluorescent filter papers. The quenching of blue emission intensity slowly weakens with decreased $H_2PO_4^-$ concentration (**Fig.III.32**) where the bright blue luminescence starts to revive when the analyte concentration was as low as 10^{-8} M. Meanwhile, when ~5 µL volume of 10^{-8} M aqueous $H_2PO_4^-$ was allowed to be spotted on a Zn(II)-coated filter paper covering an area of 1 cm^2, the LOD was found to be as low as 10.97 pg(picogram)/cm^2. Evidently, the Zn(II) complex of present chemosensor is capable of instantaneous trace quantity detection of $H_2PO_4^-$ by regulating the quenching strength through a simple and portable paper strip method in solid state.

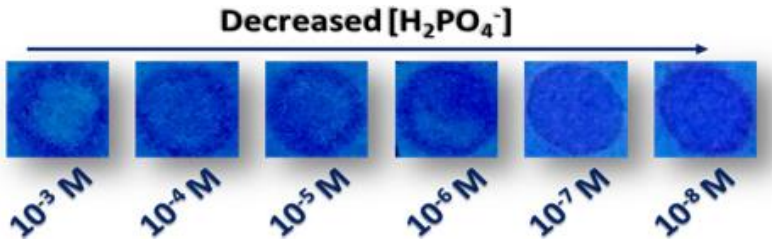

Fig.III.32 Photographs of Zn-complex embedded paper strips spotted with different concentrations of $H_2PO_4^-$ (i) 10^{-3}, (ii) 10^{-4}, (iii) 10^{-5}, (iv) 10^{-6}, (v) 10^{-7}, (vi) 10^{-8} (λ_{ex} = 365 nm).

Fluorescence images and labels have increasingly been utilized widely as the embedded security markers owing to their reluctance to be photocopied, which mostly remain invisible under day light and hardly to be duplicated.[73] Therefore, stimuli responsive fluorescence materials which exhibit definite changes in their optical features in response to the specific analyte have been considered to be the suitable candidate for architecting security devices.[74] Consequently, the reversible 'ON-OFF' fluorescence switching of present chemosensor during alternate presence of Zn^{2+} and $H_2PO_4^-$ inspires us to execute a solid state security activity with enhanced practical implication. For this, a solution-coated "Use" and "Throw" thin film fabricated upon dip coating a Whatman filter paper into a chloroform solution of HL followed by drying it under room temperature Subsequently, writing the word 'JU' with an aqueous Zn^{2+} filled pen, the HL-coated film divulges blue emission ('ON' state) only from the written portion due to feasible interaction of HL towards Zn^{2+} to form the highly emissive [Zn(L^1)OAc] complex. Interestingly, the glared emission completely fades away after washing the Zn(II)-treated film with aqueous $H_2PO_4^-$ solution ('OFF' state). (**Fig.III.33**.)

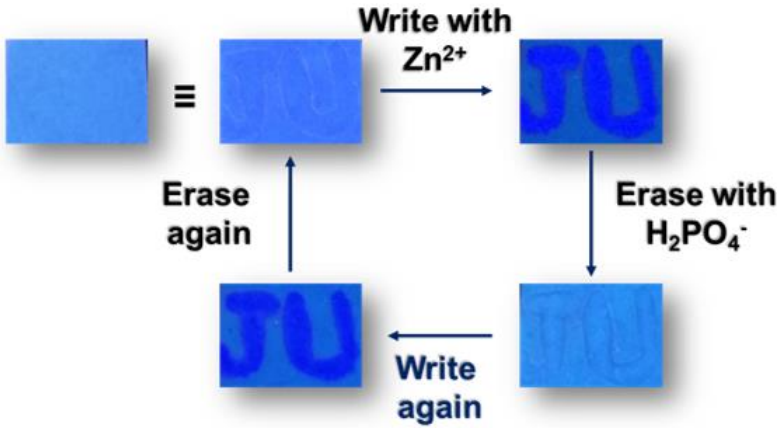

Fig.III.33. Photographs of HL coated filter paper with hand written images under illumination at 365 nm.

Moreover, the 'ON' state can be regenerated after rewriting the word 'JU' on washed surface, which evidently undergoes the 'OFF' state immediately after washing the film again This fluorescence switching property can feasibly be repeated to complete the security cycle without draining the emission property. The sensing event of [Zn(L^1)OAc] as a security label remains unaffected in presence of simple water sample containing no $H_2PO_4^-$ (**Fig.III.34**), which further reinforce selective fluorescence quenching of the chemosensor in solid state.

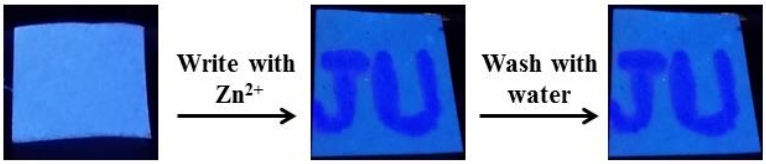

Fig.III.34. Photographs of **HL** coated filter paper with hand written images and after washing with water; λ_{ex}, 365 nm.

III.4. Conclusions

The present work sheds light on an 'ON-OFF' fluorescence switching assisted trace quantity detection of environmentally relevant $H_2PO_4^-$ ion in a desired selective and sensitive fashion based on a newly designed Zn(II) complex of 2-ethoxy-6-[1-(phenyl-pyridin-2-yl-methyl)-1H-benzoimidazol-2-yl]-phenol (HL) in DMSO-water [(9:1, v/v), pH = 7.4]. Free HL is nonfluorescent and exhibits remarkable fluorescence 'turn-on' recognition to Zn^{2+} ion out of sixteen pertinent cations (Cu^{2+}, Co^{2+}, Pb^{2+}, Zn^{2+}, Cr^{3+}, Cd^{2+}, Ca^{2+}, Al^{3+}, Fe^{3+}, Hg^{2+}, Ni^{2+}, Mn^{2+}, Ba^{2+}, Na^+, K^+, Mg^{2+} and Pd^{2+}). The desired complexation is confirmed through a ring opening pathway, where the sensitivity of the probe towards Zn^{2+} is found to be superior to other reported Zn-sensor and the LOD is considerably low, 3.2 nM. The emissive [Zn(L^1)OAc] complex is further capable of disclosing a selective fluorescence 'turn-off' detection towards $H_2PO_4^-$ out of nineteen admissible anions (HPO_4^-, PO_4^{3-}, SO_4^{2-}, SCN^-, $H_2PO_4^-$, $S_2O_3^{2-}$, S^{2-}, IO_3^-, AsO_2^-, Br^-, NO_3^-, CH_3COO^-, AsO_3^-, NO_2^-, F^-, CN^-, HF_2^-, citrate and $S_2O_5^{2-}$). The demetallation of the probe in presence of $H_2PO_4^-$ leads to a sensitive detection of the desired analyte, where the LOD is found to be as low as 0.238 μM. Subsequently, taking the advantage of sequential sensing performance of HL, a reversible and recyclable 'ON-OFF' fluorescence switch is

constructed which is capable to be operated upto 6 cycles without noticeable exhaustion in switching activity. Finally, the switchable emissive characteristics of HL triggers us to construct an INHIBIT logic gate, proficient of mimicking a smart memory circuit with two input (Zn^{2+}, $H_2PO_4^-$) and one output (λ_{em} = 461 nm) signaling propensity. Importantly, the sensitivity of the present chemosensor is successfully extended in solid state where the highly emissive [Zn(L^1)OAc] complex is found to be capable of recognizing $H_2PO_4^-$ up to 10^{-8} M level from water with the LOD of 10.97 pg(picogram)/cm^2 based on a portable and cost-effective contact mode detection on the fabricated paper strips. Furthermore, the remarkable reversibility in the optical characteristics of the chemosensor enables us to develop a disposable security device, where the desired changes of fluorescence property in presence of Zn^{2+} and $H_2PO_4^-$ results in an 'ON-OFF' switching aided security labels without adopting any complicated methodologies. Taking the results together, the present findings pave an avenue towards attaining the multi-sensing venture of biologically apposite analytes in reasonably minute quantity from a single probe where the desired selectivity, sensitivity and low LODs enable HL to be a potent sensing candidate of practical significances.

III.5. References:

1. D. W. Zhang, X. Z. Jiang, H. Q. Yang, Z. Su, E. Q. Gao, A. Martinez and G. H. Gao, *Chem. Commun.*, 2013, **49**, 6149–6151.

2. C. Warwick, A. Guerreiro and A. Soares, *Biosens. Bioelectron.*, 2013, **41**, 1–11.

3. P. A. Furman, J. A. Fyfe, M. H. St Clair, K. Weinhold, J. L. Rideout, G. A. Freeman, S. N. Lehrman, D. P. Bolognesi, S. Broder and H. Mitsuya, *Proc. Natl. Acad. Sci. U. S. A.*, 1986, **83**, 8333–8337.

4. A. Ojida, Y. Mito-oka, K. Sada and I. Hamachi, *J Am Chem. Soc.*, 2004, **126**, 2454–2463.

5. S. Khoshniat, A. Bourgine, M. Julien, P. Weiss, J. Guicheux and L. Beck, *Cell. Mol. Life Sci.*, 2011, **68**, 205–218.

6. A. T. Lawal and S. B. Adeloju, *Talanta*, 2013, **114**, 191–203.

7. H. T. Ngo, X. Liu and K. A. Jolliffe, *Chem. Soc. Rev.*, 2012, **41**, 4928–4965.

8.T. Tabary and L. Ju, *J. Immunol. Methods*, 1992, **156**, 55–60.

9. A. Bencini, F. Bartoli, C. Caltagirone and V. Lippolis, *Dyes Pigments*, 2014, **110**, 169–192.

10. D. Zhang, J. R. Cochrane, A. Martinez and G. Gao, *RSC Adv.*, 2014, **4**, 29735–29749.

11. P. A. Gale, *Chem. Commun.*, 2005, **30**, 3761–3772.

12. E. Slatopolsky, *Kidney Int.*, 2011, **79**, S3–S8.

13. R. Kumar, *Curr. Opin. Nephrol. Hypertension*, 2009, **18**, 281–284.

14. S. O. Engblom, *Biosens. Bioelectron.*, 1998, **13**, 981–994.

15. H. Kawasaki, K. Sato, J. Ogawa, Y. Hasegawa and H. Yuki, *Anal. Biochem.*, 1989, **182**, 366–370.

16. A. I. Vogel and G. H. Jeffery, Vogel's Textbook of Quantitative Chemical Analysis, Longman Scientific & Technical, 1989.

17. S. Hisham, H. A. Tajuddin, C. F. Chee, Z. A. Hasan and Z. Abdullah, *J. Lumin.* 2019, **208**, 245–252.

18. J. Wongkongkatep, A. Ojida and I. Hamachi, *Top. Curr. Chem.*, 2017, **375**, 1–33.

19. F. Wang, X. Zeng, X. Zhao, H. Lu and Q. Wang, *J. Lumin.*, 2019, **208**, 302–306.

20. A. E. Hargrove, S. Nieto, T. Zhang, J. L. Sessler and E. V. Anslyn, *Chem. Rev.*, 2011, **111**, 6603–6782.

21. A. K. H. Hirsch, F. R. Fischer and F. Diederich, *Angew Chem. Int. Ed.*, 2007, **46**, 338–352.

22. S. K. Kim, D. H. Lee, J. -I. Hong and J. Yoon, *Acc. Chem. Res.*, 2009, **42**, 23–31.

23. N. Busschaert, C. Caltagirone, W. V. Rossom, P. A. Gale, *Chem. Rev.*, 2015, **115**, 8038–8155.

24. J. Wu, W. Liu, J. Ge, H. Zhang and P. Wang, *Chem. Soc. Rev.*, 2011, **40**, 3483–3495.

25. H. T. Ngo, X. Liu and K. A. Jolliffe, *Chem. Soc. Rev.*, 2012, **41**, 4928–4965.

26. Y. L. Pak, K. M. K. Swamy and J. Yoon, *Sensors*, 2015, **15**, 24374–24396.

27. P. A. Gale, *Acc. Chem. Res.*, 2006, **39**, 465–475.

28. F. P. Schmidtchen and M. Berger, *Chem. Rev.*, 1997, **97**, 1609–1646.

29. S. Suganya, S. Naha and S. Velmathi, *ChemistrySelect*, 2018, **3**, 7231–7268.

30. X. Lou, D. Ou, Q. Li and Z. Li, *Chem. Commun.*, 2012, **48**, 8462–8477.

31. M. C. Aragoni, M. Arca, A. Bencini, C. Caltagirone, A. Garau, F. Isaia, M. E. Light, V. Lippolis, C. Lodeiro, M. Mameli, R. Montis, M. C. Mostallino, A. Pintus and S. Puc-cioni, *Dalton Trans.*, 2013, **42**, 14516–14530.

32. H. G. Lee, J. H. Lee, S. P. Jang, I. H. Hwang, S. J. Kim, Y. Kim, C. Kim and R. G. Harrison, *Inorg. Chim. Acta*, 2013, **394**, 542–551.

33. E. Oliveira, D. Genovese, R. Juris, N. Zaccheroni, J. L. Capelo, M. M. M. Raposo, S. P. G. Costa, L. Prodi and C. Lodeiro, *Inorg. Chem.*, 2011, **50**, 8834–8849.

34. Y. Ma, F. Wang, S. Kambam and X. Chen, *Sens. Actuators B Chem.*, 2013, **188**, 1116–1122.

35. Y. Kurishita, T. Kohira, A. Ojida and I. Hamachi, *J. Am. Chem. Soc.*, 2012, **134**, 18779–18789.

36. J. M. Berg and Y. Shi, *Science*, 1996, **271**, 1081–1085.

37. S. Goswami, S. Maity, A. C. Maity, A. K. Das, K. Khanra, T. K. Mandal and N. Bhattacharyya, *Tetrahedron Lett.*, 2014, **55**, 5993–5997.

38. H. D. Duong and J. I. Rhee, *Sens. Actuators B, Chem.*, 2018, **274**, 66–77.

39. D. D. Perrin, W. L. F. Armarego and D. R. Perrin, Purification of Laboratory Chemicals, Pergamon Press, Oxford, U.K., 1980.

40. S. Chaudhuri, S. C. Patra, P. Saha, A.S. Roy, S. Maity, S. Bera, P. S. Sardar, S. Ghosh, T. Weyhermüller and P. Ghosh, *Dalton Trans.*, 2013, **42**, 15028–15042.

41. A. S. M. Islam, M. Sasmal, D. Maiti, A. Dutta, B. Show M. Ali, *ACS Omega*, 2018, **3**, 10306–10316.

42. G. M. Sheldrick, *Acta Cryst.*, 2008, **64**, 112–122.

43. J. Farrugia, *J. Appl. Crystallogr.*, 1997, **30**, 565–574.

44. A. L. Spek, Platon, The Netherlands, 1999.

45. M. J. Frisch, G. W. Trucks, H. B. Schlegel, G. E. Scuseria, M. A. Robb, J. R. Cheeseman, G. Scalmani, V. Barone, B. Mennucci, G. A. Petersson, H. Nakatsuji, M. Caricato, X. Li, H. P. Hratchian, A. F. Izmaylov, J. Bloino, G. Zheng, J. L. Sonnenberg, M. Hada, M. Ehara, K. Toyota, R. Fukuda, J. Hasegawa, M. Ishida, T. Nakajima, Y. Honda, O. Kitao, H. Nakai, T. Vreven, J. A. Montgomery Jr, J. E. Peralta, F. Ogliaro, M. Bearpark, J. J. Heyd, E. Brothers, K. N. Kudin, V. N. Staroverov, R. Kobayashi, J. Normand, K. Raghavachari, A. Rendell, J. C. Burant, S. S. Iyengar, J. Tomasi, M. Cossi, N. Rega, J. M. Millam, M. Klene, J. E. Knox, J. B. Cross, V. Bakken, C. Adamo, J. Jaramillo, R. Gomperts, R. E. Stratmann, O. Yazyev, A. J. Austin, R. Cammi, C. Pomelli, J. W. Ochterski, R. L. Martin, K. Morokuma, V. G. Zakrzewski, G. A. Voth, P. Salvador, J. J. Dannenberg, S. Dapprich, A. D. Daniels, O. Farkas, J. B. Foresman, J. V. Ortiz, J. Cioslowski and D. J. Fox, Gaussian 09, Revision D.01, Gaussian Inc, Wallingford, CT, 2009.

46. A. Afonin, D. D. Toryashinova, E. Y. Schmidt, *J. Mol. Struct. (Theochem)*, 2004, **680**, 127–135.

47. M. Cossi and V. Barone, *J. Chem. Phys.*, 2001, **115**, 4708–4717.

48. M. Cossi, N. Rega, G. Scalmani and V. Barone, *J. Comput. Chem.*, 2003, **24**, 669–681.

49. H. Ito, *J. Number Theory*, 2014, **135**, 139–150.

50. S. Sivalingam, K. Debsharma, A. Dasgupta, S. Sankararaman and E. Prasad, *ChemPlusChem*, 2019, **84**, 392–402.

51. K. Debsharma, J. Santhi, B. Baire and E. Prasad, *ACS Appl. Mater. Interfaces*, 2019, **11**, 48249−48260.

52. Y. Dong, R. Fan, W. Chen, P. Wang and Y. Yang, *Dalton Trans.*, 2017, **46**, 6769–6775.

53. T. Pariat, P. M.Vérité. D. Jacquemin, J. Massue and G. Ulrich, *Dyes Pigm.*, 2021, **190**, 109338.

54. Y. Liu, X. Wang, E. Feng, C. Fan and S. Pu, *Spectrochim. Acta A*, 2021, **246**, 119052.

55. M. An, B. Kim, H. Seo, A. Helal and H. Kim, *Spectrochim. Acta A*, 2016, **169**, 87–94.

56. J. Fu, K. Yao, B. Li, H. Mei, Y. Chang and K. Xu, *Spectrochim. Acta A*, 2020, **228**, 117790.

57. N. Behera and V. Manivannan, *J. Photoch. Photobio. A*, 2018, **353**, 77–85.

58. R. Purkait, A. D. Mahapatra, D. Chattopadhyay and C. Sinha, *Spectrochim. Acta A*, 2019, **207**, 164–172.

59. S. Goswami, S. Maity, A. C Maity, A. K. Das, K. Khanra, T. K. Mandal and N. Bhattacharyya, *Tetrahedron Lett.*, 2014, **55**, 5993–5997.

60. K. Du, S. Niu, L. Qiao, Y. Dou, Q. Zhu, X. Chen and P. Zhang, *RSC Adv.*, 2017, **7**, 40615–40620.

61. A. Gogoi, S. Samanta and G. Das, *Sens. Actuators B*, 2014, **202**, 788–794.

62. S. S. Kumara, R. S. Kumara and S. K. A. Kumara, *Inorg. Chim. Acta*, 2020, **502**, 119348.

63. S. Dey, S. Maity, K. Pal, K. Jana and C. Sinha, *Dalton Trans.*, 2019, **48**, 17818–17830.

64. Y. Che, D. E. Gross, H. Huang, D. Yang, X. Yang, E. Discekici, Z. Xue, H. Zhao, J. S. Moore and L. Zang, *J. Am. Chem. Soc.*, 2012, **134**, 4978−4982.

65. S. Suganya, K. Debsharma, E. Ravindran, M. K. Mahato and E. Prasad, *ACS Appl. Polym. Mater.*, 2020, **2**, 1222−1233.

66. S. Maity, M. Shyamal, R. Maity, N. Mudi, P. Hazra, P. K. Giri, S. S. Samanta, S. Pyne and A. Misra, *Photochem. Photobiol. Sci.*, 2020, **19**, 681–694.

67. L. Patra, S. Das, S. Gharami, K. Aich and T. K. Mondal, *New J. Chem.*, 2018, **42**, 19076–19082.

68. R. Purkait, S. Dey and C. Sinha, *New J. Chem.*, 2018, **42**, 16653–16665.

69. S. Paul, S. Dey, K. Pal, S. Maity, K. Jana and C. Sinha, *ChemistrySelect*, 2020, **5**, 1–11.

70. S. Dey, R. Purkait, K. Pal, K. Jana and C. Sinha, *ACS Omega*, 2019, **4**, 8451−8464.

71. S. S. Kumar, R. S. Kumar and S. K. A. Kumar, *Inorg. Chim. Ac*ta, 2020, **502**, 119348.

72. J. Du, X. Wang, M. Jia, T. Li, J. Mao and Z. Guo, *Inorg. Chem. Commun.*, 2008, **11**, 999–1002.

73. V. K. Praveen, B. Vedhanarayanan, A. Mal, R. K. Mishra and A. Ajayaghosh, *Acc. Chem. Res.*, 2020, **53**, 496−507.

74. R. Thirumalai, R. D. Mukhopadhyay, V. K. Praveen and A. Ajayaghosh, *Sci. Rep.*, 2015, **5**, 9842.

Chapter IV

Idiosyncratic recognition of Zn^{2+} and CN^- using Pyrazolyl-Hydroxy-Coumarin scaffold and live cell imaging: Depiction of Luminescent Zn(II)-Metallocryptand.

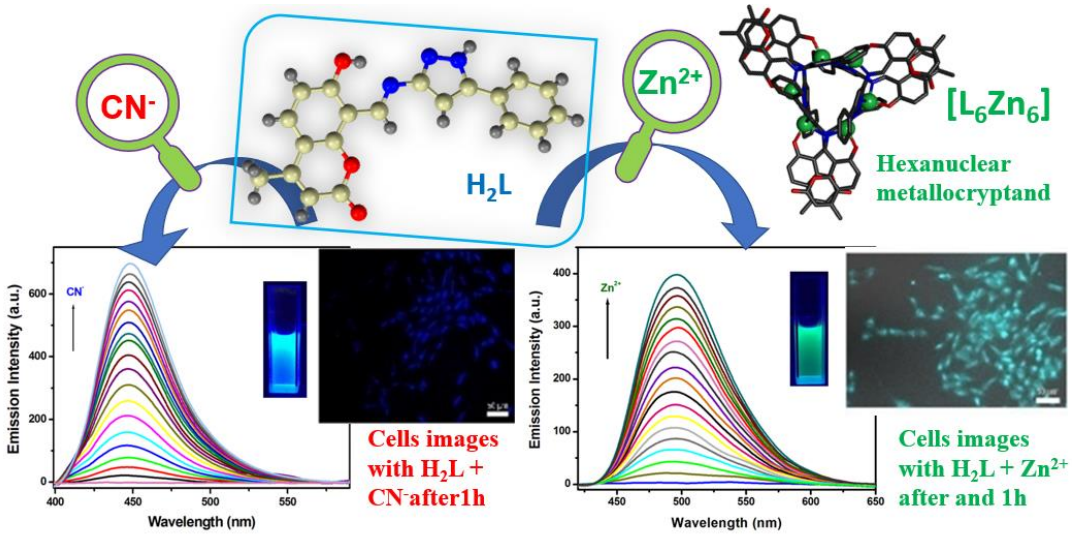

CHAPTER IV

Abstract

Multi-responsive and selective sensor design is one of the stimulating researches in sensor field. We have designed a pyrazolyl-hydroxy-coumarin scaffold, 7-hydroxy-4-methyl-8-(((5-phenyl-1H-pyrazol-3-yl)imino)methyl)-2H-chromen-2-one (H_2L) and characterized by spectroscopic data (^{1}H-NMR,^{13}C-NMR, ESI-MS, IR). The Single crystal X-Ray diffraction measurement confirms the molecular structure of the probe. It undergoes selective sensing to Zn^{2+} in presence of sixteen other cations with 'Turn On' approach through enhancement of green fluorescence (($\lambda_{em.}$= 499 nm; $\lambda_{ex.}$= 390 nm) in CH_3CN/H_2O (99:1, v/v; HEPES Buffer, pH 7.5) medium with the limit of detection (LOD) 34.76 nM. The structural depiction of isolated Zn^{2+} complex reveals cage like metallocryptand cyclic hexamer, $[Zn_6L_6]$ with 30.9% void of cavity along crystallographic c axis of approximate dimension of 7.502 × 7.050 × 7.068 Å^3. Diffusion NMR study reveals the only one type of complex in solution, having 1:1 composition, Zn^{2+}: H_2L which affirms the isolated form of the complex. On the other hand, the receptor, H_2L, recognizes very noxious anion CN^- out of sixteen anions. The product identification by spectroscopic data supports the nucleophilic addition of CN^- across the exocyclic imine (C=N) bond which shows blue emission (($\lambda_{em.}$= 447 nm; $\lambda_{ex.}$= 390 nm) and LOD is 19.91 nM. The composition of [H_2L-Zn^{2+}] and [H_2L-CN^-] are established by ^{1}H NMR titration, Job's method, ESI-MS and FTIR spectra. The efficacy of the probe is further applied for MTT Assay in MDA-MB 231 and WI-38 cell line as well as for intracellular imaging of Zn^{2+} and CN^- under Fluorescence microscope. Flow Cytometric Data has been further performed for quantitative analysis of Zn^{2+} distribution in MDA-MB 231 cells.

IV.1. Introduction

Biochemical implication of ions in human health and environment focuses on the synthetic strategy of a receptor in such a manner that the chemosensor selectively emanates recognizable signals on binding with bioactive or toxic cations and anions. Polypodal Schiff bases may synthesize multinuclear metallo-macrocycle complexes[1,2] those may act as potential magnetic materials,[3,4] homogeneous catalysts,[5] optical and electronic materials,[6,7] sensing devices[8] etc. Schiff bases with fluorogenic components like, carbazole,[9,10] quinoline,[11,12] Rhodamine,[13,14] naphthyl,[15,16] pyrenyl,[17,18] fluorenyl,[19,20] diformyl[21,22] etc. influence the emission energy, intensity, pattern and the molecules might serve as sensitive detector of ions/molecules. Fluorogenic units of Coumarin derivatives[23-25] are beneficial for their diverse pharmacological properties, low toxicity and interesting photophysical responses to analytes.

Zinc ion (Zn^{2+}) ranks second in terms of its abundance and activity in environmental and human health.[26,27] It involves in cell division, gene expression, neurotransmission, signal transduction DNA and protein synthesis.[28-30] In general, balanced concentration of Zn^{2+} is beneficial for human health while misregulation has a serious effect on life. On deficiency of Zn^{2+}, mental retardation, unbalanced metabolism are the common side effects.[31] However excess accumulation of Zn^{2+} in cells causes severe neurodegenerative disorder such as Alzheimer's disease and Parkinson's disease.[32,33] As per the WHO guidelines, the permissible limit of Zn^{2+}consumption in drinking water is 76 μM.[34] Visual detection of Zn^{2+} is a convenient approach for easy detection in the materials; bis(oxadiazole)pyridine derivative is recently demonstrated as effective Zn^{2+} fluorescent sensors[35] even in cellular environment and benzothiazole based chromogenic unit senses also Zn^{2+} colormetrically.[36] Pyrazolyl derivatives efficiently serves the purpose of colorimetric as well as fluorometric Zn^{2+} sensor.[37,38] So it is important to design analytical methods for efficient, sensitive, selective, nontoxic, cheap detection of Zn^{2+} at cellular level.

On the other hand, cyanide (CN^-), often found in the seeds of apples, Cassava and apricot kernels etc., which on consumption leads to acute toxicity as the CN^- strongly binds Fe of Cytochrome C oxidase causing the disruption of mitochondrial electron-transport process resulting in reduction of oxidative metabolism and

interferes with energy production.[39-42] In addition CN^- gets absorbed through skin and lungs and even microscopic increase in its concentration in human body causes serious hazardous to health.[43] Cyanide is used in gold and silver extraction, electroplating, plastic production, synthesis of resins, fibers and pesticides. The discharge of cyanide contaminated industrial waste in environment can results the exposure of CN^- to human health through food and drinking water.[44-46] So detection of CN^- at trace level is important owing to its extreme toxic nature and proper regulations and guidelines were imposed by WHO for monitoring of CN^- level with maximum permissible limit for consumption in drinking water is 1.9 μM.[47,48] Therefore generation and advancement of molecular probes for sensitive cyanide detection at trace level are gaining importance.

Spectroscopic methods are easily operative, rapid responsive and economical method for highly sensitive and efficient detection of ions.[49] Use of coumarin derivatives are potentially effective for sensing as well as biological application.[50,51] In this account, we design and structurally characterize coumarin based Schiff base, (Z)-7-hydroxy-4-methyl-8-(((5-phenyl-1H-pyrazol-3-yl)imino)methyl)-2H-chromen-2-one (H_2L) which serves as chemosensor for the sensing of Zn^{2+} (λ_{em} = 499 nm, LOD, 34.76 nM) and CN^- (λ_{em} = 447 nm LOD, 19.91 nM) with distinctive fluorescence responses at two emissive states in acetonitrile medium. The interaction of Zn^{2+} and H_2L has isolated a metallocryptand hexanuclear complex, $[Zn_6L_6]$. The composition and binding stoichiometry of the complex ($[H_2L\text{-}Zn^{2+}]$ and $[H_2L\text{-}CN^-]$) has been confirmed through ^{1}H-NMR, ESI-MS, IR and other spectroscopic techniques. Theoretical study has been performed for the probe H_2L along with its Zn^{2+} ($[H_2L\text{-}Zn^{2+}]$) and CN^- ($[H_2L\text{-}CN^-]$) complexes to explain the spectroscopic changes. MTT Assay of probe has been carried out in MDA-MB 231 and WI-38 cell line for cytotoxicity analysis. Distribution of Zn^{2+} and CN^- in MDA-MB 231 cells has been checked through intracellular fluorescence imaging and detailed estimation of Zn^{2+} distribution in cells was further examined through Flow Cytometric Analysis.

IV.2. Experimental section

IV.2.1. Materials and methods

All the reagents of analytical grade (A.R) were collected from the commercial suppliers and used without further purification. 3-Amino-5phenyl pyrazole, Resorcinol, Ethylacetoacetate, Hexamine were purchased from Sigma-Aldrich. Inorganic salts and other organic chemicals ($ZnCl_2$, $CdCl_2$, $HgCl_2$, $CuCl_2.2H_2O$, $CoCl_2.6H_2O$, $PbCl_2$, $AlCl_3$, $CaCl_2.6H_2O$, $FeCl_3.6H_2O$, $BaCl_2.2H_2O$, $NiCl_2.6H_2O$, NaCl, $MnCl_2.4H_2O$, $PdCl_2$, $CrCl_3.6H_2O$, KCl, $MgCl_2$, $Na_2S_2O_3.5H_2O$, K_3PO_4, NaCl, NaF, NH_4HF_2, KNO_3, KBr, $NaNO_2$, NaN_3, CH_3COONa,, KIO_3, $Na_4P_2O_7$,KI,Na_2SO_4, Na_2S, $Na_2S_2O_5$, $C_4H_9N(CN)$) were bought from TCI chemicals and Merck. For spectroscopic measurement UV graded solvents spectroscopic were used. The solvents were dried by standard procedure for spectroscopic studies.[52] Milli-Q water (Millipore) has been used for preparation of aqueous solutions of metal salts. Perkin-Elmer (2400 Series-II, Perkin Elmer, USA) CHN analyser has been used for elemental analysis purpose. The spectra were recorded by Lambda 25 spectrophotometer: UV-Vis; LS55: fluorescence and LX-1FTIR spectrophotometer: FT-IR spectra (KBr disk, 4000-400 cm^{-1}) on Perkin Elmer instruments. ^1H and ^{13}C NMR spectra were taken by Bruker 300 MHz FT-NMR spectrometer. The chemical shift (δ) of the respective NMR spectra were recorded in parts per million (ppm) with respect to trimethylsilaneas internal standard. ESI-MS spectra were obtained from HRMS spectrometer (model, XEVO-G2QTOF#YCA351).

IV.2.2. Synthesis of 7-hydroxy-4-methyl-8-(((5-phenyl-1H-pyrazol-3-yl)imino)methyl)-2H-chromen-2-one (H_2L)

7-Hydroxy-4-methyl-2-oxo-2H-chromene-8-carbaldehyde prepared following the literature procedure.[53] To a 10 mL stirred methanol solution of 7-Hydroxy-4-methyl-2-oxo-2H-chromene-8-carbaldehyde (204.18 mg, 1 mmol), a solution of 3-Amino-5-phenylpyrazol (159.19 mg, 1 mmol) in MeOH (5 mL) was slowly added in dropwise. The resulting solution, after few minutes, turned orange which on stirring for 12 h followed by refluxing for 3h isolated orange precipitate. It was filtered off and thoroughly washed with methanol, dried under vacuum. (**Scheme IV**) The compound was recrystallized by slow evaporation of DMSO/MeOH solution

(1:4, v/v) and orange block shaped crystals were isolated. Yield: 79.2% (273.32 mg). Microanalytical data ($C_{20}H_{15}N_3O_3$) Fd Calcd.(%) C, 69.50 (69.56);H, 4.38 (4.35);N, 12.23(12.17).^{1}H-NMR (300 MHz, DMSO-d_6): δ14.87 (s,1H, OH), 13.47 (s,1H, NH), 9.49 (s, 1H, CH=N), 7.89-6.96, (m, 8H, Ar-H), 6.27 (s, 1H, Ar-H), 2.42 (s, 3H, CH_3) (**Fig.IV.1)** ^{13}CNMR (75 MHz, DMSO-d_6): δ 165.20, 159.62, 156.11, 154.43, 154.37, 144.38, 130.72, 129.50, 129.36, 129.01, 125.66, 114.42, 111.75, 111.05, 106.75, 100.01, 94.42, 18.82. (**Fig.IV.2)** ESI-MS shows a molecular ion base peak at 368.0911 (Calculated m/z = 368.10 [M+Na^+]). **(Fig.IV.3)** IR Spectrum: 3207 cm^{-1}(N-H stretching, pyrazole), 2886 cm^{-1} (C-H stretching, CH_3), 1691 cm^{-1} (C=O, coumarin), 1617 cm^{-1} (C=N, imine), 1082 cm^{-1} (C-O, phenolic). (**Fig.IV.4)**

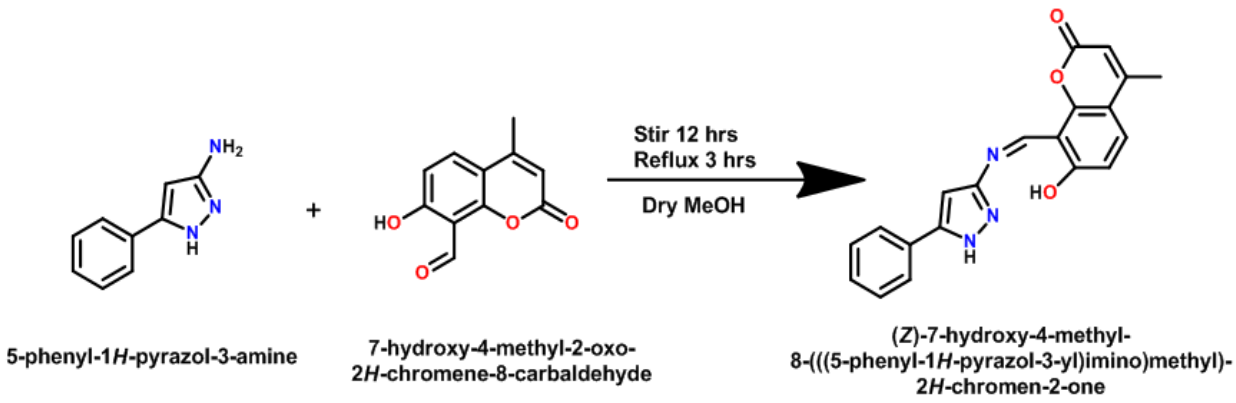

Scheme IV. Synthesis of Ligand H_2L

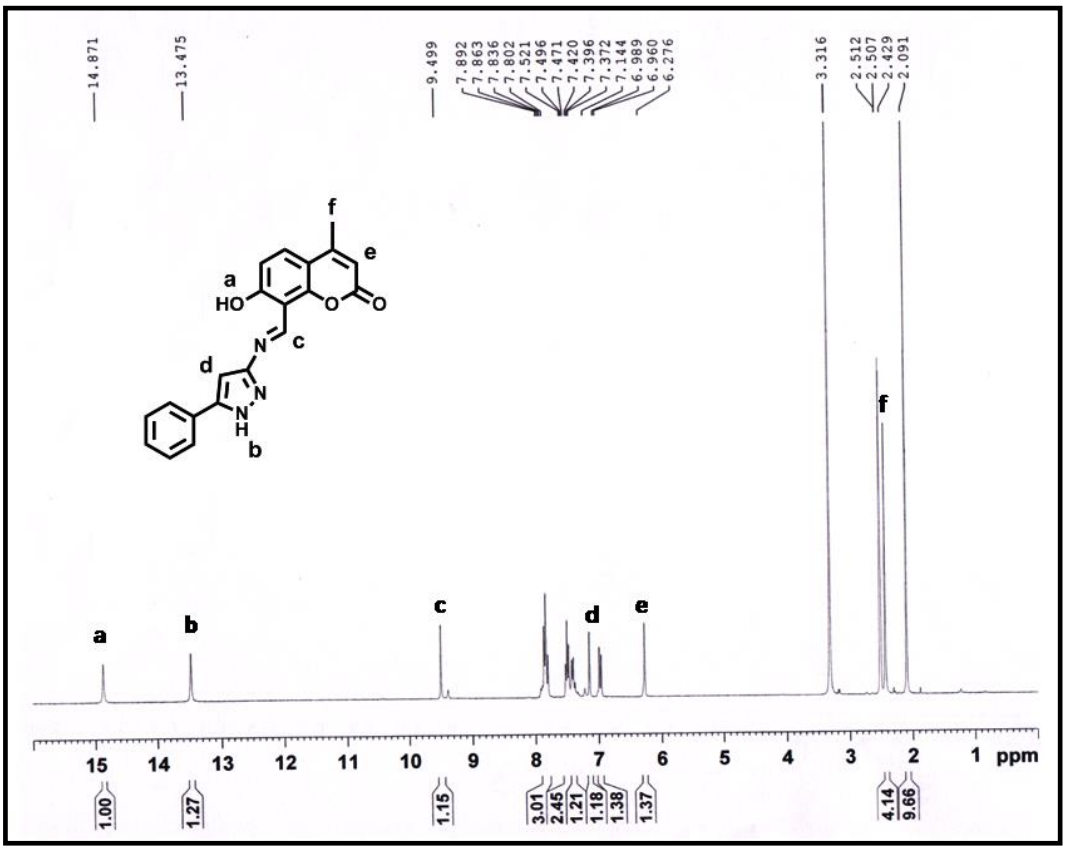

Fig.IV.1. ^{1}HNMR Spectrum (300 MHz) of the probe H_2L in DMSO-d_6

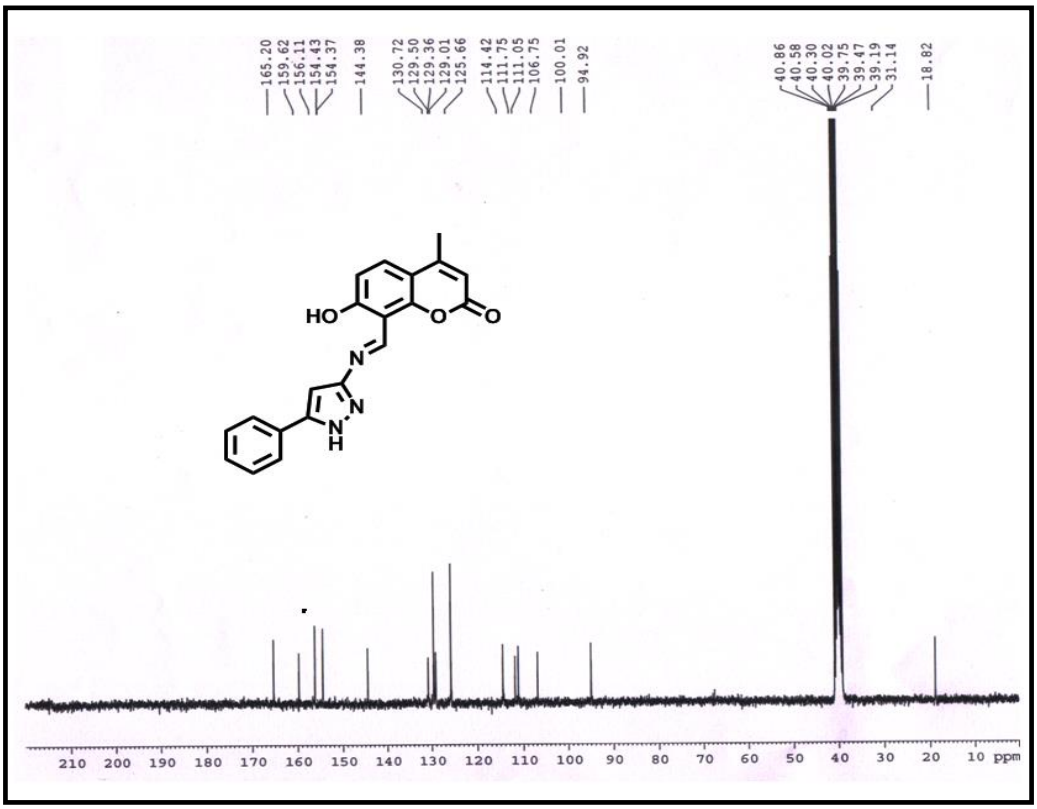

Fig.IV.2. ^{13}CNMR Spectrum (75 MHz) of H_2L in DMSO-d_6

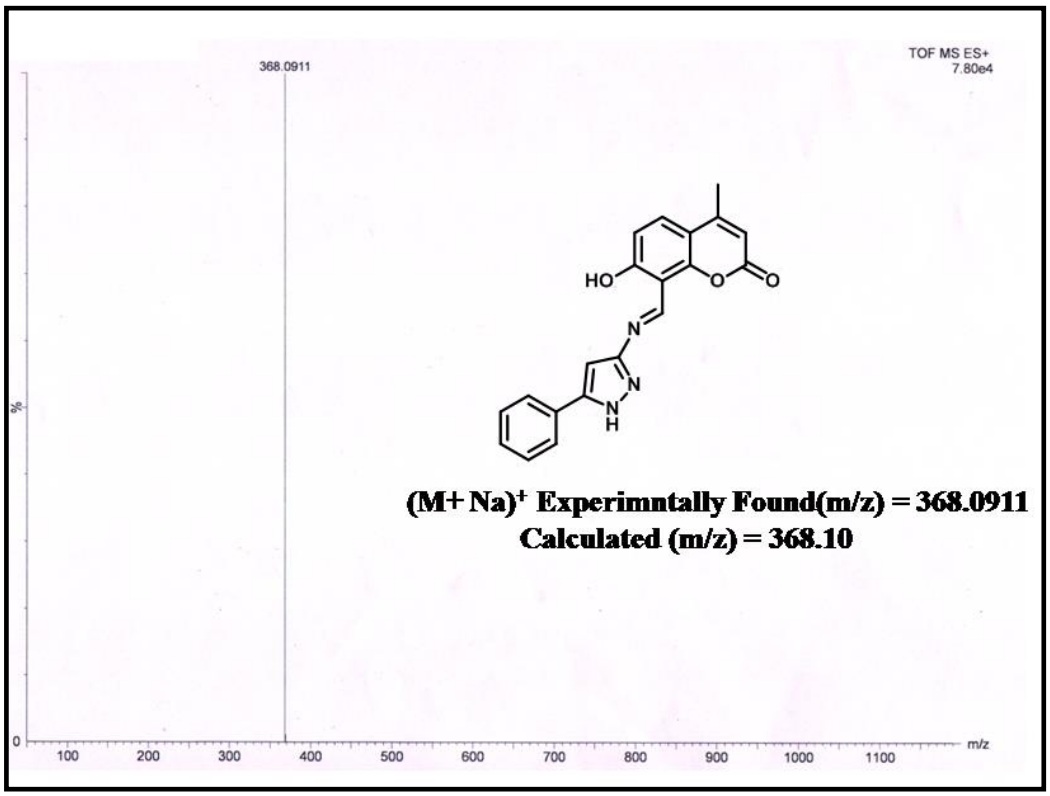

Fig.IV.3. ESI-MS Spectrum of H_2L

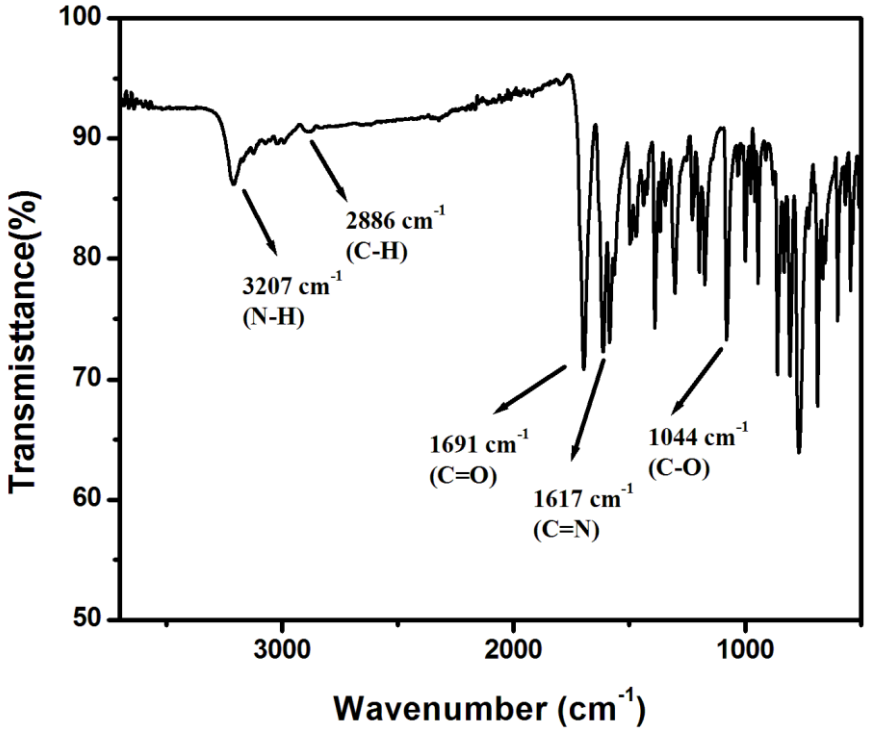

Fig.IV.4. IR Spectrum of the probe H_2L

IV.2.3. Synthesis of Hexanuclear Zinc Complex, [Zn_6L_6]

To a solution of H_2L (345 mg, 1 mmol) in 1ml DMSO, a 5 mL methanolic solution of $Zn(CH_3COO)_2.2H_2O$ (220 mg, 1 mmol) (DMSO:MeOH, v/v, 1:5) was added slowly under stirring condition for 3 h. The resulting mixture was filtered and kept isolated and allowed for slow evaporation at room temperature for few days. Needle shaped single crystals were separated and used for different physicochemical studies and suitable for X-ray Diffraction data collection. ^{1}HNMR: 9.51-9.43 (d, 1H, CH=N), 7.76-6.00 (m, 9H, Ar-H), 2.35 (s, 3H, CH_3). Microanalytical data ($C_{123}H_{89}N_{18}O_{20}SZn_6$) Fd (Calcd.) (%) C, 57.59 (57.63); H, 3.47 (3.50); N, 9.87 (9.84). IR Spectrum: υ(C=O) 1702 cm^{-1}, υ (C=N) 1573 cm^{-1}. Yield: 70%. (155 mg)

IV.2.4. X-Ray Crystallographic Measurements

Single crystals of (Z)-7-Hydroxy-4-methyl-8-(((5-phenyl-1H-pyrazol-3-yl)imino)methyl)-2H-chromen-2-one (H_2L, Orange crystal, 0.12 x 0.08 x 0.08 mm^3) and needle shaped yellowish green crystals of [Zn_6L_6] (0.27 x 0.09 x 0.05 mm^3) were obtained by slow evaporation from equimolar solution of DMSO and MeOH. Single Crystal X-ray data were collected by Bruker Apex II CCD Area Detector at 100.4K and 273K.Graphite-monochromatized Mo-Kα radiation (λ= 0.71073 Å) was used in fine-focus sealed tube. The hkl range for data collection were -15≤ h≤ 15; -16≤ k≤ 16; -14≤ l≤ 14 for the probe H_2L and -21≤ h≤ 21; -21≤k≤ 21; -29≤ l≤ 29 for [Zn_6L_6]. Diffraction was recorded within the angular range from 2.364≤ θ ≤ 27.158^o (H_2L) and 2.276≤ θ ≤ 25.495^o ([Zn_6L_6]). The intensity was corrected for Lorentz and polarisation effects and empirical absorption corrections were applied for both the probe and the complex. Data were collected applying the condition I>2σ(I). The structure was solved by direct method and followed by successive Fourier and difference Fourier syntheses. All non-hydrogen atoms were refined anisotropically. The hydrogen atoms were geometrically fixed and refined using the riding model. All calculations were carried out using SHELXL-2016/6 Program for Crystal Structure Solution, University of Gөτtingen: Göttinge,[54] ORTEP-32,[55] PLATON-99[56] and Olex 2-1.5-alpha[57] programs. The crystal data of probe H_2L and Zn^{2+} complexes have been deposited to Cambridge Crystallographic Data Centre with CCDC 2109503 and 2109502. Details of Data collection and Crystal data with some selected bond length and bond angle were listed in (**Tables IV.1,2, 3 and 4**).

Table IV.1: Crystal Data and Refined Parameters for H_2L and $[Zn_6L_6]$

Empirical formula	$C_{20}\ H_{15}\ N_3\ O_3$	$C_{245.78}H_{168.66}N_{36}O_{39.78}S_{1.57}\ Zn_{12}$
CCDC No.	2109503	2109502
Formula weight	345.35	5097.43
Temperature (K)	273(2)	100.4
System	Monoclinic	Triclinic
Space group	*P 21/c*	P -1
a (Å)	11.8984(10)	17.5384(14)
b (Å)	12.8002(10)	17.6613(12)
c (Å)	11.1706(9)	24.5865(16)
α/°	90	97.163(2)
β/°	101.831(2)	100.276(2)
γ/°	90	106.205(2)
V $(Å)^3$	1665.2(2)	7072.1(9)
Z	4	1
D(cal) /g cm^{-3}	1.378	1.197
μ/mm^{-1}	0.095	1.076
λ(Å)	0.71073	0.71073
Data[I >2σ(I)]/param	3676/237	26162/ 1546
$R_1{}^a$[I>2σ(I)]	0.0530	0.0612
$wR_2{}^b$	0.1595	0.1656
GOF[c]	1.215	1.043

$^aR_1 = \Sigma||F_o|-|F_c||/\Sigma|F_o|$; $^bwR_2 = \{\Sigma[w(F_o^2-F_c^2)^2]/\Sigma[w(F^2_o)^2]\}^{1/2}$; $w = [\sigma^2(F_o)^2 + (0.1003P)^2 + 4.9693P\ ]^{-1}$ $(F_o^2 + 2F_c^2)/3$; [c] Goodness-of-fit.

Table IV.2: Selected Bond length (Ă) of H_2L

Bond	Length (Ă)	Bond	Angle (°)
N(3)-H(3A)	0.86	N(3)-N(2)-H(3A)	123.2
N(3)-N(2)	1.345(2)	N(3)-N(2)-C(11)	103.60(16)
N(2)-C(11)	1.339(2)	N(2)-C(11)-N(1)	116.66(17)
C(11)-N(1)	1.401(2)	C(11)-N(1)-C(10)	120.49(16)
N(1)-C(10)	1.285 (2)	N(1)-C(10)-H(10)	120
C(10)-C(8)	1.452(2)	N(1)-C(10)-C(8)	119.72(17)
C(8)-C(7)	1.406 (2)	C(10)-C(8)-C(7)	121.75(15)
C(7)-O(3)	1.342(2)	C(8)-C(7)-O(3)	121.15(17)
O(3)-H(3)	0.82	C(7)-O(3)-H(3)	109.5

Table IV.3: Selected Bond length (Ă) for $[Zn_6L_6]$

Bond Length	Length (Ă)	Bond Length	Angle (°)
Zn(1)-O(1)	1.932(4)	Zn(4)-O(12)	1.945(3)
Zn(1)-N(12)	1.973(4)	Zn(4)-O(20)	2.539(4)
Zn(1)-N(13)	2.010(4)	Zn(4)-N(5)	2.087(4)
Zn(1)-N(18)	1.979(4)	Zn(4)-N(7)	1.983(4)
Zn(2)-O(6)	1.986(4)	Zn(4)-N(14)	2.007(4)
Zn(2)-O(19)	2.253(4)	Zn(5)-O(18)	1.960(4)
Zn(2)-N(1)	2.027(4)	Zn(5)-O(20)	2.360(4)
Zn(2)-N(4)	2.025(4)	Zn(5)-N(8)	2.023(4)
Zn(2)-N(16)	2.124(4)	Zn(5)-N(10)	2.126(4)
Zn(3)-O(13)	1.944(3)	Zn(5)-N(15)	2.012(4)

Zn(3)-O(19)	2.597(4)	Zn(6)-O(7)	1.938(3)
Zn(3)-N(2)	1.991(5)	Zn(6)-N(9)	2.001(4)
Zn(3)-N(3)	2.014(5)	Zn(6)-N(11)	1.983(4)
Zn(3)-N(6)	2.070(5)	Zn(6)-N(17)	1.985(4)

Table IV.4: Selected Bond Angles (°) for $[Zn_6L_6]$

Bond Angles	Degrees (°)	Bond Angle	Degrees (°)
O(1)-Zn(1)-N12	118.25(16)	O(1)-Zn(1)-N(13)	92.96(16)
N(12)-Zn(1)-N(13)	115.22(16)	N(12)-Zn(1)-N(18)	107.7(17)
O(6)-Zn(2)-O(19)	82.42(14)	O(6)-Zn(2)-N(1)	113.83(16)
O(6)-Zn(2)-N(16)	86.57(14)	O(19)-Zn(2)-N(1)	86.31(15)
O(19)-Zn(2)-N(16)	167.20(14)	N(1)-Zn(2)-N(4)	107.03(16)
N(4)-Zn(2)-N(16)	101.32(19)	O(13)-Zn(3)-O(19)	77.46(15)
O(13)-Zn(3)-N(3)	111.32(16)	O(13)-Zn(3)-N(6)	90.47(15)
O(19)-Zn(3)-N(3)	82.44(17)	O(19)- Zn(3)-N(6)	167.36(17)
N(2)-Zn(3)-N(6)	108.78(16)	N(3)-Zn(3)-N(6)	105.81(17)
O(12)-Zn(4)-N(5)	89.82(15)	O(12)-Zn(4)-N(7)	127.43(17)
O(20)-Zn(4)-N(5)	165.09(17)	O(20)-Zn(4)-N(7)	74.55(15)
N(5)-Zn(4)-N(7)	108.47(16)	N(5)-Zn(4)-N(14)	108.56(16)
O(18)-Zn(5)-O(20)	80.48(13)	O(18)-Zn(5)-N(8)	115.94(16)
O(18)-Zn(5)-N(15)	130.84(16)	O(20)-Zn(5)-N(8)	82.63(14)
O(20)-Zn(5)-N(15)	82.70(15)	N(8)-Zn(5)-N(10)	105.00(15)
N(10)-Zn(5)-N(15)	103.34(17)	O(7)-Zn(6)-N(9)	93.58(15)
O(7)-Zn(6)-N(17)	117.06(15)	N(9)-Zn(6)-N(11)	113.73(17)
N(11)-Zn(6)-N(17)	108.30(16)	Zn(1)-O(1)-C(1)	127.5(3)

Zn(6)-O(7)-C(63)	126.8(3)	Zn(3)-O(13)-C(103)	128.8(4)
Zn(5)-O(18)-C(52)	131.4(3)	Zn(2)-O(19)-Zn(3)	87.62(15)
Zn(3)-O(19)-C(02S)	128.1(3)	Zn(4)-O(20)-Zn(5)	87.89(15)
Zn(5)-O(20)-S(1)	139.3(2)	Zn(2)-N(1)-N(2)	120.4(3)
Zn(3)-N(2)-N(1)	112.8(4)	Zn(3)-N(2)-C(14)	137.7(3)
Zn(3)-N(2)-C(14)	137.7(3)	Zn(3)-N(3)-N(4)	119.8(4)
Zn(2)-N(4)-N(3)	115.2(3)	Zn(2)-N(4)-C(81)	135.8(3)
Zn(3)-N(6)-C(112)	119.2(3)	Zn(4)-N(7)-N(8)	113.9(3)
Zn(5)-N(8)-N(7)	121.5(3)	Zn(5)-N(8)-C(80)	128.0(3)
Zn(6)-N(9)-C(80)	117.0(4)	Zn(5)-N(10)-C(49)	120.6(3)
Zn(6)-N(11)-N(12)	123.9(3)	Zn(6)-N(11)-C(49)	125.9(4)
Zn(1)-N(12)-C(41)	134.0(4)	Zn(1)-N(13)-C(11)	124.4(3)
Zn(4)-N(14)-N(15)	123.1(4)	Zn(4)-N(14)-C(112)	126.3(3)
Zn(5)-N(15)-C(114)	137.7(3)	Zn(2)-N(16)-C(31)	126.0(4)
Zn(6)-N(17)-N(18)	114.6(3)	Zn(6)-N(17)-C(34)	134.5(4)
Zn(1)-N(18)-C(32)	124.8(4)	Zn(2)-O(19)-H(19)	119.8(2)
O(1)-Zn(1)-N(18)	107.72(16)	O(18)-Zn(5)-N(10)	87.83(15)
N(13)-Zn(1)-N(18)	114.52(15)	O(20)-Zn(5)-N(10)	168.04(14)
O(6)-Zn(2)-N(4)	134.84(15)	N(8)-Zn(5)-N(15)	107.12(16)
O(19)-Zn(2)-N(4)	81.62(15)	O(7)-Zn(6)-N(11)	110.73(15)
N(1)-Zn(2)-N(16)	104.21(16)	N(9)-Zn(6)-N(17)	113.04(16)
O(13)-Zn(3)-N(2)	126.67(17)	Zn(2)-O(6)-C(22)	133.3(3)
O(19)-Zn(3)-N(2)	76.26(17)	Zn(4)-O(12)-C(92)	131.1(4)
N(2)-Zn(3)-N(3)	110.20(16)	Zn(2)-O(19)-C(02S)	123.7(3)
O(12)-Zn(4)-O(20)	77.26(15)	Zn(4)-O(20)-S(1)	118.2(2)

O(12)-Zn(4)-N(14)	111.09(19)	Zn(2)-N(1)-C(12)	126.8(3)
O(20)-Zn(4)-N(14)	83.57(17)	Zn(3)-N(3)-N(4)	119.8(4)
N(7)-Zn(4)-N(14)	108.64(16)	Zn(3)-N(3)-C(89)	126.9(3)
Zn(5)-N(10)-C(50)	123.9(4)	Zn(3)-N(6)-C(101)	124.1(4)
Zn(1)-N(12)-N(11)	115.9(3)	Zn(4)-N(7)-C(72)	135.8(3)
Zn(1)-N(13)-C(12)	116.4(3)	Zn(5)-N(15)-N(14)	113.5(3)
Zn(2)-N(16)-C(32)	120.1(3)	Zn(1)-N(18)-N(17)	126.0(3)

IV.2.5. Quantum Yield and Limit of detection Calculation

Fluorescence quantum yields (Φ) were obtained by using the equation:

$$\Phi_{sample} = (OD_{std.} \times A_{sample})/(OD_{sample} \times A_{std.}) \times \Phi_{std.}$$

Where, A_{sample} and A_{std} represent the areas under the fluorescence spectral curves for sample and standard respectively. OD_{sample} and OD_{std} represents the optical densities of the sample and standard respectively at the excitation wavelength.[58,59] In this work, acidic quinine sulfate (0.1(N) H_2SO_4 solution) was taken as the standard with known quantum yield, Φstd. = 0.54 for the quantum yield calculation of ligand HL and the complex with Zn^{2+} and CN^-.

LOD determination was calculated from fluorescence Titration Experiment on gradual addition of Zn^{2+} and CN^- ion to the solution of ligand HL. Standard Deviation measured from emission intensity of ligand with addition of varying concentration of Zn^{2+} and CN^-. Limit of Detection for Zn^{2+} and CN^- determined from the equation LOD = (3σ/Slope) where σ represents standard deviation and m is the slope acquired from the plot of fluorescence titration experiment.

IV.2.6. Solution for Spectral Measurement

For UV-Vis and Fluorescence study, the ligand H_2L with concentration of $1x\ 10^{-3}$(M) was prepared in DMSO. All the cationic and anionic solutions of $1\ x\ 10^{-3}$(M) were arranged in deionized water. The Spectroscopic experiment was carried out in acetonitrile medium. A 25 μM of HL solution was prepared in 2 mL CH_3CN/H_2O (99:1, v/v) (HEPES Buffer, pH 7.5) for sensing study. To this solution 1 equivalent of metal cations were added and the sensitivity and selectivity was checked by UV-vis and Fluorescence measurement of the probe HL solution. The absorption and emission path length of cell used were 1 cm. fluorescence measurement experiments were done on excitation and emission of 12 nm x 7 nm (For Zn^{2+}) and 12 nm x 3 nm (For CN^-) slit width.

IV.2.7. DFT Computation

DFT and TD-DFT calculation were conducted to elucidate theoretical correlation with experimental spectroscopic results. Gas phase geometry of H_2L was optimized with coordinates obtained from single crystal structure using DFT/B3LYP method with 6-311G as basis set (O, N, C, H) whereas LanL2DZ basis set has been employed for the $[Zn_6L_6]$ and $[L\text{-}CN^-]$ complex of Gaussian Program Package 09.[60-62] The vibrational frequency calculation has been performed to ensure that the optimized geometries represent the local minima and the only positive Eigen values are used. To understand the change in absorption band of the probe regarding the sensing pathway towards Zn^{2+} and CN^-, selective electronic transitions were theoretically obtained by Time Dependent DFT (TD-DFT) calculation in Acetonitrile medium using conductor like polarizable continuum model (CPCM).[63-65] GAUSSSUM employed for calculation of fractional contribution of groups to the Molecular orbitals.[66]

IV.2.8. Cell line study

In the present study Human breast cancer cell line MDA-MB 231 was procured from the central cell repository of National Center for Cell Science (NCCS), Pune, India and human normal kidney epithelium cell line NKE was obtained from Bose Institute, India. All the above cell lines were cultured either in a T25 with DMEM

(for MDA-MB 231) RPMI-1640 (for, NKE) supplemented with, non-essential amino acids, 1mM sodium pyruvate, 10% Fetal bovine serum, 2 mM L-glutamine, 100 units/L penicillin,100 mg/L streptomycin, and 50 mg/L gentamycin in a 37°C humidified incubator containing 5% CO_2.

Fluorescence ability of the probe H_2L in the presence of Zn^{2+} was envisioned in living cell MDA-MB 231. Briefly, cells were grown in coverslips for 24 h in a 37°C humidified incubator containing 5% CO_2 and then either mock-treated or treated with 10μM of H_2L in the presence or absence of 10 μM Zn^{2+} and CN^- and incubated for different time period at the same temperature. The cells were washed with 1×PBS and then they were mounted on a glass slide and detected under fluorescence microscope (Leica).

Cell survivability of the ligand H_2L was studied by performing MTT cell proliferation assay and MTT assay was performed following reported procedure.[67, 68] In brief, MDA-MB 231 and NKE cells were seeded in 96-well plates at a concentration of 1×10^4 cells per well and exposed to the H_2L at different concentrations of 0 μM, 10 μM, 20 μM, 40 μM, 80 μM, 100 μM for 24 hrs. After incubation cells were washed with 1×PBS twice and MTT solution (100 μl; 0.5 mg/ml) were added to each well and incubated for 4 h at 37ºC. The resulting purple coloured formazan crystals were dissolved in DMSO and the absorbance was measured at 570 nm by using a microplate reader. Cell viability was expressed as a percentage of the control experimental setup.

IV.3. Results and Discussion

IV.3.1. Characterization of H_2L

The ^{1}HNMR spectrum (**Fig.IV.1**) of (Z)-7-hydroxy-4-methyl-8-(((5-phenyl-1H-pyrazol-3-yl)imino)methyl)-2H-chromen-2-one (H_2L) shows singlet peak at 14.87 ppm for phenolic proton (O-H) of coumarinyl group; another sharp singlet at 13.48 ppm refers to N-H proton of pyrazole moiety while the singlet at 9.50 ppm represents the imine proton (CH=N). These data confirm the formation of the Schiff base. Rest of the aromatic protons appear at 7.89 - 6.96 ppm. The signal at 6.28 and 2.42 ppm refer to the proton adjacent to aromatic-H of carbonyl unit and -CH_3 protons of coumarin ring.^{13}C-NMR spectrum (**Fig.IV.2**) also reveals characteristics signals at 165.20 and 159.62 ppm for carbonyl (C=O)-C and phenolic (C-O)-C centers while signal at 156.11

ppm represents the imine-C (HC=N)/pyrazolyl-C (C=N). Remaining Cs of the aromatic region appears at 154.43 to 94.92 ppm and -CH_3 shows a peak at 18.82 ppm. ESI-MS spectrum (**Fig.IV.3**) of the probe generates a molecular ion peak at 368.0911 [M+ Na^+] which confirms the formation of probe. FTIR spectrum exhibits stretching frequencies at 3207 cm^{-1} (υ(N-H)), 1691 cm^{-1} (υ(C=O)) and 1617 cm^{-1} (υ(C=N)) of the probe, H_2L (**Fig.IV.4**).

IV.3.2. Structural Description of H_2L

H_2L crystallizes in $P2_1/c$ space group. The molecular structure with the atom labelling scheme of H_2L is shown in **Fig.IV.5** and selected bond parameters are summarized in **Table IV.1**. The O(3)-C(7), 1.342(2) Å is longer than O(1)-C(1), 1.207(2) Å which indicate that O(3)-C(7) is phenolic type and O(1)-C(1) is ketone type. The N(1)-C(10) length is 1.285(2) Å (imine type) and shorter than N(1)-C(11), 1.401(2) Å (amine linkage). In the pyrazole ring the bond lengths are: N(2)-C(11), 1.339(2); N(3)-C(13), 1.353(3) and N(2)-N(3), 1.345(2) Å.

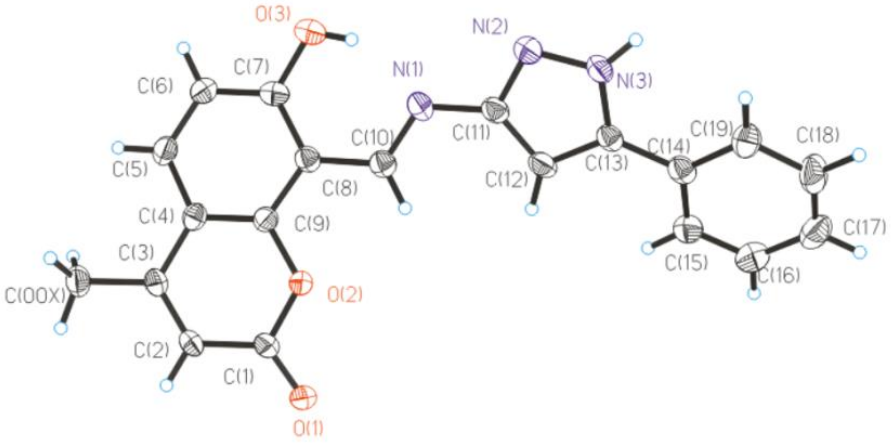

Fig.IV.5. Molecular geometry of **H_2L** in crystals (40% thermal ellipsoids, hydrogen atoms omitted for clarity).

The intermolecular and intramolecular H-bonding O---H-N (2.060 Å), N---H-O (1.843 Å) enhances the strength and stability of the probe (**Fig.IV.6(a)**). The probe has three N donor and one O donor centers in close proximity behaving as tetradentate chelating site for metal binding. The angle of deviation corresponds to plane containing the coumarin unit with respect to the plane of pyrazol fragments is 24.89° while the plane corresponds to phenyl unit exhibits a 16.19° deviation from the pyrazol plane. (**Fig.IV.6(b) (i), (ii)**)

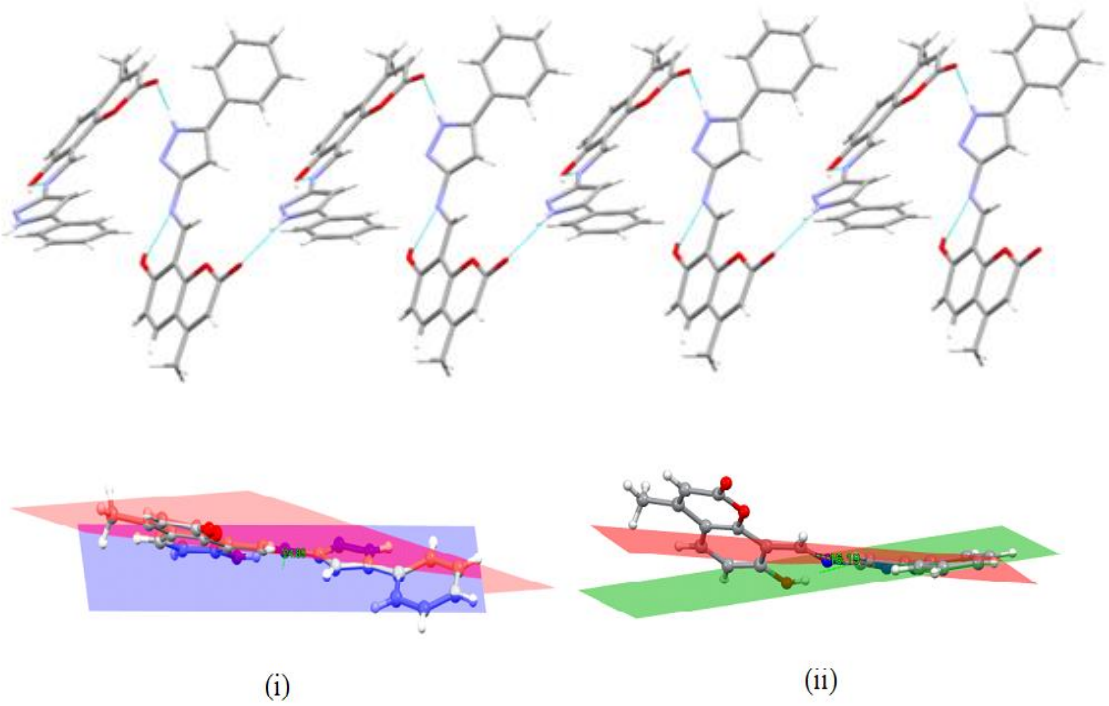

Fig.IV.6. (a) O•••NH and N•••HO interactions content in the **H_2L**; **(b)** angle of deviation of (i) coumarin and (ii) phenyl unit with respect to pyrazol plane.

IV.3.3. Spectroscopic Response towards Zn^{2+} and CN^- Sensing

The absorption spectrum of H_2L in CH_3CN/H_2O (99:1, v/v; HEPES Buffer, pH 7.5) shows transition at 316 nm who is ascribed to π–π∗ band. Upon addition of salt solutions of different cations (Cu^{2+}, Co^{2+}, Pb^{2+}, Cr^{3+}, Cd^{2+}, Ca^{2+}, Al^{3+}, Fe^{3+}, Hg^{2+}, Ni^{2+}, Mn^{2+}, Ba^{2+}, Na^+, K^+, Mg^{2+} and Pd^{2+}) the absorption wavelength more or less remains unshifted; only in case of Zn^{2+} the ligand solution shows significant red shifting of the band to 340 nm along with a low energy hump at 412 nm (**Fig.IV.7(a)**). On incremental addition of [Zn^{2+}] (1 μM) to the probe H_2L (25 μM) in the same medium, the spectral change is observed and attained saturation at 1:1 mole ratio of metal : ligand stoichiometry (**Fig.IV.7(b)**). The probe in its solution state remains colorless and transforms distinctively to greenish yellow on addition of Zn^{2+} which makes it a colorimetric responsive as well as optically detectable towards Zn^{2+} sensing.

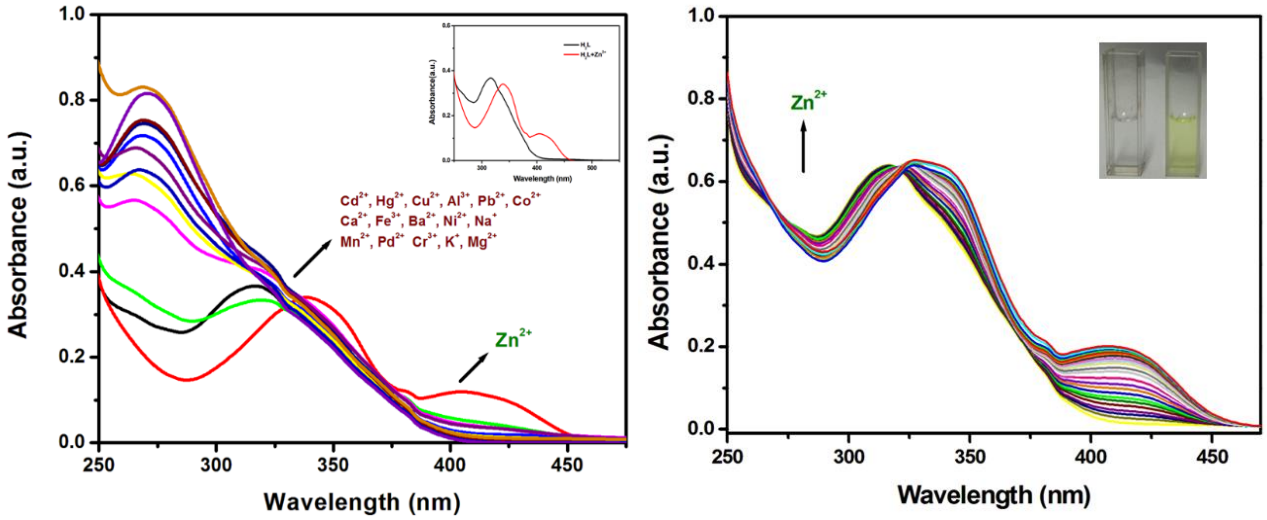

(a) **(b)**

Fig.IV.7 (a) UV-Vis Absorption Spectra of H_2L on addition of cations (2 equiv.) in (99:1, v/v) (HEPES Buffer, pH 7.5) medium. Inset: Absorption Spectrum of H_2L and H_2L+Zn^{2+}. **(b)** Change in the Absorption Spectrum of H_2L on incremental addition of Zn^{2+}.

The selectivity of H_2L to anions is also checked following similar procedure. The anions used are Cl^-, Br^-, I^-, CN^-, S^{2-}, CH_3COO^-, $C_6H_5O_7^{3-}$, $S_2O_3^{2-}$, SO_4^{2-}, F^-, SCN^-, NO_3^-, NO_2^-, $S_2O_5^{2-}$, N_3^-, IO_3^- in CH_3CN/H_2O (99:1, v/v; HEPES Buffer, pH 7.5). Noticeably, out of all anions the UV-Vis spectral change is observed only when CN^- is added. Upon addition of NEt_4CN solution to H_2L in the same medium the band at 316 nm shifts to 380 nm (**Fig.IV.8(a)**). The incremental addition of CN^- (1 μM) to H_2L solution (25 μM), results in gradual decrease of band, 316 nm and a new band appears at longer wavelength, 380 nm with a shoulder at 390 nm. The bathochromic shift on successive CN^- addition remains unchanged until a molar ratio 1:1 of H_2L to CN^- is reached (**Fig.IV.8(b)**). However, on addition of CN^- to the probe solution generates a transient straw yellow colour which rapidly changes to colourless solution. The change is visually detectable but colour of the resulting solution on addition of CN^- remains unchanged.

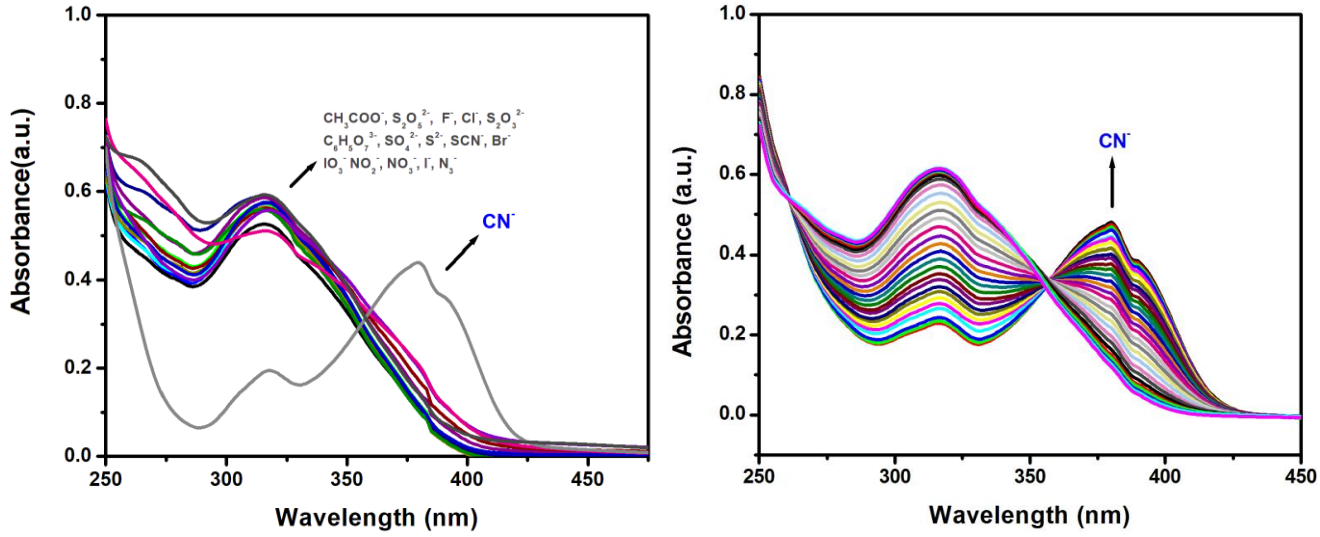

(a) **(b)**

Fig.IV.8 (a) Absorption Spectra of H_2L on addition of different anions (2 equiv.) in CH_3CN/H_2O (99:1, v/v) (HEPES Buffer, pH 7.5) medium. **(b)** Change in the absorption spectrum of H_2L on gradual addition of CN^-

Upon excitation of acetonitrile solution of H_2L at 390 nm exhibits weak fluorescence at 433 nm (ϕ = 0.006). Energy scavenging of excited species by PET and ESIPT may be the reasons for nonradiative decay process in solution phase.[69] In solid state H_2L exhibits enhanced fluorescence at longer wavelength (557 nm) with higher quantum yield (ϕ = 0.201) which may be due to molecular rigidity that induces RIR (Restricted Intramolecular Rotation) and inhibits isomerization around C=N bond (**Fig.IV.9**).[70,71]

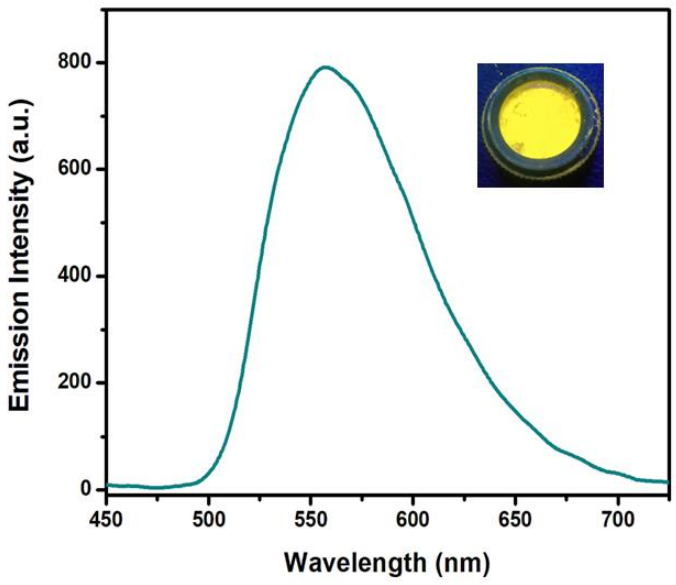

Fig.IV.9. Solid State Emission Spectrum of H_2L (Inset: images) (λ_{ex}= 390 nm).

The fluorogenic sensitivity of the probe (H_2L) was examined through change of emission intensity (λ_{ex}, 390 nm) on adding seventeen different cations in CH_3CN/H_2O (99:1, v/v; HEPES Buffer, pH 7.5). Interestingly, the fluorescence intensity of H_2L selectively enhances upon addition of Zn^{2+} (ϕ = 0.097) and is improved by 20 fold at 499 nm. (**Fig.IV.10(a)**) The enhancement may be explained on account of its complexation of H_2L with Zn^{2+} as confirmed from the crystal structure that tends to suppression of the non-radiative PET and ESIPT processes and inclusion of Chelation Enhanced Fluorescence (CHEF).[72,73] On incremental addition of [Zn^{2+}] (0-26 μM) to probe, H_2L (25 μM) in CH_3CN/H_2O (99:1, v/v) (HEPES Buffer, pH 7.5) medium, the emission intensity increases linearly with added concentration of Zn^{2+} and saturates when the molar ratio is reached at 1:1 concentration of the probe and Zn^{2+} (**Fig.IV.10(b)**). Limit of detection (34.76 nM, **Fig.IV.11**) has been evaluated from the calibrated titration profile of Zn^{2+} fluorescence titration following the 3σ/Slope method. The LOD for Zn^{2+} is much below the recommended limit by WHO.

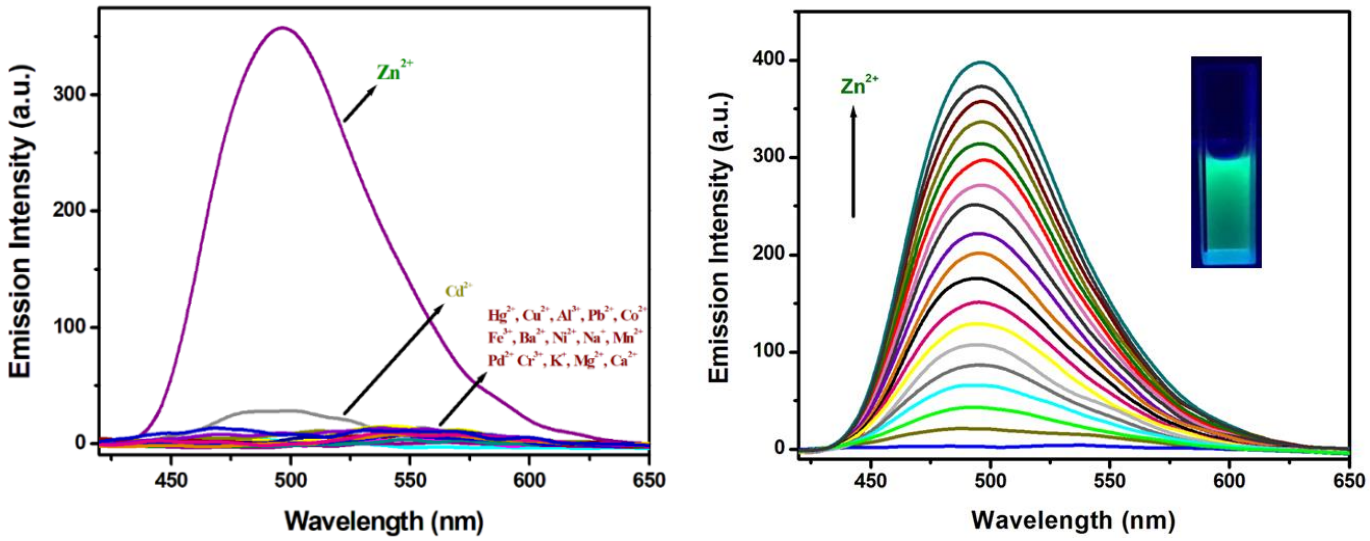

(a) **(b)**

Fig.IV.10. (a) Emission Spectra of H_2L in presence of different cations (2 equivalents) in CH_3CN/H_2O (99:1, v/v) (HEPES Buffer, pH 7.5) medium. **(b)** Change in the Fluorescence Spectrum of H_2L on successive addition of Zn^{2+} in CH_3CN/H_2O (99:1, v/v) (HEPES Buffer, pH 7.5) medium. (Inset: images) (λ_{ex}= 390 nm).

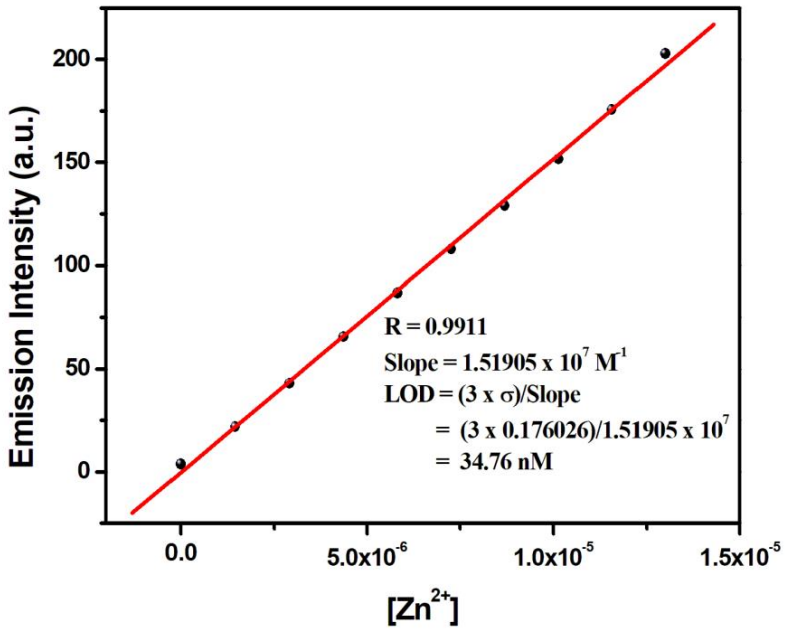

Fig.IV.11. Detection limit of H_2L for Zn^{2+} sensing.

Similar experimental method is applied for CN^- sensing as well; the probe has been treated with 2 equivalent anions in CH_3CN/H_2O (99:1, v/v) (HEPES Buffer, pH 7.5) medium. Upon excitation at 390 nm the emission appears at 447 nm. (ϕ = 0.137) In presence of only CN^-, the emission is 32-fold enhanced while other ions remain insensitive (**Fig.IV.12(a)**). The incremental addition of CN^- (0-29 μM) in the same solution of the probe (25 μM) a gradual increase in the emission intensity is observed. The plot of emission intensity *vs* [CN^-] is linear and the emission is optimized when 1 equivalent of CN^- is added (**Fig.IV.12(b)**). The LOD is 19.91 nM (3σ method) (**Fig.IV.13**).

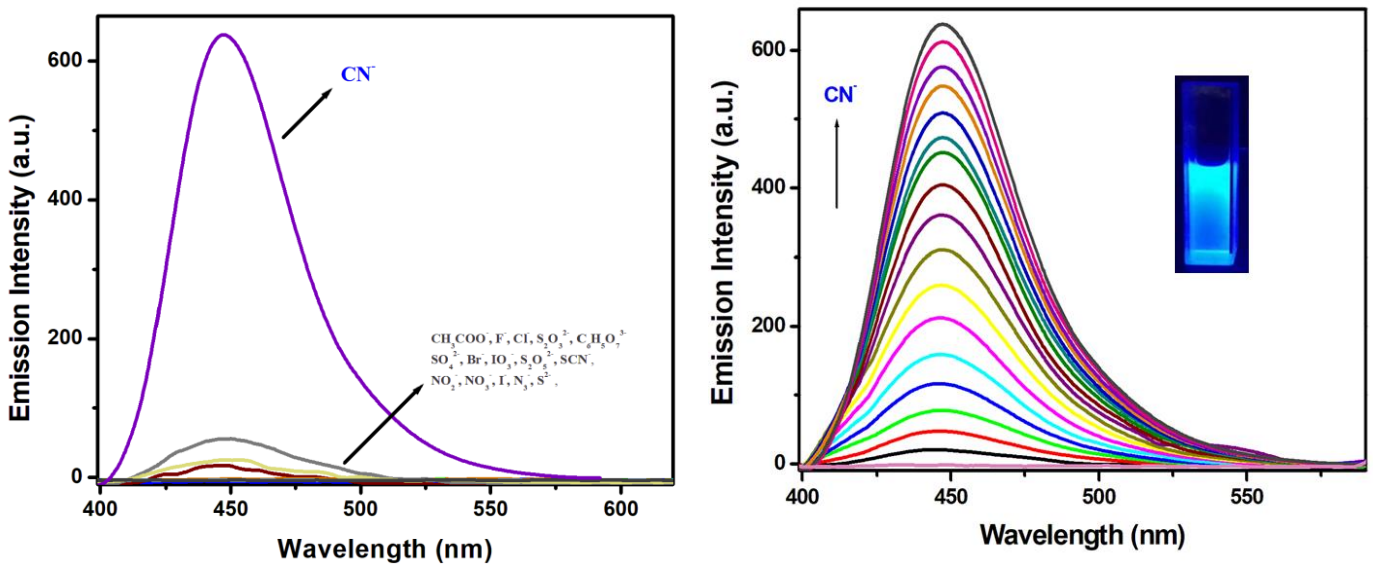

Fig.IV.12. (a) Emission Spectra of H_2L in presence of different anions (2 equivalents) in CH_3CN/H_2O (99:1, v/v) (HEPES Buffer, pH 7.5) medium. **(b)** Change in Fluorescence Spectrum of H_2L on successive addition of CN^- in CH_3CN/H_2O (99:1, v/v) (HEPES Buffer, pH 7.5) medium. (Inset: images) (λ_{ex}= 390 nm).

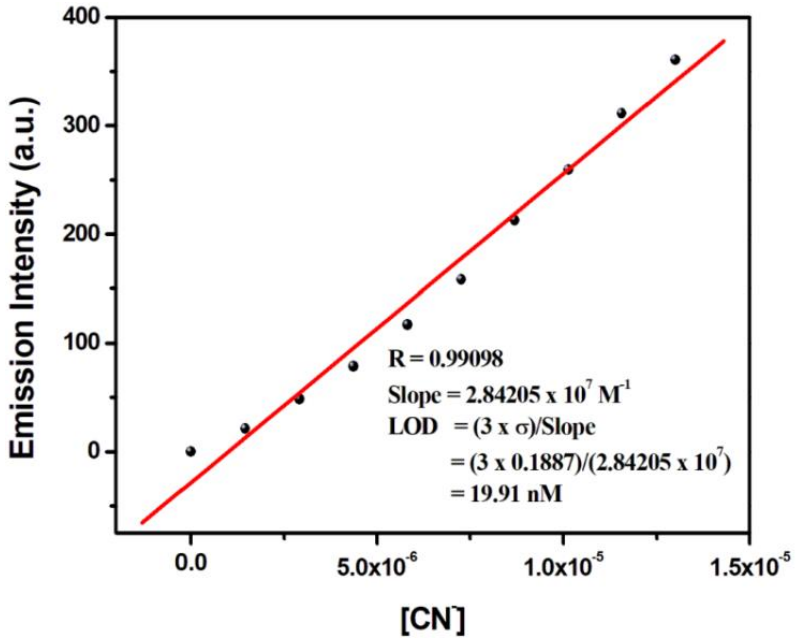

Fig.IV.13. Detection limit of H_2L towards CN^- sensing

A list of the reported probes along with their LOD value has been compared (**Table IV.5**) and it is revealed that the Pyrazolyl-Hydroxy-Coumarin probe (H_2L) serves efficiently and effectively detects Zn^{2+} and CN^-.

Table IV.5: Reported Zn^{2+} and CN^- selective probe with their LOD value

Sl. No.	Probe	Selectivity (LOD)	Solvent	Reference
1.	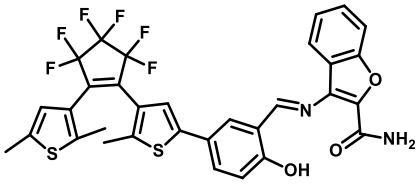	Zn^{2+} (32 nM) CN^-(13 nM)	CH_3CN	[74]
2.	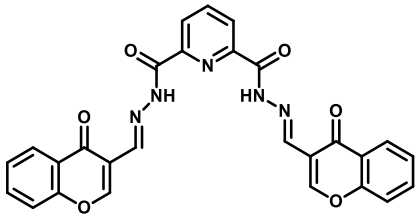	Zn^{2+} (0.87 μM) CN^- (1.56 μM)	DMSO:H_2O (9:1)	[75]
3.	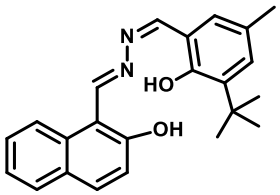	Zn^{2+} (13 nM) Cu^{2+} (1.6 μM) CN^- (0.81 μM)	H_2O	[76]
4.	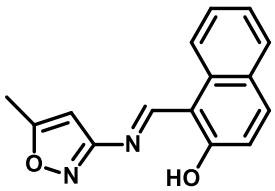	Zn^{2+}(1.29 μM) CN^- (12.3 μM)	DMF H_2O	[77]
5.	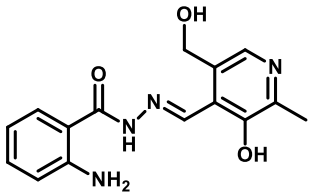	Zn^{2+} (0.302 μM) CN^-(0.153 μM)	DMSO	[78]
6.	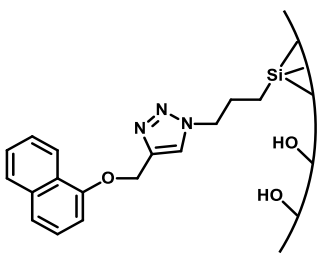	Zn^{2+} (0.23 μM) CN^- (0.39 μM)	H_2O	[79]

The idea of 1:1 mole proportion of H_2L with Zn^{2+}/ CN^- is also supported by the Job's Plot (**Fig.IV.14 (a) and (b)**). H_2L shows spontaneous responsive and separately senses Zn^{2+} and CN^- at two distinctive emissive wavelengths with a detection limit at nM range (34.76 nM for Zn^{2+} and 19.91 nM for CN^-).

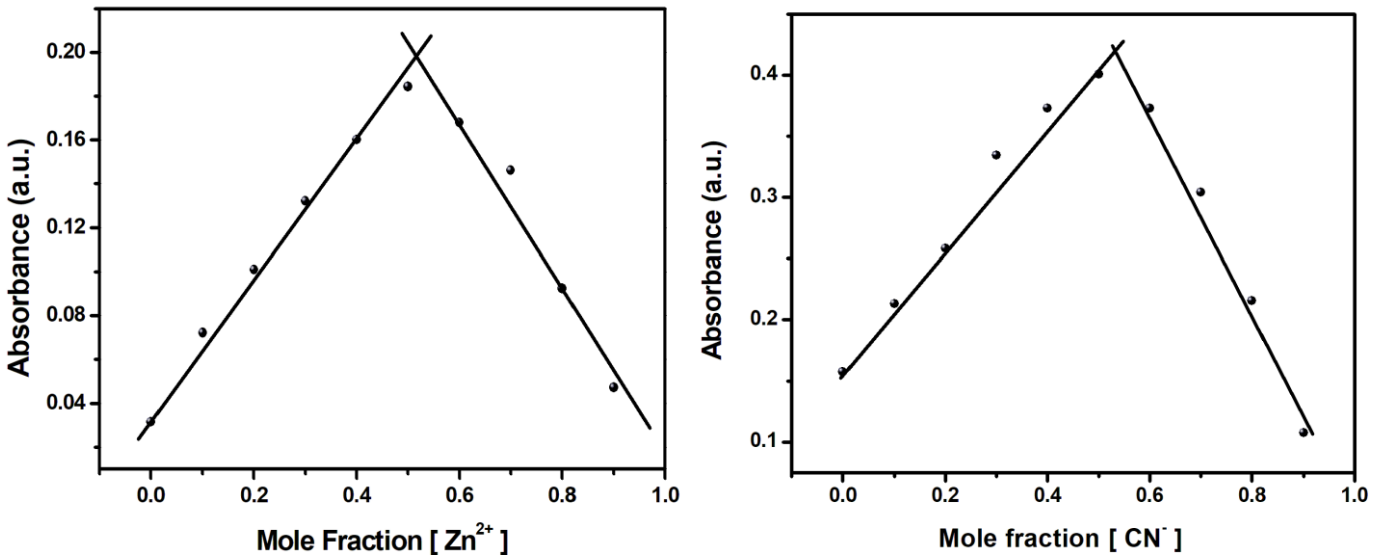

Fig. IV.14. Job's Plot for stoichiometric binding to **(a)** Zn^{2+} **(b)** CN^-.

For detailed understanding of selectivity of probe H_2L towards Zn^{2+} and CN^- sensing in presence of other ions, interference study was conducted under the identical condition. To the solution containing Zn^{2+} and H_2L, 2 equivalents of external co-cations were added at each time and their fluorescence spectra were recorded. The emission intensity of [H_2L-Zn^{2+}] in presence of Fe^{3+}, Al^{3+}, Cr^{3+} exhibits slight interferences. This may be due to the weak secondary interaction among molecular assembly of [H_2L-Zn^{2+}] and M^{3+} ($Fe^{3+,}$ $Al^{3+,}$ Cr^{3+}) [80,81] while for others cations, the emission is almost unaffected and interestingly the probe could detect Zn^{2+} even in presence of Cd^{2+} and Hg^{2+} (**Fig.IV.15**).

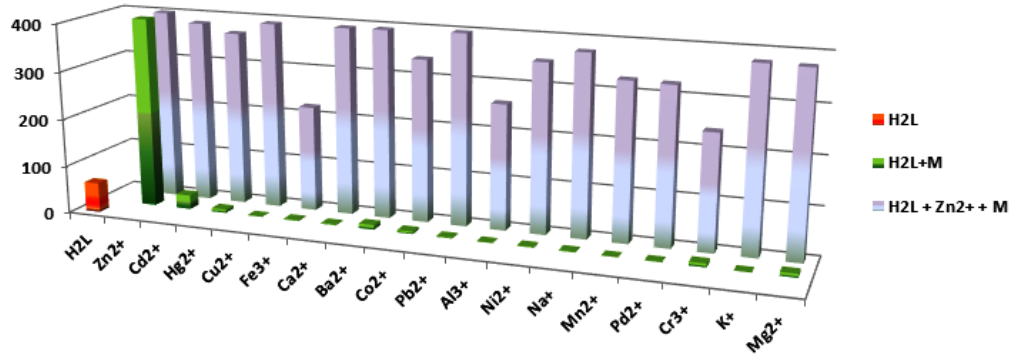

Fig.IV.15. Interference Study on Zn^{2+} Sensing.

In case of interference study of CN^- detection, 2 equivalents of external anions were added at each time to the resulting solution containing CN^- and H_2L and their emission spectra were noted. Interestingly, the impacts of interfering effects were negligible on the emission of [H_2L-CN^-] in presence of added external anions (**Fig.IV.16**). Results clearly assert the probe to be applicable for sensitive detection of Zn^{2+} and CN^-.

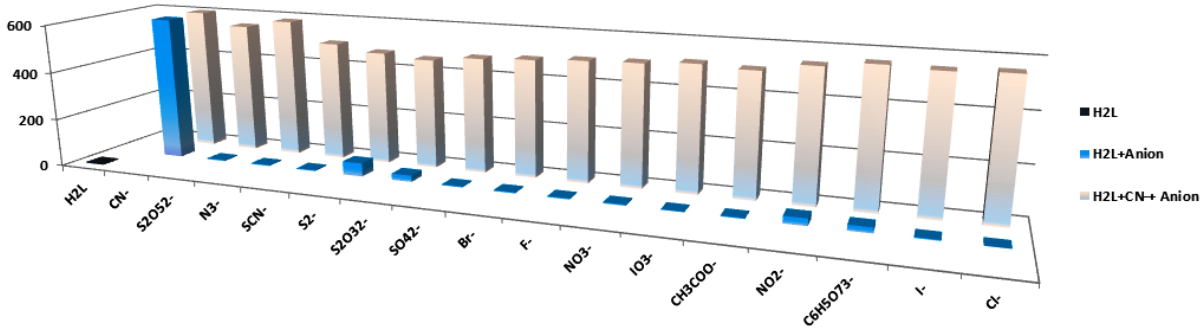

Fig.IV.16. Interference study on CN^- Sensing.

IV.3.4. ^{1}HNMR Study

The ^{1}HNMR titration explains the extent of binding of H_2L with Zn^{2+}/CN^-. For detailed understanding of interaction of H_2L on addition of Zn^{2+}, the ^{1}HNMR Titration has been performed with $Zn(CH_3COO)_2.2H_2O$ in DMSO-d_6 medium.. The ^{1}HNMR Spectrum of H_2L recorded at 298 K in DMSO-d_6 exhibited a singlet at 14.89 ppm which attributed to the resonance of phenolic proton, another singlet at 13.50 ppm assigned to resonance of pyrazolyl protons; besides, an imine singlet at 9.50 ppm, another doublet at 7.86 ppm (2H, J=7.8 Hz) integrating two protons, a doublet at 7.83 ppm (1H, J = 9.0 Hz), a triplet at 7.49 ppm (2H, J = 6.6 Hz), another triplet at 7.40 ppm (1H, J = 6 Hz), a singlet at 7.16 ppm, a doublet 6.98 ppm (1H, J = 9 Hz), singlet

at 6.28 ppm and a sharp singlet arises at 2.43 ppm attributed the resonances of three proton of aliphatic -CH_3 unit. The presence of two equivalent acetate in $Zn(CH_3COO)_2.2H_2O$ causes the deprotonation of ligand as L^{2-} to bind with Zn^{2+}. The presence of acetate ions is also confirmed from the presence of sharp singlet peak at 1.90 ppm. Addition of 0.5 equivalent Zn^{2+} results in gradual fading and broadening of phenolic peak (O-H) and pyrazol proton (N-H) at 14.89 and 13.50 ppm. On addition of 1 equivalent Zn^{2+} the disappearance of phenolic peak at 14.89 ppm along with further reduction and complete broadening of pyrazolic proton concludes its participation in complexation to Zn^{2+}. Appearance of peak at 11.99 ppm are assigned to the OH peak of CH_3COOH. The imine proton at 9.50 ppm undergoes downfield shift with respect to the protons of aromatic region. The signal at 6.99 and 6.29 ppm of the aromatic region undergoes upfield shift to 6.64 and 6. 06 ppm. The aliphatic zone corresponding to the sharp singlet signal at 2.429 ppm assigned to methyl unit shifted slight upfield from 2.43 to 2.38 ppm (**Fig.IV.17**).

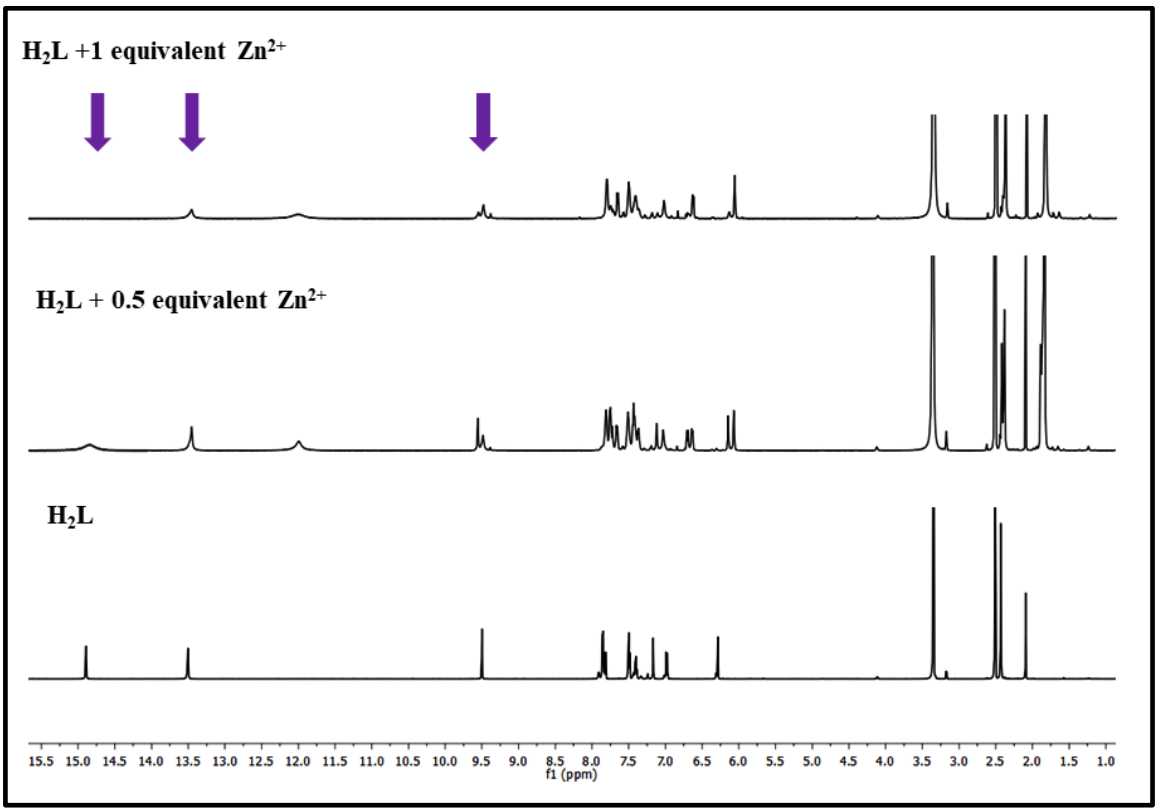

Fig.IV.17. ^{1}HNMR Titration of H_2L on successive addition of Zn^{2+} in DMSO-d_6.

The DOSY ^{1}HNMR Spectra of the *in-situ* complex generated from addition of 1 equivalent $Zn(CH_3COO_2).2H_2O$ to the probe H_2L in DMSO-d_6 clearly explains the formation of single species with a

Diffusion Coefficient of D = 2.86 x 10^{-10} m^2 s^{-1} (**Fig.IV.18**). The ^{1}HNMR spectrum of [Zn_6L_6] reveals absence of phenolic and pyrazolyl proton peaks which indicates the coordination of Zn^{2+} to L^{2-}. Further broadening of imine and aromatic signals due to complexation was also observed in the spectrum as well. (**Fig.IV.19**).

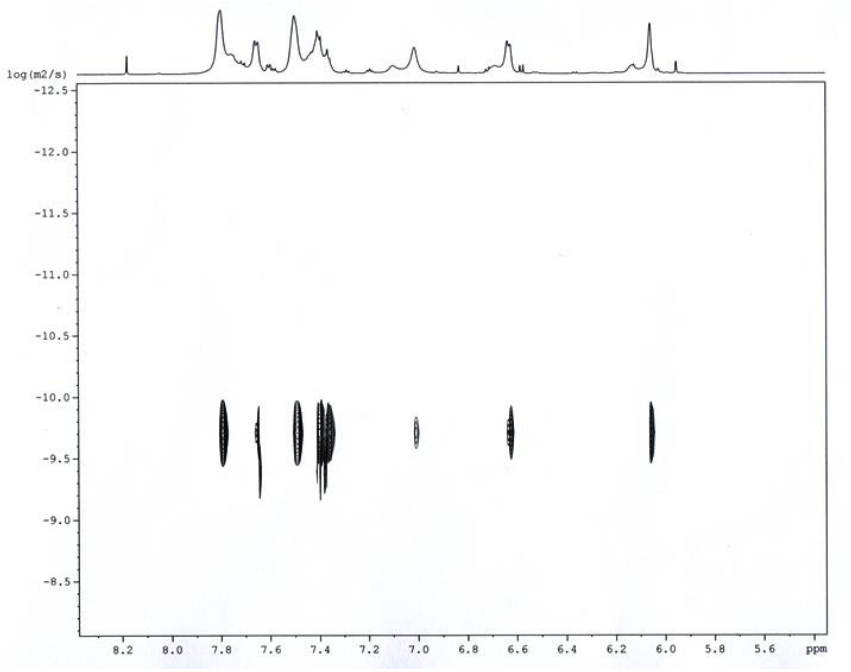

Fig.IV.18. DOSY NMR (600 MHz) of complex on addition of Zn^{2+} (1 equivalent) to H_2L in DMSO-d_6.

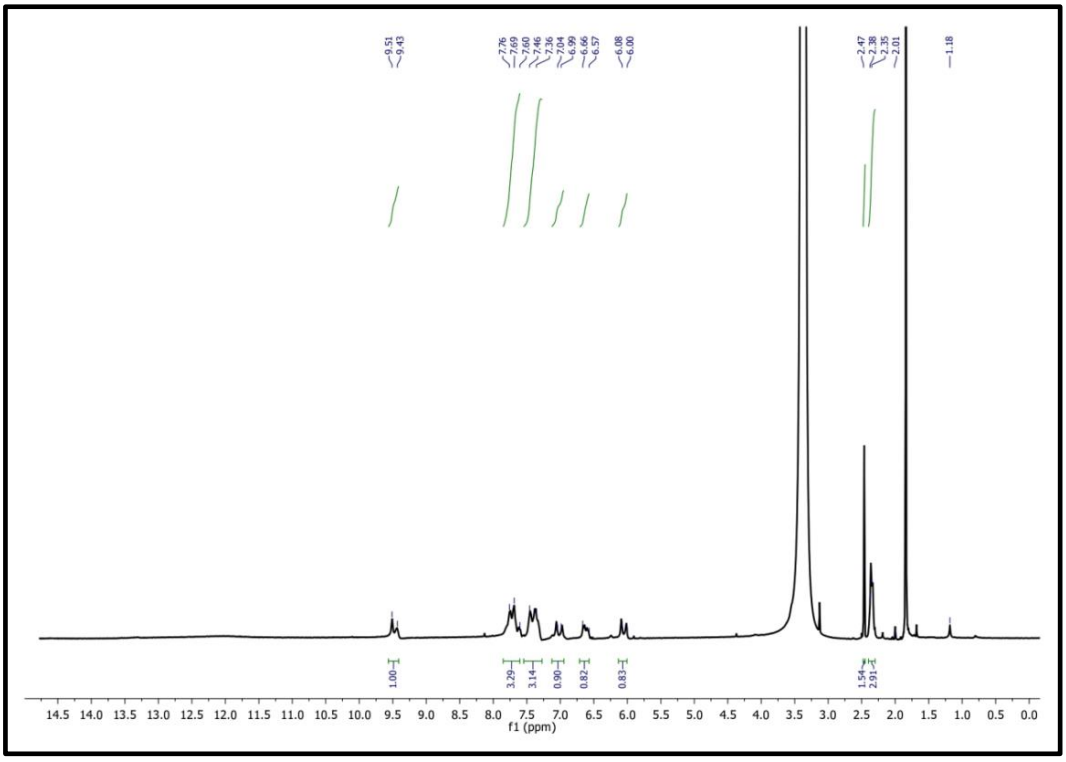

Fig.IV.19. ^{1}HNMR Spectra of Zn^{2+} Complex in DMSO-d_6

Upon addition of 0.5 equivalent CN^-, the ^{1}H-NMR titration of the probe H_2L (DMSO-d_6) shows the attenuation of the signal corresponding to -OH and -NH proton of coumarin and pyrazol unit whereas on addition of 1 equivalent CN^-, the complete disappearance of phenolic-OH peak followed by further reduction as well as broadening of NH peak clearly indicates that the interaction with CN^- proceeds through deprotonation pathway. Gradual fading of the imine singlet at 9.482 ppm is observed on adding CN^- and complete attenuation of imine singlet is noted on adding 2 equivalent of CN^- with simultaneous appearance of singlet at 5.870 and 5.500 ppm that attribute to NH and 3° CH protons. This observation supports the nucleophilic addition of cyanide to the carbon atom of imine group. The proportional broadening and upfield shifting of aryl protons also validate the adduct formation resulted from CN^- addition to H_2L (**Fig.IV.20**).

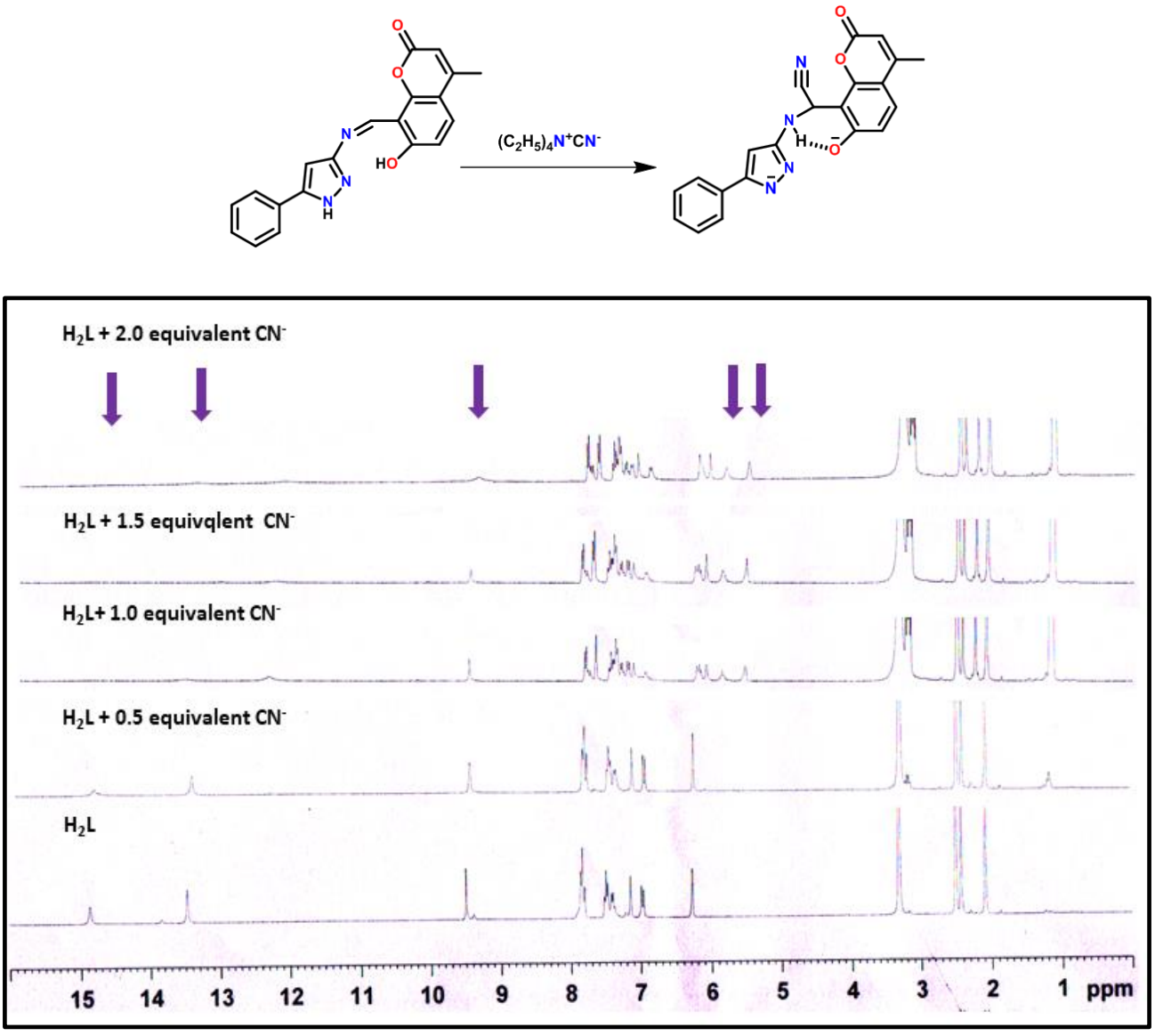

Fig.IV.20. ^{1}HNMR Titration of H_2L with successive addition of CN^- in DMSO-d_6.

Furthermore, the appearance of peak at 3.150 and 1.121 ppm due to CH_2 and CH_3 protons of EtN_4^+ in the ^{1}HNMR spectra of CN^- Complex also supports and confirms the formation of such CN^- binding adduct (**Fig.IV.21**).[82,83]

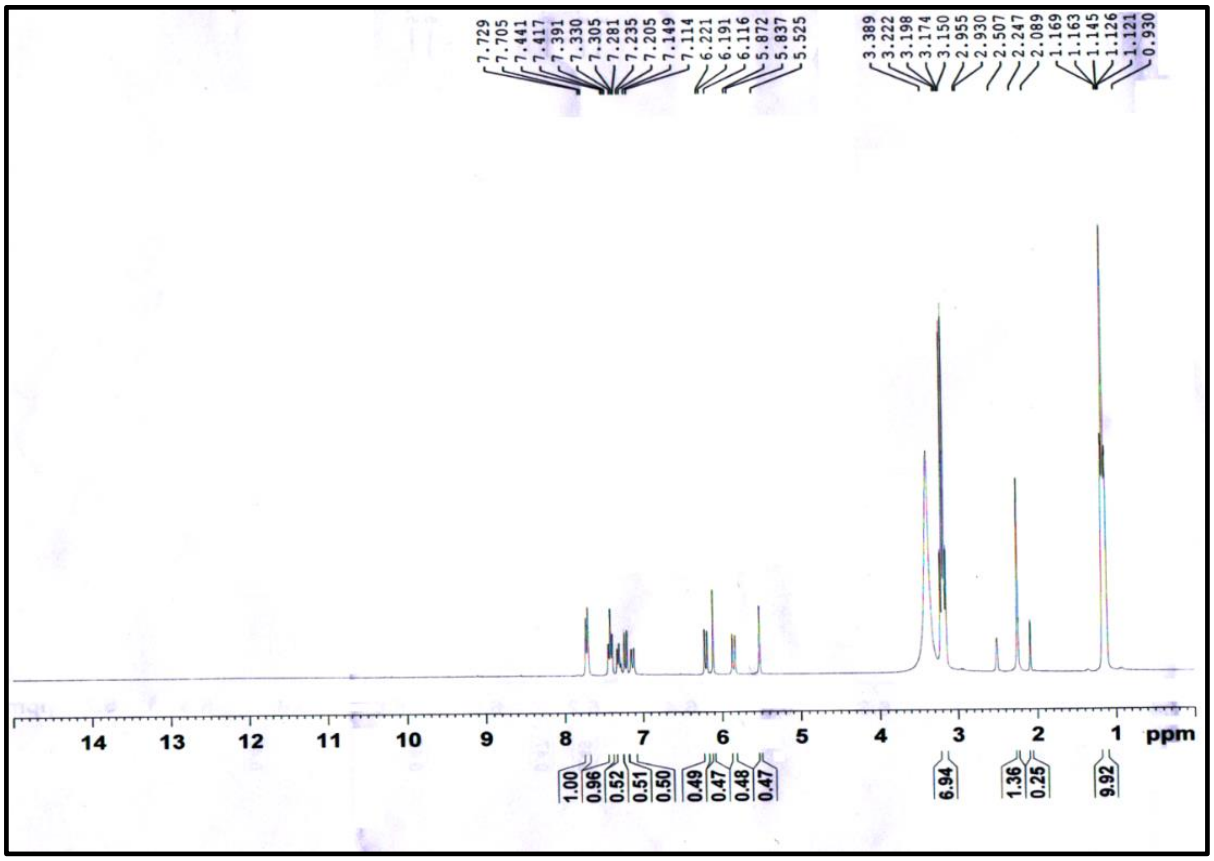

Fig.IV.21. ^{1}HNMR Spectra of CN^- Complex in DMSO-d_6.

IV.3.5. Structural Description of Hexanuclear Metallocrypytand [Zn_6L_6]

The structure of the complex forms a hexanuclear metallocryptand with Zn(II) and H_2L. [Zn_6L_6] crystallizes in *P*-1 space group. The pyrazolyl unit of H_2L forms bridged binuclear Zn(II) motif and imine phenolato pendant portion of the ligand chelates to neighboring Zn(II) center. Each Zn(II) center is chelated by N,O group of one H_2L and coordinated by two pyrazolyl-N centers from two other H_2L ligands. Thus, there are three ligands involve about each Zn(II) center. In each hexanuclear cage structure half of the Zn(II) centers form four coordinated distorted tetrahedral ZnN_3O sphere and other half Zn(II) centers form five coordinated distorted trigonal bipyramidal ZnN_3O_2 sphere. The fifth coordination center about Zn(II) is assisted from MeOH/DMSO. There are different types of macrocycle rings are formed between the zinc ion. The Zn(1) and

Zn(6) are bridged by the nitrogen atom of two diazole ring and exhibits tetrahedral geometry with Zn(1)---Zn(6) distance of 3.520 Å.

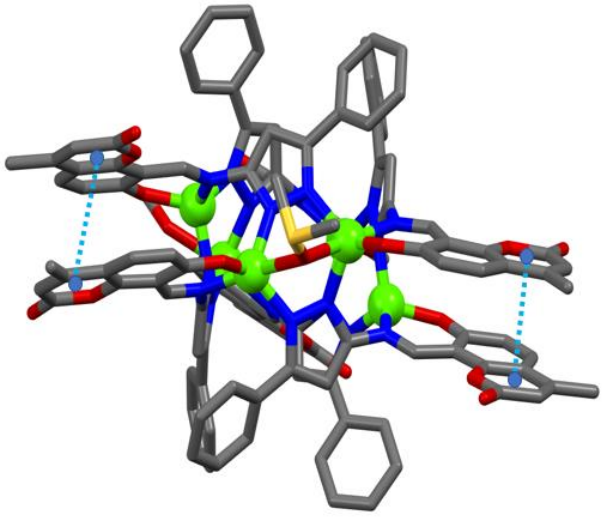

(a)

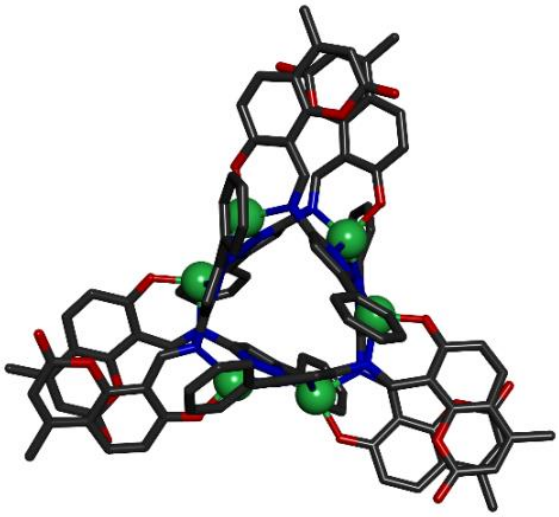

(b)

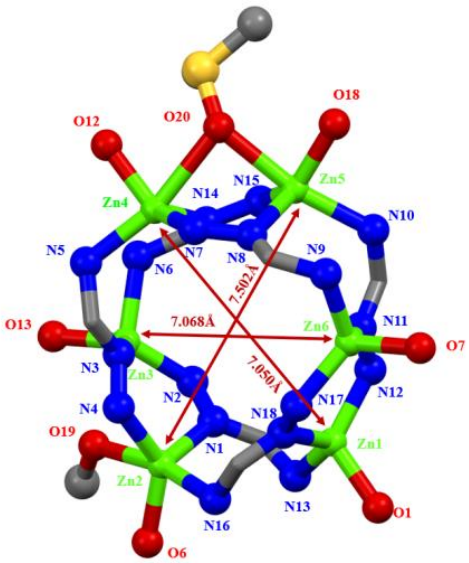

(c)

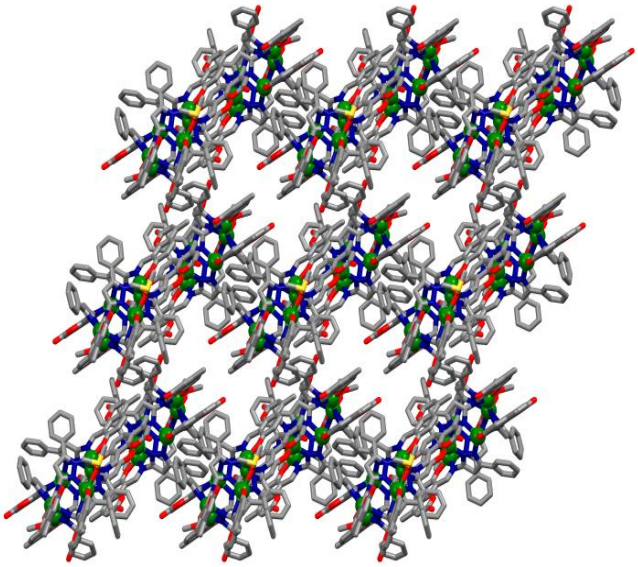

(d)

Fig.IV.22 (a) Discrete hexanuclear Zn(II) complex $[Zn_6L_6]$ showing parallel π···π interaction between coumarin units. **(b)** Top and side views of $[Zn_6L_6]$, **(c)** Linkage Framework unit of $[Zn_6L_6]$ exhibiting crown like cavity and **(d)** 3D Supramolecular assemblies along c axis.

The Zn(1)-O(1) and Zn(6)-O(7) distances are 1.932(4) and 1.938(3) Å which are similar type whereas Zn(1)-N(18), Zn(1)-N(12), Zn(1)-N(13) lengths are 1.979(4), 1.973(4), 2.010(4) Å and Zn(6)-N(17), Zn(6)-N(9) and Zn(6)-N(11) lengths are 1.985(4) 2.001(4) and 1.983(4) Å. This clearly indicates that the Zn(1) and Zn(6) are equivalent and form six membered macrocycle. Zn(2) forms distorted triagonal bipyramidal structure (ZnN_3O_2) with one MeOH molecule coordinated and bond distances are 1.986(4) (Zn(2)-O(6)), 2.027(4) (Zn(2)-N(1)), 2.025(5) (Zn(2)-N(4)), 2.253(4) (Zn(2)-O(19)) and 2.124(4) Å (Zn(2)-N(16)). The distance between the Zn(1) and Zn(2) is 4.187 Å. The Zn(3) center is tetrahedrally coordinated and the bond distances are 1.991(5) (Zn(3)-N(2)), 2.070(5) (Zn(3)-N(6)), 1.944(3) (Zn(3)-O(13)) and 2.014(4) Å (Zn(3)-N(3)). Zn(2) and Zn(3) are bridged in similar manner by the pyrazolo entity and the distance between Zn(2)----Zn(3) and Zn(3)----Zn(4) are 3.364 and 4.308 Å, respectively.The Zn(4) and Zn(5) are bridged by nitrogen atom of two diazole ring and one oxygen atom of DMSO molecule and the Zn(II) ions are formed distorted trigonal bipyramidal structure. The measure distance between Zn(4) and Zn(5) is 3.404 Å. The distances Zn(4)-O(12), 1.945(3); Zn(4)-N(5), 2.087(4); Zn(4)-N(14), 2.007(4); Zn(4)-N(7), 1.983(4); Zn(5)-O(18), 1.960(4); Zn(5)-N(8), 2.023(4); Zn(5)-N(10), 2.126(4) and Zn(5)-N(15), 2.012(4) Å are comparable with first hemisphere of the metallocryptand. The Zn(5)---Zn(6), 4.181 Å in the macrocyclic cage lies in the supramolecular framework. Six Zn(II) centres constituting eight membered macrocycle are embedded in loop and form the macrocycle. The discrete hexanuclear unit exhibits a crown like cavity in the crystal structure (**Fig.IV.22(b)**) and the diagonal distances are 7.502 (Zn(2)-Zn(5)), 7.050 (Zn(1)-Zn(4)) and 7.068 Å (Zn(3)-Zn(6)) (**Fig.IV.22(c)**). The overall crystal structure of the six nuclei and the ligands forms fifteen membered macrocycles. The solvent molecules are eliminated by Solvent Mask method from the crystal structure during refinement stage. The coumarin ring of H_2L interacts with another coumarin ring of adjacent ligand by π----π interaction at 3.471, 3.699 and 3.591 Å (**Fig.IV.22(a)**). Three dimensional supramolecular assemblies along crystallographic c axis exhibits 30.9% void space (**Fig.IV.22(d)**). The absorption spectrum of isolated complex $[Zn_6L_6]$ also exhibits bands at 335 nm and 412 nm (**Fig.IV.23(a)**) and the fluorescence spectrum of $[Zn_6L_6]$ in acetonitrile-water shows emission at 500 nm upon excitation at 390 nm in (99:1, v/v) (HEPES Buffer, pH 7.5) medium. (**Fig.IV.23(b)**).

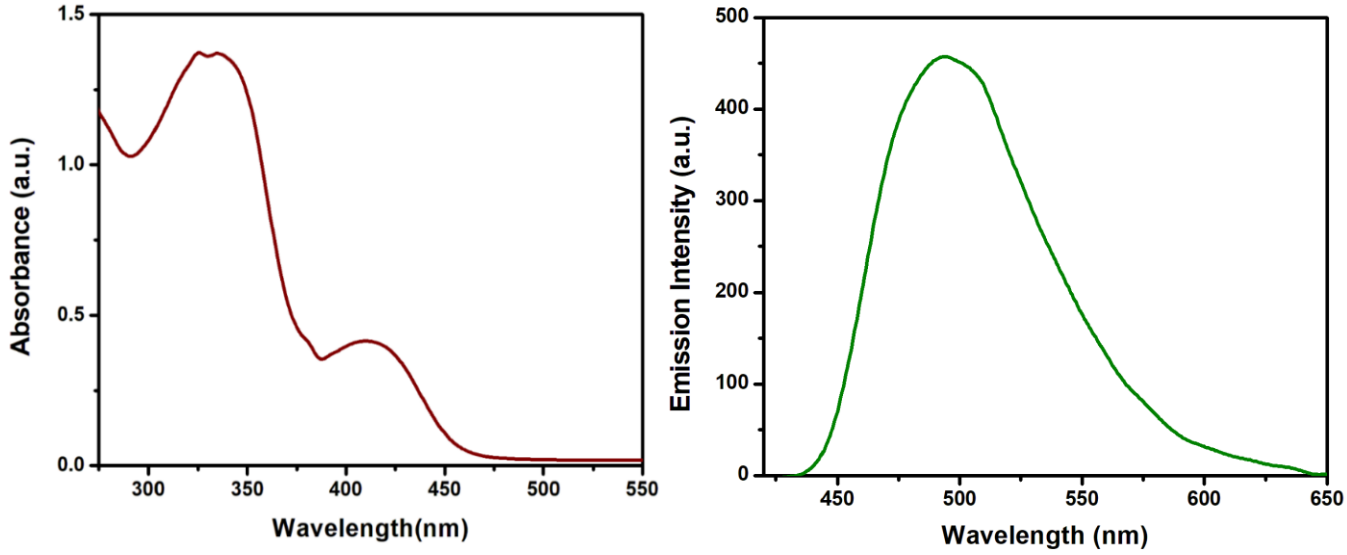

(a) **(b)**

Fig.IV.23. (a) UV-Vis Absorption Spectrum of $[Zn_6L_6]$ **(b)** Fluorescence Spectrum of $[Zn_6L_6]$

IR spectrum of $[Zn_6L_6]$ reveals broad stretching band around 3500 cm^{-1} which indicates presence of MeOH coordinated to the complex as evident from the crystal structure. The shifting of υ(C=N) from 1606 to 1573 cm^{-1} confirms its participation the coordination of L^{2-} to Zn^{2+} (**Fig.IV.24(a)**). IR Spectrum of the composite $[H_2L+CN^-]$ also exhibits stretching band at 2200 cm^{-1} which confirms CN^- addition to the probe H_2L. (**Fig.IV.24(b).**).

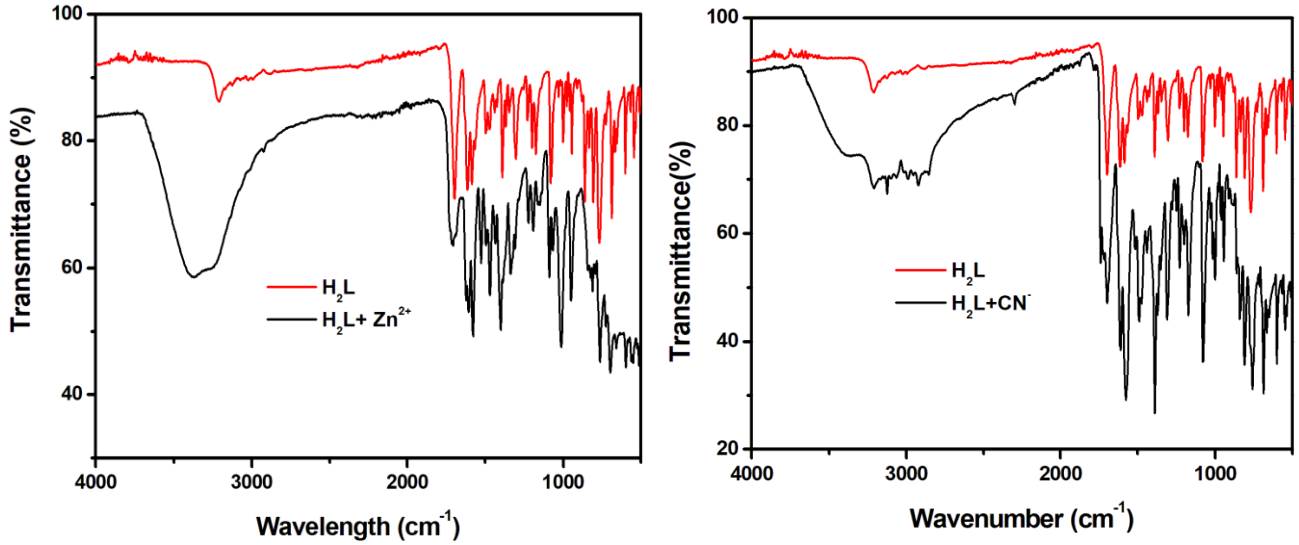

(a) **(b)**

Fig.IV.24. (a) IR Spectrum of Zn^{2+} Complex. **(b)** IR spectrum of CN^- Complex.

The ESI-MS Spectrum of CN^- complex in anion mode gives a molecular ion peak at m/z = 371 corresponding to $[HL+CN^-]$ which supports the formation of cyanide adduct along with the presence of expected deprotonated molecular ion peak of H_2L at m/z =344 corresponds to $[H_2L-H]$.[84] (**Fig.IV.25**).

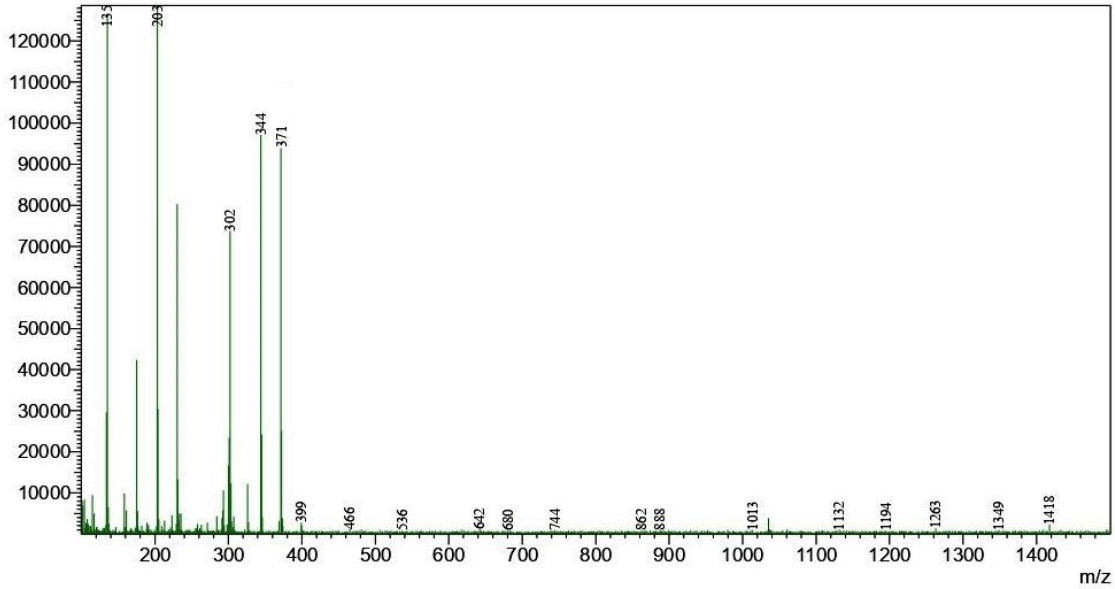

Fig.IV.25. ESI-MS of CN^- Complex.

IV.3.6. Time -Correlated Single Photon Counting (TCSPC) (Lifetime Measurement):

Average lifetime (τ_{av}) decay profile of H_2L (1.272 ns) as well as the composite of $[H_2L+Zn^{2+}]$ (3.177 ns) and $[H_2L+CN^-]$ (2.8934 ns) fits well into bi-exponential decay process (**Fig.IV.26**) proves delocalization of excited energy over the complex motifs of $[H_2L+Zn^{2+}]/[H_2L+CN^-]$

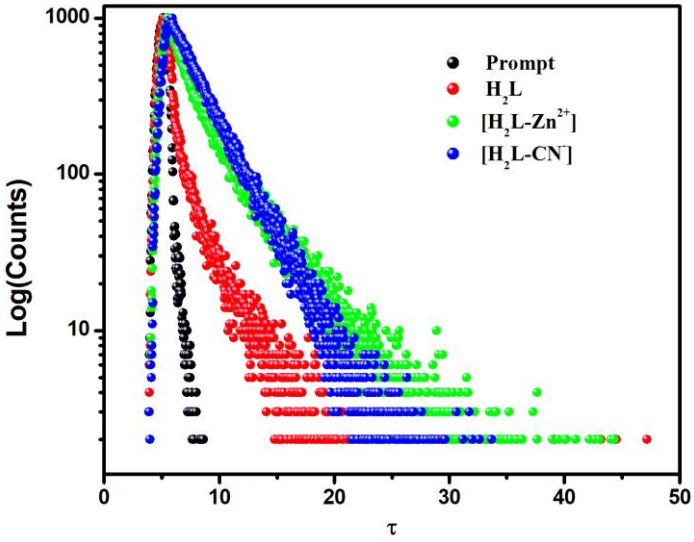

Fig.IV.26. Lifetime Plot of H_2L with Zn^{2+} and CN^-

IV.3.7 DFT Computation

To understand the probing efficiency of H_2L to Zn^{2+}/CN^- theoretical computation of H_2L and the composites were carried out by Density Functional Theory (DFT) using Gaussian Program Package 09. The DFT calculation was employed to obtain the optimized structure of ligand H_2L using B3LYP/6-311G as basis set and LanL2DZ basis set were used for $[Zn_6L_6]$ and L-CN^- complex. (**Tables IV.6**)

Tables IV.6: Optimized Geometry of H_2L, $[Zn_6L_6]$ and [L-CN^-]

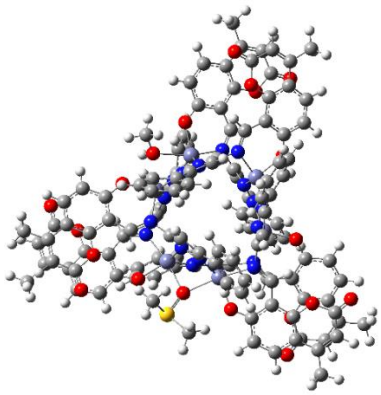	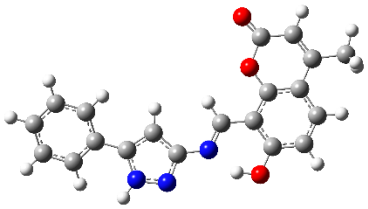	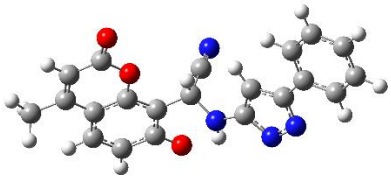
$[Zn_6L_6]$	**H_2L**	**L-CN^-**

Based on the experimental results the binding model of the respective Zn^{2+} and CN^- complexes were guided. Bond parameters obtained from optimized structure of free probe H_2L in the **Table IV.7** are compared and in well accordance with the single crystal X-Ray structure of the probe H_2L. Bond Length (Å) calc. (exp.): (C(10) – N(2)), 1.309 (1.285); (C(11)-N(1)), 1.392 (1.401); (C(7)-O(3)), 1.342 (1.349); (N(2)-N(3)), 1.367 (1.345). Bond Angles calc. (exp.): N(2)-C(11)-N(3), 117.53 (116.66); C(7)-O(3)-H, 108.56 (109.5); N(2)-N(3)-C(11), 103.60 (103.97); C(10)-N(1)-C(11) 120.49 (123.19) N(2)-N(3)-H, 118.63 (123.2).

Table IV.7: Calculated Bond Parameters obtained from DFT calculation of the optimized geometry of H_2L

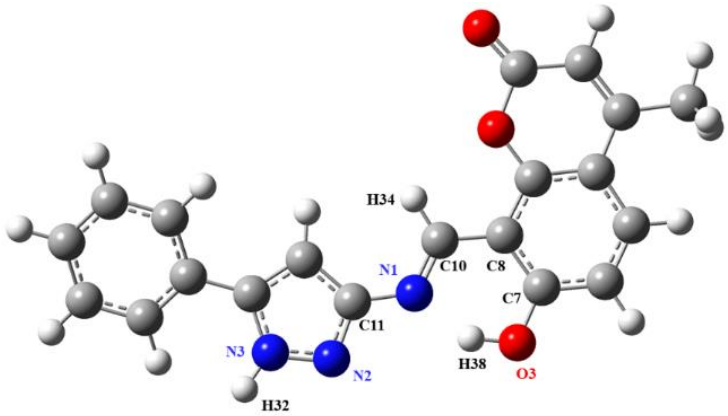

Bond Length	Theoretical Value (Ă)	Bond Angle	Theoretical Value (°)
C11-N1	1.392	N2-C11-N1	117.53
C11-N2	1.353	N2-N3-H32	118.63
N3-N2	1.367	N3-N2-C11	103.97
N1-C10	1.305	C10-C8-C7	120.95
C7-O3	1.349	C8-C7-O3	120.57
O3-H38	1.034	C7-O3-H38	108.56
N3-H32	1.005	C11-N1-C10	123.19
C10-C8	1.440	N1-C10-C8	118.91
C8-C7	1.424	N1-C10-H34	120.22

Optimized geometry and energy of the selected orbitals are enlisted in **Tables IV. 8, 9 & 10**

Table IV.8: Selected MO's of H_2L along with their energy.

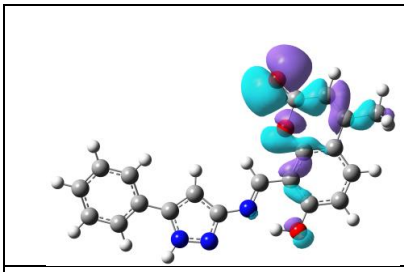	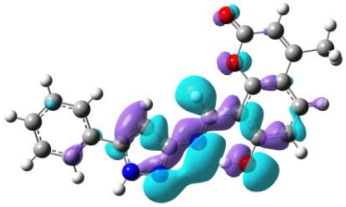	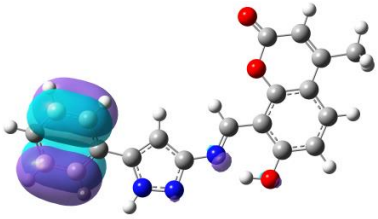
HOMO-5 **-7.49 eV**	**HOMO-4** **-7.42 eV**	**HOMO-3** **-7.3 eV**
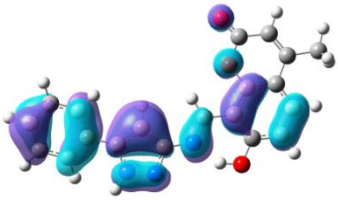	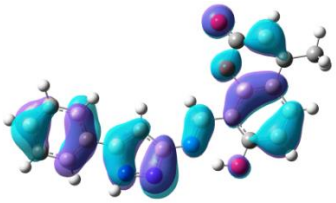	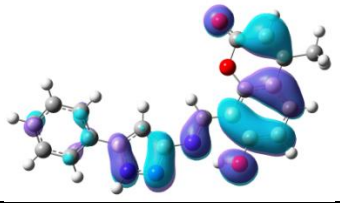
HOMO-2 **-6.59 eV**	**HOMO-1** **-6.28 eV**	**HOMO** **-5.98 eV**
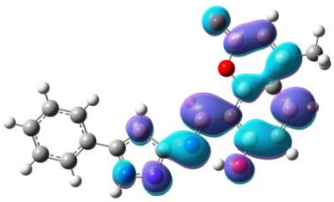	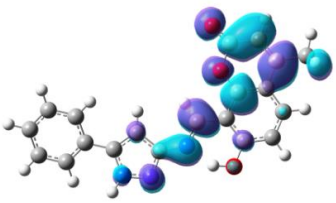	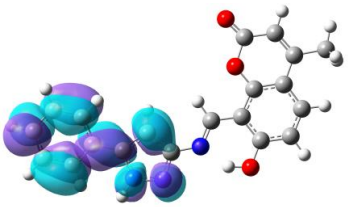
LUMO **-2.06 eV**	**LUMO+1** **-1.64 eV**	**LUMO+2** **-1.12 eV**
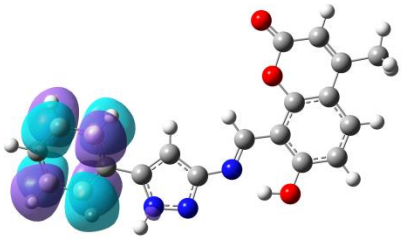	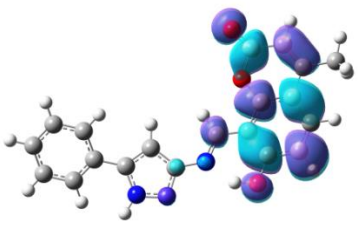	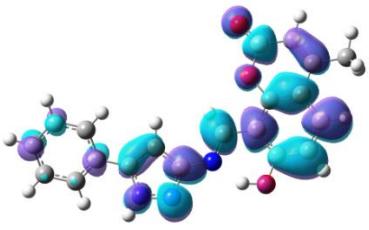
LUMO+3 **-0.44 eV**	**LUMO+4** **-0.1 eV**	**LUMO+5** **0.63 eV**

Table IV.9: Selected MO's of $[Zn_6L_6]$ Complex with their energy state

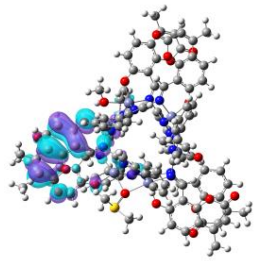	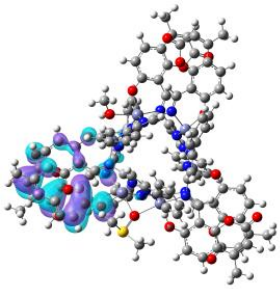	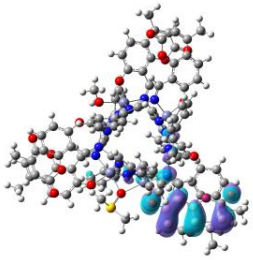
HOMO-5 **-5.98 eV**	**HOMO-4** **-5.93 eV**	**HOMO-3** **-5.85 eV**
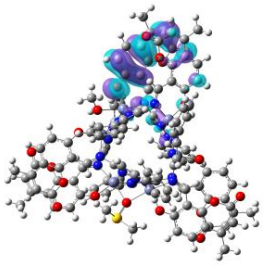	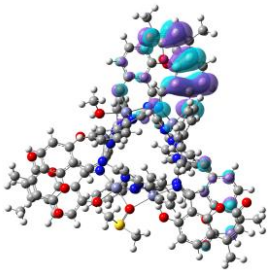	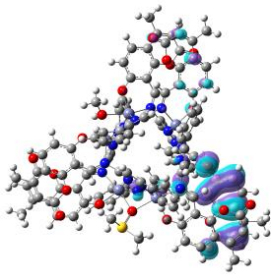
HOMO-2 **-5.84 eV**	**HOMO-1** **-5.75 eV**	**HOMO** **-5.72 eV**
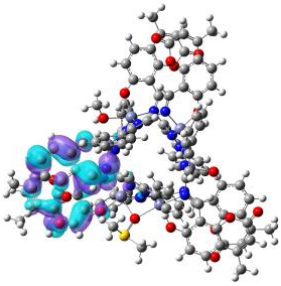	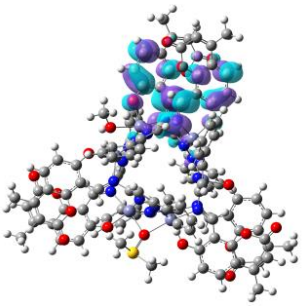	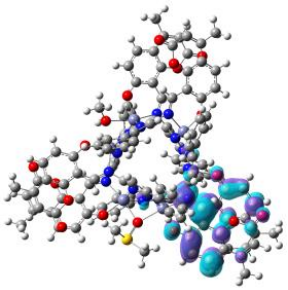
LUMO **-2.24 eV**	**LUMO+1** **-2.16 eV**	**LUMO+2** **-2.13 eV**
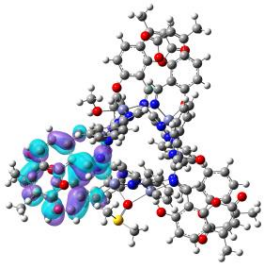	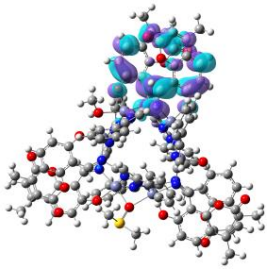	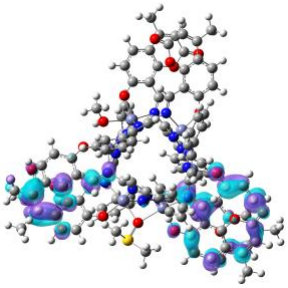
LUMO+3 **-2.05 eV**	**LUMO+4** **-2.00 eV**	**LUMO+5** **-1.95 eV**

Table IV.10: Selected MO's of L-CN^- complexes with their energy level.

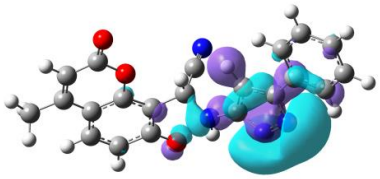	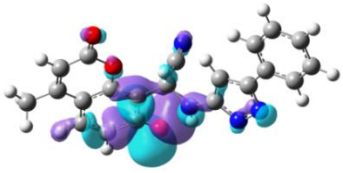	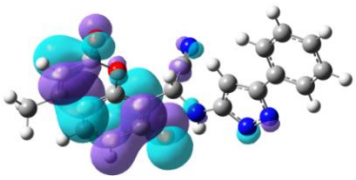
HOMO-5 **-1.03 eV**	**HOMO-4** **-0.75 eV**	**HOMO-3** **0.05 eV**
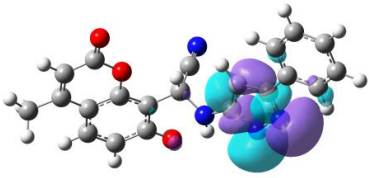	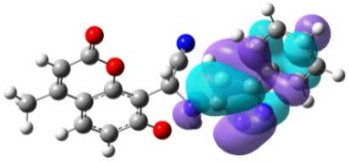	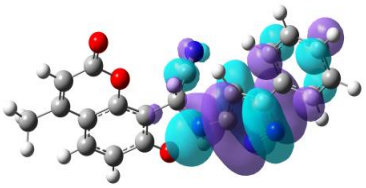
HOMO-2 **0.43 eV**	**HOMO-1** **0.61 eV**	**HOMO** **1.55 eV**
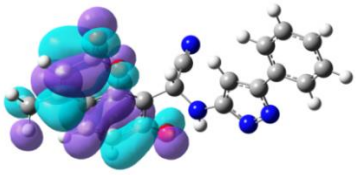	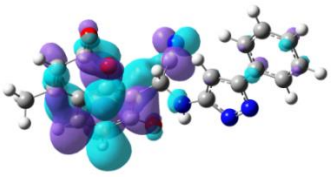	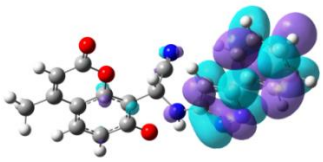
LUMO **3.34 eV**	**LUMO+1** **4.92 eV**	**LUMO+2** **4.95 eV**
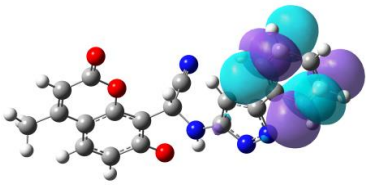	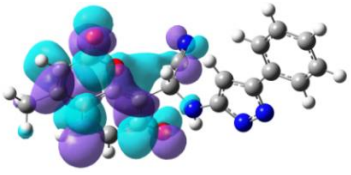	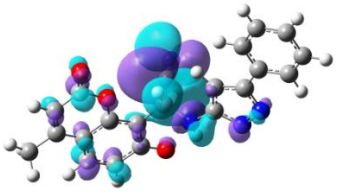
LUMO+3 **5.09 eV**	**LUMO+4** **5.42 eV**	**LUMO+5** **6.4 eV**

Electronic Transition derived from Time Dependent Density Function Theory (TD-DFT) calculation determines the HOMO-LUMO gap of the probe and the complexes. Time Dependent Density Functional Theory (TD-DFT) studies elucidate the theoretical aspects of spectral behaviour of H_2L in presence of Zn^{2+} and CN^-. HOMO-LUMO band gap of the optimized structure of H_2L, $[Zn_6L_6]$ and $[H_2L\text{-}CN^-]$ was determined as 4.53, 3.51 and 2.73 eV. The transitions obtained from TD-DFT listed in the (**Table IV.11).**

Table IV.11: TD-DFT transition of H_2L, $[Zn_6L_6]$ and $[L\text{-}CN^-]$ complex.

System	Excitation Energy (eV)	Experimental Wavelength (nm)	Theoretical Wavelength (nm)	Oscillation Frequency (f)	Key Transition
H_2L	3.9591	316	313.16	0.8159	HOMO-2→LUMO
$[Zn_6L_6]$	3.2772	339	378.32	0.0018	HOMO-1→LUMO
	3.0436	412	407.05	0.0509	HOMO-1→LUMO+1
$[L\text{-}CN^-]$	3.3103	379	374.55	0.3658	HOMO-1→LUMO

The absorption wavelength obtained from DFT calculation correlates well with experimental absorption spectra. The probe H_2L in its free state exhibits absorption band at 316 nm corresponds to the transition of HOMO-2 →LUMO. In case of hexanuclear Zn^{2+} complex $[Zn_6L_6]$, the absorption band at 339 and 412 nm are mainly ascribed due to the transition of HOMO-1→LUMO and HOMO-1→LUMO+1 respectively. For the motif $L\text{-}CN^-$, the transition HOMO-1→LUMO contributes to absorption maxima at 379 nm. The decrease in band gap of $[Zn_6L_6]$ and $L\text{-}CN^-$ by about 1.02 and 1.70 eV suitably explains the bathochromic shift in absorption Spectra of H_2L on addition of Zn^{2+} and CN^- respectively (**Fig.IV.27**).

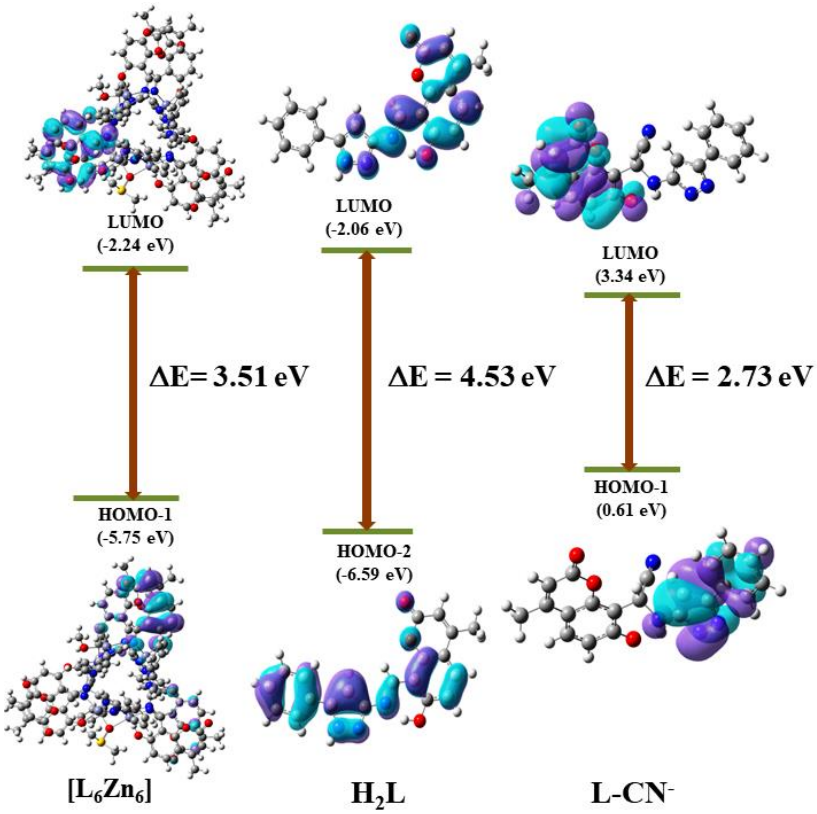

Fig.IV.27. HOMO-LUMO gap of probe H_2L, Zn^{2+} and CN^- Complexes.

IV.3.8. MTT Assay and Cell Imaging

In-vivo cell survivability and cytotoxicity of H_2L was checked on MDA-MB 231 and WI-38 cell line. The cells were treated with five different concentrations of H_2L (0 μM, 10 μM, 20 μM, 40 μM, 80 μM, 100 μM) for 24 h and results were evaluated. Cell viability was expressed as a percentage of the control experimental setup and the results of MTT assay (**Fig.IV.28**) had shown no substantial toxicities even at the concentration of 100 μM. Hence, the probe H_2L shows significant biocompatibility and favourable for biological applications.

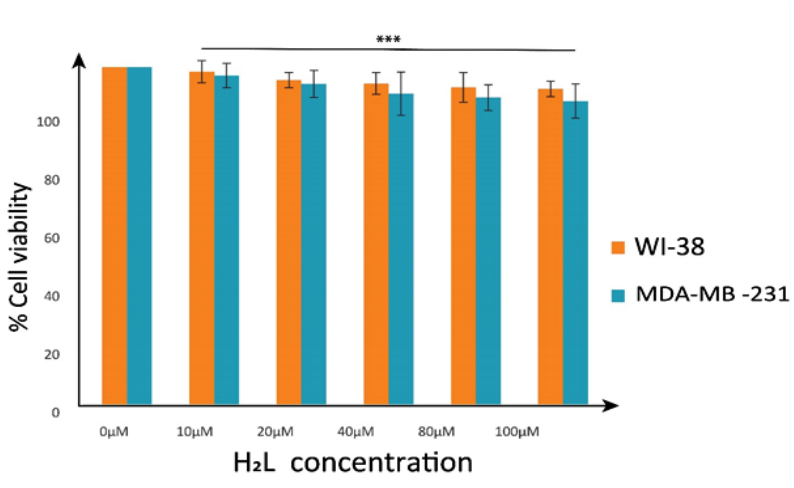

Fig.IV.28. Cell survivability (MDA-MB 231 and WI-38 cells) exposed to different H_2L concentration Data are representative of at least three independent experiments and bar graph shows mean ± SEM, ***$p < 0.001$ were interpreted as statistically significant, as compared with the control.

When MDA-MB 231 cells were treated with only Zn^{2+} and CN^- the results were ineffective (**Fig.IV.29**). Fluorescence microscopy imaging showed an increase in fluorescence intensity when MDA-MB 231 cells were exposed with both the mixture [H_2L (10 μM) + Zn^{2+} (10 μM)] (green emission, **Fig.IV.30 and 31**) and [H_2L (10 μM) + CN^-(10 μM)] (blue emission, **Fig.IV.32 and 33**) at a different incubation time frame of 30 min and 1 h. acquired using blue filter with excitation using 390 nm monochromatic laser beams. Whereas cells exposed to only the H_2L ligand (10 μM) have shown very low level of fluorescence intensity. Results from fluorescence microscopic images manifest that in presence of Zn^{2+} and CN^-, ligand H_2L emits prominent fluorescent signal.

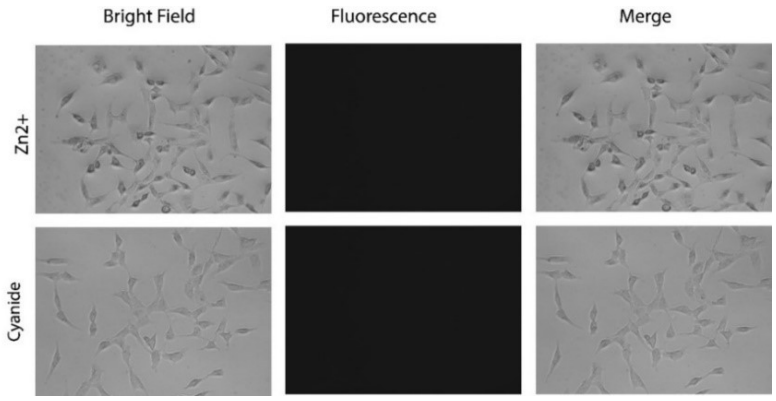

Fig.IV.29 Microscopic images of MDA-MB 231 cells treated with Zn^{2+}(10µM) and CN^-(10µM) after 30 min incubation period under bright, fluorescence and merged field.

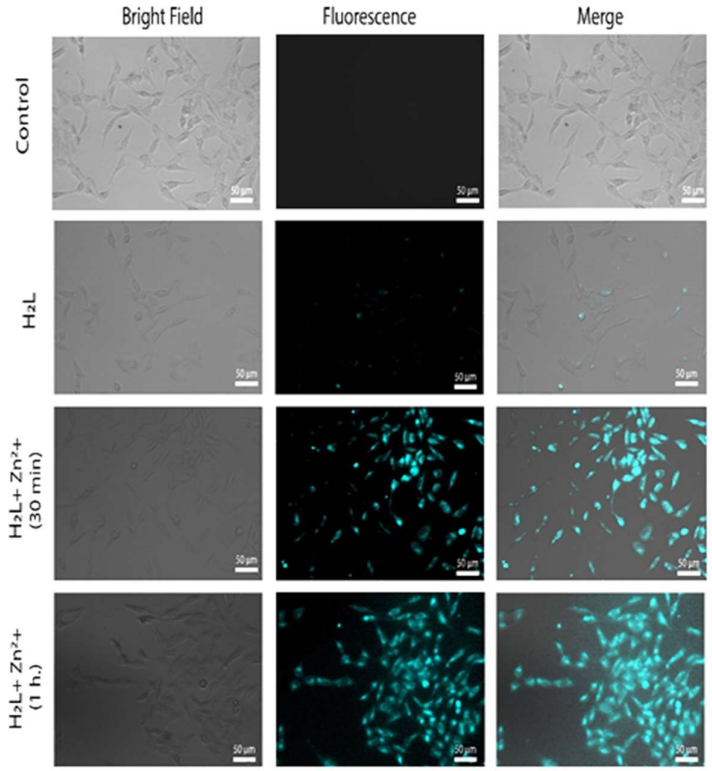

Fig.IV.30. Microscopic images of untreated MDA-MB 231 cells (Control), cells treated with H_2L (10µM), H_2L (10µM) + Zn^{2+} (10µM) after 30 min and 1h of incubation period under bright, fluorescence and merged field.

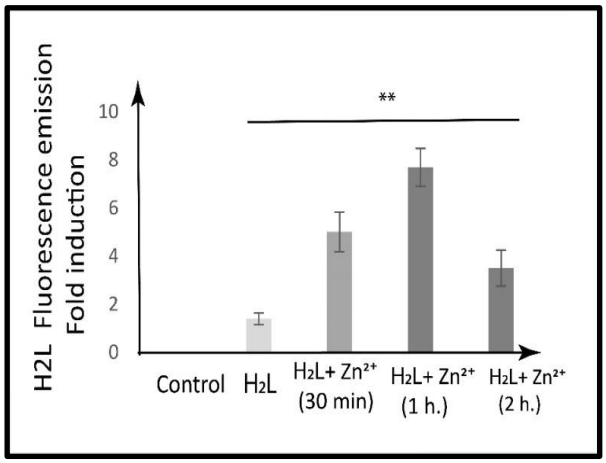

Fig.IV.31. H_2L Fluorescence emission fold induction in untreated MDA-MB 231 cells (Control), cells treated with H_2L (10µM), H_2L (10µM) + Zn^{2+} (10µM) after 30 min, 1h and 2h.

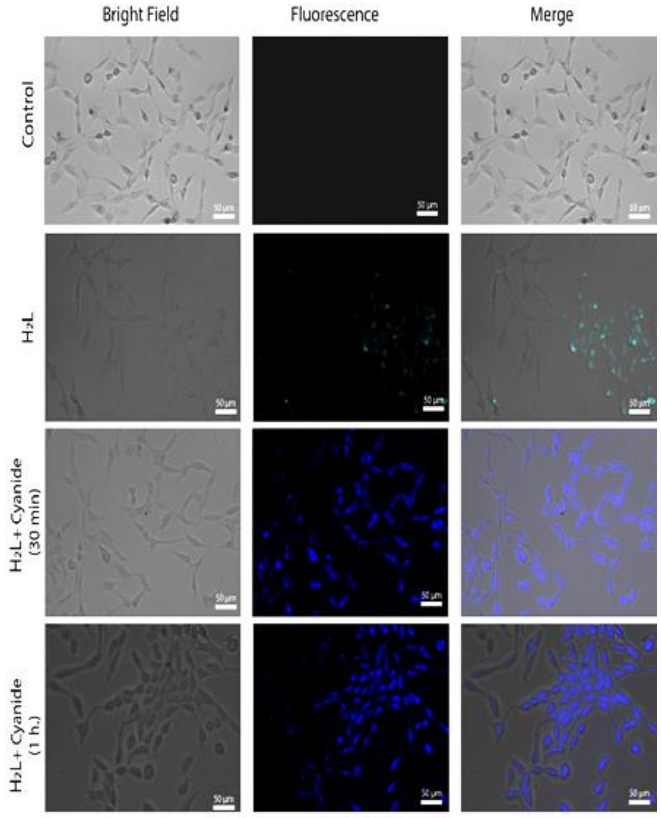

Fig.IV.32. Microscopic images of untreated MDA-MB 231 cells (Control), cells treated with H_2L (10µM), H_2L (10µM) + CN^-(10µM) after 30 min and 1h of incubation period under bright, fluorescence and merged field.

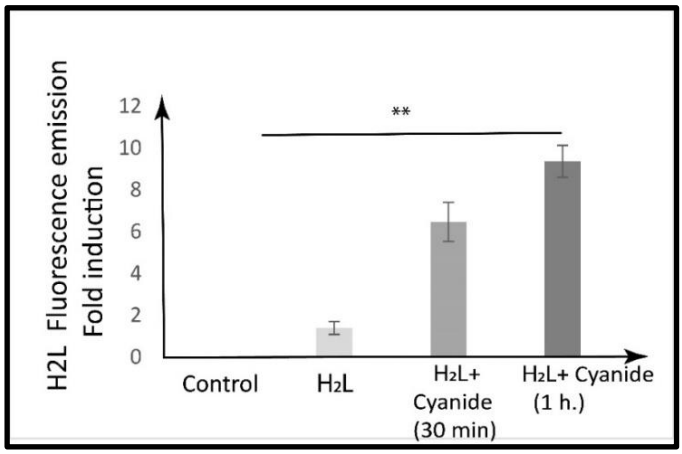

Fig.IV.33. H_2L Fluorescence emission fold induction inuntreated MDA-MB 231 cells (Control), cells treated with H_2L (10μM), H_2L (10μM) + Cyanide (10μM) after 30 min, 1hr.

FACS was performed to quantitatively analyze the population of cell that shows fluorescence emission after being either mock-treated or treated with 10 μM of ligand in the presence or absence of 10 μM Zn^{2+} at different time period. Flow cytometric data of H_2L (10 μM) + Zn^{2+} (10 μM) treated cell also showed that about 92% and 99% population of cell showed H_2L fluorescence emission after an incubation period of 30 min and 1 h respectively. Thus, we can conclude that the cells readily uptake the ligand H_2L (10 μM) in the presence of Zn^2. Further flow cytometric data also showed that in comparison to control cell, 7.46- and 9.27-fold induction in H_2L fluorescence emission in the H_2L (10 μM) + Zn^{2+} (10 μM) treated cell after an incubation period of 30 min and 1 h receptively. Results from cell trace experiment using FACS clearly shows a 92% ± 2.47 increase in the cellular population expressing fluorescence emission in ligand H_2L + Zn^{2+} treated cell, in comparison to control as well as ligand H_2L treated cell. This indicates the permeability of the ligand H_2L throughout the cell membrane and clearly justified our findings from fluorescence microscopy and also helps in quantitative analysis of Zn^{2+} distribution in live cells and showed that in the presence of Zn^{2+} and ligand H_2L results in prominent fluorescent signal (**Fig.IV.34**).

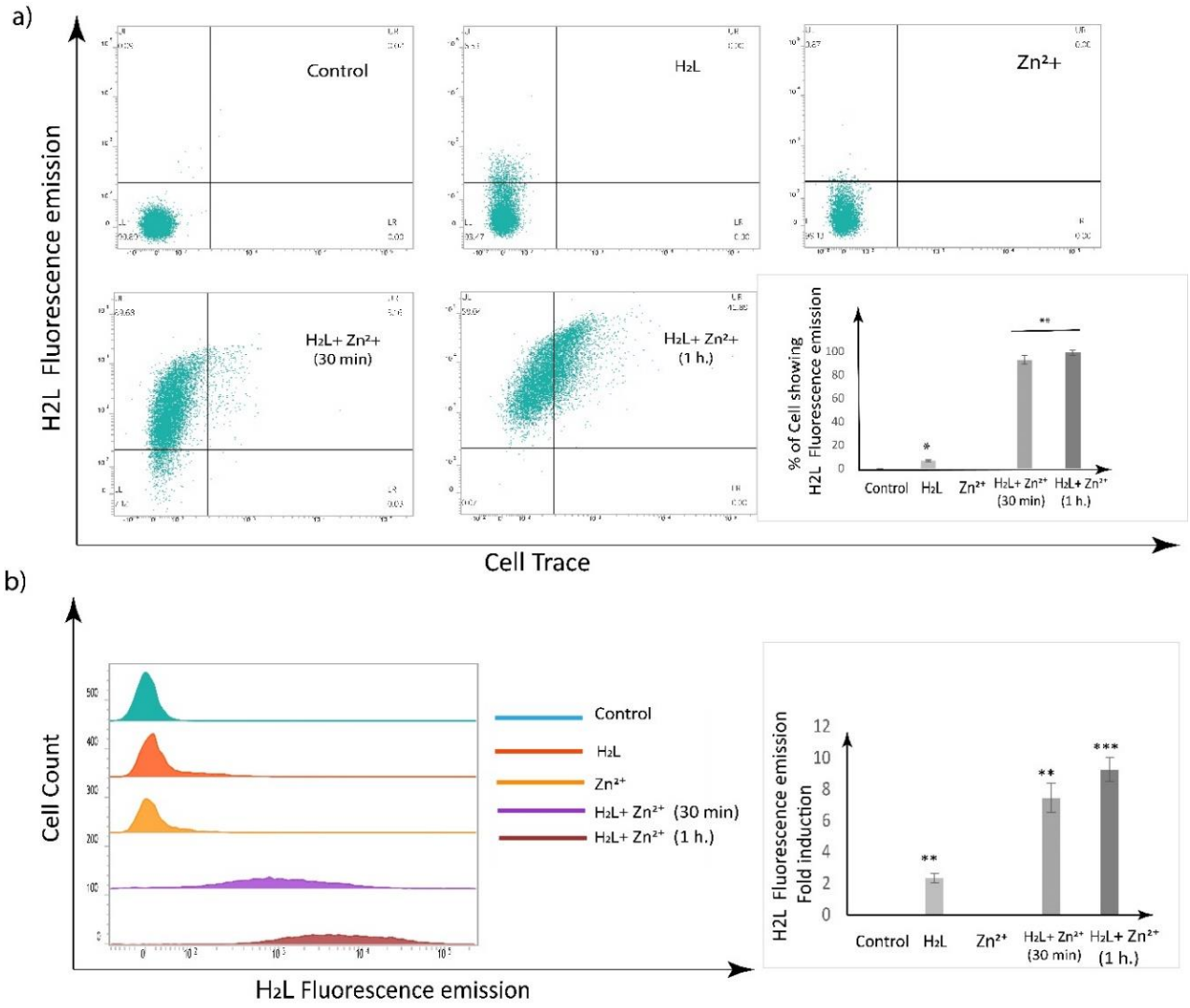

Fig.IV.34. Flow cytometric analysis of **(a)** dot plot and **(b)** bar plot untreated MDA-MB 231 cells (Control), cells treated with H_2L (10µM) + Zn^{2+}(10µM) after 30 min and 1h of incubation period. Data are representative of at least three independent experiments and bar graph shows mean ± SEM, *$p < 0.05$ **$p < 0.01$, ***$p < 0.001$ were interpreted as statistically significant, as compared with the control.

IV.4. Conclusion

7-Hydroxy-4-methyl-8-(((5-phenyl-1H-pyrazol-3-yl)imino)methyl)-2H-chromen-2-one (H_2L) has been developed for selective recognition and dual channel response to Zn^{2+} and CN^- at two emissive region following different mechanism. Detailed Structural characterization for probe H_2L and hexanuclear Complex $[Zn_6L_6]$ has been confirmed from Single Crystal X-Ray Diffraction (SCXRD) and other Instrumental analyses. The probe selectively senses Zn^{2+} through CHEF and inhibition of PET results in greenish emission (λ_{ex}= 390

nm, λ_{em}= 497 nm) while for CN^- generates bluish emission (λ_{ex}= 390 nm, λ_{em} = 447 nm) in CH_3CN/H_2O (99:1, v/v) (HEPES Buffer, pH 7.5) medium. The proposed binding mechanism and composition of the Zn^{2+} and CN^- complexes has been well accomplished by ^{1}HNMR Titration, IR and ESI-MS analysis. Limit of Detection (LOD) has been experimentally found to be 34.76 and 19.91 nM for Zn^{2+} and CN^- detection which accomplish the probe to be efficiently sensitive. DFT calculation establishes the theoretical interpretation of spectral behaviour of the probe in presence of Zn^{2+} and CN^-. The biocompatibility of the probe was established from MTT Assay in MDA-MB 231. The probe has been successfully capable of intracellular imaging of Zn^{2+} and CN^- is imaged in MDA-MB 231 cells those have been confirmed from the fluorescence microscopic images. The overall results certify that the probe as competent chemosensor of selective ion sensing and efficient detection of Zn^{2+} and CN^- with dual channel response for practical application.

IV.5. References

1. M. V. Escárcega-Bobadilla, D. Anselmo, S. J. W ezenberg, E. C. Escudero-Adán, M. M. Belmonte, E. Martin and A. W. Kleij, *Dalton Trans.*, 2012, **41**, 9766–9772

2. G. Ambrosi, M. P. Clares, I. Pont, M. Formica, V. Fusi, A. Ricci, P. Paoli, P. Rossi, E. García-España and M. Inclán., *Dalton Trans.*, 2020, **49**, 1897-1906

3. M. Gopalakrishnan,N. Krittametaporn,N.Yoshinari, T. Konno and P. Sangtrirutnugul, *New J. Chem.*, 2020,**44**, 13764-137703.

4. N. B. Nandi, A. Purkayastha, S. Roy, J. Kłak, R. Ganguly, I. Alkorta and T. K. Misra *New J. Chem.*, 2021, 45, 2742

5. N. Pinault, D. W. Bruce, *Coord. Chem. Rev.*, 2003, **241**, 1-25

6. P. Levín, D. Escudero, N. Díaz, A. Oliver, A. G. Lappin, G.Ferraudi, and L.Lemus, *Inorg. Chem.* 2020, **59**, 3, 1660–1674

7. J. Gregoliński,K. Ślepokura, and J. Lisowski, *Inorg. Chem.*2017, **56**, 12719−12727,

8.S.K.Kushvaha, B. Shankar, N. V. T. Sai, Gorantla, and K.C.Mondal, *ChemistrySelect*, 2019, **4**, 3334 –3339

9.J. Zhang, H. Cui, M. Hojo, S. Shuang, C. Dong., *Bioorg. Med. Chem. Lett.*2012, **22**, 343-346

10. L.Patra, K.Aich,S.Gharami,T. K. Mondal. *J. Lumin.*2018, **201**, 419-426.

11. G. Chakraborty, P. Das and S. K. Mandal *Mater. Adv.*, 2021, **2**, 2334-2346

12. Q. Tang, F. Dan, S. Ma, X. Zeng, H.Lan. *Chemistryselect* 2021, **6,** 6557-6563.

13. X. Tanga, J. Han, Y. Wang, L.Ni, X. Bao, L.Wang,W. Zhanga, *Spectrochim. Acta A*, 2017, **173**, 721-726.

14. C. Long, J.-H.Hu, P.-W. Ni, Z.Yina and Q.-Q. Fu. *New J. Chem.*, 2018,**42**, 17056-17061

15. S. Samanta, U. Manna, T. Raya and G. Das. *Dalton Trans*., 2015,**44**, 18902-18910

16. G.-H. Liu, Z.-Z. Chen, Y.-H. Deng, W.-K. Dong, *J.Photochem.&Photobio. A: Chemistry* 2021, **414**, 113271.

17. M. Shellaiah, Y.-T.Chen, Y.-T.Chen, N. Thirumalaivasan, B. Aazaad, K. Awasthi, K. W. Sun, S.-P.Wu, M.-C.Lin, and N. Ohta. *ACS Appl. Mater. Interfaces* 2021, **13**, 28610–28626.

18.V. Jeyasingh, K. Murugesan, S. Lakshminarayanan, N. Selvapalam, G.Das, L. Piramuthu. *Spectrochim. Acta. A: Molecular and Biomolecular Spectroscopy*2020, **234**, 118207.

19. K. D. Belfield, M. V. Bondar, A. Frazer, A. R. Morales, O. D. Kachkovsky, I. A. Mikhailov, A. E. Masunov, and O. V. Przhonska. *J. Phys. Chem. B* 2010, **114**, 9313–9321.

20. F. N. Moghadam, M. Amirnasr, S. Meghdadi, K. Eskandari, A. Buchholz, W. Plass. *Spectrochim.ActaA* 2019**,207**, 6-15.

21. J. Zhang, M. Shea, J. Lia, C. Wang, S. Wang, P. Liu, S. Zhang, J. Li. *Sens. Actuators B* 2018**, 270**, 362-370

22. K.Poongodi, P.Saravana Kumar, R. Shanmugapriya, C.Nandhini Kuppanagounder, P.Elango. *Spectrochim. Acta A*, 2021, **249**, 119288.

23. R. Purkait, A. Dey ,S. Dey, P. P. Ray and C. Sinha. *New J. Chem.* 2019, **43**, 14979-14990.

24. N. Sahu, S. Mondal, K. Naskar, A. D. Mahapatra, S. Gupta, A. M. Z. Slawin, D. Chattopadhyay, C. Sinha, *J. Mol. Struc*. 2018,**1155**, 152-164

25. R. Purkait, C. Patra, A. Das Mahapatra, D. Chattopadhyay, C. Sinha, *Sens. Actuators B.* 2018, **257**, 545-552

26. C. F. Mills, Zinc in Human Biology, edSpringer-Verlag, Berlin, 1989.

27. J. M. Berg, Y. Shi,The Galvanization of Biology: A Growing Appreciation for the Roles of Zinc,Science 1996, **271**, 1081-1085.

28. K. Wechakorn, K. Suksen, P. Piyachaturawat, P. Kongsaeree, *Sens. Actuators B* 2016**, 228**,270–277

29. C. J. Frederickson, J. Y. Koh, A. I. Bush, *Nat. Rev. Neurosci.*,2005, **6**, 449-462.

30. K. Wanga, K. Chen, T. Bian, Y. Chao, T. Yamato, F. Xing, T. J. Priora, C. Redshaw.,*Dyes and Pigments*,2021, **190** ,109300.

31. A. Kre¸ ˙zel and W. Maret, *J. Biol. Inorg Chem.*, 2006, **11**, 1049.

32. A. I. Bush, *Trends Neurosci.*,2003, **26**, 207–214

33. A. Takeda, H. Tamano, *Brain Res. Rev.*,2009, **62**, 33-34.

34. T. Tulchinsky, MD, MPH. *Public Health Reviews.*,2010, **32**, 243-255.

35. G. Ambrosi, M. Fanelli, P. Paoli, M. Formica, D. Paderni, P. Rossi, M. Micheloni, L. Giorgi and V. Fusi *Dalton Trans.*, 2020, **49**, 7496-7506.

36. C. A. S. Pothulapadu, A. Jayaraj, S. N, R. N. Priyanka, and G. Sivaraman, *ACS Omega*, 2021, **6**, 24473–24483.

37. M. Formica, G. Favi, V.Fusi, L. Giorgi, F. Mantellini, M. Micheloni. *J. Lumin.* 2018, 195, 193-200.

38. T. S.Ayshaa, M. B. I. Mohamed, M. S.E. Sedika, Y.A.Youssefa. *Dyes and Pigments*. 2021, **196,** 109795.

39. M. D.Holzbecher,M. A. Moss, H. A. Ellenberger, *J. Toxicol. Clin.Toxicol.*,1984, **22**, 341−347

40. Z. Xu,X.Chen, H. N.Kim,J.Yoon,*Chem. Soc. Rev.*,2010, **39**, 127−137.

41. B. Vennesland, E. E. Comm, C. J. Knownles, J. Westly and F. Wissing, Cyanide in Biology Academic Press: London. 1981.

42. F. R. Sidell, E. T. Takafuji, D. R. Franz, Medical Aspects of Chemical and Biological Warfare.1997.

43. G. C. Miller, C. A. Pritsos, TMS Publishing: Warrendale, PA, 2001,73−81.

44. Y. Sun, G. Wang, W. Guo, *Tetrahedron*,2009, **65**,3480−3485.

45. J. Marsden, I. House, The Chemistry of Gold Extraction; SME: Littleton, Colorado, USA, 2006**.** 67. 46. M. Sahu, A. Kumar, M. Kalyani, R. Dipti, N. B. Sharma, G. K.Patra *, Inorg. Chim. Acta*, 2021, **528**, 120600.

47. World Health Organization. Guidelines for Drinking-Water Quality, 3rd ed., Geneva, 2008; pp 188

48. J-W Hu, W.-C. Lin, S.-Y. Hsiao, Y.-H. Wu, H.-W. Chen, K.-Y. Chen, *Sens. Actuators. B.*, 2016, 233, 510-519.

49. A. Adak, R. Purkait, S. K. Manna, B. Ghosh and S. Pathak, C. Sinha, *New J. Chem.*,2019, **43**, 3899-3906

50. S. Warrier, P. S. Kharkar, *Spectrochim. Acta A*, 2018,**188**, 659-665

51. X. Sun, T. Liu, J. Sun and X.Wang *RSC Adv.*, 2020,**10**, 10826-10847

52. D. D. Perrin, W. L. F. Armarego, D. R. Perrin, Purification of Laboratory Chemicals,Pergamon Press, Oxford, U.K., 1980.

53. K. Das, U. Panda, A. Datta, S. Roy, S. Mondal, C. Massera, T. Askun, P. Celikboyun, E. Garribba, C. Sinha, K. Anand, T. Akitsug and K. Kobayashi, *New J. Chem.*,2015, **39**, 7309-7321.

54. G. M. Sheldrick, *ActaCrystallogr.*,*Sect.A: Found.Crystallogr.*, 2008, **64**, 112–122.

55. A. L. Spek, *Platon*, The Netherlands, 1999.

56. J. Farrugia, *J. Appl. Crystallogr.*, 1997, **30**, 565–565.

57. Dolomanov, O.V.; Bourhis, L.J.; Gildea, R.J.; Howard, J.A.K.; Puschmann, H., OLEX2: A complete structure solution, refinement and analysis program. *J. Appl. Cryst.*,2009,**42**, 339-341.

58. D. Maiti, A. S. M. Islam, M. Sasmal, C. Prodhan and M. Ali, Photochem. Photobiol.Sci., 2018, **17**, 1213-1221

59. A. Samui, K. Pal, P. Karmakar and S. K. Sahu, *Mater. Sci. Eng.* C, 2019, **98**, 772-781.

60. M. J. Frisch, G. W. Trucks, H. B. Schlegel, G. E. Scuseria, M. A. Robb, J. R. Cheeseman, G. Scalmani, V. Barone, B. Mennucci, G. A. Petersson, H. Nakatsuji, M. Caricato, X. Li, H. P. Hratchian, A. F. Izmaylov, J. Bloino, G. Zheng, J. L. Sonnenberg, M. Hada, M. Ehara, K. Toyota, R. Fukuda, J. Hasegawa, M. Ishida, T. Nakajima, Y. Honda, O. Kitao, H. Nakai, T. Vreven, J. A. Montgomery Jr., J. E. Peralta, F. Ogliaro, M. Bearpark, J. J. Heyd, E. Brothers, K. N. Kudin, V. N. Staroverov, R. Kobayashi, J. Normand, K. Raghavachari, A. Rendell, J. C. Burant, S. S. Iyengar, J. Tomasi, M. Cossi, N. Rega, J. M. Millam, M. Klene, J. E. Knox, J. B. Cross, V. Bakken, C. Adamo, J. Jaramillo, R. Gomperts, R. E. Stratmann, O. Yazyev, A. J. Austin, R. Cammi, C. Pomelli, J. W. Ochterski, R. L. Martin, K. Morokuma, V. G. Zakrzewski, G. A. Voth, P. Salvador, J. J. Dannenberg, S. Dapprich, A. D. Daniels, O. Farkas, J. B. Foresman, J. V. Ortiz, J. Cioslowski and D. J. Fox, Gaussian 09, Revision D.01, Gaussian Inc., Wallingford, CT, 2009.

61. A. D. Becke,*J. Chem. Phys.* 1993, **98**, 5648–5652.

62. W.R. Wadt and P.J. Hay, *J. Chem. Phys*. 1985, **82**, 299-310

63. R. Bauernschmitt and R. Ahlrichs,*Chem. Phys. Lett.* 1996, **256**, 454–464.

64. M. Cossi and V. Barone,*J. Chem. Phys.* 2001, **115**, 4708–4717.

65. M. Cossi, N. Rega, G. Scalmani and V. Barone,*J. Comput. Chem.*, 2003, **24**, 669–681.

66. N. M. O'Boyle, A. L. Tenderholt and K. M. Langner,*J. Comput. Chem.*, 2008, **29**, 839–845.

67. D. Laha, A. Pramanik, S. Chattopadhyay, S. K Dash, S. Roy, P. Pramanik, P. Karmakar, *RSC Adv.* 2015, **5**, 68169-68178.

68. K. Pal, S. Roy, P. K. Parida, A. Dutta, S. Bardhan, S. Das, K. Jana and P. Karmakar, *Mater.Sci. Eng.* C, 2019, **95**, 204-216.

69. T. Wei, J. Wang, Y. Chen and Y. Han, *RSC Adv.*, 2015,**5**, 57141-57146

70. Z. He, C. Ke, and B. Z. Tang, *ACS Omega*, 2018, **3**, 3267−3277

71. S. D. Padghan, L. C. Wang, W.C. Lin, J.W. Hu, W.C. Liu, and K.Y. Chen., *ACS Omega*,2021, **6**, 5287−5296.

72. A. Panditha, N. Uddin, C. H. Choi, H-S. Kim, *Sens. Actuators B*, 2017, **247**, 840-849

73. A. Dhara, N. Guchhait, I. Mukherjeec, A. Mukherjeec, S. C. Bhattacharya *RSC Adv.*, 2016,**6**, 105930-105939

74. W. Gao, H. Li, Y. Zhang, S. Pu., *Tetrahedron.* 2019,**75**, 2538-2546

75. K.Rezaeian, H. Khanmohammadi and A.Talebbaigy, *Anal.Methods*, 2020, **12**, 1759

76. Q. Niu, T. Sun, T. Li, Z. Guo, H. Pang Sens.Actuators B, 2018, **266**, 730–743

77. J. M. Jung, D. Yun, H. Lee, K.T. Kim, C. Kim, *Sens. Actuators B*, 2019, **297**, 126814

78. T. Anand, A. K. SK, and S. K Sahoo, *ChemistrySelect*, 2017, **2**, 7570 – 7579

79. M. Karimi, A.Badiei, G. M.Ziarani, *Inorg.Chim.Acta*, 2016,450 ,346–352.

80. S.-L. Yao, Y.-C. Xiong, X.-M. Tian, S.-J. Liu, H. Xu, T.-F. Zheng, J.-L. Chen and H.-R. Wen *CrystEngComm*, 2021,23, 1898-1905

81. L. E. Santos-Figueroa, A. Llopis-Lorente, S. Royo, F. Sancenûn, R. Martinez-Manez, A. M. Costero, S. Gil, and M. Parra *ChemPlusChem*, 2015, **80**,800 –804

82. T. Devendhiran, K. Kumarasamy, M.-C. Lin, Y. X. Yang, *Inorg. Chem. Comm.*, 2021, **134**, 108951.

83. J.-H. Hu, Y. Sun, J. Qi, Q. Li, T.-B.Wei, *Spectrochim. Acta A*, 2017,**175**, 125-133

84. S. Dey, C. Sen, C. Sinha, *Spectrochim.Acta Part A.*,2020, **225**, 117471

Chapter V

Naphthyl-Azine Scaffold: AIEgen, Reversible Acidochromism, Cyanide sensing and its application in Intracellular Imaging.

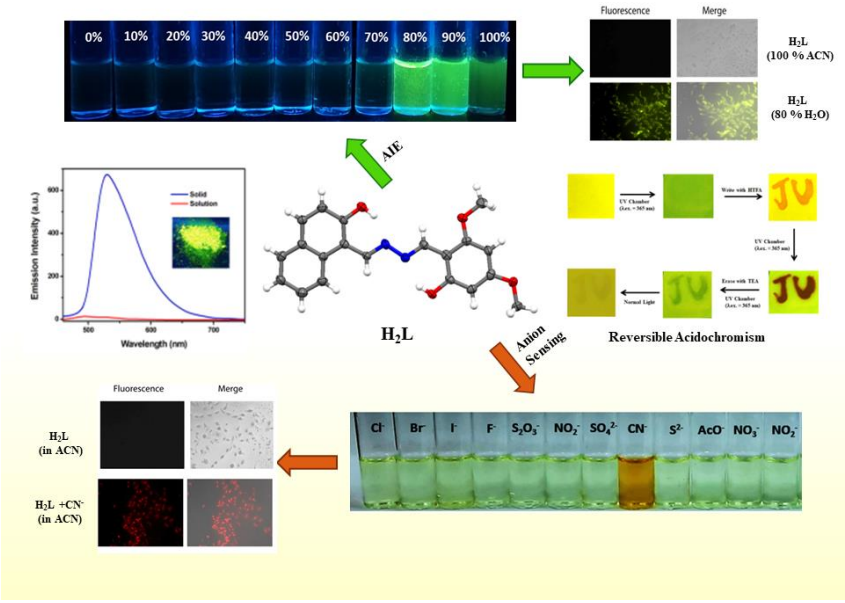

CHAPTER V

Abstract

Naphthylhydrazone derivative, 1-[(2-Hydroxy-4,6-dimethoxy-benzylidene)-hydrazonomethyl]-naphthalen-2-ol (H_2L), an AIE active probe emerges out as a promising solid-state emitter upon exercising restricted intramolecular rotation (RIR) in an ordered J-type self-assembly and accounts for solid-state sensitive fluorescence quencher of trifluoroacetic acid (HTFA) vapour with limit of detection (LOD), 1.41 ppm. A plausible mechanism of quenching may be the protonataion driven destruction of compacted arrangement in the solid state of the probe. Interestingly, H_2L executes reversible acidochromic behavior upon sequential addition of HTFA and TEA (Triethylamine, NEt_3) vapour, which has been utilized for information protection application using the "write-erase" technique. Moreover, the probe divulges a selective and sensitive colorimetric and 'turn-on' fluorogenic response towards CN^- amongst other anions, where deprotonation induced intramolecular charge transfer (ICT) ultimately determines LOD, 45.42 nM. Interestingly, the CN^--sensing activity of H_2L is found to be reversible in presence of HTFA, which can easily be cycled for several times to demonstate its potent reusability. Furthermore, cytotoxicity studies with MTT assay reveals considerable biocompatability and intracellular-imaging of the probe, which reflects the AIEgenic properties and CN^- detection in MDA-MB 231 cells as well.

V.1. Introduction

π-Conjugated organic material with fluorogenic motif exhibits tunable photophysical behavior in aggregated state and executes a vast arena of potential application including sensing, optoelectronic device formation (OLEDs, OFETs), bioimaging etc.[1-3] Aggregation has two opposite basic effects - Aggregation-caused Quenching (ACQ)[4,5] and Aggregation-induced Emission (AIE).[6]. In case of AIE property, molecular packing plays an important role behind the onset of this unusual event, where Restriction of Intramolecular Rotation (RIR) induces vigorous rigidity upon aggregation/self-assembly and prevents the continuous dissipation of energy through non-radiative relaxation.[7,8] Owing to the augmented luminescence feature accomplished with superior photostability, AIE*gens* have established themselves as the sensitive agents behind construction of efficient chemosensors for trace quantity detection of toxic ions, gases, and even explosives.[9-13] Solid luminophores owing to their high quantum efficiency are often considered as convenient multi-stimuli responsive materials in presence of external stimuli such as heat,[14] light,[15] mechanical force[16-18] and chemical vapors.[19, 20] Subsequently, fluorogenic devices fabricated for the detection of volatile acids have drawn considerable attention due to their inevitable implications for the estimation of acidity in local environment in biology, chemistry, food science, pharmacy, forensic science etc.[21] Even lower concentration of such acid vapours are potentially toxic, corrosive, irritant to skin, eyes and causes severe burn to mucous membrane of the respiratory tract.[22-24] Therefore, an increasing demand has recently been perceived for developing an improved, cost-effective, reusable and responsive materials for ultra-trace recognition of toxic acid vapors.

Side-by-side, anion sensors have also been emerged as a progressive field of research owing to their crucial roles in various biochemical and industrial processes. Out of several existing anions in surroundings, Cyanide ion (CN^-), known to be a highly toxic anion can easily bind with the iron (Fe^{3+}) centre of Cytochrome-C oxidase and causes the disruption of mitochondrial electron transport chain, which ultimately lead to hypoxia.[25,26] Also, CN^- is extremely detrimental as it gets easily absorbed through skin and induces potential damages to vascular, central nervous, endocrine and even cardiac system.[27] Extensive utilization of CN^- for different industrial processes of gold extraction, synthesis of fibers and electroplating results in its accidental

release as unprocessed waste into ecology, which severely causes environmental contamination and increases the risk of damage for human health mostly *via* oral and dermal exposure. Therefore, the permissible limit for CN^- in drinking water has been restricted to 1.9 μM by WHO.[28] Hence, an urgency for the development of efficient chromogenic and fluorogenic sensing module for visual detection of CN^- remains a top priority in the ongoing research fraternity.

In the present work, we have designed an azine derivative based on naphthyl scaffold namely 1-[(2-Hydroxy-4,6-dimethoxy-benzylidene)-hydrazonomethyl]-naphthalen-2-ol (H_2L), which exhibits excellent AIE behavior in mixed aqueous medium. The π-π stacking of naphthyl unit plays a predominant factor contributing to its interesting photophysical properties. The probe, H_2L is strongly emissive and is employed as a reversible fluorescence sensor at solid-state to HTFA/TEA (NEt_3) vapours which enables it as a promising solvent free medium for analysis and encrypted security ink application. Further the azine probe, H_2L simultaneously detects CN^- in acetonitrile medium through chromogenic response *via* selective deprotonation pathway which has been substantiated by DFT computation of the probe (H_2L) and deprotonated (L^{2-}) form. The MTT assay and intracellular-imaging application in MDA-MB Cells exhibits red emission of CN^- by H_2L emphasizes its biocompatibility and interesting photophysical properties revealing the AIEgenic behaviour at different water fractions which shows resemblances with the spectral outcomes.

V.2. Experimental Section

V.2.1. Materials and Methods

All the reagents of analytical grade (A.R) were collected and used without further purification. 2-Hydroxy-Napthaldehyde, Hydrazine Hydrate, 4,6-Dimethoxy-Salicyldehyde, Inorganic salts and other chemicals (,$Na_2S_2O_3.5H_2O$, NaCl, NaF, NH_4HF_2, KNO_3, KBr, $NaNO_2$, NaN_3 , CH_3COONa, , KIO_3, KI, Na_2SO_4, Na_2S, $C_4H_9N(CN)$, KSCN) Trifluoroacetic Acid, Triethylamine , Phosphoric acid, Propionic acid, Sulphuric acid, Methane sulfonic acid, Methacrylic acid, Heptanoic acid, Oleic acid, AcOH, HNO_3 HCl were bought from TCI chemicals and Merck. For spectroscopic measurement UV graded spectroscopic solvents were used. The solvents were dried by standard procedure for spectroscopic studies.[1]Milli-Q water (Millipore) has been used

for preparation of aqueous solutions of metal salts. Perkin-Elmer (2400 Series-II, Perkin Elmer, USA) CHN analyzer has been used for elemental analysis purpose. The spectra were recorded by Lambda 25 spectrophotometer: UV-Vis; LS55: fluorescence, LX-1FTIR and LITA spectrophotometer: FT-IR spectra (KBr disk, 4000-400 cm^{-1}) on Perkin Elmer instruments. ^1H and ^{13}C NMR spectra were taken by Bruker 300 MHz FT-NMR spectrometer. The chemical shift (δ) of the respective NMR spectra were recorded in parts per million (ppm) with respect to trimethylsilaneas internal standard. ESI-MS spectra were obtained from HRMS spectrometer (model, XEVO-G2QTOF#YCA351).

V.2.2. Synthesis of 1-[(2-Hydroxy-4,6-dimethoxy-benzylidene)-hydrazonomethyl]-naphthalen-2-ol (H_2L)

1-Hydrazonomethyl-naphthalen-2-ol was synthesized based on a literature procedure [29] To a methanolic solution (10 mL) of 1-hydrazonomethyl-naphthalen-2-ol (0.186 mg, 1 mmol), 2-hydroxy-4,6-dimethoxy-benzaldehyde (0.182 mg, 1 mmol) in MeOH (5 ml) was added dropwise slowly. The resulting solution stirred overnight followed by reflux for 3 h and a bright yellow precipitate was appeared. The precipitate was filtered, washed several times with methanol and dried under vacuum (**Scheme V**). The product was further recrystallized from a saturated solution of DMSO/Acetonitrile (1:5 v/v) through slow evaporation method and the isolated yellow needle shaped crystals were found to be suitable for single crystal X-ray diffraction. Yield: 73%. ^1H NMR ($CDCl_3$, 300 MHz): 13.12 (s, 1H, OH(1)), 12.41(s, 1H, OH(10)), 9.56 (s, 1H, N=CH(8)), 9.11 (s, 1H, N=CH(9)) 8.16-7.24 (m, 6H, Ar-H(2-7)), 6.20-6.02 (s, 2H, Ar-H(11,12)), 3.89 (s, 6H, CH_3(13,14)) (**Fig.V.1**); ^{13}C NMR ($CDCl_3$, 75 MHz) : 165.19, 163.17, 161.00, 160.68, 159.55, 158.71, 134.27, 132.58, 129.15, 128.18, 127.84, 123.68, 120.09, 119.17, 108.26, 101.29, 93.50, 90.76, 55.78, 55.56 (**Fig.V.2**). ESI-MS: 351.1333 [$M+H^+$] (**Fig.V.3**). IR spectrum: 3392 cm^{-1} (O-H stretching), 2953 & 2843 cm^{-1} (C-H stretching), 1628 & 1583 cm^{-1} (C=N stretching) (**Fig.V.4**).

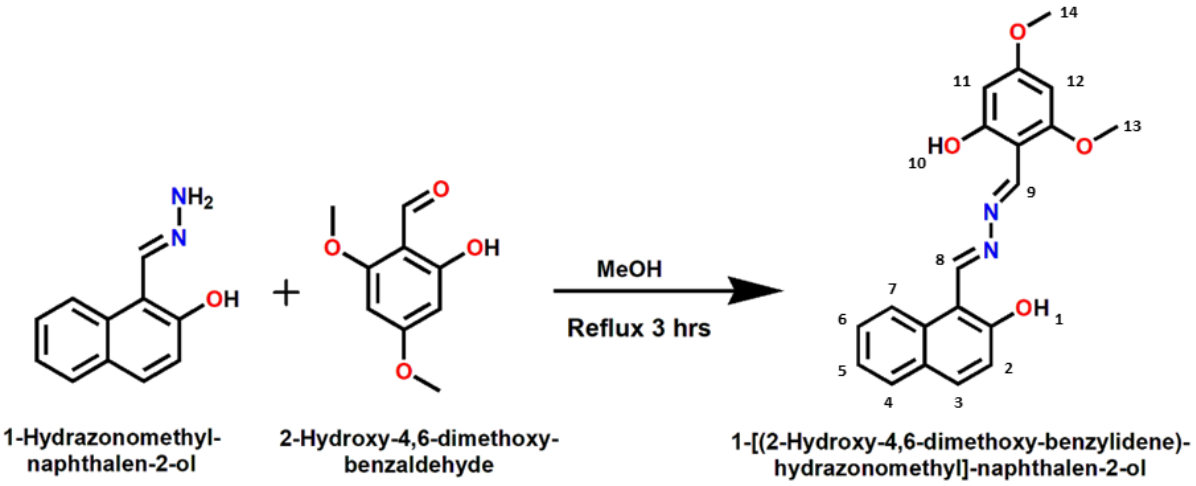

Scheme V. Synthetic Scheme of the probe H_2L

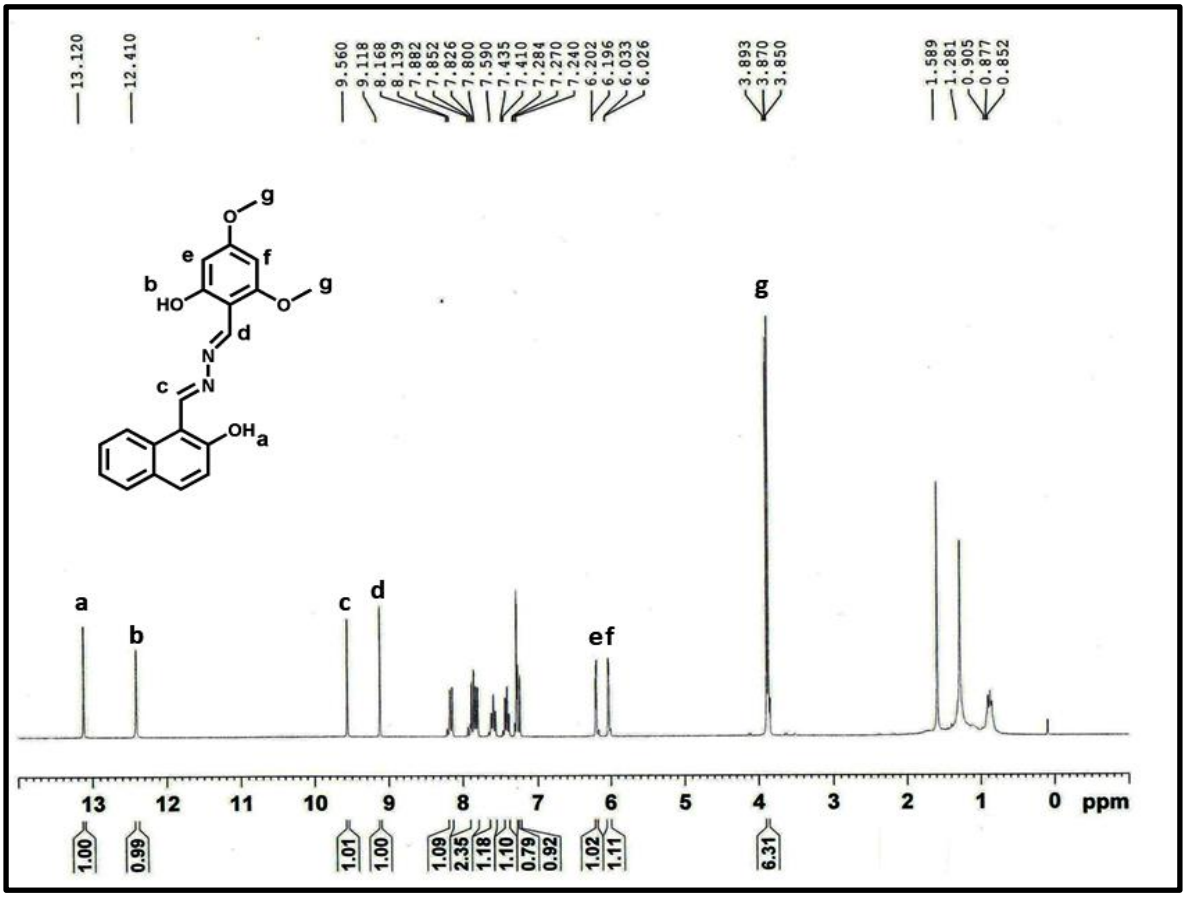

Fig.V.1. ^{1}HNMR Spectrum of the probe, H_2L ($CDCl_3$, 300 MHz)

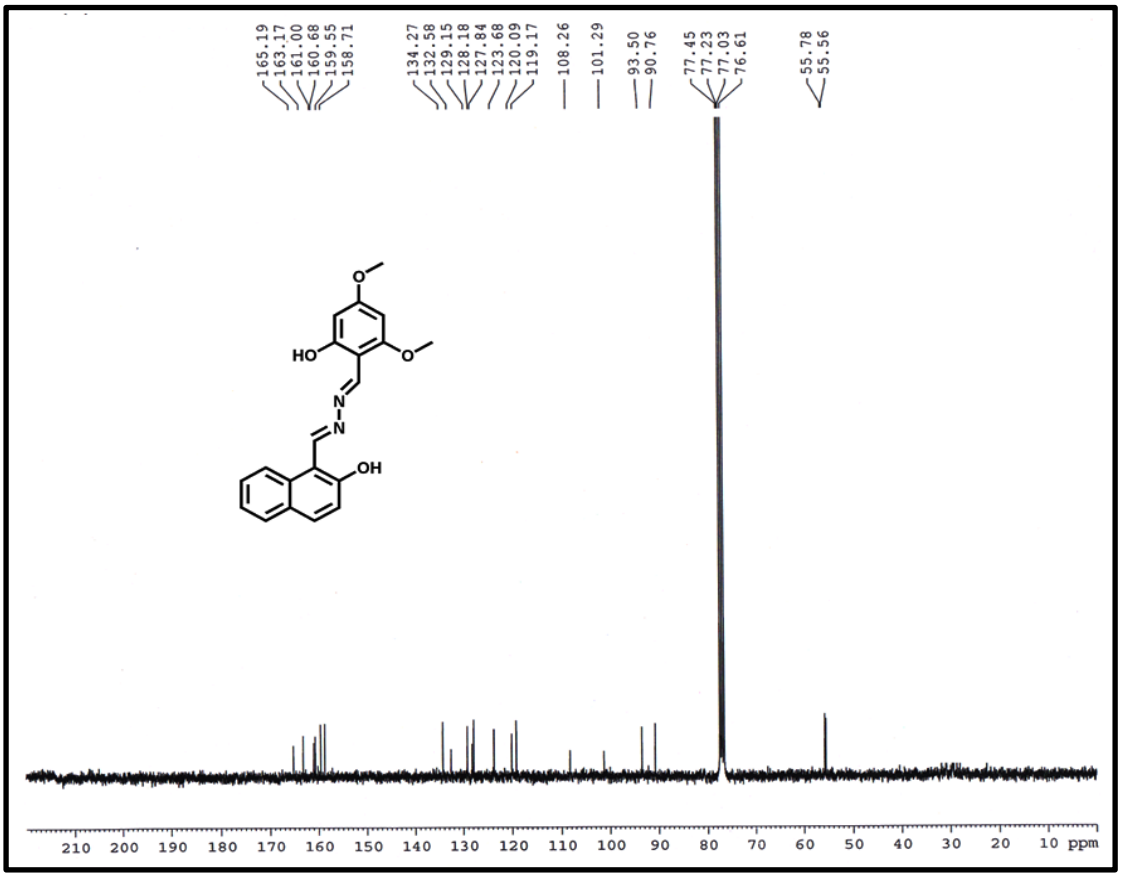

Fig.V.2. ^{13}CNMR Spectrum of the probe, H_2L ($CDCl_3$, 75 MHz)

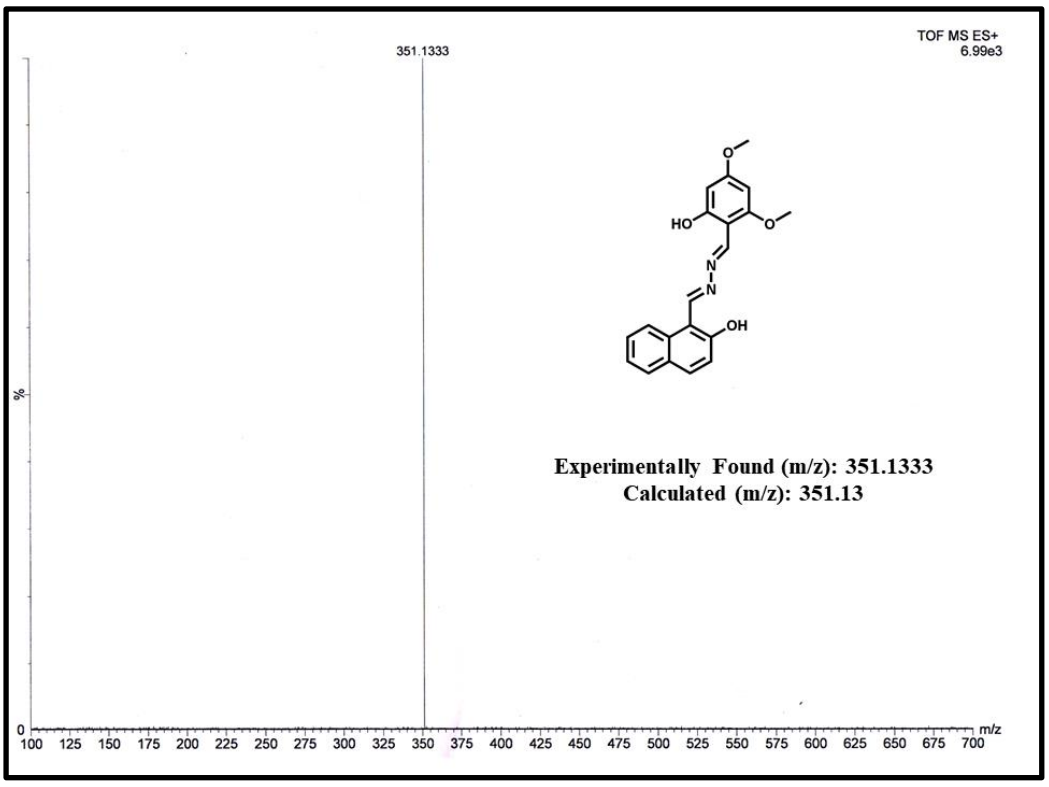

Fig.V.3. ESI-MS(+) of the Ligand H_2L

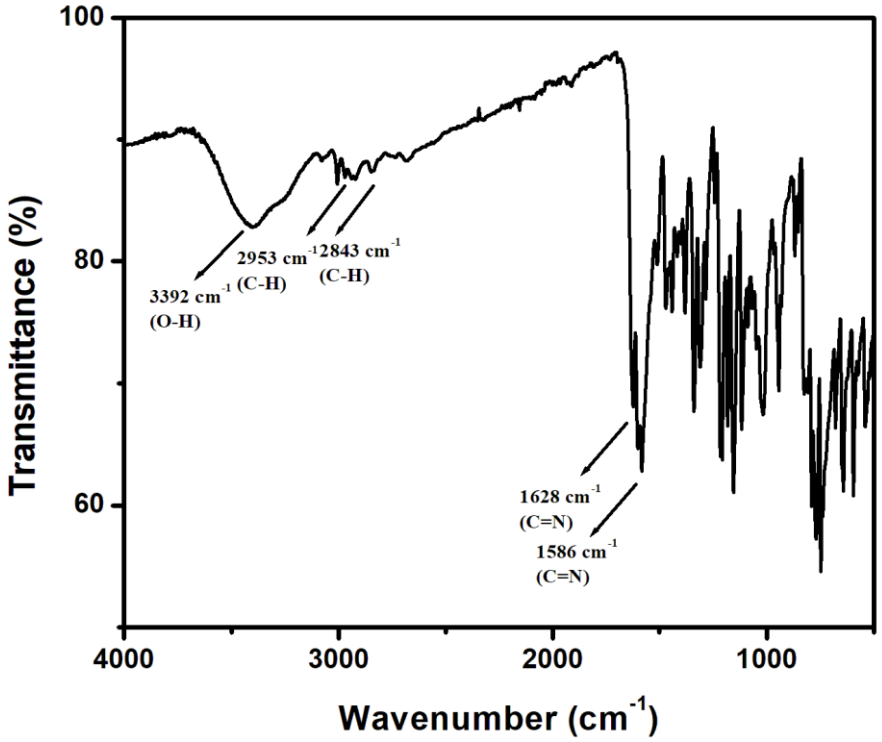

Fig.V.4. IR Spectrum of the probe H_2L

V.2.3. X-Ray Crystallographic Measurements

The needle shaped yellow single crystal (0.20 × 0.12 × 0.08 $Å^3$) of H_2L was obtained through slow evaporation technique in DMSO/Acetonitrile (1:5, v/v) medium. Single Crystal X-ray data were collected by Bruker Apex II CCD Area Detector at 100(2) K. Graphite-monochromatized Cu-Kα radiation (λ = 1.54178 Å) was used in a fine-focused sealed tube. The hkl range for data collection was $-12 \le h \le 13$;$-11 \le k \le 11$; $-37 \le l \le 37$ for the probe H_2L, where diffraction was recorded within the angular range from $2.292 \le \theta \le 73.202^o$ for H_2L. The intensity was corrected for Lorentz and polarisation effects and empirical absorption corrections were applied for both the probe and the complex. Data were collected applying the condition $I > 2\sigma(I)$. The structure was solved by direct method followed by successive Fourier and difference Fourier syntheses. All the non-hydrogen atoms were refined anisotropically. The hydrogen atoms were geometrically fixed and refined using the riding model. All calculations were carried out using SHELXL-2016/6,[30] ORTEP-32,[31] and PLATON-99[32] programs. The crystal data for the probe H_2L have been deposited to the Cambridge Crystallographic Data Centre with CCDC 2178275. The copies of this data may be picked up free of cost from the Director, CCDC,

12 Union Road, Cambridge CB2 1EZ, UK (e-mail:deposit@ccdc.cam.ac.uk or www:htpp://www.ccdc.cam.ac.uk). Details of Data collection and Crystal data were listed in **Tables V.1 and V.2.**

Table V.1. Crystal Data and Refined Parameters for H_2L

Empirical formula	$C_{20}H_{18}N_2O_4$
CCDC No.	2178275
Formula weight	350.36
Temperature (K)	100(2) K
System	Orthorhombic
Space group	P n a 21
a (Å)	11.7509(4)
b (Å)	9.3631(3)
c (Å)	30.1678(10)
α/°	90
β/°	90
γ/°	90
V $(Å)^3$	3319.21(19)
Z	8
D(cal) /g cm^{-3}	1.402
μ/mm^{-1}	0.813
λ(Å)	1.54178
Data[I >2σ(I)]/param	6304/474
$R_1{}^a$[I>2σ(I)]	0.0517
$wR_2{}^b$	0.1343
GOF[c]	1.090

[a]$R_1 = \Sigma||F_o|-|F_c||/\Sigma|F_o|$; [b]$wR_2 = \{\Sigma[w(F_o^2-F_c^2)^2]/\Sigma[w(F^2_o)^2]\}^{1/2}$; $w = [\sigma^2(F_o)^2 + (0.1003P)^2 + 4.9693P]^{-1}$ $(F_o^2 + 2F_c^2)/3$; [c] Goodness-of-fit.

Table V.2: Selected Bond length and Bond Angles of H_2L

Bond Length (Experimental)	**Å**	**Bond Angle (Experimental)**	**Degree (°)**
N2-N1	1.396	C33-N2-N1	112.45
C22-N1	1.298	C22-N1-N2	113.91
C22-C23	1.454	N1-C22-C23	120.65
C23-C24	1.400	C22-C23-C24	119.92
C24-O3	1.345	C23-C24-O3	123.07
O3-H3	0.840	C24-O3-H3	109.50
N2-C33	1.304	N2-C33-C34	131.96
C33-C34	1.440	C33-C34-C35	122.12
C34-C35	1.410	C34-C35-O8	121.31
C35-O8	1.349	C35-O8-H8	103.42
O8-H8	0.840		

V.2.4. Quantum Yield and Limit of detection Calculation

Fluorescence quantum yields (Φ) were obtained by using following equation:

$$\Phi_{sample} = (OD_{std.} \times A_{sample})/(OD_{sample} \times A_{std.}) \times \Phi_{std.}$$

Where, A_{sample} and A_{std} represent the areas under the fluorescence spectral curves for sample and standard respectively. OD_{sample} and OD_{std} represents the optical densities of the sample and standard respectively at the excitation wavelength.[33] In this work, acidic quinine sulfate (0.1N H_2SO_4 solution) was taken as the standard with known quantum yield, $\Phi_{std} = 0.54$ for quantum yields calculation of H_2L and the CN^- complex.

Limit of Detection (LOD) was calculated from absorption titration experiment on gradual addition of CN^- ion to the solution of ligand H_2L. Accordingly, standard deviation was measured from absorbance of ligand, where the limit of detection (LOD) for CN^- was determined from the equation LOD = (3σ/Slope) where, σ represents standard deviation and m is the slope acquired from the plot of absorption titration experiment.

V.2.5. Solution for Spectral Measurement

For UV-Vis and Fluorescence study, the ligand H_2L with concentration of $1x\ 10^{-3}$(M) was prepared in DMSO. All anionic solutions of $1\ x\ 10^{-3}$(M) were arranged in CH_3CN. The Spectroscopic experiment was carried out in acetonitrile medium. A 25 μM of HL solution was prepared in 2 mL CH_3CN/H_2O (99:1, v/v) (HEPES Buffer, pH 7.5) for sensing study. To this solution 2 equivalent of anions were added and the sensitivity and selectivity was checked by UV-vis and Fluorescence measurement of the probe H_2L solution. The absorption and emission path length of cell used were 1 cm. Fluorescence measurement experiments were done on excitation and emission of 12 nm x 3 nm (For HTFA vapor) and 10 nm x 10 nm (For CN^-) slit width.

V.2.6. Theoretical Calculation

The Gas-phase optimized structures of ligand H_2L and its CN^- complexes (L^{2-}) were calculated with 6311-G basis set (C, H, O, N) and B3LYP functional of Gaussian Program Package 09.[34-36] The optimized geometry of H_2L was obtained using the coordinates from single crystal structures where the vibrational frequency calculation represented the local minima with positive Eigen values. The TD-DFT calculation determined the theoretical transition in relevance to that of experimental absorption spectral behaviour in presence of CN^-, which was performed using conductor like polarizable continuum model (CPCM) in acetonitrile medium.[37-39] Fractional contribution of the orbital were calculated using GAUSSUM.[40]

V.2.7. Cell line study

In the present study, human breast cancer cell line MDA-MB-231 and human normal lung fibroblast cell line WI-38 were procured from the central cell repository of National Centre for Cell Science (NCCS), Pune, India. All the cell lines were cultured in a T25 flask with DMEM which were supplemented with 10% FBS (Fetal

bovine serum), 1mM sodium pyruvate, 2 mM L-glutamine, non-essential amino acids, 100 units/L penicillin, 100 mg/L streptomycin, and 50 mg/L gentamycin in a 37°C humidified incubator containing 5% CO_2.

V.2.8. Cytotoxicity assay

The MTT cell proliferation assay[41] was performed to assess the cytotoxic effect of the ligand H_2L in both the cancer cell line MDA-MB-231 and normal cell line WI-38. In brief, the cells were first seeded in 96-well plates at a concentration of 1×10^4 cells per well for 24 h, which were then exposed to the different working concentration of ligand H_2L in DMSO (0, 10, 20, 40, 80, 100 μM) for 24 h. After incubation, the cells were washed with 1×PBS and MTT solution (0.5 mg/ml) were added to each well and incubated for 4 h and the resulting formazan crystals were dissolved in DMSO and the absorbance was measured at 570 nm by using a microplate reader. Cell viability was expressed as a percentage of the control experimental setup.

V.2.9. Fluorescence imaging

To envision the fluorescence ability of H_2L in the presence of mixed solvent medium (water (H_2O) and acetonitrile (CH_3CN)), also in the presence of cyanide (CN^-), the fluorescence imaging was performed in cell line MDA-MB 231. Briefly, the cells were allowed to grow in cover slips for 24 h in a 37°C humidified incubator containing 5% CO_2 and then the systems were either mock-treated or treated with 10 μM of H_2L in presence and absence of CN^- (5 and 10 μM) separately both in water as well as inorganic solvent medium and incubated for 30 minutes in dark at 37ºC. The cells were washed with 1×PBS and then they were mounted on a glass slide and detected under fluorescence microscope (Olympus) using DAPI filter .[42]

V.3. Results and Discussion

V.3.1. Structural Characterization

^1H NMR spectrum of 1-[(2-Hydroxy-4,6-dimethoxy-benzylidene)-hydrazonomethyl]-naphthalen-2-ol (H_2L) (**Fig.V.1**) reveals two singlet Hs at 13.12 and 12.41 ppm who are assigned to the naphthyl-OH and dimethoxyphenyl-OH, respectively. In addition, the sharp singlets at 9.56 and 9.12 ppm are assigned to the two imine (CH=N) protons of naphthyl and dimethoxyphenyl unit, which certainly confirms the formation of

probe H_2L. The two aromatic singlets of the dimethoxyphenyl group appear at 6.20 and 6.02 ppm. An intense singlet at 3.89 ppm implies -OCH_3 protons. Other aromatic protons of H_2L observe at 8.16 – 7.24 ppm. The ^{13}C NMR spectrum of H_2L shows two peaks at 165.19 and 163.17 ppm due to C (C-O) centres attached to the methoxy unit. The two peaks at 161.00 and 160.68 ppm represent the C of (CH=N) imine signal. Phenolic (C-O) centres attributed to the peaks at 159.55 and 158.71 ppm. The remaining aromatic-C centres appear from 134.27 to 90.76 ppm. The signals for the methoxy unit are assigned at 55.78 and 55.56 ppm (**Fig.V.2**). ESI-MS analysis of H_2L shows molecular ion peak at 351.1333, which corresponds to $[M+H^+]$ formation and confirms its composition (**Fig.V.3**). IR Spectrum of H_2L exhibits stretching frequencies of two imine (C=N) groups at 1630 and1590 cm^{-1} which certifies the formation of the probe. Correspondingly, The N-N stretching band of the azine linkage appears at 1219 cm^{-1} (**Fig.V.4**).

V.3.2. Molecular Structural Description of H_2L

The emissive molecule H_2L crystallizes in orthorhombic system with Pna21 space group. The bond lengths, C22-N1 (1.296 Å) and C33-N2 (1.304 Å) exhibit imine linkage, which are found to be shorter than the distance between N1-N2 (1.400 Å) of azine function. Also, the lengths C24-O3 (1.345 Å) and C35-O8 (1.349 Å) indicate characteristic phenolic type bonding. Two methoxy groups, C37-O1 and C39-O2, are identical and exhibit a bond length 1.360 Å. (**Table V.2**). There are two types of intramolecular hydrogen bonds, viz., O3-H3···N1 (1.821 Å) and O8-H8···N2 (1.873 Å) which impart stability to the molecule (**Fig.V.5(a)**). A 2D supramolecular self-assembly is formed by various non-covalent π…π (4.312 Å) interactions (**Fig.V.5(b)**).

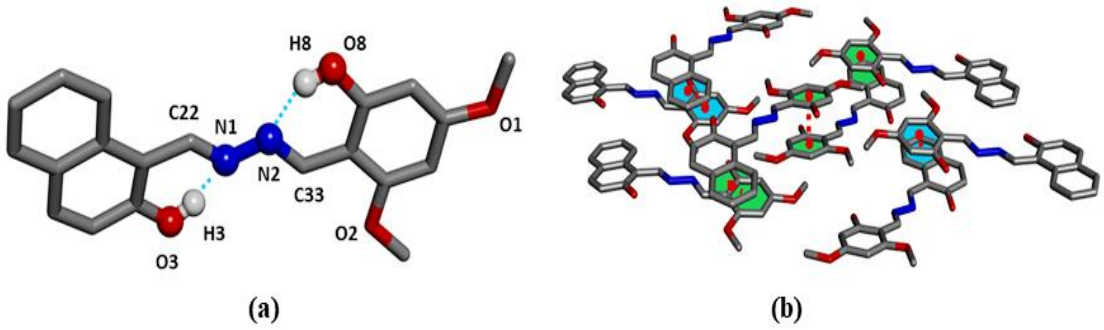

Fig.V.5 (a) Single crystal X-Ray structure of the probe. **(b)** Supramolecular assembly and occurrence of π··π interaction (4.312 Å) in molecule of H_2L due to different non-covalent interaction.

V.3.3. AIEgen Spectroscopic Study

The absorption spectrum of H_2L in acetonitrile (CH_3CN) solution exhibits multiple absorption with two intense bands at 339 and 409 nm, and are assigned to π···π* and n-π^* transitions respectively (**Fig.V.6**).

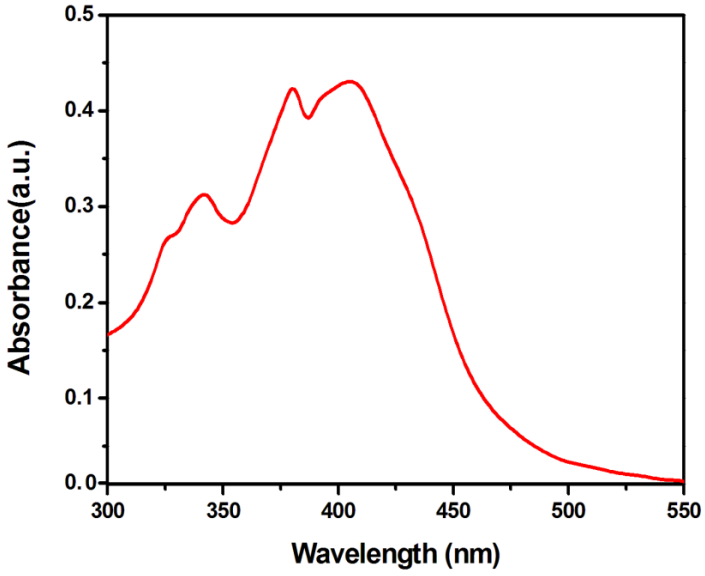

Fig.V.6. Absorption Spectrum of H_2L in CH_3CN.

The probe, H_2L is weakly emissive (λ_{em} = 503 nm; λ_{ex} = 420 nm) in pure CH_3CN (f_w = 0); on increasing addition of water (f_ws) into CH_3CN solution enhances the intensity of emission (λ_{em} = 537 nm) and the maximum intensity appears at f_w = 80%. However, further addition of water (80% < $f_w \leq$ 100%) shows gradual depletion in emission intensity presumably due to stabilization of less emissive ICT state with increasing solvent polarity. This observation refers to Aggregation Induced Enhanced Emission (AIE).[5] Moreover, increased water fractions to the solvent system of the probe lead to a bathochromic shift in the emission spectrum at f_w = 80%, emission maximum (λ_{em} = 537 nm) by 34 nm compared to pure CH_3CN (λ_{em} = 503 nm), which signifies the formation of J-type self-assembly where the instigation of RIR within the aggregated framework ultimately promotes a 152 fold enhanced fluorescence maxima together with an augmented quantum yield from 0.0025 at f_w = 0 to 0.306 at f_w = 80%, respectively (**Fig.V.7(b)**). The effect of AIE is further confirmed from the UV-photographs of H_2L in CH_3CN with varied f_ws, where execution of RIR in J-type of self-assembly confers the probe to emit bright green emission (λ_{em}, 530 nm) from CH_3CN/H_2O solvent mixture at f_w = 80% (**Fig. 7(c)**). The fluorescence (FL) spectrum in the solid phase is more intense compared

to the solution phase located at 503 nm upon excitation at 420 nm (**Fig.V.7(a)**) and λ_{em} shifts to longer wavelength.

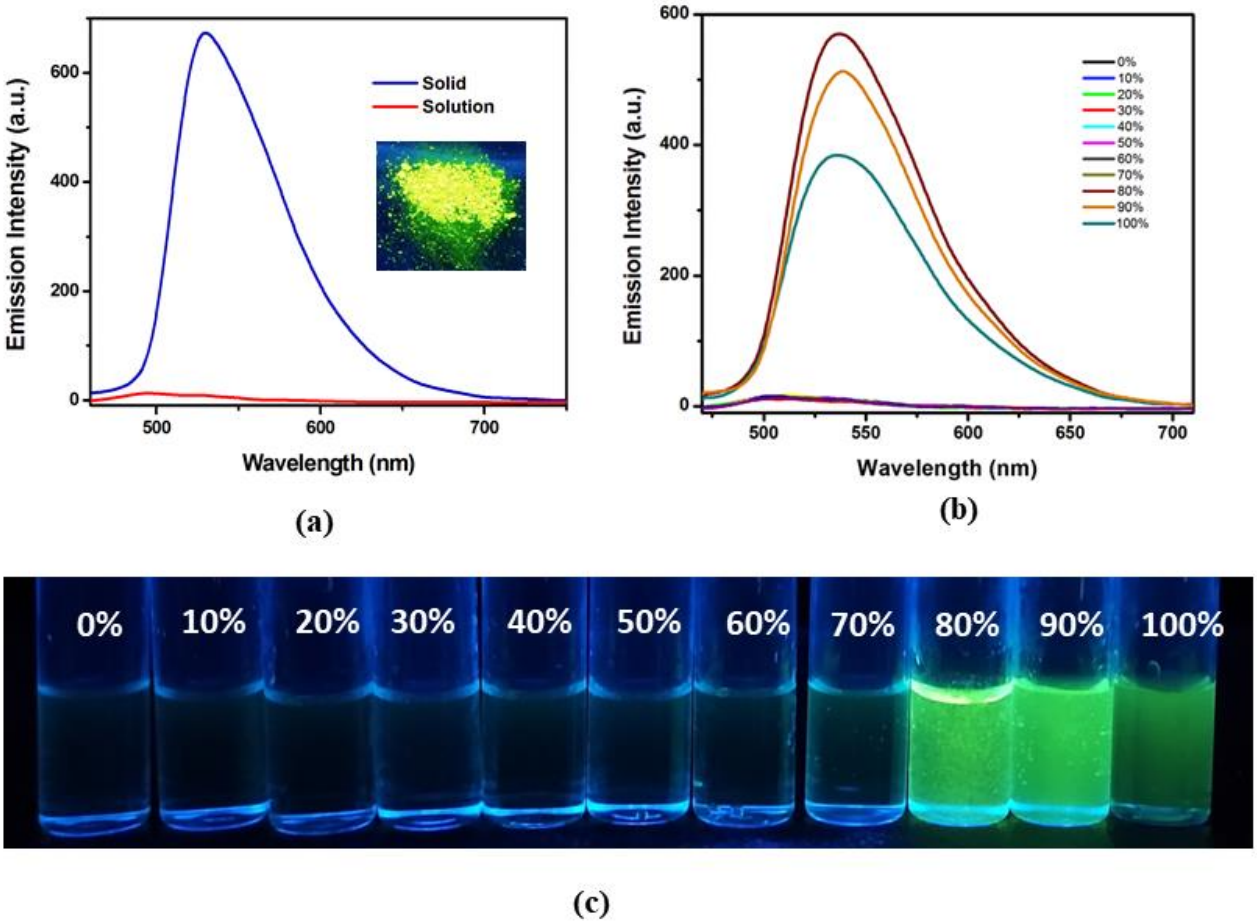

Fig.V.7. Emission spectra of the probe H_2L in **(a)** solid state (Inset: Solid State Image Under UV chamber λ_{ex} = 365 nm) **(b)** on increasing water conent in CH_3CN medium and **(c)** Vial images of AIE effect of the probe under UV chamber (λ_{ex} = 365 nm).

Apart from the fluorescence characteristics, absorption spectral measurement of the probe in CH_3CN and different CH_3CN-H_2O fraction has also been performed to explicate the AIE behaviour. Initially, H_2L exhibits absorption band at 390 nm in pure CH_3CN and upon increased f_ws, the band corresponding to f_w = 80% shows the level off tailling in the visible region (around 500-700 nm), aroused due to Mie scattering from the evolved nanoaggregates in binary solvent mixture (**Fig.V.8**).[17]

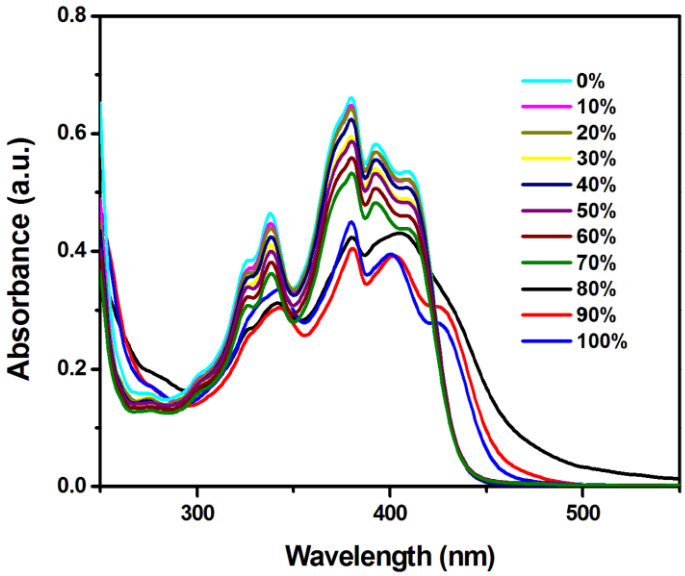

Fig.V.8. Absorption spectra of AIE phenomena of H_2L on varying CH_3CN/H_2O fraction.

Correspondingly, the Dynamic Light Scattering (DLS) measurement reveals the growth of particle size with increased f_w, which is broadened from 41.04 ± 1.0 nm in pure CH_3CN to 550 ± 6.0 nm in pure water (**Fig.V.9**).

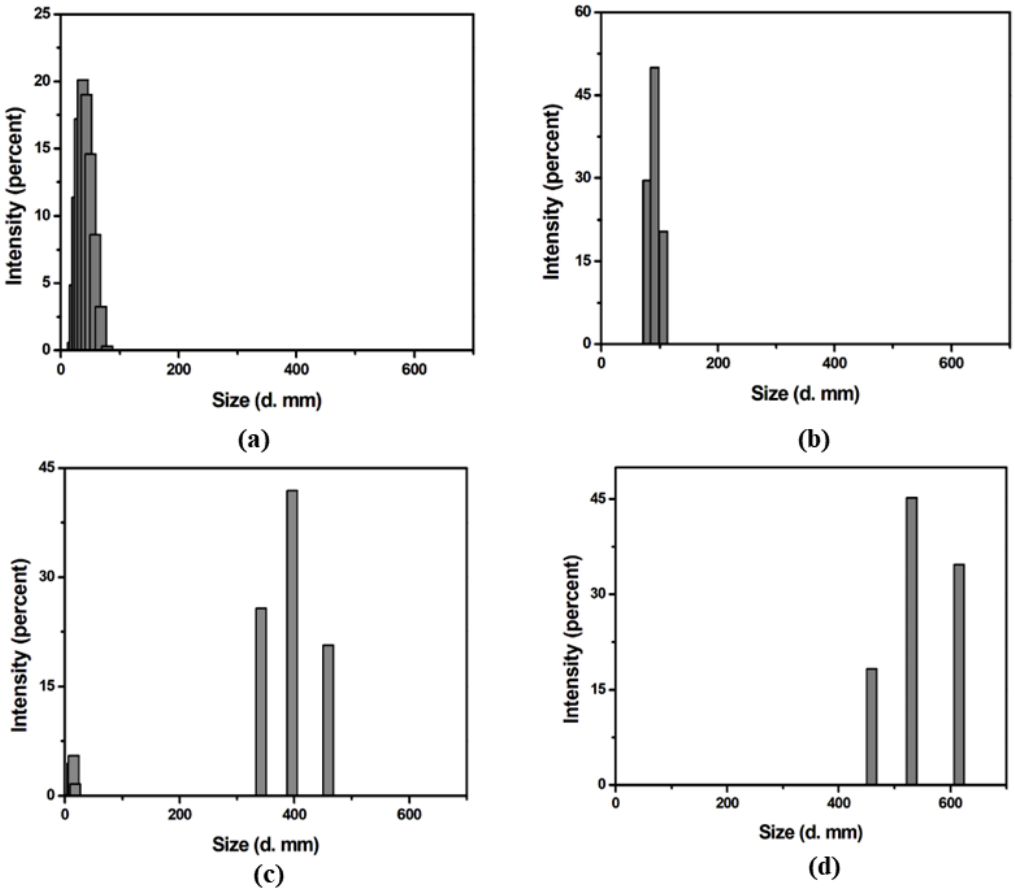

Fig.V.9. DLS Spectrum of H_2L in CH_3CN/H_2O fraction f_w (a) 0% (b) 30% (c) 80% (d) 100%

Scanning Electron Microscopic (SEM) images indicate change in the morphology of H_2L in presence of higher water fractions, where evolution of self-assembled spherical nanoparticles at f_w = 80% from a discontinuous irregular shaped particles at f_w = 0% confirms the formation such aggregates in the binary solvent mixture (**Fig.V.10**).

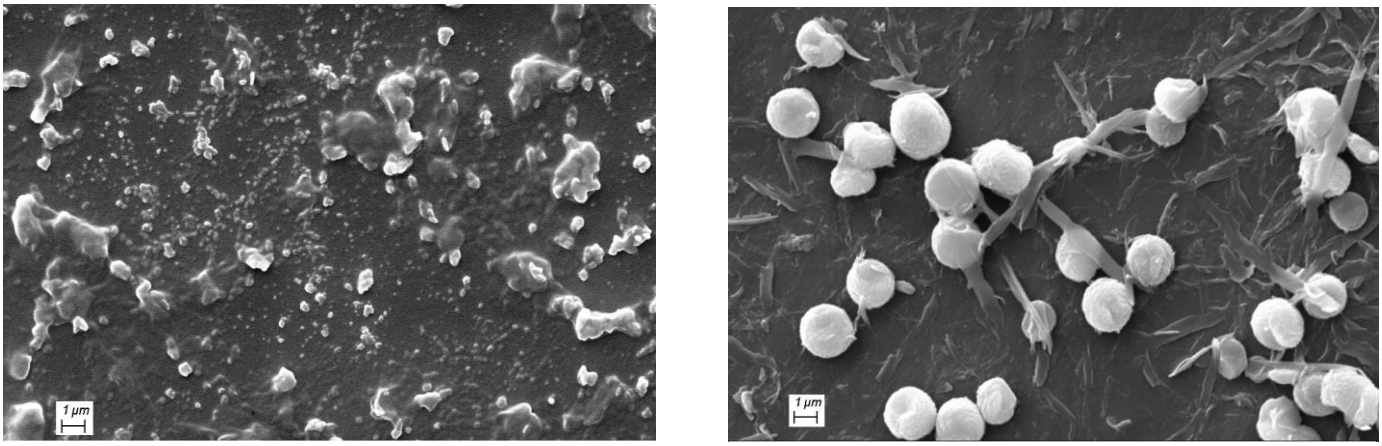

Fig.V.10. SEM images of H_2L in pure CH_3CN (f_w = 0%) (Left) and (f_w = 80%) medium (Right).

In order to understand the detailed mechanistic pathway behind AIE, viscosity-dependent fluorescence studies has been performed and the changes in the emission intensities of H_2L in CH_3CN are noted carefully with increasingly added glycerol fractions. Interestingly, upon increasing the percentage of glycerol from 0-95, the emission intensity from H_2L is concomitantly enhanced and reaches maximum at 95% gylycerol content (**Fig.V.11 (a)**). Herein, thickening of the resultant solvent mixture with increased glycerol fraction induces considerable viscous drag, which imparts rigidity to the molecule upon freezing its free rotation that inevitably elucidates more emissive behaviour for this AIE luminogen. Evidently in pure CH_3CN, free rotation of H_2L around its azine bond results in weak emission on account of non-radiative decay, whereas 41 fold augmented emission intensity in 95% gylycerol content supports the vivid effect of RIR, which enables the solid and/or aggregated state of the resultant probe to reveal the pronounced effect of AIE. Meanwhile, time resolved fluorescence decay profile of H_2L in CH_3CN/H_2O solvent mixture with different f_ws are measured, where the relaxation kinetics fits well into bi-exponential decay and shows resemblances with AIE behaviour with an increased lifetime (τ_{avg}) from 0.023 ns (f_w=0) to 4.63 ns (f_w = 80). **(Fig.V.11(b)).** [43,44]

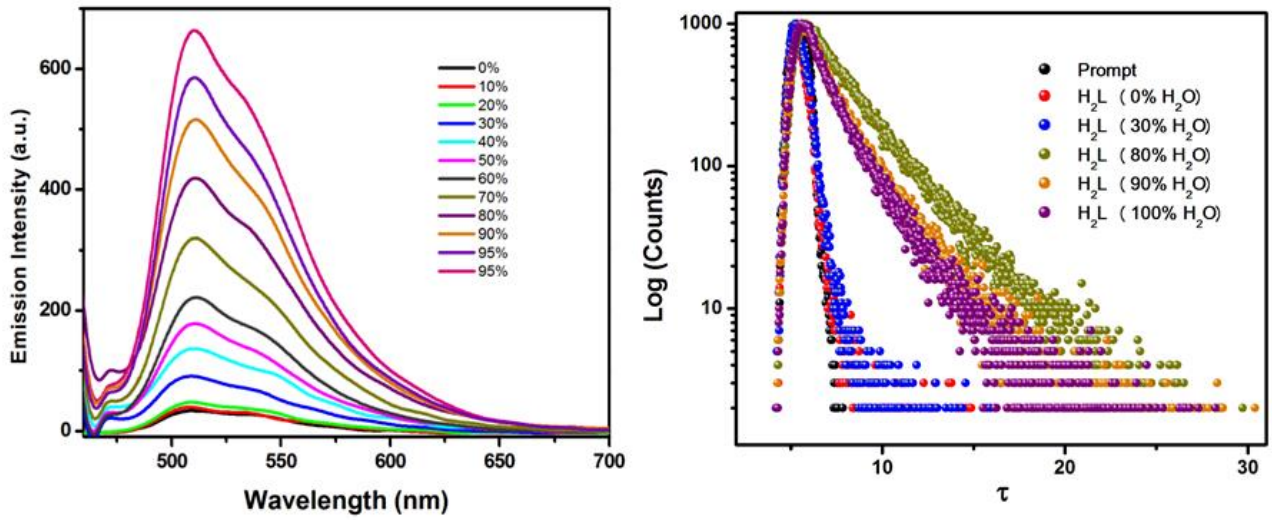

(a) **(b)**

Fig.V.11. (a) Emission spectra of H_2L in varying proportion of CH_3CN/glycerol. **(b)** Lifetime decay curve of H_2L on addition of different fraction of water.

V.3.4. Trifluoroacetic Acid (HTFA) Vapour Sensing

The enhanced fluoresence properties of aggregated state of H_2L ascertains that the resultant fluorophore might act as a promising solid state chemosensing material. The compact packing mode in solid phase results in improved fluorescence, which has further been explored as a reversible signalling protocol for a solvent-free detection to acid/base vapour. Henceforth, to check the sensory activity of aggregated H_2L, a thin film of approximately 1 cm^2 area is immersed into 10^{-3} (M) CH_2Cl_2 solution of the probe and allowed to dry in open air. Subsequently, optical behaviors of the homogeneously coated yellow-emissive thin film were noted. Firstly, the solid-state luminiscence spectrum of H_2L film reveals an intense emissive band at around 530 nm (λ_{ex} = 420 nm). Then the film upon exposure to HTFA vapour, responses rapidly through notable rapid quenching of emission, where a signficant red shift in absorption maximum indicates a distinguished chromogenic transformation from bright yellow to orange color, observed under naked eye. Such behaviour is prominent in presence of gaseous HTFA while for other acid vapours the effects are less significant even on prolonged exposure (**Fig.V.12.**).

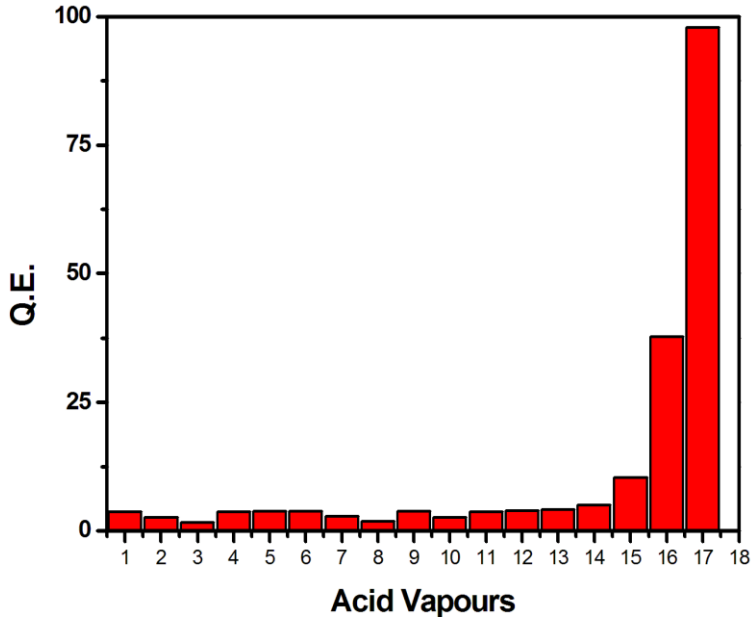

Fig.V.12. Bar plot showing Quenching Efficiencies (QE(%)) of solid emissive test kits after exposure to the saturated acid vapors of common interfering agents for 10 minutes. The analytes used are: 1. CH_3CN, 2. EtOH, 3.THF, 4. DCM, 5. n-HXN, 6. TOL, 7. phosphoric acid, 8. propionic acid, 9. sulphuric acid, 10. methane sulfonic acid, 11. methacrylic acid, 12. heptanoic acid, 13. oleic acid, 14. AcOH, 15. HNO_3 16. HCl and 17. HTFA. The emission was recorded with 5 minutes interval for each turn.

Then fluorescence titration experiment is performed for the thin film while exposing the system towards increasing concentration of HTFA vapour (0-183.35 ppm), which divulges gradual decrease in emission intensity, accompanied with shifting of the characteristics emissive band from 530 nm to 565 nm in presence of saturated HTFA vapor (**Fig.V.13(a)**). Accordingly, concentration-dependent fluorescence quenching exhibits nonlinear fluorogenic response towards entire HTFA vapor concentration, where Quenching Efficiency (QE, $1-I/I_0$) of H_2L film reaches upto 94.72%, when HTFA vapor concentration is as high as 183.35 ppm. (**Fig.V.13(b)**).

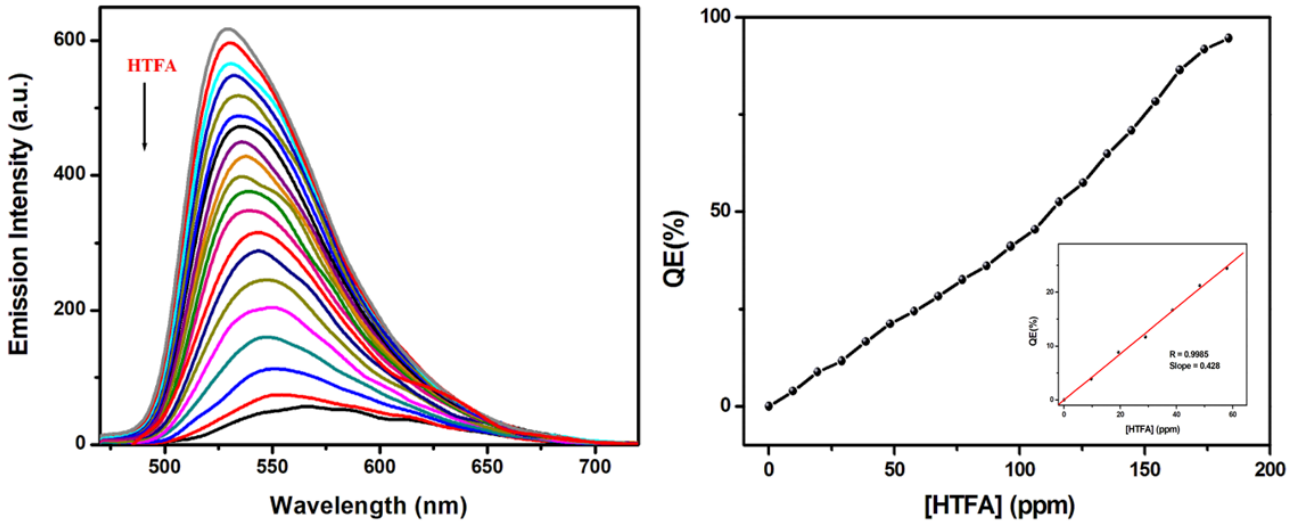

(a) **(b)**

Fig.V.13. (a) Solid-state fluoresence titration of the thin film on gradual addition of HTFA vapor **(b)** Concentration-dependent alteration in QE(%)s of H_2L in presence of HTFA.

The probe shows a rapid response time of 8.5 sec towards HTFA vapor. **(Fig. V.14(a))** Considering linear variation in QE (%)s with respect to lower HTFA vapor concentration ($0 \leq$ [HTFA] ≤ 100 ppm), Limit of detection (LOD: 3σ/slope), calculated from the luminiscence quenching titration curve is found to be as low as 1.41 ppm, which accredits the emissive self-assembled substrates as sensitive platform towards HTFA vapor detction (**Fig. V.14(b)**).

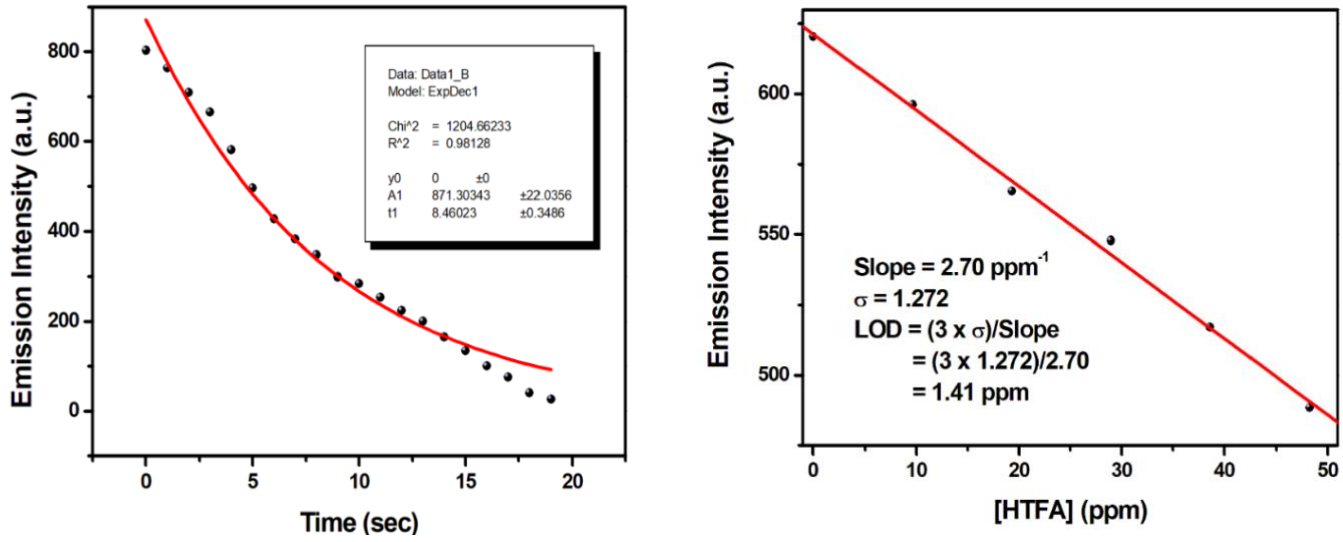

(a) **(b)**

Fig.V.14. (a) Kinetics of time dependent response Decay. **(b)** Limit of Detection for HTFA Vapor Sensing.

Next, the Stern-Volmer equation, employed on fluorogenic response of H_2L film illustrates the extent of quenching in presence of HTFA vapor. The Stern-Volmer plot of $[(I_0/I)-1]$ v/s [HTFA] displays a steep upward bending at [HTFA] > 0.52 ppm (**Fig.V.15(a)**); while a linear response is exhibited at concentration lower than that of 0.52 ppm (Inset of **Fig.V.15(a)**). The Stern-Volmer Constant (K_{SV} = 2.78 ppm^{-1}/8.0866 x 10^4 M^{-1}) is calculated from the linear segment of S-V plot, which confirms reasonable interaction between analyte and probe.[45] This proves the combination of static and dynamic quenching of emission. Also, the colorimetric response has further been verified from the remarkable red shift of the absorption band of thin film from 430 to 479 nm before and after addition of saturated HTFA vapor. (**Fig.V.15(b)**).

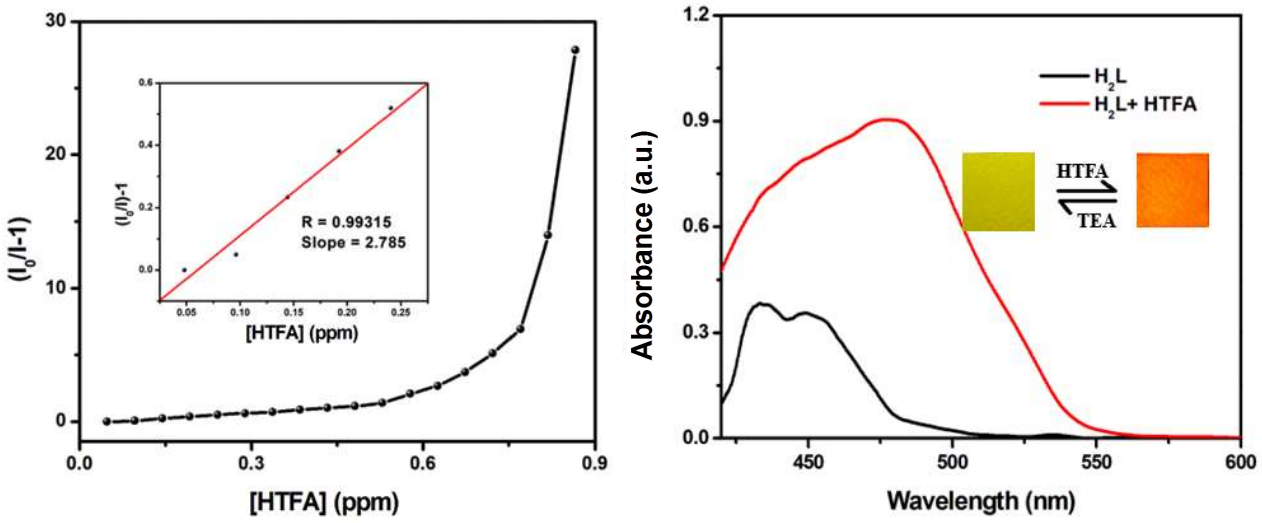

Fig.V.15. (a) Stern-Volmer plot of H_2L towards increased addition of [HTFA]. Inset: linear variation in Fluoresence intensity under lower analyte concentration. **(b)** Absorption spectra of the thin film ifself and under HTFA vapor (Inset: solid film of the probe on exposure to HTFA vapour (under normal light).

V.3.5. Reversibility of the probe in presence of HTFA/TEA vapour

Reversibility of a material has been demonstarted as an important parameter for its reusuability in the sustainable development. Accordingly, self-assembled film from H_2L is allowed to expose sequentially towards saturated vapors from HTFA and NEt_3 (TEA). Meanwhile, FESEM images clearly demonstrates the desired changes in the respective morphologies before and after treatment with HTFA vapor followed by an

exploration of the acid-treated film in TEA vapor. The morphology of free probe depicts a robust interconnecting plate like porous network of aggregated probe, which upon treatment with HTFA collapses to disorded structure, causing quenching in emission intensity. Interestingly, a densely aggregated morphology started to evolve again in presence of TEA vapor with restored emission intensity (**Fig.V.16**). Importantly, the film acts as a recyclable emissive and colorimetric optical switch which turns off its emission and alter its visible color from yellow to orange in presence of HTFA due to the disrruption in ordered morphology. Notably, it switches on original emission and recovers its yellow color under naked eye upon expsosure to TEA.

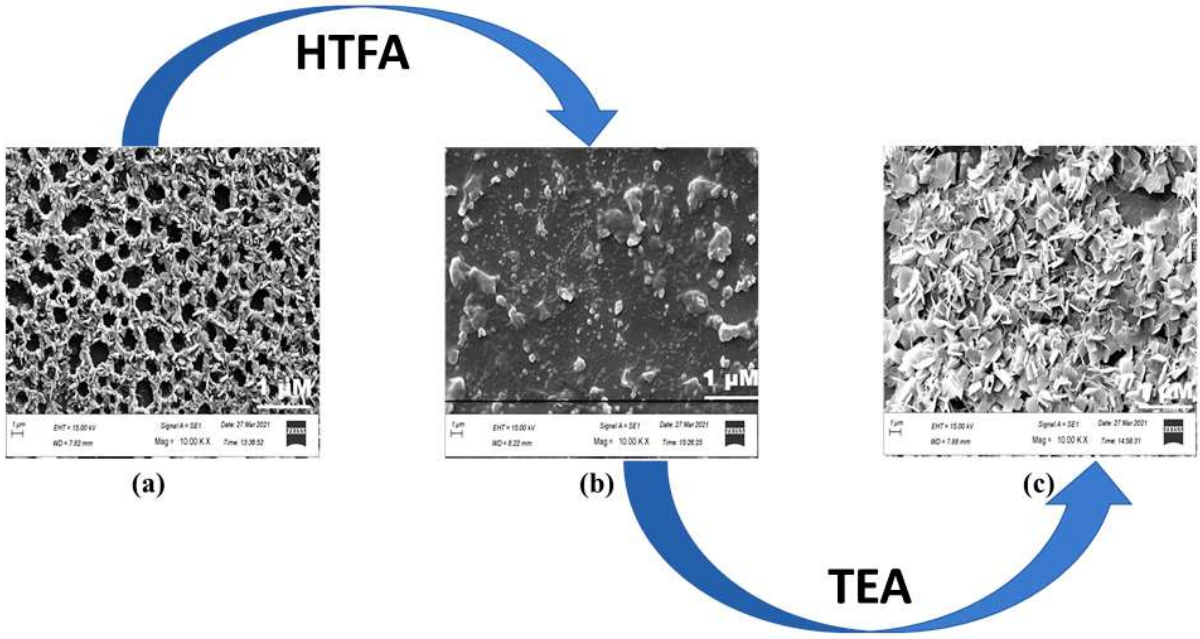

Fig.V.16. FESEM images of the H_2L **(a)** unreacted form and on treatment with **(b)** HTFA and **(c)** TEA.

The reversibilty of the probe can be repeated upto 6 cycles. **(Fig.V.17.(a))**. Powdered X-Ray Diffraction (PXRD) pattern clearly explains the reversible acidochromic behaviour of probe in presence of HTFA/TEA vapour exposure. The PXRD of free probe with sharp and intense reflection peaks changes into relatively less intense diffractogram in presence of HTFA, which almost retains back to its pattern of free probe in presence of TEA (**Fig.V.17.(b)**).

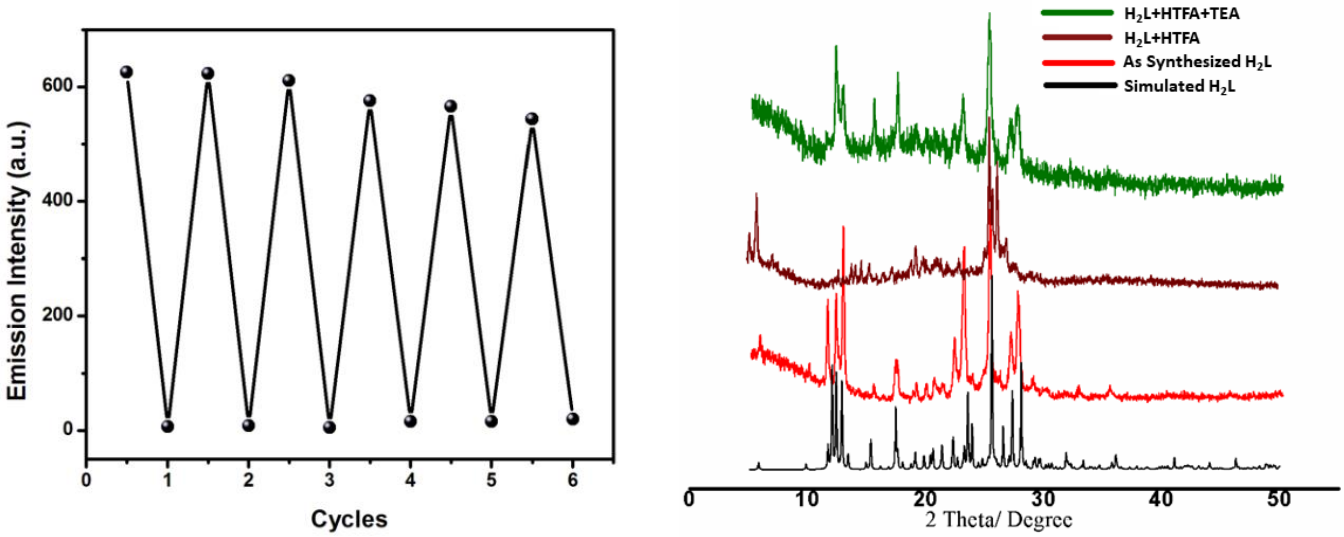

(a) **(b)**

Fig.V.17. (a) Reversibilty of the probe H_2L to HTFA/TEA cycles. **(b)** PXRD patterns of the probe in presence of HTFA, TEA.

The reversibility has been confirmed through ^{1}HNMR titration of H_2L with successive addition of HTFA and TEA in $CDCl_3$ solvent. On addition of HTFA, the phenolic protons (OH (1,10)) attributed to naphthyl and dimethoxyphenyl moeity at 13.12 and 12.41 ppm are completely vanished with the generation of broad signal at 8.95 ppm due to the protonation in imine nitrogen (N=CH(9)) of the methoxy unit. The resultant shifting in peak position is attributed to the proton transfer from the carboxylic group of HTFA to the imine N forming an ionic compound. The aromatic protons attached to the naphthyl ring remains unaltered. Out of the two aromatic protons attached to dimethoxyphenyl unit, (C-H(12)) present adjacent to the methoxy unit exhibits downfield shifts from 6.20 to 6.55 ppm while the other gets unaffected. When TEA is added to the acidified solution most of peak regenerates except the phenolic –OH signals and this phnomena may occur due to the presence of base (TEA) which capture the proton from -OH (**Fig.V.18**).[46]

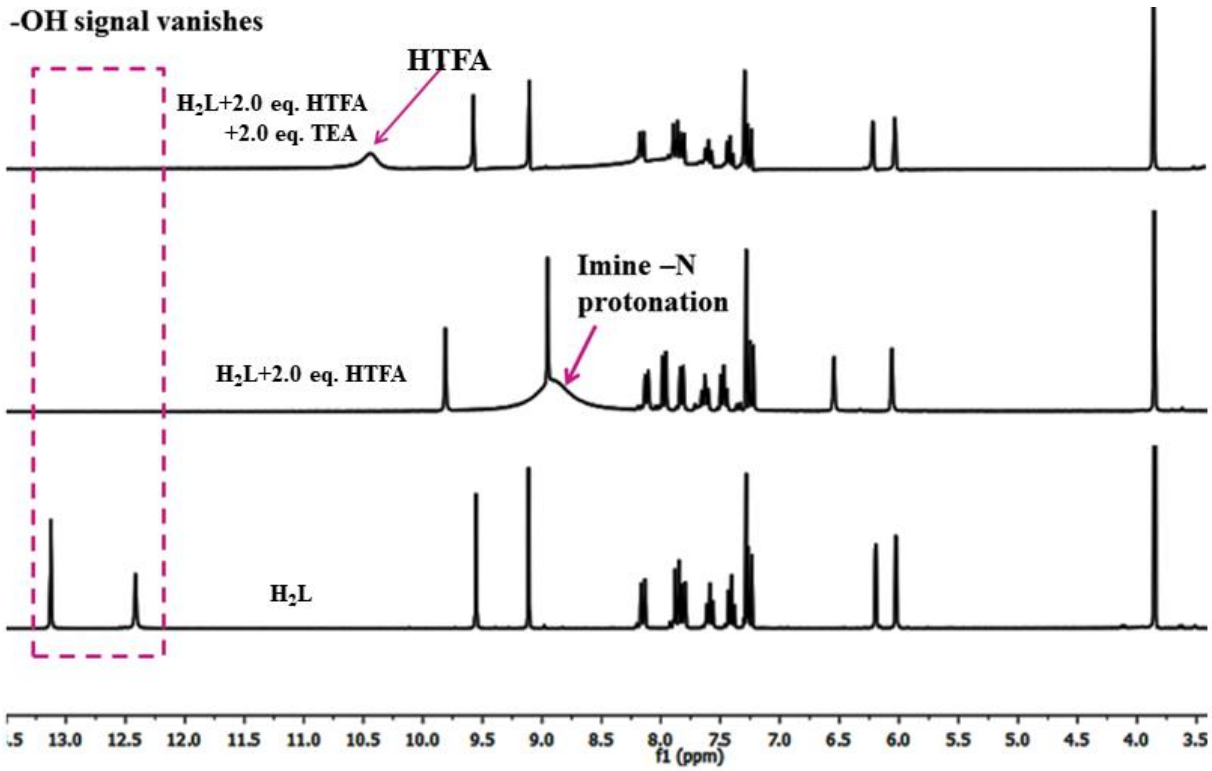

(δ, ppm)

Fig.V.18. ^{1}HNMR titration of H_2L on addition of HTFA/TEA in $CDCl_3$.

The reversible acidochromic response of the probe upon treatment with HTFA/TEA has further been employed for the fabrication of information sheilding application which enables a reusuable write-erase fluoresence platform. The non-fluorescent Whatman filter paper were dipped in CH_2Cl_2 solution of H_2L and air dried. The probe coated paper emits a bright green fluorescence upon excitation under UV chamber (λ_{ex} = 365 nm). The inscriptions referred to '**JU**' is written using CH_2Cl_2 solution of HTFA which became readable and appeared as orange color letters under normal light and exhibits quenching under UV/light irradiation. The information gets easily erased upon exposing to TEA vapor within 15 seconds after writing. Thus a rapid reversible behaviour of the probe has been verified for write-erase-write application over multiple cycles under ambident conditions (**Fig.V.19**).

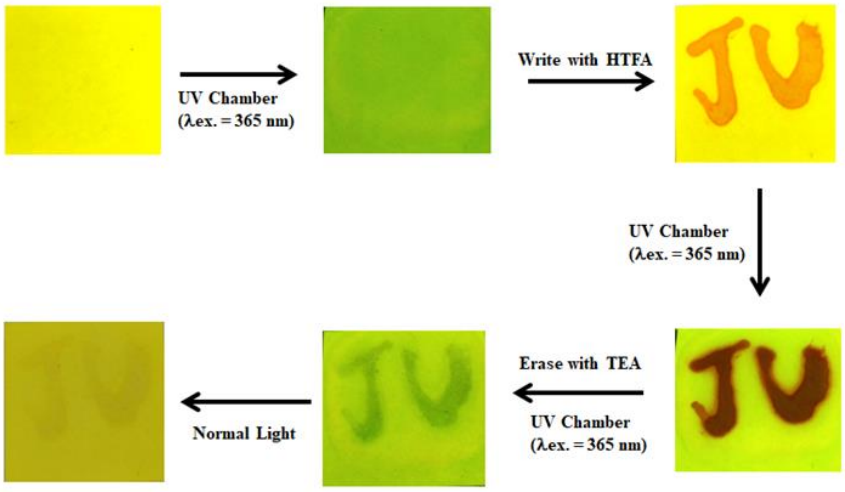

Fig.V.19. Write-Ersae-Write application of H_2L using HTFA/TEA vapour.

V.3.6. CN^- Sensing

Along with solid-state acidochromism, the probe, H_2L exhibits interesting chemosensing properties in solution phase. Conversely, the solution-phase chromogenic response from H_2L has been verified upon treating the probe with various anions (Cl^-, Br^-, I^-, CN^-, S^{2-}, CH_3COO^-, $S_2O_3^{2-}$, SO_4^{2-}, F^-, HF_2^-, SCN^-, NO_3^-, NO_2^-, N_3^-) in CH_3CN/H_2O (99:1, v/v; HEPES Buffer, pH 7.3) medium. Upon adding 2.0 equivalent of several anions, only CN^- induces a prominent naked eye colorimetric response from colourless to orange while other anions essentially remain silent. Then the selective colorimetric response has been confirmed from UV-Vis absorption study which shows the appearance of newly aroused low energy band around 479 nm specifically in case of CN^- while for the rest of the anions, the characteristic peaks remain unaffected as observed in the spectra (**Fig.V.20 (a) & (b)**). Consequently, the sensitivity of the probe was investigated in detail by UV-Vis absorption titration experiment with CN^-. On gradual addition of CN^- to the probe solution in CH_3CN/H_2O (99:1, v/v; HEPES Buffer, pH 7.3) medium, the existing absorption maxima at 381, 392 and 409 nm gradually decreases with concomitant generation of new broad band at 479 nm. Upon increased CN^- concentration, the absorption band varies linearly with a well-defined isobestic point at 430 nm and finally attains saturation after addition of 2.0 equivalents CN^- (**Fig.V.20(c)**).

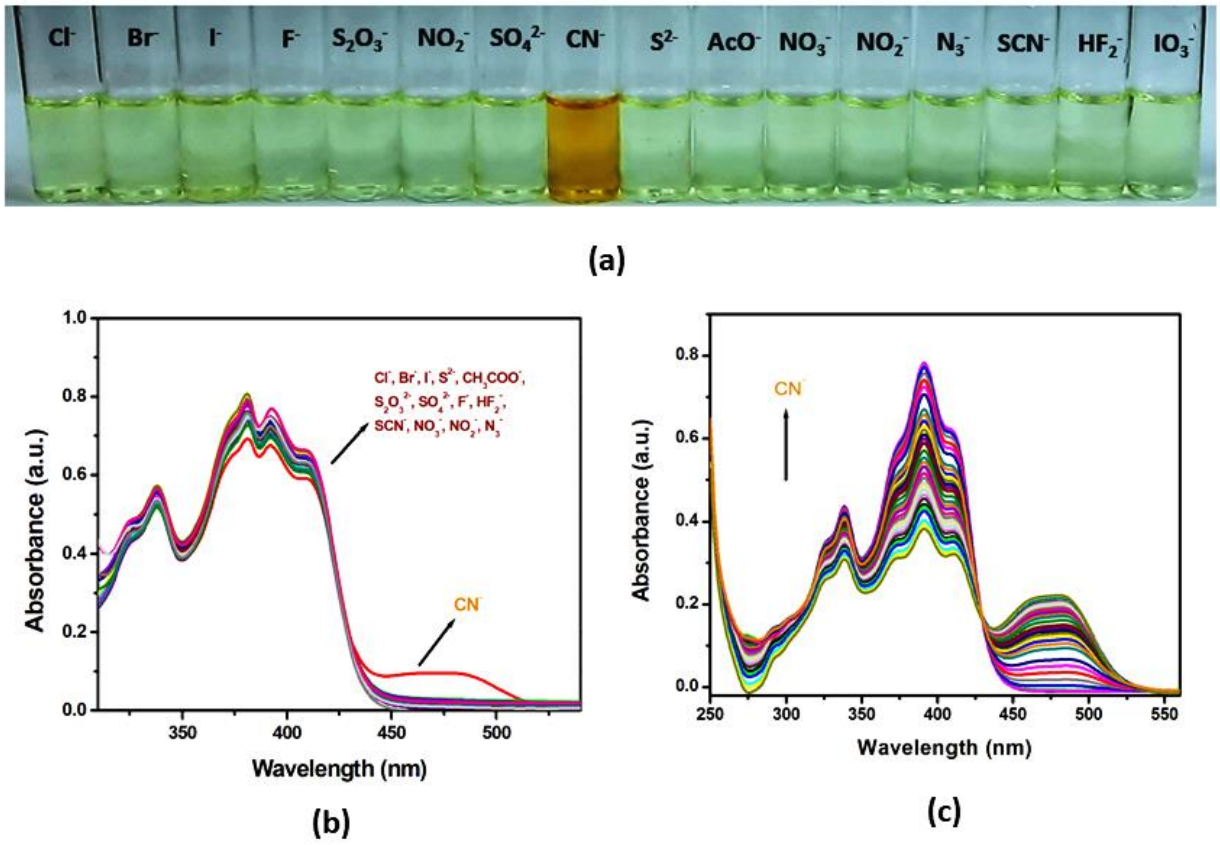

Fig.V.20.(a) Vial images. **(b)** Absorption Spectra of the probe on addition of anions (2 equivalent) in CH_3CN/H_2O (99:1, v/v; HEPES Buffer, pH 7.3) medium. **(c)** Change in Absorption Spectra of the probe on incremental addition of CN^- to H_2L in CH_3CN/H_2O (99:1, v/v; HEPES Buffer, pH 7.3) medium.

Next, the fluorogenic response of H_2L have further been examined upon monitoring variation in emission spectral response of probe in presence of aforementioned different anions (Cl^-, Br^-, I^-, CN^-, S^{2-}, CH_3COO^-, $S_2O_3^{2-}$, SO_4^{2-}, F^-, HF_2^-, SCN^-, NO_3^-, NO_2^-, N_3^-) in CH_3CN/H_2O (99:1, v/v; HEPES Buffer, pH 7.3) medium. The enhancement of emission intensity was observed only in case of CN^- while others exert negligible effect. Upon exciting the probe at 460 nm, H_2L exhibits 20 fold enhanced fluorogenic response selectively towards CN^- with emissive band centred around 565 nm. (**Fig.V.21 (a))** On incremental addition of CN^- (0-55 μM) into the probe solution (25 μM), the emission intensity gradually increases till it attains saturation on 2.0 equivalent CN^- addition and the change in emission intensity varies linearly with increasing concentration of CN^- (**Fig.V.21 (b)**).

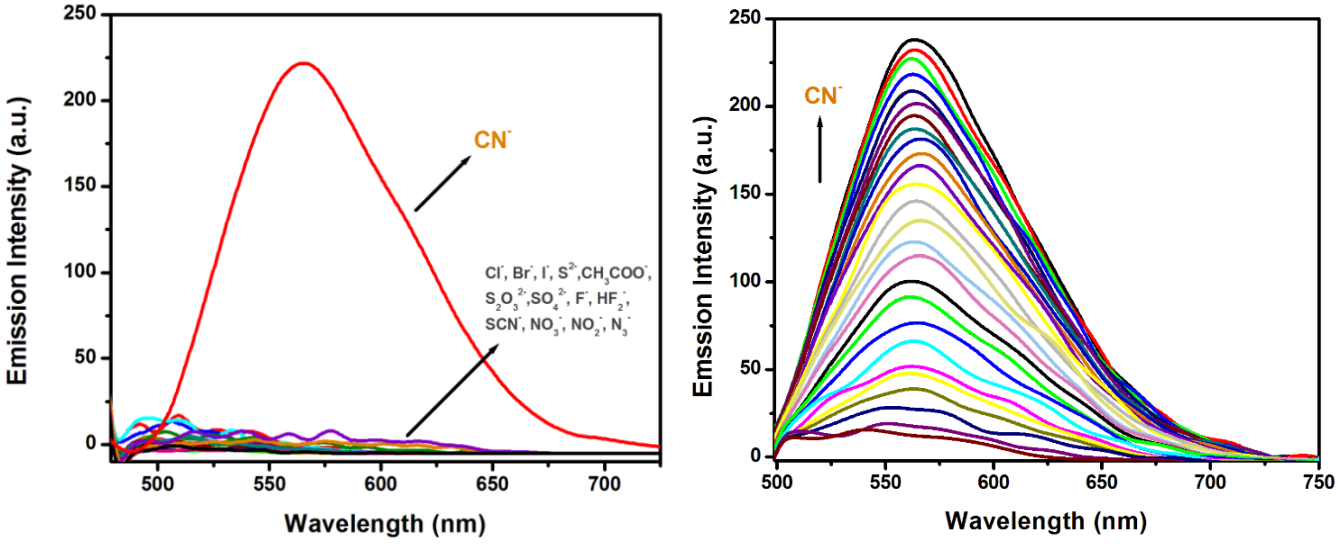

(a) **(b)**

Fig.V.21. (a) Emission spectra of H_2L on addition of different anions (2 equivalents) in CH_3CN/H_2O (99:1, v/v; HEPES Buffer, pH 7.3) medium. **(b)** Change in the emission spectra of H_2L (25 μM) on gradual addition of CN^- (0-55 μM).

Meanwhile, the limit of detection (LOD: 3σ/slope), estimated from the absorption titration curve is calculated as 45.42 nM (**Fig.V.22 (a)**), which is found to be compatible or even better than LOD of some reported colorimetric probes (**Tables V.3**). Incidentally the binding constant, evaluated from the Benesi Hildebrand plot is 9.27×10^4 M^{-1}, which indicates a stable association of probe H_2L with CN^- (**Fig.V.22 (b)**).

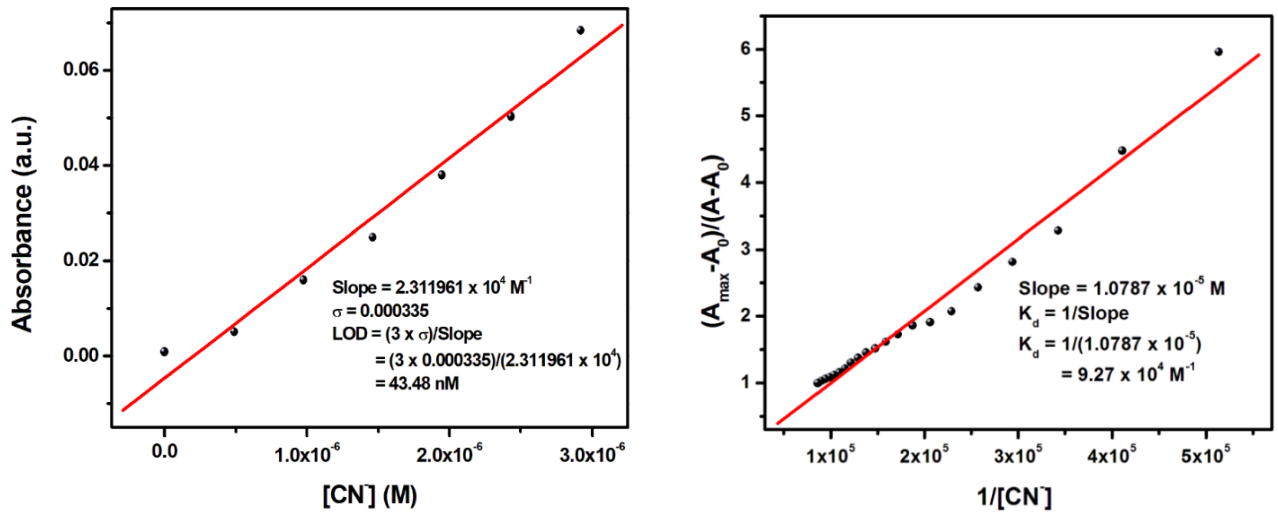

(a) **(b)**

Fig.V.22.(a) Limit of Detection for CN^- sensing of the probe H_2L. **(b)** Binding Constant (K_d) from Benesi-Hildreband Plot of the corresponding CN^- absorption titration Curve.

Table V.3: Reported Probes for CN^- detection along with their LOD

Sl. No.	Reported Probes	Solvent	LOD	References
1.	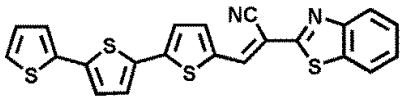	DMSO/H_2O (9:1)	0.46 μM	[47]
2.	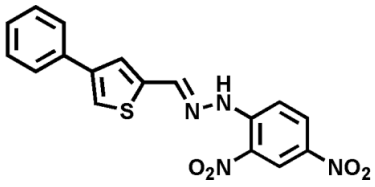	CH_3CN/H_2O (7:3)	46.2 nM	[48]
3.	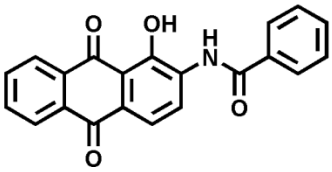	CH_3CN/H_2O (95:5)	0.22 μM	[49]
4.	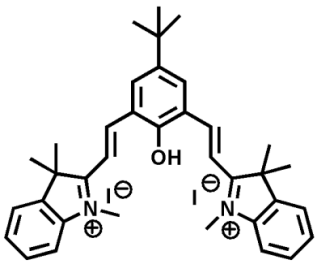	DMSO	21 nM	[50]
5.	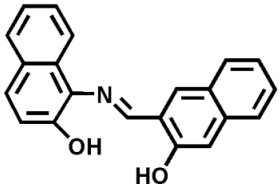	DMF/H_2O (1:1)	0.21 μM	[51]
6.	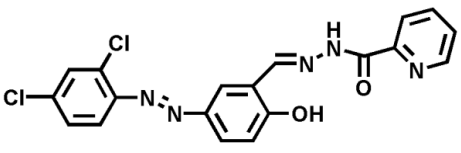	DMSO/H_2O (6:4)	6.4 μM	[52]

7.	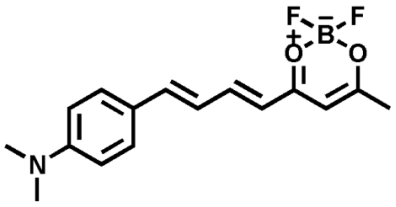	THF/H_2O (8:2)	2.23 μM	[53]
8.	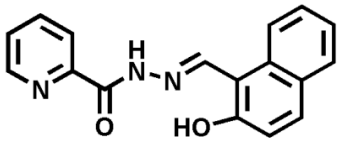	DMSO/H_2O (9:1)	7.8 μM	[54]
9.	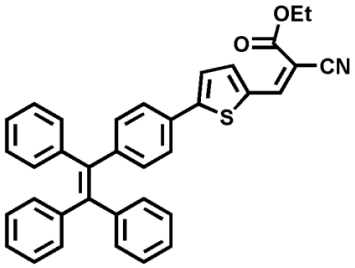	DMSO	67 nM	[55]
10.	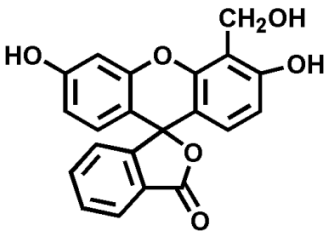	CH_3CN	3.68 μM	[56]

^{1}H NMR titration of the probe with CN^- in DMSO-d_6 explains the interaction of the probe in presence of varying proportion of CN^-. On addition of 1 equivalent CN^-, the phenolic proton (OH (1,10)) singlet of at 12.72 and 12.26 ppm attributed to naphthyl and aromatic unit disappears. The imine peak (N=CH(8)) corresponding to that of naphthyl ring undergoes significant upfield shift from 9.85 to 9.52 ppm compared to that of shifting of imine singlet (N=CH(9)) of aromatic unit from 9.02 to 8.97 ppm. The doublet signal appears at 8.61 ppm (C-H (3)) results in only downfield shift and merges with imine singlet. The remaining protons of naphthyl unit undergoes an upfield shifting where the two protons (C-H (11,12)) corresponding to the aromatic

unit exhibits marginal shifting from 6.20 to 6.16 ppm. The overall shielding effect, resulted from the negative charge of deprotonated ligand is clearly depicted in the ^1H NMR titration of the probe with CN^- (**Fig.V.23**).

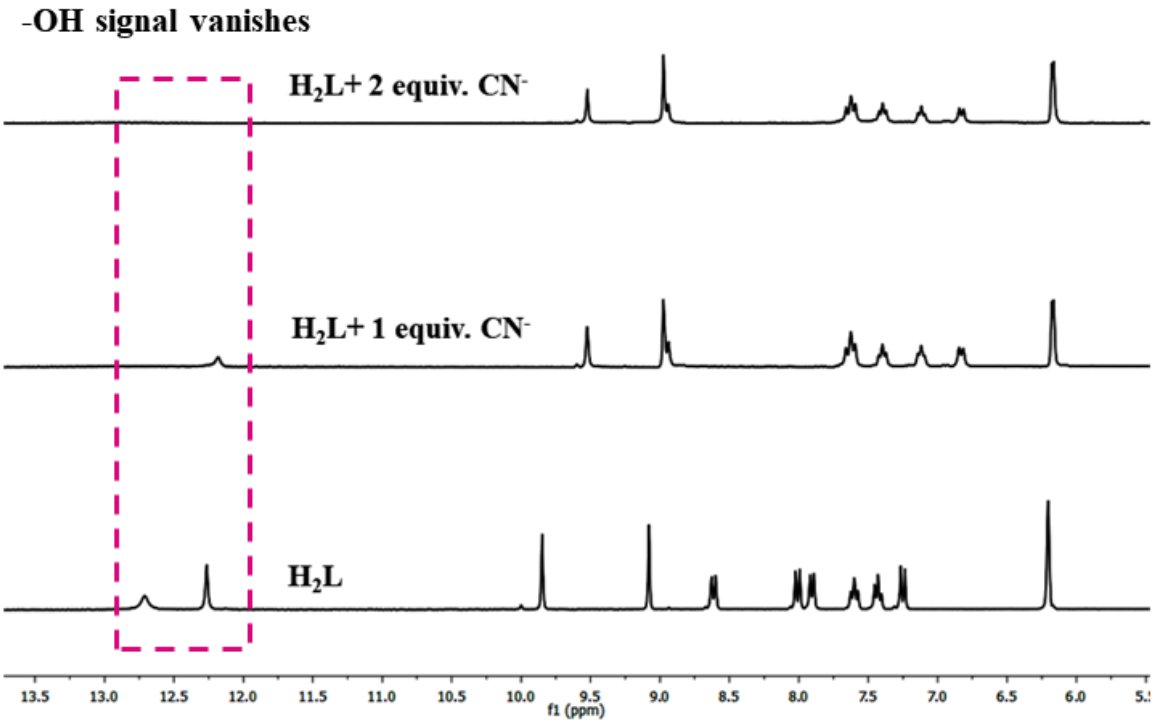

Fig.V.23. ^{1}HNMR Titration of H_2L on successive addition of CN^- (DMSO-d_6)

The deprotonation brings about a charge separation between acceptor and donor, which ultimately results in the appearance of a red-shifted low energy band at 472 nm in the absorption spectra. The enhancement in the emission spectra towards CN^- could be accredited to an extensive delocalization of charge between deprotonated oxygen centres and the aromatic as well as naphthyl rings, which breaks the intramolecular hydrogen bonding owing to charge separation and leads to an enhanced intramolecular charge transfer (ICT) for its effective "turn on" response. Nonetheless, the overall results clearly depict that the probe H_2L acts as a selective and sensitive naked eye colorimetric and "turn on" fluorogenic sensor towards CN^-.[57-61] IR spectrum of the CN^- complex indicates the absence of phenolic peak at 3393 cm^{-1} which validates deprotonation mechanism and a slight shifting of the two imine peaks at 1620 and 1583 cm^{-1} with respect to that of the free probe (**Fig.V.24**).

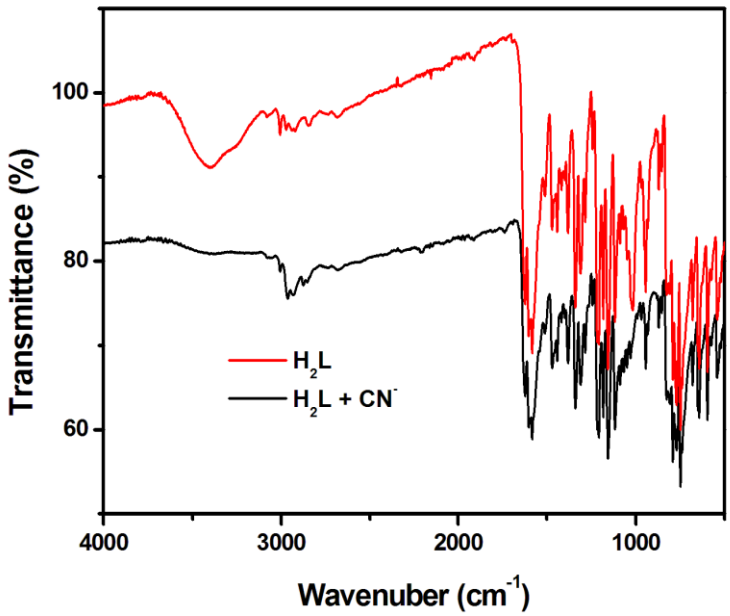

Fig.V.24. IR Spectrum of CN^- Complex.

The mass spectrum of the probe with CN^- in anionic mode gives out both the peak at m/z value of 174.2801 for its dianionic forms and 349.6396 respectively for its monoanionic form, which ascertains the desired anionic species and mechanistic pathway. (**Fig.V.25.**).

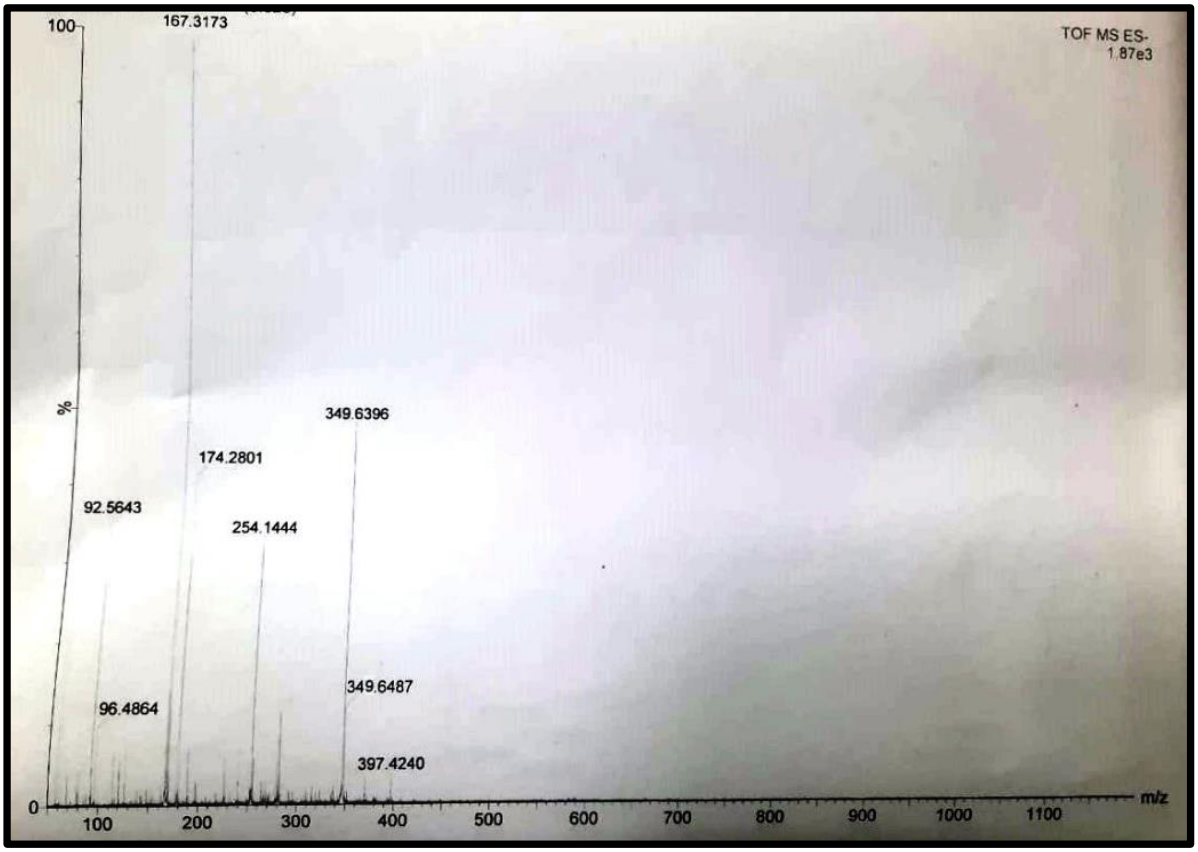

Fig.V.25. ESI-MS(-) mode of CN^- Complex (L^{2-})

V.3.7. DFT Computational Study

In order to decipher the chemosensing activity of probe in presence of CN^-, Density Functional Theory (DFT) calculation has been performed using X-Ray coordinates of the probe (H_2L) and optimised geometry of probe in presence of CN^- (L^{2-}) by B3LYP method and 6-311G basis set of Gaussian Program Package 09. The calculated theoretical bond lengths and angles of the probe are listed in **Table V.4** and the optimized geometry of the probe and its deprotonated form (L^{2-}) are represented in **Table V.5.** From the TD-DFT calculation, selected transitions are enlisted and subsequently tabulated in the **Table V.6.**

Table V.4: Theoretical Bond Length and Bond angle from Optimized structure of H_2L.

Bond Length (Theoretical)	Å	Bond Angle (Theoretical)	Degree (°)
N12-N13	1.415	C14-N13-N12	112.49
N12-C11	1.312	C11-N12-N13	113.72
C11-C10	1.447	N12- C11-C10	121.81
C10-C9	1.414	C11-C10-C9	119.44
C9-O20	1.358	C10-C9-O26	121.86
O20-H44	1.024	C9-O20-H44	108.88
N13-C14	1.303	N13-C14-C15	126.41
C14-C15	1.449	C14-C15-C16	118.91
C15-C16	1.418	C15-C16-O21	123.05
C16-O21	1.389	C16-O21-H37	113.16

Tables V.5: Optimized Geometry of H_2L and L^{2-}.

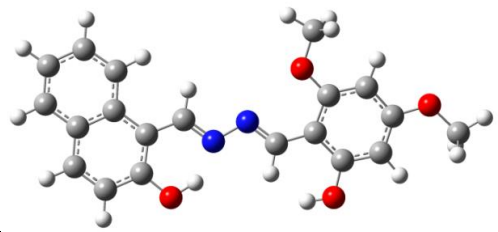	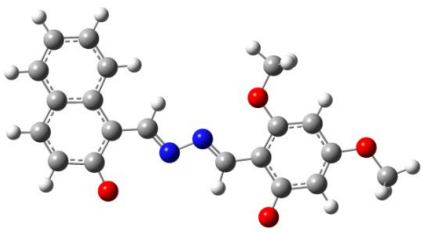
H_2L	**CN^- Complex (L^{2-})**

Table V.6: TD-DFT transition of H_2L and CN^- complex (L^{2-}.

System	Excitation Energy (eV)	Exp. Wavelength (nm)	Theor. Wavelength (nm)	Oscillation Frequency	Key Transition
H_2L	3.0311	409.04	410	1.0890	HOMO →LUMO
	3.7105	334.15	337	0.1594	HOMO-4 →LUMO
L^{2-}	2.7410	474	452.33	0.8995	HOMO →LUMO
	3.9154	338	316.66	0.0283	HOMO-1→LUMO+1

The HOMO-LUMO gap of the probe, H_2L 3.40 eV which is sternly decreased on deprotonation (L^2) upon binding with CN^-, 2.84 eV with the electronic distribution mainly concentrated on the naphthyl ring in the LUMO (**Fig.V.26**). This reduced energy gap explains the observed decrement in the absorption wavelength of the probe in presence of CN^- through deprotonation pathway. Selected orbitals along with their energy are listed in the **Tables V.7,8**.

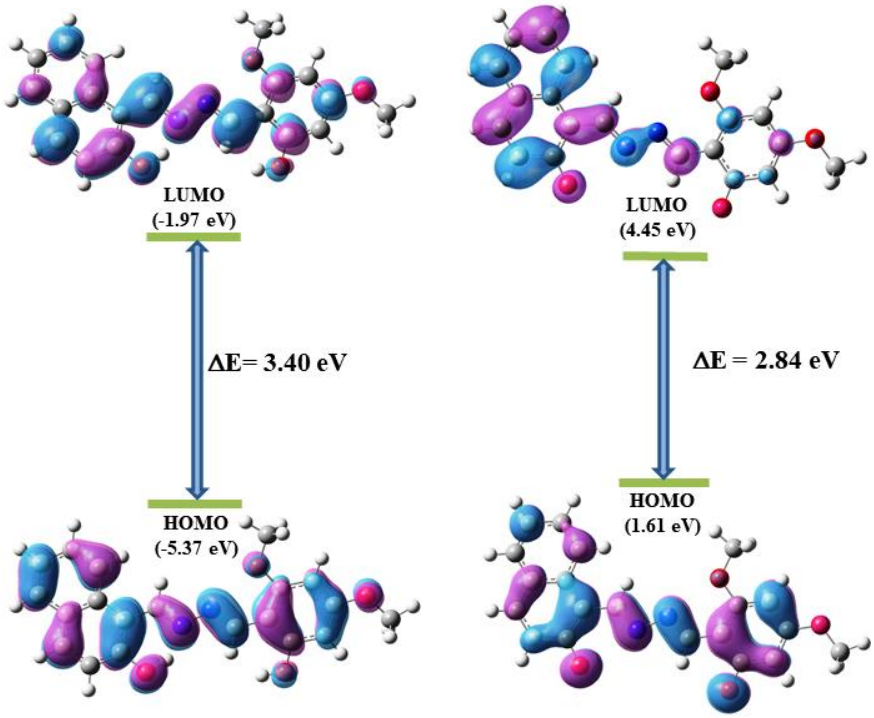

Fig.V.26. HUMO-LUMO gaps of H_2L and L^{2-} from DFT Calculations.

Tables V.7: Orbitals of H_2L and their corresponding energies

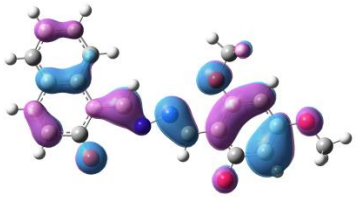 **HOMO-5** **(0.01 eV)**	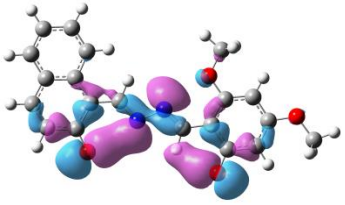 **HOMO-4** **(0.15 eV)**	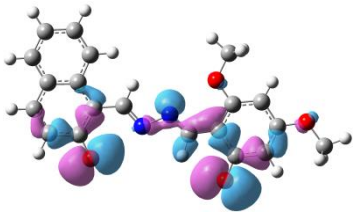 **HOMO-3** **(0.41 eV)**
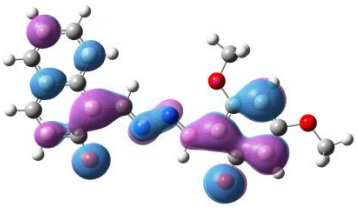 **HOMO-2** **(0.93 eV)**	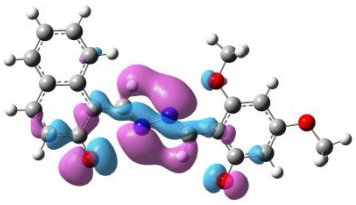 **HOMO-1** **(1.02 eV)**	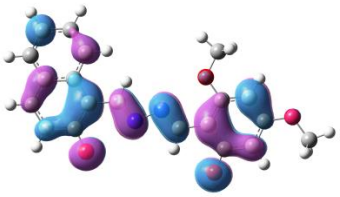 **HOMO** **(1.61 eV)**
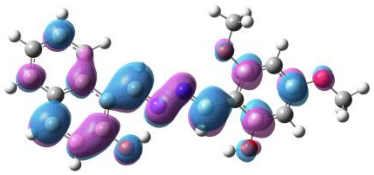 **LUMO** **(4.45 eV)**	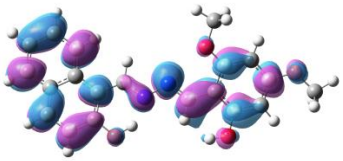 **LUMO+1** **(5.06 eV)**	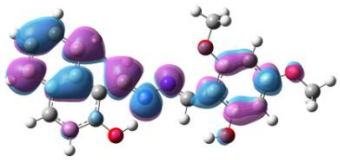 **LUMO** **(5.44 eV)**
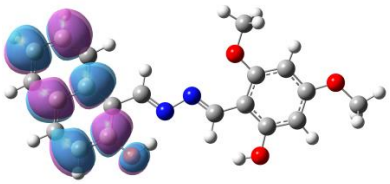 **LUMO** **(5.68 eV)**	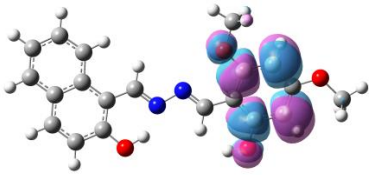 **LUMO** **(5.79 eV)**	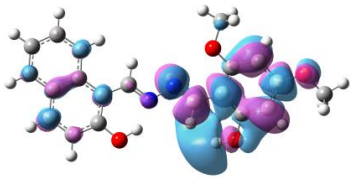 **LUMO** **(5.91 eV)**

Tables V.8: Molecular Orbitals of L^{2-} and their corresponding energies

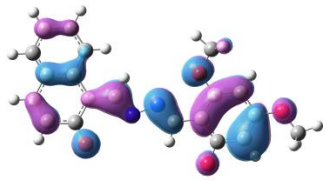 **HOMO-5** **(0.01 eV)**	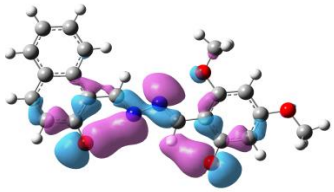 **HOMO-4** **(0.15 eV)**	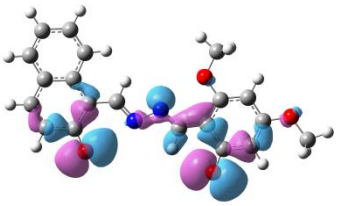 **HOMO-3** **(0.41 eV)**
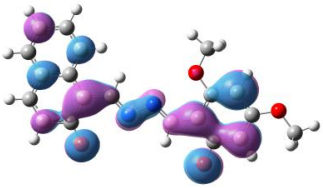 **HOMO-2** **(0.93 eV)**	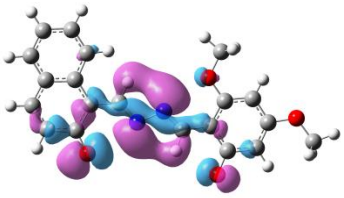 **HOMO-1** **(0.93 eV)**	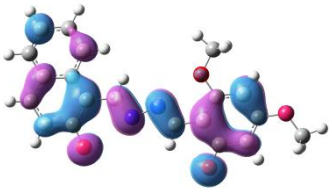 **HOMO-1** **(0.93 eV)**
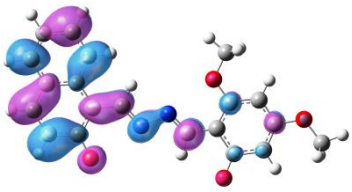 **HOMO-2** **(0.93 eV)**	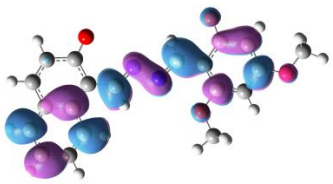 **HOMO-2** **(0.93 eV)**	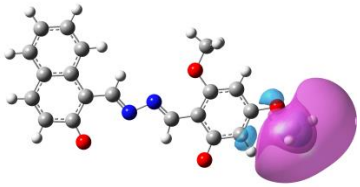 **HOMO-2** **(0.93 eV)**
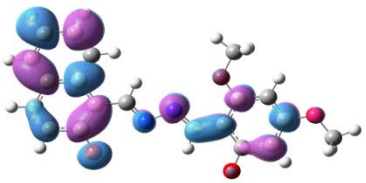 **HOMO-2** **(0.93 eV)**	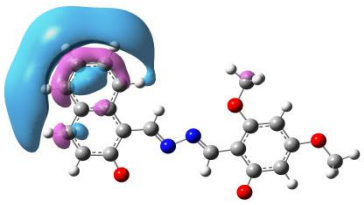 **HOMO-2** **(0.93 eV)**	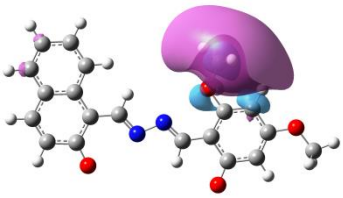 **HOMO-2** **(0.93 eV)**

V.3.8. Reversibility CN^-/HTFA

The reversibility of the CN^- detection has also been checked in presence of gradual addition of HTFA (H^+) solution [10^{-3} (M)], where restoration of original absorbance at 381, 392 and 409 nm with concomitantly reduced red-shifted absorbance at 479 nm, clearly demonstate re-protonation of L^{2-} by HTFA to unearth the original product H_2L (**Fig.V.27 (a)**). The outcome is also accompanied with decoloration of CN^--treated solution of H_2L in presence of HTFA (**Fig.V.27 (b)**). The reversible colorimetric response on addition of HTFA can be repeated up to 5 cycles.

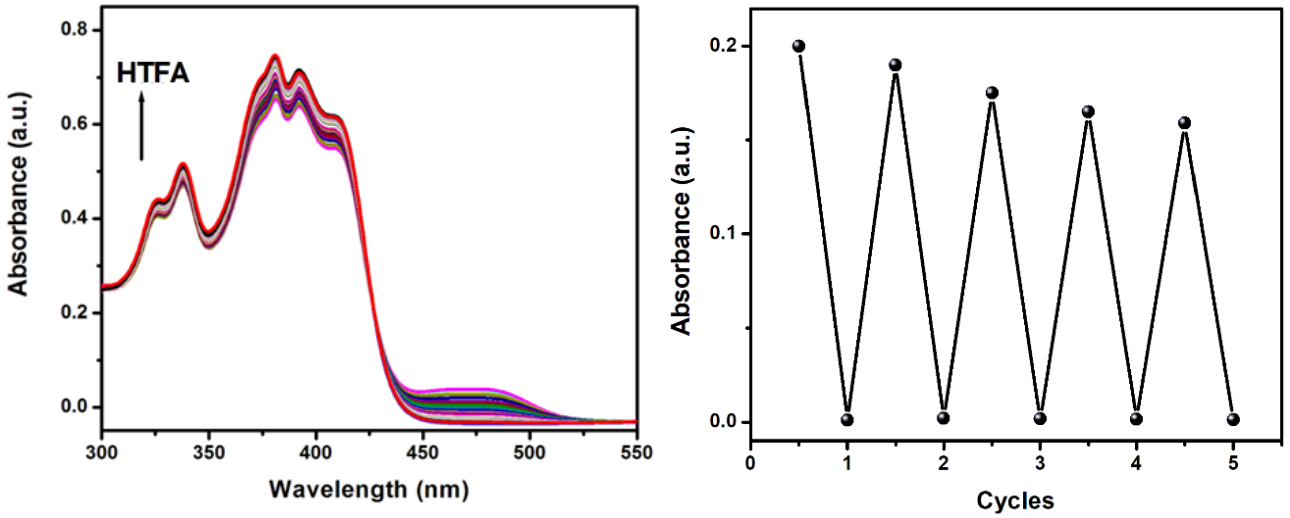

(a) **(b)**

Fig.V.27. (a) Change in the Absorption Spectra of CN^- Complex on gradual addition of TFA (H^+). **(b)** Reversible Cycles on addition of CN^-/H^+.

V.3.9. Biological Applications

In-vivo cell cytotoxicity assay of the ligand, H_2L was checked on MDA-MB 231 and WI-38 cell line. Data from MTT assay have showed minimal toxicities even at the concentration of 100 μM of ligand H_2L (**Fig. V.28**). Hence, 10 μM working concentration of the ligand H_2L was selected to perform further studies.

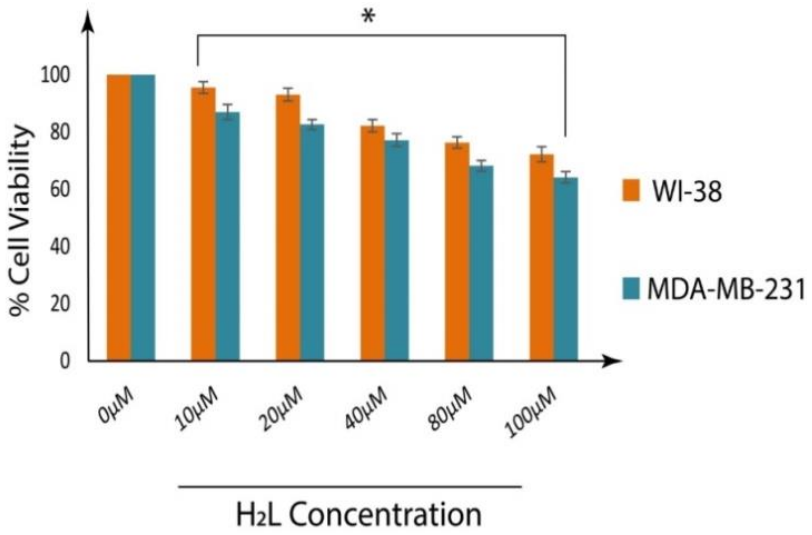

Fig.V.28. Cell survivability of MDA-MB 231 and WI-38 cells exposed to ligand H_2L concentration. Data are representative of at least three independent experiments and bar graph shows mean ± SEM, $*p < 0.001$ were interpreted as statistically significant, as compared with the control

Results from fluorescence microscopy imaging in aqueous medium showed maximum level of fluorescence intensity when MDA-MB 231 cell were treated with ligand H_2L in in 80 % H_2O + 20% CH_3CN medium at an emission level of 535 nm while a gradual decrease observed at 100% water medium and further decreases at 50 % H_2O + 50% CH_3CN medium compared to untreated as well as cells treated in CH_3CN medium whereas no fluorescence level have been found (**Fig.V.29 (a)**). While cells treated with ligand H_2L (10 μM) in combination with CN^- (5 and 10 μM respectively) in CH_3CN at an incubation time frame of 30 min a shift in fluorescence intensity from 535 nm to 650 nm have been observed compared to untreated as well as cells treated with only the ligand H_2L, which have shown no fluorescence (**Fig.V.29 (b)**). Thus we can conclude that the cells can readily uptake the ligand H_2L both in water as well as CH_3CN medium and the ligand H_2L act as a cell imaging probe in aqueous medium. Based on the exciting properties of the ligand H_2L in recognizing CN^- in CH_3CN medium it is very useful for tracking and analyzing CN^- in living systems. Hence, our synthesized ligand H_2L is biocompatible due to its minimal toxicities and favourable for biological application.

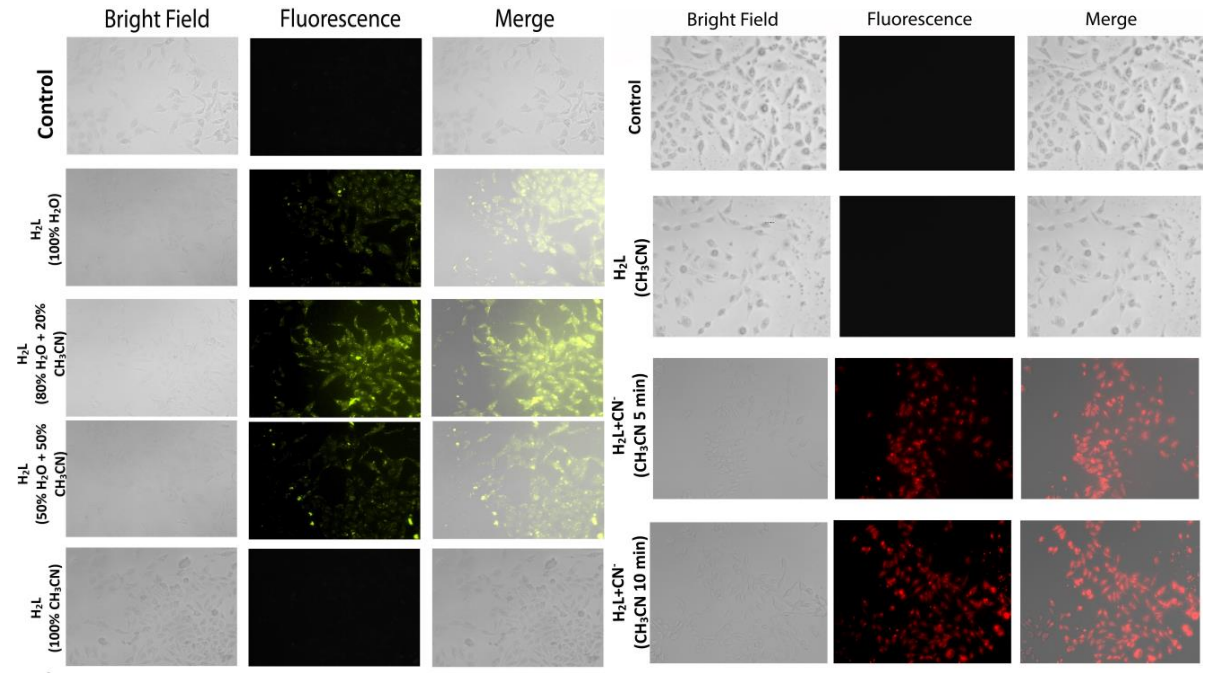

(a) **(b)**

Fig.V.29. (a) Microscopic images of untreated MDA-MB 231 cells (Control), cells treated with ligand H_2L (10 μM) in (100% water medium, 80 % H_2O + 20% CH_3CN medium , 50 % H_2O + 50% CH_3CN medium and 100% CH_3CN medium) after 30 min incubation period under bright, fluorescence and merged field. **(b)** Microscopic images of untreated MDA-MB 231 cells (Control), cells treated with ligand H_2L (10 μM) + CN^- (5 μM) and ligand H_2L (10 μM) + CN^- (10 μM) in 100% CH_3CN medium after 30 min incubation period under bright, fluorescence and merged field.

V.4. Conclusion

A multifunctional material, 1-[(2-Hydroxy-4,6-dimethoxy-benzylidene)-hydrazonomethyl]-naphthalen-2-ol (H_2L) has been well-characterized through different spectroscopic technique (NMR, ESI-MS, IR) and Single-Crystal X-ray Diffraction studies (SCXRD) confirmed the structure. The AIE active probe H_2L executes solid state emission phenomena which accounts for a solvent-free acidochromic property selectively in presence of HTFA vapor with a detection limit (LOD), 1.41 ppm. The acidochromic behaviour exhibits reversibility in presence of sequential addition of HTFA/TEA vapors, which has further been employed to develop a security encrypted device. The probe has also been applied for the colorimetric and fluorogenic detection of CN^-

specifically over a series of other compatible anions in CH_3CN/H_2O (99:1, v/v; HEPES Buffer, pH 7.3) medium with a low detection limit (LOD) 45.42 nM. MTT assay of the probe in MDA-MB 231 cells ensures biocompatibility even at higher concentration (100 μM) and has successfully been applied for intra-cellular imaging of AIE phenomena at different fraction of water content as well as for the sensitive CN^- detection which has clearly been concluded with the appearance of greenish and reddish emission in the cells.

V.5. References

1. B. Chen, B. Liu, J. Zeng, H. Nie, Y. Xiong, J. Zou, H. Ning, Z. Wang, Z. Zhao, and B. Z. Tan. *Adv. Funct. Mater*. 2018, **28**, 1803369.
2. S. Jhulki, S. Seth, A. Ghosh, T. J. Chow and J. N. Moorthy. *ACS Appl. Mater. Interfaces* 2016, **8**, 1527–1535
3. H. Li, H. Kim, J. Han, V.-N. Nguyen, X. Peng, J. Yoon. *Aggregate*, 2021, **2**, 1-30.
4. Y. Hong, J. W. Y. Lamab and B. Z. Tang. *Chem. Soc. Rev*., 2011, **40**, 5361–5388.
5. S. Sivalingam, K. Debsharma, A. Dasgupta, S. Sankararaman and E. Prasad., *ChemPlusChem* 2019, **84**, 392–402.
6. Z. He, C. Ke, and B. Z. Tang., *ACS Omega* 2018, **3**, 3267–3277
7. Y. Hong, J. W. Lam, B. Z. Tang, *Chem. Commun*. 2009, 4332-4353.
8. J. Li, W. Yang, W. Zhou, C. Li, Z. Cheng, M. Li, L. Xie and Y. Li., *RSC Adv* 2016, **6**, 35833-35841.
9. P. Alam, N.L.C. Leunga, J. Zhang, R.T.K. Kwok, J.W.Y.Lam, B. Z. Tang., *Coord. Chem. Rev* 2021, **429**, 213693.
10. H.Wan, Q. Xu, P. Gu, H. Li, D. Chen, N. Li, J. He, J. Lu., *J. Hazard. Mater*. 2021, **403**, 123656
11. M. H. Chua, K. W. Shah, H. Zhou and J. Xu., *Molecules* 2019, **24**, 1-42.
12. H. Xie, Y. Wu, Fang Zeng, J. Chena and S. Wu., *Chem. Commun*. 2017, **53**, 9813-9816.
13. S. Dey, R. Purkait, K. Pal, K. Jana, and C. Sinha. *ACS Omega* 2019, **4**, 8451–8464.
14. Y. Li, H. Li, W. Jina, X. Xua, H. Liu, Y. Ding, G. Wang, T. Zhang, Q. Peng, J. He, Q. Hu, L. Pan, K. Li., *Dyes Pigments* 2022, **202**, 110295.

15. H. Sun, J.-Y. Li, F.-F. Han, R. Zhang, Y. Zhao, B.-X. Miao, Z.-H. Ni., *Dyes Pigments* 2019, **167**, 143-150.
16. L. Huang, Y. Qiu, C. Wu, Z. Ma, Z. Shen and X. Ji., *J. Mater. Chem. C*, 2018, **6**, 10250-10255.
17. K. Debsharma, J. Santhi, B. Baire and E. Prasad., *ACS Appl. Mater. Interfaces* 2019, **11**, 48249−48260.
18. S. Suganya, K. Debsharma, E. Ravindran, M. K. Mahato and E. Prasad., *ACS Appl.Polym. Mater.* 2020, **2**, 1222-1233.
19. H. Zhu, J. Huang, L. Kong, Y.Tian, J. Yang., *Dyes and Pigments*, 2018, **151**, 140-148.
20. J. Hua, Y. Liu, X. Zhanga, H. Han, Z. Li, T. Han., *Dyes and Pigments.* 2021, **192**, 109393.
21. S. Cui, B. Wang, Y. Teng, Z. Wan, Y. Zan, L. Chen, Y. Li, X. Yan., *Sens. Actuators B: Chem.* 2021, **344**, 130120.
22. V. Ramanathan, P.J. Crutzen, J.T. Kiehl, D. Rosenfeld., *Science* 2001, **294**, 2119-2124
23. S. Gupta, M. D. Milton., *Dyes Pigments* 2019, **165**, 474-487.
24. P. Xue, J. Ding, Y. Shen, H. Gao, J. Zhao, J. Sun, R. Lu, *J. Mater. Chem. C* 2017, **5,** 11532-11541.
25. Z. Xu, X. Chen, H. N. Kim, J. Yoon, *Chem. Soc. Rev.* 2010, **39**, 127−137.
26. F.J. Baud. Cyanide: critical issues in diagnosis and treatment. 2007, **26**, 191-201.
27. S. Paul, S. Maity, S. Halder, B. Dutta, S. Jana, K. Janab and C. Sinha., *Dalton Trans.*, 2022, **51**, 3198-3212
28. Guidelines for drinking-water quality, World Health Organization, Geneva, Switzerland (1996)
29. S. Paul, S. Dey, K. Pal, S. Maity, K. Jana, C. Sinha., *ChemistrySelect* 2020, **5**, 15233-15242.
30. G. M. Sheldrick, *Acta Crystallogr. Sect.A: Found.Crystallogr*., 2008, **64**, 112–122.
31. A. L.Spek, *Platon*, The Netherlands, 1999.
32. J. Farrugia, *J. Appl. Crystallogr.*, 1997, **30**, 565–565.
33. D. Maiti, A. S. M. Islam, M. Sasmal, C. Prodhan and M. Ali, *Photochem. Photobiol.Sci*., 2018, **17**, 1213-1221.
34. M. J. Frisch, G. W. Trucks, H. B. Schlegel, G. E. Scuseria, M. A. Robb, J. R. Cheeseman, G. Scalmani, V. Barone, B. Mennucci, G. A. Petersson, H. Nakatsuji, M. Caricato, X. Li, H. P. Hratchian, A. F.

Izmaylov, J. Bloino, G. Zheng, J. L. Sonnenberg, M. Hada, M. Ehara, K. Toyota, R. Fukuda, J. Hasegawa, M. Ishida, T. Nakajima, Y. Honda, O. Kitao, H. Nakai, T. Vreven, J. A. Montgomery Jr., J. E. Peralta, F. Ogliaro, M. Bearpark, J. J. Heyd, E. Brothers, K. N. Kudin, V. N. Staroverov, R. Kobayashi, J. Normand, K. Raghavachari, A. Rendell, J. C. Burant, S. S. Iyengar, J. Tomasi, M. Cossi, N. Rega, J. M. Millam, M. Klene, J. E. Knox, J. B. Cross, V. Bakken, C. Adamo, J. Jaramillo, R. Gomperts, R. E. Stratmann, O. Yazyev, A. J. Austin, R. Cammi, C. Pomelli, J. W. Ochterski, R. L. Martin, K. Morokuma, V. G. Zakrzewski, G. A. Voth, P. Salvador, J. J. Dannenberg, S. Dapprich, A. D. Daniels, O. Farkas, J. B. Foresman, J. V. Ortiz, J. Cioslowski and D. J. Fox, Gaussian 09, Revision D.01, Gaussian Inc., Wallingford, CT, 2009.

35. A. D. Becke, *J. Chem. Phys.* 1993, **98**, 5648–5652.
36. W.R. Wadt and P.J. Hay, *J. Chem. Phys.* 1985, **82**, 299-310
37. R. Bauernschmitt and R. Ahlrichs, *Chem. Phys. Lett.* 1996, **256**, 454–464.
38. M. Cossi and V. Barone, *J. Chem. Phys.* 2001, **115**, 4708–4717.
39. M. Cossi, N. Rega, G. Scalmani and V. Barone, *J. Comput. Chem.*, 2003, **24**, 669–681.
40. N. M. O'Boyle, A. L. Tenderholt and K. M. Langner, *J. Comput. Chem.*, 2008, **29**, 839–845.
41. D. Laha, A. Pramanik, S. Chattopadhyay, S. K Dash, S. Roy, P. Pramanik, P. Karmakar, *RSC Adv.* 2015, **5**, 68169-68178.
42. M. Mandal, D. Sain, Md. M. Islam, D. Banik, M. Periyasamy, S. Mandal, A. K. Mahapatra and A. Kar., *Anal.Methods*, 2021, **13**, 3922 - 3929.
43. M. Mathivanan, B.Tharmalingam, O. Anitha, C.-H. Lin, V. Thiagarajan and B. Murugesapandian , *Mater. Chem. Front.*, 2021, **5**, 8183-8196.
44. X. Feng, J. Zhang, Z. Hu, Q. Wang, M. M. Islam, J.-S. Ni, M. R. Elsegood, J. W. Lam, E. Zhou and B. Z. Tang., *J. Mater. Chem. C*, 2019, **7**, 6932–6940.
45. P. Alam, N. L. C. Leung, H. Su, Z. Qiu, R.T. K. Kwok, J. W. Y. Lam and B. Z. Tang. *Chem. Eur. J.* 2017, **23**, 14911–14917.
46. M. E. Abdelhamid, T. Murdoch, T. L. Greaves, *Phys. Chem. Chem. Phys*., 2015, **17**, 17967

47. Q. Niu, L. Lan, T. Li, Z. Guo, T. Jiang, Z. Zhao, Z. Feng, J. Xi., *Sens. & Actuators: B. Chem.* 2018, **276**, 13–22.

48. P. Karuppusamy, S. Sarveswari. *J. Mol. Struct.*, 2022, **1248**, 131494.

49. R. Shanmugapriya, P. Saravana Kumar, S. Ponkarpagam, C. Nandhini, K.N. Vennila, A. G. Al-Sehemi, M. Pannipara, K. P. Elango., *J. Mol. Struct.*, 2022, **1251**, 132081.

50. T. P. Martyanov, A. A. Kudrevatykh, E. N. Ushakov, D.V. Korchagin, I. V. Sulimenkov, S. G. Vasil'ev, S. P. Gromov, L. S. Klimenko., *Tetrahedron,* 2021, **93**, 132312.

51. 5. B. Yilmaz, M. Keskinates, Z. Aydin, M. Bayrakci., *J. Photochem. & Photobio. A: Chem.*, 2022, **424**, 113651

52. 6. Z. Li, C. Liu, S. Wang, L. Xiao, X. Jing., *Spectrochim. Acta A,* 2019, **210**, 321–328.

53. 7. Y. Gao, M. Li, X. Tian, K.Xu, S.Gong, Y. Zhang, Y.Yang, Z. Wang, S. Wang. *Spectrochim. Acta A,* 2022, **271**, 120882.

54. 8. S. Dey, C. Sen, C. Sinha, *Spectrochim.Acta Part A.*,2020, **225**, 117471.

55. G.A. Zalmi, D.N. Nadimetla, P. Kotharkar, A. L. Puyad, M. Kowshik, and S. V. Bhosale., *ACS Omega* 2021, **6**, 16704−16713.

56. R. V. Rathod, S. Bera, D. Mondal., *Spectrochim. Acta A,* 2020, **238**, 118419.

57. Q. Niu, T. Sun, T. Li, Z. Guo, H. Pang. *Sens. Actuators B: Chem*. 2018, **266**,730–743.

58. M. Sahu, A. Kumar, M. K. Rout, D. Nikunj, B. Sharma, G. K. Patra., *Inorg. Chim. Acta.*, 2021, **528**, 120600.

59. R. Bhaskar, S. Sarveswari. *Inorg. Chem. Commun*. 2019, **102**, 83-89.

60. D. Udhayakumari., *Sens. Actuators B Chem.*, 2018, **259**, 1022-1057.

61. S. Panja , A. Panja and K. Ghosh. *Mater. Chem. Front.*, 2021, **5**, 584-602.

Chapter VI

Tangible Coumarinyl-Pyridyl Schiff base Appended Carboxylato Bridging Zinc(II) 2D Coordination Polymer : Electrical Property and Anti-carcinogenic Application.

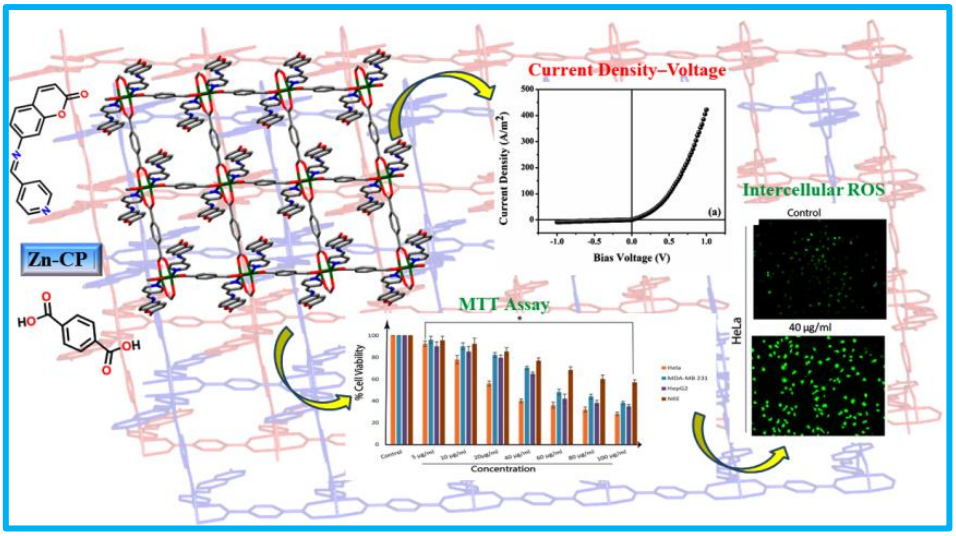

CHAPTER VI

Abstract

Coumarinyl-Pyridyl Schiff base coordinated terephthalato bridging Zn(II) 2D co-ordination polymer, $[Zn_2(BDC)_4(QPR)_2(H_2O)]_n$ (Zn(II)-CP) (BDC^{2-} = 1,4-benzenedicarboxylato; QPR = 7-[(Pyridin-4-ylmethylene)-amino]-chromen-2-one) is structurally confirmed by Single Crystal X-Ray Diffraction measurements. The optical band gap obtained from Tauc's plot is 2.91 eV which insists to fabricate a device to measure electrical conductivity, Λ, 8.07×10^{-3} S m^{-1} (dark) and 9.26×10^{-3} S m^{-1} (light) which suggests the semiconducting property of the material. The MTT assay determines the cytotoxicity in the selected human cancer cell lines, HeLa (Cervical Cancer), HepG2 (Liver Cancer) and MDA-MB 231 (Breast Cancer), relative to the normal kidney epithelial cell line NKE and its efficacy in inhibiting proliferation of HeLa (IC_{50}, 21.02) is highest relative to two other cancer cells (IC_{50} : 42.22 (HepG2) and 46.37 (MDA-MB 231)).

VI.1. Introduction

Zn(II) (d^{10}) compounds are widely used in different fields, while its application in the area of energy and biological materials are very stimulating.[1] On considering the sustainable health, the use of phytochemicals as food/food supplement/drugs or pharmaceuticals has been receiving a great attention. Towards this approach, Coumarin and its derivatives are widely used for stress-related disorder, a potential ROS (Reactive Oxygen species) scavenger and in different biomedical applications. Therefore, the coordination complexes of Coumarinyl-Zn(II) or their coordination polymers (Zn(II)-CPs) can be recognized as an emerging and effective functional material for societal applications in different area.[2-7] Coordination Polymers (CPs) and/or Porous Coordination Polymers (PCPs) are diversely applied in the field of gas sorption, catalysis, biological applications, electrical conductivity, magnetic, sensing, electrochemical CO_2 reduction, solar energy harvesting etc.[8-21] Structural architecture of the CP dictates its functional behaviour with metal ion as node and the organic ligand as bridging agent.[22-24] Depending on the variation in structural dimension (1D, 2D or 3D) due to different spatial arrangements; properties and applications of the CPs inflate extensively.[25,26] Generally, redox inactive metal centres and carbon compacted ligand based CPs are electrically non-conducting. But, in recent times, CPs have emerged as distinctive solid-state materials with interesting conductive behaviour as Schottky diode. CPs based on the d^{10} configuration (Zn^{2+}) and conjugated carboxylate linkers are known to exhibit semiconducting device. Dicarboxylic acids are the key constituent of coordination polymers.[27,28.] In this work, coumarinyl-pyridine Schiff base ligand, a π-conjugated monodentate N donor, is used in conjunction with dicarboxylato bridging motif (terephthalic acid) to architect a 2D Zn(II)-CP. It is used to fabricate Schottky diode device and the relevant studies have been discussed in detail. Density Functional Theory (DFT) calculation has been attempted for optimization of the geometry of asymmetric unit of Zn(II)-CP and the resultant band gap shows close resemblance to the value obtained from Tauc's Plot. In addition, the anticancer activity of the compound has been explored against different cells (HeLa (Cervical Cancer), HepG2 (Liver Cancer) and MDA-MB 231 (Breast Cancer)) and highest efficiency is observed in case of HeLa cells.

VI.2. Experimental Section

VI..2.1. Materials and Methods

Analytical grade reagents (AR) were collected from the Merck (India), Himedia (India), Invitrogen (India), SRL (India) and TCI chemicals. For spectroscopic measurement spectroscopic graded solvents were directly used. Other solvents were dried by standard procedure for spectroscopic studies. Water from Milli-Q water (Millipore) was collected for preparation of aqueous solutions of metal salts. Perkin-Elmer (2400 Series-II, Perkin Elmer, USA) CHN analyzer was used for collecting the elemental analysis data. Other instruments such as, Perkin Elmer Lambda 25 UV-Visible spectrophotometer for absorption spectral studies; Infrared (IR) spectrum (4000−500 cm^{-1}) was taken on a Bruker ALPHA II spectrometer in an attenuated total reflectance (ATR) mode. ^{1}H and ^{13}C NMR spectra were taken by Bruker 300 MHz FT-NMR spectrometer. The chemical shift (δ) of the respective NMR spectra were recorded in parts per million (ppm) with respect to trimethylsilane as internal standard. ESI-MS spectra were obtained from HRMS spectrometer (model, XEVO-G2QTOF#YCA351).

VI..2.2. Synthesis of the Ligand 7-[(Pyridin-4-ylmethylene)-amino]-chromen-2-one (QPR)

7-Amino coumarin was synthesized modifying the literature procedure.[29] To a methanol (15 mL) solution of 7-amino coumarin (161.16 mg, 1 mmol), 4-pyridine carbaldehyde (107.11 mg, 10 mmol) (5 mL) was added dropwise and yellow solution was stirred overnight followed by reflux for 7 h; then filtered and allowed for slow evaporation; light brown crystalline compound of 7-[(Pyridin-4-ylmethylene)-amino]-chromen-2-one (QPR) was obtained. (**Scheme VI**) Yield: 190.11 mg 75.7%. Elemental analysis (%) calcd for $C_{15}H_{10}N_2O_2$: C, 71.70; H, 4.41; N, 11.90; found: C, 71.61; H, 4.35; N, 11.96. ^{1}H-NMR (DMSO-d_6, 300 MHz): 8.76 (s, 3H, CH=N, Pyr-H(1,3)), 8.10-8.07 (d, 2H, Ar-H(7)), 7.87-7.85 (d, 2H, Pyr-H(2)), 7.72-7.71 (d, 1H, Ar-H(4)), 7.65-7.62 (t, 1H, Ar-H(6)) 7.50-7.47 (d, 1H, Ar-H(5)) 6.57-6.54 (d, 1H, Ar-H(8)).(**Fig.VI.1**) ^{13}C-NMR (DMSO-d_6, 75MHz): 160.47, 160.30, 152.79, 151.00, 147.10, 144.50, 142.76, 125.64, 122.68, 121.12, 119.72, 117.76, 117.33 (**Fig.VI.2**). ESI-MS (+) shows a molecular ion base peak at 251.0318 (Calculated m/z =

251.082). (**Fig.VI.3**). IR Spectrum: 3036 cm^{-1} (C-H stretching), 1705 cm^{-1} (C=O stretching), 1594 cm^{-1} (C=N stretching); (**Fig.VI.4**)

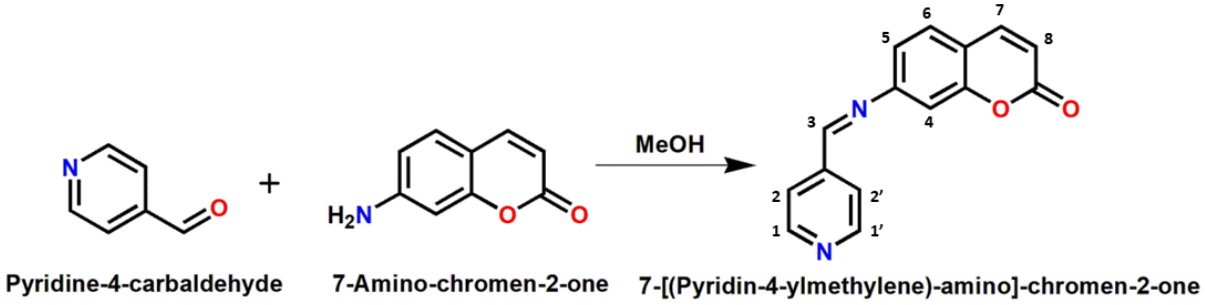

Scheme VI. Synthesis of QPR

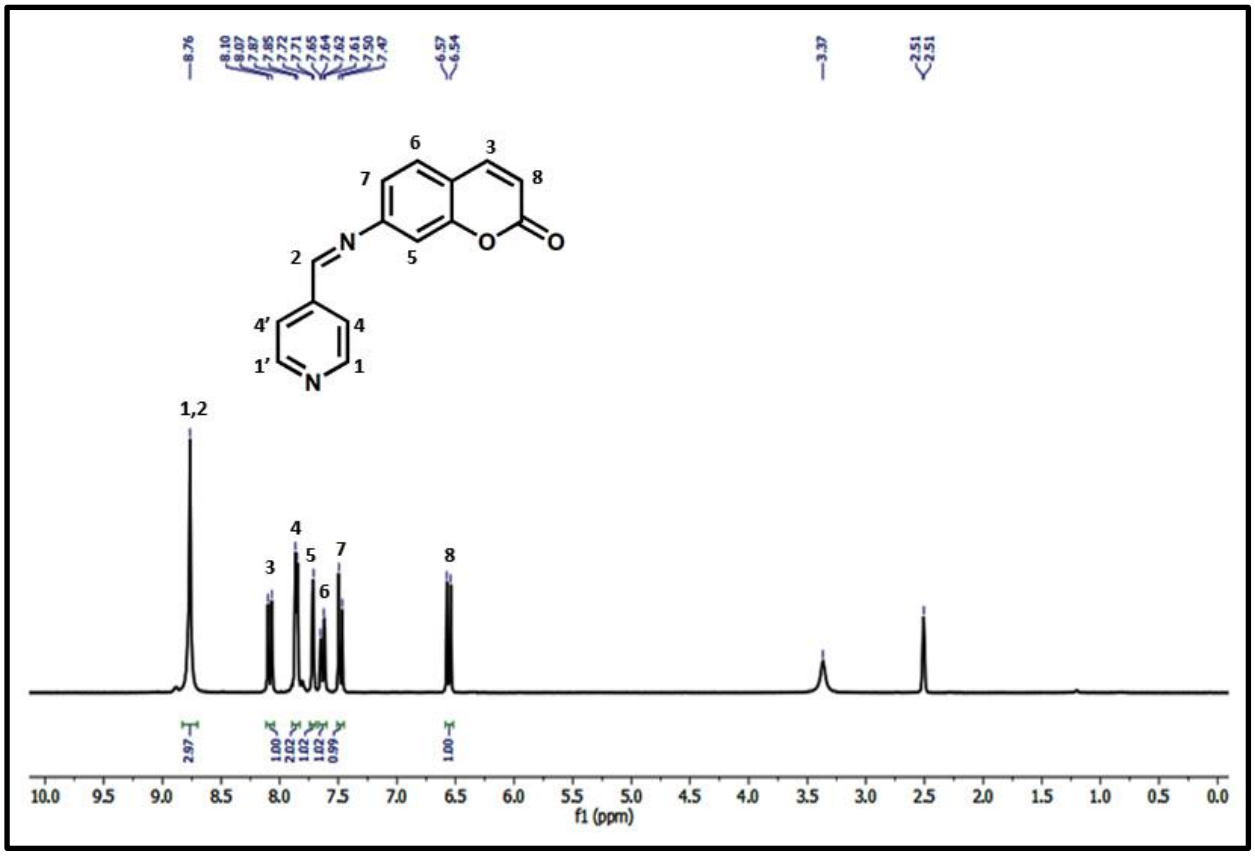

Fig.VI.1. ^{1}HNMR Spectrum of the ligand QPR.

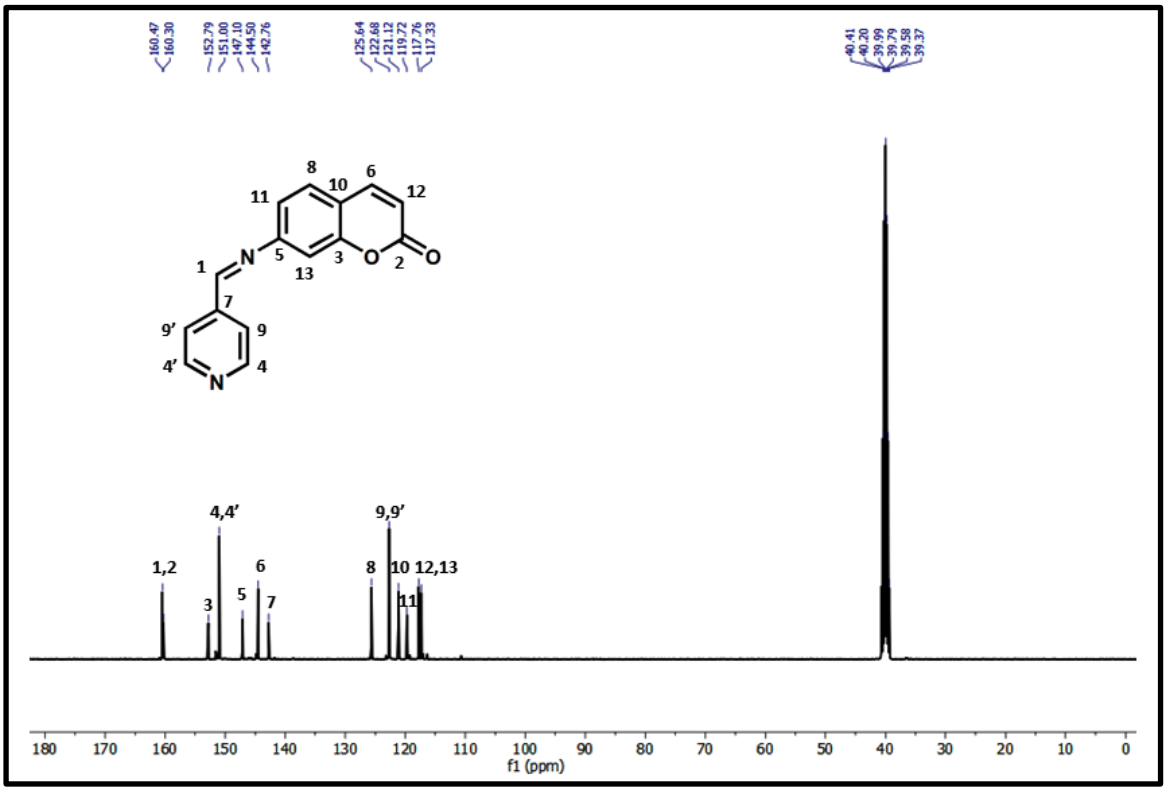

Fig.VI.2. ^{13}CNMR Spectrum of the Ligand QPR

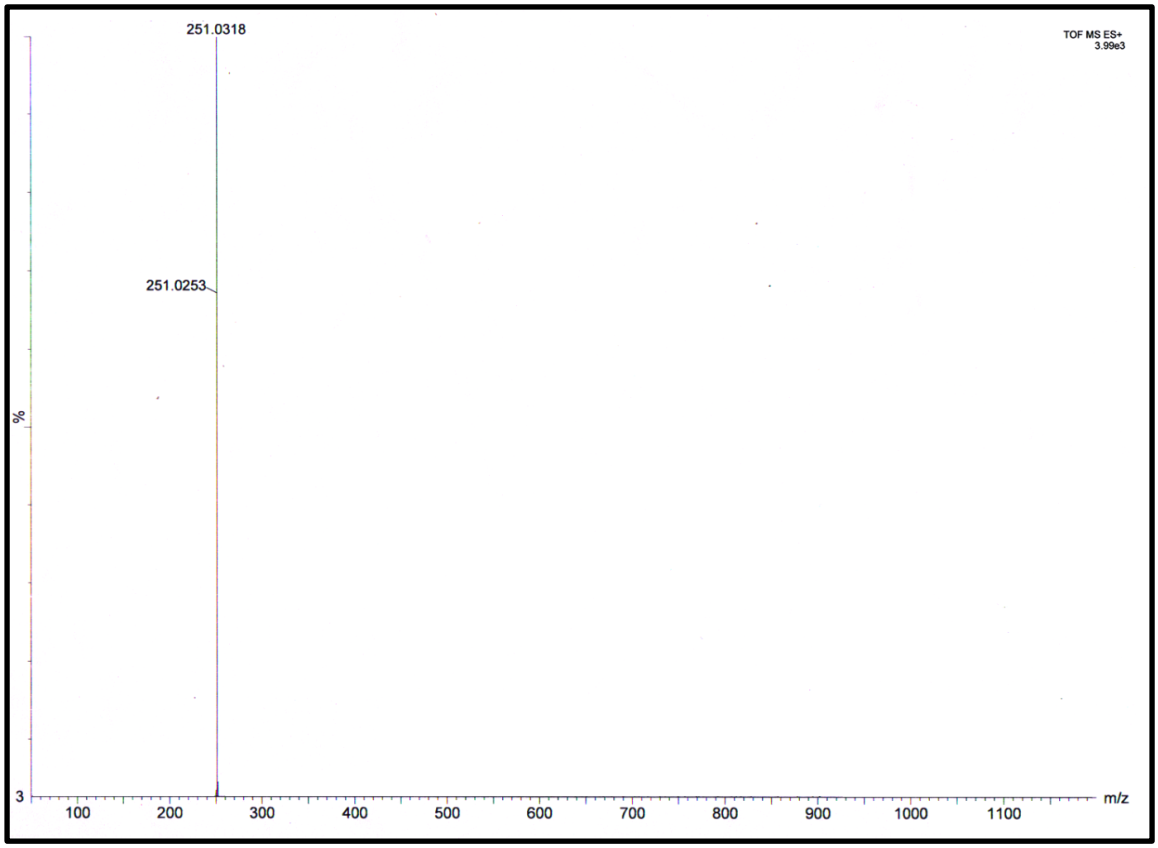

Fig.VI.3. ESI-MS of the Ligand QPR

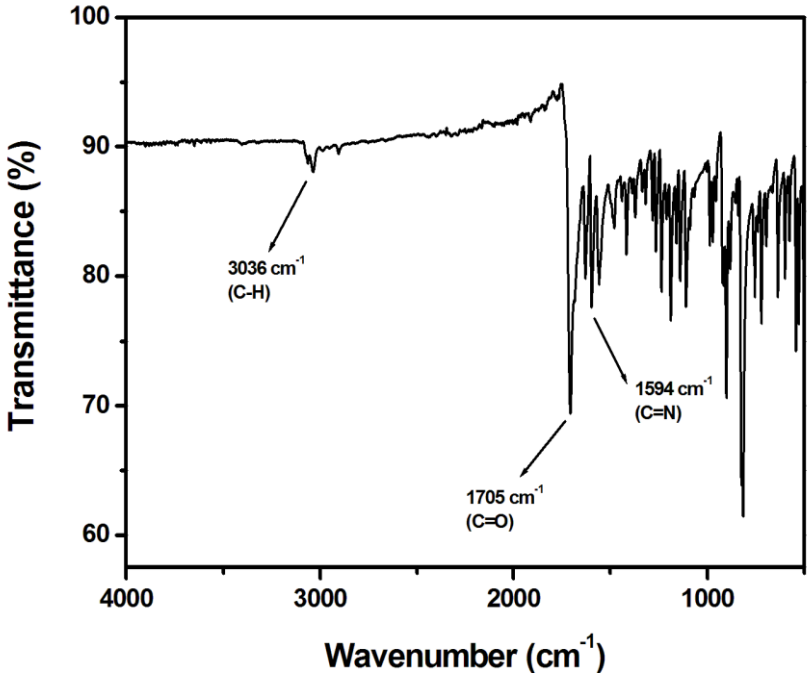

Fig.VI.4. IR Spectrum of Ligand QPR

VI.2.3. Synthesis of $[Zn_2(BDC)_4(QPR)_2(H_2O)]_n$, (Zn(II)-CP)

A methanol (3 mL) solution of QPR (75.081 mg, 0.3 mmol) was carefully layered at the interface of the aqueous solution (2 mL) of $Zn(NO_3)_2.6H_2O$ (83.847 mg, 0.3 mmol) maintained with aqueous-methanol buffer solution (MeOH:H_2O, 1:1, v/v, 3 mL). To the resulting solution, an ethanolic solution of H_2BDC (49.8 mg, 0.3 mmol) and Et_3N (0.031 g, 0.3 mmol) were slowly layered and allowed to diffuse for several weeks. Brown crystals were deposited on glass wall after three weeks and were collected carefully. Yield: 59.07 mg, 65.6 %. Elemental analysis (%) calcd for $C_{24}H_{18}N_2O_7Zn$: C, 56.32; H, 3.55; N, 5.47; found: C, 56.23; H, 3.51, N, 5.51. IR Spectrum: 1726 cm^{-1} (C=O stretching), 1630 cm^{-1} (C=O stretching), 1555 cm^{-1} (C=N stretching). (**Fig.VI.5**)

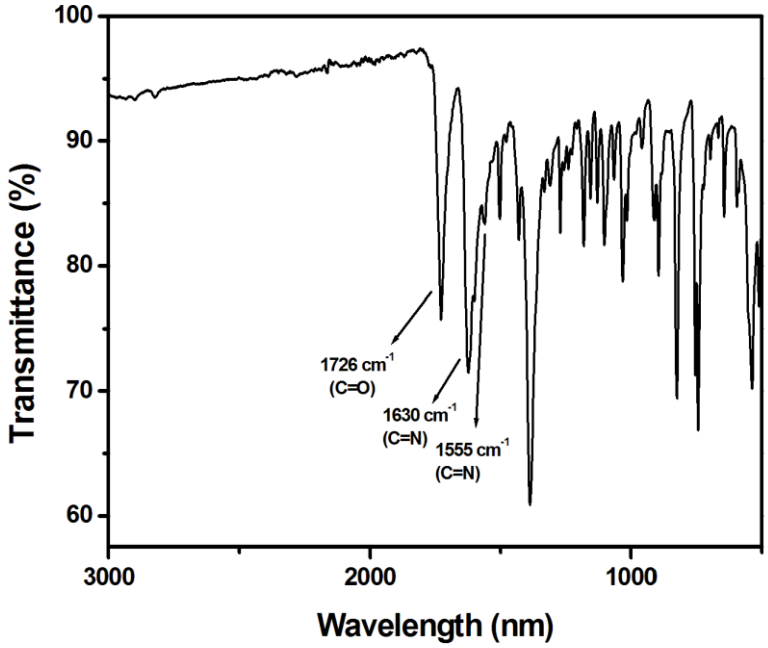

Fig.VI.5. IR Spectrum of Zn(II)-CP.

VI..2.4. X-Ray Diffraction Measurement

Brown single crystal of Zn(II)-CP of suitable dimension (0.13×0.09×0.05 mm^3) was mounted for single crystal X-ray diffraction (SCXRD) analysis and data collected using Bruker SMART APEX II diffractometer having graphite-monochromatic MoKα radiation (λ = 0.71073 Å). Structural arrangements of the single crystal were solved using the SHELX-97[30] PLATON-99[31] and ORTEP-32,[32] package. Non-hydrogen atoms of the single crystal were refined with anisotropic thermal parameters. Crystal-orientation matrices and unit cell parameters of the crystal were determined following least-squares refinement of all reflections within the hkl range −13 < h < 13, −13 < k < 13, −13 < l < 13. The diffraction angle was recorded within the angle from 1.937 ≤ θ ≤ 27.203°. All the hydrogen atoms were geometrically fixed and constrained to ride on their parent atoms. All the crystallographic data are listed in **Table VI.1.** Selected Bond Length and Bond Parameters are listed in **Table VI.2 & VI.3.** The crystal data have been deposited to Cambridge Crystallographic Data Centre with **CCDC No.** 2191815.

Table VI.1: Crystal Data and Refined Parameters for Zn(II)-CP

Empirical formula	$C_{24}\ H_{18}\ N_2\ O_7\ Zn$
CCDC No.	2191815
Formula weight	511.79
Temperature (K)	273 K
System	Triclinic
Space group	P -1
a (Å)	10.3582(13)
b (Å)	10.8566(13)
c (Å)	10.8861(13)
α/°	79.654(4)
β/°	70.435(3)
γ/°	77.041(3)
V $(Å)^3$	1116.8(2)
Z	2
D(cal) /g cm^{-3}	1.522
μ/mm^{-1}	1.149
λ(Å)	0.71073
Data[I >2σ(I)]/param	4925/310
R_1[a][I>2σ(I)]	0.0372
wR_2[b]	0.1104
GOF[c]	1.150

[a]$R_1 = \Sigma||F_o|-|F_c||/\Sigma|F_o|$; [b]$wR_2 = \{\Sigma[w(F_o^2-F_c^2)^2]/\Sigma[w(F^2_o)^2]\}^{1/2}$; $w = [\sigma^2(F_o)^2 + (0.1003P)^2 + 4.9693P]^{-1}$ $(F_o^2 + 2F_c^2)/3$; [c] Goodness-of-fit.

Table VI.2: Selected Bond Length for the following Zn(II)-CP

Bond-Length	**Å**
Zn(1) - O(1)	2.0667(18)
Zn(1) - O(2)	2.0750(19)
Zn(1) - O(3)	2.0151(17)
Zn(1) - O(4)	2.0264(18)
Zn(1) - N(1)	2.036(2)

Table VI.3: Selected Bond Angles for the following Zn(II)-CP

Bond Angle	**Degree (°)**
O(1) - Zn(1) - O(4)	90.09(8)
O(1) - Zn(1) - N(1)	104.85(8)
O(1) - Zn(1) - O(2)b	158.34(8)
O(1) - Zn(1) - O(3)[b]	87.34(8)
O(4) - Zn(1) - N(1)	99.02(8)
O(4) - Zn(1) - O(2)[b]	85.85(8)
O(4) - Zn(1) - O(3)[b]	158.52(8)
N(1) - Zn(1) - O(2)[b]	96.80(8)
N(1) - Zn(1) - O(3)[b]	102.26(8)
O(2)b - Zn(1) - O(3)[b]	88.70(8)
Zn(1) - O(1) - C(20)	110.70(16)
C(20) - O(2) - Zn(1)[b]	145.75(16)
C(16) - O(3) - Zn(1)[b]	125.72(17)
Zn(1) - O(4) - C(16)	129.27(15)
Zn(1) - N(1) - C(1)	123.11(18)
Zn(1) - N(1) - C(5)	119.4(2)

[b] 2-x,1-y,-z.

VI.2.5. DFT computation

Optimization of the gas phase geometry of the Zn(II)-CP was carried out using Density Functional Theory (DFT) calculation of Gaussian Program Package 09. All calculations were performed using SCXRD coordinates and B3LYP method. LanL2DZ basis set were employed for all elements including Zn.[33-35] Different electronic transitions were theoretically determined using the time-dependent density functional theory (TDDFT) formalism calculation.[36-38] Vibrational frequency calculations were performed to ensure that the DFT-optimized geometries represent the local minima and only positive eigenvalues.[39]

VI.2.6. Fabrication and characterization of ITO/Compound/Al based Schottky Barrier Diode

Thin film semiconducting device of Zn(II)-CP was used to carry out electrical characterization of the material. ITO (Indium Tin Oxide) coated glass substrate has been used for the study, and it was cleaned with 2-propanol, acetone, and deionized water in an ultrasonic bath for 12 minutes respectively. The glass substrate was simply dried in a N_2 environment. The synthesized chemical produced a homogenous dispersion using N, N dimethyl formamide (DMF) as the dispersive medium. With use of a Spin Coating Unit, the dispersion has been spin coated on the conducting side of ITO coated glass at 1500 rpm for 2 minutes. The film thickness was tested using a surface profiler after complete vacuum drying and the measured value is nearly one micrometer. A vacuum coating device (HINDHIVAC) using the evaporation process with an electron beam discharge at pressure of about 10^{-6} Torr deposited aluminum (Al) metal onto the thin film. Finally, Metal Semiconductor (MS) junction Schottky Diode (SD) with Al as the metal electrode was fabricated in an ITO/Zn(II)-CP/Al sandwich arrangement. At the time of metal deposition, the effective diode area (A) was kept as 7.065×10^{-6} m^2 using a shadow mask.

The current–voltage (I–V) properties of the device was measured in the dark and light (intensity ~100 $mWcm^{-2}$) with a Keithley 2635B source meter utilizing the two-probe approach at a bias voltage range of -1 V to 1V for electrical characterization. All preparations and measurements were completed at room temperature and under natural conditions.

VI.2.7. Cell culture and maintenance

To perform the present study three cancerous cancer cell lines - HeLa (human cervical cancer cell line), MDA-MB-231 (triple negative breast cancer cell line) HepG2 (human liver cancer cell line) and human normal kidney epithelialcell line NKE were obtained from Bose Institute, Kolkata. All the above cell lines were maintained using DMEM (for HeLa, MDA-MB-231 and HepG2) or RPMI medium (for NKE), supplemented with 10% FBS, 2 mM L-glutamine, 100 mg/L streptomycin, 100 units/L penicillin, non-essential amino acids, 1mMsodium pyruvate, and 50 mg/L gentamycin in a 37°C humidified incubator containing 5% CO_2.

VI.2.8. In-vitro cell survivability assay

Along with three cell lines (HeLa, HepG2, MDA-MB-231) Etoposide was used as a standard chemotherapeutic agent considering its tremendous anti-proliferative activity. Cells were seeded in 96-well plates at 1×10^4 cells per well and exposed to different concentration of Zn(II)-CP (0-100 µg/Ml) for 24 h. Following this the cells were washed with 1×PBS and then incubated by MTT solution (0.5 mg/mL) for 3-4 h at 37ºC and resulting formazan crystals formed were further dissolved in DMSO and the absorbance was observed at 570 nm wavelength, and the obtained results were compared with control cells.

VI.2.9. Annexin V-FITC/PI staining for apoptosis assay

Induction of apoptosis has been quantified *via* flow cytometric analysis utilizing the Annexin V-FITC apoptosis detection kit (BD Bioscience).[40] Briefly, HeLa cells were seeded in a 6 well plate at a density of 1×10^6 cells /ml for a time period of 24 h and treated with compound Zn(II)-CP (10 µg/ml, 20 µg/ml, and 40 µg/ml) for the interval of 24 h. After treatment cells were trypsinized and re-suspended in 100µL of 1X binding buffer solution and incubated with 5 µL of annexin V-FITC and 5 µL of PI for 15 min at room temperature in dark and data was acquired using BD FACS Verse flow cytometer (BD Biosciences, San Jose, CA). Annexin V/FITC positive cells were regarded as apoptotic cells analysed using Cell Quest Software (BD Biosciences).

VI.2.10. Measurement of cellular ROS using DCFDA

To estimate the intercellular ROS generation upon Zn(II)-CP treatment, DCFDA method was used.[41] HeLa cells were seeded in a 6 well plate and treated with the compound, Zn(II)-CP (10 µg/ml, 20 µg/ml, and 40 µg/ml) for the time period of 24 h. Post treatment cells were washed with 1XPBS and incubated with 10 µM H_2DCFDA for 30 min at 37° C. For fluorescent imaging, H_2DCFDA incubated cells were washed, resuspended in 1x PBS and directly imaged under fluorescent microscope (Leica).

VI.3. Results and Discussion

VI.3.1 Crystal Structure of Zn(II)-CP

$[Zn_2(BDC)_4(QPR)_2(H_2O)]_n$ (**Zn(II)-CP**) crystallizes in triclinic system having space group *P*-1 with Z=2. In the crystal structure the metal centre has been coordinated with dicarboxylic acid and coumarin appended nitrogen donor ligands. Zn(II) centres are in distorted square pyramidal coordination sphere; the square plane is formed by two chelated carboxylato-O,O rings of two BDC^{2-} and apical position is occupied by pyridyl-N of QPR to form ZnO_4N unit. Two Zn(II) centres are bridged by $–COO^-(BDC^{2-})$ in a paddle wheel pattern. The bond lengths of square pyramidal ZnO_4N unit are Zn(1)-O(1), 2.0670(18); Zn(1)-O(2), 2.0745 (19); Zn(1)-O(3), 2.0153(16); Zn(1)-O(4), 2.0263 (17); Zn(1)-N(1) 2.036(2) Å which support the geometrical distortion of the molecular geometry. Thus, molecular units are assembled to form 2D square-grid arrangement (**Fig. VI.6. (a) & (b)**). Some of the reported Pyridyl-N coordinated Zn(II) Coordination Polymer exhibits similar coordination environment and their structural parameters are represented in **Table VI.4.** The bond parameters of Zn(II)-CP are comparable with published results.[42-46]

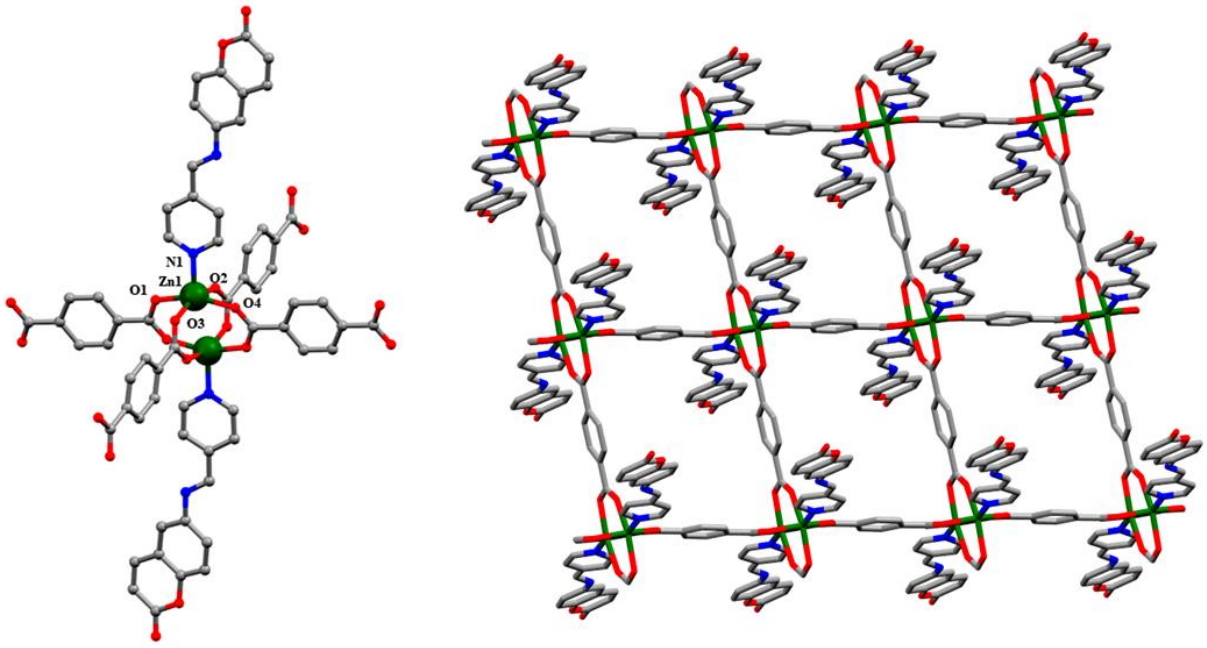

(a) **(b)**

Fig.VI.6. (a) Coordination unit around metal centre of Zn(II)-CP **(b)** Two Dimensional Network of Zn(II)-CP generated through terephthalate bridging.

Table VI.4: Summarized Bond Distance of Reported Zn(II) Coordination Polymer.

Sl. No.	Coordination Polymer	Bond Distance (Å)	Reference
1.	$[Zn(adc)(4\text{-}nvp)_2(H_2O)_2]_n$	2.200(13)–2.172(13) (Zn-N) 2.075(11)–2.156(10) (Zn-O) 2.779–3.001(C–H···π)	[42]
3.	$[Zn(adc)(4\text{-}spy)_2(H_2O)_2]_n$	2.140(2)–2.148(2) (Zn–N) 2.0999(14)-2.1357(15) (Zn-O) 2.716 (O···O)	[43]
4.	$[Zn_2(DABA)_4(4,4'\text{-}BPY)]_n$	2.045(4)-2.064(4) (Zn-N) 2.003(4)-2.075(4) (Zn-O) 3.066–3.454 (C–H…π)	[44]
5.	$[Zn(ADC)(PBT)_2(H_2O)_2]_n$	2.159(4)- 2.158(4) (Zn-N) 2.092(3)- 2.158(3) (Zn-O) 3.489(8)-3.685(8) (C–H···π)	[45]
6.	[Zn(glu)(4-nvp)]	2.039(2) (Zn–N) 2.026(2)-2.053(2) (Zn-O)	

		2.934 (Zn···Zn)	[46]
7	$[Zn_2(BDC)_4(QPR)_2(H_2O)]_n$ (**Zn(II)-CP**)	2.036(2) (Zn-N) 2.0153(16) – 2.0745(19) (Zn-O) 2.980 (Zn···Zn)	Present work

Four BDC^{2-} form bridges between two Zn(II) centres and QPR is appended through pyridyl-N coordination to Zn(II). The bridged linker repeats to develop 2D polymeric pattern. The Zn----Zn distance is 2.980 Å. Molecular forms in 2D–arrangement are self-assembled through secondary interactions to generate 3D supramolecule (**Fig. VI.7 (a), (b) & (c)**).

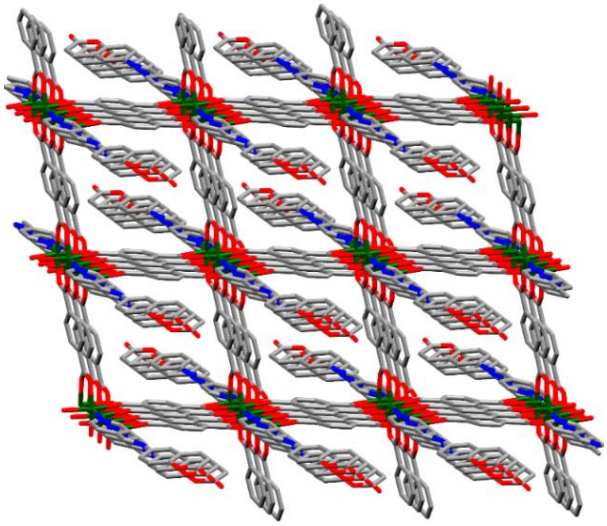

(a)

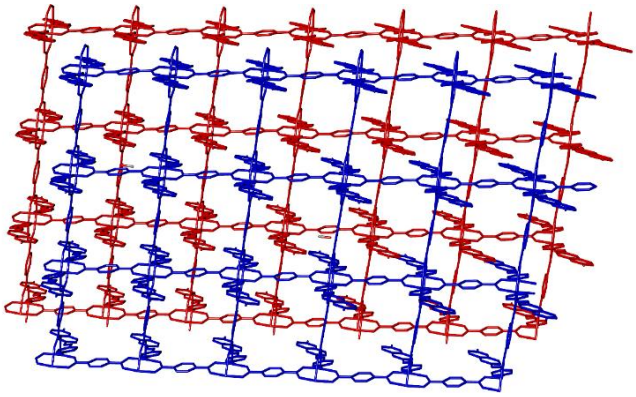

(b)

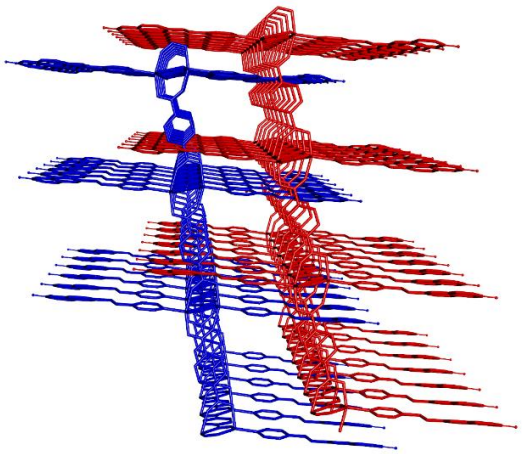

(c)

Fig.VI.7. (a) Supramolecular Assembly of Zn(II)-CP. **(b) & (c)** Interpenetration of 2D layers has been exhibited in view of self-assembly of Zn(II)-CP.

In addition, the intramolecular noncovalent interactions (C(5)-H(5)···O(4) = 2.55 Å) and intermolecular (C(13)-H(13)···O(2) = 2.60 Å (symmetry: 1-x,1-y,1-z), C(23)-H(23)···O5 = 2.49 Å (symmetry: -x,1-y,1-z)) hydrogen bonds make 3D superstructure; the C-H ···π (C(8)-H(8) ···Cg(5)) = 2.49 Å; (Cg(5) = C(21)-C(22)-C(23)-C(21)- C(22)-C(23)) and π···π (Cg(3)···Cg(3)=3.891 Å; Cg(3) = C(7)-C(8)-C(9)-C(10)-C(11)-C(12)) interactions are responsible to make the structure more robust. Again, PXRD determines the phase purity of powdered form of **Zn(II)-CP**. The PXRD pattern of the as-synthesized **Zn(II)-CP** shows resemblance with major peaks of the spectra of simulated geometry obtained from the single crystal X-ray data which validates the purity and consistency of the bulk material (**Fig. VI.8**).

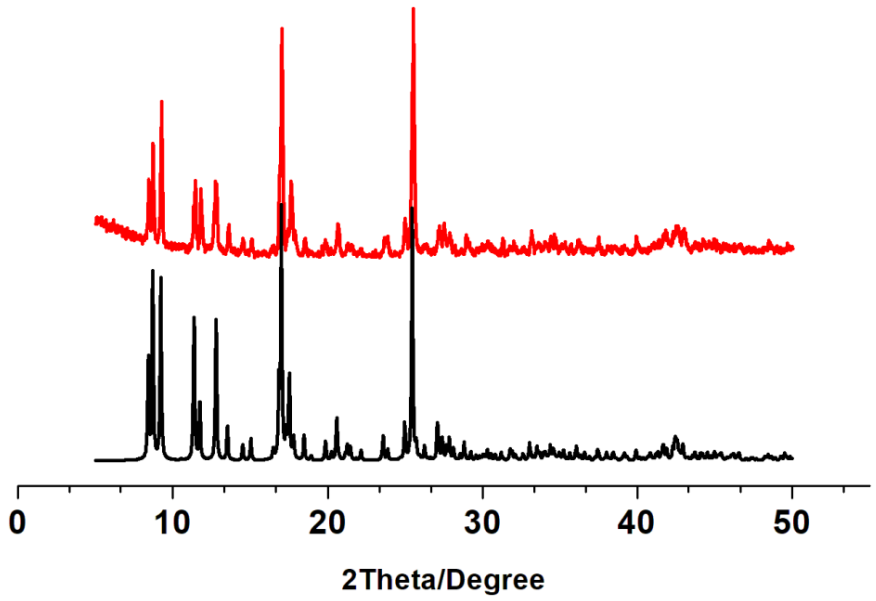

Fig.VI.8. Powdered X-Ray Diffraction (PXRD) of Zn(II)-CP [Simulated (black) and As Synthesized (red)]

VI.3.2. DFT Computational Study

Optimization of the asymmetric unit of Zn(II)-CP was performed using the coordinates of SXCRD in order to obtain the theoretical band gap corresponding to HOMO-LUMO difference ((ΔE = 3.68 eV, **Fig.VI.9**) which correlates well with the band gap of 2.91 eV evaluated from Tauc's plot (**Fig.VI.10**, *vide infra*). However, a increment in the theoretical band gap may be attributed to the geometrical factor which was restricted for single motif in DFT calculation. For coordination polymer with d^{10} system, the band edges depend on the

electronic state of the geometrical framework. Some selected orbitals along with their respective energies are listed in **Table VI.5**.

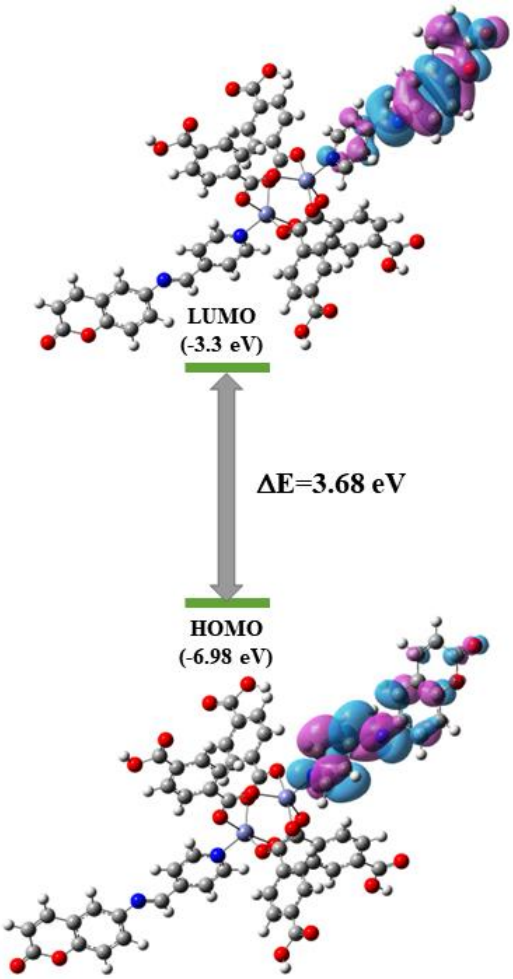

Fig.VI.9. HOMO-LUMO gap of Zn(II)-CP from DFT calculation

Table VI.5: Selected Orbitals of Zn(II)-CP along with their energy.

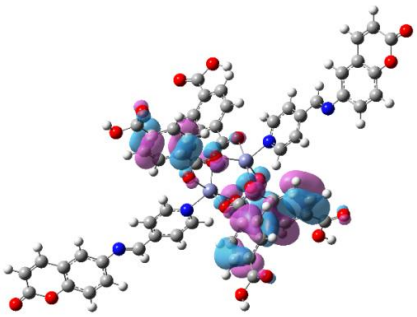 **HOMO-5 (-7.43 eV)**	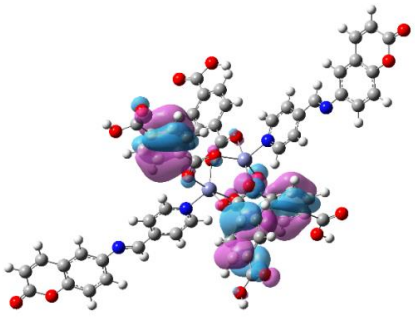 **HOMO-4 (-7.41 eV)**

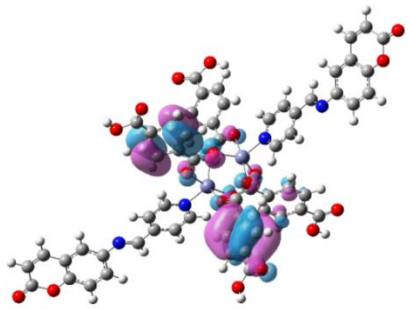

HOMO-3
(-7.38 eV)

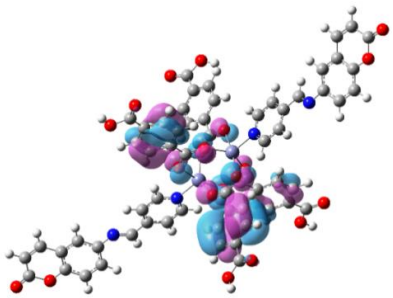

HOMO-2
(-7.33 eV)

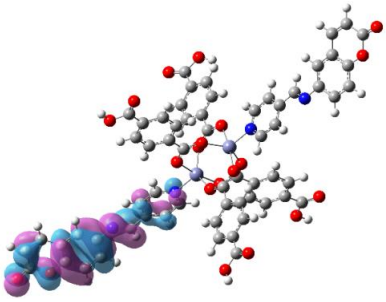

HOMO-1
(-7.03 eV)

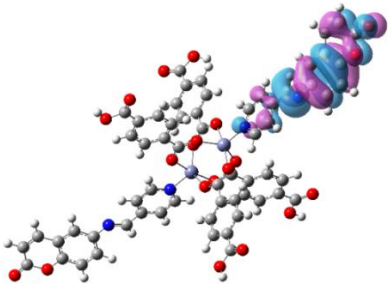

HOMO
(-6.98 eV)

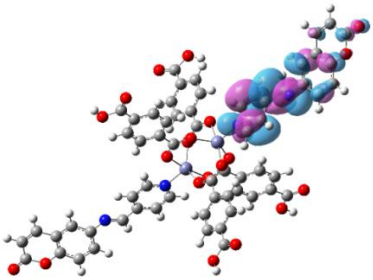

LUMO
(-3.3 eV)

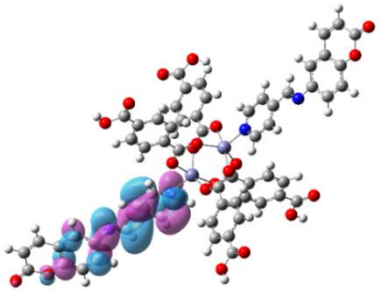

LUMO+1
(-3.29 eV)

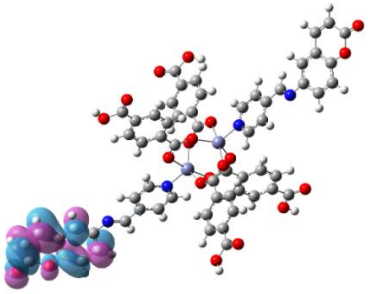

LUMO+2
(-2.78 eV)

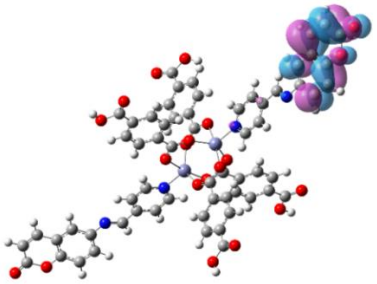

LUMO+3
(-2.76 eV)

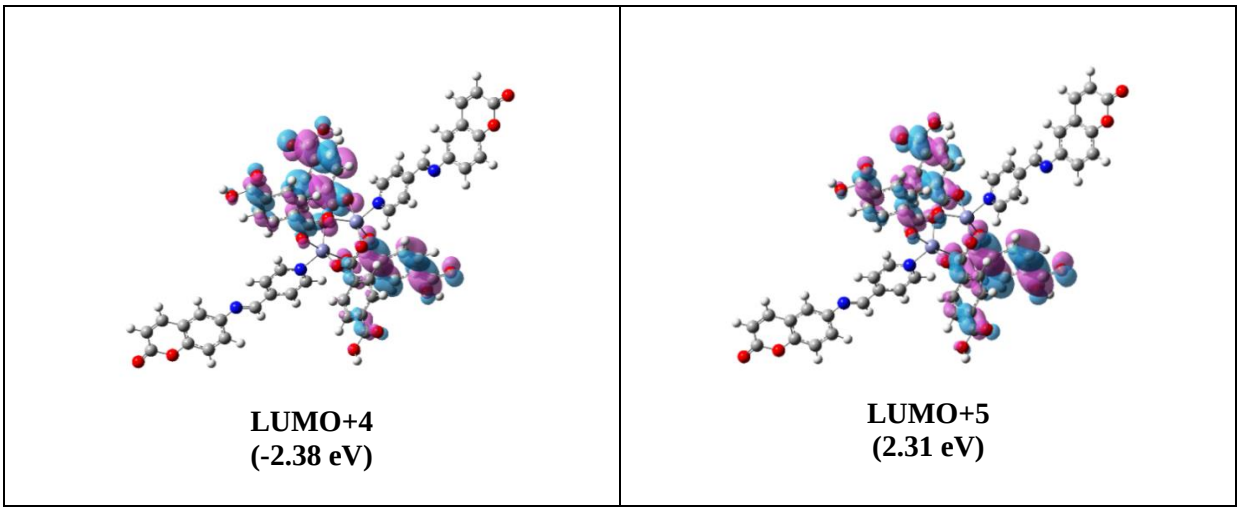

VI.3.3. Opto-electrical Property

The UV-Vis spectrum (200 – 700 nm) of Zn(II)-CP dispersion in DMF has determined the optical band gap, 2.91 eV, by Tauc's equation (Eq. VI.1, **Fig.VI.10**)[47, 48].

$$(\alpha h\upsilon)^n = c(h\upsilon - E_g) \qquad \text{(VI. 1)}$$

(α = the absorption coefficient, h = Planck's constant, υ = frequency, E_g = the optical band gap energy, c = a constant and n = the order of energy transition which is taken as ½ for indirect allowed transition).

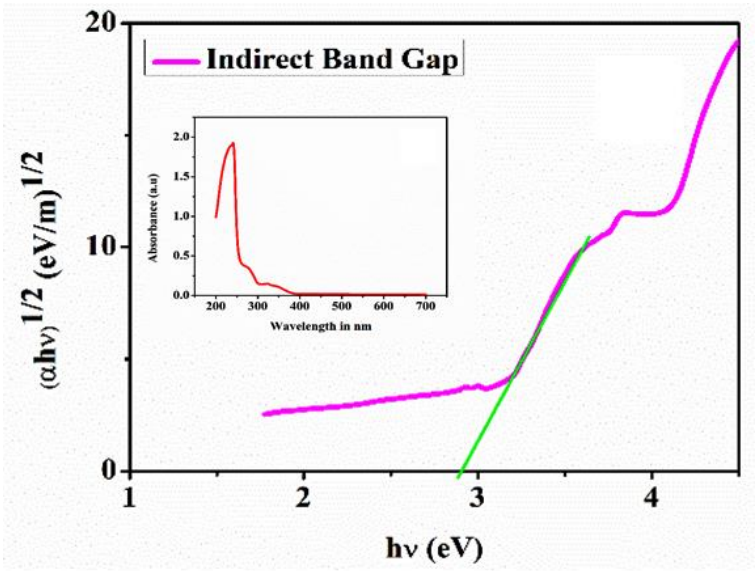

Fig.VI.10. Tauc's plot to determine the indirect allowed band gap energy of Zn(II)-CP. (Inset: UV-Vis absorption spectrum of the material.

The device's I–V characteristic was recorded both in dark and light, and the results are depicted in **Fig.VI.11** (inset logarithmic current vs voltage) The measured conductivity of Zn(II)-CP is 8.07×10^{-3} S m^{-1} (dark) and is enhanced by about 15% upon irradiation with light (9.26×10^{-3} S m^{-1}) which suggests the semiconducting property of the material. Zn(II), a d^{10}, unlike to show conductivity; Zn-O (carboxylato) is covalent in nature and certainly does not favour through bond electrical transport. Hence the conductivity arises from metal dependent charge transport through non-covalent H-bonding interactions. The electron density concerted as evident from the DFT calculation suggest that Zn(II)-CP influences of on the conductivity. The nonlinear rectifying nature of the representative I–V characteristics of the Al/compound interface was obvious, confirming Schottky barrier diode (SBD) development at the MS contact. At ±1 V, the compound's rectification ratios (I_{on}/I_{off}) were discovered to be 17.65 and 19.22 respectively. However, compound has a low photosensitivity which is enhanced by about 15%.

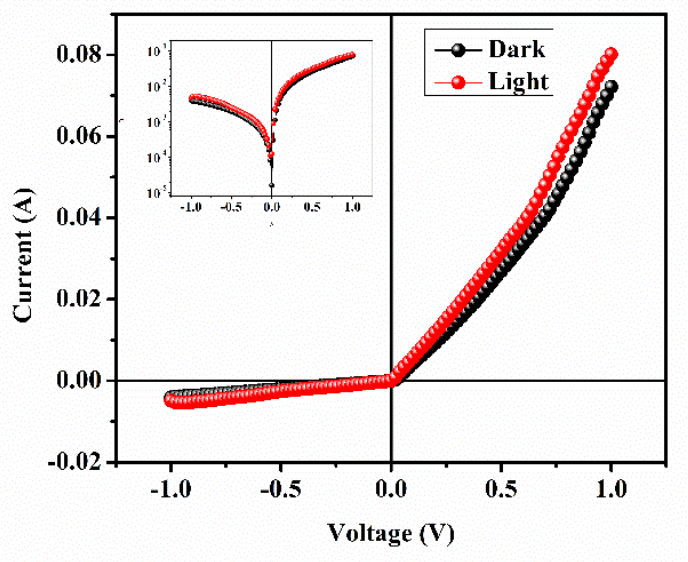

Fig.VI.11. Characteristics curve in linear scale (Inset: logarithmic scale) for ITO/Compound/Al configuration.

I–V measurements are commonly used for calculation of various SD factors. Pure thermionic emission is assumed to be the major transport process in SDs for this reason. The experimental I–V data in this circumstance may be explained by the Eq. VI.2:

$$I = I_{sat}[exp\frac{\beta}{\eta}V - 1] \qquad \text{(VI. 2)}$$

where I represent diode current density at bias V, η is the ideality factor, $\beta=(q/kT)$ represents inverse thermal voltage and I_{sat} denotes saturation current density as given by Eq. VI.3:

$$I_{sat} = AA^{*}T^{2}\exp(-\beta\varphi) \qquad \text{(VI. 3)}$$

A give the diode area, A* represents modified Richardson constant and φ denotes Schottky barrier height (SBH). The modified Richardson constant is considered as 1.206×10^{6} $AK^{-2}m^{-2}$.

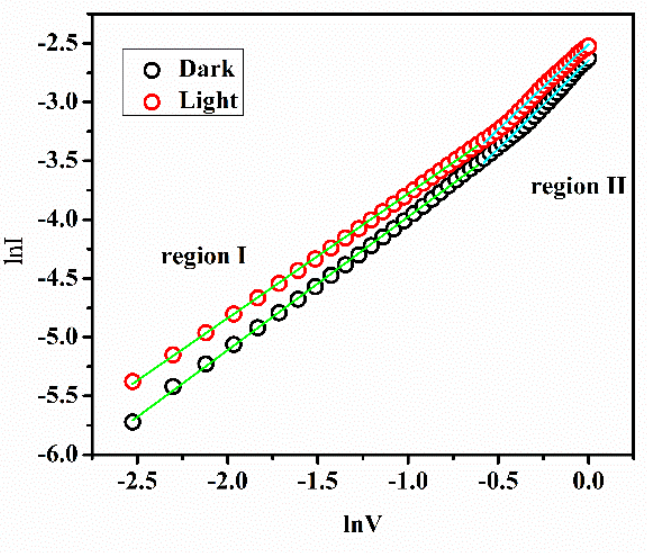

Fig.VI.12. ln I vs ln V plot for fabricated Schottky device

The ln I vs. lnV graph is plotted for the forward bias voltage regime (**Fig.VI.12**) and has been linearly fitted for better understanding of the charge transport process through MS interface. Slope corresponding to region I is ~ 1 that indicates the that carrier transport events were dominated by Ohmic conduction. The slope in region II is ~ 2, that exposes the Space Charge Limited Conduction (SCLC) mechanism which is due to trap assisted carrier transitions.

Because of existence of a parasitic series resistance (Rs) impacts the I–V characteristics mostly at high voltages, Eq. 2 can be rearranged to generate Eq. VI.4: [49]

$$I = I_{sat}[exp\frac{\beta}{\eta}(V - IR_s) - 1] \qquad \text{(VI. 4)}$$

Where, IR_S term indicates the voltage drop across series resistance of a semiconductor diode. Inserting saturation current density value from Eq.3 into Eq.4, and differentiate with respect to lnI, we get Eq. VI. 5.

$$\frac{dV}{dlnI} = IAR_S + \frac{\eta}{\beta} \quad \text{(VI. 5)}$$

For constructed Schottky device, the ideality factor (η) and series resistance (R_s) were determined from dV/dlnI vs I plot (**Fig.VI.13 (a), (b)**). In I-V characteristics curve for dV/dlnI vs I curves of diode curves of diode, linearity was discovered in downward curvature zone of forward bias. The ideality factor and series resistance in this region were calculated from slope and intercept. The ideality factor for the compound deviated from 1 due to inhomogeneity at the MS junction. Ideality factor nearly equals to 2 indicates recombination is limited by both majority and minority carriers. at dark condition. Under light illumination the fabricated diode behaves more ideal.

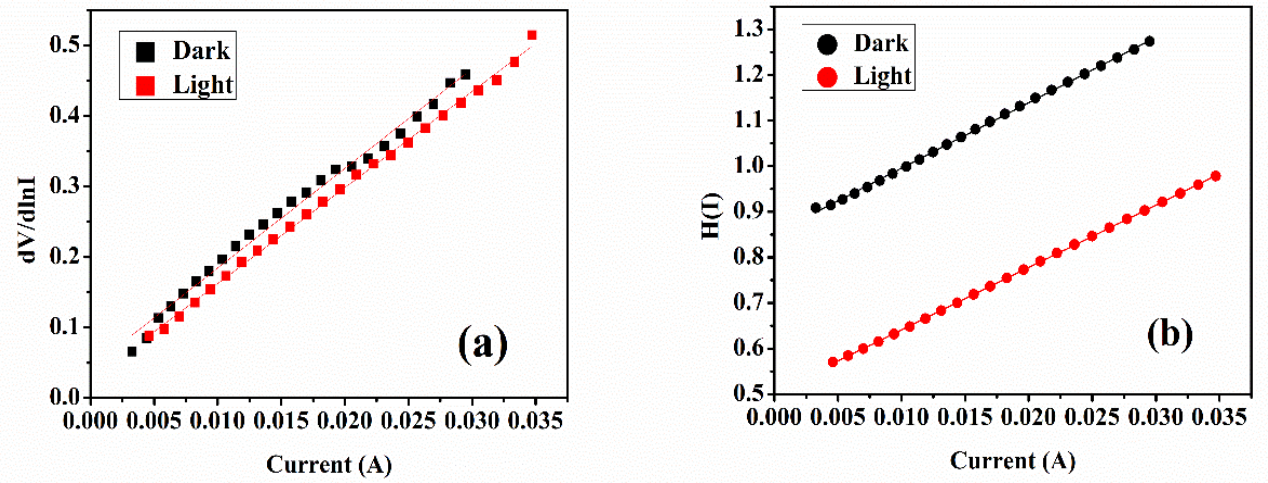

Fig.VI.13. (a) dV/dlnI and **(b)** H(I) vs current density plot for Zn(II)-CP based Schottky diode.

In the Cheung model, the current density-reliant function H(I) can be expressed as (Eq. VI.6).[50]

$$H(I) = V - \frac{\eta}{\beta} \ln\left(\frac{I}{AA^*T^2}\right) = IAR_S + \eta\varphi \quad \text{(VI.6)}$$

Schottky barrier height of the device was determined using the relevant $H(J_d)$ versus J_d graph. In the low potential area, this plot, like the dV/dlnI vs I plot, indicated linearity. The series resistance (Rs) and barrier height (φ_B) were estimated from H(I) vs I plot are represented in **Table VI.6**. Series resistance values obtained from two different procedures (dV/dlnI and H(I)) were nearly equal and also very low with reference to Coordination Polymer semiconductor. This generally depends on many different factors including the

semiconductor thin-film morphology in the vicinity of the contact interface, the contact work function, and the energetic landscape of the material.[45, 51,52,]

Table VI.6: Schottky diode parameters of Zn(II)-CP fabricated device

Condition	Rectification Ratio	Conductivity (S m^{-1})	Ideality factor	Barrier height φ_B (eV)	R_s from dV/dlnI (Ω)	R_s from H(I) (Ω)
Dark	17.65	8.07×10^{-3}	1.64	0.52	14.14	14.35
Light	19.22	9.26×10^{-3}	0.99	0.51	13.63	13.67

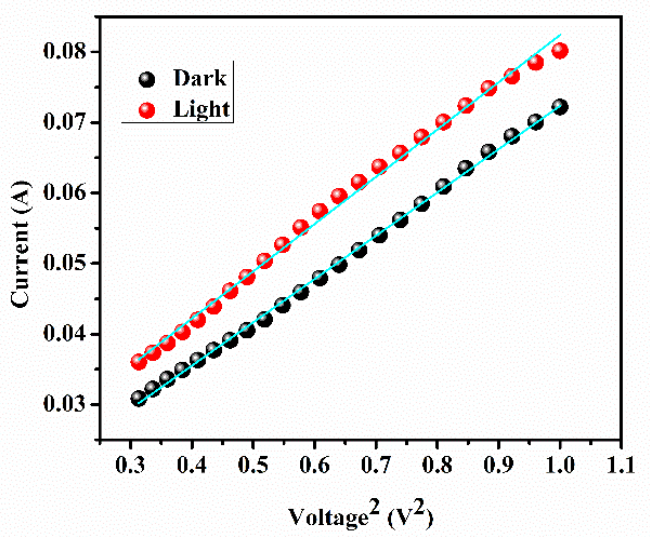

Fig.VI.14. Current density vs. voltage^2 graph for SCLC region

In SCLC region (region II) charge transport parameters (e.g. carrier concentration, mobility, transit time and density of states) was calculated to further investigate the device. Considering the slope of I vs. V^2 graphs of region II (**Fig.VI.14**), mobility (μ) of the charge carrier was estimated from Mott-Gurney equation using space charge limited current density theory. The corresponding Eq. VI.7 is [53]

$$I = \frac{9\,A\,\mu\,\varepsilon_0\varepsilon_r}{8}\left(\frac{V^2}{d^3}\right) \qquad \text{(VI.7)}$$

ε_0 and ε_r is the absolute permittivity and relative dielectric constant of the compound respectively. ε_r (= 1.08) ε_r was extracted from capacitance versus logarithm of frequency (**Fig.VI.15**) using the equation written below in Eq. VI. 8.

$$\varepsilon_r = \frac{1}{\varepsilon_0}\frac{C_{sat}\, d}{A} \quad \text{(VI.8)}$$

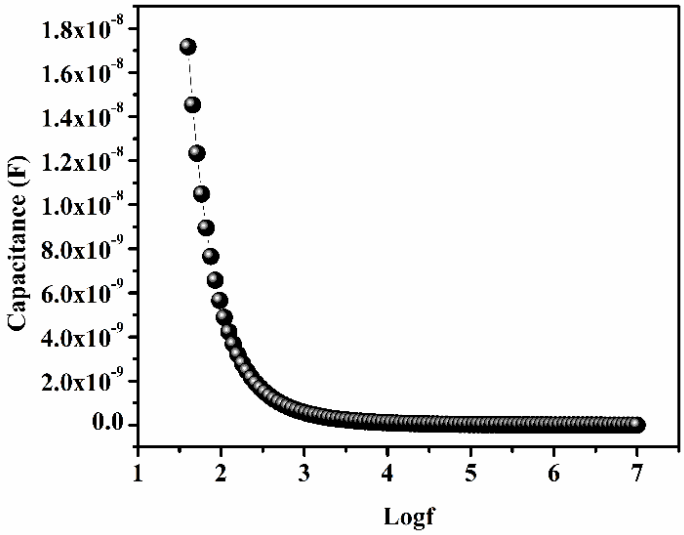

Fig.VI.15. Capacitance versus logarithm of frequency plot

The time of flight (τ) of the carrier is the time required to transit from compound to aluminum through MS junction. From the slope of I-V curve of region-II, τ was derived using Eq.VI.9.[54]

$$\tau = \frac{9\ A\ \varepsilon_0\ \varepsilon_r}{8\ d}\left(\frac{V}{I}\right) \quad \text{(VI.9)}$$

Charge carrier concentration (N) near the Fermi level and density of states had been also calculated (**Table VI.7**) with the help of the following Eqs. VI.10, 11.[55,56]

$$N = \frac{\sigma_{SCLC}}{q\,\mu} \quad \text{(VI.10)}$$

$$N_s = \frac{2\varepsilon_0\varepsilon_r(V_2 - V_1)}{d^2\Delta E_F} \quad \text{(VI.11)}$$

Where ΔE_F represents the shift in quasi-Fermi level and can be determined from the subsequent Eq. VI. 12.

$$\Delta E_F = kTln\left(\frac{I_2V_1}{I_1V_2}\right) \quad \text{(VI.12)}$$

Table VI.7: Charge Transport Parameters of the device

Condition	Mobility (μ) ($m^2V^{-1}S^{-1}$)	Time of flight τ (Å)	Carrier Concentration N (m^{-3})	Density of States N_s (m^{-3})
Dark	8.08×10^{-4}	7.95	1.03×10^{20}	7.45×10^{21}
Light	8.82×10^{-4}	7.24	1.01×10^{20}	9.36×10^{21}

VI.3.4. Cytotoxicity study against several cancer cell lines

Results from MTT assay in terms of IC_{50} value (**Fig.VI.16(a) and (c)**) show that the Zn(II)-CP shows cytotoxicity in most of the selected human cancer cell lines, like HeLa, HepG2, MDA-MB 231 relative to the normal kidney epithelial cell line NKE and its efficacy in inhibiting proliferation of HeLa ($IC_{50:}$ 21.02 ± 1.57) was highest as compared to other cancer cells (HepG2 $IC_{50:}$ 42.22 ± 3.45, MDA-MB 231 $IC_{50:}$ 46.37 ± 3.06). Thus, based on this study HeLa was selected for further study. Phase contrast microscopic imaging of compound Zn(II)-CP treated HeLa cell was performed which revealed that as compare to control experiment, treated setup showed concentration-dependent increase in the level of morphological change to induce death in HeLa cells (**Fig.VI.16 (b)**)

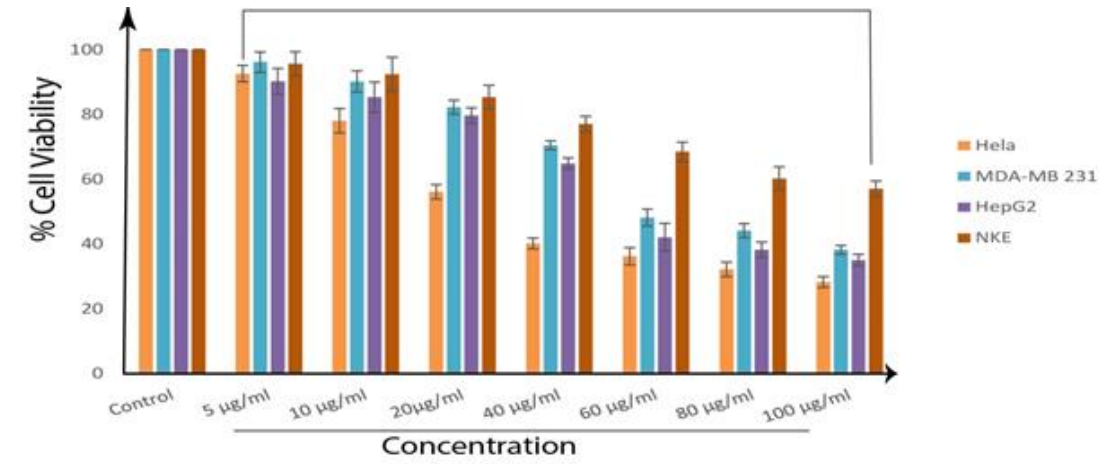

B)

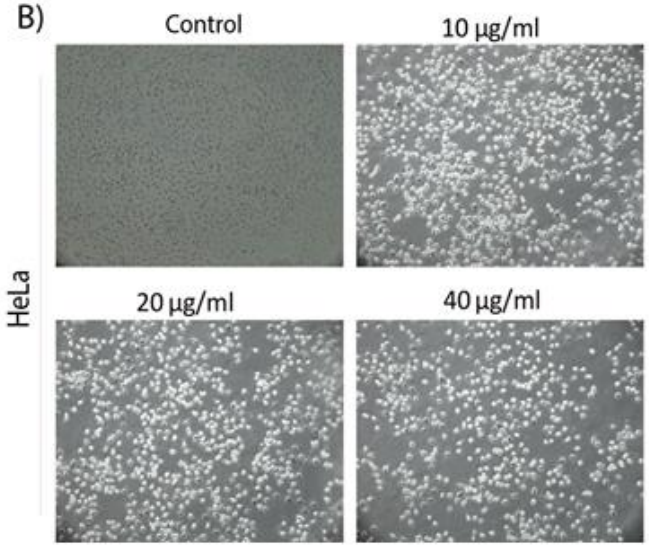

C)

IC50 Concentration (µg/ml)

Cell Lines	Compound	Etoposide
HeLa	21.02 ± 1.57	14.26 ± 3.26
MDA-MB-231	46.37 ± 3.06	20.03 ± 1.98
HepG2	42.22 ± 3.45	22.38± 3.22
NKE	≥100	34.05 ±2.46

Fig.VI.16. In vitro cytotoxicity was measured by MTT **(a)** Bar graph and Table **(b)** Phase contrast microscopic imaging of compound Zn(II)-CP (10 µg/ml, 20 µg/ml, and 40µg/ml) treated HeLa. Results were expressed as

mean ± SEM. *(P ≤0.01-0.05) is the level of significance in respect with the control. **(c)** showing IC_{50} values of Compound Zn(II)-CP in various cancer cell lines including HeLa, MDA-MB 231, HepG2 (cancer cells), and NKE (human normal kidney epithelialcell line).

VI.3.5. Zn(II)-CP treatment promotes apoptotic cell death and involves intracellular ROS generation

To understand the mechanism of anti-proliferation potential of the compound Zn(II)-CP, we have studied the generation of intracellular Reactive Oxygen Species (ROS) accumulation, H_2DCFDA fluorescence assay was performed with Fluorescence microscopic imaging. From H_2DCFDA assay of Zn(II)-CP co treated cells showed a dose dependent increase in greenish emission intensity on compared to that of the control untreated cells indicating intracellular ROS generation even at a concentration 10 µg/ml and in comparison, to control its fluorescence intensity increases to 2.24, 4.25 and 4.92-fold respectively upon 10 µg/ml, 20 µg/ml, and 40 µg/ml Zn(II)-CP treatment for 24 h. Nonetheless, HeLa cells pre-treated with 10 mM N-Acetyl-Cysteine (NAC), a potent and widely accepted inhibitor of ROS, reduced compound Zn(II)-CP induced ROS generation in comparison to Zn(II)-CP treatment alone, at a concentration of 40 µg/ml (**Fig.VI.17(a)**).

Results from Annexin V-FITC/PI flow cytometric assay also showed a dose dependent increased in the number of apoptotic cell population upon treatment of Zn(II)-CP. As shown in (**Fig.VI.17(b)**) 10 µg/ml, 20 µg/ml, and 40 µg/ml Zn(II)-CP treatment for 24 h increased the annexin V-$FITC^+/PI^-$ (early apoptotic) and annexin V-$FITC^+/PI^+$ (late apoptotic) cell population to 24.39%, 35.15% and 69.35% respectively in comparison to 2.24% in control experiment. Therefore, it is very clear that compound Zn(II)-CP mediated anti-proliferative potential may be mediated by ROS mediated apoptosis of the HeLa cells.

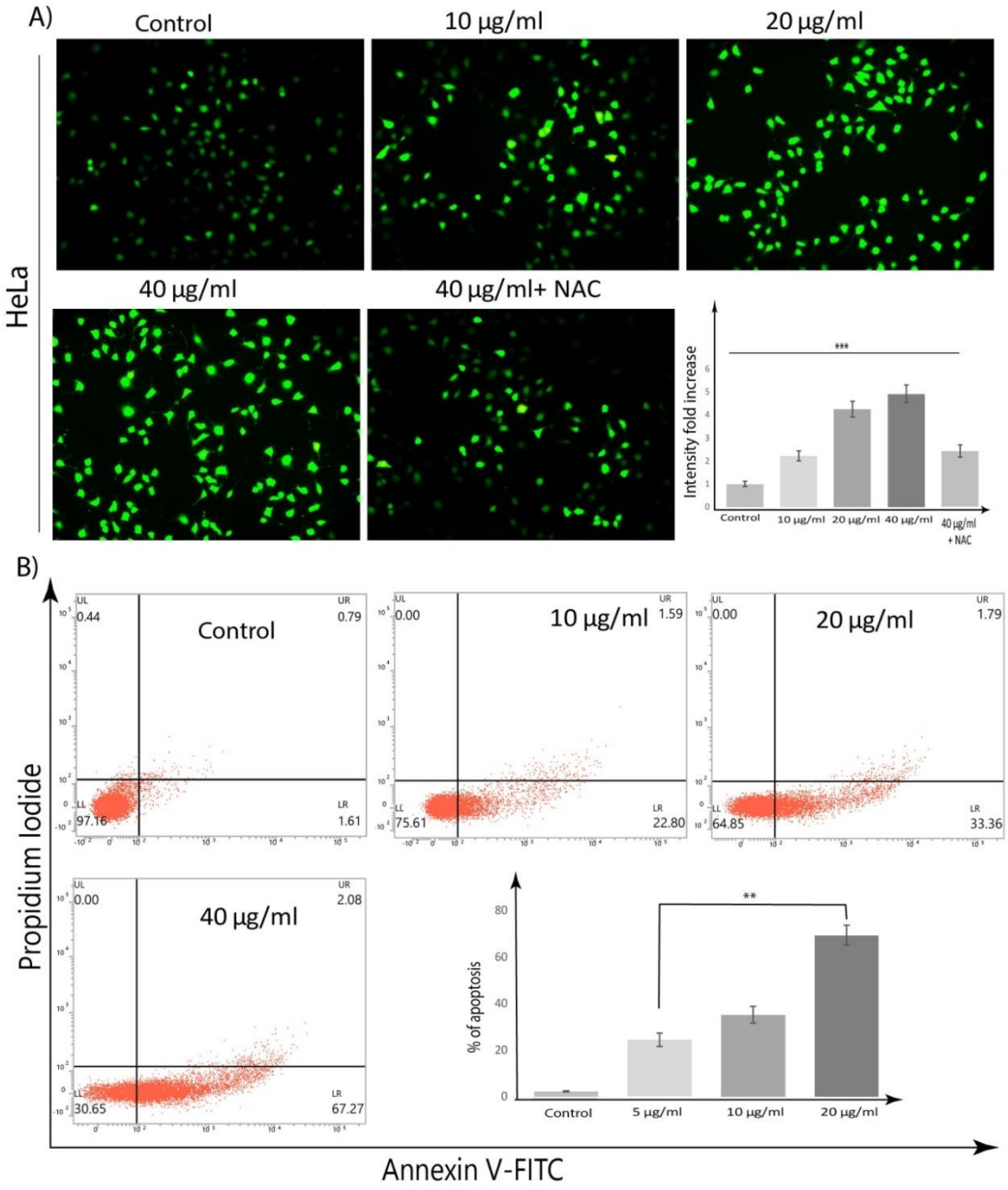

Fig.VI.17. (a) Concentration-dependent increase in intercellular ROS accumulation of HeLa cells, in response to Compound Zn(II)-CP treatment. Post treatment with Zn(II)-CP (10 µg/ml, 20 µg/ml, 40 µg/ml and Pre-treatment with NAC) for 24 h, cells were stained with H2DCFDA and fluorescence microscopic was performed. **(b)** Concentration-dependent increase in annexin V-FITC/PI-positive (Apoptosis) population of HeLa cells, in response to Zn(II)-CP treatment. Post treatment with Zn(II)-CP (10µg/ml, 20 µg/ml, and 40µg/ml) for 24 hr cells were stained with annexin V-FITC/PI and analyzed in FACS.

VI.4. Conclusion

In summary, multifunctional applications of Zn-coordination polymer, $[Zn_2(BDC)_4(QPR)_2(H_2O)]_n$ (Zn(II)-CP) (BDC^{2-}, 1,4-benzenedicarboxylato; QPR, 7-[(Pyridin-4-ylmethylene)-amino]-chromen-2-one) are recorded in this work. From the best of our knowledge, the coumarin decorated probe 7-[(Pyridin-4-ylmethylene)-amino]-chromen-2-one has been utilized first time in the construction of coordination network. In view of the structural architecture, this material has also been quite unique to make a square grid framework within the molecular assembly. However, low band gap (2.91 eV) electrical property can be tempted to fabricate a semiconducting Schottky diode device. Besides, the biological activity of the compound is also simulating; the Zn(II)-CP has revealed the effective anticancer property and highest efficiency is shown against HeLa cell line (IC_{50}, 21.02±1.57). Recent technological advancement and biological requirement can be utilized for substantial use of this material in laboratory to land applications.

VI.5. References:

1. S. L. Sensi, P. Paoletti, A. I. Bush, and I. Sekler. *Nat. Rev. Neurosci*., 2009, **10**, 780-791.
2. S. Paul, S. Maity, S. Halder, B. Dutta, S. Jana, K. Jana and C. Sinha. *Dalton Trans*., 2022, **51**, 3198-3212.
3. S. Brase, F. Glaser, T. Hurrle, Coumarins. In Privileged Scaffolds in Medicinal Chemistry: Design, Synthesis, Evaluation. *The Royal Society of Chemistry*, 2016 287−311.
4. Anamika, D. Utreja, Ekta, N. Jain, S. Sharma, *Curr. Org. Chem.* **2019**, *22*, 2509−2536.
5. R. H. Flatman, A. Eustaquio, S.-M. Li, L. Heide, A. Maxwell, *Antimicrob. Agents Chemother*. 2006, **50**, 1136−1142.
6. D. Egan, R. O. Kennedy, E. Moran, D. Cox, E. Prosser, R. D. Thornes, *Drug Metab Rev.* 1990**, 22**,503-29.
7. A. Stefanachi, F. Leonetti, L. Pisani, M. Catto, A. Carotti, *Molecules.* 2018, **23**,1-34.
8. B. Sandhya, D. Giles, V. Mathew, G. Basavarajaswamy, R. Abraham *Eur. J. Med. Chem.* 2011, **46**, 4696-4701.

9. S. R. Batten, S. M. Neville, and D. R. Turner, Coordination Polymers: Design, Analysis and Application, *Royal Society of Chemistry*, London, 2009
10. M. C. Hong, and L. Chen, John Wiley & Sons, Inc., Design and Construction of Coordination Polymers Hoboken, New Jersey, 2009.
11. S. Kitagawa, R. Kitaura, and S. I. Noro, *Angew. Chem., Int. Ed.*, 2004, 43, 2334–2375.
12. Z. Chen, L. Yin, X. Mi, S. Wang, F. Cao, Z. Wang, Y. Li, J. Lua and J. Dou, *Inorg. Chem. Front.*, 2018, **5**, 2314-2320.
13. J. Gu, M. Wen, Y. Cai, Z. Shi, D. S. Nesterov, M. V. Kirillova and A. M. Kirillov, *Inorg. Chem.* 2019, **58**, 5875–5885.
14. A. Chandra, M. Das, K. Pal, S. Jana, B. Dutta, P. P. Ray, K. Jana, and C. Sinha. *ACS Omega*, 2019, **4**, 17649−17661
15. B. Dutta, A. Dey, C. Sinha, P. P. Ray, M. H. Mir. *Inorg. Chem.*, 2018, **57**, 8029–8032.
16. D. Maspoch, D. Ruiz-Molinaa, J. Veciana, *J. Mater. Chem.*, 2004, **14**, 2713-2723.
17. S. Jana, A. Ray, A. Chandra, M. S. E. Fallah, S. Das, and C. Sinha, *ACS Omega*, 2020, **5**, 274–280.
18. Q. Liu, X. Liu, C. Shi, Y. Zhang, X. Feng, M. L. Cheng, S. Sua and J. Gu. *Dalton Trans*., 2015, **44**, 19175-19184.
19. M. Lippi, M. Cametti. *Coord. Chem. Rev.*, 2021, **430**, 213661.
20. L. Fan, D. Zhao, H. Zhang, F. Wang, B. Li, L. Yang, Y. Deng, X. Zhan. *Microporous and Mesoporous Mater*. 2021, **326**, 111396
21. Y.-Q. Zhang, V. A. Blatov, T.-R. Zheng, C.-H. Yang, L.-L. Qian, K. Li, B. L. Li, and Wu. B.; *Dalton Trans*., 2018, **47**, 6189-6198.
22. X. Zhang, X. Zhuang, N. Zhang, C. Ge, X. Luo, J. Li, J. Wu, Q. Yang, and R. Liu. *Cryst. Eng. Comm*., 2019, **21**, 1948-1955.
23. X. Zhang, V. Vieru, X. Feng, J. L. Liu, Z. Zhang, B. Na, W. Shi, B. W. Wang, A. K. Powell, L. F. Chibotaru, S. Gao, P. Cheng, and J. R. Long, *Angew. Chem., Int. Ed.*, 2015, **54**, 9861–9865
24. B. Dutta, A. Dey, C. Sinha, P. P. Ray, and M. H. Mir, *Dalton Trans.*, 2019, **48**, 11259-11267

25. J. Duan, W. Jin, and S. Kitagawa *Coord. Chem. Rev.*, 2017, **332**, 48–74 .

26. B. Dutta, S. M. Pratik, S. Jana, C. Sinha, A. Datta, M. H. Mir, *Chemistry Select*, 2018, **3**, 4289−4291.

27. W. J. Li, J. Liu, Z. H. Sun, T. F. Liu, J. Lü, S. Y. Gao, C. He, R. Cao, J. H. Luo, *Nat. Commun.* 2016, **7**, 11830−11837.

28. K. Naskar, A. Dey, B. Dutta, F. Ahmed, C. Sen, M. H. Mir, P. P. Roy, and C. Sinha, *Cryst. Growth Des.* 2017, **17**, 3267–3276

29. Q. Lin, C. Bao, G. Fan, S. Cheng, H. Liu, Z. Liu, and L. Zhu. *J. Mater. Chem.*, 2012**, 22**, 6680-6688

30. G. M. Sheldrick, *ActaCrystallogr.,Sect.A: Found.Crystallogr*., 2008, **64**, 112–122.

31. A. L.Spek, *Platon*, The Netherlands, 1999.

32. J. Farrugia, *J. Appl. Crystallogr.*, 1997, **30**, 565–565.

33. M. J. Frisch, G. W. Trucks, H. B. Schlegel, G. E. Scuseria, M. A. Robb, J. R. Cheeseman, G. Scalmani, V. Barone, B. Mennucci, G. A. Petersson, H. Nakatsuji, M. Caricato, X. Li, H. P. Hratchian, A. F. Izmaylov, J. Bloino, G. Zheng, J. L. Sonnenberg, M. Hada, M. Ehara, K. Toyota, R. Fukuda, J. Hasegawa, M. Ishida, T. Nakajima, Y. Honda, O. Kitao, H. Nakai, T. Vreven, J. A. Montgomery Jr., J. E. Peralta, F. Ogliaro, M. Bearpark, J. J. Heyd, E. Brothers, K. N. Kudin, V. N. Staroverov, R. Kobayashi, J. Normand, K. Raghavachari, A. Rendell, J. C. Burant, S. S. Iyengar, J. Tomasi, M. Cossi, N. Rega, J. M. Millam, M. Klene, J. E. Knox, J. B. Cross, V. Bakken, C. Adamo, J. Jaramillo, R. Gomperts, R. E. Stratmann, O. Yazyev, A. J. Austin, R. Cammi, C. Pomelli, J. W. Ochterski, R. L. Martin, K. Morokuma, V. G. Zakrzewski, G. A. Voth, P. Salvador, J. J. Dannenberg, S. Dapprich, A. D. Daniels, O. Farkas, J. B. Foresman, J. V. Ortiz, J. Cioslowski and D. J. Fox, Gaussian 09, Revision D.01, Gaussian Inc., Wallingford, CT, 2009.

34. A. D. Becke, *J. Chem. Phys.* 1993, **98**, 5648–5652.

35. W.R. Wadt and P.J. Hay, *J. Chem. Phys.* 1985, **82**, 299-310

36. R. Bauernschmitt and R. Ahlrichs, *Chem. Phys. Lett.* 1996, **256**, 454–464.

37. M. Cossi and V. Barone, *J. Chem. Phys.* 2001, **115**, 4708–4717.

38. M. Cossi, N. Rega, G. Scalmani and V. Barone, *J. Comput. Chem.*, 2003, **24**, 669–681.

39. N. M. O'Boyle, A. L. Tenderholt and K. M. Langner, *J. Comput. Chem.*, 2008, **29**, 839–845.

40. T. Mosmann, *J. Immunol. Methods* 1983, **65**, 55–63

41. E. Miller, *Methods Mol. Med.* 2004, **88**, 191–202.

42. B. Dutta, A. Dey, S. Maity, C. Sinha, P. P. Ray and M. H. Mir. *ACS Omega* 2018, **3**, 12060–12067

43. B. Dutta, A. Dey, K. Naskar, S. Maity, F. Ahmed, S. Islam, C. Sinha, P. Ghosh, P. P. Ray and M. H. Mir. *New J. Chem.*, 2018,**42**, 10309-10316.

44. S. Jana, J. Datta, S. Maity, B. Thakurta, P. P. Ray, C. Sinha. *Cryst. Growth Des.* 2021, 21, 5240–5250

45. K. Naskar, S. Sil, N. Sahu, B. Dutta, A. M. Z. Slawin, P. P. Ray and C. Sinha. *Cryst. Growth Des.*, 2019, 19, 2632–2641.

46. B. Dutta, C. Sinha and M. H. Mir. *Chem. Commun.*, 2019,**55**, 11049-11051.

47. S. N. Abeysingha, R. P. Wijesundera, C. V. Hettiarachchi, I. R. Perera. *Mater. Chem. Phys.*, 2020, **251**, 123109

48. P. Das, B. Pal, J. Datta, M. Das, S. Sil, and P. P. Ray, *J. Phys. Chem. Solids*, 2021, **148**, 109706

49. M. Das, P. Das, J. Datta, D. Das, S. Acharya, and P. P. Ray, *Mater. Sci. Semicond. Process*, 2021, **130**, 105799.

50. S. K. Cheung, and N. W. Cheung, *Appl. Phys. Lett.* 1986, **49**, 85-87.

51. S. Naaz, P. Das, A. Frontera, B. Dutta, S. Khan, P. P. Ray and M. H. Mir. *Cryst. Growth Des.* 2022, 22, 9, 5189–5197.

52. A. Allain, J. Kang, K. Banerjee and A. Kis. *Nature Materials*, 2015, 14, 1195-1205.

53. P. Das, S. Majumdar, A. Dey, S. Mandal, A. Mondal, S. Chakrabarty, P. P. Ray and B. Dey. *New J. Chem.*, 2021, **45**, 15920-15927.

54. S. Halder, A. Dey, A. Bhattacharjee, J. O. Castro, A. Frontera, P. P. Ray and P. Roy. *Dalton Trans.***,** 2017,**46**, 11239-11249.

55. B. Dutta, J. Datta, S. Maity, C. Sinha, D. Sun, P. P. Ray, and M. H. Mir, *Phys. Chem. Chem. Phys.*, 2018, **20**, 24744-24749.

56. B. Dutta, K. Pal, K. Jana, C. Sinha, M. H. Mir. *ChemistrySelect*, 2019, **4**, 9947-9951.

Chapter VII

Conclusion

VII.1. Conclusion

The research work in this Thesis focuses on the characterisation of Schiff bases those have been considered as a versatile chemosensors for the recognition of bio-relevant ions/molecules at a very low concentration (μM to nM) level. The coordination environment of such molecule with metal centre can form discrete complex and coordination polymers (CPs) who have been characterised by the spectroscopic data and the structural confirmation by Single Crystal X-Ray Diffraction Data.

VII.2. A Fluorogenic Triphenyl-Amine-Naphthyl-Hydrazide Probe Selective for Cu^{2+} and Cysteine Detection via an ON-OFF-ON Logic path with Real Applications. (Chapter II)

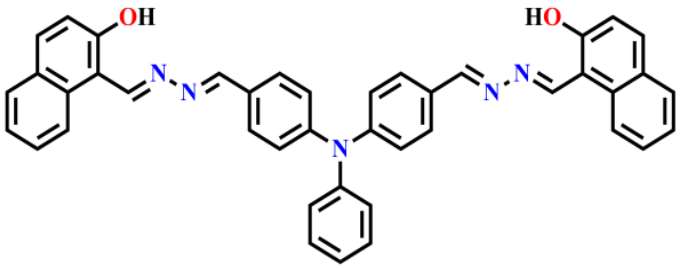

1,1'-((1E,1'E)-((2E,2'E)(((phenylazanediyl)bis(4,1-phenylene))bis-(methanylylidene))bis-(hydrazine-2,1-diylidene))bis(methanylylidene))bis(naphthalen-2-ol)

1,1'-((1E,1'E)-((2E,2'E)(((phenylazanediyl)bis(4,1-phenylene))bis-(methanylylidene))bis-(hydrazine-2,1-diylidene))bis(methanylylidene))bis(naphthalen-2-ol), H_2L produced as a result of condensation reaction which exhibits intense emission in solution and solid phase with substantial sensitivity and selectivity towards Cu^{2+} over a series of ions and oxidizing agents. In presence of Cu^{2+} the emission (λ_{em}, 550 nm; λ_{abs}, 420 nm) gets selectively quenched (CHEQ) with a detection limit of 7.3 nM in 7:3(v/v) CH_3CN/H_2O medium (HEPES buffer, pH 7.2). The interaction of Cu^{2+} with the probe has been experimentally determined. (**Fig.VII.2.1. (a),(b)**) On addition of cysteine to L-Cu^{2+}ensemble, the emission intensity (550 nm) enhances which accounts the release of Cu^{2+} from the non-emissive complex and restores the total fluorogenic efficiency of probe, H_2L (LOD (Cysteine), 36 nM). (**Scheme VII.2**) This ON-OFF-ON reversibility mechanism attributed for the

construction of IMPLICATION Logic gate (**Fig.VII.2.2. (a), (b)**). Results from MTT Assay in WI-38 Cell ensures its biocompatibility and Intracellular imaging in Hep G2 cells shows its sensing applicability in cells.

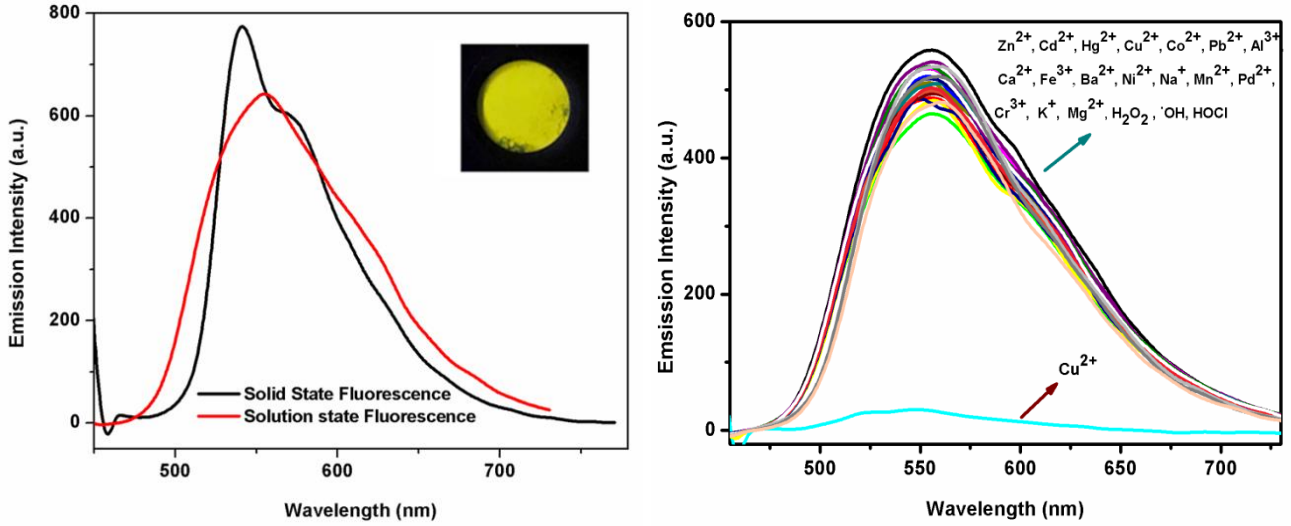

(a) **(b)**

Fig.VII.2.1. (a) Solid and solution state emission spectra of H_2L (λ_{ex} 430 nm); Inset: solid state images under UV light **(b)** Fluorescence spectra of H_2L in presence of different analytes.

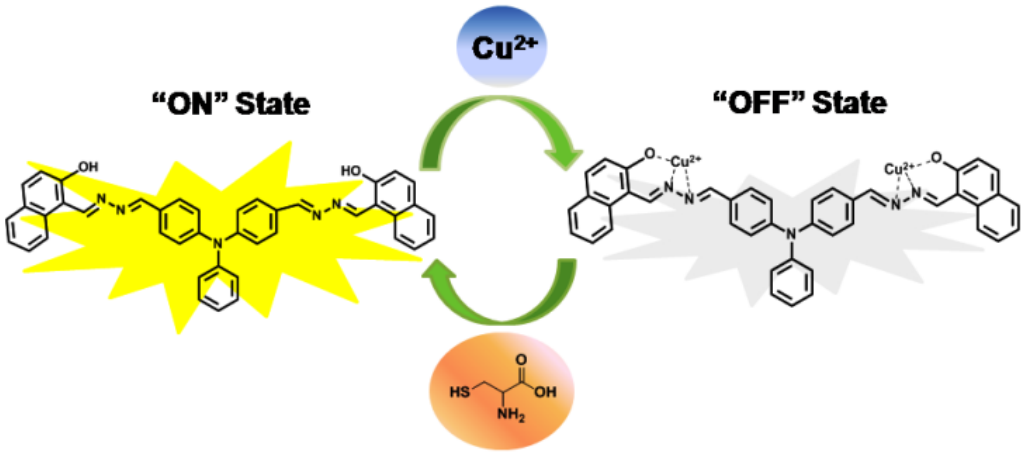

Scheme VII.2. Schematic Representation of the reversible chemosensor H_2L for Cu^{2+} and Cysteine sensing.

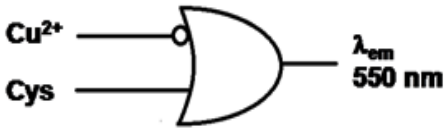

INPUT 1 Cu^{2+}	INPUT 2 Cys	OUTPUT λ_{em} = 550 nm
0	0	1
1	0	0
0	1	1
1	1	1

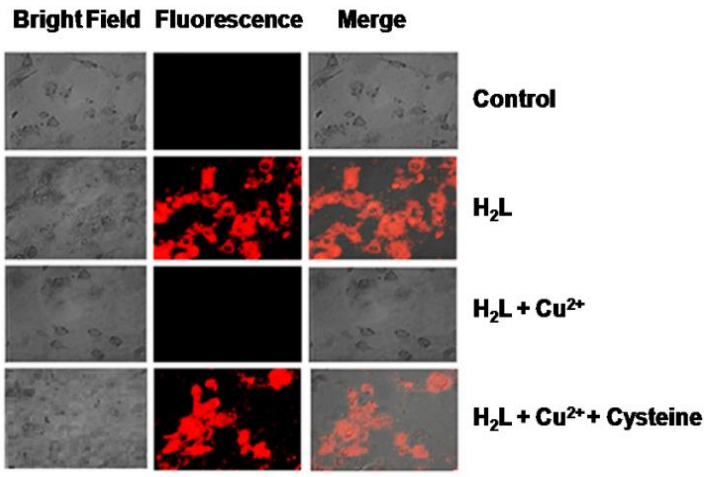

(a) **(b)**

Fig.VII.2.2. (a) Molecular IMPLICATION Logic gate construction for Cu^{2+} and Cys. **(b)** Bright field, fluorescence and merged microscopic images of untreated HepG2 (Control), cells treated with H_2L(10 μM), Cu^{2+}(20 μM), Cys (40 μM).

VII.3. A Highly Emissive Zn(II)-pyridyl-benzimidazolyl-phenolato based Chemosensor : Detection of $H_2PO_4^-$ via "Use" and "Throw" Device Fabrication. (Chapter III)

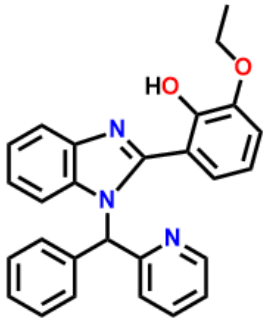

2-Ethoxy-6-[1-(phenyl-pyridin-2-yl-methyl)-1H-benzoimidazol-2-yl]-phenol

2-Ethoxy-6-[1-(phenyl-pyridin-2-yl-methyl)-1H-benzoimidazol-2-yl]-phenol, HL synthesized by the standard condensation reaction between amine and aldehyde to formm C=N coupling product and the single crystal X-ray diffraction measurement confirms the geometry. The probe recognizes Zn^{2+} (λ_{ex} =350 nm, λ_{em} = 461 nm) through CHEF mechanism in 9:1 (v/v) DMSO/H_2O (HEPES Buffer, pH=7.4) medium in presence of sixteen other cations at the limit of detection (LOD) 3.2 nM. (**Fig.VII.3.1. (a), (b)**) The emissive [$Zn(L^1)OAc$]

complex is further capable of disclosing a selective fluorescence 'turn-off' detection towards $H_2PO_4^-$ out of nineteen admissible anions The demetallation of the resulting complex in presence of $H_2PO_4^-$ leads to such response with LOD is found to be as low as 0.238 μM. Further this ON-OFF reversible switching behaviour of the probe has been employed to construct an INHIBIT logic gate with inputs input (Zn^{2+}, $H_2PO_4^-$) and one output (λ_{em} = 461 nm) (**Fig.VII.3.2. (a), (b)**). The sensitivity of the present chemosensor is successfully extended in solid state where the highly emissive [Zn(L^1)OAc] complex is found to be capable of recognizing $H_2PO_4^-$ up to 10^{-8} M level from water with the LOD of 10.97 pg (picogram)/cm^2 based on a portable and cost-effective contact mode detection on the fabricated paper strips. Subsequently, writing the word 'JU' with an aqueous Zn^{2+} filled pen, the HL-coated film divulges blue emission ('ON' state) only from the written portion due to feasible interaction of HL towards Zn^{2+} to form the highly emissive [Zn(L^1)OAc] complex. Interestingly, the glared emission completely fades away after washing the Zn(II)-treated film with aqueous $H_2PO_4^-$ solution ('OFF' state). (**Fig.VII.3.3 (a),(b)**)

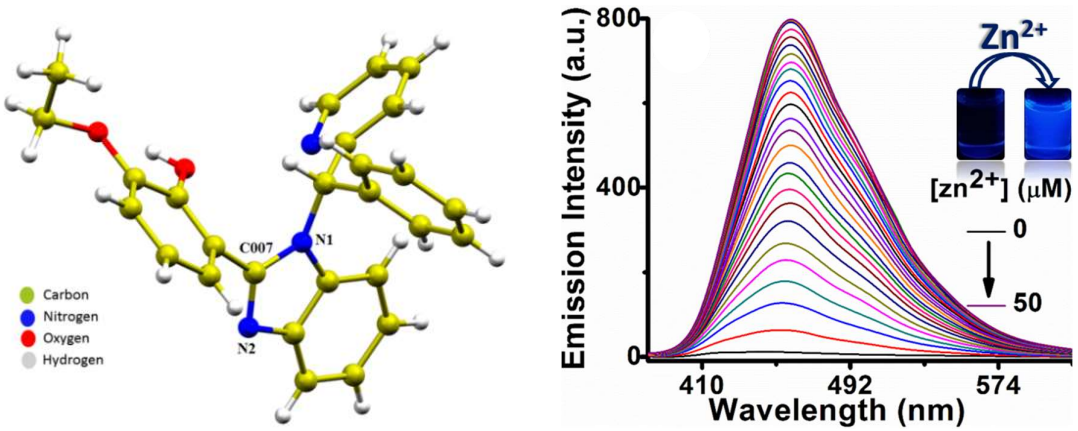

(a) **(b)**

Fig.VII.3.1. (a) Single crystal X-Ray structure of the probe, HL. **(b)** Change in the fluorescence spectrum of HL (50 μM) on successive addition of Zn^{2+} ion (0-50 μM) in 9:1 (v/v) DMSO/H_2O (HEPES Buffer, pH=7.4) (λ_{ex} = 350 nm). Corresponding inset indicates photographs of HL (50 μM) and its Zn(II)-complex taken under UV lights (λ_{ex} = 365 nm) .

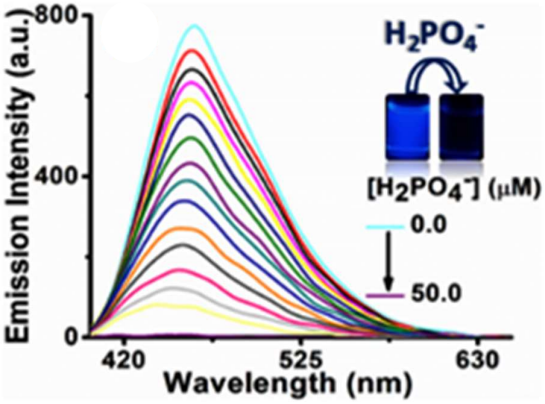

(a)

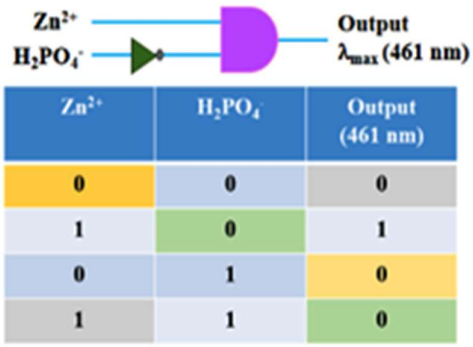

Zn^{2+}	$H_2PO_4^-$	Output (461 nm)
0	0	0
1	0	1
0	1	0
1	1	0

(b)

Fig.VII.3.2 (a) Change in emission spectra of [Zn(L^1)OAc] complex upon successive addition of $H_2PO_4^-$ (λ_{ex} = 350 nm). Inset of the figure represents photographs of Zn(II)-complex before and after treatment with $H_2PO_4^-$, taken under UV lights (λ_{ex} = 365 nm). **(b)** INHIBIT logic gate and truth table for two inputs: Zn^{2+} and $H_2PO_4^-$ and single output: λ_f = 461 nm.

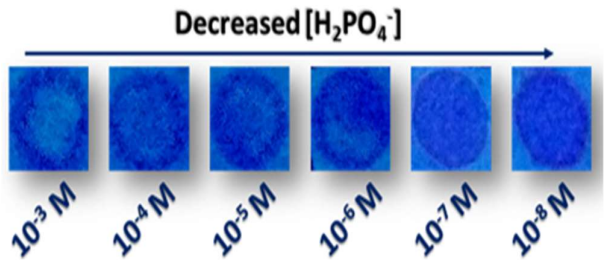

(a)

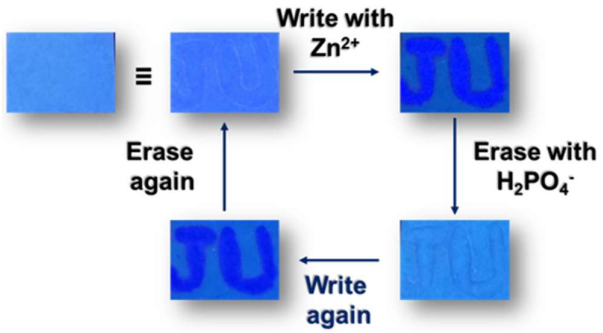

(b)

Fig.VII.3.3. (a) Photographs of Zn-complex embedded paper strips spotted with different concentrations of $H_2PO_4^-$ (i) 10^{-3}, (ii) 10^{-4}, (iii) 10^{-5}, (iv) 10^{-6}, (v) 10^{-7}, (vi) 10^{-8} (λ_{ex} = 365 nm). **(b)** Photographs of HL coated filter paper with hand written images under illumination at 365 nm.

VII.4. Idiosyncratic recognition of Zn^{2+} and CN^- using Pyrazolyl-Hydroxy-Coumarin scaffold and live cell imaging: Depiction of Luminescent Zn(II)-Metallocryptand. (Chapter IV)

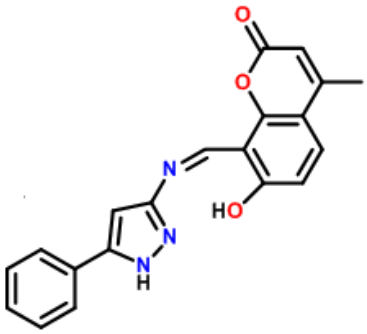

7-Hydroxy-4-methyl-8-(((5-phenyl-1H-pyrazol-3-yl)imino)methyl)-2H-chromen-2-one

7-Hydroxy-4-methyl-8-(((5-phenyl-1H-pyrazol-3-yl)imino)methyl)-2H-chromen-2-one, H_2L a Schiff base prepared and crystallized in monoclinic system (**Fig.VII.4.1(a)**). This synthesized scaffold is significantly emissive in solid phase. However, in solution phase it exhibits weak emission and serves as dual channel sensor Zn^{2+} (λ_{ex}= 390 nm, λ_{em} = 497 nm) and CN^- (λ_{ex}= 390 nm, λ_{em} = 447 nm) with two distinctive emission wavelengths in emission in CH_3CN/H_2O (99:1, v/v) (HEPES Buffer, pH 7.5) medium (**Fig.VII.4.1.(b), (c)**). The LOD is found to be 34.76 (Zn^{2+}) and 19.91 nM (CN^-) which accredits that the probe is sufficiently sensitive. The greenish emission accounted on interaction with Zn^{2+} is explained due to CHEF and inhibition of PET. The chelation involves the formation of hexanuclear metallocryptand $[Zn_6L_6]$ which is confirmed by Single Crystal X-Ray Diffraction data (**Fig.VII.4.2**). In case of CN^-, the bluish emission generates follows the plausible mechanism of nucleophilic addition of CN^- to the probe. The composition of the respective [H_2L-Zn^{2+}] and [H_2L-CN^-] complexes have been well accomplished through experimental results. MTT Assay and intracellular imaging of Zn^{2+} and CN^- in MDA-MB 231 embellishes its biocompatibility and sensing ability at cellular level (**Fig.VII.4.3(a),(b)**).

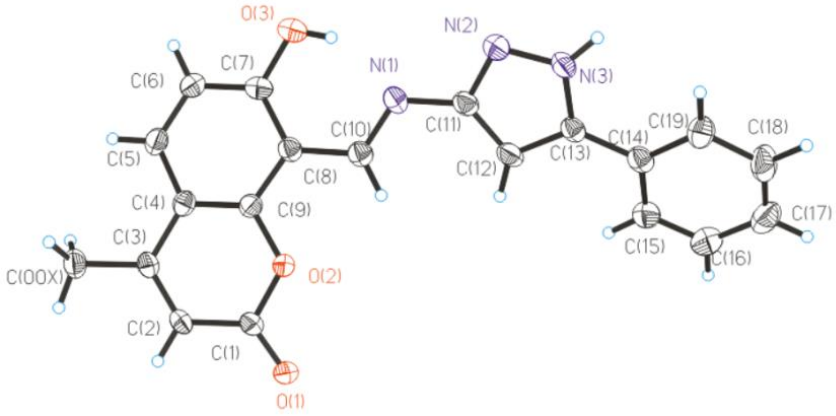

(a)

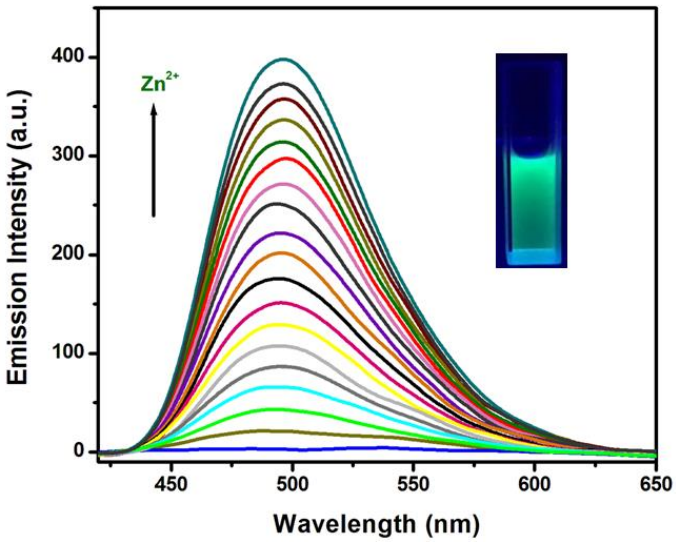

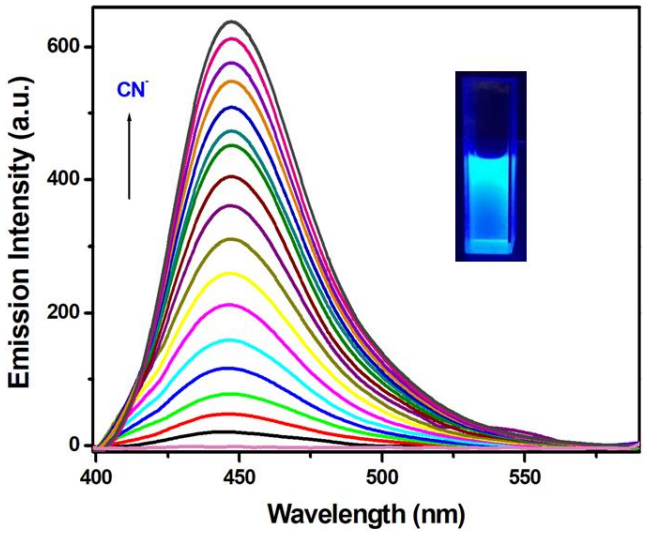

(b) **(c)**

Fig.VII.4.1. (a) Molecular geometry of **H_2L** in crystals (40% thermal ellipsoids, hydrogen atoms are omitted for clarity). **(b)** Change in the Fluorescence Spectrum of H_2L on successive addition of Zn^{2+} in CH_3CN/H_2O (99:1, v/v) (HEPES Buffer, pH 7.5) medium. (Inset: images) (λ_{ex}= 390 nm). **(c)** Change in Fluorescence Spectrum of H_2L on successive addition of CN^- in CH_3CN/H_2O (99:1, v/v) (HEPES Buffer, pH 7.5) medium. (Inset: Vial images) (λ_{ex}= 390 nm).

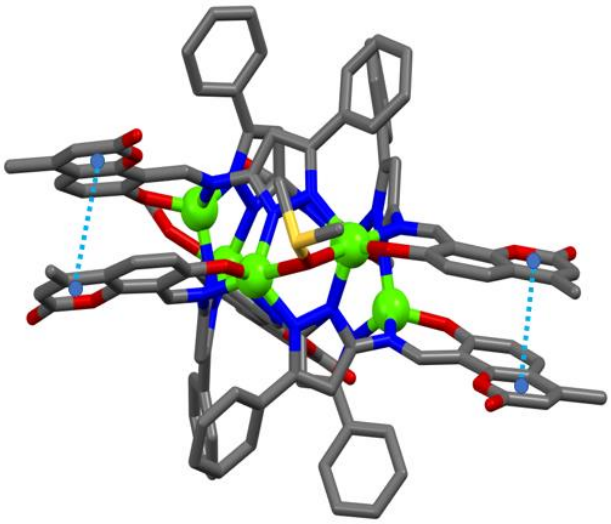

Fig.VII.4.2. Molecular structure of Hexanuclear Zn(II) complex [Zn_6L_6].

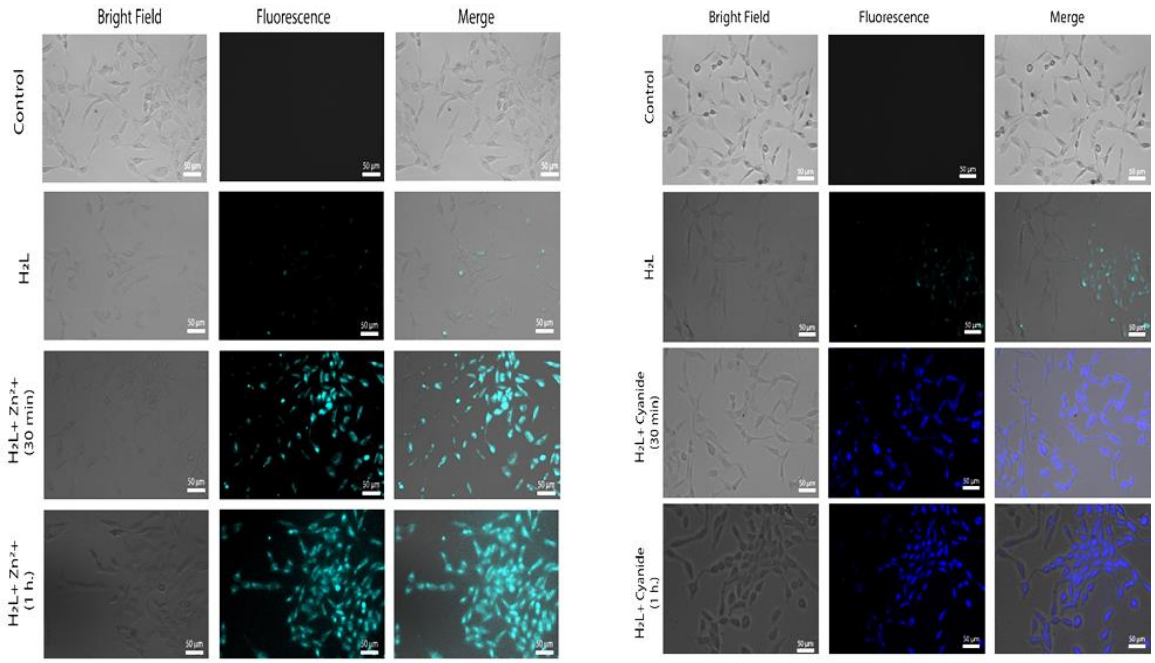

(a) **(b)**

Fig.VII.4.3. (a) Microscopic images of untreated MDA-MB 231 cells (Control), cells treated with H_2L (10μM), H_2L (10μM) + Zn^{2+} (10μM) after 30 min and 1h of incubation period under bright, fluorescence and merged field. **(b)** Microscopic images of untreated MDA-MB 231 cells (Control), cells treated with H_2L (10 μM), H_2L (10 μM) + CN^-(10 μM) after 30 min and 1h of incubation period under bright, fluorescence and merged field.

VII.5. Naphthyl-Azine Scaffold: AIEgen, Reversible Acidochromism, Cyanide sensing and its application in Intracellular Imaging. (Chapter V)

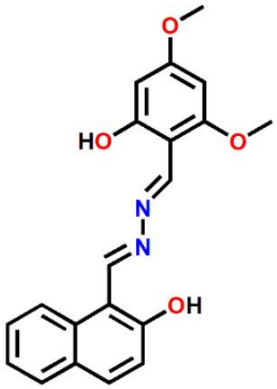

1-[(2-Hydroxy-4,6-dimethoxy-benzylidene)-hydrazonomethyl]-naphthalen-2-o

1-[(2-Hydroxy-4,6-dimethoxy-benzylidene)-hydrazonomethyl]-naphthalen-2-ol, H_2L produced via imine formation through condensation method. This versatile functionalized AIE active material and has been characterized by spectroscopic data. (λ_{ex} = 420 nm, λ_{em}=530 nm) (**Fig.VII.5.1(a), (b) and (c)**). The probe H_2L executes solid state emission which accounts for a solvent-free acidochromic property in presence of HTFA (Trifluoroacetic Acid) vapor with a detection limit (LOD), 1.41 ppm and exhibits reversibility upon exposure to HTFA/TEA (Triethylamine) vapour. In a sequential order of exposure of H_2L to HTFA-TEA vapour cycle to fabricate security encrypted device (**Fig.VII.5.2(a)**). The probe was further employed for chromogenic and fluorogenic detection of CN^- (λ_{ex} = 460 nm, λ_{em} = 565 nm) specifically over a series of other compatible anions in CH_3CN/H_2O (99:1, v/v; HEPES Buffer, pH 7.3) medium. The deprotonation-protonation of H_2L has experimentally been verified and estimated LOD is 45.42 nM (**Fig.VII.5.2(b), (c)**). Biological study of the probe in MDA-MD-231 cells has been explored through cytotoxicity analysis which assures its bio-applicability even at substantial concentration. Cellular imaging of AIE behaviour and CN^- detection is well demonstrated through the appearance of greenish and reddish emission (**Fig.VII.5.3(a),(b)**).

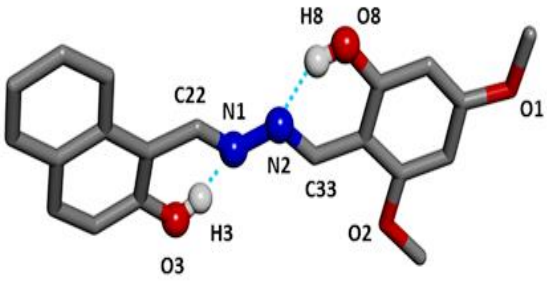

(a)

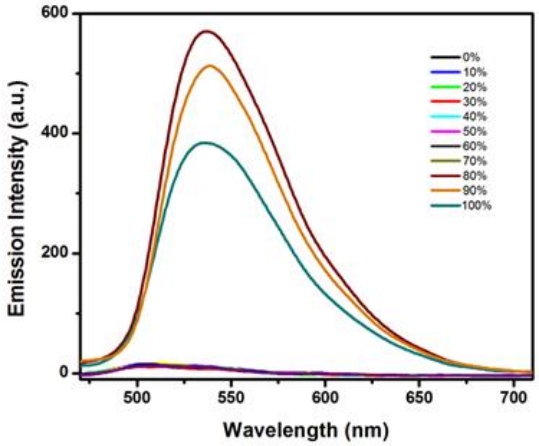

(b)

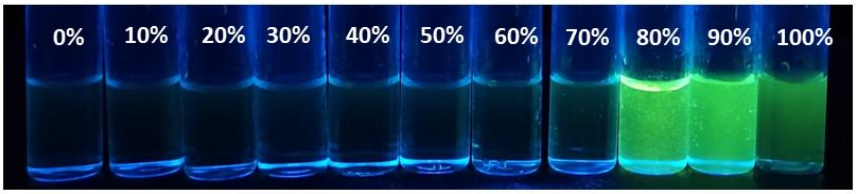

(c)

Fig.VII.5.1. (a) Single crystal X-Ray structure of the probe. **(b)** Emission spectra of H_2L in on increasing water conent in CH_3CN medium. **(c)** Vial images of AIE effect of probe under UV chamber (λ_{ex} = 365 nm).

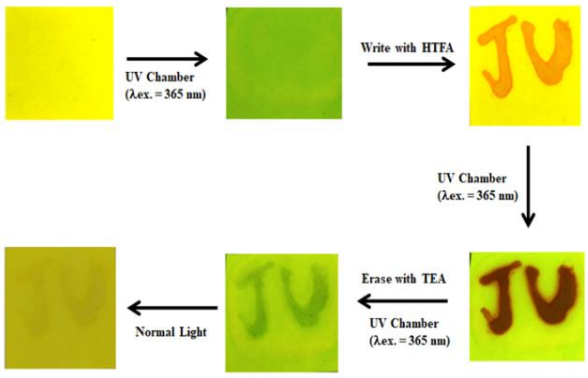

(a)

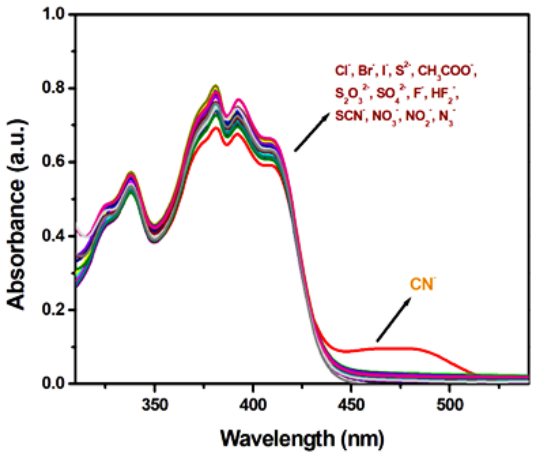

(b)

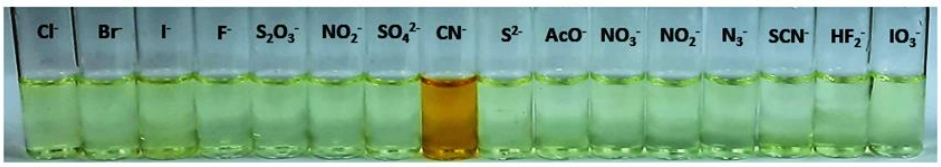

(c)

Fig.VII.5.2. (a) Write-Ersae application of H_2L using HTFA/TEA vapour. **(b)** Absorption Spectra of H_2L on addition of anions (2 eqv.) in CH_3CN/H_2O (99:1, v/v; HEPES Buffer, pH 7.3) medium. **(c)** Vial images.

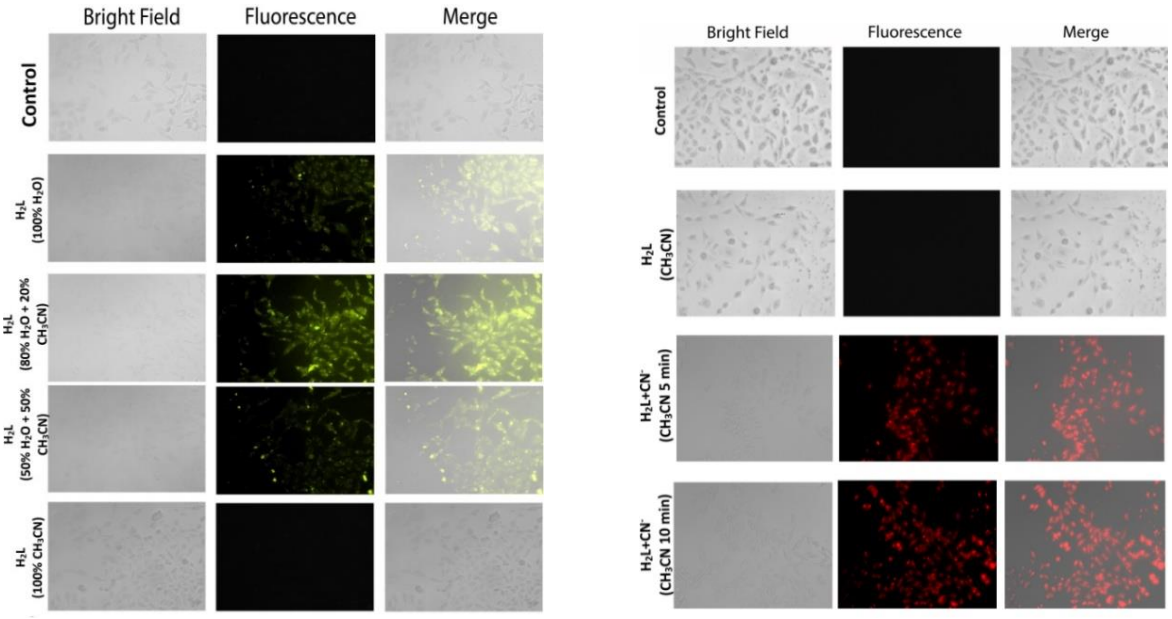

(a) **(b)**

Fig.VII.5.3. (a) Microscopic images of untreated MDA-MB 231 cells (Control), cells treated with ligand H_2L (10 μM) in (100% water medium, 80 % H_2O + 20% CH_3CN medium , 50 % H_2O + 50% CH_3CN medium and 100% CH_3CN medium) after 30 min incubation period under bright, fluorescence and merged field. **(b)** Microscopic images of untreated MDA-MB 231 cells (Control), cells treated with ligand H_2L (10 μM) + CN^- (5 μM) and ligand H_2L (10 μM) + CN^- (10 μM) in 100% CH_3CN medium after 30 min incubation period under bright, fluorescence and merged field.

VII.6. Tangible Coumarinyl-Pyridyl Schiff base Appended Carboxylato Bridging Zinc(II) 2D Coordination Polymer : Electrical Property and Anti-carcinogenic Application. (Chapter VI)

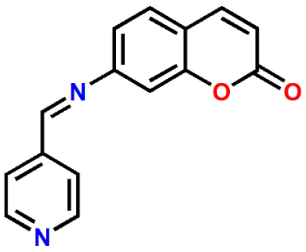

7-[(Pyridin-4-ylmethylene)-amino]-chromen-2-one (QPR)

7-[(Pyridin-4-ylmethylene)-amino]-chromen-2-one, QPR is synthesized and formulated from the conventional Schiff Base process. This pendant N-donor ligand is characterized and used for the construction of

Coumarinyl-Pyridyl Schiff base coordinated terephthalato bridging Zn(II) 2D co-ordination polymer, $[Zn_2(BDC)_4(QPR)_2(H_2O)]_n$ (Zn(II)-CP) (BDC^{2-}, 1,4-benzenedicarboxylato (**Fig.VI.6.1).**

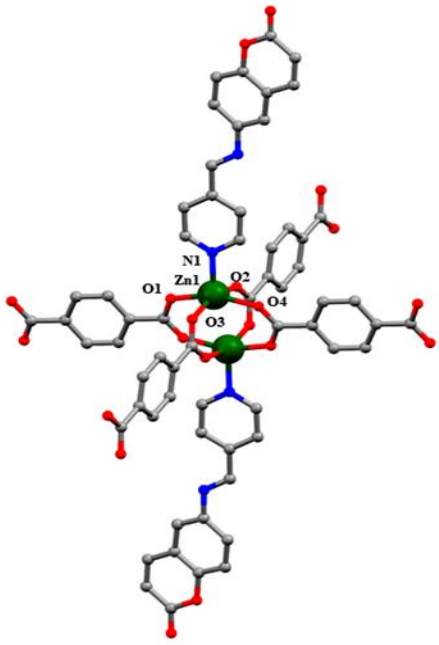

Fig.VI.6.1. Coordination unit around metal centre of Zn(II)-CP.

The coumarin decorated Zn-CP has been rarely reported, therefore forms a unique and innovative entity in the field of coordination network. The low band gap of 2.91 eV (Tauc's Plot) in Zn(II)-CP insists to fabricate a semiconducting Schottky diode device which exhibits 8.07×10^{-3} S m^{-1} (dark) and 9.26×10^{-3} S m^{-1} (light) **(Fig.VII.6.2 Table VII.6**). Further it reveals an effective anticancer property showing significant efficacy against HeLa cell line (IC_{50}, 21.02±1.57) and Zn(II)-CP induced ROS generation (**Fig.VI.6.3 (a), (b)&(c)**).

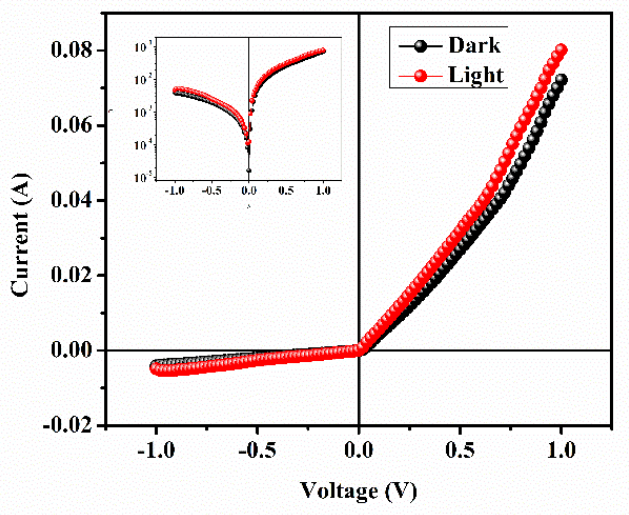

Fig.VII.6.2. Characteristics curve for ITO/Compound/Al configuration in linear & logarithmic (Inset) scale.

Table VII.6. Schottky diode parameters of Zn(II)-CP fabricated device

Condition	Rectification Ratio	Conductivity (S m^{-1})	Ideality factor	Barrier height φ_B (eV)	R_s from dV/dlnI (Ω)	R_s from H(I) (Ω)
Dark	17.65	8.07×10^{-3}	1.64	0.52	14.14	14.35
Light	19.22	9.26×10^{-3}	0.99	0.51	13.63	13.67

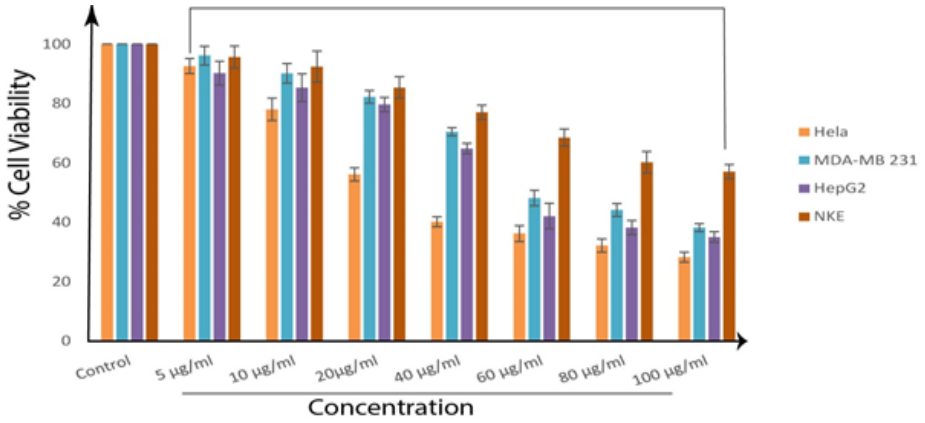

(a)

C)

IC50 Concentration (µg/ml)

Cell Lines	Compound	Etoposide
HeLa	21.02 ± 1.57	14.26 ± 3.26
MDA-MB-231	46.37 ± 3.06	20.03 ± 1.98
HepG2	42.22 ± 3.45	22.38± 3.22
NKE	≥100	34.05 ±2.46

(b)

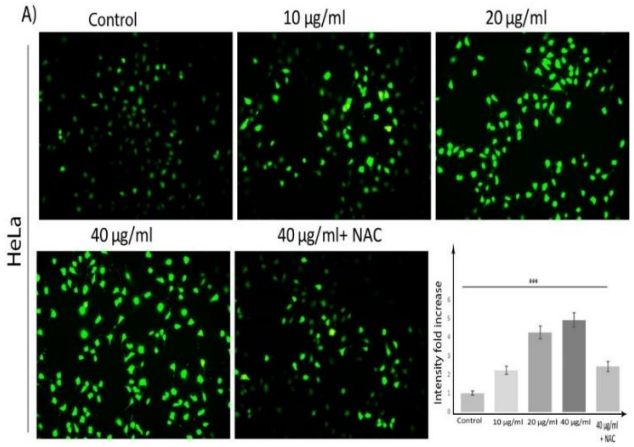

(c)

Fig.VII.6.3. (a) In vitro cytotoxicity was measured by MTT in different cell line HeLa, MDA-MB 231, HepG2 (cancer cells), and NKE (human normal kidney epithelialcell line. **(b)** showing IC_{50} values of Compound Zn(II)-CP in various cancer cell lines including HeLa, MDA-MB 231, HepG2 (cancer cells), and NKE (human normal kidney epithelialcell line. **(c)** Concentration-dependent increase in intercellular ROS accumulation of HeLa cells, in response to Zn(II)-CP treatment. Post treatment with Zn(II)-CP (10 µg/ml, 20 µg/ml, 40 µg/ml and Pre-treatment with NAC) for 24 h, cells were stained with H_2DCFDA and fluorescence microscopic was performed.

List of publications

1. **Sukanya Paul**, Sunanda Dey, Kunal Pal, Suvendu Maity, Kuladip Jana, Chittaranjan Sinha, **A Fluorogenic Triphenyl-Amine-Naphthyl-Hydrazide Probe Selective for Cu^{2+} and Cysteine Detection via an ON-OFF-ON Logic path with Real Applications**, *ChemistrySelect*, 2020, **5**, 15233-15242.
2. **Sukanya Paul**, Suvendu Maity, Satyajit Halder, Basudeb Dutta, Srikanta Jana, Kuladip Jana and Chittaranjan Sinha**, Idiosyncatic recognition of Zn^{2+} and CN^- using pyrazolyl-hydroxy-coumarin scaffold and live cell imaging: depiction of luminescent Zn(ii)-metallocryptand**, *Dalton Transaction*, 2022, **51**, 3198-3212.
3. Sunanda Dey, **Sukanya Paul**, Kingshuk Debsharma, and Chittaranjan Sinha, **A highly emissive Zn(ii)-pyridyl-benzimidazolyl-phenolato-based chemosensor: detection of $H_2PO_4^-$*via* "use" and "throw" device fabrication,** *Anal. Methods*, 2021, **13**, 5282–5292.
4. Manik Shit, **Sukanya Paul**, Taposi Chatterjee, Basudeb Dutta and Chittaranjan Sinha, **Towards Design of Energy Efficient Semiconducting Material: An Example of 1D Cd(II)-2,5-thiophene dicarboxylato Co-ordination Polymer,** *ES Energy & Environment*, 2022, **16**, 40-46.
5. Kaushik Naskar, Anup Kumar Bhanja **Sukanya Paul**, Kunal Pal and Chittaranjan Sinha, **Trace Quantity Detection of $H_2PO_4^-$ by Fluorescent Metal–Organic Framework (F-MOF) and Bioimaging Study,** *Crystal Growth & Design*, 2020, **20**, 6453−6460.
6. Srikanta Jana, Suhana Karim, **Sukanya Paul**, Ennio Zangrando, M. Salah El Fallah, Debasis Das and Chittaranjan Sinha, **Carboxylato bridging Cu(II) coordination polymer: Structure, magnetism and catalytic reduction of nitrophenols,** *Journal of Molecular Structure*, 2021, **1245**, 131058.

Conference Attended

1. **Poster Presentation:** Sukanya Paul and Chittaranjan Sinha.

   Poster Title: A Fluorogenic Schiff base based on Triphenylamine-Naphthyl Hydrazide for detection of Cu^{2+}.

   "Chemical Sciences: Today and Tomorrow (CSTT-2019)" organized by Indian Chemical Society (2019).

2. **Poster Presentation:** Sukanya Paul and Chittaranjan Sinha.

   Poster Title: Idiosyncratic recognition of Zn^{2+} and CN^- using Pyrazolyl-Hydroxy-Coumarin scaffold and live cell imaging: Depiction of Luminescent Zn(II)-Metallocryptand.

   "58^{th} Annual Convention of Chemists & International Conference on Recent Trends in Chemical Science (ACC-RTCS-2021)."

3. **Participation:** Participated in seven national and International conferences.

Awards and Recognition

1. NET Council of Scientific & Industrial Research (CSIR), India. **File No.**: 09/096(0936)/2017-EMR-I.
2. **Professor A.K. Dey Memorial Award** was achieved for poster presentation in "58^{th} Annual Convention of Chemists & International Conference on Recent Trends in Chemical Science (ACC-RTCS-2021)."

Copyrights and Permission

1. ***Chapter II***

2. ***Chapter III***

3. ***Chapter IV***

Analytical Chemistry

A Fluorogenic Triphenyl-Amine-Naphthyl-Hydrazide Probe Selective for Cu^{2+} and Cysteine Detection via an ON-OFF-ON Logic path with Real Applications

Sukanya Paul,[a] Sunanda Dey,[a] Kunal Pal,[b, c] Suvendu Maity,[a] Kuladip Jana,[c] and Chittaranjan Sinha*[a]

1,1′-((1E,1′E)-((2E,2′E)(((phenylazanediyl)bis(4,1-phenylene))bis-(methanylylidene))bis- (hydrazine-2,1-diylidene))bis(methanylylidene))bis(naphthalen-2-ol), **H_2L** shows high fluorescence emission (λ_{em}, 550 nm; λ_{abs}, 420 nm) which is selectively quenched by Cu^{2+} in presence of many other biologically important ions. The limit of detection (LOD), 7.3 nM is much lower than WHO recommended maximum permissible limit (20 μM) of Cu^{2+} consumption in human body. The binding fashion of the probe to Cu^{2+} ion is 1:2 mole ratio and has been confirmed by Job's plot and ESI-MS spectral data. The binding constant for Cu^{2+} is 4.93×10^{10} M^{-2} which also indicates sufficient stability and 1:2 complexation. On addition of cysteine to L-Cu^{2+}ensemble,the emission intensity (550 nm) enhances which accounts the release of Cu^{2+} from the non-emissive complex and restores the total fluorogenic efficiency of probe, **H_2L** (LOD (Cysteine), 36 nM). Thus, ON-OFF-ON mechanism of **H_2L** has been utilized for selective and specific detection of Cu^{2+} and Cysteine over several other amino acids. In addition to this, the probe is treated on WI-38 cell line to check cytotoxicity. This chemosensor, **H_2L** has been successfully applied to examine intracellular trace quantity of Cu^{2+} and Cysteine concentration in Hep G2 Cell lines.

Introduction

One-third of naturally abundant elements constitute life in different proportions. Amongst nine 3d transition elements, Copper (II) ion occupies the third most abundant transition metal ions in human bodies and plays vibrant roles in many essential physiological processes in organisms. Many biochemical reactions are directly/indirectly regulated by copper such as oxygen transportation by hemocyanin, electron transport redox enzymes, Blue copper protein, lactase, Cytochrome *c* oxidase, superoxide dismutase, ascorbate oxidase, pigmentation of the skin, repairing of connective tissues, etc.[1,2] However, congestion of copper can cause unadorned neurodegenerative diseases such as Alzheimer's, Parkinson's and prion diseases.[3–5] Biological requirement of copper in the normal human body is 15.7 −23.6 μM.[6] So, a constant monitoring of Cu^{2+}ion concentration in environment and health is very much important. Under the guideline of US Environmental Protection Agency (EPA) the maximum permissible limit of Cu^{2+} ion concentration in drinking water is 1.3 ppm (20 μM).[7] For these reasons, considerable efforts have been devoted to the development of analytical techniques for the accurate and precise measurements of copper in the consumed items and body organs. Therefore a facile analytical method for specific and sensitive detection for Cu^{2+} must be developed. Spectrofluorometric method is more convenient and approachable for detection of ions and molecules by qualitative and quantitative analysis owing to their interesting features such as easy modification, simplicity, cost effective and time saving over various known techniques such as redox titration, complexometric titrations, atomic absorption spectrometry,[8] inductively coupled plasma mass spectroscopy (ICPMS),[9] inductively coupled plasma-atomic emission spectrometry (ICPAES), and voltammetry which requires a much more costly and sophisticated management.[10,11] Design of chemosensors aimed at detection of ions and molecules are increasingly drawing attention in different fields of science and technology[12,13] Chemosensors based on Schiff base scaffold with Coumarin,[14–16] Rhodamine B,[17–19] Fluorescein,[20] Pyrrole,[21] derivatives has been used for Cu^{2+} detection.

Biothiols mainly Cysteine (Cys), Homocysteine (Hcy) and Glutathione (GSH) play a prominent role in various cellular processes. Cysteine one of the essential thiol containing amino acids serves as building block of protein synthesis and helps in detoxification and metabolism of living systems.[22] Free intracellular concentration of cysteine in human body is of the order 20–300 μM.[23] Scarcity in the level of cellular Cys could induce diseases such as retarded growth, fat loss, lethargy, skin lesions and hematopiesis decrease.[24–28] On the other hand an increase in Cys concentration would lead to neurotoxicity.[29,30] A balanced concentration and important role of cysteine in living system leads to monitoring and detection of cysteine essential for human health concern. An effective method for detection

[a] *S. Paul, S. Dey, Dr. S. Maity, Prof. C. Sinha*
Department of Chemstry, Jadavpur University, Kolkata-700 032, India
E-mail: crsjuchem@gmail.com
[b] *K. Pal*
Department of Life Science and Biotechnology, Jadavpur University, Kolkata-700032, India
[c] *K. Pal, Dr. K. Jana*
Division of Molecular Medicine, Bose Institute, Kolkata-700056, India

Supporting information for this article is available on the WWW under https://doi.org/10.1002/slct.202003797

and discrimination of Cys amongst various others biothiols and amino acids is quite challenging and much more essential as it would help in better understanding of its role in physiological system and early diagonisis of its related disease.

Recent works focused on designing chemosensors which includes metal complex as well as organic fluorophores for specific detection of Cys where the functional unit of the probes interacts with the thiol group of Cys which enables for selective response towards Cys sensing. Different chemosensors responds towards Cys sensing through different reaction mechanism such as nucleophilic aromatic substitution,[31,30] addition,[33] intramolecular reaarangement,[34,35] and displacement approach.[36] Based on the displacement approach, the probe has been developed for detection of Cys.

In this work, we report a Schiff base probe obtained by linking two units namely 1-(hydrazonomethyl)naphthalene-2-ol and 4,4′-diformyl triphenylamine. Details of probe characterization, spectral studies along with the theoretical computation has been reported in this work. The strong emissive nature of the ligand is distinctive for Cu^{2+} amongst all other competitive cations in the solution phase. The sensing is analyzed through "turn-off" fluorescence of probe on interaction with selectively Cu^{2+} ion in the solution state. The non-fluorescent L-Cu^{2+} in presence of Cysteine leads to decomplexation of Cu^{2+} from H_2L resulting in "turn on" fluorescence approach for detection of Cys as well as in cellular level. A MTT assay for the probe and Cell-imaging were done for the highly fluorescent probe H_2L along with intracellular detection of Cu^{2+} and Cys in HepG2 cell line. Increase or decrease of biologically relevant ion and molecular concentration from a permissible limit in cells is toxic and sometimes fatal. Hence, determination of ion and molecule concentration in trace level is a challenging task. Herein, we report a system which detects Cu^{2+} and Cysteine (Cys) with a very low detection limit.

Results and Discussion

Characterization of H_2L

The condensation of 4,4-Di formylTriphenylamine and1-(hydrazonomethyl)naphthalene-2-ol in 1:2 molar ratio synthesizes the probe **H_2L**. (Scheme S1). The probe **H_2L** shows relatively better solubility in $CDCl_3$, so the probe has been well characterized by ^{1}HNMR and ^{13}CNMR in $CDCl_3$ solvent. ^{1}HNMR ($CDCl_3$) of the probe represents a strongly deshielded singlet peak at 13.440 ppm for the phenolic (–OH) proton. Another sharp singlet appears at 9.728 ppm is attributed to imine proton (CH=N) attached to the naphthyl moiety and a peak at 8.657 ppm is assigned for the imine proton (CH=N) bonded to the diformyl unit of triphenyl amine in relatively deshielded zone confirms the formation of Schiff base. A doublet signal at 8.215 ppm corresponds to proton peak situated at para position to the imine group of the naphthyl fragment. The signals from 8.186 to 7.207 ppm represent the protons of aromatic region of the molecule. (Figure S1) ^{13}CNMR ($CDCl_3$) of the probe H_2L includes a signal at 161.13 to 160.79 ppm which corresponds for two imine carbon (CH=N) and phenolic (C–OH) peaks. The peaks at 150.01 and 146.28 ppm may be due to C–N carbon of triphenyl fragment. The regions from 134.44 to 108.48 ppm may include the rest of the carbon atom and thus confirms the formation of Schiff base (Figure S2). ESI-MS analysis shows the spectral peak with m/z at 638.2539 and 639.2458 and supports the desired formulation of the probe.(Figure S3) In FTIR spectrum of **H_2L**, the elimination of ν(CHO), 1690 cm^{-1} from 4,4′-diformyltriphenylamine and ν(NH_2) at 3312 cm^{-1} of 1-(hydrazonomethyl)naphthalene-2-ol along with appearance of new band at 1605 cm^{-1}which is assigned to ν(C=N) and supports the coupling of –CHO and –NH_2 (Figure S4). The purity of the ligand **H_2L** was further analyzed by High-performance Liquid Chromatograhy (HPLC) technique. The probe **H_2L** was eluted using 0.012% TFA as the aqueous mobile phase and 40% acetonitrile medium as the organic mobile phase having a flow rate of 1 mL/min. The result shows that the signal appeared in chromatogram was observed for 10^{-3}(M) concentration of the probe **H_2L** with retention time at 7.211 min. (Figure S5)[37]

Sensing of Cu^{2+}

In UV-Vis spectral studies, **H_2L** exhibits a high intense absorption band at 428 nm with a shoulder hump at 326 nm in 7:3(v/v) CH_3CN/H_2O medium (HEPES buffer, pH 7.2) which may arise due to π-π* transition. Sensitivity of probe **H_2L** has been checked in presence of various metal ions (Zn^{2+}, Cd^{2+}, Hg^{2+}, Co^{2+}, Pb^{2+}, Al^{3+}, Ca^{2+}, Fe^{3+}, Ni^{2+}, Na^{+}, Mn^{2+}, Pd^{2+}, Cr^{3+}, K^{+}, $Mg^{2+}$and Cu^{2+}) and selective oxidizing agents ($^{\cdot}OH$, H_2O_2, HOCl) in 7:3(v/v) CH_3CN/H_2O medium (HEPES buffer, pH 7.2) and it shows appreciably no change in the characteristic absorption band of the ligand while it shows unprecedented effect upon addition of Cu^{2+} ion. The absorption band in UV-Vis spectrum of the corresponding ligand **H_2L** is red shifted upon addition of 2 equivalent (20 μM) Cu^{2+} ion from 326 to 335 nm and 428 to 439 nm which accounts for its specificity towards Cu^{2+} ion even in presence of other competitive ions and oxidizing agents. (Figure 1).

The DFT computation technique is used to calculate the molecular energy levels of H_2L and its Cu^{2+}-complex. Optimized geometry of **H_2L** and L-Cu^{2+} along with some selected frontier molecular functions with their energy were listed in the supporting files (Figure S6, S7 and S8).TD-DFT study reveals the theoretical aspects of the observed spectroscopic changes of H_2L towards Cu^{2+}.(Table S1 and S3). The HUMO-LUMO energies (Figure 2) for **H_2L** are −5.61 eV and −2.24 eV and the energy difference is 3.37 eV and after interaction with Cu^{2+} the HOMO LUMO energies are −3.51 eV and −0.52 eV and the energy gap is diminished to 2.99 eV. The UV-Vis absorption spectrum of L-Cu^{2+} (335, 439 nm) is red shifted compared to **H_2L** (326, 428 nm) and has been supported by energy calculation. Fractional contribution of groups in frontier molecular orbitals for **H_2L** and L-Cu^{2+} were calculated by GASSSUM and are listed in the supporting information.(Table S2 and S4[‡]).

With incremental addition of Cu^{2+} ion (0–20 μM) to the probe solution in 7:3(v/v) CH_3CN/H_2O medium (HEPES buffer, pH 7.2), the absorption intensity at 428 nm gradually decreases

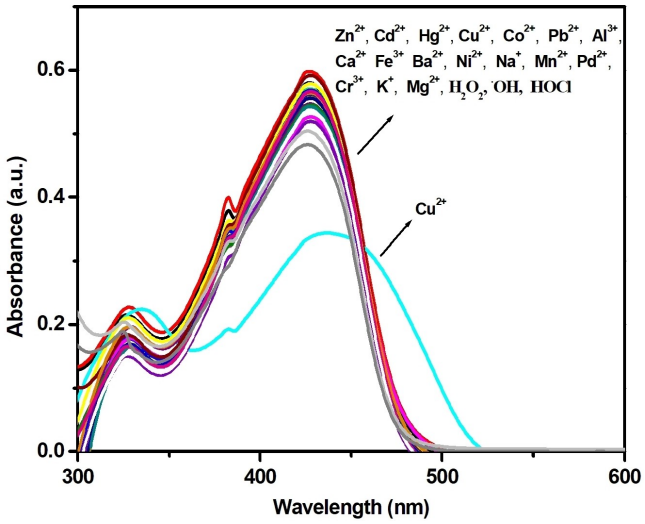

Figure 1. UV-Vis spectra of H_2L in presence of various cations and oxidizing agents (H_2L:cation and oxidizing agent; 1:2) in in CH_3CN/H_2O(7:3,v/v) medium HEPES Buffer pH = 7.2.

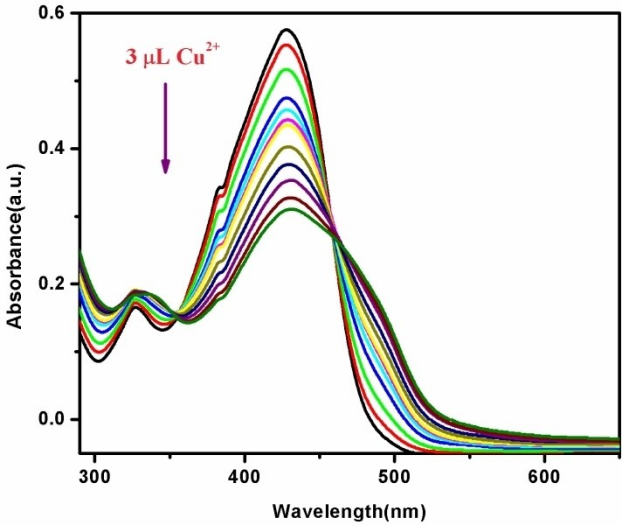

Figure 3. Change in absorption spectrum of H_2L (10 μM) upon gradual addition of Cu^{2+} ions (0-20 μM).

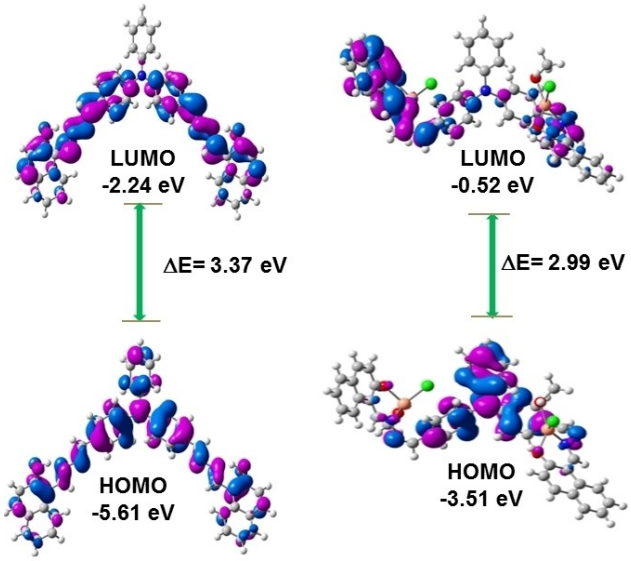

Figure 2. HOMO-LUMO gap of H_2L and L-Cu^{2+}.

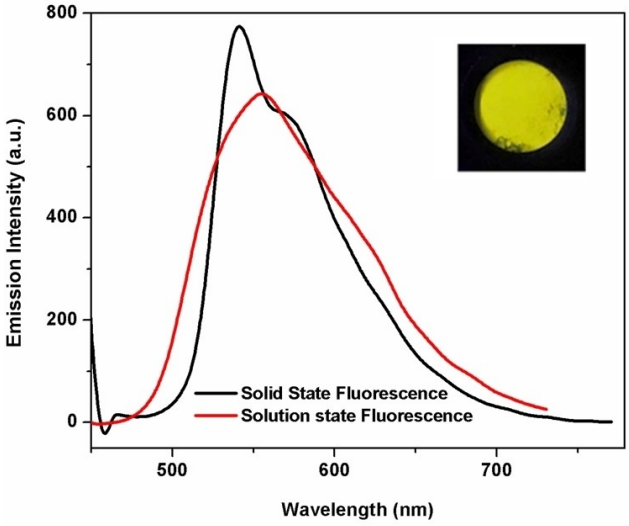

Figure 4. Solid and solution state emission spectra of H_2L (λ_{ex} 430 nm); Inset: solid state images under UV light.

while that of the peak at 326 nm shows a slight increase in the absorption intensity with two isosbestic points at 354 nm and 461 nm. On increasing concentration of Cu^{2+} to probe the characteristic band at 428 nm is shifted to 439 nm (Figure 3).

Luminophores based on hydrazide Schiff Base shows strong fluorescence in solid state.[38,39] Enhancement of emission intensity in solid state may be attributed to the Restricted Intramolecular Rotation (RIR) inhibiting the non radiative decay through rotation around C=N.[40] The probe, H_2L, in solid state shows strong emission at 540 nm with a shoulder at 570 nm upon excitation on 430 nm (Figure 4). H_2L may exist in keto and enol form which may exhibit emission at two different wavelengths; 540 and 570 nm respectively. The proton transfer may assist imine-phenol to keto-amine tautomerisation.[41–45] (Scheme S2) The probe H_2L in solution phase exhibits only single band at 550 nm.

The effect on emissive properties of H_2L in semi-aqueous phase was checked by adding various cations like Zn^{2+}, Cd^{2+}, Hg^{2+}, Co^{2+}, Pb^{2+}, Al^{3+}, Ca^{2+}, Fe^{3+}, Ni^{2+}, Na^{+}, Mn^{2+}, Pd^{2+}, Cr^{3+}, K^{+}, Mg^{2+}, Cu^{2+} and oxidizing agents like H_2O_2, $^{\cdot}OH$, HOCl in which the probe gets selectively quenched only in presence of Cu^{2+} ion (Figure 5(a)).Vial images were taken in presence of various metal ions in 7:3(v/v) CH_3CN/H_2O medium (HEPES buffer, pH 7.2) at room temperature with ligand to metal in the ratio of 1:2 (Figure 5(b)) and it shows negligible effect on the emission of the probe except Cu^{2+}. The change in the emission spectrum in its fluorometric titration of H_2L upon addition of

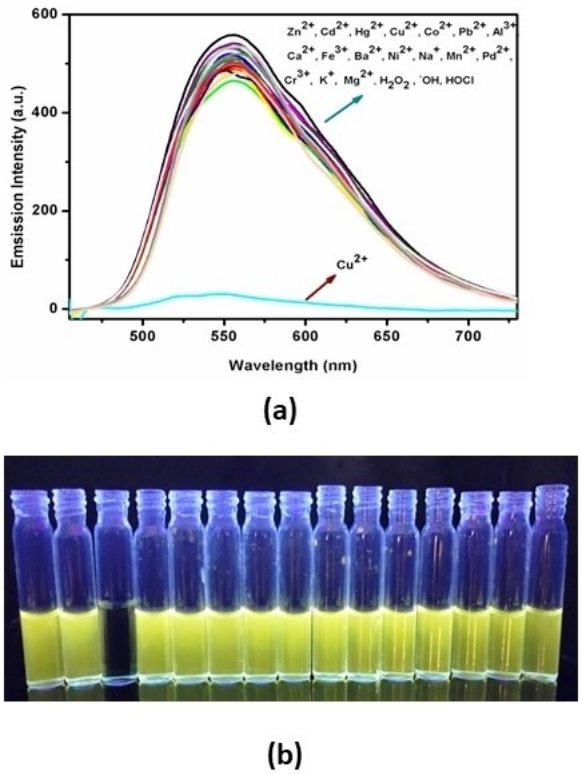

Figure 5. (a) Fluorescence spectra of H_2L in presence of different cations and oxidizing agents (2 equivalent) (b) image of the probe with various cations (left to right: H_2L, Zn^{2+}, Cu^{2+},Cd^{2+}, Hg^{2+}, Co^{2+}, Al^{3+}, Ca^{2+}, Fe^{3+}, Ni^{2+}, Na^{+}, Mn^{2+}, Pd^{2+}, $Cr^{3+}$and Mg^{2+}) under 365 nm UV light.

Cu^{2+} was carried out in 7:3(v/v) CH_3CN/H_2O medium (HEPES buffer, pH 7.2) (Figure 6).A quantitative analysis was done on quenching the emission of **H_2L** by successive addition of 2μL of

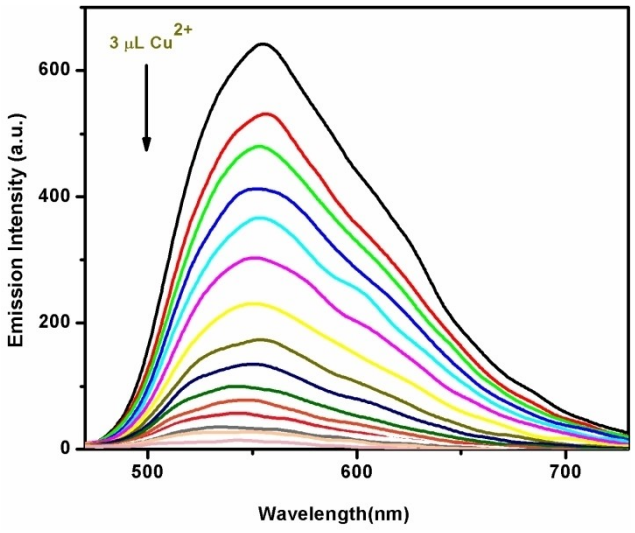

Figure 6. Fluorescence titration profile of **H_2L** on successive addition of Cu^{2+} in CH_3CN/H_2O(7:3,v/v) medium HEPES Buffer pH = 7.2, λ_{ex}, 430 nm.

Cu^{2+} (0-20 μM) stock solution to 20 μL of ligand (10 μM) in 7:3(v/v) CH_3CN/H_2O medium (HEPES buffer, pH 7.2).The emission intensity at 550 nm (quantum yield $\Phi = 0.23$) gradually decreases on titration with incremental addition of Cu^{2+} concentration and exhibited a good linearity. The **H_2L** scaffold has a pair of N,O chelating sites and can chelate to two Cu^{2+} ions. On addition of 2 equivalent of Cu^{2+} the emission intensity is quenched with a stoichiometric preference of the Ligand: Metal in 1:2 mole ratio. The ligand, H_2L chelates Cu^{2+}, the paramagnetic and Chelation Enhanced Quenching (CHEQ) may be the reason to sequester the emission.[46–48] Detection for Cu^{2+} by **H_2L** using a semi aqueous medium enables the use of green and safe solvent system for sensing studies.

The competitive study was conducted to check the selectivity of **H_2L** towards Cu^{2+} ion in presence of other cations such as Zn^{2+}, Cd^{2+}, Hg^{2+}, Co^{2+}, Pb^{2+}, Al^{3+}, Ca^{2+}, Fe^{3+}, Ni^{2+}, Na^{+}, Mn^{2+}, Pd^{2+}, Cr^{3+}, K^{+}, Mg^{2+} and anions (F^{-}, HF_2^{-}, PO_4^{3-}, $H_2PO_4^{-}$, IO_3^{-}, $S_2O_3^{2-}$, $S_2O_5^{-}$, I^{-}, HPO_4^{2-}, $PO_4^{3-}OAc^{-}$,SO_4^{2-},F^{-}, NO_3^{-}, Cl^{-}, Br^{-}, CN^{-}, AsO_2^{-}, S^{2-}, AsO_4^{3-} and $P_2O_7^{4-}$). The experiment was carried out on addition of 2.0 equivalent Cu^{2+} to the solution of 1.0 equivalent H_2L in 7:3 (v/v) CH_3CN/H_2O medium (HEPES buffer, pH 7.2) and to this complex solution, 2.0 equivalent of other cations are added at each time. Results (Figure S9) shows that there is no such interference in the detection of Cu^{2+} ion in presence of other cations. The effect of anions on the analysis of Cu^{2+} is also checked (Figure S10) and it is found that no anion (2.0 equivalent Cu^{2+} to the solution of 1.0 equivalent **H_2L** and 4.0 equivalent of anions) has impact on the determination of it. So the probe detects efficiently in presence of external ions and can be accredited as highly sensitive probe in detection of Cu^{2+} ions. The "turn-off" response of Cu^{2+} was examined in presence of co-existed ions which could minimally affect its quenching phenomenon. The fluorescence intensity of **H_2L** remains unchanged under a series of pH from 2.0 to 8.0.Upon addition of Cu^{2+} to H_2L solution emission is quenched within pH, 6.0 – 8.0 (Figure S11). Hence the probe can be used for detection of Cu^{2+} under normal physiological pH.

The limit of detection (LOD) of Cu^{2+} by **H_2L** was experimentally determined by (3σ/S) method where σ is the standard deviation; S is the slope of the calibrated curve resulted from fluorescence titration profile of **H_2L** by successive addition of Cu^{2+} ions. The LOD was experimentally calculated and it is compared with some published data (**Table S5**). From the titration, the detection limit (LOD) calculated for Cu^{2+} was found to be 7.3 nM. (Figure S12) which is fairly less than the recommended permissible limit for Cu^{2+} (20 μM) in drinking water by WHO.[7] The reports are available for Cu^{2+} sensing using different fluorogenic sensors like pyrene appended imine-phenol (LOD,1.21 μM in CH_3CN/HEPES Buffer),[7] Coumarin-napthol probe (LOD, 12.7 nM in DMSO/HEPES buffer),[14] Rhodamine-benzothiazole (LOD, 6.89 μM in CH_3CN/water),[20] pyrrole appended chromen-ol (LOD, 0.512 μM in DMSO/PBS buffer)[45], naptholhydrazide (LOD, 223 nM in PBS buffer)[46] and dicyanomethylene-4H-pyran picolinate derivative (LOD, 23 nM in DMSO/PBS Buffer);[49] The present probe **H_2L** shows better efficiency (LOD, 7.3 nM). Hence, the probe is applicable and suitable for detection of Cu^{2+} in trace quantity.

Binding preference and stoichiometric study for Cu^{2+} ion

Analysis of binding of ligand with Cu^{2+} in (7:3(v/v) CH_3CN/H_2O medium (HEPES buffer, pH 7.2)) was evident from Job's Plot which hints the stoichiometric preference of **H_2L** complexation towards Cu^{2+} (Figure S13).[50] The maxima in Job's plot correspond to mole fraction of 0.67 which indicates a complex formation of **H_2L** to Cu^{2+} in 1:2 modes

A change in the ^{1}HNMR spectra of **H_2L** was observed on addition of varying concentration of Cu^{2+} in DMSO-d_6 (Figure 7). The ^{1}HNMR spectral difference of **H_2L**, on addition of Cu^{2+} in varying proportion observes a significant change to peak at 13.2 ppm, phenolic proton attached to the naphthyl moiety. In presence of 1 equivalent of Cu^{2+}, phenolic OH proton peak gets attenuated and on 2.0 equivalents it vanishes completely which is an indication of deprotonation of **H_2L** and complexation to Cu^{2+} through O donor centres. Due to gradual addition of Cu^{2+}, the aromatic protons get broadened and a slightly downshifted. The complete disappearance of hydroxyl proton peak of **H_2L** on 2.0 equivalent additions of Cu^{2+} intimates at preferential complex formation in 1:2 ratios. The reduced peak of imine CH=N peak also indicates its participationin binding.

On ESI-MS analysis, a molecular ion peak appears at m/z = 767.0098 corresponds to $[HL+Cu+Cl+MeOH+H]^+$ reveals a 1:1 binding stochiometry between **H_2L** and Cu^{2+} and confirms 1:1 complex formation and another peak at 895.9957 corresponds to $[L+2Cu+2Cl+2MeOH+H]^+$ which reveals interaction of **H_2L** to Cu^{2+} in 1:2 stochiometry binding mode.(Figure S14).

Infrared spectrum of the complex shows a broad peak at 3370 cm^{-1} which may be due to ν(OH)of coordinated MeOH and a high intense broad peak at 1585 cm^{-1} is assigned to coordinated C=N and in free ligand (**H_2L**) it appears at 1605 cm^{-1}. The coordination of imine-N to Cu^{2+} is supposed to responsible for elongation of C=N bond length and is shifting to lower energy. A band at 1317 cm^{-1} corresponds to O–H bending; the C–N and C–O stretching appear at 1280 and 1172 cm^{-1}respectively in the complex. (Figure S15).

The binding constantis $K_D = 4.93\times10^{10}\ M^{-2}$ (R = 0.99637)as obtained from the plots of $((F_{max}\text{-}F_0)/(F\text{-}F_0))$ vs. $1/[Cu^{2+}]^2$ using the linear Benesi-Hildebrand expression (Figure S16). This also supports the fact that Cu^{2+} has a strong binding affinity for ligand with N and O chelating centres with results of 1:2 binding mode of H_2L to Cu^{2+} and thus have a sufficient stability.[51]

The lifetime decay profile of **H_2L** and L-Cu^{2+} fits well into bi-exponential fashion. The time resolved fluorescence spectroscopic study reveals a lifetime of 0.32688 ns (**H_2L**) which on addition of Cu^{2+} decreases to 0.298222 ns (Figure 8). On increasing the concentration of Cu^{2+}, lifetime of the complex remains invariant which signifies a static quenching and the quenching takes place at ground state complex formation.[52]

The Stern Volmer (S–V) constant, $K_{sv} = 0.217\times10^6\ M^{-1}$ (R = 0.98719) as calculated using the equation $[I_0/I] = 1 + K_{sv}[Q]$for static quenching (Figure 9 and 10). The plot shows linearity upto 20 μM and accounts the static quenching and on above 20 μM of $[Cu^{2+}]$ it shows an upward bend along with inclusion of dynamic process. The constancy of lifetime of the excited state fluorophore even on addition of Cu^{2+}further confirms the static quenching.[53,54]

Recovery Study from Municipal supplied Water Sample

To analyze the reliability of the use of H_2L for the fluoroscence detection method of Cu^{2+}, a recovery study was performed utilizing municipal supplied water in Kolkata by Standard addition method. The calibration plot on varying the concentration of Cu^{2+} from 0 to 10 μM and keeping the concentration of ligand 10 μM fixed7:3(v/v) CH_3CN/H_2Omedium (HEPES buffer, pH 7.2) (Figure S17).The drinking water was collected from Jadavpur, Kolkata supplied by Kolkata Municipal Corporation in specific bottle. Unknown concentration of $Cu^{2+}$is

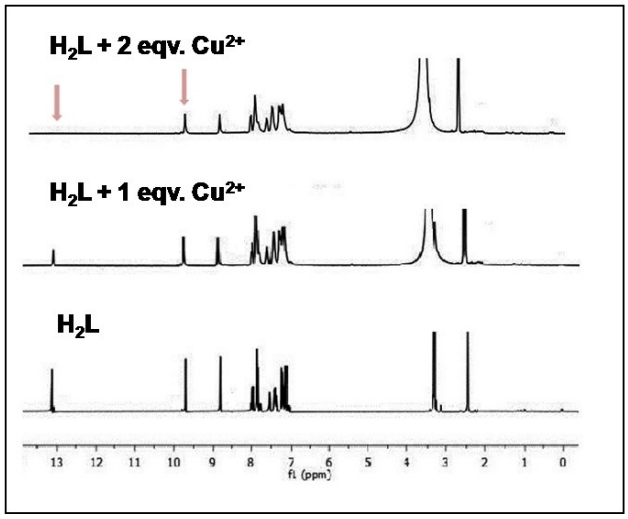

Figure 7. ^{1}HNMR titration of **H_2L** on successive addition of Cu^{2+} in DMSO-d_6.

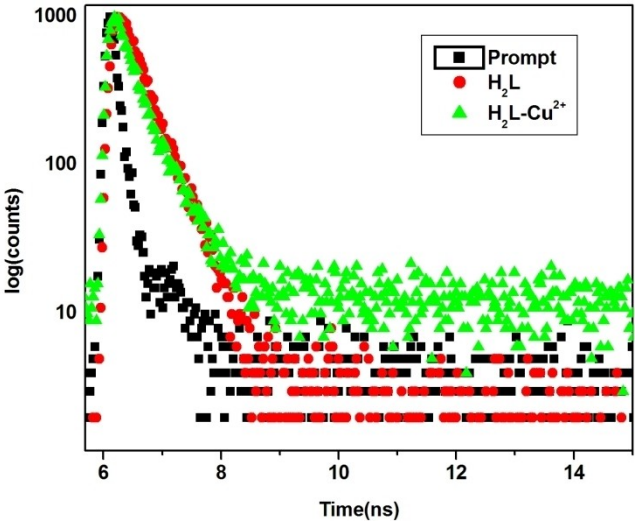

Figure 8. Fluorescence lifetime plot of **H_2L** and on Cu^{2+} addition in CH_3CN/H_2O (7:3, v/v) HEPES Buffer medium pH = 7.2.

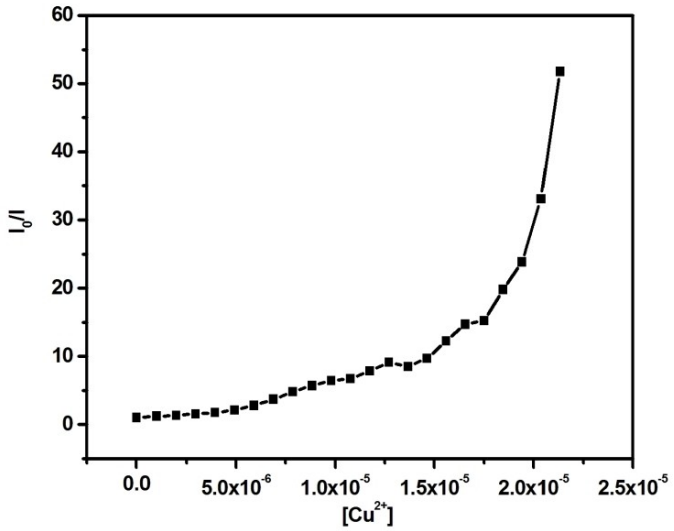

Figure 9. Stern-Volmer plot of $[Cu^{2+}]$ against I_0/I.

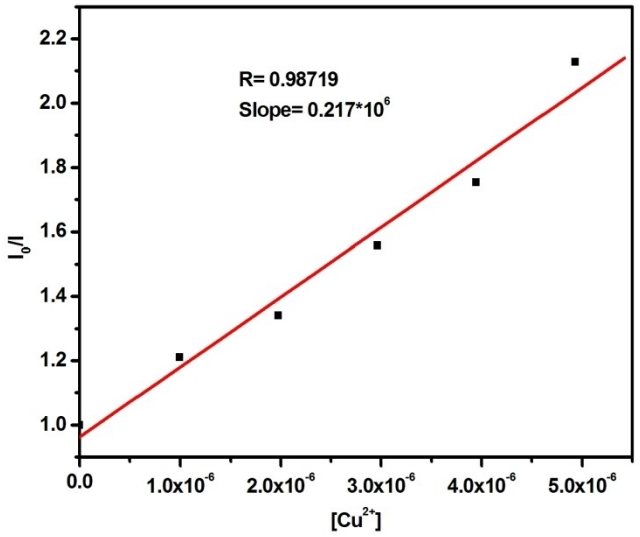

Figure 10. Stern-Volmer constant (K_{sv}) obtained from the above given plot.

determined from the calibration plot (Table 1). The recovery study of $Cu^{2+}$is satisfactory to >85%. This experiment exhibited a rapid and inexpensive application for sensing of Cu^{2+} in municipal supplied water.[55]

Table 1. Recovery of Cu^{2+} from drinking water sample using H_2L.

Sample	Added Cu^{2+}	Emission Intensity	Experimentally Found	Recovery (%)
Drinking Water	2	410	1.73	86.5
	4	357	3.52	88
	6	271	5.51	91.18

Detection of Cysteine

The strong affinity of Cysteine (Cys) towards Cu^{2+} has shown the use of L-$Cu^{2+}$for the sensing of Cysteine in 7:3(v/v) CH_3CN/H_2O medium (HEPES buffer, pH 7.2). The selectivity of Cys to Cu^{2+} from insitu generated L-Cu^{2+} non emissive complex, results in recovery of emission and turn on response towards Cys detection in semi-aqueous medium. To a solution of L-Cu^{2+} in 7:3(v/v) CH_3CN/H_2O medium (HEPES buffer, pH 7.2) 5 equivalent of amino acids (Alanine (Ala), Leucine (Leu), Methionine (Met), Serine (Ser), Proline (Pro), Glutamic acid (Glu), Aspartic acid (Asp), Glutathione (GSH), Glycine (Gly), Histidine (His), Valine (Val), Lysine (Lys), Homocysteine (Hcy)) were added and their fluorescence spectra were measured (Figure 11). The result shows that the fluorescence of the probe (H_2L) is recovered from the quenched complex, L-Cu^{2+} ensembles only in case of Cys whereas for other amino acids/ biothiols remain unaffected. On addition of 40 μM Cys, a 30 fold significant fluorescence enhancement was observed whereas only 5.6 and 9.7 fold enhancement was observed in case of GSH and Hcy.

Fluorescence titration was conducted on addition of varying amounts of Cys to the solution of L-Cu^{2+}. On gradual addition of (0–40 μM) Cys to a solution of 10 μM L-Cu^{2+} in7:3(v/v) CH_3CN/H_2O medium (HEPES buffer, pH 7.2), the intensity of spectra gradually increases and recovers to that of **H_2L**.(Figure 12) Scheme 1 represents the reversibility of the emissive probe **H_2L** which quenches in presence of Cu^{2+} and simultaneously the ensemble L-Cu^{2+} detect Cys by restoring the emission of the probe.

The emission intensity changes at 550 nm when plotted against Cys concentration exhibited a linear correlation. The detection limit (3σ/S method) for Cys is 36 nM (R = 0.99695) which is sufficiently low making it applicable for sensitive

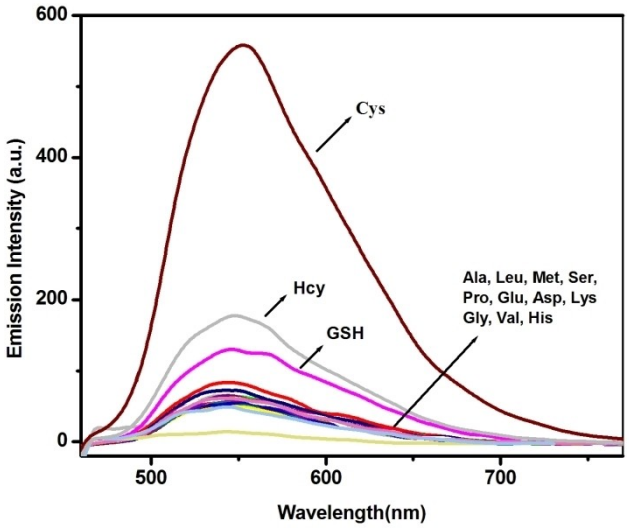

Figure 11. Fluorescence spectra of L-Cu^{2+} in presence of different biothiols and amino acids (4equivalent) 7:3(v/v) CH_3CN/H_2O medium (HEPES buffer, pH 7.2).

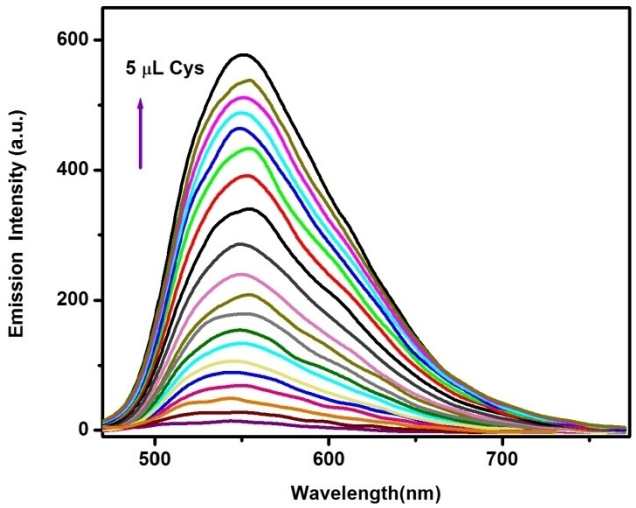

Figure 12. Fluorescence Spectra of L-Cu^{2+} on addition of varying amounts of Cys (0-40 μM) λ_{ex} = 430 nm.

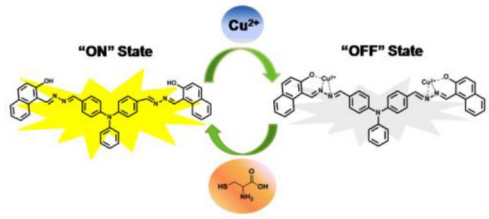

Scheme 1. Schematic Representation for Cys sensing by non-fluorescent L–Cu^{2+} ensemble.

detection in living system (Figure S18). The LOD value has also been compared with the reported LOD value of Cu^{2+} selective probes for cysteine (Cys) detection which are listed in the supporting information (Table S6). Most of the Cu^{2+} selective probes available in literature can detect in μM concentration while few reported are shown with LOD in nM range such as Zhang et al reported a Cu^{2+} selective PSMA coated carbon dot chemosensor which detects Cys with LOD value of 78 nM.[56] Wu reported aminoantipyrine-naphthyl moiety for Cys sensor (LOD 84 nM).[57] Zhang and his co workers synthesized a coumarin-appended naphthyl Cu^{2+} selective ensemble for cysteine detection (LOD-15 nM).[58]

The Binding constant from B–H plot is 0.95×10^4 M^{-1} which sugggests Cys forms stable association with Cu^{2+} which release the probe and resulted in regeneration of emission (Figure S19).The overall pattern of the emission spectrum after addition of 40 μM of Cys matches closely with the native fluorescence spectrum of **H_2L**. This clearly supports the fact that on addition of cysteine, it leads to the liberation of **H_2L**.The specificity of L-Cu^{2+} towards Cys was further checked in presence of competitive amino acids and the resulting emission intensities illustrates the fact that the response of L-Cu^{2+} to Cys is highly specific without any interference of the added competitive amino acids (Figure S20). This behavior may reasonably due to high nucleophilicity of thiolate group and steric influence which may play a prominent role in its selectivity to Cys.[57,58]

The UV-Vis absorption spectra of L-Cu^{2+} on addition of biothiols and several other amino acid were investigated in 7:3(v/v) CH_3CN/H_2O medium (HEPES buffer, pH 7.2). On addition of increasing concentration of (0–40 μM) Cys the band intensity at 439 nm gradually increases and shifted to the absorption spectrum of the probe **H_2L** at 430 nm. The absorption spectrum of **H_2L** gets completely recovered on addition of 40 μM of Cys to L-Cu^{2+}.(Figure S21). Noticeably the addition of other amino acids and biothiols induces no such effect on the absorption spectrum of L-Cu^{2+}.(Figure 13).

The formation of Cu-Cys Complex on addition of Cys to L-Cu^{2+} was further confirmed from ESI-MS Spectrum. The peak at m/z = 239 may be due to $[Cys + Cu + Cl + H_2O + H]^+$ andconfirms the formation of 1:1 stochiometric complex between Cys and Cu. Another peak appears at m/z = 302 may be assigned to $[2Cys + Cu + H]^+$ reveals a 1:2 stochiomeric complex along with liberation of **H_2L** which is clearly confirmed from the peak at m/z = 638. (Figure S22)

Reversibility is one of the prominent factors for chemosensors for recognition of important analytes. The regeneration of **H_2L** on addition of Cys to the solution of L-Cu^{2+} results in reversibility of fluorescence response which can be repeated upto 5 times by modulation of Cu^{2+}/Cys addition in 7:3(v/v) CH_3CN/H_2O medium (HEPES buffer, pH 7.2) making the probe **H_2L** as reversible fluorescence ON-OFF-ON chemosensor for detection of Cu^{2+} and Cys. (Figure 14)

Logic Behaviour

A molecule with appreciable sensitivity can be beneficial for construction of intregated logic gates.[59] The probe generates a highly emissive band at 550 nm in 7:3(v/v) CH_3CN/H_2O medium

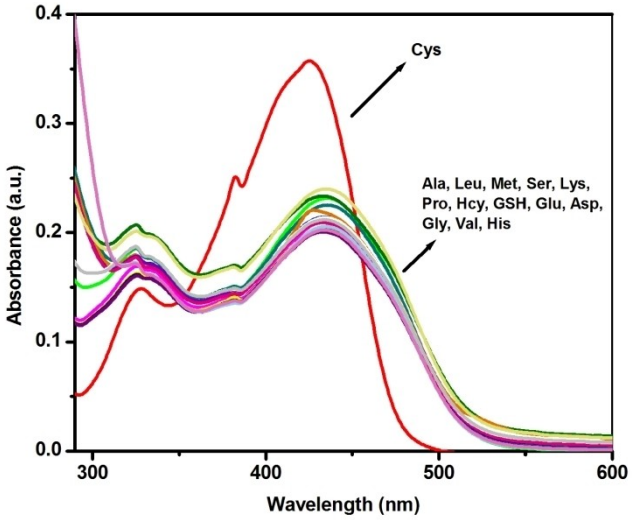

Figure 13. Absorption Spectra of L-Cu^{2+} on addition of different Amino Acids (4 equivalent) in 7:3(v/v) CH_3CN/H_2O medium (HEPES buffer, pH 7.2).

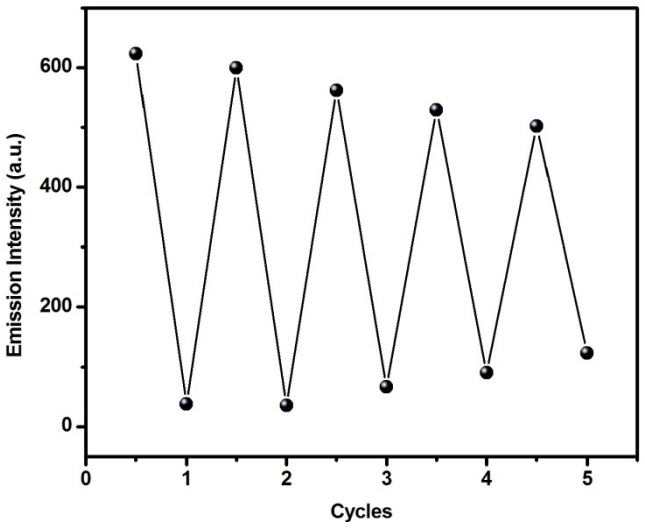

Figure 14. Emission Intensity at 550 nm change on alternative addition of Cu^{2+}/Cys with concentration in 7:3(v/v) CH_3CN/H_2O medium (HEPES buffer, pH 7.2).

(HEPES buffer, pH 7.2) which selectively quenches by Cu^{2+} and this ensemble in presence of Cys results regeneration of emission. Here the probe H_2L operates on two emission states 'ON' and 'OFF' which can be analyzed as a molecular logic gate with two chemical inputs. The two input-1(Cu^{2+}) and input-2(Cys) can be considered for the development of IMPLICATION logic gate. Monitoring the fluorescent emission as the output signal, 1 is considered if it is present and 0 if it is absent. The input and output string are connected with combination of H_2L, Cu^{2+} and Cysteine and represented in the truth table. (Figure 15)

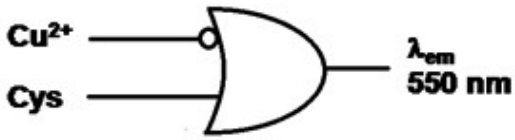

INPUT 1 Cu^{2+}	INPUT 2 Cys	OUTPUT λ_{em} = 550 nm
0	0	1
1	0	0
0	1	1
1	1	1

Figure 15. Molecular IMPLICATION Logic gate construction for Cu^{2+} and Cys.

Cell Study

In order to check the cellular toxicity of the probe **H_2L**, an in vitro cytotoxicity study was estimated for assuring its biocompatibility on WI-38 cell line. The cells were treated with five different concentrations (20 μM, 40 μM, 60 μM, 80 μM and 100 μM ml^{-1}) for 24 h and followed by MTT assay. It was evaluated from the experimental observation that the ligand exhibited no significant toxicities even at the highest concentration of 100 μM (Figure 16). Therefore the results ensure that the biocompatibility of **H_2L** applicable to living systems. The cellular internalisation study of **H_2L** was carried out in the hepatocellular carcinoma cells. The cellular uptake of **H_2L** (10 μM), Cu^{2+}salt (20 μM) and cysteine (40 μM) by HepG2 cells were examined through the fluorescence microscopy study.

A prominent red signal observed for cells treated with the probe. The prominent red fluorescence is observed as the compound penetrates into the cells which in turn results in the red emission. The red signal immediately disappears after addition of 20 μM of Cu^{2+} salt. To perform the fluorescence imaging of Cys in Hep G2 cells, 40 μM of Cys added to cells incubated with L–Cu^{2+} which resulted in reappearance of bright red fluorescence. The concentration of free copper ions has been estimated to be of the order of 10^{-18}—10^{-13} M in yeast cells and in human cells. So we can easily comprehend that the quantity within the cellular mileu is too low for our sensor **H_2L** to detect (Limit of detection 7.3 nM) Therefore the insitu detection of Cu^{2+}/Cys is not possible by employing our sensing probe, H_2L.[60] However, the overall results show that the cells can readily uptake **H_2L**, Cu^{2+} and Cys with a prominent response at cellular level (Figure 17).

Conclusion

A Highly Emissive Diformyl triphenyl-naphthyl hydrazide based probe has been synthesized and well characterized. The strongly emissive probe shows efficient sensitivity and selectiv-

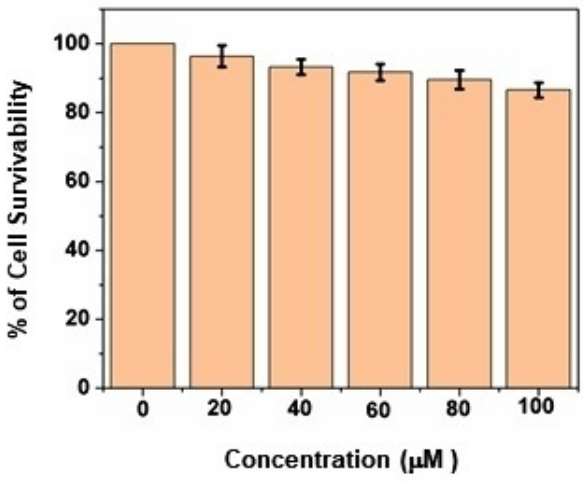

Figure 16. Cell survivability of the ligand on WI-38 cell line.

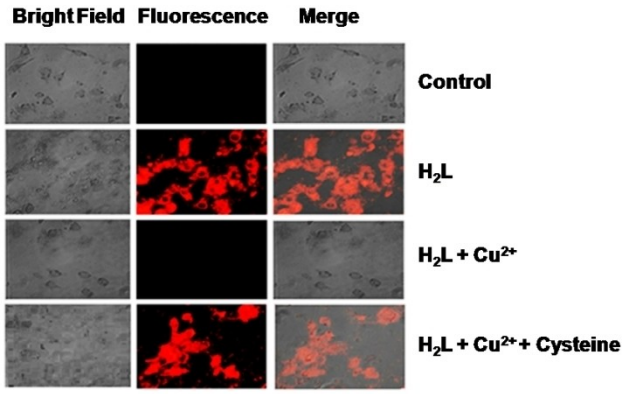

Figure 17. Bright field, fluorescence and merged microscopic images of untreated HepG2 (Control), cells treated with H_2L(10 μM), Cu^{2+}(20 μM), Cys (40 μM).

ity for Cu^{2+} ion through turn off approach over a series of important cations with a low detection limit of 7.3 nM under physiological condition. The interaction of Cu^{2+} with the probe has been experimentally determined. DFT and TDDFT calculation were in accordance with the experimental results. The L-Cu^{2+} complex is applied for selective detection of Cys amongst other biothiols and amino acids with LOD value of 36 nM for Cys. The strong affinity of Cys towards Cu^{2+} leads to the recovery of emission of **H_2L** turning it to be a reversible ON-OFF-ON chemosensor and can be beneficial for construction of IMPLICATION logic gate. A MTT study in WI-38 Cell and fluorescence cell imaging in Hep G2 cells shows biocompatibility of the probe for sensing application at cellular level.

Supporting Information Summary

The details of experimental section, different spectral characterization figures (^{1}HNMR, ^{13}CNMR, ESI-MS, FT-IR, HPLC) and required additional spectra are included in the corresponding supporting information file.

Acknowledgement

The work has been supported by the Laboratory Facilities of Jadavpur University, West Bengal India. Council of Scientific and Industrial Research (CSIR, Sanction No.: 01(2894)/2017/EMR-II), New Delhi is acknowledged for their Research Fund. S.P. is obliged to Council of Scientific and Industrial Research (CSIR, File No.: 09/096(0936)/2017-EMR-1) for granting the research Fellowship. Basudeb Dutta, Aliah University, Kolkata-700160, West Bengal, India is acknowledged for his kind support and contribution to my research work.

Conflict of Interest

The authors declare no conflict of interest.

Keywords: Cu^{2+}-sensor · Computational Chemistry · Cysteine Detection · HepG2 Cell Imaging · Fluorescent Probes · Naphthylhydrazide Schiff base

[1] P. Kaur, S. Kaur, K. Singh, *Inorg. Chem. Commun.* **2009**, *12*, 978–981.
[2] W. Wang, A. Fu, J. You, G. Gao, J. Lan, L. Chen, *Tetrahedron* **2010**, *66*, 3695–3701.
[3] K. J. Barnham, C. L. Masters, A. I. Bush, *Nat. Rev. Drug Discovery* **2004**, *3*, 205–214.
[4] Y. K. Jang, U. C. Nam, H. L. Kwon, I. H. Hwang, C. Kim, *Dyes Pigm.* **2013**, *99*, 6–13.
[5] E. Gaggelli, H. Kozlowski, D. Valensin, G. Valensin, *Chem. Rev.* **2006**, *106*, 1995–2044.
[6] M. Li, H. Ge, R. L. Arrowsmith, V. Mirabello, S. W. Botchway, W. Zhu, S. I. Pascu, T. D. James, *Chem. Commun.* **2014**, *50*, 11806–11809.
[7] S. Goswami, S. Chakraborty, S. Paul, S. Halder, S. Panja, S. K. Mukhopadhyay, *Org. Biomol. Chem.* **2014**, *12*, 3037–3044.
[8] J. S. Becker, A. Matusch, C. Depboylu, J. Dobrowolska, M. V. Zoriy, *Anal. Chem.* **2007**, *79*, 6074–6080.
[9] Y. Liu, P. Liang, L. Guo, *Talanta* **2005**, *68*, 25–30.
[10] Y. Zheng, Q. Huo, P. Kele, F. M. Andreopoulos, S. M. Pham, R. M. Leblanc, *Org. Lett.* **2001**, *3*, 3277–3280.
[11] C. Sinha, A. Adak, R. Purkait, S. K. Manna, B. Ghosh, S. Pathak, *New J. Chem.* **2019**, *43*, 3899–3906.
[12] S. Dey, S. Maity, K. Pal, K. Jana, C. Sinha, *Dalton Trans.* **2019**, *48*, 17818–17830.
[13] B. Dutta, R. Purkait, S. Bhunia, S. Khan, C. Sinha, M. H. Mir, *RSC Adv.* **2019**, *9*, 38718–38723.
[14] S. Wang, Z. Wang, Y. Yin, J. Luo, L. Kong , *J. Photochem. Photobiol. A: Chem* **2017**, *333*, 213–219.
[15] O. García-Beltrán, N. Mena, L. C. Friedrich, J. C. Netto-Ferreira, V. Vargas, F. H. Quina, M. T. Nú˜nez, B. K. Cassels, *Tetrahedron Lett.* **2012**, *53*, 5280–5283.
[16] G. Yin, J. Yao, S. Hong, Y. Zhang, Z. Xiao, T. Yu, H. Li, P. Yin, *Analyst* **2019**, *144*, 6962–6967.
[17] V. Dujols, F. Ford, A. W. Czarnik, *J. Am. Chem. Soc.* **1997**, *119*, 7386–7387.
[18] L. Tang, X. Dai, X. Wen, D. Wu, Q. Zhang, *Spectrochim. Acta Part A* **2015**, *139*, 329–334.
[19] Z.-H. Xu, H.-W. Wang, X.-F. Hou, W.-L. Xu, T.-C. Xiang, C.-Z. Wu, *Sens. Actuators B* **2014**, *201*, 469–474.
[20] B. Muthuraj, R. Deshmukh, V. Trivedi, P. K. Iyer, *ACS Appl. Mater. Interfaces* **2014**, *6*, 6562–6569.
[21] Y. Wang, H. Wu, W.-N. Wu, S.-J. Li, Z.-H. Xu, Z.-Q. Xu, Y.-C. Fan, X.-L. Zhao, B–Z. Liu, *Sens. Actuators B* **2018**, *260*, 106–115 .
[22] T. P. Dalton, H. G. Shertzer, A. Puga, *Pharmacol. Toxicol.* **1999**, *39*, 67–101.
[23] E. Weerapana, C. Wang, G. Simon, F. Richter, S. Khare, M. Dillon, D. Bachovchin, K. Mowen, D. Baker, B. Cravatt, *Nature* **2010**, *468*, 790–795.
[24] J. Shao, H. Guo, S. Ji, J. Zhao, *Biosens. Bioelectron.* **2011**, *26*, 3012–3017.
[25] H.-Y. Shiu, M.-K. Wong, C.-M. Che, *Chem. Commun.* **2011**, *47*, 4367–4369.
[26] Y. Tang, H.-R. Yang, H.-B. Sun, S.-J. Liu, J.-X. Wang, Q. Zhao, X.-M. Liu, W.-J. Xu, S.-B. Li, W. Huang, *Chem. Eur. J.* **2013**, *19*, 1311–1319.
[27] F. Wang, Z. Guo, X. Li, X. Li, C. Zhao, *Chem. Eur. J.* **2014**, *20*, 11471–11478.
[28] Y. Shi, J. Yao, Y. Duan, Q. Mi, J. Chen, Q. Xu, G. Zhang, Y. Zhou, J. Zhang, *Med. Chem.* **2013**, *23*, 2538–2542.
[29] X. Chen, H. Xu, S. Ma, H. Tong, K. Lou, W. Wang, *RSC Adv.* **2018**, *8*, 13388–13392.
[30] D. Maheshwaran, S. Priyanga, R. Mayilmurugan, *Dalton Trans.* **2017**, *46*, 11408–11417.
[31] X. Gao, X. Li, L. Li, J. Zhou, H. Ma, *Chem. Commun.* **2015**, *51*, 9388–9390.
[32] G. Yin, T. Niu, Y. Gan, T. Yu, P. Yin, H. Chen, Y. Zhang, H. Li, S. Yao, *Angew. Chem. Int. Ed.* **2018**, *57*, 4991–4994.
[33] Z. Mao, M. Wang, J. Liu, L.-J. Liu, S. M.-Y. Lee, C.-H. Leung, D.-L. Ma, *Chem. Commun.* **2016**, *52*, 4450–4453.
[34] M. Tang, L. Wu, D. Wu, C. Huang, W. Zhu, Y. Xu, X. Qian, *RSC Adv.* **2016**, *6*, 34996–35000.
[35] R. Xie, Y. Li, Z. Zhou, X. Pang, C. Wu, P. Yin, H. Li, *Anal. Bioanal. Chem.* **2020**, *412*, 5539–5550.

[36] Y. W. Choi, J. J. Lee, G. R. Youand, C. Kim, *RSC Adv.* **2015**, *5*, 38308–38315.
[37] D. Śmiłowicz, N. M. -Nolte, *J. Inorg. Biochem.* **2020**, *206*, 111410.
[38] V. S. Padalkar, S. Seki, *Chem. Soc. Rev.* **2016**, *45*, 169–202.
[39] R. Hu, S. Li, Y. Zeng, J. Chen, S. Wang, Y. Li, *Phys. Chem. Chem. Phys.* **2011**, *13*, 2044–2051.
[40] P. P. Soufeena, T. A. Nibila, K. K. Aravindakshan, *Spectrochimica ActaA: Mol.Biomol. Spectrosc.* **2019**, *223*, 117201.
[41] Z. Tu, M. Liu, Y. Qian, G. Yang, M. Cai, L. Wang, W. Huang, *RSC Adv.* **2015**, *5*, 7789–7793.
[42] Z. Tu, Q. Zhang, M. Liu, Y. Qian, L. Wang, W. Huang, *J. Mater. Sci.* **2016**, *51*, 2972–2979.
[43] G. Yang, K. Zhang, F. Gong, M. Liu, Z. Yang, J. Ma, S. Li, *Sens. Actuators B* **2011**, *155*, 848–853.
[44] R. Hu, J. Feng, D. Hu, S. Wang, S. Li, Y. Li, G. Yang, *Angew. Chem.* **2010**, *49*, 4915–4918.
[45] S. Bhardwaj, N. Maurya, A. K. Singh, R. Varshney, P. Roy, *RSC Adv.* **2016**, *6*, 102096–102101.
[46] B. Liu, H. Zhou, B. Yang, X. Hu, *Sens. Actuators B* **2017**, *246*, 554–562.
[47] H. S. Jung, J. H. Han, Z. H. Kim, C. Kang, J. S. Kim, *Org. Lett.* **2011**, *13*, 5056–5059.
[48] C. Yin, J. Li, F. Huo, *Curr. Med. Chem.* **2019**, *26*, 3958–4002.
[49] B. Gu, L. Huang, Z. Xu, Z. Tan, M. Hu, Z. Yang, Y. Chen, C. Peng, W. Xiao, D. Yu, H. Li *Sens. Actuators B* **2018**, *273*, 118–125.
[50] P. Singha, H. Singha, G. Bhargavab, S. Kumara, *J. Mater. Chem. C* **2015**, *3*,5524–5532.
[51] D. Zhao, T. M. Swager, *Macromolecules* **2005**, *38*, 9377–9384.
[52] J. Ding, L. Yuan, L. Gao, J. Chen, *J. Lumin.* **2012**, *132*, 1987–1993.
[53] V. Sharma, D. De, S. Pal, P. Saha, P. K. Bharadwaj, *Inorg. Chem.* **2017**, *56*, 8847–8855.
[54] S. Dey, R. Purkait, K. Pal, K. Jana, C. Sinha, *ACS Omega* **2019**, *4*, 8451–8464.
[55] R. Jiang, N. Liu, F. Li, W. Fu, Y. Zhou, Y. Zhang, *Polymer.* **2018**, *10*, 786.
[56] H. Fang, N. Wang, L. Xie, P. Huang, K.-Y. Deng, F.-Y. Wu, *Sens. Actuators B* **2019**, *294*, 69–77.
[57] Y. Wang, Q. Meng, Q. Han, G. He, Y. Hu, H. Feng, H. Jia, R. Zhang, Z. Zhang, *New J. Chem.* **2018**, *42*, 15839–15846.
[58] H. Zhao, Y. Luo, H. Wang, T. Guo, H. Zhou, H. Tan, Z. Zhou, Y. Long, Z. Tang, *ChemistrySelect* **2018**, *3*, 1521–1526.
[59] X. Tian, Z. P. Dong, J. R. Hou, R. Wang, J. T. Ma, *J. Lumin* **2014**, *145*, 459–465.
[60] H. Tapiero, D. M. Townsend, K. D. Tew, *Biomed Pharmacother.* **2003**, *57*, 386–398.

Submitted: September 29, 2020
Accepted: December 15, 2020

Dalton Transactions

ROYAL SOCIETY OF CHEMISTRY

PAPER

View Article Online
View Journal | View Issue

Cite this: *Dalton Trans.*, 2022, **51**, 3198

Idiosyncatic recognition of Zn^{2+} and CN^- using pyrazolyl-hydroxy-coumarin scaffold and live cell imaging: depiction of luminescent Zn(II)-metallocryptand†

Sukanya Paul,[a] Suvendu Maity,[a] Satyajit Halder,[b] Basudeb Dutta,[c] Srikanta Jana,[a] Kuladip Jana[b] and Chittaranjan Sinha *[a]

Received 28th October 2021,
Accepted 17th January 2022

DOI: 10.1039/d1dt03654h

rsc.li/dalton

Multi-responsive and selective sensor design is one of the stimulating research areas in the sensors field. We have designed a pyrazolyl-hydroxy-coumarin scaffold, 7-hydroxy-4-methyl-8-(((5-phenyl-1*H*-pyrazol-3-yl)imino)methyl)-2*H*-chromen-2-one (H_2L) and characterized it by spectroscopic techniques (^1H NMR, ^{13}C NMR, ESI-MS, IR). The single crystal X-ray diffraction measurement confirms the molecular structure of the probe. It shows the selective sensing of Zn^{2+} in the presence of sixteen other cations with 'Turn On' approach through the enhancement of green florescence ((λ_{em} = 499 nm; λ_{ex} = 390 nm) in CH_3CN/H_2O (99 : 1, v/v; HEPES buffer, pH 7.5) medium with the limit of detection (LOD) of 34.76 nM. The structural depiction of the isolated Zn^{2+} complex reveals cage like metallocryptand cyclic hexamer, $[Zn_6L_6]$ with 30.9% void of cavity along the crystallographic *c* axis of approximate dimension of 7.502 × 7.050 × 7.068 $Å^3$. The diffusion NMR study reveals only one type of complex in the solution, having 1 : 1 composition, *i.e.*, $Zn^{2+} : H_2L$, which affirms the isolated form of the complex. On the other hand, the receptor, H_2L, recognizes the very noxious anion CN^- out of sixteen anions. The product identification using spectroscopic techniques supports the nucleophilic addition of CN^- across the exocyclic imine (C═N) bond, which shows blue emission ((λ_{em} = 447 nm; λ_{ex} = 390 nm), and the LOD was 19.91 nM. The composition of $[H_2L–Zn^{2+}]$ and $[H_2L–CN^-]$ was established by ^1H NMR titration, Job's method, ESI-MS, and FTIR spectra. The efficacy of the probe was further studied using MTT assay in MDA-MB 231 and WI-38 cell line as well as for the intracellular imaging of Zn^{2+} and CN^- using a fluorescence microscope. Flow Cytometry was further performed for the quantitative analysis of Zn^{2+} distribution in MDA-MB 231 cells.

Introduction

The biochemical implication of ions in human health and environment focuses on the synthetic strategy of a receptor in such a manner that the chemosensor selectively emits recognizable signals on binding with bioactive or toxic cations and anions. Polypodal Schiff bases may synthesize multinuclear metallo–macrocycle complexes,[1,2] which may act as potential magnetic materials,[3,4] homogeneous catalysts,[5] optical and electronic materials,[6,7] sensing devices,[8] *etc*. Schiff bases with fluorogenic components such as carbazole,[9,10] quinoline,[11,12] rhodamine,[13,14] naphthyl,[15,16] pyrenyl,[17,18] fluorenyl,[19,20] and diformyl[21,22] influence the emission energy, intensity, pattern, and the molecules might serve as sensitive detectors of ions/molecules. Fluorogenic units of Coumarin derivatives[23–25] are beneficial for their diverse pharmacological properties, low toxicity, and interesting photophysical responses to analytes.

Zinc ion (Zn^{2+}) ranks second in terms of its abundance and activity in environmental and human health.[26,27] It is involved in cell division, gene expression, neurotransmission, signal transduction DNA, and protein synthesis.[28–30] In general, the balanced concentration of Zn^{2+} is beneficial for human health while misregulation has a serious effect on life. In the deficiency of Zn^{2+}, intellectual disability and unbalanced metabolism are the common side effects.[31] However, excess accumulation of Zn^{2+} in cells causes severe neurodegenerative disorder such as Alzheimer's disease and Parkinson's

[a]*Department of Chemistry, Jadavpur University, Kolkata 700 032, India. E-mail: crsjuchem@gmail.com*
[b]*Division of Molcular Medicine, Bose Institute, Kolkata 700056, India*
[c]*Department of Chemical Science, Indian Institute of Science and Education Research, Kolkata, Mohanpur 741246, India*

†Electronic supplementary information (ESI) available. CCDC 2109503 and 2109502. For ESI and crystallographic data in CIF or other electronic format see DOI: 10.1039/d1dt03654h

disease.[32,33] As per the WHO guidelines, the permissible limit of Zn^{2+} consumption in drinking water is 76 μM.[34] The visual detection of Zn^{2+} is a convenient approach for easy detection in materials; bis(oxadiazole)pyridine derivative has been recently demonstrated as an effective Zn^{2+} fluorescent sensor[35] even in cellular environment and the benzothiazole-based chromogenic unit also senses Zn^{2+} colormetrically.[36] Pyrazolyl derivatives efficiently serve the purpose of colorimetric as well as fluorometric Zn^{2+} sensors.[37,38] Thus, it is important to design analytical methods for the efficient, sensitive, selective, nontoxic, and cheap detection of Zn^{2+} at the cellular level.

On the other hand, cyanide (CN^-), often found in the seeds of apples, Cassava, and apricot, on consumption leads to acute toxicity as the CN^- strongly binds Fe of Cytochrome C oxidase, causing the disruption of mitochondrial electron-transport process, resulting in the reduction of oxidative metabolism and interference with energy production.[39–42] In addition, CN^- gets absorbed through skin and lungs and even a microscopic increase in its concentration in the human body causes serious hazards to health.[43] Cyanide is used in gold and silver extraction, electroplating, plastic production, synthesis of resins, fibers, and pesticides. The discharge of cyanide-contaminated industrial waste in environment can result in the exposure of CN^- to humans through food and drinking water.[44–46] Thus, the detection of CN^- at the trace level is important owing to its extremely toxic nature and proper regulations, and guidelines were imposed by WHO for the monitoring of CN^- level with the maximum permissible limit for consumption in drinking water of 1.9 μM.[47,48] Therefore, the generation and advancement of molecular probes for sensitive cyanide detection at the trace level are gaining importance.

Spectroscopic methods are easily operative, show rapid responsive, and are an economical method for the highly sensitive and efficient detection of ions.[49] The use of coumarin derivatives are potentially effective for sensing as well as biological applications.[50,51] In this account, we design and structurally characterize coumarin-based Schiff base, (*Z*)-7-hydroxy-4-methyl-8-(((5-phenyl-1*H*-pyrazol-3-yl)imino)methyl)-2*H*-chromen-2-one (H_2L), which serves as a chemosensor for the sensing of Zn^{2+} (λ_{em} = 499 nm, LOD, 34.76 nM) and CN^- (λ_{em} = 447 nm LOD, 19.91 nM) with distinctive fluorescence responses at two emissive states in acetonitrile medium. The interaction of Zn^{2+} and H_2L has isolated a metallocryptand hexanuclear complex, $[Zn_6L_6]$. The composition and binding stoichiometry of the complex ($[H_2L–Zn^{2+}]$ and $[H_2L–CN^-]$) has been confirmed through ^1H NMR, ESI-MS, IR, and other spectroscopic techniques. Theoretical study has been performed for the probe H_2L along with its Zn^{2+} ($[H_2L–Zn^{2+}]$) and CN^- ($[H_2L–CN^-]$) complexes to explain the spectroscopic changes. The MTT assay of the probe has been carried out in MDA-MB 231 and WI-38 cell lines for cytotoxicity analysis. The distribution of Zn^{2+} and CN^- in MDA-MB 231 cells has been checked through intracellular fluorescence imaging and the detailed estimation of Zn^{2+} distribution in the cells was further examined through Flow cytometric analysis.

Experimental methods

Experimental section (ESI†) includes detail of reagents, common instruments, spectroscopic analysis, and biochemical investigations.

Synthesis of 7-hydroxy-4-methyl-8-(((5-phenyl-1*H*-pyrazol-3-yl) imino)methyl)-2*H*-chromen-2-one (H_2L)

7-hydroxy-4-methyl-2-oxo-2*H*-chromene-8-carbaldehyde was prepared following the literature procedure.[52] To a 10 mL stirred methanol solution of 7-hydroxy-4-methyl-2-oxo-2*H*-chromene-8-carbaldehyde (204.18 mg, 10 mmol), a solution of 3-amino-5-phenylpyrazol (159.19 mg, 10 mmol) in MeOH (5 mL) was slowly added dropwise. The resulting solution, after a few minutes, turned orange, which on stirring for 12 h, followed by refluxing for 3 h, isolated the orange precipitate. It was filtered off and thoroughly washed with methanol, and dried under vacuum (Scheme 1). The compound was recrystallized by the slow evaporation of DMSO/MeOH solution (1 : 4, v/v) and orange block-shaped crystals were isolated. Yield: 79.2%.

Synthesis of hexanuclear zinc complex, $[Zn_6L_6]$

To a solution of H_2L (345 mg, 1 mmol) in 1 mL DMSO, a 5 mL methanolic solution of $Zn(CH_3COO)_2{\cdot}2H_2O$ (220 mg, 1 mmol) (DMSO : MeOH, v/v, 1 : 5) was added slowly under stirring condition for 3 h. The resulting mixture was filtered and kept isolated and allowed for slow evaporation at room temperature for few days. Needle-shaped single crystals were separated and

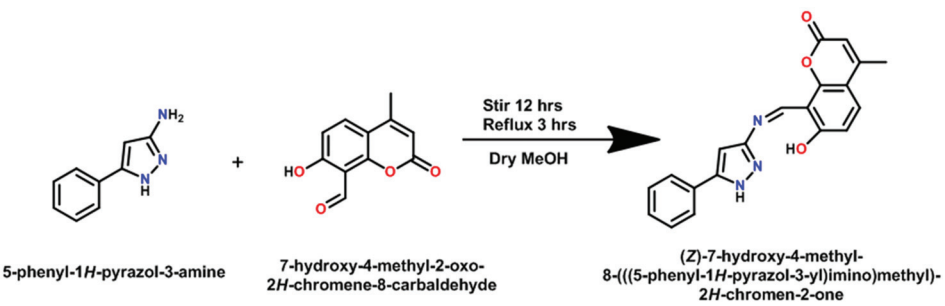

Scheme 1 Synthesis of ligand H_2L.

used for different physicochemical studies and X-ray diffraction data collection. ^{1}H NMR: 9.51–9.43 (d, 1H, CH=N), 7.76–6.00 (m, 9H, Ar–H), 2.35 (s, 3H, CH_3) (Fig. S1†). Microanalytical data ($C_{123}H_{89}N_{18}O_{20}SZn_6$) Fd (calcd) (%) C, 57.59 (57.63); H, 3.47 (3.50); N, 9.87 (9.84). IR Spectrum: ν(C=O) 1702 cm^{-1}, ν(C=N) 1573 cm^{-1}. Yield: 70%.

X-ray crystallographic measurements

Single crystals of (*Z*)-7-hydroxy-4-methyl-8-(((5-phenyl-1*H*-pyrazol-3-yl)imino)methyl)-2*H*-chromen-2-one (H_2L, orange crystal, 0.12 × 0.08 × 0.08 mm^3) and needle shaped yellowish-green crystals of [Zn_6L_6] (0.27 × 0.09 × 0.05 mm^3) were obtained by slow evaporation from an equimolar solution of DMSO and MeOH. Single crystal X-ray data were collected by a Bruker Apex II CCD Area Detector at 100.4 K and 273 K. Graphite-monochromatized Mo-Kα radiation (λ = 0.71073 Å) was used in a fine-focus sealed tube. The *hkl* range for data collection were $-15 \le h \le 15$; $-16 \le k \le 16$; $-14 \le l \le 14$ for the probe H_2L and $-21 \le h \le 21$; $-21 \le k \le 21$; $-29 \le l \le 29$ for [Zn_6L_6]. Diffraction was recorded within the angular range from $2.364 \le \theta \le 27.158°$ (H_2L) and $2.276 \le \theta \le 25.495°$ ([Zn_6L_6]). The intensity was corrected for Lorentz and polarization effects and empirical absorption corrections were applied for both the probe and the complex. Data were collected applying the condition $I > 2\sigma(I)$. The structure was solved by direct methods, followed by successive Fourier and difference Fourier syntheses. All non-hydrogen atoms were refined anisotropically. The hydrogen atoms were geometrically fixed and refined using the riding model. All calculations were carried out using SHELXL-2016/6 Program for Crystal Structure Solution, University of Göτtingen: Göttinge,[53] ORTEP-32,[54] PLATON-99,[55] and Olex 2-1.5-alpha[56] programs. The crystal data of the probe H_2L and Zn^{2+} complexes have been deposited at the Cambridge Crystallographic Data Centre with CCDC 2109503 and 2109502. Details of data collection and crystal data with some selected bond lengths and bond angles were listed in (Tables S1, S2, S3, and S4†).

DFT computation

DFT and TD-DFT calculations were conducted to elucidate theoretical correlation with experimental spectroscopic results. Gas phase geometry of H_2L was optimized with coordinates obtained from the single crystal structure using the DFT/B3LYP method with 6-311G as the basis set (O, N, C, H), whereas the LanL2DZ basis set has been employed for the [Zn_6L_6] and [L–CN$^-$] complex of Gaussian Program Package 09.[57–59] Vibrational frequency calculation has been performed to ensure that the optimized geometries represent the local minima and only the positive eigen values are used. To understand the change in the absorption band of the probe regarding the sensing pathway toward Zn^{2+} and CN$^-$, selective electronic transitions were theoretically obtained by time-dependent DFT (TD-DFT) calculation in acetonitrile medium using a conductor such as polarizable continuum model (CPCM).[60–62] GAUSSSUM employed for the calculation of fractional contribution of the groups to the molecular orbitals.[63]

Cell line study

In the present study, human breast cancer cell line MDA-MB 231 was procured from the central cell repository of National Center for Cell Science (NCCS), Pune, India and human normal kidney epithelium cell line NKE was obtained from Bose Institute, India. All the above cell lines were cultured either in a T25 with DMEM (for MDA-MB 231) RPMI-1640 (for, NKE) supplemented with non-essential amino acids, 1 mM sodium pyruvate, 10% Fetal bovine serum, 2 mM L-glutamine, 100 units per L penicillin, 100 mg L^{-1} streptomycin, and 50 mg L^{-1} gentamycin in a 37 °C humidified incubator containing 5% CO_2.

The fluorescence ability of the probe H_2L in the presence of Zn^{2+} was envisioned in living cell MDA-MB 231. Briefly, the cells were grown in coverslips for 24 h in a 37 °C humidified incubator containing 5% CO_2 and then either mock-treated or treated with 10 μM of H_2L in the presence or absence of 10 μM Zn^{2+} and CN$^-$ and incubated for different time periods at the same temperature. The cells were washed with 1× PBS and then they were mounted on a glass slide and detected under a fluorescence microscope (Leica).

The cell survivability of the ligand H_2L was studied by performing MTT cell proliferation assay and MTT assay was performed by following the reported procedure.[64,65] In brief, MDA-MB 231 and NKE cells were seeded in 96-well plates at a concentration of 1 × 10^4 cells per well and exposed to H_2L at different concentrations of 0 μM, 10 μM, 20 μM, 40 μM, 80 μM, and 100 μM for 24 h. After incubation, the cells were washed with 1× PBS twice and MTT solution (100 μL; 0.5 mg mL^{-1}) were added to each well and incubated for 4 h at 37 °C. The resulting purple colored formazan crystals were dissolved in DMSO and the absorbance was measured at 570 nm using a microplate reader. Cell viability was expressed as a percentage of the control experimental setup.

Results and discussion

Characterization of H_2L

The ^{1}H-NMR spectrum (Fig. S1†) of (*Z*)-7-hydroxy-4-methyl-8-(((5-phenyl-1*H*-pyrazol-3-yl)imino)methyl)-2*H*-chromen-2-one (H_2L) shows a singlet peak at 14.87 ppm for phenolic proton (O–H) of coumarinyl group; another sharp singlet at 13.48 ppm refers to the N–H proton of the pyrazole moiety, while the singlet at 9.50 ppm represents the imine proton (CH=N). These data confirm the formation of the Schiff base. Rest of the aromatic protons appear at 7.89–6.96 ppm. The signal at 6.28 and 2.42 ppm refer to the proton adjacent to the aromatic-H of carbonyl unit and the –CH_3 protons of coumarin ring. The ^{13}C NMR spectrum (Fig. S2†) also reveals characteristics signals at 165.20 and 159.62 ppm for carbonyl (C=O)–C and phenolic (C–O)–C centers while the signal at 156.11 ppm represents the imine-C (HC=N)/pyrazolyl–C (C=N). The remaining Cs of the aromatic region appears in the range of 154.43 to 94.92 ppm and –CH_3 shows a peak at 18.82 ppm. The ESI-MS spectrum (Fig. S3†) of the probe generates a mole-

cular ion peak at 368.0911 [M + Na^+], which confirms the formation of the probe. The FTIR spectrum exhibits stretching frequencies at 3207 cm^{-1} (ν(N–H)), 1691 cm^{-1} (ν(C=O)), and 1617 cm^{-1} (ν(C=N)) of the probe, H_2L (Fig. S4†).

Structural description of H_2L

H_2L crystallizes in the $P2_1/c$ space group. The molecular structure with the atom labelling scheme of H_2L is shown in Fig. 1 and selected bond parameters are summarized in Table S1.† The O(3)–C(7), 1.342(2) Å is longer than O(1)–C(1), 1.207(2) Å, which indicates that O(3)–C(7) is a phenolic type and O(1)–C(1) is a ketone type. The N(1)–C(10) length is 1.285(2) Å (imine type) and shorter than N(1)–C(11), 1.401(2) Å (amine linkage). In the pyrazole ring, the bond lengths are: N(2)–C(11), 1.339 (2); N(3)–C(13), 1.353(3), and N(2)–N(3), 1.345(2) Å. The intermolecular and intramolecular H-bonding O···H–N (2.060 Å), N···H–O (1.843 Å) enhances the strength and stability of the probe (Fig. 2a). The probe has three N donor and one O donor centers in close proximity behaving as tetradentate chelating site for metal binding. The angle of deviation corresponds to the plane containing the coumarin unit with respect to the plane of the pyrazol fragments is 24.89°, while the plane corresponding to the phenyl unit exhibits a 16.19° deviation from the pyrazol plane (Fig. 2b(i) and (ii)).

Spectroscopic response toward Zn^{2+} and CN^- sensing

The absorption spectrum of H_2L in CH_3CN/H_2O (99 : 1, v/v; HEPES buffer, pH 7.5) shows transition at 316 nm, which is ascribed to the π–π* band. Upon the addition of salt solutions of different cations (Cu^{2+}, Co^{2+}, Pb^{2+}, Cr^{3+}, Cd^{2+}, Ca^{2+}, Al^{3+}, Fe^{3+}, Hg^{2+}, Ni^{2+}, Mn^{2+}, Ba^{2+}, Na^+, K^+, Mg^{2+}, and Pd^{2+}), the absorption wavelength more or less remains unshifted; only in

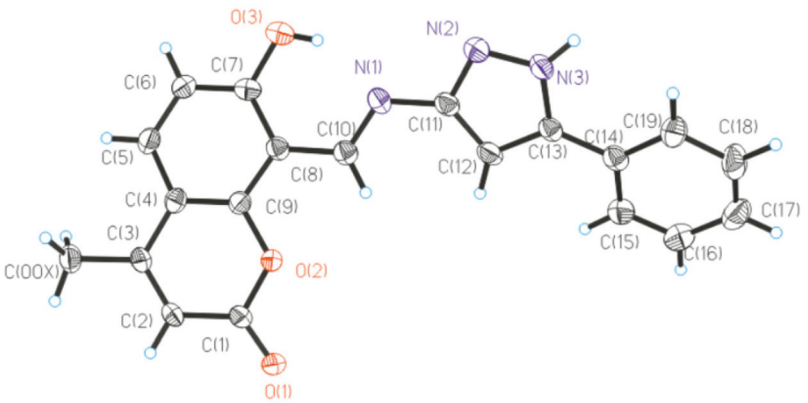

Fig. 1 Molecular geometry of H_2L in crystals (40% thermal ellipsoids, hydrogen atoms are omitted for clarity).

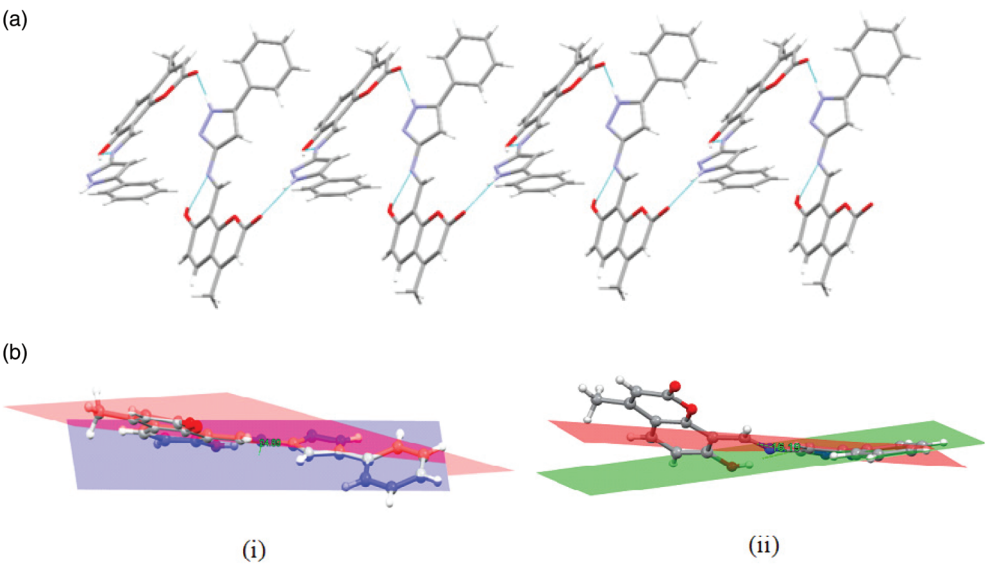

Fig. 2 (a) O···NH and N···HO interactions content in the H_2L; (b) angle of deviation of (i) coumarin and (ii) phenyl unit with respect to the pyrazol plane.

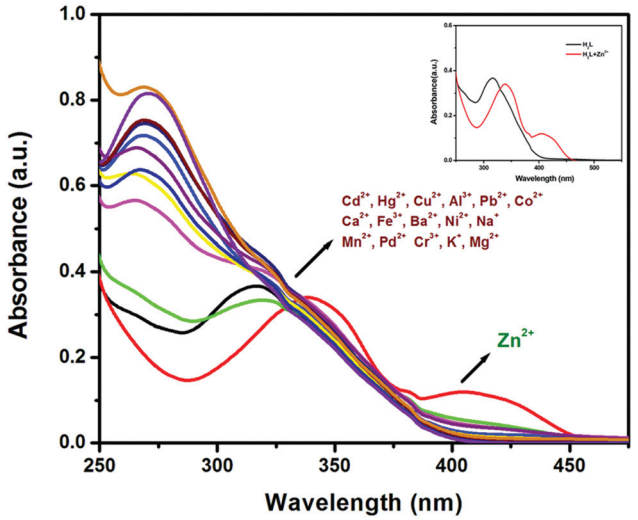

Fig. 3 UV-Vis absorption spectra of H_2L on the addition of cations (2 equiv.) in (99 : 1, v/v) (HEPES buffer, pH 7.5) medium. Inset: absorption spectrum of H_2L and $H_2L + Zn^{2+}$.

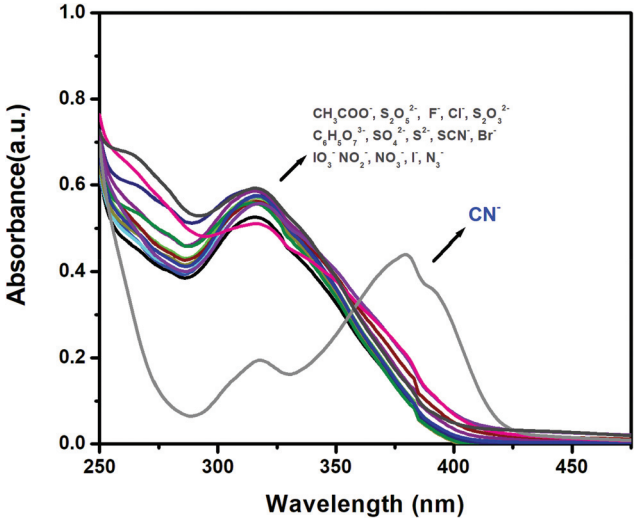

Fig. 5 Absorption spectrum of H_2L on the addition of different anions (2 equiv.) in CH_3CN/H_2O (99 : 1, v/v) (HEPES buffer, pH 7.5) medium.

the case of Zn^{2+}, the ligand solution shows a significant red shifting of the band to 340 nm along with a low energy hump at 412 nm (Fig. 3). On the incremental addition of [Zn^{2+}] (1 μM) to the probe H_2L (25 μM) in the same medium, a spectral change is observed that attained saturation at the 1 : 1 mole ratio of metal : ligand stoichiometry (Fig. 4). The probe in its solution state remains colorless and transforms distinctively to greenish-yellow on the addition of Zn^{2+}, which makes it colorimetric responsive as well as optically detectable toward Zn^{2+} sensing.

The selectivity of H_2L to anions is also checked by following a similar procedure. The anions used are Cl^-, Br^-, I^-, CN^-, S^{2-}, CH_3COO^-, $C_6H_5O_7^{3-}$, $S_2O_3^{2-}$, SO_4^{2-}, F^-, SCN^-, NO_3^-, NO_2^-, $S_2O_5^{2-}$, N_3^-, and IO_3^- in CH_3CN/H_2O (99 : 1, v/v; HEPES buffer, pH 7.5). Noticeably, out of all the anions, the UV-Vis spectral change is observed only when CN^- is added. Upon the addition of NEt_4CN solution to H_2L in the same medium, the band at 316 nm shifts to 380 nm (Fig. 5).

The incremental addition of CN^- (1 μM) to H_2L solution (25 μM) results in a gradual decrease of the 316 nm band and a new band appears at a longer wavelength, 380 nm with a shoulder at 390 nm. The bathochromic shift on successive CN^- addition remains unchanged until a molar ratio 1 : 1 of H_2L to CN^- is reached (Fig. 6). However, the addition of CN^- to the probe solution generates a transient straw yellow color, which rapidly changes to a colorless solution. The change is visually detectable but the color of the resulting solution on the addition of CN^- remains unchanged.

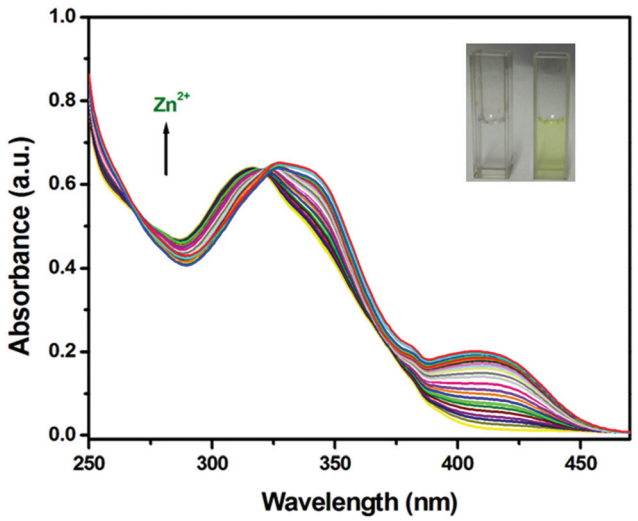

Fig. 4 Change in the absorption spectrum of H_2L on the incremental addition of Zn^{2+}.

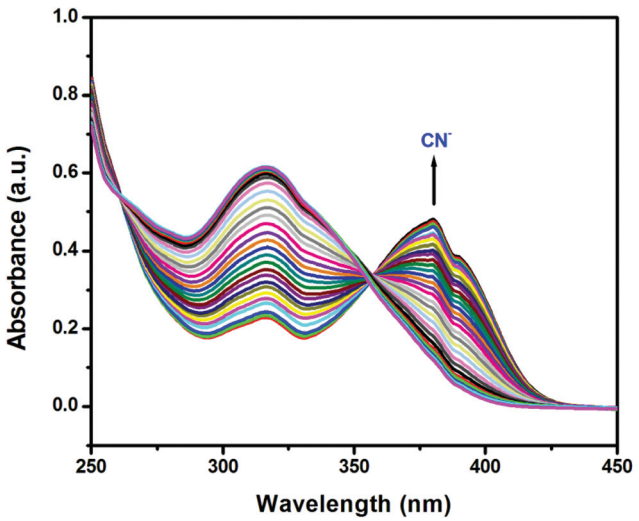

Fig. 6 Change in the absorption spectrum of H_2L on the gradual addition of CN^-.

Luminescence study

Upon the excitation of acetonitrile solution of H_2L at 390 nm, weak fluorescence at 433 nm (ϕ = 0.006) is observed. The energy scavenging of the excited species by PET and ESIPT may be the reasons for the nonradiative decay process.[66] In the solid state, H_2L exhibits enhanced fluorescence at longer wavelength (557 nm) with a higher quantum yield (ϕ = 0.201), which may be due to molecular rigidity that induces RIR (Restricted Intramolecular Rotation) and inhibits isomerization around the C=N bond (Fig. S5†).[67,68] The fluorogenic sensitivity of the probe (H_2L) was examined through the change in the emission intensity (λ_{ex}, 390 nm) on adding seventeen different cations in CH_3CN/H_2O (99 : 1, v/v; HEPES buffer, pH 7.5). Interestingly, the fluorescence intensity of H_2L selectively enhances upon the addition of Zn^{2+} (ϕ = 0.097) and is improved by 20-fold at 499 nm (Fig. 7). The enhancement may be explained on account of its complexation of H_2L with Zn^{2+} as confirmed from the crystal structure that tends to suppress the non-radiative PET and ESIPT processes and inclusion of Chelation-Enhanced Fluorescence (CHEF).[69,70]

On the incremental addition of [Zn^{2+}] (0–26 μM) to the probe, H_2L (25 μM) in CH_3CN/H_2O (99 : 1, v/v) (HEPES buffer, pH 7.5) medium, the emission intensity increases linearly with increasing concentration of Zn^{2+} and saturates when the molar ratio is reached at 1 : 1 concentration of the probe and Zn^{2+} (Fig. 8). The limit of detection (34.76 nM, Fig. S6†) has been evaluated from the calibrated titration profile following the 3σ/Slope method. The LOD for Zn^{2+} is much below the recommended limit by WHO. A similar experimental method is applied for CN^- sensing as well; the probe has been treated with 2 equivalent anions in CH_3CN/H_2O (99 : 1, v/v) (HEPES buffer, pH 7.5) medium. Upon excitation at 390 nm, the emission appears at 447 nm (ϕ = 0.137). In the presence of only CN^-, the emission is 32-fold enhanced while other ions remain insensitive (Fig. 9). On the incremental addition of

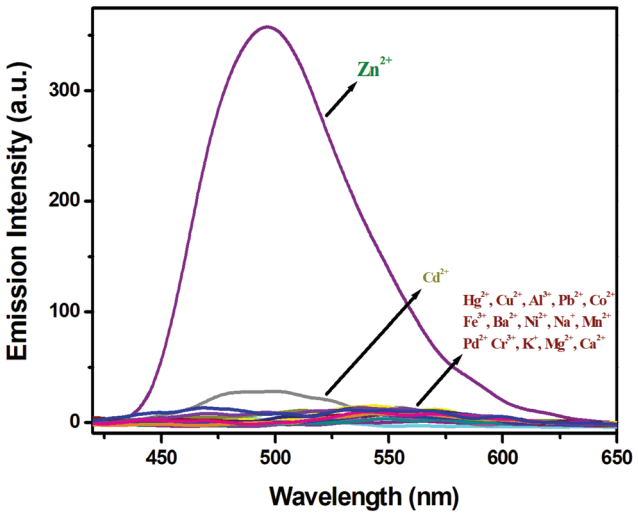

Fig. 7 Emission spectra of H_2L in the presence of different cations (2 equivalents) in CH_3CN/H_2O (99 : 1, v/v) (HEPES buffer, pH 7.5) medium.

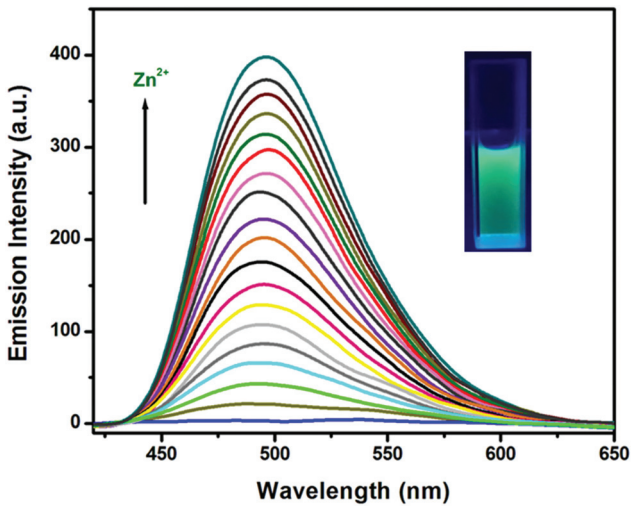

Fig. 8 Change in the fluorescence spectrum of H_2L on the successive addition of Zn^{2+} in CH_3CN/H_2O (99 : 1, v/v) (HEPES buffer, pH 7.5) medium (Inset: images) (λ_{ex} = 390 nm).

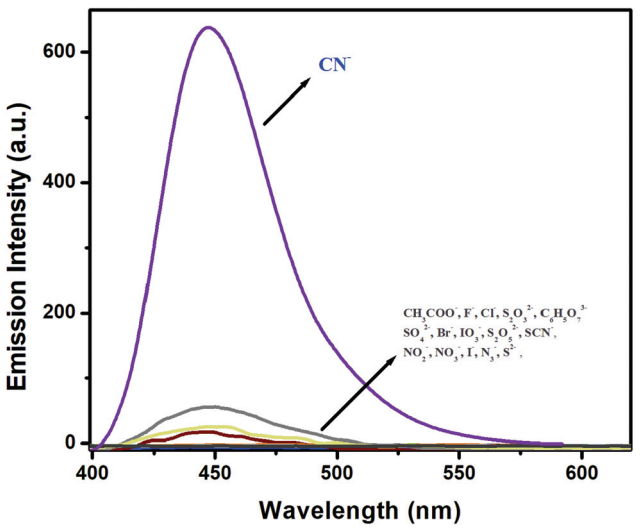

Fig. 9 Emission spectra of H_2L in the presence of different anions (2 equivalents) in CH_3CN/H_2O (99 : 1, v/v) (HEPES buffer, pH 7.5) medium.

CN^- (0–29 μM) in the same solution of the probe (25 μM), a gradual increase in the emission intensity is observed. The plot of emission intensity *vs.* [CN^-] is linear and the emission is optimized when 1 equivalent of CN^- is added (Fig. 10). The LOD is 19.91 nM (3σ method) (Fig. S7†).

The idea of 1 : 1 mole proportion of H_2L with Zn^{2+}/CN^- is also supported by the Job's Plot (Fig. S8 and S9†). H_2L shows spontaneous response and separately senses Zn^{2+} and CN^- at two distinctive emissive wavelengths with a detection limit in the nM range (34.76 nM for Zn^{2+} and 19.91 nM for CN^-). A list of the reported probes along with their LOD value has been compared (Table S5†) and it is revealed that the Pyrazolyl-Hydroxy-Coumarin probe (H_2L) serves efficiently and effectively detects Zn^{2+} and CN^-.

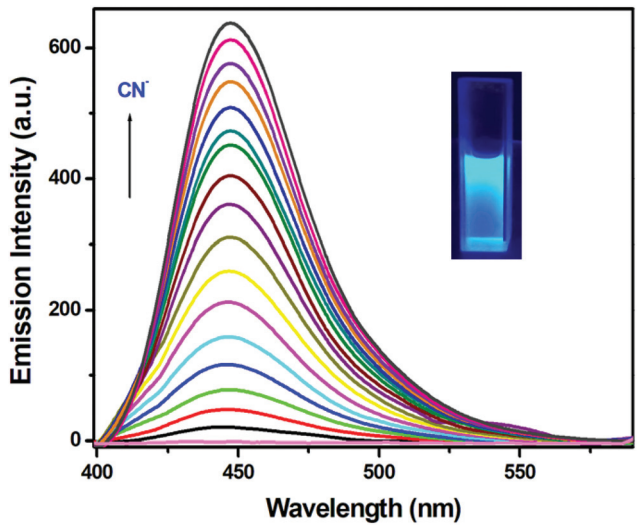

Fig. 10 Change in fluorescence spectrum of H_2L on the successive addition of CN^- in CH_3CN/H_2O (99 : 1, v/v) (HEPES buffer, pH 7.5) medium (Inset: images) (λ_{ex} = 390 nm).

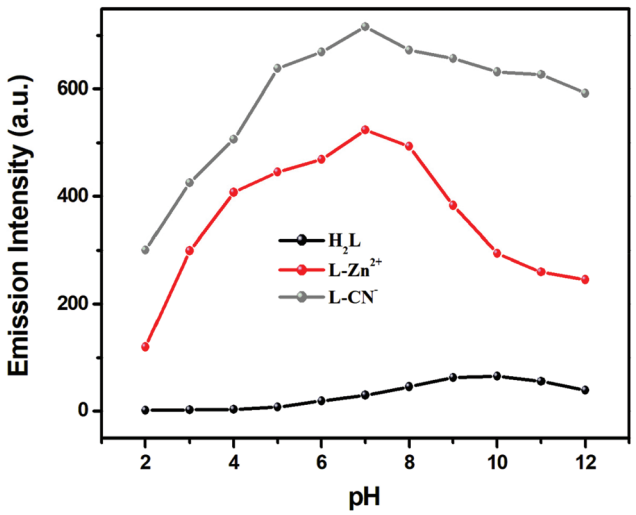

Fig. 11 pH effect on Zn^{2+} and CN^- sensing of the probe H_2L.

To further investigate the influence of pH on the sensing efficacy of the probe, the fluorescence of the H_2L, [H_2L–Zn^{2+}], and [H_2L–CN^-] were closely monitored under the pH range of 2–12. For the Zn^{2+} complex, on going from pH 2 to 6, a steady increase in the emission intensity was observed. The maximum emission in the presence of Zn^{2+} is achieved at pH 7 due to the formation of the [H_2L–Zn^{2+}] species. However, a decrease in the emission intensity at pH > 8 of the [H_2L–Zn^{2+}] complex may be ascribed due to the formation of the oxo-hydroxo-Zn(II) species with increasing basicity, which may interfere with the availability of free Zn^{2+} for complexation with the ligand. The emission intensity on the addition of CN^- is influenced in acidic pH from 2 to 4, which may be ascribed to the formation of HCN species, which may interfere and weaken the extent of nucleophilic addition, thereby accounting for reduced emission in acidic medium. The emission efficiency is maximum at pH 7 while on increasing the pH from 8 to 12, the extent of decrease in the emission intensity was marginal (Fig. 11).

For the detailed understanding of the selectivity of probe H_2L toward Zn^{2+} and CN^- sensing in the presence of other ions, the interference study was conducted under identical conditions. To the solution containing Zn^{2+} and H_2L, 2 equivalents of external co-cations were added to each time and their fluorescence spectra were recorded. The emission intensity of [H_2L–Zn^{2+}] in the presence of Fe^{3+}, Al^{3+}, and Cr^{3+} exhibits slight interferences. This may be due to the weak secondary interaction among the molecular assembly of [H_2L–Zn^{2+}] and M^{3+} (Fe^{3+}, Al^{3+}, Cr^{3+}),[71,72] while for other cations, the emission is almost unaffected and interestingly, the probe could detect Zn^{2+} even in the presence of Cd^{2+} and Hg^{2+} (Fig. S10†). In the case of the interference study of CN^- detection, 2 equivalents of external anions were added at each time to the resulting solution containing CN^- and H_2L and their emission spectra were noted. Interestingly, the impacts of interfering effects were negligible on the emission of [H_2L–CN^-] in the presence of added external anions (Fig. S11†). The results clearly assert the probe to be applicable for the sensitive detection of Zn^{2+} and CN^-.

The ^1H NMR titration explains the extent of binding of H_2L with Zn^{2+}/CN^-. For a detailed understanding of the interaction of H_2L on the addition of Zn^{2+}, the ^1H NMR titration was performed with $Zn(CH_3COO)_2{\cdot}2H_2O$ in DMSO-d_6 medium. The ^1H NMR Spectrum of H_2L recorded at 298 K in DMSO-d_6 exhibited a singlet at 14.89 ppm, which is attributed to the resonance of the phenolic proton, another singlet at 13.50 ppm is assigned to the resonance of pyrazolyl protons; besides, an imine singlet at 9.50 ppm, another doublet at 7.86 ppm (2H, J = 7.8 Hz) integrating two protons, a doublet at 7.83 ppm (1H, J = 9.0 Hz), a triplet at 7.49 ppm (2H, J = 6.6 Hz), another triplet at 7.40 ppm (1H, J = 6 Hz), a singlet at 7.16 ppm, a doublet 6.98 ppm (1H, J = 9 Hz), singlet at 6.28 ppm, and a sharp singlet arises at 2.43 ppm is attributed the resonances of three proton of the aliphatic -CH_3 unit. The presence of two equivalent acetate in $Zn(CH_3COO)_2{\cdot}2H_2O$ causes the deprotonation of the ligand to L^{2-} to bind with Zn^{2+}. The presence of acetate ions is also confirmed from the presence of a sharp singlet peak at 1.90 ppm. The addition of 0.5 equivalent Zn^{2+} results in the gradual fading and broadening of the phenolic peak (O–H) and pyrazol proton (N–H) at 14.89 and 13.50 ppm, respectively. On the addition of 1 equivalent Zn^{2+}, the disappearance of the phenolic peak at 14.89 ppm along with the further reduction and complete broadening of the pyrazolic proton concludes its participation in the complexation to Zn^{2+}. The appearance of the peak at 11.99 ppm is assigned to the OH peak of CH_3COOH. The imine proton at 9.50 ppm undergoes a downfield shift with respect to the protons of the aromatic region. The signal at 6.99 and 6.29 ppm of the aromatic region undergoes an upfield shift to 6.64 and 6.06 ppm, respectively. The aliphatic zone corresponding to the sharp singlet signal at

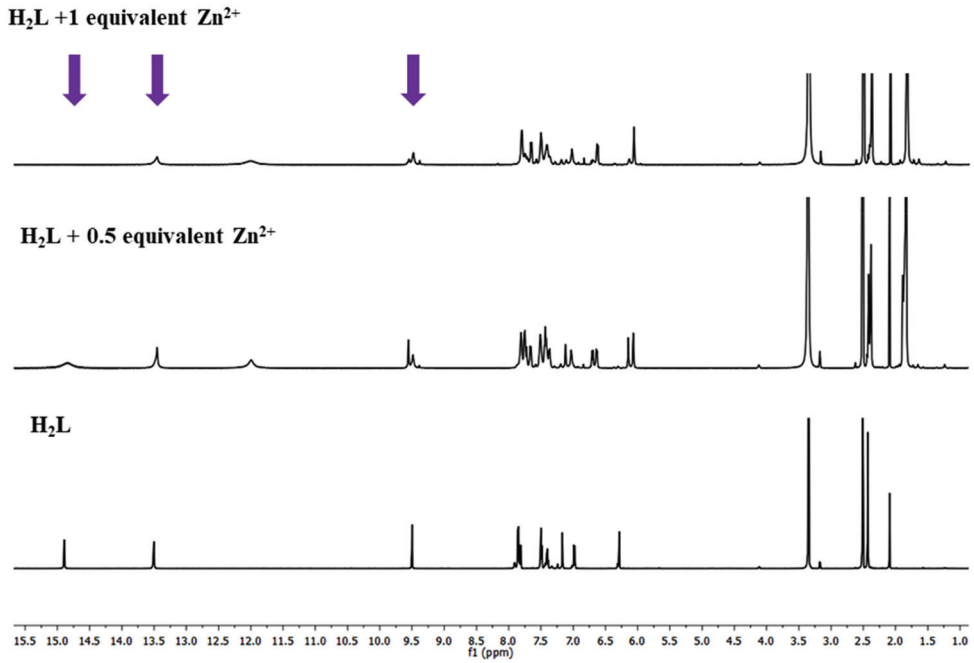

Fig. 12 ^{1}H NMR titration of H_2L on the successive addition of Zn^{2+} in DMSO-d_6.

2.429 ppm is assigned to the methyl unit shifted slightly upfield from 2.43 to 2.38 ppm (Fig. 12).

The DOSY ^{1}H NMR Spectra of the *in situ* complex generated from the addition of 1 equivalent $Zn(CH_3COO_2)\cdot 2H_2O$ to the probe H_2L in DMSO-d_6 clearly explains the formation of a single species with a diffusion coefficient of $D = 2.86 \times 10^{-10}$ m^2 s^{-1} (Fig. 13). The ^{1}H NMR spectrum of $[Zn_6L_6]$ reveals the absence of phenolic and pyrazolyl proton peaks, which indicates the coordination of Zn^{2+} to L^{2-}. The further broadening of imine and aromatic signals due to complexation was also observed in the spectrum (Fig. S12†).

Upon the addition of 0.5 equivalent CN^{-}, the ^{1}H NMR titration of the probe H_2L (DMSO-d_6) shows the attenuation of the signal corresponding to the –OH and –NH proton of coumarin

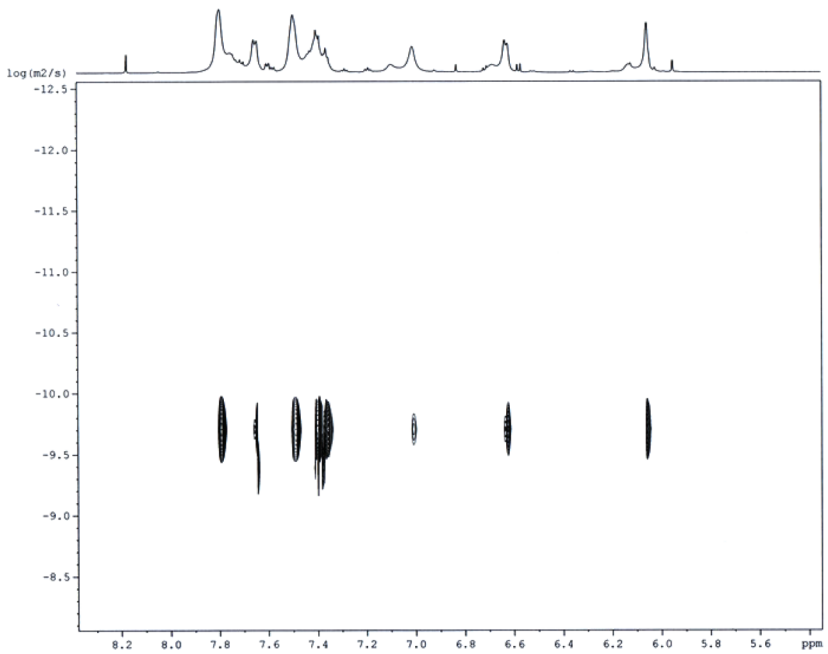

Fig. 13 DOSY NMR (600 MHz) of the resulting complex on the addition of 1 equivalent Zn^{2+} to the probe H_2L in DMSO-d_6.

and pyrazol unit, whereas on addition of 1 equivalent CN^-, the complete disappearance of the phenolic–OH peak, followed by further reduction, as well as the broadening of the NH peak clearly indicates that the interaction with CN^- proceeds through the deprotonation pathway. The gradual fading of the imine singlet at 9.482 ppm is observed on adding CN^- and the complete attenuation of the imine singlet is noted on adding 2 equivalents of CN^- with the simultaneous appearance of the singlet at 5.870 and 5.500 ppm, which attributes to NH and 3° CH protons. This observation supports the nucleophilic addition of cyanide to the carbon atom of the imine group. The proportional broadening and upfield shifting of the aryl protons also validate adduct formation resulting from CN^- addition to the probe H_2L (Fig. 14). Furthermore, the appearance of the peak at 3.150 and 1.121 ppm due to CH_2 and CH_3 protons of EtN_4^+ in the ^1H NMR spectra of the CN^- complex also supports and confirms the formation of such a CN^- binding adduct (Fig. S13†).[73,74]

The average lifetime (τ_{av}) decay profile of H_2L (1.272 ns) as well as the composite of [H_2L + Zn^{2+}] (3.177 ns) and [H_2L + CN^-] (2.8934 ns) fits well into the bi-exponential decay process (Fig. 15). This proves the delocalization of excited energy over the complex motifs of the [H_2L + Zn^{2+}]/[H_2L + CN^-] composite.

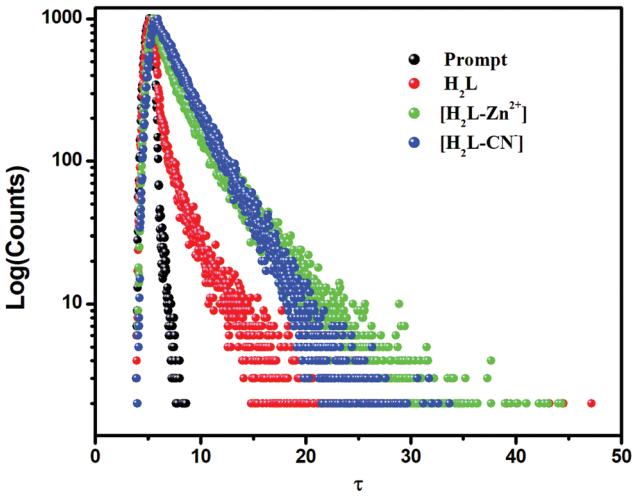

Fig. 15 Lifetime plot of H_2L with Zn^{2+} and CN^-.

Structural description of hexanuclear metallocrypytand [Zn_6L_6]

The structure of the complex forms a hexanuclear metallocryptand (Fig. 16) with Zn(II) and H_2L. [Zn_6L_6] crystallizes in the $P\bar{1}$ space group. The pyrazolyl unit of H_2L forms a bridged binuclear Zn(II) motif and the imine phenolato pendant portion of

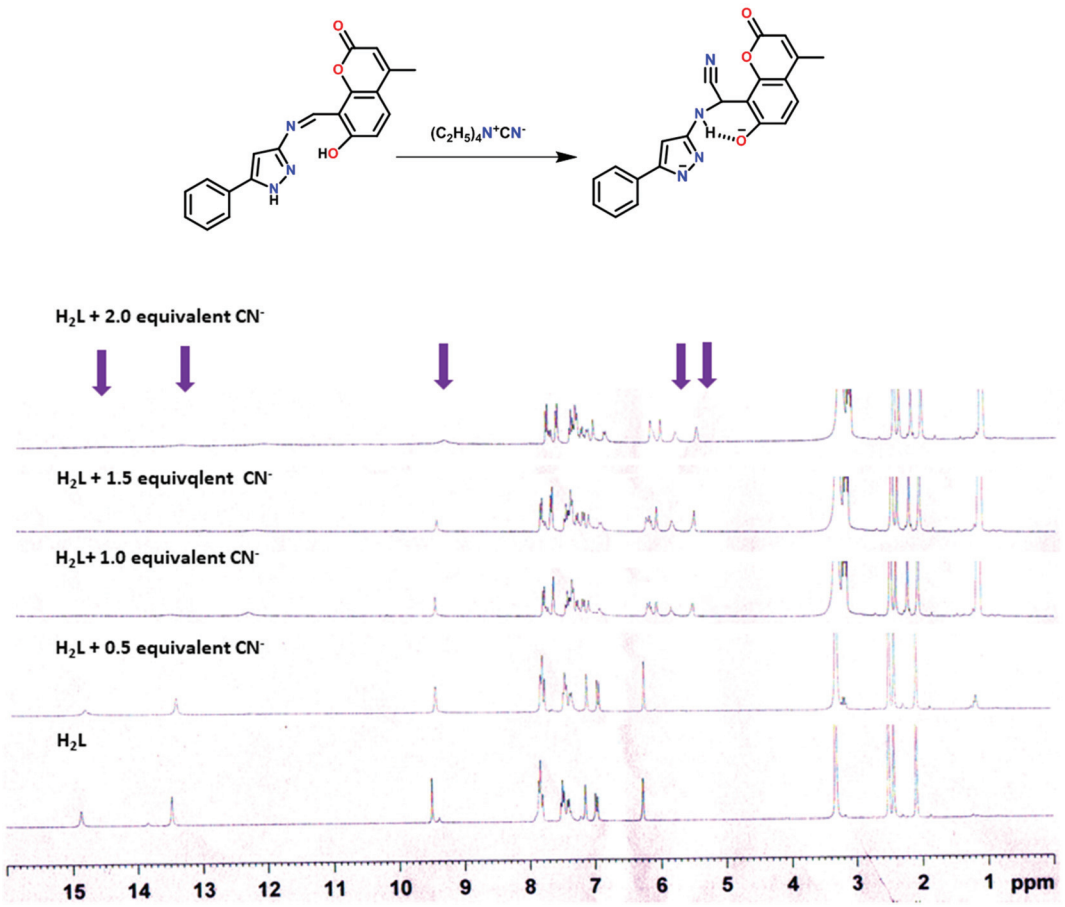

Fig. 14 ^1H NMR titration of H_2L with the successive addition of CN^- in DMSO-d_6.

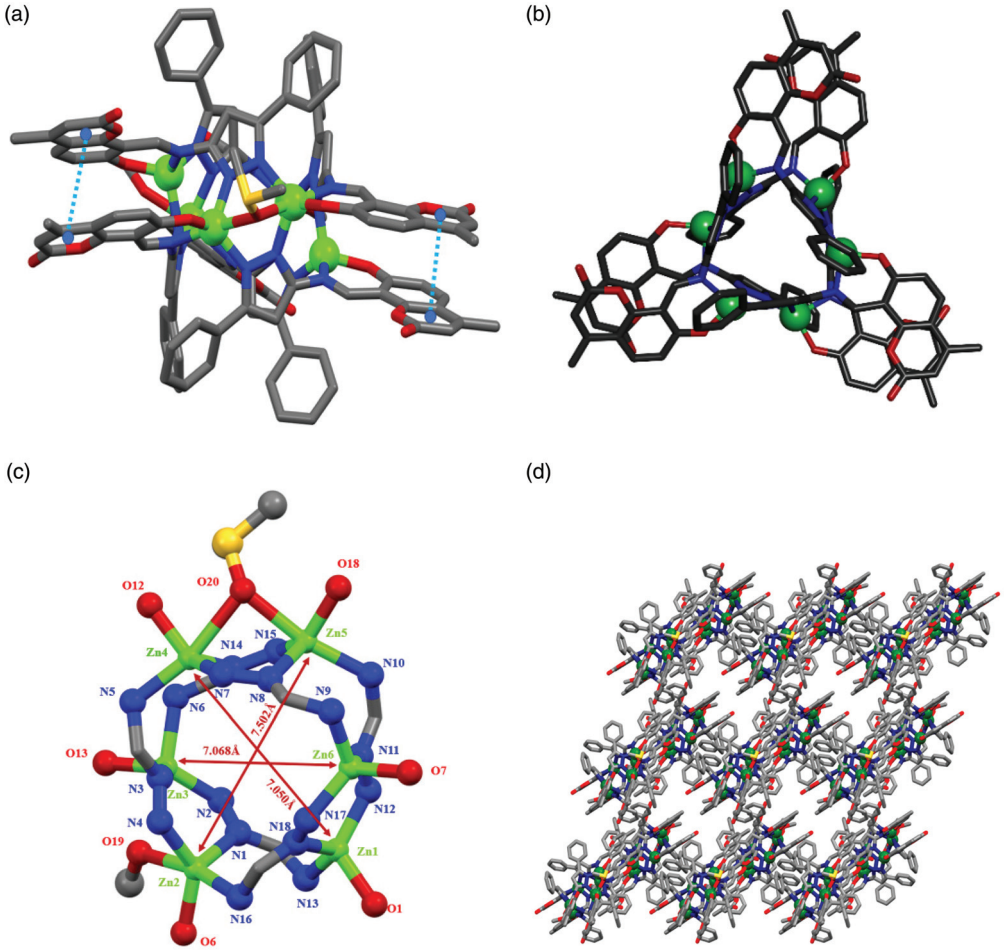

Fig. 16 (a) Discrete hexanuclear Zn(II) complex $[Zn_6L_6]$ showing parallel π···π interaction between the coumarin units. (b) Top and side views of $[Zn_6L_6]$. (c) Linkage framework unit of $[Zn_6L_6]$ exhibiting crown-like cavity and (d) 3D supramolecular assemblies along the *c* axis.

the ligand chelates to the neighboring Zn(II) center. Each Zn(II) center is chelated by the N,O group of one H_2L and coordinated by two pyrazolyl-N centers from two other H_2L ligands. Thus, there are three ligands that are involved in each Zn(II) center. In each hexanuclear cage structure, half of the Zn(II) centers form four-coordinated distorted tetrahedral ZnN_3O sphere and other half Zn(II) centers form five coordinated distorted trigonal bipyramidal ZnN_3O_2 sphere. The fifth coordination center about Zn(II) is assisted by MeOH/DMSO. There are different types of macrocycle rings formed between the zinc ion. Zn(1) and Zn(6) are bridged by the nitrogen atom of the two diazole rings and exhibits tetrahedral geometry with a Zn(1)···Zn(6) distance of 3.520 Å.

The Zn(1)–O(1) and Zn(6)–O(7) distances are 1.932(4) and 1.938(3) Å, which are of a similar type, whereas Zn(1)–N(18), Zn(1)–N(12), and Zn(1)–N(13) lengths are 1.979(4), 1.973(4), and 2.010(4) Å; also, the Zn(6)–N(17), Zn(6)–N(9), and Zn(6)–N(11) lengths are 1.985(4), 2.001(4), and 1.983(4) Å, respectively. This clearly indicates that Zn(1) and Zn(6) are equivalent and form a six-membered macrocycle. Zn(2) forms a distorted triagonal bipyramidal structure (ZnN_3O_2) with one MeOH molecule coordinated and the bond distances are 1.986(4) (Zn(2)–O(6)), 2.027(4) (Zn(2)–N(1)), 2.025(5) (Zn(2)–N(4)), 2.253(4) (Zn(2)–O(19)), and 2.124(4) Å (Zn(2)–N(16)). The distance between the Zn(1) and Zn(2) is 4.187 Å. The Zn(3) center is tetrahedrally coordinated and the bond distances are 1.991(5) (Zn(3)–N(2)), 2.070(5) (Zn(3)–N(6)), 1.944(3) (Zn(3)–O(13)), and 2.014(4) Å (Zn(3)–N(3)). Zn(2) and Zn(3) are bridged in a similar manner by the pyrazolo entity and the distance between Zn(2)···Zn(3) and Zn(3)···Zn(4) are 3.364 and 4.308 Å, respectively. The Zn(4) and Zn(5) are bridged by the nitrogen atom of two diazole ring and one oxygen atom of the DMSO molecule and the Zn(II) ions form a distorted trigonal bipyramidal structure. The measured distance between Zn(4) and Zn(5) is 3.404 Å. The distances Zn(4)–O(12), 1.945(3); Zn(4)–N(5), 2.087(4); Zn(4)–N(14), 2.007(4); Zn(4)–N(7), 1.983(4); Zn(5)–O(18), 1.960(4); Zn(5)–N(8), 2.023(4); Zn(5)–N(10), 2.126(4), and Zn(5)–N(15), 2.012(4) Å are comparable with the first hemisphere of the metallocryptand. The Zn(5)···Zn(6) distance of 4.181 Å in the macrocyclic cage lies in the supramolecular framework. Six Zn(II) centers constituting eight membered macrocycle are embedded in a loop and form the macrocycle. The discrete

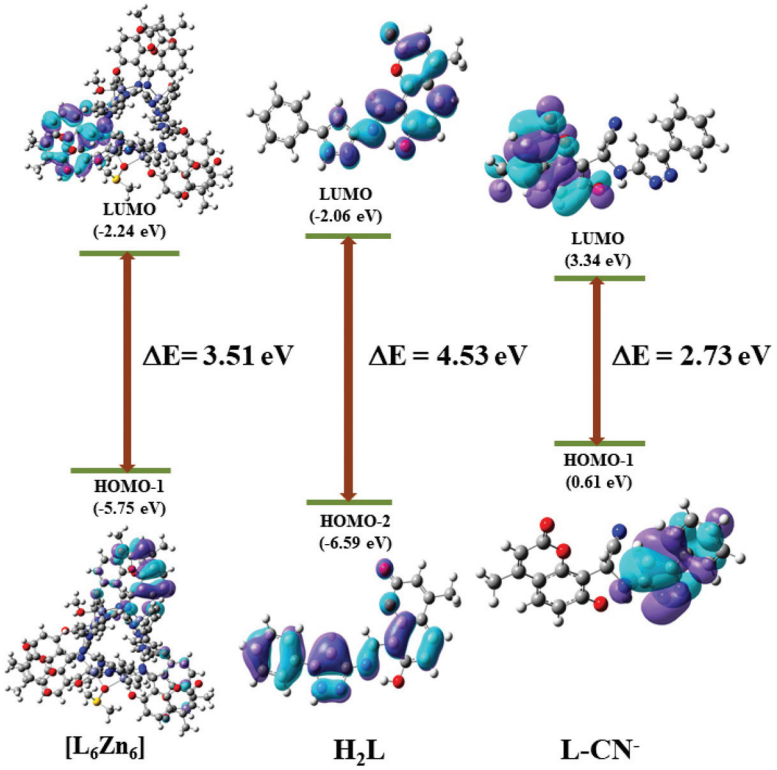

Fig. 17 HOMO–LUMO gap of the probe H_2L, Zn^{2+}, and CN^- Complexes.

hexanuclear unit exhibits a crown-like cavity in the crystal structure (Fig. 16b) and the diagonal distances are 7.502 (Zn(2)–Zn(5)), 7.050 (Zn(1)–Zn(4)), and 7.068 Å (Zn(3)–Zn(6)) (Fig. 16c). The coumarin ring of H_2L interacts with another coumarin ring of the adjacent ligand by the π···π interaction at 3.471, 3.699, and 3.591 Å (Fig. 16a). Three dimensional supramolecular assemblies along the crystallographic *c* axis exhibit 30.9% void space (Fig. 16d). The overall crystal structure of the six nuclei and the ligands forms fifteen-membered macrocycles. The solvent molecules are eliminated by the solvent mask method from the crystal structure during the refinement stage. The absorption spectrum of the isolated complex $[Zn_6L_6]$ also exhibits bands at 335 nm and 412 nm (Fig. S14†). The fluorescence spectrum of $[Zn_6L_6]$ in acetonitrile–water shows emission at 500 nm upon excitation at 390 nm (Fig. S15†). The IR spectrum of $[Zn_6L_6]$ reveals a broad stretching band at about 3500 cm^{-1}, which indicates the presence of MeOH coordinated to the complex, as evident from the crystal structure. The shifting of ν(C=N) from 1606 to 1573 cm^{-1} confirms its participation in the coordination of L^{2-} to Zn^{2+} (Fig. S16†). The IR spectrum of the composite $[H_2L + CN^-]$ also exhibits the stretching band at 2200 cm^{-1}, which confirms the CN^- addition to the probe (Fig. S17†). The ESI-MS Spectrum of the CN^- complex in the anion mode gives a molecular ion peak at m/z = 371 corresponding to $[HL + CN^-]$, which supports the formation of the cyanide adduct along with the presence of the expected deprotonated molecular ion peak of H_2L at m/z = 344 corresponding to $[H_2L - H]$[75] (Fig. S18†).

DFT computation

To understand the probing efficiency of H_2L for Zn^{2+}/CN^-, the theoretical computation of H_2L and the composites were carried out by Density Functional Theory (DFT) using Gaussian Program Package 09. The DFT calculation was employed to obtain the optimized structure of the ligand H_2L using B3LYP/6-311G as the basis set and the LanL2DZ basis set were used for $[Zn_6L_6]$ and L–CN^- complex (Table S6†). Based on the experimental results, the binding model of the respective Zn^{2+} and CN^- complexes were guided. The bond parameters obtained from the optimized structure of the free probe H_2L in the ESI (Table S7†) are compared and in accordance with the single crystal X-ray structure of the probe H_2L. The optimized geometry and energy of the selected orbitals are enlisted in the ESI (Tables S8, S9, S10†). Bond Length (Å) calc. (exp.): (C(10)–N(2)), 1.309 (1.285); (C(11)–N(1)), 1.392 (1.401); (C(7)–O(3)), 1.342 (1.349); (N(2)–N(3)), 1.367 (1.345). Bond angles calc. (exp.): N(2)–C(11)–N(3), 117.53 (116.66); C(7)–O(3)–H, 108.56 (109.5); N(2)–N(3)–C(11), 103.60 (103.97); C(10)–N(1)–C(11) 120.49 (123.19) N(2)–N(3)–H, 118.63 (123.2). Electronic transition derived from Time Dependent Density Function Theory (TD-DFT) calculation determines the HOMO–LUMO gap of the probe and the complexes. Time Dependent Density Functional Theory (TD-DFT) studies elucidate the theoretical aspects of the spectral behavior of H_2L in the presence of Zn^{2+} and CN^-. The HOMO–LUMO band gap of the optimized structure of H_2L, $[Zn_6L_6]$, and $[L–CN^-]$ was deter-

mined as 4.53, 3.51, and 2.73 eV, respectively. The transition obtained from the TD-DFT of the respective structure are listed in Table S11.† The absorption wavelength obtained from DFT calculation correlates well with the experimental absorption spectra. The probe H_2L in its free state exhibits a absorption band at 316 nm corresponding to the transition of HOMO−2 → LUMO. In the case of the hexanuclear Zn^{2+} complex $[Zn_6L_6]$, the absorption bands at 339 and 412 nm are mainly ascribed to the transition of HOMO−1 → LUMO and HOMO−1 → LUMO + 1, respectively. For the motif L-CN^-, the transition HOMO−1 → LUMO contributes to the absorption maxima at 379 nm. The decrease in the band gap of $[Zn_6L_6]$ and L-CN^- by about 1.02 and 1.70 eV suitably explains the bathochromic shift in the absorption spectra of H_2L on the addition of Zn^{2+} and CN^-, respectively (Fig. 17).

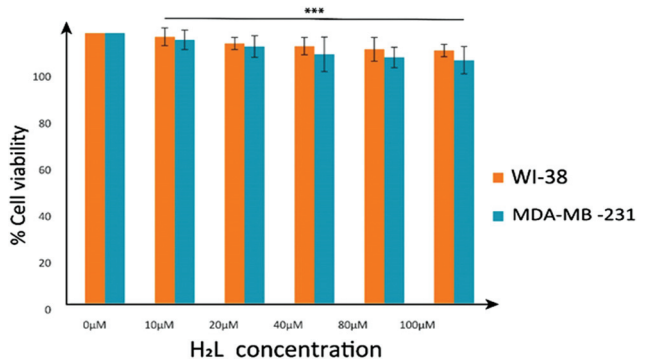

Fig. 18 Cell survivability (MDA-MB 231 and WI-38 cells) exposed to different H_2L concentration. Data are representative of at least three independent experiments and bar graph shows mean ± SEM, ***p < 0.001 were interpreted as statistically significant, as compared with the control.

MTT assay and cell imaging

In vivo cell survivability and cytotoxicity of H_2L was checked on MDA-MB 231 and WI-38 cell line. The cells were treated with five different concentrations of H_2L (0 μM, 10 μM, 20 μM, 40 μM, 80 μM, 100 μM) for 24 h and the results were evaluated. Cell viability was expressed as a percentage of the control experimental setup and the results of the MTT assay (Fig. 18) have shown no substantial toxicities even at the concentration of 100 μM. Hence, the probe H_2L shows significant biocompatibility and favorable for biological applications.

When MDA-MB 231 cells were treated with only Zn^{2+} and CN^-, the results were ineffective (Fig. S19†). Fluorescence microscopy imaging showed an increase in the fluorescence intensity when MDA-MB 231 cells were exposed with both the mixture [H_2L (10 μM) + Zn^{2+} (10 μM)] (green emission, Fig. 19(a) and Fig. S20†) and [H_2L (10 μM) + CN^- (10 μM)] (blue emission, Fig. 19(b) and S21†) at a different incubation time frame of 30 min and 1 h acquired using a blue filter with excitation using 390 nm monochromatic laser beams. On the other hand, the cells exposed to only the H_2L ligand (10 μM) have shown a very low level of florescence intensity. Results from the fluorescence microscopic images manifest that in the presence of Zn^{2+} and CN^-, ligand H_2L emits a prominent fluorescence signal.

FACS was performed to quantitatively analyze the population of the cell that shows fluorescence emission after being

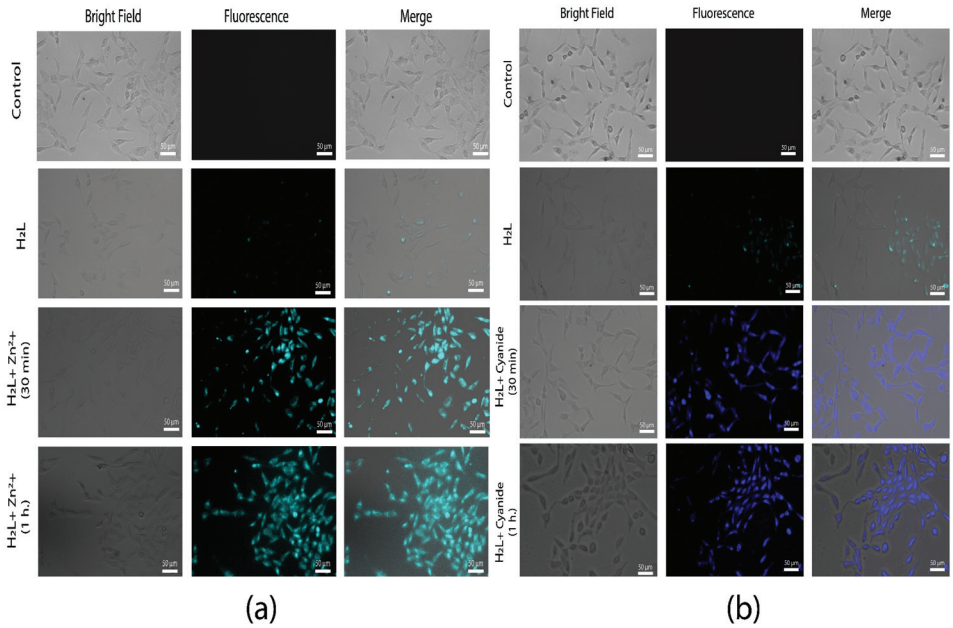

Fig. 19 Microscopic images of untreated MDA-MB 231 cells (Control), cells treated with H_2L (10 μM), (a) H_2L (10 μM) + Zn^{2+} (10 μM), (b) H_2L (10 μM) + CN^- (10 μM) after 30 min and 1 h of incubation period under bright, fluorescence, and merged field.

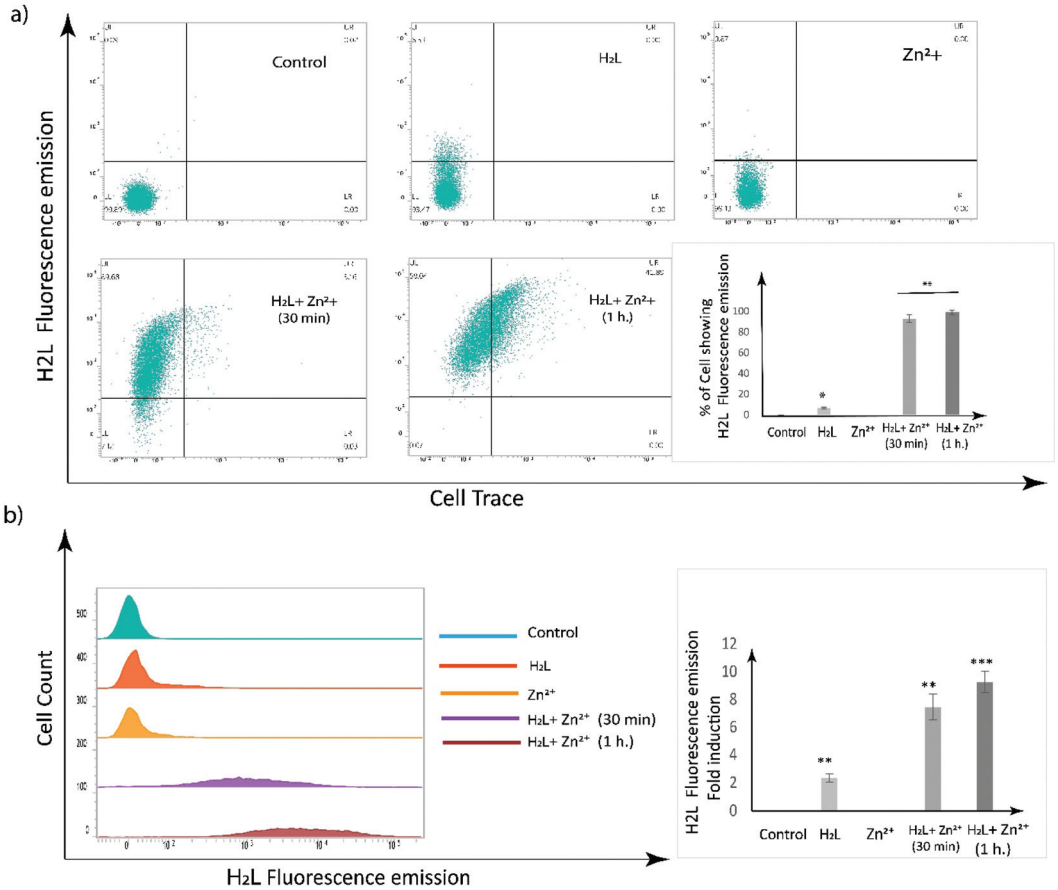

Fig. 20 Flow cytometric dot plot (a) and histogram (b) analysis of untreated MDA-MB 231 cells (Control), cells treated with H_2L (10 μM) + Zn^{2+} (10 μM) after 30 min and 1 h of incubation period. Data are representative of at least three independent experiments and the bar graph shows mean ± SEM, *$p < 0.05$ **$p < 0.01$, ***$p < 0.001$ were interpreted as statistically significant, as compared with the control.

either mock-treated or treated with 10 μM of the ligand in the presence or absence of 10 μM Zn^{2+} at different time periods. Flow cytometric data of H_2L (10 μM) + Zn^{2+} (10 μM) treated cell also showed that about 92% and 99% population of the cell showed H_2L florescence emission after an incubation period of 30 min and 1 h, respectively. Thus, we can conclude that the cells readily uptake the ligand H_2L (10 μM) in the presence of Zn^{2+}. Further, the flow cytometric data also showed that in comparison to the control cell, there is 7.46- and 9.27-fold induction in fluorescence emission in the H_2L (10 μM) + Zn^{2+} (10 μM) treated cell after an incubation period of 30 min and 1 h, receptively. Results from the cell trace experiment using FACS clearly shows a 92% ± 2.47 increase in the cellular population, expressing fluorescence emission in the ligand H_2L + Zn^{2+} treated cell, in comparison to the control as well as the ligand H_2L-treated cell. This indicates the permeability of the ligand H_2L throughout the cell membrane and clearly justified our findings from fluorescence microscopy and also helps in the quantitative analysis of Zn^{2+} distribution in live cells and showed that the presence of Zn^{2+} and ligand H_2L results in a prominent fluorescent signal (Fig. 20).

Conclusion

7-hydroxy-4-methyl-8-(((5-phenyl-1*H*-pyrazol-3-yl)imino)methyl)-2*H*-chromen-2-one (H_2L) has been developed for selective recognition and dual channel response to Zn^{2+} and CN^- at two emissive regions following a different mechanism. Detailed structural characterization for the probe H_2L and hexanuclear complex $[Zn_6L_6]$ has been confirmed from single crystal X-ray diffraction (SCXRD) and other instrumental analyses. The probe selectively senses Zn^{2+} through CHEF and inhibition of PET results in greenish emission (λ_{ex} = 390 nm, λ_{em} = 497 nm) while CN^- generates bluish emission (λ_{ex} = 390 nm, λ_{em} = 447 nm) in CH_3CN/H_2O (99 : 1, v/v) (HEPES buffer, pH 7.5) medium. The proposed binding mechanism and composition of the Zn^{2+} and CN^- complexes has been well accomplished by ^1H NMR titration, IR, and ESI-MS analysis. The Limit of Detection (LOD) has been experimentally found to be 34.76 and 19.91 nM for Zn^{2+} and CN^- detection, which accomplishes the probe to be efficiently sensitive. DFT calculation establishes the theoretical interpretation of the spectral behavior of the probe in the presence of Zn^{2+} and CN^-. The biocompatibility of the probe was established from the MTT assay in MDA-MB 231. The NKE cell

line has been successfully capable of the intracellular imaging of Zn^{2+} and CN^- is imaged in MDA-MB 231 cells, which have been confirmed from the fluorescence microscopic images. The overall results certify that the probe is a competent chemosensor for selective ion sensing and efficient detection of Zn^{2+} and CN^- with dual channel response for practical applications.

Conflicts of interest

The authors declare no conflict of Interest.

Acknowledgements

The work has been supported by the Laboratory Facilities of Jadavpur University, West Bengal India. Council of Scientific and Industrial Research (CSIR, Sanction No.: 01(2894)/2017/EMR-II), New Delhi is acknowledged for their Research Fund. S. P. is obliged to Council of Scientific and Industrial Research (CSIR, File No.: 09/096(0936)/2017-EMR-1) for granting the research Fellowship. Mr Barun Majumder, Bose Institute is acknowledged for his kind contribution in DOSY NMR analysis.

References

1 M. V. Escárcega-Bobadilla, D. Anselmo, S. J. W. Ezenberg, E. C. Escudero-Adán, M. M. Belmonte, E. Martin and A. W. Kleij, *Dalton Trans.*, 2012, **41**, 9766–9772.
2 G. Ambrosi, M. P. Clares, I. Pont, M. Formica, V. Fusi, A. Ricci, P. Paoli, P. Rossi, E. García-España and M. Inclán, *Dalton Trans.*, 2020, **49**, 1897–1906.
3 M. Gopalakrishnan, N. Krittametaporn, N. Yoshinari, T. Konno and P. Sangtrirutnugul, *New J. Chem.*, 2020, **44**, 13764–137703.
4 N. B. Nandi, A. Purkayastha, S. Roy, J. Kłak, R. Ganguly, I. Alkorta and T. K. Misra, *New J. Chem.*, 2021, **45**, 2742.
5 N. Pinault and D. W. Bruce, *Coord. Chem. Rev.*, 2003, **241**, 1–25.
6 P. Levín, D. Escudero, N. Díaz, A. Oliver, A. G. Lappin, G. Ferraudi and L. Lemus, *Inorg. Chem.*, 2020, **59**(3), 1660–1674.
7 J. Gregoliński, K. Ślepokura and J. Lisowski, *Inorg. Chem.*, 2017, **56**, 12719–12727.
8 S. K. Kushvaha, B. Shankar, N. V. T. S. M. Gorantla and K. C. Mondal, *ChemistrySelect*, 2019, **4**, 3334–3339.
9 J. Zhang, H. Cui, M. Hojo, S. Shuang and C. Dong, *Bioorg. Med. Chem. Lett.*, 2012, **22**, 343–346.
10 L. Patra, K. Aich, S. Gharami and T. K. Mondal, *J. Lumin.*, 2018, **201**, 419–426.
11 G. Chakraborty, P. Das and S. K. Mandal, *Mater. Adv.*, 2021, **2**, 2334–2346.
12 Q. Tang, F. Dan, S. Ma, X. Zeng and H. Lan, *Chemistryselect*, 2021, **6**, 6557–6563.
13 X. Tanga, J. Han, Y. Wang, L. Ni, X. Bao, L. Wang and W. Zhanga, *Spectrochim. Acta, Part A*, 2017, **173**, 721–726.
14 C. Long, J.-H. Hu, P.-W. Ni, Z. Yina and Q.-Q. Fu, *New J. Chem.*, 2018, **42**, 17056–17061.
15 S. Samanta, U. Manna, T. Raya and G. Das, *Dalton Trans.*, 2015, **44**, 18902–18910.
16 G.-H. Liu, Z.-Z. Chen, Y.-H. Deng and W.-K. Dong, *J. Photochem. Photobiol., A*, 2021, **414**, 113271.
17 M. Shellaiah, Y.-T. Chen, Y.-T. Chen, N. Thirumalaivasan, B. Aazaad, K. Awasthi, K. W. Sun, S.-P. Wu, M.-C. Lin and N. Ohta, *ACS Appl. Mater. Interfaces*, 2021, **13**, 28610–28626.
18 V. Jeyasingh, K. Murugesan, S. Lakshminarayanan, N. Selvapalam, G. Das and L. Piramuthu, *Spectrochim. Acta, Part A*, 2020, **234**, 118207.
19 K. D. Belfield, M. V. Bondar, A. Frazer, A. R. Morales, O. D. Kachkovsky, I. A. Mikhailov, A. E. Masunov and O. V. Przhonska, *J. Phys. Chem. B*, 2010, **114**, 9313–9321.
20 F. N. Moghadam, M. Amirnasr, S. Meghdadi, K. Eskandari, A. Buchholz and W. Plass, *Spectrochim. Acta, Part A*, 2019, **207**, 6–15.
21 J. Zhang, M. Shea, J. Lia, C. Wang, S. Wang, P. Liu, S. Zhang and J. Li, *Sens. Actuators, B*, 2018, **270**, 362–370.
22 K. Poongodi, P. Saravana Kumar, R. Shanmugapriya, C. Nandhini Kuppanagounder and K. P. Elango, *Spectrochim. Acta, Part A*, 2021, **249**, 119288.
23 R. Purkait, A. Dey, S. Dey, P. P. Ray and C. Sinha, *New J. Chem.*, 2019, **43**, 14979–14990.
24 N. Sahu, S. Mondal, K. Naskar, A. D. Mahapatra, S. Gupta, A. M. Z. Slawin, D. Chattopadhyay and C. Sinha, *J. Mol. Struct.*, 2018, **1155**, 152–164.
25 R. Purkait, C. Patra, A. Das Mahapatra, D. Chattopadhyay and C. Sinha, *Sens. Actuators, B*, 2018, **257**, 545–552.
26 C. F. Mills, *Zinc in Human Biology*, Springer-Verlag, Berlin, 1989.
27 J. M. Berg and Y. Shi, The Galvanization of Biology: A Growing Appreciation for the Roles of Zinc, *Science*, 1996, **271**, 1081–1085.
28 K. Wechakorn, K. Suksen, P. Piyachaturawat and P. Kongsaeree, *Sens. Actuators, B*, 2016, **228**, 270–277.
29 C. J. Frederickson, J. Y. Koh and A. I. Bush, *Nat. Rev. Neurosci.*, 2005, **6**, 449–462.
30 K. Wanga, K. Chen, T. Bian, Y. Chao, T. Yamato, F. Xing, T. J. Priora and C. Redshaw, *Dyes Pigm.*, 2021, **190**, 109300.
31 A. Krężel and W. Maret, *JBIC, J. Biol. Inorg. Chem.*, 2006, **11**, 1049.
32 A. I. Bush, *Trends Neurosci.*, 2003, **26**, 207–214.
33 A. Takeda and H. Tamano, *Brain Res. Rev.*, 2009, **62**, 33–34.
34 T. Tulchinsky, *Public Health Rev.*, 2010, **32**, 243–255.
35 G. Ambrosi, M. Fanelli, P. Paoli, M. Formica, D. Paderni, P. Rossi, M. Micheloni, L. Giorgi and V. Fusi, *Dalton Trans.*, 2020, **49**, 7496–7506.
36 C. A. S. Pothulapadu, A. Jayaraj, S. N, R. N. Priyanka and G. Sivaraman, *ACS Omega*, 2021, **6**, 24473–24483.
37 M. Formica, G. Favi, V. Fusi, L. Giorgi, F. Mantellini and M. Micheloni, *J. Lumin.*, 2018, **195**, 193–200.

38 T. S. Aysha, M. B. I. Mohamed, M. S. E. Sedik and Y. A. Youssef, *Dyes Pigm.*, 2021, **196**, 109795.
39 M. D. Holzbecher, M. A. Moss and H. A. Ellenberger, *J. Toxicol., Clin. Toxicol.*, 1984, **22**, 341–347.
40 Z. Xu, X. Chen, H. N. Kim and J. Yoon, *Chem. Soc. Rev.*, 2010, **39**, 127–137.
41 B. Vennesland, E. E. Comm, C. J. Knownles, J. Westly and F. Wissing, *Cyanide in Biology*, Academic Press, London, 1981.
42 F. R. Sidell, E. T. Takafuji and D. R. Franz, *Medical Aspects of Chemical and Biological Warfare*, 1997.
43 G. C. Miller and C. A. Pritsos, *Cyanide: Social, Industrial, and Economic Aspects*, TMS Publishing, Warrendale, PA, 2001, pp. 73–81.
44 Y. Sun, G. Wang and W. Guo, *Tetrahedron*, 2009, **65**, 3480–3485.
45 J. Marsden and I. House, *The Chemistry of Gold Extraction*, SME, Littleton, Colorado, USA, 2006, p. 67.
46 M. Sahu, A. Kumar, M. Kalyani, R. Dipti, N. B. Sharma and G. K. Patra, *Inorg. Chim. Acta*, 2021, **528**, 120600.
47 World Health Organization, *Guidelines for Drinking-Water Quality*, 3rd edn, Geneva, 2008, p. 188.
48 J.-W. Hu, W.-C. Lin, S.-Y. Hsiao, Y.-H. Wu, H.-W. Chen and K.-Y. Chen, *Sens. Actuators, B*, 2016, **233**, 510–519.
49 A. Adak, R. Purkait, S. K. Manna, B. Ghosh, S. Pathak and C. Sinha, *New J. Chem.*, 2019, **43**, 3899–3906.
50 S. Warrier and P. S. Kharkar, *Spectrochim. Acta, Part A*, 2018, **188**, 659–665.
51 X. Sun, T. Liu, J. Sun and X. Wang, *RSC Adv.*, 2020, **10**, 10826–10847.
52 K. Das, U. Panda, A. Datta, S. Roy, S. Mondal, C. Massera, T. Askun, P. Celikboyun, E. Garribba, C. Sinha, K. Anand, T. Akitsug and K. Kobayashi, *New J. Chem.*, 2015, **39**, 7309–7321.
53 G. M. Sheldrick, *Acta Crystallogr., Sect. A: Found. Crystallogr.*, 2008, **64**, 112–122.
54 A. L. Spek, *Platon*, The Netherlands, 1999.
55 J. Farrugia, *J. Appl. Crystallogr.*, 1997, **30**, 565–565.
56 O. V. Dolomanov, L. J. Bourhis, R. J. Gildea, J. A. K. Howard and H. Puschmann, OLEX2: A complete structure solution, refinement and analysis program, *J. Appl. Crystallogr.*, 2009, **42**, 339–341.
57 M. J. Frisch, G. W. Trucks, H. B. Schlegel, G. E. Scuseria, M. A. Robb, J. R. Cheeseman, G. Scalmani, V. Barone, B. Mennucci, G. A. Petersson, H. Nakatsuji, M. Caricato, X. Li, H. P. Hratchian, A. F. Izmaylov, J. Bloino, G. Zheng, J. L. Sonnenberg, M. Hada, M. Ehara, K. Toyota, R. Fukuda, J. Hasegawa, M. Ishida, T. Nakajima, Y. Honda, O. Kitao, H. Nakai, T. Vreven, J. A. Montgomery Jr., J. E. Peralta, F. Ogliaro, M. Bearpark, J. J. Heyd, E. Brothers, K. N. Kudin, V. N. Staroverov, R. Kobayashi, J. Normand, K. Raghavachari, A. Rendell, J. C. Burant, S. S. Iyengar, J. Tomasi, M. Cossi, N. Rega, J. M. Millam, M. Klene, J. E. Knox, J. B. Cross, V. Bakken, C. Adamo, J. Jaramillo, R. Gomperts, R. E. Stratmann, O. Yazyev, A. J. Austin, R. Cammi, C. Pomelli, J. W. Ochterski, R. L. Martin, K. Morokuma, V. G. Zakrzewski, G. A. Voth, P. Salvador, J. J. Dannenberg, S. Dapprich, A. D. Daniels, O. Farkas, J. B. Foresman, J. V. Ortiz, J. Cioslowski and D. J. Fox, *Gaussian 09, Revision D.01*, Gaussian Inc., Wallingford, CT, 2009.
58 A. D. Becke, *J. Chem. Phys.*, 1993, **98**, 5648–5652.
59 W. R. Wadt and P. J. Hay, *J. Chem. Phys.*, 1985, **82**, 299–310.
60 R. Bauernschmitt and R. Ahlrichs, *Chem. Phys. Lett.*, 1996, **256**, 454–464.
61 M. Cossi and V. Barone, *J. Chem. Phys.*, 2001, **115**, 4708–4717.
62 M. Cossi, N. Rega, G. Scalmani and V. Barone, *J. Comput. Chem.*, 2003, **24**, 669–681.
63 N. M. O'Boyle, A. L. Tenderholt and K. M. Langner, *J. Comput. Chem.*, 2008, **29**, 839–845.
64 D. Laha, A. Pramanik, S. Chattopadhyay, S. K. Dash, S. Roy, P. Pramanik and P. Karmakar, *RSC Adv.*, 2015, **5**, 68169–68178.
65 K. Pal, S. Roy, P. K. Parida, A. Dutta, S. Bardhan, S. Das, K. Jana and P. Karmakar, *Mater. Sci. Eng., C*, 2019, **95**, 204–216.
66 T. Wei, J. Wang, Y. Chen and Y. Han, *RSC Adv.*, 2015, **5**, 57141–57146.
67 Z. He, C. Ke and B. Z. Tang, *ACS Omega*, 2018, **3**, 3267–3277.
68 S. D. Padghan, L. C. Wang, W. C. Lin, J. W. Hu, W. C. Liu and K. Y. Chen, *ACS Omega*, 2021, **6**, 5287–5296.
69 A. Panditha, N. Uddin, C. H. Choi and H.-S. Kim, *Sens. Actuators, B*, 2017, **247**, 840–849.
70 A. Dhara, N. Guchhait, I. Mukherjeec, A. Mukherjeec and S. C. Bhattacharya, *RSC Adv.*, 2016, **6**, 105930–105939.
71 S.-L. Yao, Y.-C. Xiong, X.-M. Tian, S.-J. Liu, H. Xu, T.-F. Zheng, J.-L. Chen and H.-R. Wen, *CrystEngComm*, 2021, **23**, 1898–1905.
72 L. E. Santos-Figueroa, A. Llopis-Lorente, S. Royo, F. Sancenûn, R. Martinez-Manez, A. M. Costero, S. Gil and M. Parra, *ChemPlusChem*, 2015, **80**, 800–804.
73 T. Devendhiran, K. Kumarasamy, M.-C. Lin and Y. X. Yang, *Inorg. Chem. Commun.*, 2021, **134**, 108951.
74 J.-H. Hu, Y. Sun, J. Qi, Q. Li and T.-B. Wei, *Spectrochim. Acta, Part A*, 2017, **175**, 125–133.
75 S. Dey, C. Sen and C. Sinha, *Spectrochim. Acta, Part A*, 2020, **225**, 117471.

Analytical Methods

ROYAL SOCIETY OF CHEMISTRY

PAPER

View Article Online
View Journal | View Issue

Cite this: *Anal. Methods*, 2021, **13**, 5282

A highly emissive Zn(II)-pyridyl-benzimidazolyl-phenolato-based chemosensor: detection of $H_2PO_4^-$ *via* "use" and "throw" device fabrication†

Sunanda Dey,‡[ab] Sukanya Paul,‡[a] Kingshuk Debsharma‡[c] and Chittaranjan Sinha *[a]

2-Ethoxy-6-[1-(phenyl-pyridin-2-yl-methyl)-1*H*-benzoimidazol-2-yl]-phenol (HL) selectively serves as a sensitive 'turn on' Zn^{2+} sensor in 9 : 1 (v/v) DMSO/H_2O (HEPES buffer, pH = 7.4) medium in the presence of sixteen other cations at the limit of detection (LOD) of 3.2 nM. The strong blue emission of the complex, {[Zn(L^1)OAc]} (HL^1 = benzimidazolyl ring-opening structure of HL) (λ_{em}, 461 nm), is quenched by $H_2PO_4^-$ in the presence of eighteen other anions and the LOD is 0.238 μM. The emission of the complex is due to restricted intramolecular rotation (RIR) followed by chelation-enhanced fluorescence (CHEF). The quenching of the emission of [Zn(L^1)OAc] by $H_2PO_4^-$ (in the presence of other P^Vs (inorganic and biological) as well as additional anions) is due to the 'turn off' fluorescence *via* the demetallation and release of the nonfluorescent ligand, HL, and $[Zn(H_2PO_4)]^+$. An INHIBIT logic gate memory circuit of the probe HL was devised with Zn^{2+} and $H_2PO_4^-$ as two consecutive inputs. The percentage of $H_2PO_4^-$ recovery was excellent and was obtained from distilled, tap, and drinking water sources. The bright blue emission of [Zn(L^1)OAc] further triggered the fabrication of ready-made portable thin films of the Zn-complex, which executed a cost-effective 'on-site' solid-state contact mode detection of $H_2PO_4^-$ with selectivity at the picogram level (10.97 pg cm^{-2}) by monitoring the intensities of quenched spots under UV light upon varying the analyte concentration from 10^{-8} to 10^{-3} M. Finally, taking advantage of reversible fluorescence switching, a simple and definite ion-responsive security feature was successfully embedded into a "use" and "throw" solution-coated paper strip of the Zn(II)-pyridyl-benzimidazolyl-phenolato-based chemosensor, which efficiently detected $H_2PO_4^-$ in water by a successive 'ON–OFF' fluorescence switching-driven security activity without any exhaustion of the emission phenomenon.

Received 15th September 2021
Accepted 13th October 2021

DOI: 10.1039/d1ay01575c

rsc.li/methods

Introduction

Phosphates (P^V), inorganic phosphates (PO_4^{3-}, $H_2PO_4^-$, HPO_4^{2-}, $P_2O_7^{4-}$, $P_3O_{10}^{5-}$, polyphosphates) and biogenic phosphates (AMP^{2-}, ADP^{3-} and ATP^{4-}, nucleic acids, phospholipids) are ubiquitous in ecology and the environment, and have attracted considerable attention owing to their inevitable relevance in energy metabolism, signal transduction, regulation of protein and genetic information transfer[1,2] and manufacturing of antiviral as well as chemotherapeutic drugs.[3,4] Khoshniat *et al.* reviewed and suggested that the local phosphate concentration in serum acts as a signal regulating agent for some important biological events like those affecting bones, teeth, muscles, or vascular calcification.[5] Phosphates are useful genetic components for the development of essential biopolymers – DNA, RNA, and phospholipids, along with the transcription of energy and signal *via* the development of bioproteins like adenosine triphosphate (ATP).[6–9] Essentially, phosphates have been extensively utilized as nutrients and fertilizers for all plants and crops in agricultural processes.[10] However, their excessive dispensation together with the uncontrolled discharge of such ions/compounds in the environment through wind erosion and surface runoff from terrestrial to aquatic ecosystems, triggered by anthropogenic activities such as agriculture, animal husbandry, and others causes a severe threat to human health and living organisms. The over-leakage of inorganic phosphates as agricultural waste eventually results in eutrophication of the aquatic bodies *via* the decomposition and depletion of dissolved oxygen due to excessive algal growth in water.[11] Therefore, the permissible level of phosphate in drinking water has been minimized by WHO to 1 mg L^{-1}.[6] Irregular concentrations of phosphate in the

[a]*Department of Chemistry, Jadavpur University, Kolkata 700 032, India. E-mail: crsjuchem@gmail.com*

[b]*Department of Chemistry, Mrinalini Datta Mahavidyapith, Birati, Kolkata 700051, India*

[c]*Department of Chemistry, Indian Institute of Technology Madras, Chennai 600036, India*

† Electronic supplementary information (ESI) available: The spectral characterization figures, theoretical calculation parameters and other additional required UV-Vis and fluorescence spectra. See DOI: 10.1039/d1ay01575c

‡ Authors contribute equally.

human body lead to the clinical diagnostics of various disorders related to vitamin D deficiency, mineral and bone syndrome,[12] illnesses like hyperparathyroidism, hypertension,[13] Franconia disorder,[14,15] hyperphosphatemia and cardiovascular complications.[6] On considering their importance in both biology and environment, great efforts have been made toward the trace level detection of P^V in analytical biochemistry.

Various techniques based on gravimetry, volumetry, spectrophotometry, electrochemistry, and enzymatic coupled reactions have been adopted for the quantitative estimation of P^V.[16] In most cases, the methods have been developed with reference to the yellow molybdophosphate. However, these methods suffer from a serious drawback of acidic pH conditions (conc. HNO_3) and the use of hazardous chemicals. Of these methods, fluorescence molecular sensors specific to inorganic phosphate (Pi) are highly sensitive, selective, inexpensive and simple. Hydrogen bonding, pi-interactions, self-assembly for the aggregation induced emission/quenching, coordination of oxoanions, chemical reactions, displacement approaches, *etc.* are the advanced procedures for ion detection by molecular fluorescence sensing techniques.[17–19] Due to their importance in biology and the environment, considerable attention has been given to the development of systems capable of the selective sensing of phosphates and their related compounds. Several comprehensive reviews describing the recognition of phosphate molecules by artificial receptors have been published.[20–28]

Of the various intrinsic forms of phosphorus, dihydrogen phosphate ($H_2PO_4^-$) has been considered as a predominant component of inorganic phosphate owing to its prevailing equilibrium between two other basic anions, HPO_4^{2-} and PO_4^{3-}, at physiological pH.[16] Therefore, the sensitive and selective detection of $H_2PO_4^-$ as a primary target analyte is a topic of paramount importance. In this aspect, the design of fluorogenic metal complexes that could selectively interact with $H_2PO_4^-$ through altering its emission by desired physical or chemical methods is of utmost priority.[1,6]

Sequential "ON–OFF" fluorescence switching formulated on the direct coordination of a metal ion to the organic scaffold followed by its demetallation with the desired anion based on the relay displacement process not only successfully resolves the prolonged dearth of phosphate detection but also has the added benefit of dual sensing (metal ions and anions) with the exchangeable indicator in a single chemosensor framework, where the sensing mechanism remains independent of the analyte structure.[29,30] Among the different metal ions, the second most abundant essential element Zn(II) imparts a sensitive recognition towards $H_2PO_4^-$ and is biologically important.[31–36] The lack of a spectroscopic signature of Zn(II) due to its intrinsic ($3d^{10}$) electronic configuration can be successfully resolved by its spontaneous tendency to divulge a feasible complexation with varied organic chemosensors, which ultimately tune the photophysics of the luminogenic receptor through the real-time modulation of the fluorescence signal upon hampering the metal-induced electronic communication in the presence of the required anion.[37] Taking inspiration from the simultaneous detection of multi-analytes, the present study unearths an easily made novel benzimidazole appended probe, 2-ethoxy-6-[1-(phenyl-pyridin-2-yl-methyl)-1*H*-benzoimidazol-2-yl]-phenol (HL), based on a single-step Schiff base condensation, where the targeted detection requires merely ambient conditions. Unlike most of the unstable phosphate sensors having poor sensitivity,[38] the present receptor unveils sensitive and selective relay recognition of $H_2PO_4^-$ both in the solution and solid states *via* the "ON–OFF" fluorescence switching of the sensor, triggered by a ring opening chelation of Zn^{2+} followed by its displacement by $H_2PO_4^-$, with desired accuracy and comparability in each recognition step.

Experimental section

Materials and methods

2-Benzoylpyridine, *o*-phenylenediamine, 3-ethoxysalicylaldehyde were purchased from Sigma-Aldrich. Inorganic salts (cation sources: $Zn(OAc)_2\cdot 2H_2O$, $Cd(OAc)_2$, $Hg(OAc)_2$, $CuCl_2\cdot 2H_2O$, $CoCl_2\cdot 6H_2O$, $PbCl_2$, $Al(NO_3)_3\cdot 9H_2O$, $CaCl_2\cdot 6H_2O$, $FeCl_3\cdot 6H_2O$, $BaCl_2\cdot 2H_2O$, $NiCl_2\cdot 6H_2O$, NaCl, $MnCl_2\cdot 4H_2O$, $PdCl_2$, $CrCl_3\cdot 6H_2O$, KCl, $MgCl_2$; anion sources: KH_2PO_4, $Na_2S_2O_3\cdot 5H_2O$, K_3PO_4, NaCl, NaF, NH_4HF_2, KNO_3, KBr, $NaNO_2$, NaN_3, Na_3AsO_4, CH_3COONa, $NaAsO_2$, KIO_3, $Na_4P_2O_7$, KI, Na_2SO_4, Na_2S, and $Na_2S_2O_5$) were bought from Merck. For spectroscopic measurements, spectroscopic grade solvents were used from TCI. The solvents were dried by the standard procedure for spectroscopic studies.[39] Milli-Q water (Millipore) was used for the preparation of aqueous solutions of metal salts. A PerkinElmer (2400 Series-II, PerkinElmer, USA) CHN analyzer was utilized for elemental analysis purposes. The spectra were recorded by a Lambda 25 spectrophotometer: UV-Vis; LS55: fluorescence and LX-1FTIR spectrophotometer: FT-IR spectra (KBr disk, 4000–400 cm^{-1}) on PerkinElmer instruments. ^1H and ^{13}C NMR spectra were taken by a Bruker 500 MHz FT-NMR spectrometer. The chemical shift (δ) of the respective NMR spectra were recorded in parts per million (ppm) with respect to trimethylsilane (TMS) as the internal standard. ESI-MS spectra were obtained using an HRMS spectrometer (model, XEVO-G2QTOF#YCA351).

2-Ethoxy-6-[1-(phenyl-pyridin-2-yl-methyl)-1*H*-benzoimidazol-2-yl]-phenol (HL)

N-(Phenyl-pyridin-2-yl-methyl)-benzene-1,2-diamine (**A**) was synthesized by following the literature procedure.[40] To dry a methanol solution (10 mL) of **A** (0.275 g, 1.0 mmol), 3-ethoxysalicylaldehyde (0.166 g, 1.0 mmol in 15 mL methanol) was added gradually and the mixture was stirred for 12 h. The clear

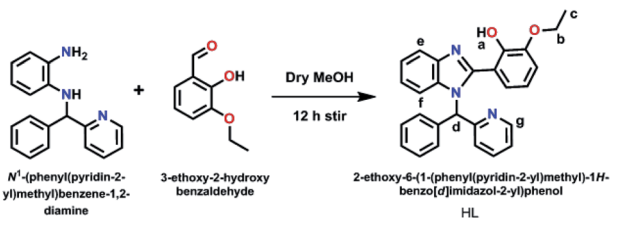

Scheme 1 Synthesis of the probe, HL.

solution was allowed to evaporate slowly (Scheme 1) to isolate yellow-colored prismatic crystals (0.305 g, yield ~72%) after two weeks, which were characterized by various spectroscopic techniques including single-crystal X-ray diffraction measurements.

Quantum yield and limit of detection calculations

Fluorescence quantum yields (ϕ) were obtained by using the following equation:

$$\phi_{\text{sample}} = (\text{OD}_{\text{std.}} \times A_{\text{sample}})/(\text{OD}_{\text{sample}} \times A_{\text{std.}}) \times \phi_{\text{std.}}$$

where A_{sample} and $A_{\text{std.}}$ represent the areas under the fluorescence spectral curves for the sample and standard respectively. $\text{OD}_{\text{sample}}$ and $\text{OD}_{\text{std.}}$ represent the optical densities of the sample and standard, respectively, at that excitation wavelength. In this work, acidic quinine sulfate (0.1(N) H_2SO_4 solution) was taken as the standard with a known quantum yield of 0.54.[41]

The LOD was calculated from the fluorescence titration experiment with the gradual addition of Zn^{2+} into the solution of probe HL. The standard deviation was measured from the emission intensity of the probe at varying concentrations. The limit of detection was determined from the equation, $\text{LOD} = 3\sigma/m$, where, σ represents the standard deviation and the slope (m) was acquired from the plot of the fluorescence titration experiment.

Solution preparation for UV-Vis and fluorescence spectral measurements

The probe solution (HL, 1×10^{-3} M) was prepared in DMSO (AR). All the salt solutions (1×10^{-3} M) were taken in deionized water. A 50 μM solution of HL was prepared with (9 : 1, v/v; DMSO/H_2O (HEPES buffer, pH 7.4)). To this solution, 1.0 equivalent of salt solution was added at room temperature (298 K) with the appropriate correction of the dilution factor and the sensitivity and selectivity were checked by spectroscopic measurements. A two and four-faced quartz cell with a path length of 1 cm were used for the absorption and emission measurements, respectively. Fluorescence experiments were carried out with 15 and 5 nm excitation and emission slit widths.

X-ray crystallography of HL

Yellow prismatic crystals of HL ($0.19 \times 0.03 \times 0.06$ mm^3), suitable for diffraction study, were obtained upon the slow evaporation of the ethanolic solution of the probe at room temperature. Single-crystal X-ray data were collected using a Bruker Apex II CCD Area Detector at 273(2) K. The crystal data and refinement parameters are tabulated in Table S1 (ESI†). Graphite-monochromatized MoKα radiation (λ = 0.71073 Å) was used in a fine-focus sealed tube. The *hkl* range for data collection was $-10 \le h \le 10$; $-12 \le k \le 12$; $-27 \le l \le 27$. Diffraction was recorded within the angular range of $2.185 \le \theta \le 24.993°$. The intensity was corrected for Lorentz and polarization effects with the application of rectified empirical absorption data, collected under the condition of $I > 2\sigma(I)$. The structure was solved by the direct method, followed by successive Fourier and difference Fourier syntheses. All non-hydrogen atoms were refined anisotropically. The hydrogen atoms were geometrically fixed and refined using the riding model. All calculations were carried out using the SHELXL-97,[42] ORTEP-32 (ref. 43) and PLATON-99 (ref. 44) programs. The crystal data of HL were deposited to the Cambridge Crystallographic Data Centre with CCDC 2038659.†

Time-resolved fluorescence decay measurement

A time-correlated single-photon counting spectrometer (Horiba Jobin Yvon) having a diode laser as an excitation source (λ_{ex} = 390 nm) with a pulse repetition rate of 1 MHz was utilized for fluorescence decay profile measurement. The respective emission maxima were taken for the collection of decay curves, which were further analyzed using an IBH DAS6 software with suitable fitting according to the following equation:

$$I(t) = \sum_i A_i \, e^{-\tau/\tau_i}$$

where, τ_i is the luminescence lifetime of the i^{th} species and A_i represents the amplitude of the corresponding decay. During fitting, a range of valid χ^2 values were employed accordingly. For evaluating the characteristic times, a bi-exponential decay model was utilized based on the following equation:

$$\tau_{\text{avg}} = \frac{\sum \tau_i B_i}{\sum_i B_i}$$

where, τ and B represent the lifetime and its respective amplitude.

DFT computations

Density Functional Theory (DFT) and Time Depended-DFT (TD-DFT) calculations were performed to explicate the theoretical correlation with experimental analyses. The gas-phase full geometry optimization of HL was carried out using the GEN basis set with the B3LYP functional in the Gaussian program package Gaussian 09.[45] The LanL2DZ basis set was employed for full geometry optimization of the Zn complex. The absence of any imaginary frequencies in the vibrational frequency calculations of the probe and its complex ensured that the optimized geometries attained the respective energy minima.[46] Subsequently, the entire vibrational analyses were performed with respect to all geometrical variables, regardless of any geometrical constraints. Electronic transitions were obtained theoretically by TD-DFT calculations in DMSO medium using a Conductor-like Polarizable Continuum Model (CPCM)[47,48] and the GAUSSSUM[49] was used for the calculation of the fractional contribution of groups in the molecular orbitals.

Results and discussion

General information for probe HL

The ^{1}H NMR spectrum of 2-ethoxy-6-[1-(phenyl-pyridin-2-yl-methyl)-1*H*-benzoimidazol-2-yl]-phenol (HL) showed a singlet

peak at 9.52 ppm which was assigned to the phenolic proton (–OH). Also, a singlet signal at 8.52 ppm was allotted to the aromatic-C–H (H_g), adjacent to the pyridyl-*N*. The remaining aromatic protons appeared from 6.71 to 7.78 ppm. The sharp singlet peak due to the tertiary C–H (H_d) appeared at 6.13 ppm. The methylene (–CH_2–) proton (H_b) of the ethoxy (–O–CH_2–CH_3) group was at 4.09–4.13 ppm and the methyl (–CH_3) proton (H_c) was observed at 1.32 ppm (Fig. S1, ESI†). The ^{13}C NMR spectrum showed a peak at 157.6 ppm due to the presence of the C–N of the pyridine ring and other aromatic carbon appeared between 113.59–149.65 ppm. The resonance signals for the methylene carbon (–CH_2–) of –O–CH_2–CH_3 and the primary carbon (–CH_3) appeared at 64.73 and 15.10 ppm, respectively (Fig. S2, ESI†); thus, the probe carried the benzimidazole derivative. This was also confirmed from the single-crystal structure determination (Fig. 1). The ESI-MS analysis showed molecular ion peaks at *m*/*z*, 422.1845 and 444.4698, which were assigned to [M + H^+] and [M + Na^+] ions peaks, respectively, supporting the structure of HL (Fig. S3, ESI†). The FT-IR spectrum exhibited stretching frequencies at 2900 and 1591 cm^{-1}, respectively corresponding to the vibrations of the tertiary C–H and C=N units in the probe (Fig. S4, ESI†). The phenolic –OH stretching was observed at 3448 cm^{-1}. All the characterizations and spectroscopic data are provided in the ESI.†

The single-crystal X-ray structure of HL is shown in (Fig. 1), it crystallizes in the orthorhombic crystal system with the space group $P2_12_12_1$. The molecular lattice consists of one discrete unit and details of the bond parameters like selected bond length and bond angle are listed in the ESI.† The bond lengths of C(007)–N(2) and C(007)–N(1) are 1.307(9) and 1.374(9) Å, respectively, which confirm the formation of the imine and amine linkages in the probe. The HL has three N donors and one O donor for chelation with metal ions and demonstrates tetradentate NNNO-type coordination based on the proximity of the chelating sites. A supramolecular assembly was formed in this crystal unit along the '*c*-axis' through weak intermolecular interactions (Fig. S5, ESI†).

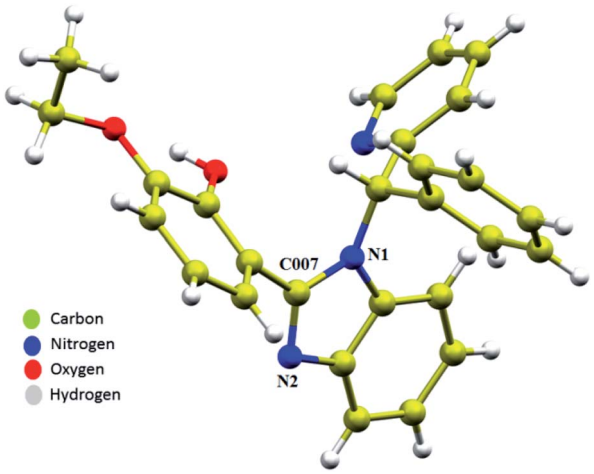

Fig. 1 Single-crystal X-ray structure of the probe, HL.

The spectroscopic behaviour of HL toward metal ions and selectivity for Zn^{2+} ions

The UV-Vis absorption spectrum of the probe, HL (9 : 1 (v/v) DMSO/H_2O; HEPES buffer, pH = 7.4) exhibited absorption bands at 265 and 285 nm and a weak shoulder at 335 nm (Fig. S6, ESI†). The fluorescence spectrum exhibited very weak emission ($\phi_{[HL]} = 0.0051$) upon excitation at 350 nm in the same medium (9 : 1 (v/v) DMSO/H_2O (HEPES buffer, pH = 7.4)). The poor luminogenic behavior of the probe in the free-state was demonstrated by twisting the structural framework, which enabled the unrestricted rotation of the tethered 2-ethoxy phenol and phenyl pyridine substituents with respect to the benzimidazole unit. The torsional angles of the C4–C5–C007–N2, C6–C5–C007–N1, and N1–C7–C18–N3 planes are 58.14°, 64.18° and 38.09°, respectively (Fig. S7, Table S2, ESI†), which indicate the free rotation of the probe and the resulting weak luminescence in the excited state.[50,51]

Sensitivity experiments of the probe were carried out in the presence of 1.0 equivalent of different essential cations such as Cu^{2+}, Co^{2+}, Pb^{2+}, Zn^{2+}, Cr^{3+}, Cd^{2+}, Ca^{2+}, Al^{3+}, Fe^{3+}, Hg^{2+}, Ni^{2+}, Mn^{2+}, Ba^{2+}, Na^+, K^+, Mg^{2+} and Pd^{2+} in 9 : 1 (v/v) DMSO/H_2O (HEPES buffer, pH = 7.4) and the fluorescence spectra were recorded (Fig. 2a). Interestingly, out of all the cations, the probe selectively sensed Zn^{2+} ions with the enhancement of the emission band centered at 461 nm (λ_{ex} = 350 nm). A significant enhancement (~80 fold) of the emission was observed in the case of Zn^{2+} ions, whereas ~6 fold enhancement was observed for Cd^{2+} ions, and the rest of the metal ions caused insignificant changes in the emission intensity. The probe showed a distinctive blue emission only in the presence of Zn^{2+} ions (inset of Fig. 2b) and such high emission may be explained by the suppression of the existing free rotations in HL accompanied by

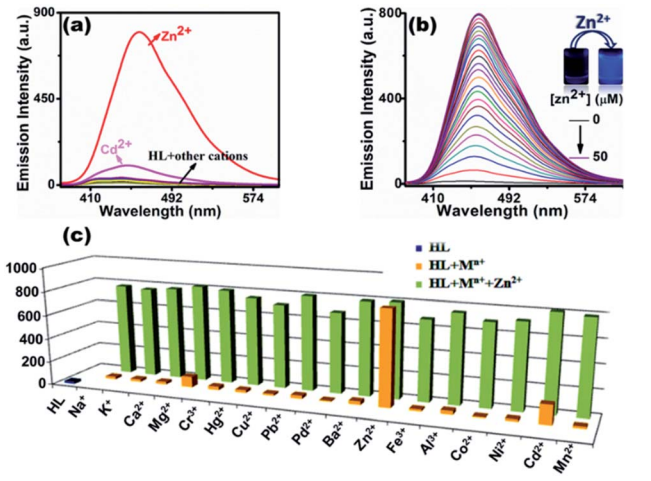

Fig. 2 (a) Emission spectra of HL (50 μM) in the presence of different cations (1.0 equivalent) in 9 : 1 (v/v) DMSO/H_2O (HEPES buffer, pH = 7.4) (λ_{ex} = 350 nm). (b) Changes in the fluorescence spectrum of HL (50 μM) on the successive addition of Zn^{2+} ions (0–50 μM) in 9 : 1 (v/v) DMSO/H_2O (HEPES buffer, pH = 7.4) (λ_{ex} = 350 nm). The inset shows photographs of HL (50 μM) and its Zn(II)-complex taken under UV light (λ_{ex} = 365 nm). (c) Interference study on Zn^{2+} sensing in the presence of external cations.

the introduction of Chelation Enhanced Fluorescence (CHEF) with augmentation of the molecular rigidity.[52,53]

Inspired by the selective 'turn-on' recognition towards Zn^{2+}, with the gradual addition of the analyte to the 50 μM probe solution (9 : 1 (v/v) DMSO/H_2O; HEPES Buffer, pH = 7.4), the emission intensity at 461 nm significantly increased (Fig. 2b) and varied linearly with [Zn^{2+}] until the emission reached the saturation level of the 1.0 equivalent of Zn^{2+}. At this stage, the probe shows remarkable turn-on sensitivity towards Zn^{2+} ions.

Eventually, the limit of detection (LOD) was determined from the fluorescence titration profile by following the 3σ/slope method. The calculated LOD for Zn^{2+} is 3.2 nM (Fig. S8, ESI†), which is much lower than the permissible level recommended by the WHO and implies that the probe is highly sensitive towards Zn^{2+} ions with a very efficient LOD as compared to most of the reported probes (Table S3, ESI†). The quantum yield calculated for the complex [Zn(L^1)OAc] ($\phi = 0.391$) was found to be reasonably higher than that of the free probe, HL ($\phi_{[HL]} = 0.0051$). Since the non-emissive probe HL becomes selectively highly luminescent on coordination to Zn^{2+} ($\lambda_{em} = 461$ nm) out of sixteen biologically important metal ions, the specific behavior of Zn^{2+} can presumably be explained based on the suitable size of the ion, which fits in the NNNO chelate cavity and elevates the CHEF process in a dominating fashion. Furthermore, the Lewis acidity of Zn^{2+} makes it appropriate for robust and selective interactions with the hard N and O centers of the probe, which reinforces the emission intensity by resisting the free rotations and also the vibrational relaxation of the pendant substituents in HL. The disfavored size and electronic characteristics of other ions in the present case make them unfit for such emission enhancement.

The absorbance change in HL was also recorded with the incremental addition of Zn^{2+} (9 : 1 (v/v) DMSO/H_2O, HEPES buffer, pH = 7.4), where the absorption intensity at 325 nm increased with a red shift to 362 nm (Fig. S9, ESI†). On further addition of Zn^{2+}, the unchanged absorbance spectrum indicated that the saturation was attained with a stoichiometry of 1 : 1 for complexation and the red shift in the absorption spectra also remained unchanged with the successive addition of Zn^{2+} when 1 : 1 complexation was attained. The sensitivity of the probe was further tested in the presence of other co-cations to check the interference in the detection of Zn^{2+}. The competitive study was performed by the addition of 2.0 equivalent of other cations to the solution containing HL and Zn^{2+}, *i.e.* the *in situ*-generated [Zn(L^1)OAc] complex. It was found that the interfering effects were negligible in the detection of Zn^{2+} in the presence of external cations (Fig. 2c).

The change in the emission of the probe was insensitive to a wide range of pH (2–12). However, on the addition of 1.0 equivalent of Zn^{2+} to the probe solution, the emission intensity increased from pH 5 to 12 and appreciable emission was observed in the basic pH (>7) regime (Fig. S10, ESI†). The effect of pH on the luminescence properties of [Zn(L^1)OAc] was examined. The non-luminescent nature of the free probe due to the unrestricted rotation of its twisted counterparts was hardly affected by the variation of the pH values, which resulted in the unaltered photoluminescence characteristics of HL throughout the entire pH regime (2–12). However, in acidic pH (<5), the N, N, N, and O units in HL became inefficient for binding with Zn^{2+}, presumably due to the possible protonation of the coordinating sites, which eventually led to poor emission features. Conversely, with increased pH values, the respective coordinating units become available for efficient chelation with 1 equivalent Zn^{2+} where vigorous restriction of existing free rotation in [Zn(L^1)OAc] complex effectuates chelation enhanced fluorescence (CHEF) emission from pH 5 to 12 and appreciable emission is observed in the basic pH (>7) regime. Hence, the probe is also applicable for recognizing Zn^{2+} ions at normal physiological pH. The binding affinity of HL towards Zn^{2+} was experimentally determined from the Benesi–Hildebrand equation ($[(F_{max} - F_0)/(F - F_0)]$ *vs.* $1/[Zn^{2+}]$) and the binding constant K_d was estimated as 2.93×10^4 M^{-1}, which suggests a strong interaction and association between HL and Zn^{2+} (Fig. S11, ESI†). The stoichiometry of the complex Zn^{2+}-HL was examined by the Job plot, which showed an inflexion corresponding to the mole fraction of 0.5 and suggested 1 : 1 complexation (Fig. S12, ESI†). ESI-MS of the [HL-Zn^{2+}] complex also supports the 1 : 1 complex formation. The mass peak at m/z = 486.0937 corresponds to the [HL–H + Zn]$^+$ ion, which accounts for a 1 : 1 binding along with ring-opening of the cyclic benzimidazole moiety (Fig. S13, ESI†). To understand the binding approach of HL towards Zn^{2+} and the proposed composition of the zinc complex, ^{1}H-NMR titration (500 MHz, DMSO-d_6) of the probe was conducted with the successive addition of Zn^{2+} (Fig. 3).

On the successive addition of different concentrations of $Zn(OAc)_2 \cdot 2H_2O$ into the probe solution, the phenolic OH peak intensity at 9.52 ppm gradually disappeared and completely

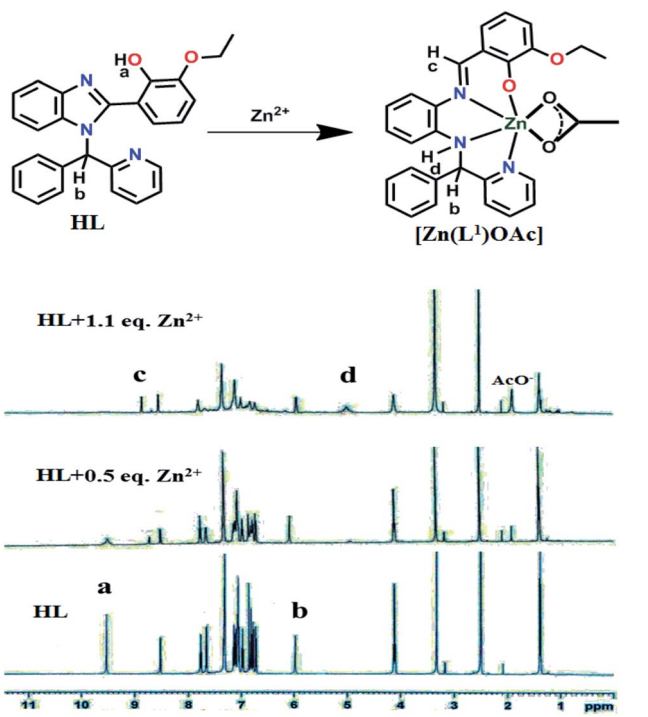

Fig. 3 ^{1}H-NMR titration of HL on the successive addition of Zn^{2+} in DMSO-d_6.

vanished with the 1 : 1 stoichiometric addition. The appearance of two new peaks at 8.90 and 5.02 ppm can be assigned to the imine (CH=N) and NH protons, which suggest that chelation prefers the ring-opening event in the presence of Zn^{2+}. The appearance of a peak at 1.88 ppm indicated the presence of acetate (AcO^-) in the [Zn(L^1)OAc] complex. The broadening of the aromatic peak also confirmed the participation of Zn^{2+} in binding. Together, the results explain the ring-opening phenomena towards Zn^{2+} binding. This is reasonably due to the involvement of the Zn^{2+} chelation-induced five-membered ring-opening reaction.[54] The kinetics of Zn^{2+} sensing *via* the ring-opening of the cyclic benzimidazole moiety of HL has been evaluated by fitting the emission intensity into a single-exponential equation,[55] and the response time has been calculated to be as low as 0.05 s (Fig. S14, ESI†). The rapid response time indicates the instantaneous reaction of the probe towards Zn^{2+} ions.

The presence of the medium intense broad stretching band at 3343 cm^{-1} indicates ν(N–H) along with the presence of tertiary ν(C–H) at 2975 cm^{-1} (Fig. S15, ESI†), which confirms the chelation that proceeds through the ring-opening reaction. A shift in ν(C=N) stretching from 1592 to 1599 cm^{-1} indicated its participation in the chelation process with Zn^{2+}, and the appearance of an intense band at 1614 cm^{-1} was presumably ascribed to ν(N–H) bending as well. The acetate (–COO) group might associate with metal ions in different modes, which was assigned to the [Zn–(O–C–O)] chelation. For the [Zn(L^1)OAc] complex, the bands at 1585 and 1393 cm^{-1} plausibly refer to the asymmetric and symmetric binding of the acetate group. The merged IR spectra of HL and its Zn-complex are also included in the supporting information file (Fig. S16, ESI†) for better understanding.

DFT computation

To explain the change in bond parameters on the interaction of HL with Zn^{2+}, the optimized structure of HL and [Zn(L^1)OAc] were calculated using the DFT/B3LYP computational method (Fig. S17, ESI†). The bond lengths and bond angles were calculated from the optimized cyclic structure of HL (Tables S4 and S5, ESI†), which are in good correlation with the parameters obtained from X-ray measurements as shown for HL (length; Å) calc. (exp.): C007–N1 1.39 (1.37), N1–C7 1.46 (1.47), C18–N3 1.33 (1.39), C007–N2 1.31 (1.30), O2–H2 0.96 (0.82) and bond angle (°): calc.(exp.) C007–N1–C7 124.89 (124.48), N1–C7–C18 111.70 (112.10), C18–N3–C14 118.48 (118.39), N1–C007–N2 113.01 (112.6), C007–N2–C9 105.60 (105.22), N2–C007–C5 121.69 (123.36), C6–C1–O1 113.28 (114.51), C6–O2–H2 107.78 (110).

To explain the spectroscopic response of HL towards Zn^{2+}, Time-Dependent Density Functional Theory (TD-DFT) was performed. The highest occupied molecular orbital (HOMO) and lowest unoccupied molecular orbital (LUMO) of HL and its zinc complex ([Zn(L^1)OAc]) along with some selected Frontier molecular orbitals are shown in Table S6 and S7 (ESI†). Using the CPCM method in the DMSO solvent medium, the ground state electronic spectra for the probe and its zinc complexes were obtained. The absorption band at 335 nm for HL may be ascribed to the HOMO-1 → LUMO transition, and for the complex, the absorption maximum at 362 nm was contributed by the HOMO-1 → LUMO transition. Some other possible electronic transitions are also tabulated in Table S8 and S9, ESI.† The band gap of 4.7 eV was calculated for HL, which was further diminished to 4.13 eV for the [Zn(L^1)OAc] complex. This decrement by 0.57 eV explains the red shift behavior in the UV-Vis absorption spectra of the Zn-complex with respect to HL itself (Fig. 4). The band gap does not support the examination of the compounds for the photoconductivity experiments.

The coordination of HL with Zn^{2+} opens the ring and makes a more planar structure as compared to the free one. This is quite evident from the energy-optimized structure of [Zn(L^1)OAc], where the dihedral angles 162.40° (45–17–47–3), 170.12° (17–47–3–10) and 149.07° (13–1–47–17) in the energy-optimized complex were found to be comparatively lower as compared to HL (Fig. S18, Table S10, ESI†). Thus, the planar geometry helps with better electronic delocalization throughout the structure and has a lowered energy gap with respect to that of HL, which possibly explains the red-shifted absorption spectrum of the Zn-complex.[56]

Detection of $H_2PO_4^-$ by emissive [Zn(L^1)OAc]

The complex, [Zn(L^1)OAc], shows strong emission at 461 nm upon excitation at 350 nm (9 : 1 (v/v) DMSO/H_2O, HEPES buffer, pH = 7.4). Interestingly, the higher emission of [Zn(L^1)OAc] is quenched upon the addition of $H_2PO_4^-$ ion selectively, where other P^Vs remain silent. Henceforth, the fluorescence quenching of [Zn(L^1)OAc] was monitored through a titration experiment with increasingly added $H_2PO_4^-$ (Fig. 5a). On the gradual addition of $H_2PO_4^-$ (0–50 μM) to the [Zn(L^1)OAc] complex in 9 : 1 (v/v) DMSO/H_2O (HEPES buffer, pH = 7.4), the emission intensity decreased linearly and was completely quenched with the addition of 1.0 equivalent of $H_2PO_4^-$. From the fluorescence titration curve, the detection limit was experimentally determined to be 0.238 μM based on the 3σ/slope method (Fig. S19, ESI†).

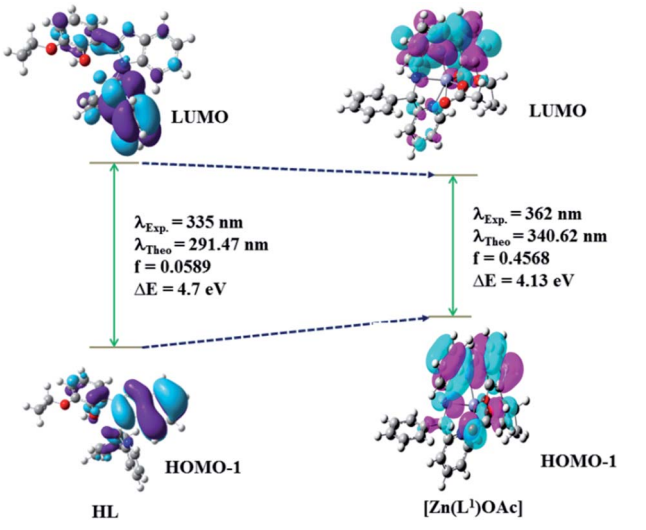

Fig. 4 The electronic transitions of HL and its respective zinc complex.

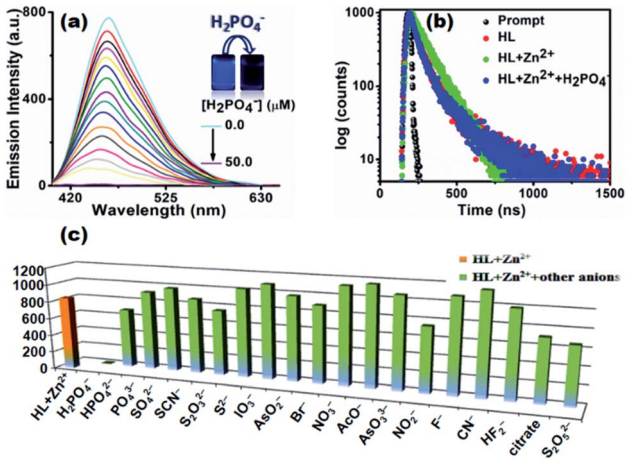

Fig. 5 (a) Change in the emission spectra of the [Zn(L^1)OAc] complex upon the successive addition of $H_2PO_4^-$ (λ_{ex} = 350 nm). The inset represents photographs of the Zn(II)-complex before and after treatment with $H_2PO_4^-$, taken under UV lights (λ_{ex} = 365 nm). (b) Time-resolved fluorescence spectroscopy of the probe, HL, on the addition of Zn^{2+} and $H_2PO_4^-$ in 9 : 1 (v/v) DMSO/H_2O (HEPES buffer, pH = 7.4). (c) The emission intensity of [Zn(L^1)OAc] in the presence of 1.0 equivalent of various anions in 9 : 1 (v/v) DMSO/H_2O (HEPES buffer, pH = 7.4) (λ_{ex} = 350 nm).

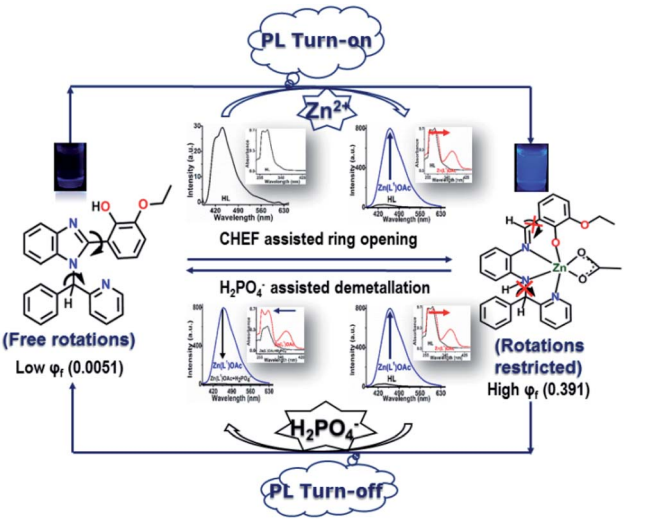

Scheme 2 The proposed mechanism for the sensing of $H_2PO_4^-$ ions by the [Zn(L^1)OAc] complex.

The binding constant was also calculated and found to be 3.224×10^4 M^{-1}, which showed sufficient stability on binding with $H_2PO_4^-$ (Fig. S20, ESI†). The average fluorescence lifetime decay for the probe fits into bi-exponential decay (τ_{HL} 1.909 ns) and is lower than that of the Zn(II)-complex (τ_{comp}, 2.907 ns) (Fig. 5b, Table 1). Upon the addition of $H_2PO_4^-$, the lifetime of the resultant system further decreased to 1.829 ns. The enhanced lifetime value of the Zn-complex was justified by the decrement of non-radiative relaxation from 521.16×10^6 to 209.5×10^6 s^{-1} of the excited state (Table 1) because of the rigidification of the overall structural framework on coordination to Zn(II).[57,58]

Eventually, the increased radiative dissipation of the excited energy from 2.67×10^6 to 134.5×10^6 s^{-1} resulted in a higher fluorescence quantum yield (0.391 *vs.* 0.0051 in free HL) and caused ~1.52 times enhancement in the fluorescence lifetime of [Zn(L^1)OAc]. On the other hand, the decrement in τ of [Zn(L^1)OAc] with the addition of $H_2PO_4^-$ is comparable to that of the average lifetime of the free probe.[59] Moreover, the selectivity over additional anions, such as Cl^-, Br^-, I^-, HPO_4^{2-}, CN^-, S^{2-}, PO_4^{3-}, AcO^-, $S_2O_3^{2-}$, IO_3^-, SO_4^{2-}, citrate, F^-, $S_2O_5^{2-}$, AsO_3^{3-}, AsO_2^-, SCN^-, NO_3^-, NO_2^-, HF_2^- towards [Zn(L^1)OAc] emission is also inspected by adding 1.0 equivalent into the complex solution, which did not show any significant effect on the emission intensity of the Zn-complex (Fig. 5c). Concurrently, the quenching can be explained by its favorability towards Zn^{2+} ions, which may tend to demetallate the [Zn(L^1)OAc] complex. Thus, the probe, HL, can be used for the simultaneous detection of Zn^{2+} and $H_2PO_4^-$. The UV-Vis absorption spectrum showed a decrease in intensity at 362 and 285 nm upon the gradual addition of $H_2PO_4^-$ (0–50 μM) (Fig. S21, ESI†). To verify the respective interactions between $H_2PO_4^-$ and [Zn(L^1)OAc], ESI-MS was inspected by adding $H_2PO_4^-$ to the *in situ* generated complex in the solution phase. The mass spectrum showed a base peak at 422.1367, which ascertained the mass of HL + H^+, whereas the peak at 162.3632 corresponds to $[Zn(H_2PO_4)]^+$ (Fig. S22, ESI†). In the ^1H NMR measurement, the addition of $H_2PO_4^-$ (1.1 equiv.) to the resulting mixture of HL and Zn^{2+} (1.0 equiv.) regenerated the probe HL by removing Zn^{2+} from the [Zn(L^1)OAc] complex, shown in (Fig. S23, ESI†). Evidently, the kinetics of the fluorescence quenching of the emissive [Zn(L^1)OAc] in the presence of $H_2PO_4^-$ was also monitored by fitting the intensity decay to a single-exponential equation and the calculated response time was found to be 0.02 s (Fig. S24, ESI†). Due to the strong affinity towards Zn^{2+}, $H_2PO_4^-$ is used for gravimetric estimation in analytical chemistry and, in the present case, the removal of Zn^{2+} from the complex has been assessed as the recovery of the free probe, HL. Hence, the proposed mechanism for the sensing of $H_2PO_4^-$ ions by [Zn(L^1)OAc] complex can be represented by Scheme 2.

Table 1 Photophysical parameters of HL, HL + Zn^{2+} and HL + Zn^{2+} + $H_2PO_4^-$

Systems	λ_a (nm)	λ_f (nm)	τ_f (ns)	ϕ_f	$k_r{}^a$ (s^{-1})/10^6	$k_{nr}{}^b$ (s^{-1})/10^6
Free HL	265, 285, 335[c]	~460	1.91	0.0051	2.67	521.16
HL + Zn^{2+}	262, 288, 362	461	2.91	0.391	134.50	209.50
HL + Zn^{2+} + $H_2PO_4^-$	264, 288, 334[c]	~460	1.83	0.0039	2.13	544.62

[a] $k_r = \phi_f/\tau_f$. [b] $k_{nr} = (1/\tau_f) - k_r$. [c] shoulder band.

Table 2 Recovery of $H_2PO_4^-$ by the [Zn(L^1)OAc] complex from real water samples

Sample	Added $H_2PO_4^-$ (M)	Detected $H_2PO_4^-$ (M)	Recovery (%)	Error (%)
Tap water	0.5×10^{-6}	0.505×10^{-6}	101	1.0
	1.0×10^{-6}	0.991×10^{-6}	99.1	0.9
	2.0×10^{-6}	1.99×10^{-6}	99.5	0.5
Distilled water	0.5×10^{-6}	0.493×10^{-6}	98.6	1.4
	1.0×10^{-6}	0.992×10^{-6}	99.2	0.8
	2.0×10^{-6}	1.94×10^{-6}	97.0	3.0
Drinking water	0.5×10^{-6}	0.479×10^{-6}	95.8	4.2
	1.0×10^{-6}	0.972×10^{-6}	97.2	2.8
	2.0×10^{-6}	1.934×10^{-6}	96.7	3.3

Recently, the accumulation of phosphate in surface water created great concern for water bodies and human health.[6] Henceforth, it is of importance to track and recover phosphates from real water sources in order to maintain the quality of the potable water. The excellent selectivity of [Zn(L^1)OAc] towards $H_2PO_4^-$ together with reasonable sensitivity inspired us to further explore its practical application as a sensing agent as well as a recovery agent for $H_2PO_4^-$ from the real water samples. In this regard, we have utilized tap water, distilled water, and drinking water spiked with trace quantities of the requisite analyte (0.5–2.0 μM) without any further processing.

The percentage of $H_2PO_4^-$ recovery by the Zn(II) complex (Table 2) is in the range of 95.8 to 101 with a minimal percentage error (0.5–4.2).

Reversibility study and logic gate behavior

Reversibility and recyclability are considered the most prominent factors when it comes to the practicability of the chemosensor.[60] The CHEF-induced fluorescence of HL on the addition of Zn^{2+} and its simultaneous quenching in the presence of $H_2PO_4^-$ can be repeated for up to 6 cycles upon modulation of $Zn^{2+}/H_2PO_4^-$ addition in 9 : 1 (v/v) DMSO/H_2O (HEPES buffer, pH = 7.4) (Fig. 6a). Based on the switchable emissive characteristics of HL towards Zn^{2+} and $H_2PO_4^-$ (Fig. 6b), an INHIBIT logic gate can be constructed with input signals of Zn^{2+} and $H_2PO_4^-$ as INPUT 1 (In Z) and INPUT 2 (In P) and the emission intensity at 461 nm as the output signal. The strong emission can be denoted as the "ON" state and represented as 1, while that of the quenched state can be considered as the "OFF" state, which is represented by 0. The truth table (Fig. 6c) and the set-reset memory device (Fig. 6d) were constructed for the given logical circuit and the output is considered as 1 when it results in the enhancement of emission.[61]

Practical application of [Zn(L^1)OAc] complex for sensing of $H_2PO_4^-$ in solid-state with devising a "use" and "throw" security marker

Fluorescent chemosensors, capable of exhibiting quantitative detection of bioactive analytes in the solid-state overrules the traditional sensors owing to their additional advantages in terms of cost-effective 'on-site' recognition of a particular analyte with better sensitivity and improved LOD without much necessity for sophisticated instruments.[62,63] Considering the importance of phosphates in the environment and industry, it is necessary to detect $H_2PO_4^-$ in a solid platform which practically offers a quick response and is easy to handle. In order to achieve selective solid-state detection of $H_2PO_4^-$, disposable paper strips of Whatman 41 are soaked with probe solution (HL) and air-dried. Then, the aqueous solution of Zn^{2+} (10^{-3} M) is sprayed over the strip, which reveals blue fluorescence from the treated area while illuminated under UV light (λ_{ex} = 365 nm) (Fig. S25(i), ESI†). Interestingly, the bright blue fluorescence selectively fades away when the strip is treated with an aqueous solution of $H_2PO_4^-$ (10^{-3} M) (Fig. S25(ii), ESI†) out of eighteen other anions. The observation clearly indicates the selective detection of $H_2PO_4^-$ by the Zn(II) complex of pyridyl-benzimidazolyl-phenolato in the solid-state. Subsequently, to inspect the sensitivity of Zn(II)-coated paper strips, the concentration-dependent fluorescence quenching of the Zn(II) complex is readily monitored by simply varying the aqueous concentration of $H_2PO_4^-$ from 10^{-3} M to 10^{-8} M upon spotting different concentrations on the fluorescent filter papers. The quenching of blue emission intensity slowly weakens with decreased $H_2PO_4^-$ concentration (Fig. 7) where the bright blue luminescence starts to revive when the analyte concentration was as low as 10^{-8} M. Meanwhile, when ~5 μL volume of 10^{-8} M aqueous $H_2PO_4^-$ was allowed to be spotted on a Zn(II)-coated filter paper covering an area of 1 cm^2, the LOD was found to be as low as 10.97 pg(picogram) cm^{-2}. Evidently, the Zn(II) complex of the present chemosensor is capable of instantaneous trace quantity detection of $H_2PO_4^-$ by regulating the quenching strength through a simple and portable paper strip method in the solid-state.

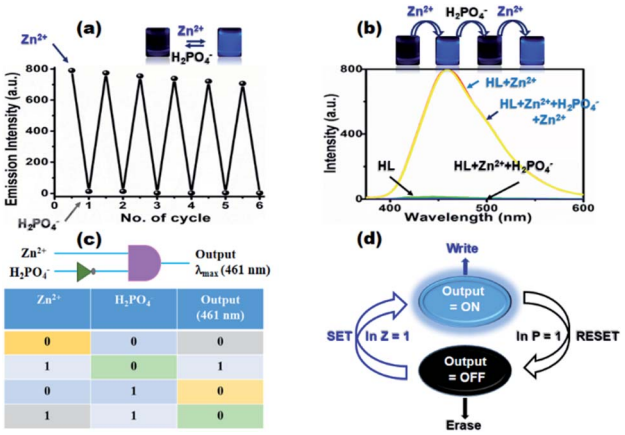

Fig. 6 (a) Recyclability of HL on the addition of $Zn^{2+}/H_2PO_4^-$ up to 6 cycles. (b) Variation in PL characteristics of HL (50 μM; λ_{ex} = 350 nm) upon simultaneous addition of Zn^{2+} and $H_2PO_4^-$ (1 cycle). Insets of figures (a) and (b) represent chronological changes in emission color of HL upon successive addition of Zn^{2+} and $H_2PO_4^-$, taken under UV light (λ_{ex} = 365 nm). (c) INHIBIT logic gate and truth table for two inputs: Zn^{2+} and $H_2PO_4^-$ and single output: λ_f = 461 nm. (d) Schematic representations of SET/RESET memorized write/erase logic circuit based on reversible ON/OFF fluorescence switching behavior.

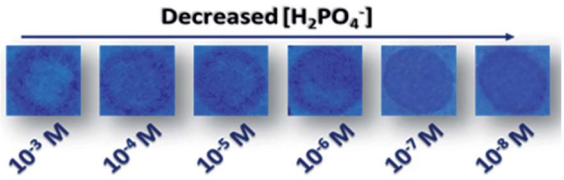

Fig. 7 Photographs of Zn-complex-embedded paper strips spotted with different concentrations of $H_2PO_4^-$: (i) 10^{-3}, (ii) 10^{-4}, (iii) 10^{-5}, (iv) 10^{-6}, (v) 10^{-7}, (vi) 10^{-8} (λ_{ex} = 365 nm).

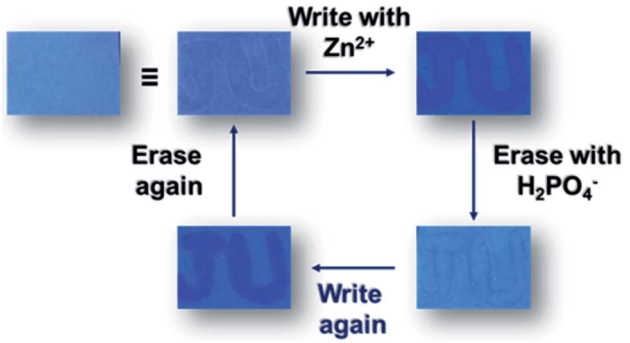

Fig. 8 Photographs of the HL-coated filter paper with handwritten images under illumination at 365 nm.

Fluorescence images and labels have been increasingly utilized as embedded security markers due to their reluctance to be photocopied; they mostly remain invisible under daylight and are difficult to duplicate.[64] Therefore, stimuli-responsive fluorescence materials that exhibit definite changes in their optical features in response to the specific analyte have been considered to be suitable candidates for architecting security devices.[65] Consequently, the reversible 'ON–OFF' fluorescence switching of the present chemosensor during the alternate presence of Zn^{2+} and $H_2PO_4^-$ inspired us to execute a solid-state security activity with enhanced practical implication. For this, a solution-coated "use" and "throw" thin film was fabricated upon dip-coating a Whatman filter paper into a chloroform solution of HL followed by drying it at room temperature [Fig. 8 (i)].

Subsequently, on writing the word 'JU' with an aqueous Zn^{2+}-filled pen, the HL-coated film divulged blue emission ('ON' state) only from the written portion [Fig. 8 (ii)] due to the feasible interaction of HL with Zn^{2+} to form the highly emissive [Zn(L^1)OAc] complex. Interestingly, the glaring emission completely faded away after washing the Zn(II)-treated film with aqueous $H_2PO_4^-$ solution ('OFF' state) [Fig. 8 (iii)]. Moreover, the 'ON' state could be regenerated after rewriting the word 'JU' on the washed surface [Fig. 8 (iv)], which underwent the 'OFF' state immediately after washing the film again [Fig. 8 (v)]. This fluorescence switching property can feasibly be repeated to complete the security cycle without draining the emission property. The sensing event of [Zn(L^1)OAc] as a security label remained unaffected in the presence of a simple water sample containing no $H_2PO_4^-$ (Fig. S26, ESI†), which further reinforced the selective fluorescence quenching of the chemosensor even in the solid-state.

Conclusions

The present work sheds light on an 'ON–OFF' fluorescence switching-assisted trace quantity detection of environmentally relevant $H_2PO_4^-$ ions in a desired selective and sensitive fashion based on a newly designed Zn(II) complex of 2-ethoxy-6-[1-(phenyl-pyridin-2-yl-methyl)-1*H*-benzoimidazol-2-yl]-phenol (HL) in DMSO-water [(9 : 1, v/v), pH = 7.4]. Free HL is non-fluorescent and exhibits remarkable fluorescence 'turn-on' recognition of Zn^{2+} ions out of sixteen pertinent cations (Cu^{2+}, Co^{2+}, Pb^{2+}, Zn^{2+}, Cr^{3+}, Cd^{2+}, Ca^{2+}, Al^{3+}, Fe^{3+}, Hg^{2+}, Ni^{2+}, Mn^{2+}, Ba^{2+}, Na^+, K^+, Mg^{2+} and Pd^{2+}). The desired complexation was confirmed through a ring-opening pathway, where the sensitivity of the probe towards Zn^{2+} was found to be superior to other reported Zn-sensors and the LOD was considerably low at 3.2 nM. The emissive [Zn(L^1)OAc] complex is capable of disclosing a selective fluorescence 'turn-off' detection towards $H_2PO_4^-$ out of nineteen admissible anions (HPO_4^-, PO_4^{3-}, SO_4^{2-}, SCN^-, $H_2PO_4^-$, $S_2O_3^{2-}$, S^{2-}, IO_3^-, AsO_2^-, Br^-, NO_3^-, CH_3COO^-, AsO_3^-, NO_2^-, F^-, CN^-, HF_2^-, citrate and $S_2O_5^{2-}$). The demetallation of the probe in the presence of $H_2PO_4^-$ leads to the sensitive detection of the desired analyte, where the LOD was found to be as low as 0.238 μM. Subsequently, taking advantage of the sequential sensing performance of HL, a reversible and recyclable 'ON–OFF' fluorescence switch was constructed, which is capable of operating for up to 6 cycles without noticeable exhaustion in switching activity. Finally, the switchable emissive characteristics of HL triggered us to construct an INHIBIT logic gate, capable of mimicking a smart memory circuit with two-input signals (Zn^{2+}, $H_2PO_4^-$) and one-output (λ_{em} = 461 nm) signaling propensities. Importantly, the sensitivity of the present chemosensor was successfully extended in the solid-state where the highly emissive [Zn(L^1)OAc] complex was found to be capable of recognizing $H_2PO_4^-$ for up to the 10^{-8} M level from water with the LOD of 10.97 pg(picogram) cm^{-2} based on a portable and cost-effective contact mode detection on the fabricated paper strips. Furthermore, the remarkable reversibility in the optical characteristics of the chemosensor enabled us to develop a disposable security device, where the desired changes in the fluorescence properties in the presence of Zn^{2+} and $H_2PO_4^-$ resulted in 'ON–OFF' switching aided security labels without adopting any complicated methodologies. The present findings pave the way towards attaining the multi-sensing of biologically apposite analytes in reasonably minute quantities from a single probe where the desired selectivity, sensitivity and low LODs enable HL to be a potent sensing candidate of practical significance.

Author contributions

Sunanda Dey, Sukanya Paul and Kingshuk Debsharma contributed equally in synthesis, characterisation,

photophysical application, theoretical calculations, as well as writing the manuscript and ESI.†

Conflicts of interest

The authors declare no conflicts of interest.

Acknowledgements

The authors are grateful to Council of Scientific and Industrial Research, India (CSIR, Sanction no. 01(2894)/17/EMR-II), New Delhi and Jadavpur University, Kolkata for the financial support and instrumental facilities respectively. S. P. thankful to the Council of Scientific and Industrial Research (CSIR), Govt. of India for research fellowship. Dr Suvendu Maity, R. K. Mission Residential College, Narendrapur is gratefully acknowledged for crystallographic measurements.

Notes and references

1 D. W. Zhang, X. Z. Jiang, H. Q. Yang, Z. Su, E. Q. Gao, A. Martinez and G. H. Gao, *Chem. Commun.*, 2013, **49**, 6149–6151.
2 C. Warwick, A. Guerreiro and A. Soares, *Biosens. Bioelectron.*, 2013, **41**, 1–11.
3 P. A. Furman, J. A. Fyfe, M. H. St Clair, K. Weinhold, J. L. Rideout, G. A. Freeman, S. N. Lehrman, D. P. Bolognesi, S. Broder and H. Mitsuya, *Proc. Natl. Acad. Sci. U. S. A.*, 1986, **83**, 8333–8337.
4 A. Ojida, Y. Mito-oka, K. Sada and I. Hamachi, *J. Am. Chem. Soc.*, 2004, **126**, 2454–2463.
5 S. Khoshniat, A. Bourgine, M. Julien, P. Weiss, J. Guicheux and L. Beck, *Cell. Mol. Life Sci.*, 2011, **68**, 205–218.
6 A. T. Lawal and S. B. Adeloju, *Talanta*, 2013, **114**, 191–203.
7 H. T. Ngo, X. Liu and K. A. Jolliffe, *Chem. Soc. Rev.*, 2012, **41**, 4928–4965.
8 T. Tabary and L. Ju, *J. Immunol. Methods*, 1992, **156**, 55–60.
9 A. Bencini, F. Bartoli, C. Caltagirone and V. Lippolis, *Dyes Pigm.*, 2014, **110**, 169–192.
10 D. Zhang, J. R. Cochrane, A. Martinez and G. Gao, *RSC Adv.*, 2014, **4**, 29735–29749.
11 P. A. Gale, *Chem. Commun.*, 2005, **30**, 3761–3772.
12 E. Slatopolsky, *Kidney Int.*, 2011, **79**, S3–S8.
13 R. Kumar, *Curr. Opin. Nephrol. Hypertens.*, 2009, **18**, 281–284.
14 S. O. Engblom, *Biosens. Bioelectron.*, 1998, **13**, 981–994.
15 H. Kawasaki, K. Sato, J. Ogawa, Y. Hasegawa and H. Yuki, *Anal. Biochem.*, 1989, **182**, 366–370.
16 A. I. Vogel and G. H. Jeffery, *Vogel's Textbook of Quantitative Chemical Analysis*, Longman Scientific & Technical, 1989.
17 S. Hisham, H. A. Tajuddin, C. F. Chee, Z. A. Hasan and Z. Abdullah, *J. Lumin.*, 2019, **208**, 245–252.
18 J. Wongkongkatep, A. Ojida and I. Hamachi, *Top. Curr. Chem.*, 2017, **375**, 1–33.
19 F. Wang, X. Zeng, X. Zhao, H. Lu and Q. Wang, *J. Lumin.*, 2019, **208**, 302–306.
20 A. E. Hargrove, S. Nieto, T. Zhang, J. L. Sessler and E. V. Anslyn, *Chem. Rev.*, 2011, **111**, 6603–6782.
21 A. K. H. Hirsch, F. R. Fischer and F. Diederich, *Angew. Chem., Int. Ed.*, 2007, **46**, 338–352.
22 S. K. Kim, D. H. Lee, J.-I. Hong and J. Yoon, *Acc. Chem. Res.*, 2009, **42**, 23–31.
23 N. Busschaert, C. Caltagirone, W. V. Rossom and P. A. Gale, *Chem. Rev.*, 2015, **115**, 8038–8155.
24 J. Wu, W. Liu, J. Ge, H. Zhang and P. Wang, *Chem. Soc. Rev.*, 2011, **40**, 3483–3495.
25 H. T. Ngo, X. Liu and K. A. Jolliffe, *Chem. Soc. Rev.*, 2012, **41**, 4928–4965.
26 Y. L. Pak, K. M. K. Swamy and J. Yoon, *Sensors*, 2015, **15**, 24374–24396.
27 P. A. Gale, *Acc. Chem. Res.*, 2006, **39**, 465–475.
28 F. P. Schmidtchen and M. Berger, *Chem. Rev.*, 1997, **97**, 1609–1646.
29 S. Suganya, S. Naha and S. Velmathi, *ChemistrySelect*, 2018, **3**, 7231–7268.
30 X. Lou, D. Ou, Q. Li and Z. Li, *Chem. Commun.*, 2012, **48**, 8462–8477.
31 M. C. Aragoni, M. Arca, A. Bencini, C. Caltagirone, A. Garau, F. Isaia, M. E. Light, V. Lippolis, C. Lodeiro, M. Mameli, R. Montis, M. C. Mostallino, A. Pintus and S. Puc-cioni, *Dalton Trans.*, 2013, **42**, 14516–14530.
32 H. G. Lee, J. H. Lee, S. P. Jang, I. H. Hwang, S. J. Kim, Y. Kim, C. Kim and R. G. Harrison, *Inorg. Chim. Acta*, 2013, **394**, 542–551.
33 E. Oliveira, D. Genovese, R. Juris, N. Zaccheroni, J. L. Capelo, M. M. M. Raposo, S. P. G. Costa, L. Prodi and C. Lodeiro, *Inorg. Chem.*, 2011, **50**, 8834–8849.
34 Y. Ma, F. Wang, S. Kambam and X. Chen, *Sens. Actuators, B*, 2013, **188**, 1116–1122.
35 Y. Kurishita, T. Kohira, A. Ojida and I. Hamachi, *J. Am. Chem. Soc.*, 2012, **134**, 18779–18789.
36 J. M. Berg and Y. Shi, *Science*, 1996, **271**, 1081–1085.
37 S. Goswami, S. Maity, A. C. Maity, A. K. Das, K. Khanra, T. K. Mandal and N. Bhattacharyya, *Tetrahedron Lett.*, 2014, **55**, 5993–5997.
38 H. D. Duong and J. I. Rhee, *Sens. Actuators, B*, 2018, **274**, 66–77.
39 D. D. Perrin, W. L. F. Armarego and D. R. Perrin, *Purification of Laboratory Chemicals*, Pergamon Press, Oxford, U.K., 1980.
40 S. Chaudhuri, S. C. Patra, P. Saha, A. S. Roy, S. Maity, S. Bera, P. S. Sardar, S. Ghosh, T. Weyhermüller and P. Ghosh, *Dalton Trans.*, 2013, **42**, 15028–15042.
41 A. S. M. Islam, M. Sasmal, D. Maiti, A. Dutta, B. Show and M. Ali, *ACS Omega*, 2018, **3**, 10306–10316.
42 G. M. Sheldrick, *Acta Crystallogr., Sect. A: Found. Crystallogr.*, 2008, **64**, 112–122.
43 J. Farrugia, *J. Appl. Crystallogr.*, 1997, **30**, 565–574.
44 A. L. Spek, *Platon*, The Netherlands, 1999.
45 M. J. Frisch, G. W. Trucks, H. B. Schlegel, G. E. Scuseria, M. A. Robb, J. R. Cheeseman, G. Scalmani, V. Barone, B. Mennucci, G. A. Petersson, H. Nakatsuji, M. Caricato, X. Li, H. P. Hratchian, A. F. Izmaylov, J. Bloino, G. Zheng, J. L. Sonnenberg, M. Hada, M. Ehara, K. Toyota, R. Fukuda, J. Hasegawa, M. Ishida, T. Nakajima, Y. Honda, O. Kitao, H. Nakai, T. Vreven, J. A. Montgomery Jr,

J. E. Peralta, F. Ogliaro, M. Bearpark, J. J. Heyd, E. Brothers, K. N. Kudin, V. N. Staroverov, R. Kobayashi, J. Normand, K. Raghavachari, A. Rendell, J. C. Burant, S. S. Iyengar, J. Tomasi, M. Cossi, N. Rega, J. M. Millam, M. Klene, J. E. Knox, J. B. Cross, V. Bakken, C. Adamo, J. Jaramillo, R. Gomperts, R. E. Stratmann, O. Yazyev, A. J. Austin, R. Cammi, C. Pomelli, J. W. Ochterski, R. L. Martin, K. Morokuma, V. G. Zakrzewski, G. A. Voth, P. Salvador, J. J. Dannenberg, S. Dapprich, A. D. Daniels, O. Farkas, J. B. Foresman, J. V. Ortiz, J. Cioslowski and D. J. Fox, *Gaussian 09, Revision D.01*, Gaussian Inc, Wallingford, CT, 2009.

46 A. Afonin, D. D. Toryashinova and E. Y. Schmidt, *J. Mol. Struct.: THEOCHEM*, 2004, **680**, 127–135.

47 M. Cossi and V. Barone, *J. Chem. Phys.*, 2001, **115**, 4708–4717.

48 M. Cossi, N. Rega, G. Scalmani and V. Barone, *J. Comput. Chem.*, 2003, **24**, 669–681.

49 H. Ito, *J. Number Theor.*, 2014, **135**, 139–150.

50 S. Sivalingam, K. Debsharma, A. Dasgupta, S. Sankararaman and E. Prasad, *ChemPlusChem*, 2019, **84**, 392–402.

51 K. Debsharma, J. Santhi, B. Baire and E. Prasad, *ACS Appl. Mater. Interfaces*, 2019, **11**, 48249–48260.

52 Y. Dong, R. Fan, W. Chen, P. Wang and Y. Yang, *Dalton Trans.*, 2017, **46**, 6769–6775.

53 T. Pariat, P. M. Vérité, D. Jacquemin, J. Massue and G. Ulrich, *Dyes Pigm.*, 2021, **190**, 109338.

54 S. Dey, S. Maity, K. Pal, K. Jana and C. Sinha, *Dalton Trans.*, 2019, **48**, 17818–17830.

55 Y. Che, D. E. Gross, H. Huang, D. Yang, X. Yang, E. Discekici, Z. Xue, H. Zhao, J. S. Moore and L. Zang, *J. Am. Chem. Soc.*, 2012, **134**, 4978–4982.

56 S. Suganya, K. Debsharma, E. Ravindran, M. K. Mahato and E. Prasad, *ACS Appl. Polym. Mater.*, 2020, **2**, 1222–1233.

57 S. Maity, M. Shyamal, R. Maity, N. Mudi, P. Hazra, P. K. Giri, S. S. Samanta, S. Pyne and A. Misra, *Photochem. Photobiol. Sci.*, 2020, **19**, 681–694.

58 L. Patra, S. Das, S. Gharami, K. Aich and T. K. Mondal, *New J. Chem.*, 2018, **42**, 19076–19082.

59 R. Purkait, S. Dey and C. Sinha, *New J. Chem.*, 2018, **42**, 16653–16665.

60 S. Paul, S. Dey, K. Pal, S. Maity, K. Jana and C. Sinha, *ChemistrySelect*, 2020, **5**, 1–11.

61 S. Dey, R. Purkait, K. Pal, K. Jana and C. Sinha, *ACS Omega*, 2019, **4**, 8451–8464.

62 S. S. Kumar, R. S. Kumar and S. K. A. Kumar, *Inorg. Chim. Acta*, 2020, **502**, 119348.

63 J. Du, X. Wang, M. Jia, T. Li, J. Mao and Z. Guo, *Inorg. Chem. Commun.*, 2008, **11**, 999–1002.

64 V. K. Praveen, B. Vedhanarayanan, A. Mal, R. K. Mishra and A. Ajayaghosh, *Acc. Chem. Res.*, 2020, **53**, 496–507.

65 R. Thirumalai, R. D. Mukhopadhyay, V. K. Praveen and A. Ajayaghosh, *Sci. Rep.*, 2015, **5**, 9842.

JOHN WILEY AND SONS LICENSE
TERMS AND CONDITIONS

Sep 13, 2022

This Agreement between JADAVPUR UNIVERSITY -- SUKANYA PAUL ("You") and John Wiley and Sons ("John Wiley and Sons") consists of your license details and the terms and conditions provided by John Wiley and Sons and Copyright Clearance Center.

License Number	5386991343067
License date	Sep 13, 2022
Licensed Content Publisher	John Wiley and Sons
Licensed Content Publication	ChemistrySelect
Licensed Content Title	A Fluorogenic Triphenyl-Amine-Naphthyl-Hydrazide Probe Selective for Cu2 and Cysteine Detection via an ON-OFF-ON Logic path with Real Applications
Licensed Content Author	Chittaranjan Sinha, Kuladip Jana, Suvendu Maity, et al
Licensed Content Date	Dec 28, 2020
Licensed Content Volume	5
Licensed Content Issue	48
Licensed Content Pages	10

Type of use	Dissertation/Thesis
Requestor type	Author of this Wiley article
Format	Print and electronic
Portion	Full article
Will you be translating?	No
Title	Synthesis and characterization of Schiff bases and their diverse applications
Institution name	Jadavpur University
Expected presentation date	Jan 2023
Requestor Location	JADAVPUR UNIVERSITY Dept of Chemistry Kolkata, other India Attn: JADAVPUR UNIVERSITY
Publisher Tax ID	EU826007151
Total	0.00 USD

Terms and Conditions

TERMS AND CONDITIONS

This copyrighted material is owned by or exclusively licensed to John Wiley & Sons, Inc. or one of its group companies (each a"Wiley Company") or handled on behalf of a society with which a Wiley Company has exclusive publishing rights in relation to a particular work (collectively "WILEY"). By clicking "accept" in connection with completing this licensing transaction, you agree that the following terms and conditions apply to this transaction (along with the billing and payment terms and conditions established by the Copyright

Clearance Center Inc., ("CCC's Billing and Payment terms and conditions"), at the time that you opened your RightsLink account (these are available at any time at http://myaccount.copyright.com).

Terms and Conditions

- The materials you have requested permission to reproduce or reuse (the "Wiley Materials") are protected by copyright.

- You are hereby granted a personal, non-exclusive, non-sub licensable (on a stand-alone basis), non-transferable, worldwide, limited license to reproduce the Wiley Materials for the purpose specified in the licensing process. This license, **and any CONTENT (PDF or image file) purchased as part of your order,** is for a one-time use only and limited to any maximum distribution number specified in the license. The first instance of republication or reuse granted by this license must be completed within two years of the date of the grant of this license (although copies prepared before the end date may be distributed thereafter). The Wiley Materials shall not be used in any other manner or for any other purpose, beyond what is granted in the license. Permission is granted subject to an appropriate acknowledgement given to the author, title of the material/book/journal and the publisher. You shall also duplicate the copyright notice that appears in the Wiley publication in your use of the Wiley Material. Permission is also granted on the understanding that nowhere in the text is a previously published source acknowledged for all or part of this Wiley Material. Any third party content is expressly excluded from this permission.

- With respect to the Wiley Materials, all rights are reserved. Except as expressly granted by the terms of the license, no part of the Wiley Materials may be copied, modified, adapted (except for minor reformatting required by the new Publication), translated, reproduced, transferred or distributed, in any form or by any means, and no derivative works may be made based on the Wiley Materials without the prior permission of the respective copyright owner.**For STM Signatory Publishers clearing permission under the terms of the STM Permissions Guidelines only, the terms of the license are extended to include subsequent editions and for editions in other languages, provided such editions are for the work as a whole in situ and does not involve the separate exploitation of the permitted figures or extracts,** You may not alter, remove or suppress in any manner any copyright, trademark or other notices displayed by the Wiley Materials. You may not license, rent, sell, loan, lease, pledge, offer as security, transfer or assign the Wiley Materials on a stand-alone basis, or any of the rights granted to you hereunder to any other person.

- The Wiley Materials and all of the intellectual property rights therein shall at all times remain the exclusive property of John Wiley & Sons Inc, the Wiley Companies, or their respective licensors, and your interest therein is only that of having possession of and the right to reproduce the Wiley Materials pursuant to Section 2 herein during the continuance of this Agreement. You agree that you own no right, title or interest in or to the Wiley Materials or any of the intellectual property rights therein. You shall have no rights hereunder other than the license as provided for above in Section 2. No right, license or interest to any trademark, trade name, service mark or other branding ("Marks") of WILEY or its licensors is granted hereunder, and you agree that you shall not assert any such right, license or interest with respect thereto

- NEITHER WILEY NOR ITS LICENSORS MAKES ANY WARRANTY OR REPRESENTATION OF ANY KIND TO YOU OR ANY THIRD PARTY, EXPRESS, IMPLIED OR STATUTORY, WITH RESPECT TO THE MATERIALS OR THE ACCURACY OF ANY INFORMATION CONTAINED IN THE MATERIALS, INCLUDING, WITHOUT LIMITATION, ANY IMPLIED WARRANTY OF MERCHANTABILITY, ACCURACY, SATISFACTORY

QUALITY, FITNESS FOR A PARTICULAR PURPOSE, USABILITY, INTEGRATION OR NON-INFRINGEMENT AND ALL SUCH WARRANTIES ARE HEREBY EXCLUDED BY WILEY AND ITS LICENSORS AND WAIVED BY YOU.

- WILEY shall have the right to terminate this Agreement immediately upon breach of this Agreement by you.

- You shall indemnify, defend and hold harmless WILEY, its Licensors and their respective directors, officers, agents and employees, from and against any actual or threatened claims, demands, causes of action or proceedings arising from any breach of this Agreement by you.

- IN NO EVENT SHALL WILEY OR ITS LICENSORS BE LIABLE TO YOU OR ANY OTHER PARTY OR ANY OTHER PERSON OR ENTITY FOR ANY SPECIAL, CONSEQUENTIAL, INCIDENTAL, INDIRECT, EXEMPLARY OR PUNITIVE DAMAGES, HOWEVER CAUSED, ARISING OUT OF OR IN CONNECTION WITH THE DOWNLOADING, PROVISIONING, VIEWING OR USE OF THE MATERIALS REGARDLESS OF THE FORM OF ACTION, WHETHER FOR BREACH OF CONTRACT, BREACH OF WARRANTY, TORT, NEGLIGENCE, INFRINGEMENT OR OTHERWISE (INCLUDING, WITHOUT LIMITATION, DAMAGES BASED ON LOSS OF PROFITS, DATA, FILES, USE, BUSINESS OPPORTUNITY OR CLAIMS OF THIRD PARTIES), AND WHETHER OR NOT THE PARTY HAS BEEN ADVISED OF THE POSSIBILITY OF SUCH DAMAGES. THIS LIMITATION SHALL APPLY NOTWITHSTANDING ANY FAILURE OF ESSENTIAL PURPOSE OF ANY LIMITED REMEDY PROVIDED HEREIN.

- Should any provision of this Agreement be held by a court of competent jurisdiction to be illegal, invalid, or unenforceable, that provision shall be deemed amended to achieve as nearly as possible the same economic effect as the original provision, and the legality, validity and enforceability of the remaining provisions of this Agreement shall not be affected or impaired thereby.

- The failure of either party to enforce any term or condition of this Agreement shall not constitute a waiver of either party's right to enforce each and every term and condition of this Agreement. No breach under this agreement shall be deemed waived or excused by either party unless such waiver or consent is in writing signed by the party granting such waiver or consent. The waiver by or consent of a party to a breach of any provision of this Agreement shall not operate or be construed as a waiver of or consent to any other or subsequent breach by such other party.

- This Agreement may not be assigned (including by operation of law or otherwise) by you without WILEY's prior written consent.

- Any fee required for this permission shall be non-refundable after thirty (30) days from receipt by the CCC.

- These terms and conditions together with CCC's Billing and Payment terms and conditions (which are incorporated herein) form the entire agreement between you and WILEY concerning this licensing transaction and (in the absence of fraud) supersedes all prior agreements and representations of the parties, oral or written. This Agreement may not be amended except in writing signed by both parties. This Agreement shall be binding upon and inure to the benefit of the parties' successors, legal representatives, and authorized assigns.

- In the event of any conflict between your obligations established by these terms and conditions and those established by CCC's Billing and Payment terms and conditions,

these terms and conditions shall prevail.

- WILEY expressly reserves all rights not specifically granted in the combination of (i) the license details provided by you and accepted in the course of this licensing transaction, (ii) these terms and conditions and (iii) CCC's Billing and Payment terms and conditions.

- This Agreement will be void if the Type of Use, Format, Circulation, or Requestor Type was misrepresented during the licensing process.

- This Agreement shall be governed by and construed in accordance with the laws of the State of New York, USA, without regards to such state's conflict of law rules. Any legal action, suit or proceeding arising out of or relating to these Terms and Conditions or the breach thereof shall be instituted in a court of competent jurisdiction in New York County in the State of New York in the United States of America and each party hereby consents and submits to the personal jurisdiction of such court, waives any objection to venue in such court and consents to service of process by registered or certified mail, return receipt requested, at the last known address of such party.

WILEY OPEN ACCESS TERMS AND CONDITIONS

Wiley Publishes Open Access Articles in fully Open Access Journals and in Subscription journals offering Online Open. Although most of the fully Open Access journals publish open access articles under the terms of the Creative Commons Attribution (CC BY) License only, the subscription journals and a few of the Open Access Journals offer a choice of Creative Commons Licenses. The license type is clearly identified on the article.

The Creative Commons Attribution License

The Creative Commons Attribution License (CC-BY) allows users to copy, distribute and transmit an article, adapt the article and make commercial use of the article. The CC-BY license permits commercial and non-

Creative Commons Attribution Non-Commercial License

The Creative Commons Attribution Non-Commercial (CC-BY-NC)License permits use, distribution and reproduction in any medium, provided the original work is properly cited and is not used for commercial purposes.(see below)

Creative Commons Attribution-Non-Commercial-NoDerivs License

The Creative Commons Attribution Non-Commercial-NoDerivs License (CC-BY-NC-ND) permits use, distribution and reproduction in any medium, provided the original work is properly cited, is not used for commercial purposes and no modifications or adaptations are made. (see below)

Use by commercial "for-profit" organizations

Use of Wiley Open Access articles for commercial, promotional, or marketing purposes requires further explicit permission from Wiley and will be subject to a fee.

Further details can be found on Wiley Online Library
http://olabout.wiley.com/WileyCDA/Section/id-410895.html

Other Terms and Conditions:

v1.10 Last updated September 2015

Questions? customercare@copyright.com or +1-855-239-3415 (toll free in the US) or +1-978-646-2777.

CCC Marketplace™

Order Number: 1263085
Order Date: 30 Aug 2022

Payment Information

SUKANYA PAUL
paulsukanya10@gmail.com
Payment method: Invoice

Billing Address:
Miss SUKANYA PAUL
JADAVPUR UNIVERSITY
Dept of Chemistry
Kolkata
India

+91 9775997854
paulsukanya10@gmail.com

Customer Location:
Miss SUKANYA PAUL
JADAVPUR UNIVERSITY
Dept of Chemistry
Kolkata
India

Order Details

1. Dalton transactions : an international journal of inorganic chemistry

Billing Status: Open

Article: Idiosyncratic recognition of Zn2+ and CN- using Pyrazolyl-Hydroxy-Coumarin scaffold and live cell imaging: Depiction of Luminescent Zn(II)-Metallocryptand

Order License ID	1263085-1	**Type of use**	Republish in a thesis/dissertation
Order detail status	Completed		
ISSN	1477-9226	**Publisher**	ROYAL SOCIETY OF CHEMISTRY
		Portion	Page

0.00 USD
Republication Permission

LICENSED CONTENT

Publication Title	Dalton transactions : an international journal of inorganic chemistry	**Rightsholder**	Royal Society of Chemistry
		Publication Type	Journal
Article Title	Idiosyncratic recognition of Zn2+ and CN- using Pyrazolyl-Hydroxy-Coumarin scaffold and live cell imaging: Depiction of Luminescent Zn(II)-Metallocryptand	**Start Page**	3198
		End Page	3212
		Issue	8
		Volume	51
Author/Editor	Royal Society of Chemistry (Great Britain)		
Date	01/01/2003		
Language	English		

Country	United Kingdom of Great Britain and Northern Ireland

REQUEST DETAILS

Portion Type	Page	**Rights Requested**	Main product
Page range(s)	3198-3212	**Distribution**	Worldwide
Total number of pages	15	**Translation**	Original language of publication
Format (select all that apply)	Print, Electronic	**Copies for the disabled?**	No
Who will republish the content?	Author of requested content	**Minor editing privileges?**	No
Duration of Use	Life of current edition	**Incidental promotional use?**	No
Lifetime Unit Quantity	Up to 499	**Currency**	USD

NEW WORK DETAILS

Title	Synthesis and characterization of Schiff bases and their diverse applications	**Institution name**	JADAVPUR UNIVERSITY
		Expected presentation date	2023-01-16
Instructor name	SUKANYA PAUL		

ADDITIONAL DETAILS

The requesting person / organization to appear on the license	Jadavpur University

REUSE CONTENT DETAILS

Title, description or numeric reference of the portion(s)	Synthesis and characterization of Schiff bases and their diverse applications	**Title of the article/chapter the portion is from**	Idiosyncratic recognition of Zn2+ and CN- using Pyrazolyl-Hydroxy-Coumarin scaffold and live cell imaging: Depiction of Luminescent Zn(II)-Metallocryptand
Editor of portion(s)	Paul, Sukanya; Maity, Suvendu; Halder, Satyajit; Dutta, Basudeb; Jana, Srikanta; Jana, Kuladip; Sinha, Chittaranjan	**Author of portion(s)**	Paul, Sukanya; Maity, Suvendu; Halder, Satyajit; Dutta, Basudeb; Jana, Srikanta; Jana, Kuladip; Sinha, Chittaranjan
Volume of serial or monograph	51	**Issue, if republishing an article from a serial**	8
Page or page range of portion	3198-3212	**Publication date of portion**	2022-02-22

Total Items: 1

Subtotal: 0.00 USD

Order Total: 0.00 USD

Marketplace Order General Terms and Conditions

The following terms and conditions ("General Terms"), together with any applicable Publisher Terms and Conditions, govern User's use of Works pursuant to the Licenses granted by Copyright Clearance Center, Inc. ("CCC") on behalf of the applicable Rightsholders of such Works through CCC's applicable Marketplace transactional licensing services (each, a "Service").

1) **Definitions.** For purposes of these General Terms, the following definitions apply:

"License" is the licensed use the User obtains via the Marketplace platform in a particular licensing transaction, as set forth in the Order Confirmation.

"Order Confirmation" is the confirmation CCC provides to the User at the conclusion of each Marketplace transaction. "Order Confirmation Terms" are additional terms set forth on specific Order Confirmations not set forth in the General Terms that can include terms applicable to a particular CCC transactional licensing service and/or any Rightsholder-specific terms.

"Rightsholder(s)" are the holders of copyright rights in the Works for which a User obtains licenses via the Marketplace platform, which are displayed on specific Order Confirmations.

"Terms" means the terms and conditions set forth in these General Terms and any additional Order Confirmation Terms collectively.

"User" or "you" is the person or entity making the use granted under the relevant License. Where the person accepting the Terms on behalf of a User is a freelancer or other third party who the User authorized to accept the General Terms on the User's behalf, such person shall be deemed jointly a User for purposes of such Terms.

"Work(s)" are the copyright protected works described in relevant Order Confirmations.

2) **Description of Service.** CCC's Marketplace enables Users to obtain Licenses to use one or more Works in accordance with all relevant Terms. CCC grants Licenses as an agent on behalf of the copyright rightsholder identified in the relevant Order Confirmation.

3) **Applicability of Terms.** The Terms govern User's use of Works in connection with the relevant License. In the event of any conflict between General Terms and Order Confirmation Terms, the latter shall govern. User acknowledges that Rightsholders have complete discretion whether to grant any permission, and whether to place any limitations on any grant, and that CCC has no right to supersede or to modify any such discretionary act by a Rightsholder.

4) **Representations; Acceptance.** By using the Service, User represents and warrants that User has been duly authorized by the User to accept, and hereby does accept, all Terms.

5) **Scope of License; Limitations and Obligations.** All Works and all rights therein, including copyright rights, remain the sole and exclusive property of the Rightsholder. The License provides only those rights expressly set forth in the terms and conveys no other rights in any Works

6) **General Payment Terms.** User may pay at time of checkout by credit card or choose to be invoiced. If the User chooses to be invoiced, the User shall: (i) remit payments in the manner identified on specific invoices, (ii) unless otherwise specifically stated in an Order Confirmation or separate written agreement, Users shall remit payments upon receipt of the relevant invoice from CCC, either by delivery or notification of availability of the invoice via the Marketplace platform, and (iii) if the User does not pay the invoice within 30 days of receipt, the User may incur a service charge of 1.5% per month or the maximum rate allowed by applicable law, whichever is less. While User may exercise the rights in the License immediately upon receiving the Order Confirmation, the License is automatically revoked and is null and void, as if it had never been issued, if CCC does not receive complete payment on a timely basis.

7) **General Limits on Use.** Unless otherwise provided in the Order Confirmation, any grant of rights to User (i) involves only the rights set forth in the Terms and does not include subsequent or additional uses, (ii) is non-exclusive and non-transferable, and (iii) is subject to any and all limitations and restrictions (such as, but not limited to, limitations on duration of use or circulation) included in the Terms. Upon completion of the licensed use as set forth in the Order Confirmation, User shall either secure a new permission for further use of the Work(s) or immediately cease any new use of the Work(s) and shall render inaccessible (such as by deleting or by removing or severing links or other locators) any further copies of the Work. User may only make alterations to the Work if and as expressly set forth in the Order Confirmation. No Work may be used in any way that is

defamatory, violates the rights of third parties (including such third parties' rights of copyright, privacy, publicity, or other tangible or intangible property), or is otherwise illegal, sexually explicit, or obscene. In addition, User may not conjoin a Work with any other material that may result in damage to the reputation of the Rightsholder. User agrees to inform CCC if it becomes aware of any infringement of any rights in a Work and to cooperate with any reasonable request of CCC or the Rightsholder in connection therewith.

8) **Third Party Materials.** In the event that the material for which a License is sought includes third party materials (such as photographs, illustrations, graphs, inserts and similar materials) that are identified in such material as having been used by permission (or a similar indicator), User is responsible for identifying, and seeking separate licenses (under this Service, if available, or otherwise) for any of such third party materials; without a separate license, User may not use such third party materials via the License.

9) **Copyright Notice.** Use of proper copyright notice for a Work is required as a condition of any License granted under the Service. Unless otherwise provided in the Order Confirmation, a proper copyright notice will read substantially as follows: "Used with permission of [Rightsholder's name], from [Work's title, author, volume, edition number and year of copyright]; permission conveyed through Copyright Clearance Center, Inc." Such notice must be provided in a reasonably legible font size and must be placed either on a cover page or in another location that any person, upon gaining access to the material which is the subject of a permission, shall see, or in the case of republication Licenses, immediately adjacent to the Work as used (for example, as part of a by-line or footnote) or in the place where substantially all other credits or notices for the new work containing the republished Work are located. Failure to include the required notice results in loss to the Rightsholder and CCC, and the User shall be liable to pay liquidated damages for each such failure equal to twice the use fee specified in the Order Confirmation, in addition to the use fee itself and any other fees and charges specified.

10) **Indemnity.** User hereby indemnifies and agrees to defend the Rightsholder and CCC, and their respective employees and directors, against all claims, liability, damages, costs, and expenses, including legal fees and expenses, arising out of any use of a Work beyond the scope of the rights granted herein and in the Order Confirmation, or any use of a Work which has been altered in any unauthorized way by User, including claims of defamation or infringement of rights of copyright, publicity, privacy, or other tangible or intangible property.

11) **Limitation of Liability.** UNDER NO CIRCUMSTANCES WILL CCC OR THE RIGHTSHOLDER BE LIABLE FOR ANY DIRECT, INDIRECT, CONSEQUENTIAL, OR INCIDENTAL DAMAGES (INCLUDING WITHOUT LIMITATION DAMAGES FOR LOSS OF BUSINESS PROFITS OR INFORMATION, OR FOR BUSINESS INTERRUPTION) ARISING OUT OF THE USE OR INABILITY TO USE A WORK, EVEN IF ONE OR BOTH OF THEM HAS BEEN ADVISED OF THE POSSIBILITY OF SUCH DAMAGES. In any event, the total liability of the Rightsholder and CCC (including their respective employees and directors) shall not exceed the total amount actually paid by User for the relevant License. User assumes full liability for the actions and omissions of its principals, employees, agents, affiliates, successors, and assigns.

12) **Limited Warranties.** THE WORK(S) AND RIGHT(S) ARE PROVIDED "AS IS." CCC HAS THE RIGHT TO GRANT TO USER THE RIGHTS GRANTED IN THE ORDER CONFIRMATION DOCUMENT. CCC AND THE RIGHTSHOLDER DISCLAIM ALL OTHER WARRANTIES RELATING TO THE WORK(S) AND RIGHT(S), EITHER EXPRESS OR IMPLIED, INCLUDING WITHOUT LIMITATION IMPLIED WARRANTIES OF MERCHANTABILITY OR FITNESS FOR A PARTICULAR PURPOSE. ADDITIONAL RIGHTS MAY BE REQUIRED TO USE ILLUSTRATIONS, GRAPHS, PHOTOGRAPHS, ABSTRACTS, INSERTS, OR OTHER PORTIONS OF THE WORK (AS OPPOSED TO THE ENTIRE WORK) IN A MANNER CONTEMPLATED BY USER; USER UNDERSTANDS AND AGREES THAT NEITHER CCC NOR THE RIGHTSHOLDER MAY HAVE SUCH ADDITIONAL RIGHTS TO GRANT.

13) **Effect of Breach.** Any failure by User to pay any amount when due, or any use by User of a Work beyond the scope of the License set forth in the Order Confirmation and/or the Terms, shall be a material breach of such License. Any breach not cured within 10 days of written notice thereof shall result in immediate termination of such License without further notice. Any unauthorized (but licensable) use of a Work that is terminated immediately upon notice thereof may be liquidated by payment of the Rightsholder's ordinary license price therefor; any unauthorized (and unlicensable) use that is not terminated immediately for any reason (including, for example, because materials containing the Work cannot reasonably be recalled) will be subject to all remedies available at law or in equity, but in no event to a payment of less than three times the Rightsholder's ordinary license price for the most closely analogous licensable use plus Rightsholder's and/or CCC's costs and expenses incurred in collecting such payment.

14) **Additional Terms for Specific Products and Services.** If a User is making one of the uses described in this Section 14, the additional terms and conditions apply:

a) ***Print Uses of Academic Course Content and Materials (photocopies for academic coursepacks or classroom handouts).*** For photocopies for academic coursepacks or classroom handouts the following additional terms apply:

i) The copies and anthologies created under this License may be made and assembled by faculty members individually or at their request by on-campus bookstores or copy centers, or by off-campus copy shops and other similar entities.

ii) No License granted shall in any way: (i) include any right by User to create a substantively non-identical copy of the Work or to edit or in any other way modify the Work (except by means of deleting material immediately preceding or following the entire portion of the Work copied) (ii) permit "publishing ventures" where any particular anthology would be systematically marketed at multiple institutions.

iii) Subject to any Publisher Terms (and notwithstanding any apparent contradiction in the Order Confirmation arising from data provided by User), any use authorized under the academic pay-per-use service is limited as follows:

A) any License granted shall apply to only one class (bearing a unique identifier as assigned by the institution, and thereby including all sections or other subparts of the class) at one institution;

B) use is limited to not more than 25% of the text of a book or of the items in a published collection of essays, poems or articles;

C) use is limited to no more than the greater of (a) 25% of the text of an issue of a journal or other periodical or (b) two articles from such an issue;

D) no User may sell or distribute any particular anthology, whether photocopied or electronic, at more than one institution of learning;

E) in the case of a photocopy permission, no materials may be entered into electronic memory by User except in order to produce an identical copy of a Work before or during the academic term (or analogous period) as to which any particular permission is granted. In the event that User shall choose to retain materials that are the subject of a photocopy permission in electronic memory for purposes of producing identical copies more than one day after such retention (but still within the scope of any permission granted), User must notify CCC of such fact in the applicable permission request and such retention shall constitute one copy actually sold for purposes of calculating permission fees due; and

F) any permission granted shall expire at the end of the class. No permission granted shall in any way include any right by User to create a substantively non-identical copy of the Work or to edit or in any other way modify the Work (except by means of deleting material immediately preceding or following the entire portion of the Work copied).

iv) Books and Records; Right to Audit. As to each permission granted under the academic pay-per-use Service, User shall maintain for at least four full calendar years books and records sufficient for CCC to determine the numbers of copies made by User under such permission. CCC and any representatives it may designate shall have the right to audit such books and records at any time during User's ordinary business hours, upon two days' prior notice. If any such audit shall determine that User shall have underpaid for, or underreported, any photocopies sold or by three percent (3%) or more, then User shall bear all the costs of any such audit; otherwise, CCC shall bear the costs of any such audit. Any amount determined by such audit to have been underpaid by User shall immediately be paid to CCC by User, together with interest thereon at the rate of 10% per annum from the date such amount was originally due. The provisions of this paragraph shall survive the termination of this License for any reason.

b) ***Digital Pay-Per-Uses of Academic Course Content and Materials (e-coursepacks, electronic reserves, learning management systems, academic institution intranets).*** For uses in e-coursepacks, posts in electronic reserves, posts in learning management systems, or posts on academic institution intranets, the following additional terms apply:

i) The pay-per-uses subject to this Section 14(b) include:

A) **Posting e-reserves, course management systems, e-coursepacks for text-based content,** which grants authorizations to import requested material in electronic format, and allows electronic access

to this material to members of a designated college or university class, under the direction of an instructor designated by the college or university, accessible only under appropriate electronic controls (e.g., password);

B) **Posting e-reserves, course management systems, e-coursepacks for material consisting of photographs or other still images not embedded in text,** which grants not only the authorizations described in Section 14(b)(i)(A) above, but also the following authorization: to include the requested material in course materials for use consistent with Section 14(b)(i)(A) above, including any necessary resizing, reformatting or modification of the resolution of such requested material (provided that such modification does not alter the underlying editorial content or meaning of the requested material, and provided that the resulting modified content is used solely within the scope of, and in a manner consistent with, the particular authorization described in the Order Confirmation and the Terms), but not including any other form of manipulation, alteration or editing of the requested material;

C) **Posting e-reserves, course management systems, e-coursepacks or other academic distribution for audiovisual content,** which grants not only the authorizations described in Section 14(b)(i)(A) above, but also the following authorizations: (i) to include the requested material in course materials for use consistent with Section 14(b)(i)(A) above; (ii) to display and perform the requested material to such members of such class in the physical classroom or remotely by means of streaming media or other video formats; and (iii) to "clip" or reformat the requested material for purposes of time or content management or ease of delivery, provided that such “clipping” or reformatting does not alter the underlying editorial content or meaning of the requested material and that the resulting material is used solely within the scope of, and in a manner consistent with, the particular authorization described in the Order Confirmation and the Terms. Unless expressly set forth in the relevant Order Conformation, the License does not authorize any other form of manipulation, alteration or editing of the requested material.

ii) Unless expressly set forth in the relevant Order Confirmation, no License granted shall in any way: (i) include any right by User to create a substantively non-identical copy of the Work or to edit or in any other way modify the Work (except by means of deleting material immediately preceding or following the entire portion of the Work copied or, in the case of Works subject to Sections 14(b)(1)(B) or (C) above, as described in such Sections) (ii) permit "publishing ventures" where any particular course materials would be systematically marketed at multiple institutions.

iii) Subject to any further limitations determined in the Rightsholder Terms (and notwithstanding any apparent contradiction in the Order Confirmation arising from data provided by User), any use authorized under the electronic course content pay-per-use service is limited as follows:

A) any License granted shall apply to only one class (bearing a unique identifier as assigned by the institution, and thereby including all sections or other subparts of the class) at one institution;

B) use is limited to not more than 25% of the text of a book or of the items in a published collection of essays, poems or articles;

C) use is limited to not more than the greater of (a) 25% of the text of an issue of a journal or other periodical or (b) two articles from such an issue;

D) no User may sell or distribute any particular materials, whether photocopied or electronic, at more than one institution of learning;

E) electronic access to material which is the subject of an electronic-use permission must be limited by means of electronic password, student identification or other control permitting access solely to students and instructors in the class;

F) User must ensure (through use of an electronic cover page or other appropriate means) that any person, upon gaining electronic access to the material, which is the subject of a permission, shall see:

- a proper copyright notice, identifying the Rightsholder in whose name CCC has granted permission,
- a statement to the effect that such copy was made pursuant to permission,

- a statement identifying the class to which the material applies and notifying the reader that the material has been made available electronically solely for use in the class, and

- a statement to the effect that the material may not be further distributed to any person outside the class, whether by copying or by transmission and whether electronically or in paper form, and User must also ensure that such cover page or other means will print out in the event that the person accessing the material chooses to print out the material or any part thereof.

G) any permission granted shall expire at the end of the class and, absent some other form of authorization, User is thereupon required to delete the applicable material from any electronic storage or to block electronic access to the applicable material.

iv) Uses of separate portions of a Work, even if they are to be included in the same course material or the same university or college class, require separate permissions under the electronic course content pay-per-use Service. Unless otherwise provided in the Order Confirmation, any grant of rights to User is limited to use completed no later than the end of the academic term (or analogous period) as to which any particular permission is granted.

v) Books and Records; Right to Audit. As to each permission granted under the electronic course content Service, User shall maintain for at least four full calendar years books and records sufficient for CCC to determine the numbers of copies made by User under such permission. CCC and any representatives it may designate shall have the right to audit such books and records at any time during User's ordinary business hours, upon two days' prior notice. If any such audit shall determine that User shall have underpaid for, or underreported, any electronic copies used by three percent (3%) or more, then User shall bear all the costs of any such audit; otherwise, CCC shall bear the costs of any such audit. Any amount determined by such audit to have been underpaid by User shall immediately be paid to CCC by User, together with interest thereon at the rate of 10% per annum from the date such amount was originally due. The provisions of this paragraph shall survive the termination of this license for any reason.

c) ***Pay-Per-Use Permissions for Certain Reproductions (Academic photocopies for library reserves and interlibrary loan reporting) (Non-academic internal/external business uses and commercial document delivery).*** The License expressly excludes the uses listed in Section (c)(i)-(v) below (which must be subject to separate license from the applicable Rightsholder) for: academic photocopies for library reserves and interlibrary loan reporting; and non-academic internal/external business uses and commercial document delivery.

i) electronic storage of any reproduction (whether in plain-text, PDF, or any other format) other than on a transitory basis;

ii) the input of Works or reproductions thereof into any computerized database;

iii) reproduction of an entire Work (cover-to-cover copying) except where the Work is a single article;

iv) reproduction for resale to anyone other than a specific customer of User;

v) republication in any different form. Please obtain authorizations for these uses through other CCC services or directly from the rightsholder.

Any license granted is further limited as set forth in any restrictions included in the Order Confirmation and/or in these Terms.

d) ***Electronic Reproductions in Online Environments (Non-Academic-email, intranet, internet and extranet).*** For "electronic reproductions", which generally includes e-mail use (including instant messaging or other electronic transmission to a defined group of recipients) or posting on an intranet, extranet or Intranet site (including any display or performance incidental thereto), the following additional terms apply:

i) Unless otherwise set forth in the Order Confirmation, the License is limited to use completed within 30 days for any use on the Internet, 60 days for any use on an intranet or extranet and one year for any other use, all as measured from the "republication date" as identified in the Order Confirmation, if any, and otherwise from the date of the Order Confirmation.

ii) User may not make or permit any alterations to the Work, unless expressly set forth in the Order Confirmation (after request by User and approval by Rightsholder); provided, however, that a Work consisting of photographs or other still images not embedded in text may, if necessary, be resized, reformatted or have its resolution modified without additional express permission, and a Work consisting of audiovisual content may, if necessary, be "clipped" or reformatted for purposes of time or content management or ease of delivery (provided that any such resizing, reformatting, resolution modification or “clipping” does not alter the underlying editorial content or meaning of the Work used, and that the resulting material is used solely within the scope of, and in a manner consistent with, the particular License described in the Order Confirmation and the Terms.

15) **Miscellaneous.**

a) User acknowledges that CCC may, from time to time, make changes or additions to the Service or to the Terms, and that Rightsholder may make changes or additions to the Rightsholder Terms. Such updated Terms will replace the prior terms and conditions in the order workflow and shall be effective as to any subsequent Licenses but shall not apply to Licenses already granted and paid for under a prior set of terms.

b) Use of User-related information collected through the Service is governed by CCC's privacy policy, available online at www.copyright.com/about/privacy-policy/.

c) The License is personal to User. Therefore, User may not assign or transfer to any other person (whether a natural person or an organization of any kind) the License or any rights granted thereunder; provided, however, that, where applicable, User may assign such License in its entirety on written notice to CCC in the event of a transfer of all or substantially all of User's rights in any new material which includes the Work(s) licensed under this Service.

d) No amendment or waiver of any Terms is binding unless set forth in writing and signed by the appropriate parties, including, where applicable, the Rightsholder. The Rightsholder and CCC hereby object to any terms contained in any writing prepared by or on behalf of the User or its principals, employees, agents or affiliates and purporting to govern or otherwise relate to the License described in the Order Confirmation, which terms are in any way inconsistent with any Terms set forth in the Order Confirmation, and/or in CCC's standard operating procedures, whether such writing is prepared prior to, simultaneously with or subsequent to the Order Confirmation, and whether such writing appears on a copy of the Order Confirmation or in a separate instrument.

e) The License described in the Order Confirmation shall be governed by and construed under the law of the State of New York, USA, without regard to the principles thereof of conflicts of law. Any case, controversy, suit, action, or proceeding arising out of, in connection with, or related to such License shall be brought, at CCC's sole discretion, in any federal or state court located in the County of New York, State of New York, USA, or in any federal or state court whose geographical jurisdiction covers the location of the Rightsholder set forth in the Order Confirmation. The parties expressly submit to the personal jurisdiction and venue of each such federal or state court.

CCC Marketplace™

Order Confirmation

Thank you, your order has been placed. An email confirmation has been sent to you. Your order license details and printable licenses will be available within 24 hours. Please access Manage Account for final order details.

This is not an invoice. Please go to manage account to access your order history and invoices.

CUSTOMER INFORMATION

Payment by invoice: You can cancel your order until the invoice is generated by contacting customer service.

Billing Address

Miss SUKANYA PAUL
JADAVPUR UNIVERSITY
Dept of Chemistry
Kolkata
India

+91 9775997854
paulsukanya10@gmail.com

Customer Location

Miss SUKANYA PAUL
JADAVPUR UNIVERSITY
Dept of Chemistry
Kolkata
India

PO Number (optional)

N/A

Payment options

Invoice

PENDING ORDER CONFIRMATION

Confirmation Number: Pending

Order Date: 13-Sep-2022

1. Analytical methods

0.00 USD

Article: A Highly Emissive Zn(II)-pyridyl-benzimidazolyl-phenolato based Chemosensor: Detection of $H_2PO_4^-$ via "Use" and "Throw" Device Fabrication

Order License ID	Pending	**Publisher**	RSC Publishing
ISSN	1759-9679	**Portion**	Page
Type of Use	Republish in a thesis/dissertation		

LICENSED CONTENT

Publication Title	Analytical methods	**Publication Type**	e-Journal
		Start Page	5282
		End Page	5292

Article Title	A Highly Emissive Zn(II)-pyridyl-benzimidazolyl-phenolato based Chemosensor: Detection of H2PO4– via “Use” and “Throw” Device Fabrication	**Issue**	44
		Volume	13
		URL	http://www.rsc.org/Publishing/Journals/AY/index.asp
Author/Editor	Royal Society of Chemistry (Great Britain)		
Date	01/01/2009		
Language	English		
Country	United Kingdom of Great Britain and Northern Ireland		
Rightsholder	Royal Society of Chemistry		

REQUEST DETAILS

Portion Type	Page	**Rights Requested**	Main product
Page range(s)	5282-5292	**Distribution**	Worldwide
Total number of pages	11	**Translation**	Original language of publication
Format (select all that apply)	Print, Electronic	**Copies for the disabled?**	No
Who will republish the content?	Author of requested content	**Minor editing privileges?**	Yes
Duration of Use	Life of current edition	**Incidental promotional use?**	No
Lifetime Unit Quantity	Up to 499	**Currency**	USD

NEW WORK DETAILS

Title	Synthesis and characterization of Schiff bases and their diverse applications	**Institution name**	Jadavpur University
		Expected presentation date	2022-09-16
Instructor name	SUKANYA PAUL		

ADDITIONAL DETAILS

Order reference number	N/A	**The requesting person / organization to appear on the license**	Jadavpur University

REUSE CONTENT DETAILS

Title, description or numeric reference of the portion(s)	Synthesis and characterization of Schiff bases and their diverse applications	**Title of the article/chapter the portion is from**	A Highly Emissive Zn(II)-pyridyl-benzimidazolyl-phenolato based Chemosensor: Detection of H2PO4– via “Use” and “Throw” Device Fabrication
Editor of portion(s)	Dey, Sunanda; Paul, Sukanya; Debsharma, Kingshuk; Sinha, Chittaranjan		
Volume of serial or monograph	13		

Page or page range of portion	5282-5292	**Author of portion(s)**	Dey, Sunanda; Paul, Sukanya; Debsharma, Kingshuk; Sinha, Chittaranjan
		Issue, if republishing an article from a serial	44
		Publication date of portion	2021-11-18

Total Items: 1

Total Due: 0.00 USD

Accepted: Marketplace Order General Terms and Conditions and any applicable Publisher Terms and Conditions